Conference Proceedings of the Society for Experimental Mechanics Series

Tom Proulx *Editor*

Application of Imaging Techniques to Mechanics of Materials and Structures, Volume 4

Proceedings of the 2010 Annual Conference on Experimental and Applied Mechanics

SEM Springer

Conference Proceedings of the Society for Experimental Mechanics Series

Series Editor
Tom Proulx
Society for Experimental Mechanics, Inc.,
Bethel, CT, USA

For further volumes:
http://www.springer.com/series/8922

Tom Proulx
Editor

Application of Imaging Techniques to Mechanics of Materials and Structures, Volume 4

Proceedings of the 2010 Annual Conference on Experimental and Applied Mechanics

Springer

Editor
Tom Proulx
The Society for Experimental Mechanics,
7 School Street
06801-1405 Bethel
USA

ISSN 2191-5644 ISSN 2191-5652 (electronic)
ISBN 978-1-4419-9528-5 ISBN 978-1-4419-9796-8 (eBook)
DOI 10.1007/978-1-4419-9796-8
Springer New York Heidelberg Dordrecht London

Library of Congress Control Number: 2011922268

Printed on acid-free paper

Springer is part of Springer Science+Business Media (www.springer.com)

Preface

Application of Imaging Techniques to Mechanics of Materials and Structures represents one of six tracks of technical papers presented at the Society for Experimental Mechanics Annual Conference & Exposition on Experimental and Applied Mechanics, held at Indianapolis, Indiana, June 7-10, 2010. The full proceedings also include volumes on Dynamic Behavior of Materials, Role of Experimental Mechanics on Emerging Energy Systems and Materials, Experimental and Applied Mechanics, along with the 11th International Symposium on MEMS and Nanotechnology, and the Symposium on Time Dependent Constitutive Behavior and Failure/Fracture Processes.

Each collection presents early findings from experimental and computational investigations on an important area within Experimental Mechanics. The current volume on the Application of Imaging Techniques to Mechanics of Materials and Structures includes studies on model identification/inverse problem, composites, microscale applications, biological materials, residual stresses, infrared imaging and thermomechanics, digital image correlation, full-field volumetric measurements, soft materials, development in optical techniques, and high strain rate/dynamics.

It is clear that within the last 10 years, imaging techniques have spread very widely within the experimental mechanics community thanks to readily available digital cameras and other imaging techniques, such as SEM, AFM, X-ray tomography, MRI etc. The objective of this track is to share experience on how such rich experimental data can help experimentalists and modeling scientists to better understand and simulate the behavior of materials and structures. It was originally envisioned by the organizers to cover a wide range of applications and techniques to encourage cross-fertilization over disciplines and problem types. This goal has been reached, in large part due to the support provided by several Technical Divisions and dedicated session organizers.

The organizers would like to thank the authors, presenters, session organizers and session chairs for their participation in this track.

The Society would like to thank the organizers of the track, Fabrice Pierron, *Arts et Métiers ParisTech* and Michael A. Sutton, *University of South Carolina* for their efforts.

Bethel, Connecticut

Dr. Thomas Proulx
Society for Experimental Mechanics, Inc

Contents

Proceedings of the SEM Annual Conference
June 7-10, 2010 Indianapolis, Indiana USA

Identification from full-field measurements: a promising perspective in experimental mechanics

M. Grédiac

Clermont Université
Université Blaise Pascal & IFMA, EA 3867, Laboratoire de Mécanique et Ingénieries
BP 10448, F-63000 Clermont-Ferrand, France

ABSTRACT

This paper deals with the use of full-field measurement techniques in experimental solid mechanics. The main techniques used in practice are briefly described and the different types of applications are classified according to their link with modelling. Finally, one these applications: identification of constitutive parameters from full-field measurements is developed in more detail.

INTRODUCTION

Full-field measurement techniques such as digital image correlation, moiré interferometry, speckle or grid method are now widely used in the experimental mechanics community. Such techniques provide displacement and/or strain maps, which are very useful to analyze phenomena that occur during mechanical tests. These techniques are also completed by infrared thermography which provides another type of information: temperature changes on the specimen surface.

The main features of these two families of techniques are given in the first section of the paper. Different types of applications are then shortly described in the second section. One of these applications is finally highlighted: the identification of constitutive parameters from this type of measurements. This topic is in fact very specific because of the nature of the data that are processed: fields of measurements, in other words, a wealth of quasi-continuous information which, in addition, is generally noisy. Specific strategies have been recently developed for processing this specific type of data. They are briefly described in this last part of the paper.

FULL-FIELD MEASUREMENT TECHNIQUES

Kinematical measurement

From an historical point of view, displacements were the first quantities measured with full-field measurement techniques. Various techniques are described in the literature. They can be classified using the physical phenomenon that is used to provide the desired quantity. Interferometry between laser beams has given birth to different techniques, the most popular ones being moiré interferometry and speckle interferometry. In the first case, a diffraction grating characterized by a very small pitch (typically 1200 lines/mm) must cover the surface under investigation. Interference of two laser beams on the grating gives rise to a fringe pattern [1]. In the second case, a random distribution of “grains” whose size is some micrometers is obtained by diffraction thanks to the roughness of the surface under investigation [2]. Subtracting images obtained after and before applying load provides fringes. Fringe patterns are related to the displacement along a given direction since the phase of these fringes is proportional to this quantity. Deducing displacement maps from fringes requires specific operations such as phase shifting [3] or phase unwrapping [4]. It must be pointed out that moiré interferometry and speckle interferometry are very sensitive because of the very nature of the physical phenomenon involved. Displacements

T. Proulx (ed.), *Application of Imaging Techniques to Mechanics of Materials and Structures, Volume 4*, Conference Proceedings of the Society for Experimental Mechanics Series 14, DOI 10.1007/978-1-4419-9796-8_1, © The Society for Experimental Mechanics, Inc. 2013

are measured under quasi-static load, but they can also be obtained in dynamics using specific optical arrangement. Classically, vibration modes are measured in this case. The main drawbacks of these techniques are first the fact that lasers must be used, thus leading to some complicated setups, and second that fringes obtained are generally very sensitive to vibrations. In addition, a grating featuring a very small pitch must be transferred on the surface of the specimen under investigation in case of moiré interferometry. For these reasons, these techniques are often difficult to implement in industrial environments.

Purely geometric techniques such as digital image correlation [5] or grid method [6] represent a good alternative to the techniques described above. They rely on a much simpler principle since they merely consist in marking the surface of the specimen with speckles or with regular grids, respectively, and to track this surface marking with suitable algorithms that process images of the surface taken by a camera and deduce displacement fields. The first of these two techniques is more user-friendly since painting speckles with a paint spray for instance is easier than marking the surface with grids. The natural contrast of the surface under investigation is even sufficient in certain cases. Concerning the second technique, grids can be either transferred [7] or engraved [8] with a suitable strategy.

Strains are generally deduced from displacements simply by numerically differentiating them. Noise corrupts however the results, so displacement fields must be smoothed beforehand. Since smoothing impairs spatial resolution, this procedure is somewhat tricky in many cases. Hence calculating strain maps from images of the surface marking is really an issue that has been addressed using specific procedures, [9][10] for instance.

As a last remark, it must be pointed out that recent advances in tomography and image processing has made it possible to measure 3D displacements in the bulk of some materials. In this case, digital image correlation is performed, the equivalent of the small squared images used for performing correlation being small cubes [11]. The requirement is to obtain a 3D marking of the material, but this is possible for all types of materials.

Thermal measurements

Temperature fields are directly measured with infrared cameras. In fact, temperature variations that occur during mechanical tests are interesting quantities since they may be caused by heat sources due to some specific phenomena related to the mechanical response of the constitutive material. Within the framework of elasticity, thermal stress analysis relies on the proportionality between temperature variation and variation of the trace of the stress tensor: temperature slightly increases as this trace decreases and vive versa. This technique has led to many applications [12] for instance. If other phenomena such as plasticity or damage occur, temperature variations may become more significant and related to some localized heat sources. Retrieving heat source distributions provides an information which is relevant for analysing localized phenomena such as necking or deformation bands which occur in some materials or alloys [13][14]. This is however a difficult task because first- or second-order derivatives of noisy measurements must be performed. Moreover, the number of pixels available in infrared camera sensors is generally lower than the number of pixels of CCD cameras. Consequently, such heat sources are generally obtained with a spatial resolution that is lower than the spatial resolution in displacement or strain.

APPLICATIONS OF FULL-FIELD MEASUREMENT TECHNIQUES IN EXPERIMENTAL SOLID MECHANICS

Measuring displacements, strains and temperature variations is useful in many cases, as can be observed in the literature where an increasing number of papers deals with the use of such techniques for characterizing materials and structures. In fact, the original aspect of full-field measurement techniques compared to classical measuring devices is their ability to detect and to quantify heterogeneities in displacement, strain and temperature variation maps. In Ref. [15] dealing with the use of full-field measurement techniques in composite material characterization, it is suggested to classify the different applications in seven groups which can be distinguished with their link with modelling. This classification can easily be extended to any type of material. In this context, the different types of applications are as follows:

1- Non destructive testing and inspection. In this case, full-field measurement methods are used to reveal local defects due to the manufacturing process for instance. These defects cause the strain fields or the temperature variation fields to be locally heterogeneous. The location and sometimes the nature of the defects are detected, but it must be pointed out that observations remain at a qualitative level. See for instance Ref. [16] where sandwich structures are inspected.

2- Verification of boundary and loading conditions. Mechanical tests are usually carried out to measure relevant parameters which are used to feed mechanical models. These tests are interpreted under some assumptions like the homogeneity of strain fields which are not always valid. Full-field measurement techniques are well suited to detect the influence of the loading device or of free boundaries which can disturb this homogeneity. See for instance Ref. [17] where full-field methods are used to check boundary conditions during the ASTM C273 shear test. Another similar issue is to measure the actual loading distribution applied on a specimen. See for instance Ref [18] where dynamic loads applied to a three-point bending specimen are detected and quantified using a high-speed camera and digital image correlation.

3- Experimental evidence of local gradients due to materiel heterogeneities. Many materials such as composites or concrete are heterogeneous at different scales, thus leading to local variations of the strain distribution around their average value. This is probably the most popular application of full-field measurement techniques. See for instance the study of the failure mechanics in laminates with dropped plies [19].

4- Crack characterization. High gradients often give rise to cracks whose geometry in terms of opening, shape or location is characterized thanks to displacement discontinuities. See for instance Ref. [20] devoted to the measurement of the displacement/strain distributions at a crack tip using digital image correlation..

5- Verification of assumptions used for building up mechanical models. Modelling the mechanical response of structures is often based on some assumptions on the displacement field. Their suitability is crucial to insure the relevancy of the model. The relevancy of these assumptions can be assessed thanks to full-field measurements. See for instance Ref. [21] where the section warping through the thickness of bent beams is measured to discuss some higher-order theories used in laminated beams.

6- Validation of models. Models can be validated by comparing calculated and measured displacement fields. See for instance Ref. [22] where some models developed for predicting the buckling of columns and resulting degradation in laminates are analysed with the moiré method.

7- Identification of constitutive parameters. Full-field measurements can be used to identify the parameters which govern a model assumed to be *a priori* relevant.

This last issue is in fact very original since it specifically involves full-field measurements. Its also gives the opportunity to deduce constitutive parameters from heterogeneous strain or temperature variation maps that can occur in very general cases while the classical material characterization approach relies on tests raising homogeneous distributions or heterogeneous distributions for which an analytical relationship exists between load and measured quantity (bending tests on beams for instance). The advantages of this type of procedure are threefold:

- First, a greatest number of parameters can be identified at the same time, thus leading to a reduction of the number of tests to be performed. For composite materials for instance, three different tensile tests are generally carried out to measured the governing parameters assuming the response is linear elastic and orthotropic (tensile test along two perpendicular directions plus a shear or an off-axis test) whereas one test only is required if full-field measurement techniques are used and applied on tests giving rise to heterogeneous strain fields. The reason for this is the fact that the whole set of parameters influences the mechanical response of the specimen. Hence they can be identified is a suitable strategy is used since no direct relationship generally exists between unknown parameters and measurements.

- Second, this is the only route which is available for characterizing heterogeneous materials since strain or temperature variation fields are heterogeneous in this case. Indeed, classical characterization procedures are not suitable for such materials.

- Finally, parameters can be identified on specimens that can potentially exhibit more complicated geometries than the classical rectangular-shaped coupons generally used in tensile or bending tests for instance. Moreover, complex loading or loading paths can be investigated. Hence portions of industrial structural components can be directly tested, so constitutive parameters that are identified are potentially more representative of the actual response of the *in situ* material. One can also imagine to optimize the shape and the loading of the specimen to satisfy some constraints fixed *a priori* such as minimization of noise effect on identified parameters.

The objective of the following section is to give an overview on the different identification methods suitable for full-field measurements. Only kinematical measurements are addressed (displacements and strain) for thee sake of simplicity.

IDENTIFICATION OF CONSTITUTIVE PARAMETERS FROM FULL-FIELD MEASUREMENTS

Statement of the problem

Retrieving constitutive parameters from full-field measurements can be considered as an inverse problem which can be stated as follows. A solid of any shape is considered. It is subjected to a given load whose distribution remains generally unknown, only the resulting force being measured in practice. A certain type of constitutive equations is chosen *a priori* for its relevancy and the objective is to retrieve the parameters than govern the constitutive equations assuming that displacement or strain distributions are measured on the surface of the specimen. Since the specimen is generally flat and subjected to an in-plane loading, measurements on the surface are representative of the through-thickness displacement and strain distributions.

An important remark is that no closed-form solution for the actual displacement/strain field is available in the general case. Hence the problem of extracting the parameters governing the constitutive equations from the displacement/strain fields is not trivial. Different strategies have been proposed and employed in the recent past for solving this problem. A review of these methods is available in Ref. [23]. They are briefly described below.

Model updating

This approach is the most popular one since it generally involves a well-known numerical tool: the finite element method. The first step is to construct a model of the specimen under load and to compute the displacement or the strain fields with a first set of constitutive parameters using either an analytical (if available) or a numerical (this is the general case) solution. A cost function is then constructed with the point-to-point squared difference between any measured quantity and its calculated counterpart. This cost function is finally minimized with respect to the unknown parameters. The main advantage of this approach is its versatility. Moreover, it is not limited to field measurements and can also potentially involve a restricted number of measurements. The drawback is the fact that iterative calculations must be performed in any case to compute the strain/displacement fields for each loop. Finally, it is not always convenient to model correctly the boundary conditions since the loading distribution must be entered in the model whereas only the resulting force applied on the specimen is measured in practice. This method has been widely used in the recent past. Various types of materials and measurements have been considered. In Refs. [24] and [25] for instance, an orthotropic composite material is characterized within the framework of linear elasticity from displacements measured with moiré interferometry and digital image correlation, respectively. More complicated constitutive equations can also be considered. See for instance Ref. [26] in which parameters of an elasto-plastic law are caracterized.

Constitutive gap method

A similar technique is the constitutive gap method. It relies on a so-called constitutive gap defined by the following quantity

$$E(v,\tau,A)=\frac{1}{2}\int_V\left(\tau-A:\varepsilon(v)\right)A^{-1}\left(\tau-A:\varepsilon(v)\right)dV. \qquad (1)$$

where τ is a given stress field, ε is the strain field defined from a given displacement field v and A is the compliance tensor of the material. This quantity has been introduced first in Ref. [26] for assessing the quality of the solutions given by finite element programmes. $E(v, \tau, A)$ is null if equilibrium is satisfied and if the components of A are the actual ones for a given displacement/strain field. In the current context of parameter identification, the procedure consist in minimizing $E(v, \tau, A)$ alternatively. The first type of minimization is performed with respect to the components of A assuming that τ is fixed, the second one with respect to the stress components assuming that the components of A are fixed. This approach has been used for instance in Ref. [27] to find the constitutive parameters governing an elasto-plastic law. It must also be pointed out that it is possible to identify the unknown parameters zone by zone, thus allowing to characterize heterogeneous materials.

Equilibrium gap method

This method has been specifically developed for full-field measurements. It merely relies on the local equations of equilibrium that are discretized using a mesh of the specimen. The equilibrium of each element is written and the constitutive equations are introduced [28]. In case of elasticity, it can be shown that the rigidity contrast distribution over the specimen can be identified. Consequently, this approach seems to be well suited for characterizing the spatial distribution of damage, as shown in Ref. [29] for instance.

Virtual fields method

This method also relies on equilibrium, but written with its weak form, namely with the principle of virtual work. The principle is valid for any kinematically virtual displacement field [30]. The method consists in introducing the constitutive equations in the principle of virtual work and then to write this principle with different independent virtual displacement fields [31]. In case of constitutive equations depending linearly of the constitutive parameters, it can be shown that a system of linear equations is obtained where the constitutive parameters are the unknowns, each equation being the principle of virtual work written with a virtual displacement field independent of the other ones. This system can be inverted is the actual strain distribution is heterogeneous, thus leading to a direct determination of the parameters. Specific strategies have been developed for determining the virtual fields since this is a key-issue in this method. For instance, it can be shown that the virtual field that minimizes noise effect on identified parameters (in other words, that leads to the most robust identification) is unique in a given basis if functions used for expressing the virtual fields [32]. This method has been applied in many different cases of loadings and constitutive equations [33].

CONCLUSION

This paper is a brief overview of the different full-field measurement techniques that are available and of their use in experimental solid mechanics. Much effort has been done in the recent past for developing these techniques, thus lending credence to them in this particular context. Several challenges are however still ahead of the scientific community, for instance, improving the metrological performance of the techniques or developing the numerical procedures proposed for extracting constitutive parameters from full-field measurements, as illustrated by the increasing number of papers devoted to these topics recently published in the literature.

REFERENCES

[1] Post, D., Han, B., and Ifju, P., High sensitivity moiré: experimental analysis for mechanics and materials, Springer- Verlag, New York, 1994

[2] JACQUOT P., Speckle interferometry: A review of the principal methods in use for experimental mechanics applications, Strain, 44, 57-69, 2008

[3] Kujawinska, M., Use of phase-stepping automatic fringe analysis in moiré Interferometry, Applied Optics, 26, 4712-4714, 1987.

[4] HUNTLEY J.M., SALDNER H., Temporal phase unwrapping algorithm for automated interferogram analysis, Applied Optics, 32, 3047-3052, 1993

[5] Sutton M., Orteu J.-J., Schreier H. W., Image correlation for shape, motion and deformation measurements, Springer, 2009

[6] Surrel Y., Fringe Analysis, in Photomechanics, Topics Appli. Phys. 77, P.K. Rastogi, 55-102, 2000,

[7] Piro J.L., Grédiac M., Producing and transferring low-spatial-frequency grids for measuring displacement fields with moiré and grid methods, Experimental Techniques, 28(4), 23-26, 2004

[8] Moulart R., Rotinat R., Pierron F., Lerondel G., On the realization of microscopic grids for local strain measurement by direct interferometric photolithography. Optics and Lasers in Engineering, 45(12), 1131-1147, 2007

[9] Badulescu C., Grédiac M., Mathias J.-D., Investigation of the grid method for accurate in-plane strain measurement, Measurement Science and Technology, 20:095102, 2009

[10] Avril S., Feissel P., Pierron F., Villon P., Comparison of two approaches for controlling the uncertainty in data differentiation: application to full-feild measurements in solid mechanics. Measurement Science and Technology, 21:015703, 2010.

[11] Buffiere J.-Y., Maire E., Adrien J., Masse J.P., Boller E., In Situ Experiments with X ray Tomography: an Attractive Tool for Experimental Mechanics, Experimental Mechanics, 50(3), 289 – 305, 2010
[12] Journal of Strain Analysis for Engineering Design, special issue in honour of emeritus Professor P. Stanley: thermal techniques for stress analysis and damage assessment, 43(6), 2008
[13] Chrysochoos, A. and Louche, H., Thermographic analysis of localization mechanisms in mild steels, Comptes Rendus Académie des Sciences Série II Fascicule B - Mécanique, 326, 345-352, 1998
[14] Chrysochoos, A. Louche, H., An infrared image processing to analyse the calorific effects accompanying strain localisation, International Journal of Engineering Science, 38, 1759-1788, 2000
[15] Grédiac M., The use of full-field measurement methods in composite material characterization : interest and limitations, Composites Part A, 35, 751-761, 2004
[16] M. Vickstrom and J. Backlund and K. A. Olsson, Non-destructive testing of sandwich construction using thermography, Composite Structures, 13, pp. 49-65, 1989
[17] Dufort L., Grédiac M., Experimental evidence of parasitic effects in the shear test on sandwich beams, Experimental Mechanics, 42(2), pp. 186-193, Society for Experimental Mechanics, 2002
[18] Pierron, F., Sutton M.A., Tiwari V., Ultra high speed DIC on a three point bending test mounted on a Hopkinson bar, in this volume.
[19] Xing, Y. M., Yun H., Dai F.L., An experimental study of failure mechanisms in laminates with dropped plies, Composite Science and Technology, 59, pp. 1527-1531, 1999
[20] Réthoré, J., Roux, S., Hild, F., Hybrid analytical and extended finite element method (HAX-FEM): A new enrichment procedure for cracked solids, International Journal for Numerical Methods in Engineering, 81(3), 268-285, 2010
[21] Dufort L., Grédiac M., Surrel Y., Experimental evidence of the cross section warping in short composite beams under three point bending, Composite Structures, 51, 37-47, 2001
[22] Papila, M., Akgun, A., Niu X., Ifju P., Post-buckling of composite I sections. Part 2 : experimental validation, Journal of Composite Materials, 35(9), pp. 797-821, 2001
[23] Avril S., Bonnet M., Bretelle A.S., Grédiac M., Hild F., Ienny P., Latourte F., Lemosse D., Pagano S., Pagnacco S., Pierron F., Overview of identification methods of mechanical parameters based on full-field measurements, Experimental Mechanics, 48(4), 381-402, 2008
[24] Molimard J, Le Riche R, Vautrin A, Lee JR, Identification of the four orthotropic plate stiffnesses using a single open-hole tensile test, Experimental Mechanics, 45(5), 404-411, 2005
[25] Cooreman S., Lecompte D., Sol H., Vantomme J., Debruyne D., Identification of Mechanical Material Behavior Through Inverse Modeling and DIC, Experimental Mechanics, 48(4), 421-433, 2008
[26] Meuwissen M. H. H., Oomens, C. W. J., Baailens F. P. T., Petterson R., Janssen J. D., Determination of the elasto-plastic properties of aluminium using a mixed numerical-experimental method, Journal of Materials Processing Technology, 75:204–211, 1998
[26] Moës E.S., Ladevèze P., Douchin B, Constitutive relation error estimators for (visco)plastic finite element analysis with softening, Computational Methods in Applied Mechanical Engineering, 176, 247–264, 1999
[27] Latourte F., Chrysochoos A., Pagano S., Wattrisse B., Elastoplastic behavior identification for heterogeneous loadings and materials, Experimental Mechanics, 48(4), 435-449, 2008
[28] Claire, D., Hild F., Roux S., A finite element formulation to identify damage fields, International Journal for Numerical Methods in Engineering, 61:189–208, 2004
[29] Crouzeix L., Perie J. N., Collombet F., Douchin B., An orthotropic variant of the equilibrium gap method applied to the analysis of a biaxial test on a composite material, Composites/Part A, 40(11), 1732-1740, 2009
[30] Dym C.L., Shames I.H. Solid Mechanics: A Variational Approach, McGraw-Hill Book Company, Inc, New York, 1973
[31] Grédiac M., Principe des travaux virtuels et identification, Comptes Rendus Mécanique, 309, 1-3, 1989
[32] Avril S., Grédiac M., Pierron F., Sensitivity of the virtual fields method to noisy data, Computational Mechanics, 34, 439-452, 2004
[33] Grédiac M., Pierron F., Avril S., Toussaint E., The Virtual Fields Method for extracting constitutive parameters from full-field measurements: a review, Strain, 42, 233-253, 2006

Proceedings of the SEM Annual Conference
June 7-10, 2010 Indianapolis, Indiana USA

Identification of Cohesive-Zone Laws from Crack-tip Deformation Fields

Soonsung Hong
Department of Mechanical Engineering, Michigan State University,
East Lansing, Michigan 48824
shong@egr.msu.edu

ABSTRACT

A hybrid framework for inverse analysis of crack-tip cohesive zone model was developed to determine cohesive zone laws from full-field measurement of crack-tip fields by combining analytical, experimental and numerical approaches. The framework is based on the analytical solution method developed to extract cohesive-zone laws from elastic far-fields by using eigenfunction expansion of cohesive crack-tip fields and path-independent integrals. Electronic Speckle Patten Interferometry (ESPI) was used to provide crack-tip deformation fields as input data for the inverse analysis. To overcome ill-conditioning of the inverse problem, a global noise reduction algorithm was developed by implementing a PDE-constrained error minimization problem. The analytical, experimental and numerical approaches were combined to extract cohesive zone laws of fracture processes in glassy polymers, so called crazing. The results demonstrated that the inverse analysis framework provided a systematic and rigorous method to obtain cohesive-zone laws from experimental measurements, so that more realistic cohesive zone modeling can be achieved to predict fracture processes in various engineering materials and interfaces.

INVERSE PROBLEM OF COHESIVE ZONE MODEL

The cohesive zone model, depicted in Figure 1, has been widely used to represent the complex nonlinear fracture processes in various ductile or quasi-brittle materials, as well as to describe frictional-slip and adhesion between two elastic bodies. One of the major difficulties in applying the cohesive zone model is the lack of well-established experimental methods to determine realistic traction-separation laws. This is a challenging inverse boundary value problem that seeks unknown constitutive cohesive-zone laws from far-field experimental measurements. The fact that there are very little analytical studies on the general form of cohesive crack-tip fields has made the problem very difficult. Consequently, the majority of studies on this inverse problem rely upon optimal parameter estimation based on numerical solutions of forward problems, such that sensitivity and uniqueness of the outcome can not be easily addressed. In addition, the inverse problem is inherently ill-conditioned because extracting source parameters from rapidly decaying field is extremely sensitive to the noise in the input data. Therefore, in this study, a framework developed by Hong and Kim [1] for the inverse analysis of the crack-tip cohesive zone model is employed to obtain realistic cohesive zone laws of crazing by following a series of experimental, numerical and analytical procedures.

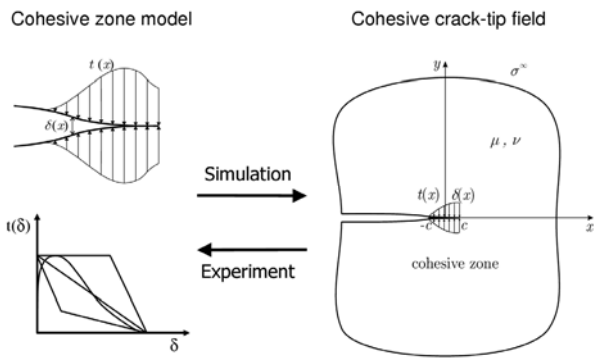

FIGURE 1. Cohesive zone modeling of fracture

T. Proulx (ed.), *Application of Imaging Techniques to Mechanics of Materials and Structures, Volume 4*, Conference Proceedings of the Society for Experimental Mechanics Series 14, DOI 10.1007/978-1-4419-9796-8_2, © The Society for Experimental Mechanics, Inc. 2013

INTEGRATED APPROACH

Optical measurement of crack-tip deformation field

Electronic Speckle Pattern Interferometry (ESPI) was used to measure crack-tip displacement fields in a region surrounding a crack-tip [2]. Non-contacting and whole-field measurement capability of the ESPI was proven to effective to provide elastic deformation fields surrounding a fracture process zone that can be used as input data for the inverse analysis. A laser speckle interferometer setup shown in Figure 2 was used to measure in-plane displacement fields around a crack tip during four-point bending fracture tests of glassy polymers. The optical measurement system is designed to provide far-field elastic deformation fields surrounding a fracture process zone with a high sensitivity and a high spatial resolution suitable for the inverse analysis of the crack-tip cohesive zone problem.

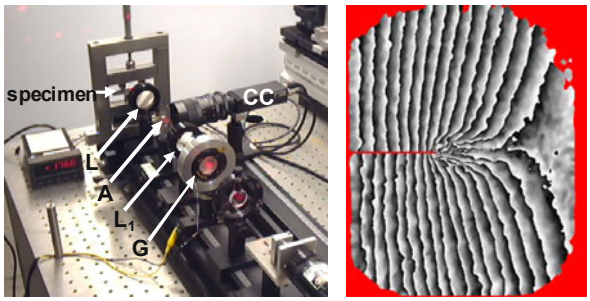

FIGURE 2. Four-beam speckle interferometer setup and a crack-tip displacement field in vertical direction.

Numerical noise reduction in full-field data

A numerical noise reduction algorithm, called Equilibrium Smoothing Method [2], is used to overcome the severe ill-conditioning in the inverse problem by removing experimental noises in the full-field data. The equilibrium smoothing method uses the governing field equation of isotropic linear elasticity as a constraint for a PDE-constrained error minimization problem, in order to extract a smooth equilibrium field that is closest to an experimentally measured displacement field in the least-square sense. Also, an additional constraint of cubic-spline smoothing is imposed along the boundary of the domain. The equilibrium smoothing algorithm is applied to remove experimental noises in the crack tip displacement field measured by the speckle interferometer.

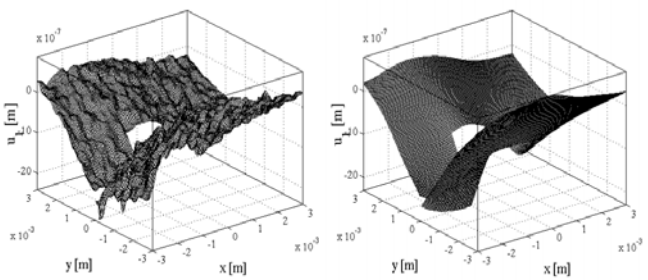

FIGURE 3. Horizontal displacement fields before and after equilibrium smoothing

Extracting cohesive zone laws of crazing

The analytical solution method of the inverse problem [1] is used to extract a cohesive-zone law, i.e. a traction-separation law from the elastic far-field surrounding a crack-tip fracture process zone. The solution method uses a general form of cohesive crack-tip fields expressed as eigenfunction expansions of the plane elastic field in a complex variable representation. In case of Mode-I, the cohesive traction and the separation-gradient within the cohesive zone ($-c \le x \le c$) are expressed in terms of two analytic functions, $F(x)$ and $G(x)$, from the general-form complex functions, as

$$t(x) = \sqrt{x+c}\, F(x)$$

$$b(x) = -\frac{d\delta(x)}{dx} = \frac{\kappa+1}{2\mu}\sqrt{c-x}\; G(x)$$

where $\kappa = 3 - 4\nu$ for plane strain, $\kappa = (3-\nu)/(1+\nu)$ for plane stress and ν is Poisson's ratio. Using the Chebyshev polynomial of the second kind, the cohesive traction and the separation gradient can be represented with a set of cohesive crack-tip eigenfunctions which is complete and orthogonal in the sense of the interaction J-integral at far field as well as at the cohesive-zone faces. Then, the coefficients of the eigenfunctions in the J-orthogonal representation are extracted directly, using the interaction J-integrals at far field between the physical field and auxiliary probing fields. Then, the separation profile within the cohesive zone is found by

$$\delta(x) = \int_x^c b(\xi)\, d\xi\,.$$

The parametric relationship between the traction and the separation within the cohesive zone provides a cohesive zone law. The cohesive zone laws of environmental crazing in PMMA and multiple crazing in HIPS obtained by the proposed inversion method [2] are shown in Figure 4. It was concluded that the proposed inverse analysis scheme could provide a systematic way of empirically finding the shape of the cohesive zone laws governed by the different micro-mechanisms of fracture.

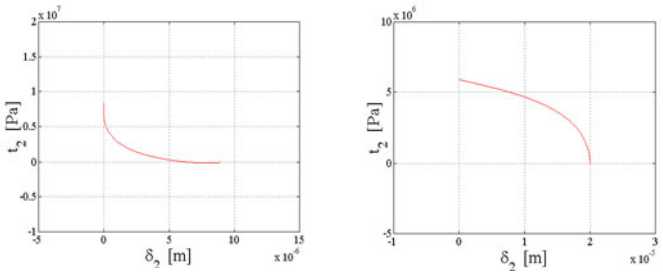

FIGURE 4. Cohesive zone laws of environment crazing in PMMA and multiple crazing in HIPS

REFERENCES

[1] Hong, S., Kim, K.S., 2003. Extraction of cohesive-zone laws from elastic far-fields of a cohesive crack tip: a field projection method. Journal of the Mechanics and Physics of Solids 51 (7), 1267-1286.

[2] Hong, S., Chew, H.B., Kim, K.S., 2009. Cohesive-zone laws for void growth - I. Experimental field projection of crack-tip crazing in glassy polymers. Journal of the Mechanics and Physics of Solids 57 (8), 1357-1373.

Proceedings of the SEM Annual Conference
June 7-10, 2010 Indianapolis, Indiana USA

Recovery of 3D stress intensity factors from surface full-field measurements

Stéphane Andrieux[a] and Thouraya N. Baranger[b]

[a] *Mechanics of Durable Industrial Structures Laboratory, UMR CNRS-EDF 2832, Clamart, France.*
[b] *Université de Lyon*
Contact and Structural Mechanics Laboratory, CNRS UMR5259, F69621, France; Université Lyon 1, Villeurbanne, F-69622, France, Thouraya.Baranger@univ-lyon1.fr

ABSTRACT

The identification of cracks stress intensity factors (SIFs) in elastic solids from full-field in-plane displacement field measurements is addressed. Because it is known that significant three dimensional effects alter the values of plane stress computed SIFs, and that the overall geometry of the crack front plays also a role, the problem of SIF's identification is tackled here in the full three-dimensional framework. First is derived a data completion method in elasticity enabling the determination of the elastic displacement and stress fields inside the solid, or in the part where the behavior remain elastic, from surface displacements including the case of only in-plane displacement fields measurements over a traction-free surface. Then usual numerical methods for the computation of SIF or energy release rates are used. Numerical applications in three-dimensional elasticityfor true 3D geometry and loading are presented.

Three dimensional effects in linear fracture mechanics

The determination of the stress intensity factors (SIF's) in linear fracture mechanics from full field in-plane (surface) displacement relies generally on the hypothesis of plane elasticity, that is the measured displacement fields are supposed to be the displacement of a plane problem. This hypothesis is obviously adopted because of the impossibility of measuring optically either simultaneously the in-plane and out-of-plane surface displacements, or the displacement inside the solid. Unfortunately it is known that three-dimensional effects alter significantly the value of the SIF's at the surface and in the bulk of the solid.

Parsons *et al.* [1] studied numerically the simple problem of an edge crack in a plate under tension with thickness *h*. The results show that the in-plane stresses, $\sigma_{\alpha\beta}$ ($\alpha,\beta=r,\theta$), are nearly constant through the thickness with the normal stresses dropping off by approximately 25% at the free surfaces. The out-of-plane stress, σ_{33} has considerable variation through the thickness. The results show also that in the center of the plate, very close to the crack tip, the stress field is a plane strain fields. Further away from the crack, $r \approx 0.33h$ the field is a plane stress field. Very close to the crack-tip plane strain predominates except in a boundary layer near the free surfaces. Rosakis and Ravi-Chankar [2] showed that the size of the three dimensional effect on the surface fields extends approximately to a radius equal to half the thickness *h* of the solid. Sinha *et al*. [3] investigated mode-mixity for interfacial cracks in PMMA/Al specimen subject to three points bending by experimental interferometric means coupled with finite element analysis. For dominant tensile stress conditions, plane stress conditions are not established along the bond line, even far away from the crack tip. At other polar directions (65° to 1 35 °) plane stress conditions are encountered at distances greater than 0.3*h*. However, there is a significant reduction of these strong 3D effects for dominant shear stress conditions. For small quarter-elliptical corner cracks in elastic plates subjected to tension, Zhang and Guo [4] obtained by finite element analysis that strong 3D effects exist within a radial distance of the crack tip ranging from 4.6 to 0.7 *a*, *a* being the minor semi axis, for aspect ratio *c*/*a* ranging from 0.2 to 1.

T. Proulx (ed.), *Application of Imaging Techniques to Mechanics of Materials and Structures, Volume 4*, Conference Proceedings of the Society for Experimental Mechanics Series 14, DOI 10.1007/978-1-4419-9796-8_3, © The Society for Experimental Mechanics, Inc. 2013

To relax the limitations due to the assumption of plane displacement fields for the computation of SIFs and energy release rates from surface measurements, we propose to compute these quantities from 3D fields that will have been extended into the solid from the surface tangential displacement fields usually measured on stress free portions of the boundary of the 3D solidA “data completion” method is then a first necessary step. Then usual numerical methods for the computation of SIFs or energy release rates are used. This approach opens a new field of application of surface displacement measurements for linear mechanics purposes, namely the determination of SIFs for “true” 3D experiments, as illustrated below.

Extending the fields inside the solid: the data completion method

The method has then to produce a 3D equilibrium elastic displacement field in the solid, provided the displacement field and the surface traction fields are known on a part of the boundary, and the distribution of the elastic properties of the material that constitutes the solid is given. This problem is known as a Cauchy problem for the Lamé operator. The Cauchy problem has been extensively studied for the Laplace operator, but more recently interest for the Lamé operator has appeared in linearized elasticity (see Andrieux and Baranger [5] for the analysis of the literature of this field). Very few authors deal with this 3D problem because of the complexity of extending their method to 3D situations or because of computational costs. A large amount of work addresses only homogeneous and isotropic media. The present formulation aims simultaneously at more generality in order to deal with more realistic applications and more computational efficiency in order to deal with large 3D situations. It extends the method given in Andrieux *et al,* [6], for the Cauchy problem for the Laplace operator.

An elastic three-dimensional solid Ω is considered, the boundary of which is separated into three non-overlapping parts.

- On the first part, denoted by Γ_m, the surface tractions $\boldsymbol{T}^m$ **and** the displacement field $\boldsymbol{U}^m$ are known (measured),
- On the second part, Γ_b, usual boundary conditions are known (combination of surface tractions and displacement field components); these boundary conditions will be denoted generally by:

$$B\boldsymbol{u} = \boldsymbol{b} \tag{1}$$

- On the third part, Γ_u, the external forces $\boldsymbol{T}^u$ or the displacement $\boldsymbol{U}^u$ are prescribed; **both** of these are unknown.

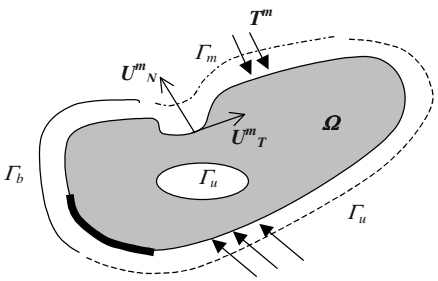

Figure 1: Definition of the three parts of the boundary

Provided the Hooke’s tensor **A** of the elastic material that forms the solid is known, even possibly depending on space, the Cauchy problem is the following:

Cauchy problem for the Elasticity operator:

Given:

The surface traction field $\boldsymbol{T}^m$ and displacement field $\boldsymbol{U}^m$ on Γ_m,
The vector $\boldsymbol{b}$ of usual boundary conditions on Γ_b,

Find the surface tractions $\boldsymbol{T}^u$ and displacement $\boldsymbol{U}^u$ such that an elastic displacement field $\boldsymbol{u}$ satisfies:

$$\begin{cases} div(A:\varepsilon(\boldsymbol{u}))=0 & in\ \Omega \\ A:\varepsilon(u).n=\boldsymbol{T}^m,\ \boldsymbol{u}=\boldsymbol{U}^m & on\ \Gamma_m \\ B\boldsymbol{u}=b & on\ \Gamma_b \\ A:\varepsilon(\boldsymbol{u}).n=T^u,\ \boldsymbol{u}=\boldsymbol{U}^u & on\ \Gamma_u \end{cases} \tag{2}$$

The general method proposed in [5],[6] to solve the Cauchy problem is to derive a functional of the unknown fields on Γ_u, say ($\boldsymbol{\tau}$, $\boldsymbol{\upsilon}$), where (possibly local) minima deliver the desired pair of fields ($\boldsymbol{T}^m$, $\boldsymbol{U}^m$). Building this functional follows two steps. First, the two following elastic displacement fields $\boldsymbol{u_1}$ and $\boldsymbol{u_2}$ are defined, as functions respectively of ($\boldsymbol{b}$, $\boldsymbol{U}^m$, $\boldsymbol{\tau}$) and ($\boldsymbol{b}$, $\boldsymbol{T}^m$, $\boldsymbol{\upsilon}$). They correspond to the solutions of two well-posed classical mixed elasticity problems.

$$\begin{cases} div(\mathrm{A}:\varepsilon(\boldsymbol{u}_1))=0 & in\ \Omega \\ \boldsymbol{u}_1=\boldsymbol{U}^m & on\ \Gamma_m \\ B\boldsymbol{u}_1=\boldsymbol{b} & on\ \Gamma_b \\ \mathrm{A}:\varepsilon(\boldsymbol{u}_1).\boldsymbol{n}=\boldsymbol{\tau} & on\ \Gamma_u \end{cases} \qquad \begin{cases} \mathrm{div}(\mathrm{A}:\varepsilon(\boldsymbol{u}_2))=0 & in\ \Omega \\ \mathrm{A}:\varepsilon(\boldsymbol{u}_2).\boldsymbol{n}=\boldsymbol{T}^m & on\ \Gamma_m \\ \mathrm{B}\boldsymbol{u}_2=\boldsymbol{b} & on\ \Gamma_b \\ \boldsymbol{u}_2=\upsilon & on\ \Gamma_u \end{cases} \tag{3}$$

Since whenever the two fields $\boldsymbol{u_1}$ and $\boldsymbol{u_2}$ coincide ($\boldsymbol{\tau}$,$\boldsymbol{\upsilon}$) is a solution ($\boldsymbol{T}^u$, $\boldsymbol{U}^u$) of the Cauchy problem, the second step consists in the introduction of a functional measuring the gap between the two fields. The choice of this functional here is the error in the semi-norm of elastic energy:

$$\boldsymbol{J}(\boldsymbol{u}_1,\boldsymbol{u}_2)=\frac{1}{2}\int_\Omega A:\varepsilon(\boldsymbol{u}_1-\boldsymbol{u}_2):\varepsilon(\boldsymbol{u}_1-\boldsymbol{u}_2)d\Omega \tag{4}$$

The problem is then formulated via the minimization of the energy error functional: *Find* ($\boldsymbol{\tau}$, $\boldsymbol{\upsilon}$) *that minimize:*

$$E(\boldsymbol{\tau},\boldsymbol{\upsilon})\equiv \boldsymbol{J}(\boldsymbol{u}_1,\boldsymbol{u}_2)=\frac{1}{2}\int_\Omega A:\varepsilon(\boldsymbol{u}_1-\boldsymbol{u}_2):\varepsilon(\boldsymbol{u}_1-\boldsymbol{u}_2) \tag{5}$$

$$\text{with}\qquad \boldsymbol{u}_1=\boldsymbol{u}_1(\boldsymbol{b},\boldsymbol{U}^m,\boldsymbol{\tau}),\boldsymbol{u}_2=\boldsymbol{u}_2(\boldsymbol{b},\boldsymbol{T}^m,\boldsymbol{\upsilon})\ solution\ of\ (3)$$

Complete justification of this formulation can be found in [5]. For computational purpose, an alternative form of the functional is derived involving only surface integrals, by exploiting the equilibrium properties of the $\boldsymbol{u}$ fields.

$$E(\boldsymbol{\tau},\boldsymbol{\upsilon})=\frac{1}{2}\int_{\Gamma_m}(A:\varepsilon(\boldsymbol{u}_1(\boldsymbol{\tau})).\boldsymbol{n}-\boldsymbol{T}^m).(\boldsymbol{U}^m-\boldsymbol{u}_2(\boldsymbol{\upsilon}))d\Gamma+\frac{1}{2}\int_{\Gamma_u}(\boldsymbol{\tau}-A:\varepsilon(\boldsymbol{u}_2(\boldsymbol{\upsilon})).\boldsymbol{n}).(\boldsymbol{u}_1(\tau)-\boldsymbol{\upsilon})d\Gamma \tag{6}$$

This last expression is used in the computations and avoids any domain integration. It involves both surfaces Γ_m and Γ_u. The method is very similar in the case where only tangential surface displacements are measured [5], and can be then used when the displacement field is obtained by digital image correlation.

Computation of 3D SIFs and energy release rates

Once the data completion problem is solved, one is equipped with a elastic displacement filed within the entire structure, on the finite element mesh that has been used for the computation of the fields $\boldsymbol{u}_1$ and $\boldsymbol{u}_2$.When convergence is reached $\boldsymbol{u}_1$ equals $\boldsymbol{u}_2$, and in the applications the $\boldsymbol{u}_1$ field is used as the “true” elastic field in the solid, meeting the surface measurements. Then usual numerical methods for computing the SIFs and the energy release rates (Code_Aster, [7]) can be employed. In the following applications, the solid is a plate, lying in the *x-y* plane and the crack front is parameterized with the *z*-coordinate. The SIFs are computed by least-square fitting of the asymptotic form (near the crack tip) of the elastic displacement field:

$$K_i(z) = \sqrt{\frac{\pi}{8}} \frac{E}{(1-\varepsilon_i \nu)(1+\nu) r_m^2} \int_0^{r_m} \left[u_i(r,\pi,z) - u_i(r,-\pi,z) \right] \sqrt{r}\, dr \quad , i = I, II, III \quad , \varepsilon_I = \varepsilon_{II} = 1,\ \varepsilon_{III} = 0 \tag{7}$$

Whereas the global energy release rate G and the local one $g(z)$ are computed via the Irwin's formula :

$$g(z) = \frac{(1-\nu^2)}{E} \left(K_I^2(z) + K_{II}^2(z) + \frac{1}{1-\nu} K_{III}^2(z) \right) \ , \quad G = \int_0^h g(z) dz \tag{8}$$

Determination of 3D KIFs for a straight crack in a thick plate from surface displacements measurements

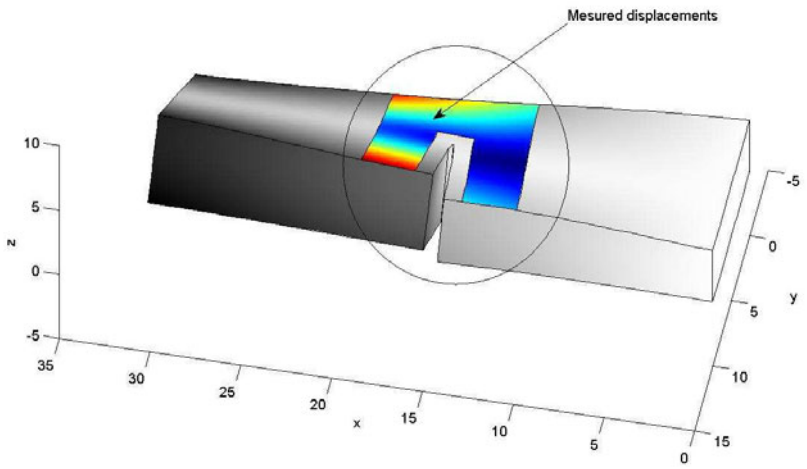

Figure 2: The studied solid with crack under a mixed Mode-I, II, III loading.

We consider the solid shown on figure 2. The applied load induces a mix of Mode I, II, III and the mixity coefficient varies along the crack front. The Cauchy data consist on displacement measurements on a well-defined area around the crack as shown on the figure 2. The surface tractions on this area are equal to zero. The data completion problem is defined on a part of this solid which is defined on figure 2. Figure 3 presents the data completion domain, with the boundary Γ_m of the Cauchy data and the boundary Γ_u where displacements and tractions have to be identified. Figure 4 presents the associated used FEM mesh. The material has the following properties: $E=2.08\ 10^{11}$ and $\nu=0.3$. The identified Stress Intensity Factors and release energy rates are evaluated using the field u_1 obtained from the minimization problem defined above (eq .5)

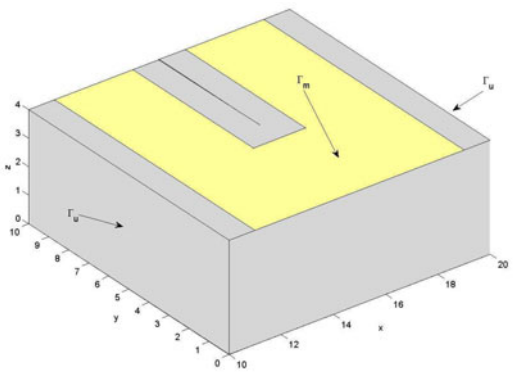

Figure 3: Geometry and boundaries of the data completion domain

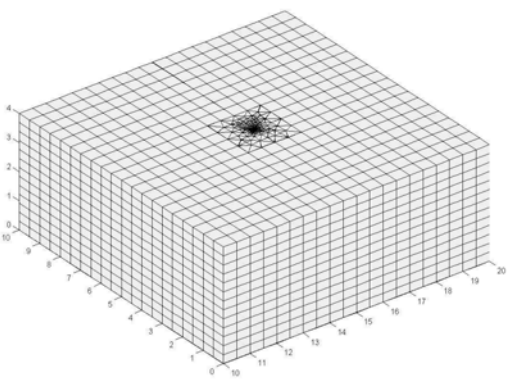

Figure 4: FEM mesh of the data completion domain

Three cases were studied:

- ✓ Case 1: we use Cauchy displacement data taken on the patch defined by the area on the face located at z=4. We consider that the all the displacement components u_x, u_y and u_z are known on this patch.
- ✓ Case 2: idem case 1 except that we consider only the tangential displacement components u_x and u_y are known.
- ✓ Case 3: we use Cauchy displacement data taken on the two identical patches located at z=0 and z=4, respectively. We consider only the tangential displacement components u_x and u_y are known.

Figure 5 shows the results obtained in the case 1. We observe a very good agreement between the exact values of SIFs' and the identified ones. Figure 6 shows results obtained in the case 2 and 3. Here, we observe in the case 2, a degradation of identification results, which is more important for mode I and III than the mode II. These results have required many more iterations in the minimization process, than those of the case 1. However, when increasing the amount of data, and if we arrange geometrically the information by using both faces of the muoc-up, then even with tangential data only, we obtain again a good agreement between the *exact* and identified values with the same computational cost.

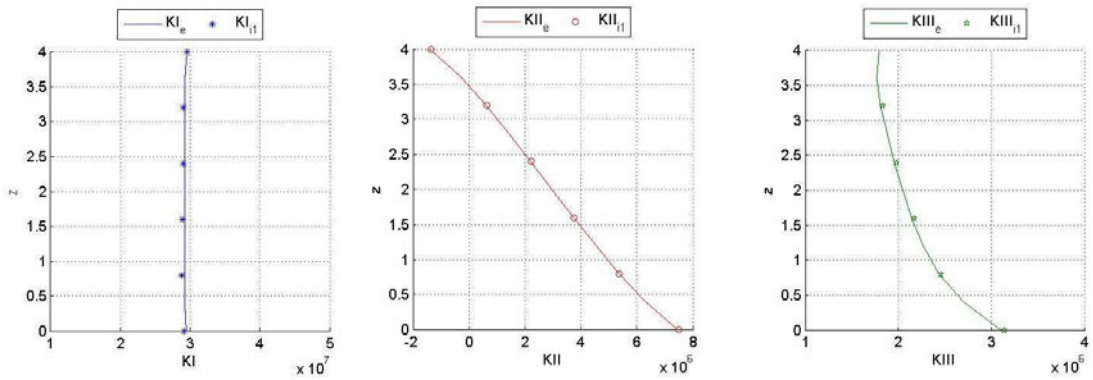

Figure 5: Identified Stress Intesity Factors KI_i, KII_i and $KIII_i$ along the crack front using full displacement field (u_x, u_y, u_z) on Γ_m. Comparison with *exact* values KI_e, KII_e, $KIII_e$. Indexes *e* and *i* indicate exact and identified values, respectively. Indexes *1* indicate case 1. (Pa.m$^{1/2}$)

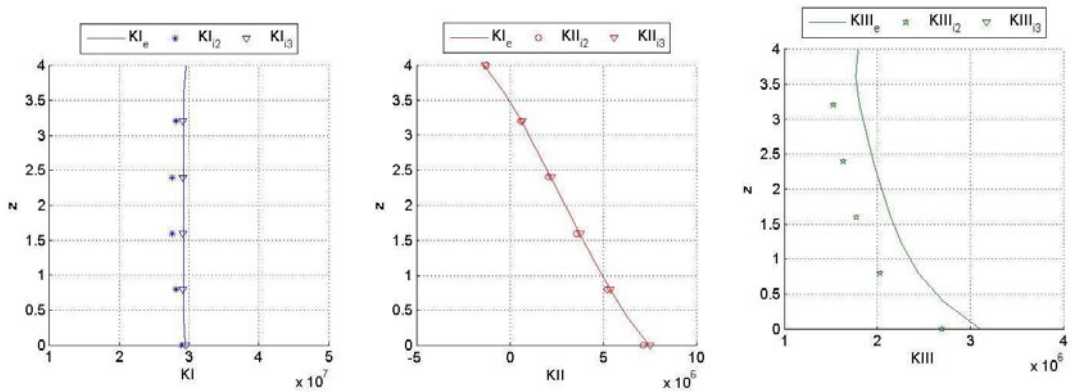

Figure 6: Identified Stress Intensity Factors KI_i, KII_i and $KIII_i$ along the crack front using tangential displacement field (u_x, u_z) on Γ_m. Comparison with *exact* values KI_e, KII_e, $KIII_e$. Indexes *e* and *i* indicate exact and identified values, respectively. Indexes *2* and *3* indicate case 2 and case 3, respectively. (Pa.m$^{1/2}$)

Figure 7 shows the identified local release energy obtained in the three cases defined above and compared to the *exact* one. The same remarks can do that for SIFS. The global release energy values obtained are summerized in the table 1:

	Case 1	Case 2	Case 3
Identified	15369	14339	15508
Relative error	1.49%	8.05%	0.56%

Table 1: Release energy. Comparison between the three cases and the exact computation: G_e=15596 Pa.m

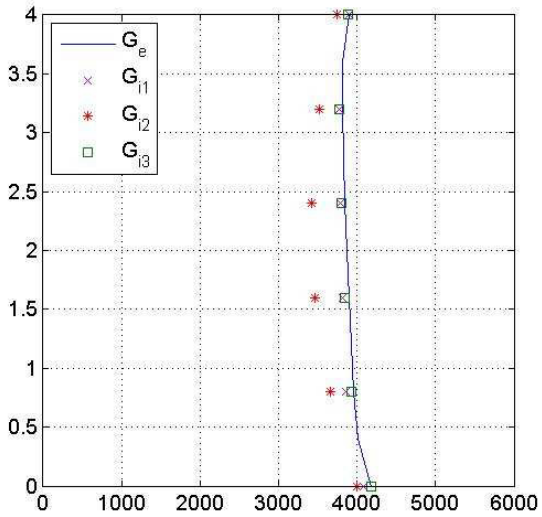

Figure 7: Identified local energy release rate $g_i(z)$ along the crack front and comparison with the exact one. Indexes *e* and *i* indicate exact and identified values, respectively. Indexes *1*, *2* and *3* indicate case 1, case 2 and case 3, respectively (Pa)

Conclusion

In this paper we present an energy minimsation method, based on solving a Cauchy problem [5], in order to identify the Stress Intensity Factors of a crack in three-dimensional domain. This method uses measured displacement data on an accessible face of the solid. It also can be applied only on a part of the solid arround the crack. The identification results are in good agreement with the exact computation one. However, when the displacement measurements are obtained via optic technics, only the tangential components to the surface are available, then the choice of the location and the amount of the measure are important for the quality of the identification results and the computational cost. The presented method can be easily implemented in industrial finite element software in order to deal with industrial identification problems. No regularization is needed. However, in the case of industrial applications, the data are often severely altered by noise. Hence, the identification will also be altered by this noise. The effect of noise has been examined for the Cauchy problem for the Laplacian operator in a previous paper of Andrieux et. al. [3]; incorporation of some kind of regularization seems to be requisite in the method as soon as the noise is above 5%.

References

[1] Parsons ID, Hall JF, and Rosakis A, A finite element investigation of the elastostatic state near a three dimensional edge crack, *20th Midwestern Mechanics Conference* 14(b), 729–734, 1987

[2] Rosakis A.J., Ravi-Chankar K, On the crack tip stress state: an experimental evaluation of three-dimensional effect, *Int. J. Solids and Structures*, 22(2), pp 121-136., 1986

[3] Sinha J.K., Tippur H.V., Xu L. An interferometric and finite element investigation of interfacial crack tip fields: role of mode-mixity on 3-D stress variation, *Int. J. Solids. Structures*, Vol. 43, N°6, pp 741-754, 1997

[4] Zhang B., W. Guo, Three-dimensional effect stress state around quarter-elliptical corner cracks in elastic plates subjected to uniform tension loading, *Engineering fracture Mechanics*, 74, pp 386-398, 2007

[5] Andrieux S., Baranger T.N. An energy error-based method for the resolution of the Cauchy problem in 3D linear elasticity*, Computer Methods in Applied Mechanics and Engineering*, **197**, 9-12, 902-920, 2008,

[6] Andrieux S., Baranger T.N. and Ben Abda A. Solving Cauchy problem by minimizing an energy-like functional, *Inverse Problems* 22, 115-133, 2006

[7] Code_Aster, Reference, validation and user's manuals, 2010, *www.code_aster.org*

Proceedings of the SEM Annual Conference
June 7-10, 2010 Indianapolis, Indiana USA

Characterization of aluminum alloys using a 3D full field measurement

Marco Rossi, Arts et Métiers ParisTech,
rue St. Dominique, 51000 Châlons-en-Champagne, m.rossi@ensam.eu
Gianluca Chiappini, Università Politecnica delle Marche,
via brecce bianche, 60100 Ancona, g.chiappini@univpm.it
Marco Sasso, Università Politecnica delle Marche,
via brecce bianche, 60100 Ancona, m.sasso@univpm.it

ABSTRACT
In the 2009 SEM Conference in Albuquerque, a measurement technique that combines the digital image correlation and the fringe projection was proposed by the authors to evaluate the 3D displacement of a specimen during a tensile test: the DIC is used to measure the in-plane displacement on both faces of the specimen while the fringe projection and phase shifting is used to reconstruct the shape with a high spatial resolution. In this work, the mentioned experimental technique was employed to characterize the plastic behavior of an aluminum alloy. First a 3D mesh was utilized to regularize the measured data and to get the strain field inside the specimen, in such way the full strain history of the test was reconstructed until failure. Then the Virtual Fields Method was adopted to identify the parameters of an anisotropic plasticity model. A comparison with FEM was also made to assess the correctness of the identified parameters.

INTRODUCTION
The characterization of the plastic behavior of metals is commonly obtained by means of uniaxial tensile tests. The main limit of such tests is the occurrence of a necking that starts after the maximum load is reached and leads the specimen to a premature fracture.
In order to characterize the material behavior at larger strains, more sophisticated tests can be used, for instance torsion tests, hydraulic bulge tests or bending tests [1-3]. In general an inverse approach with FEM is also required to identify the parameters of the constitutive equation when a complex state of stress is obtained in the specimen during the test [4-10].
Another possibility is to use the strain field, measured on the specimen surface with a full-field optic technique, to identify directly the parameters of the constitutive model [11]. On this subject, the Virtual Fields Method [12] is a well established technique to identify the constitutive equations starting from strain data and some applications to isotropic plasticity were already presented in the literature [13,14].
The goodness of the strain measure is a fundamental issue for a successful identification. Different techniques are available to measure the displacement field on a surface, the most used are based on the numerical correlation of white light speckle images and considerable results can be obtained in terms of accuracy [15]. Recently the strain measurement has been extended to the three-dimensional space and commercial software is available to measure the 3D displacement on a surface. A 3D measurement system becomes mandatory when the geometry of the surface to be measured is not more planar.
In the present paper the surface displacement field on a tensile test was achieved using a technique that combines DIC and fringe projection [16], the 3D measurement is required because the surface of the specimen becomes curved after the occurrence of the localized necking through the thickness. With this system, it had been possible to evaluate the strain history of the specimen at large strains, up to the final fracture.
Starting from the surface displacement, the through thickness strain distribution was computed using a 3D mesh, where the displacement of the nodes inside the specimen has been achieved by an interpolation, involving Beziér curves.
A procedure to compute the stress field from the strain data, neglecting the elastic part of the strain, is also proposed here, the Hill48 yield criterion for normal anisotropy was applied. The resultant stress-strain history was used to characterize the plastic behavior of the material at large strains by the Virtual Fields Method.

T. Proulx (ed.), *Application of Imaging Techniques to Mechanics of Materials and Structures, Volume 4*, Conference Proceedings of the Society for Experimental Mechanics Series 14, DOI 10.1007/978-1-4419-9796-8_4, © The Society for Experimental Mechanics, Inc. 2013

3D STRAIN FIELD RECONSTRUCTION

The material employed is a 6061 aluminum, the specimen was extracted from a 4mm thick plate and it is shown in Fig. 1. The specimen has a non-standard dog bone shape, the central zone is 20×20 mm and it is connected to the ends with an 8 mm fillet radius. This particular geometry allows to have limited elongation and forces the localized necking to occur in the center of the specimen.

Figure 1: Specimen with speckle pattern

The experimental setup is shown in Fig. 2; a Zwick-Roell electromechanical tensile machine was used to perform the tensile test. The force is measured with a 50 kN load cell and the displacement by an LVDT on the crosshead. The test was performed in displacement control and a rate of 0.2 mm/min was set to the crosshead. The 3D displacement surface field was measured using a symmetric configuration on the two sides of the specimen. A complete description of the measurement technique is given in the reference [16].

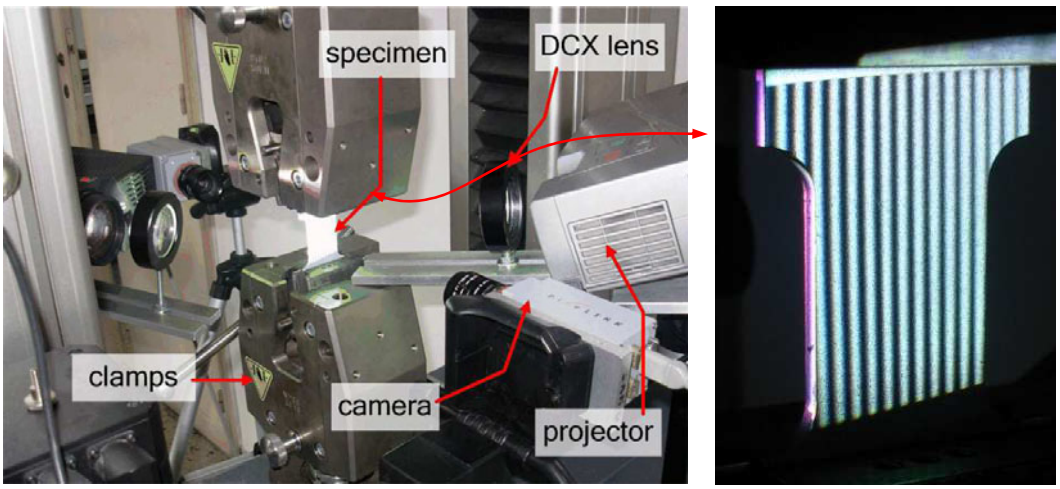

Figure 2: Test rig for combined techniques: specimen, tensile machine and vision system and particular specimen during the test with the surface illuminated by the fringes

After the post-processing, at each acquisition time step *t* two surface meshes are available, one for each surface. The node coordinates are given in a three dimensional Cartesian space, where the *x*-axis is aligned with the tensile force the *y*-axis is the transverse direction and the *z*-axis is the through thickness direction. At the first step, the two meshes are overlapping since the specimen is flat and at each node N^f on the front surface corresponds a node N^r on the rear surface.

From these experimental data a 3D model of the specimen was built using brick elements. Only a half of the specimen was represented since the displacement has been considered symmetric respect to the plane *x*-*y*. At each time step, the following procedure was used to achieve the current coordinate of the nodes.

- The coordinates of the nodes *N* of the reconstructed symmetric specimen surface are obtained as an average of the N^f and N^r coordinates respect to the mid-plane.
- At each node *N* a normal versor $\hat{\mathbf{n}}$ is computed as the average of the normal versors of the adjacent faces.
- A point $\mathbf{P_0}$ is obtained as the intercept of the $\hat{\mathbf{n}}$ direction with the mid-plane of the specimen, the one with $z=0$ in the chosen coordinate system.

- A quadratic Beziér curve is built using three points, ($\mathbf{P_N}$, $\mathbf{P_0}$, $\mathbf{P_{-N}}$) where $\mathbf{P_N}$ is the position of the node *N*, $\mathbf{P_0}$ is the point computed at the precedent step and $\mathbf{P_{-N}}$ is the point symmetric to $\mathbf{P_N}$ respect to the *x-y* plane.
- The coordinates of the through thickness nodes are obtained dividing the curve by the number of elements along the thickness.

At each surface node *N* the correspond Beziér curve writes:

$$C(t) = (1-t)^2 \mathbf{P_N} + 2(1-t)t\mathbf{P_0} + t^2 \mathbf{P_{-N}} \quad \text{with} \quad t \in [0,1] \tag{1}$$

the curve is symmetric respect to the x-y plane, then when *t*=0.5 the curve indicates the coordinates of the node in the mid-plane. The intermediate nodes are computed using a step for *t* that is 0.5 divided by the number of element through thickness. A geometric representation of the following procedure is illustrated in Fig. 3.

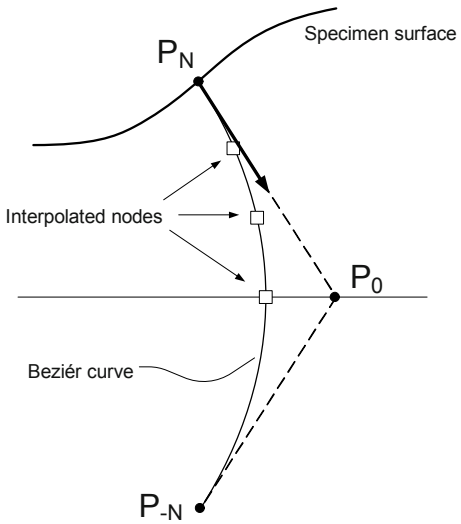

Figure 3: Scheme for the nodal coordinates interpolation along the thickness.

Fig. 4 shows the obtained results, three elements are used along the thickness. On the left is illustrated the undeformed configuration, on the right the deformed configuration at the final time step. In the visualization, a cut allows to observe the strain concentration that occurs at the center of the specimen, obtained thanks to the adopted interpolation along the thickness.

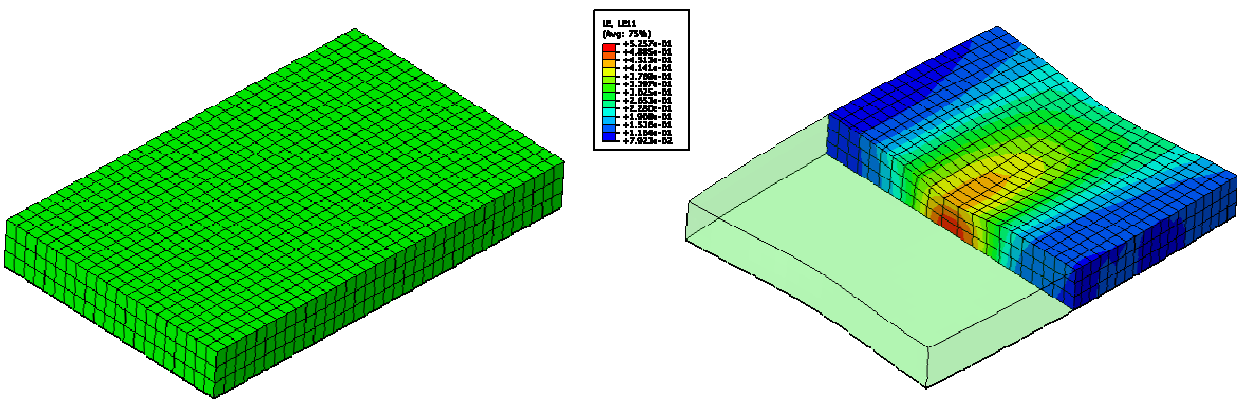

Figure 4: undeformed and deformed 3D mesh obtained using a post-elaboration of the experimental surface data.

THEORETIC MODELS

The identification is based on the Virtual Fields Method for non-linear materials [13], a brief description is given below. The principle of virtual work, for a solid of any shape of volume *V* and boundary surface ∂V , in the case of small perturbations and absence of body forces, can be written as:

$$\int_V \boldsymbol{\sigma} : \boldsymbol{\varepsilon}^* dV = \int_{\partial V} \mathbf{F} \cdot \mathbf{u}^* dS \tag{2}$$

where **σ** is the stress tensor, **F** the forces acting at the boundary, **u*** a kinematically admissible virtual field and **ε*** the correspondent virtual strain field. The first term of Equation 2 represents the virtual work of the internal forces W_i and the second term represents the virtual work of the external forces W_e. The virtual displacement can be chosen in such way that the only external forces involved are the global loads measured by the load cells of the experimental equipment.

The stress field is computed from the reconstructed strain field using a constitutive relation the will depend on a set of parameters **P** that are the unknowns to be identified. The best set of parameters is identified by a minimization of the cost function Φ:

$$\Phi(\mathbf{P}) = \sum_{j=1}^{n} \sqrt{\left(w_e^j - w_i^j \right)^2} \tag{3}$$

.

The passage from the strain to the stress field is a crucial point for the correct identification of the material parameters. The elastic part of the strain tensor is neglected, it is assumed that the measured strain is only the plastic one. This hypothesis is valid only for large strains when the plastic flow is completely developed.

The Hill48 anisotropic model [17], reduced to the normal anisotropy, was employed to achieve the stresses. The yielding locus *F* for a general stress state is written respect to an equivalent stress σ_{eq}:

$$F(\boldsymbol{\sigma}) = \left[f(\sigma_y - \sigma_z)^2 + g(\sigma_z - \sigma_x)^2 + h(\sigma_x - \sigma_y)^2 + l\tau_{yz} + m\tau_{zx} + n\tau_{xy} \right] - \sigma_{eq}^2 = 0 \tag{4}$$

as occur for the classic Von Mises theory, the hydrostatic part of the stress tensor does not influence the yielding point, then Equation 4 can be rewritten in terms of the deviatoric stress tensor **S**

$$F(\mathbf{S}) = \left[f(S_y - S_z)^2 + g(S_z - S_x)^2 + h(S_x - S_y)^2 + lS_{yz} + mS_{zx} + nS_{xy} \right] - \sigma_{eq}^2 = 0 \tag{5}$$

where:

$$S_{ij} = \sigma_{ij} + \delta_{ij}\sigma_{kk} \tag{6}$$

the equivalent stress depends on the hardening of the material and thus on the amount of plastic deformation reached by the material point. We used a modified power law to describe the hardening behavior:

$$\sigma_{eq} = K(\varepsilon_{eq} + \varepsilon_0)^N \tag{7}$$

where ε_{eq} is the equivalent plastic strain which is a function of the strain history. As mentioned above, only the normal anisotropy was taken into account [18], under this assumptions the parameters of Equation 5 can be rewritten in terms of the Lankford parameter *R* that represents the ratio of the transverse strain to the through thickness strain in a uniaxial tensile test [19], it writes:

$$f = \frac{1}{(1+R)}; g = \frac{1}{(1+R)}; h = \frac{R}{(1+R)}; l = \frac{3}{2}; m = \frac{3}{2}; n = \frac{(1+2R)}{(1+R)}; \tag{8}$$

the increment of the plastic strain at the time increment *dt* is given by:

$$d\boldsymbol{\varepsilon}_p = d\lambda \hat{\mathbf{n}}_\varepsilon \tag{9}$$

where $d\lambda$ is a plastic multiplier and $\hat{\mathbf{n}}_\varepsilon$ is a versor that indicates the direction of the plastic strain. According to the normality rule, the direction of the strain increment is normal to the yielding surface. Analytically, the strain direction is obtained by:

$$\hat{\mathbf{n}}_\varepsilon = \frac{\partial F(\mathbf{S})}{\partial \mathbf{S}} \cdot \left\| \frac{\partial F(\mathbf{S})}{\partial \mathbf{S}} \right\|^{-1} \tag{10}$$

the deviatoric stress tensor can be expressed as well in terms of its direction and the radius *R* of the yielding surface in the yielding point:

$$\mathbf{S} = R\hat{\mathbf{n}}_S \tag{11}$$

the radius *R* is obtained as a function of the equivalent stress by putting Equation 11 in Equation 5, if follows:

$$R = \sigma_{eq} \left[f(n_y - n_z)^2 + g(n_z - n_x)^2 + h(n_x - n_y)^2 + l \cdot n_{yz} + m \cdot n_{zx} + n \cdot n_{xy} \right]^{-1} \tag{12}$$

in the present problem the direction of the strain increment is known since it is known the strain history of the specimen at each time step. By inverting Equation 10 it is possible to obtain the direction of the deviatoric stress vector at each step, the radius *R* is computed using Equation 12 and Equation 7 to achieve the equivalent stress σ_{eq} related to the current amount of equivalent plastic strain, finally the deviatoric stress is computed by Equation 11. It is important to underline that only the deviatoric stress can be determined: because of the incompressibility, only five of the six strain components are independent, indeed the normal components are constrained by the following rule:

$$d\varepsilon_x + d\varepsilon_y + d\varepsilon_z = 0 \tag{13}$$

a similar relation is valid for the normal components of the deviatoric stress, therefore it is possible to invert Equation 10 because there are five unknowns and five independent equations. In order to obtain the stress tensor from the deviatoric stress, the plane stress condition was applied. This assumption is justified by the low thickness of the considered geometry, it follows:

$$\begin{cases} \sigma_x = 2S_x + S_y \\ \sigma_y = S_x + 2S_y \\ \sigma_z = 0 \end{cases} \quad \begin{cases} \tau_{xy} = S_{xy} \\ \tau_{yz} = S_{yz} \\ \tau_{zx} = S_{zx} \end{cases}. \tag{14}$$

Using this approach, the stress field can be derived from the strain field as a function of four unknown K, ε_0, N and *R* respectively, that can be identified by a minimization of function Φ of Equation 3.

PARAMETER IDENTIFICATION

In order to identify the parameters two virtual fields have been chosen and introduced in Equation 2, they are respectively:

$$\mathbf{u}_1^* = \begin{Bmatrix} x \\ 0 \\ 0 \end{Bmatrix} \quad \text{with} \quad \boldsymbol{\varepsilon}_1^* = \begin{bmatrix} 1 & 0 & 0 \\ 0 & 0 & 0 \\ 0 & 0 & 0 \end{bmatrix} \tag{15}$$

and

$$\mathbf{u}_2^* = \begin{Bmatrix} 0 \\ xy(x-L) \\ 0 \end{Bmatrix} \quad \text{with} \quad \boldsymbol{\varepsilon}_2^* = \begin{bmatrix} 0 & y(x-L/2) & 0 \\ y(x-L/2) & x(x-L) & 0 \\ 0 & 0 & 0 \end{bmatrix} \tag{16}$$

the two virtual fields were used to evaluate two cost functions Φ_1 and Φ_2 by Equation 3, then a global cost function was evaluated as a combination of the two:

$$\Phi = k_1\Phi_1 + k_2\Phi_2$$

where k_1 and k_2 are two weighting constants. The cost function was minimized using the Nelder-Mead simplex algorithm implemented in Matlab. The identified parameters are shown in Table 1.

K (MPa)	ε_0	N	R
307.4	0.0112	0.0723	0.59

Table 1: Identified parameters

At this point, a FEM model of the experimental test was run using the identified parameters as input for the constitutive model. In Fig 5 is illustrated a comparison of the force evaluated by the FEM and the one measured by the test and a comparison of the thickness reduction in the two cases.

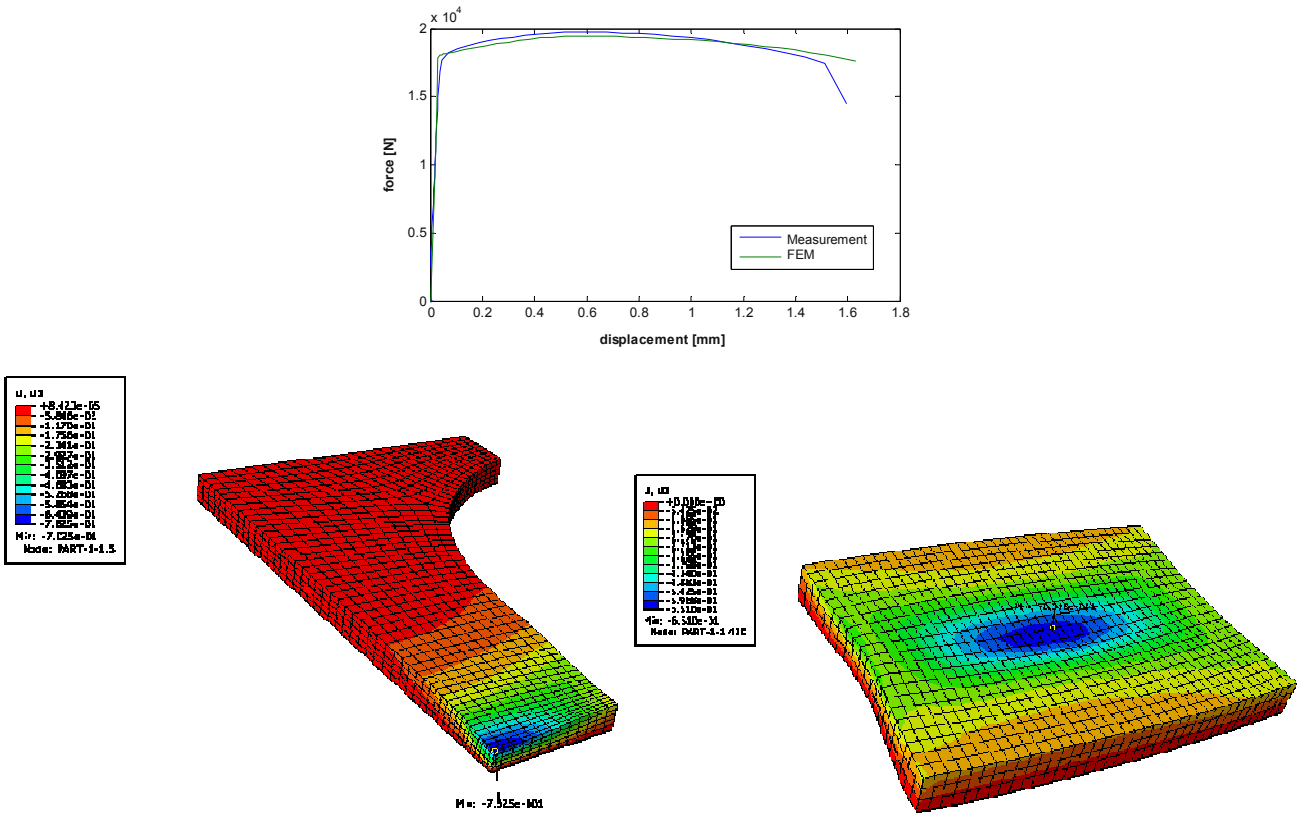

Figure 5: Comparison between FEM and experiments: Force vs Displacement, contour map of the displacement in the thickness direction U_z

The agreement between measurement data and FEM is fairly good. The minimum measured thickness is 2.728 mm while the FEM gives 2.625 mm, the width of the minimum section measures 18.14 mm while a value of 17.91 is obtained by FEM.

CONCLUSION

In this work it is presented a procedure to identify the plastic behavior of a metal using 3D displacement data. A three dimensional strain field is obtained using surface measurements and a non-linear interpolation across the thickness. From the strain field, the stress field is computed and the VFM is applied to identify the parameters of the constitutive equation using two independent virtual fields. In order to assess the effectiveness of the evaluated solution a FE model was built to reproduce the experimental test using the identified parameters as input in the constitutive equation. The global response in terms of force and thickness reduction is satisfying, nevertheless more aspects have still to be evaluated in following works, for instance, the influence of noise, the robustness of the optimization algorithm, the transferability of the results to different geometries.

REFERENCES

[1] Laws V., Derivation of the tensile stress-strain curve from bending data. J Mater Sci 16:1299-1304,1981
[2] Mayville R.A., Finnie I., Uniaxial stress-strain curves from a bending test. Exp Mech 22:197–201,1982
[3] Brunet M., Morestin F., Godereaux S., Nonlinear kinematic hardening identification for anistropic sheet metals with bending-undbending tests. J. Eng. Mater. Technol, 123: 378-383, 2001
[4] Ling Y., Uniaxial true stress-strain after necking. AMP J Technol, 5: 37-48, 1996
[5] Mahnken R., Stein E., The identification of parameters for visco-plastic models via finite-elements methods and gradient methods. Model Simulation Mater Sci Eng 2: 596-616, 1994
[6] Meuwissen M.H.H., Oomens C.W.J., Baaijens F.P.T., Petterson R., Janssen J.D., Determination of the elasto-plastic properties of aluminum using a mixed numerical-experimental method. J Mater Process Technol 75: 204-211, 1998
[7] Okada H., Fukui Y., Kumazawa N., An inverse analysis determining the elastic-plastic stress-strain relationship using nonlinear sensitivities. Comput Model Simulation Eng 4(3): 176-185, 1999
[8] Hoc T., Crépin J., Gélébart L., Zaoui A., A procedure for identifying the plastic behavior of single crystals from the local response of polycrystals. Acta Materialia 51: 5477-5488, 2003
[9] Kajberg J., Lindkvist G, Characterization of materials subjected to large strains by inverse modeling based on in-plane displacement fields. Int J Solids Struct 41: 3439-3459, 2004
[10] Cooreman S., Lecompte D., Sol H., Vantomme J., Debruyne D., Elasto-plastic material parameter identification by inverse methods: Calculation of the sensitivity matrix. Int J Solids STruct 44(13): 4329-4341, 2007
[11] Rossi M., Broggiato G.B., Papalini S., Application of digital image correlation to the study of planar anisotropy of sheet metals at large strains. Meccanica, 43: 185-199, 2008
[12] Grédiac M., Pierron F., Avril S., Toussant E., The virtual fields method for extracting constitutive parameters from full-fields measurements: a review. Strain 42:233-253, 2006
[13] Grédiac M., Pierron F., Applying the virtual field method to the identification of elasto-plastic constitutive parameters. Int. J. Plasticity 22(4): 602-627, 2006
[14] Pannier Y., Avril S., Rotinat R., Pierron F., Identification of elasto-plastic sonstitutive parameters from statically undetermined tests using the virtual fields method. Exp Mech 46(6): 735-755, 2006
[15] Borggiato G.B., Adaptive image correlation technique for full-field strain measurement. In: Proceedings of ICEM 12 – 12th international conference on experimental mechanics, Bari, Italy
[16] Sasso M., Rossi M., Chiappini G., Palmieri G., Sheet metals testing with combined fringe projection and digital image correlation. In: Proceedings of SEM 2009, Albuquerque, New Mexico.
[17] Hill R., A theory of yielding and plastic flow in anisotropic metals. Proc. Roy. Soc. Lond. Ser. A 193: 281-297, 1948
[18] Chakrabarty J., Applied plasticity. Srpinger, New York, Chap 6, 2000
[19] Lankford W.I., Snyder S.C., Bauscher J.A., New criteria for predicting the press performance of deep-drawing sheets, Trans ASM 42:1196-1232, 1950

Proceedings of the SEM Annual Conference
June 7-10, 2010 Indianapolis, Indiana USA

Low Strain Rate Measurements on Explosives Using DIC

Bruce J. Cunningham, cunningham1@llnl.gov
Franco J. Gagliardi, gagliardi7@llnl.gov
Lou Ferranti Jr., ferranti1@llnl.gov

Lawrence Livermore National Laboratory
Energetic Materials Center
P.O. Box 808, L-282, Livermore, CA 94550, USA

Abstract: Digital Image Correlation (DIC) is a technique that has a wide range of applications. At the High Explosives Applications Facility (HEAF), Lawrence Livermore National Laboratory, we are using DIC to perform a variety of strain measurements on plastic bonded explosives (PBXs). Because of the nature of these highly filled polymer composite materials, some conventional strain measurement devices, for example strain gages, cannot be used to measure strain reliably. While there are some drawbacks to DIC, there are also many advantages to this non-contact, optically based measurement system.

We have been successful in using DIC to measure strain in high strain rate experiments involving explosively driven plates. However, in this paper we will focus on our application of DIC to low strain rate measurements. Included in the work to be discussed will be DIC measurements of thermal expansion, Poisson's ratio, strain derived from axial-torsion loading, and tensile creep. For each measurement type we provide some details on the additional hardware required and on the requisite modifications to our existing equipment. Also, in each case we will assess the effectiveness of our approach and, where applicable, compare results to those obtained using more traditional measurement techniques.

Introduction

For more than ten years our group has focused on measuring the mechanical properties of compacted explosives. Aside from safety related concerns associated with the fact that these materials have the capacity to release energy rapidly, our group is interested, primarily, in increasing our understanding of their behavior as structural materials. Measurements that we have performed over the years have included, among others, strain response to uniaxial tensile and compression stress, creep, confined creep, fracture, mechanical response to thermal effects, and so forth. The multi-component nature of these composites, and in some cases constituent behaviors, often result in relatively complex, and in some cases unusual material responses. The polymer components tend to cause the response of these materials to be quite temperature and strain rate dependant. In addition, we have found that the surfaces of these polymer-bound pressed materials are such that strain gages do not adhere well to them, particularly at elevated temperatures. As a consequence, we have a strong interest in new property measurement techniques, especially those that will work well and safely with our somewhat specialized materials. Aside from the measurement capabilities that DIC provides, the fact that it is non-contact and is optically based are significant.

Materials Tested

The materials with which we are primarily concerned are composites, usually consisting of an energetic combined with of one or more polymer binders. In order to maintain high energy densities while at the same time achieving good material strengths, the ratio of binder to explosive generally ranges from about 5 to 15% by weight. Because of the significant property differences between the constituents, the mechanical behaviors of these materials tend to be more than usually complex. Further, these materials are most often highly temperature and strain rate dependant, a consequence largely attributable to the presence of the polymer binder.

T. Proulx (ed.), *Application of Imaging Techniques to Mechanics of Materials and Structures, Volume 4*, Conference Proceedings of the Society for Experimental Mechanics Series 14, DOI 10.1007/978-1-4419-9796-8_5, © The Society for Experimental Mechanics, Inc. 2013

Although we have tested a variety of PBXs, in recent years, our focus has been on a subset of the PBX family known as IHEs (Insensitive High Explosives). IHEs are limited to those PBX's for which the energetic constituent is a material called TATB (1,3,5-triamino-2,4,6-trinitrobenzene). In a world where safety is becoming progressively more important, this energetic's insensitivity to stimuli such as impact, friction electrical spark and elevated temperature make TATB attractive in certain applications, especially weapons. Common examples of TATB-based formulations are LX-17-1 (Livermore's IHE variant, consisting of 7.5% Kel-F 800 binder and 92.5% TATB) and PBX 9502 (Los Alamos's variant, consisting of 5% Kel-F 800 binder and 95% TATB).

Our test specimens are produced in several ways. Cylindrical specimens that we use for compression testing may be produced by coring and finish machining from large billets of material that are formed by heating the material to 105 ˚C and then compacting it hydrostatically, at pressures of 145 – 201 MPa. Alternately, compression cylinders may be individually pressed directly to shape using dies and plungers. Tensile specimens, that have a more complex geometry, are machined from billets or from larger mechanically pressed parts. See Figure 1.

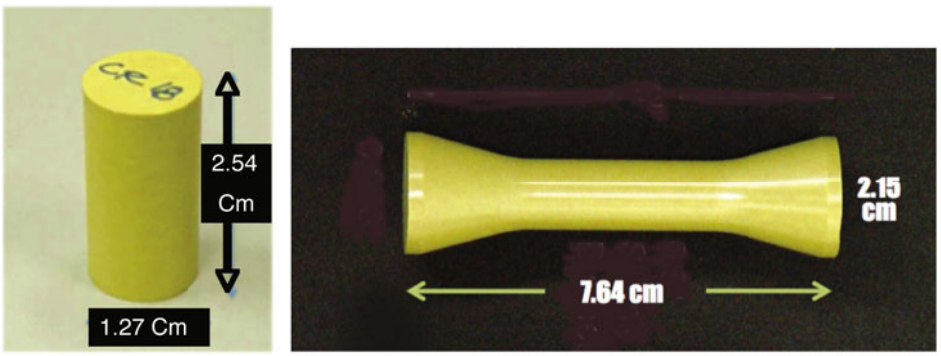

Figure 1 – PBX compression (left) and tension (right) specimens.

Instrumentation

For our low strain rate experiments we have acquired several pieces of DIC related equipment, including Correlated Solutions DIC software, a computer cart with processor, display, and data acquisition hardware, a laptop with software and interfacing, a pair of Point Grey Grasshopper CCD cameras (5 megapixel resolution, with a maximum frame rate of 5 Frames Per Second), a pair of Point Grey Flea CCD cameras, 5 FPS, 35mm and 75 mm C-mount lenses, LED and fiber optic lighting, a tripod and mounting hardware. See Figure 2.

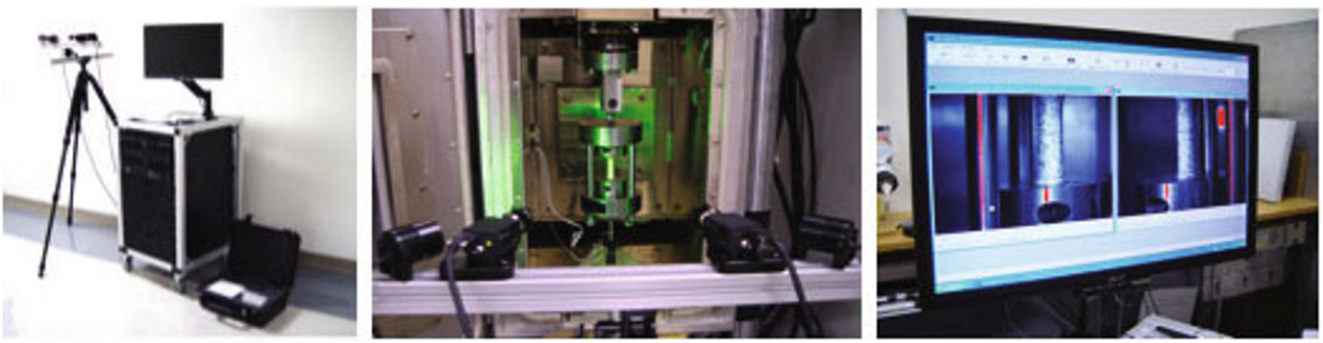

Figure 2 – DIC measurement equipment.

Testing

Thermal Expansion Measurements

Unlike metals, which tend to have coefficients of thermal expansion that are relatively constant over wide ranges of temperature, the IHEs exhibit expansion behaviors that are quite temperature dependant, especially above the Kel-F 800 binder glass transition temperature of approximately 28˚C [1]. Also, this material can be quite anisotropic, depending on how it is compacted. A third complexity is that compactions containing TATB will exhibit permanent growth (called “ratchet growth”) when temperature cycled [2].

Our standard method for measuring thermal expansion in PBXs is through the use of a thermal-mechanical analyzer (TA Instruments TMA model 2940). The temperature range capability of this instrument is approximately -160˚C, up in excess of 400˚C. Complex temperature profiles may be programmed into the instrument’s computer control system and the instrument allows iterative patterns such as temperature cycling. This device allows automated expansion measurement on samples in sizes up to approximately 10 mm in diameter by 10 mm high. Expansion measurements may be performed in one direction at a time.

Alternately, we have been experimenting with DIC as a means to measure thermal expansion on considerably larger parts than our TMA system will allow. In this application, DIC also provides the advantage of allowing expansion measurements to be made in several directions simultaneously. This capability is particularly valuable in the cases where the material in question displays anisotropic expansion behavior. Typically, our interest is in temperatures that lie within a range of about -54 to +74˚C. To perform thermal expansion measurements using DIC, we modified our resistance heated and liquid nitrogen (LN) cooled MTS (Mechanical Test System) environmental chamber by removing the door and replacing it with a 50.8 mm thick insulating foam sheet equipped with a 3 mm thick low-reflection optical window. This window allowed us to focus our pair of DIC cameras on objects situated inside the chamber while controlling the specimen temperature. Through experimentation, we found that increasing the temperature of the chamber up to just above 70˚C worked well and created few problems with our DIC measurements. In decreasing temperatures below 0˚C, however, we began experiencing problems with condensation on the outer surface of the window. In addition, as temperatures decreased further, we found that pulsed LN vapor began to cloud the images, and that ice crystals beginning to form on the specimen surface. Through trial and error, we discovered that the periodic application of warm air to the window, using a heat gun, largely corrected the condensation problem. Ice crystal formation should be reduced significantly by flowing dry inert gas across the face of the sample, or testing in an inert atmosphere. The problem with liquid nitrogen vapor clouding the image was eventually solved by bringing the specimen to the desired low temperature and then shutting the LN off. We then allowed the specimen to warm slowly while we measured the increasing strain. The test setup and example data for measurements made on 25.4 mm diameter by 25.4 mm high cylindrical LX-17 specimens are shown in Figure 3. Note the anisotropic expansion behavior in the sample’s axial and transverse directions.

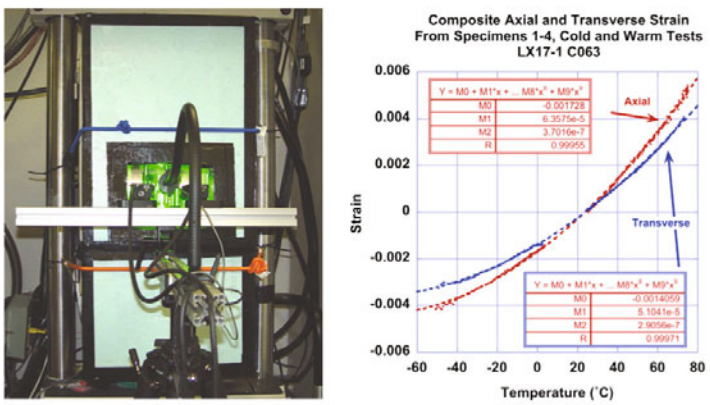

Figure 3 – The MTS test chamber modified for CTE measurements (left) and example expansion data from measurements made on LX-17 (right). Note the anisotropy in the material’s expansion behavior.

Our DIC technique has certain disadvantages when compared to the TMA. The TMA is automated and once programmed, can produce its data with little interference on the part of the operator. Also, data produced by our DIC instrument has a somewhat lower strain resolution than does the TMA. However, in comparing results from measurements made by the two systems when measuring expansion on comparable material samples, their results appear to be quite similar.

Poisson's Ratio Measurements

In the past, we have attempted to measure Poisson's ratio (the ratio of transverse strain to axial strain under conditions of uniaxial stress) on PBX samples. Our previous attempts involved the simultaneous application of axial and transverse extensometers to tensile and compression specimens with cylindrical cross sections. Results from using this method were erratic. This was partly due to the fact that Poisson's ratio is indeed a ratio of two different measurements. This results, inherently, in data with a somewhat larger than usual amount of scatter. In addition, because the materials that we are dealing with are not continuous, but are instead composites containing discrete particles, there is a predisposition to variation in behavior, especially when point-to-point measurements are performed.

In this application, DIC has the advantage of averaging strains over large surface areas and of providing both axial and transverse strain data from the same measurement. None-the-less, because of the problems with scatter we have found that Poisson's ratio measurements from DIC are best determined by performing several redundant tests and then averaging the results. Figure 4 shows Poison's ratio data that was obtained on LX-17-1. Note that the data shown indicates an average initial Poisson's ratio value of approximately -0.43, but that the absolute value of the Poisson's ratio then increases as the test continues. A value of 0.5 is reached at a level of indicated axial compressive strain of approximately 0.010. Thereafter, it continues to increase with increasing strain, achieving absolute values well in excess of 0.5. The reason for what might at first appear to be a non-physical result is that voids develop within the specimen as this material is deformed. These voids, which are largely the consequence of separation between the binder and energetic crystal surfaces, result in material bulking (that is to say, it's volume increases). Because this is so, under conditions of large strains, Poisson's ratio values can become quite large, as is seen in the data.

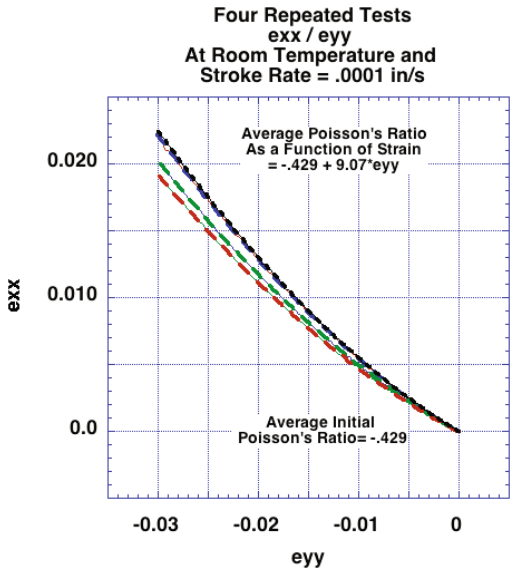

Figure 4 - DIC measured Poisson's ratio for four redundant LX17-1 compression tests. Note that the average initial value is -0.429 but that the absolute value of the ratio increases with increasing axial strain. The value exceeds 0.5 at a compressive strain of around 10,000 microstrain. This is possible because the material bulks due to void formation as material damage accumulates.

Axial-Torsion Testing

For some time, we have been interested in examining the failure behavior of PBXs under conditions of combined loading. We conducted a series of experiments on a plastic bonded explosive identified as LX-14, an energetic consisting of 95.5 % HMX (octahydro-1,3,5,7-tetranitro-1,3,5,7-tetrazocine) and 4.5% Estane binder, by weight. Our earlier experiments, reported in detail at last year's SEM Conference in Albuquerque [3], included roughly 10 experiments on tubular specimens that were subjected to various levels of compressive stress, and then twisted about their axis until failure occurred. We found in these tests that the material failed in tension, or in shear, depending on the level of axial compressive load present. At the time of these tests, we were able to monitor only

the compression load, the applied torque, and the angular rotation. Lacking the means to do so, we were unable to measure shear or other strains on these relatively small samples. With DIC, we have acquired the capacity to monitor strains as they develop on the specimen's surface. Figure 5 shows an image of the experimental setup, along with example strain data that was acquired using the DIC system. From examining the data, we note that there is evidence of non-uniform loading. We have also noted that the strains shown are greater than we had anticipated, prior to testing. Although unconfirmed at this time, we speculate that these higher strains are due to the fact that the loads applied are significant relative to the material's strength and, consequently, the samples are undergoing a significant amount of slow, time-based deformation (creep) as the test is taking place.

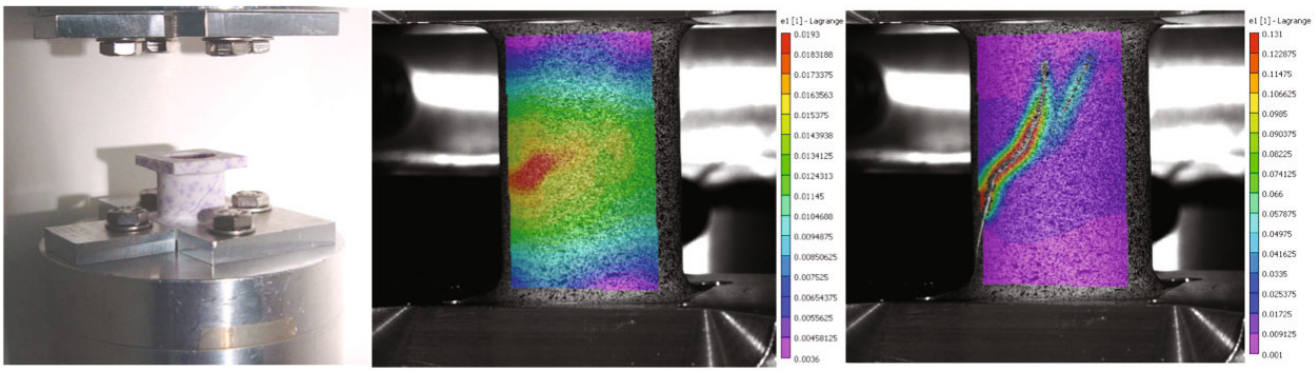

Figure 5 – Experimental setup and DIC principal strain maps from a combined compression and torsion loading test, pre and post failure. Specimen shown at left is an earlier, shorter torsion tube design.

Tensile Creep

In the past, we have performed a great deal of work measuring IHE creep-strain in compression using methods centered around the use of LVDTs (linear variable differential transformers) for long-term creep and recovery strain measurement. We also employ extensometers to measure strain during the brief load application and load removal phases of our tests. We reported on this work in some detail at the SEM conferences in 2008 and 2009 [4,5]. Our methods involved techniques that inferred creep and recovery strains based on the relative motion of the compressive loading platens (the fixture surfaces used to apply load to the cylindrical samples). This method works well in compression, because the entire specimen is being compressed and therefore the compressed region is well defined (it is simply the full length of the test cylinder). For tensile creep, however, our standard specimen is a one-piece, 73 mm long "dog bone" shape, with flared grip-ends. See Figure 1. When gripped by the ends and subjected to a fixed-value tensile load, the material will deform over time until fracture eventually occurs. Unlike the case with the compression sample, where the affected portion of the sample is well defined and where the loading is relatively uniform, this is not the case with our tension tests when using the sample. This is because the elongation that takes place in the sample will occur not only in the constant diameter portion of the specimen, but also, non-uniformly and to an indeterminable extent, within the cone grips as well.

Because of this problem, alternate approaches to tensile creep measurement are required. We are experimenting with DIC as a means to monitor developing tensile creep strain in our specimens. Since creep testing normally takes place over extended time periods, we initially performed some experiments to convince ourselves that the CCD (charge coupled device) sensor portion of the system would be sufficiently stable to give reliable long-term results. These experiments, which included focusing the cameras on a patterned aluminum plate for a period of ten days, indicated to us that the system should indeed be adequately stable, provided care was taken to ensure that relative motion between the cameras resulting from a physical disturbance or from temperature changes, did not occur to any significant extent during the test. It is believed that, while paired camera motion relative to the specimen may, and, in fact, is likely to occur due to "sag" or to temperature fluctuations in the surrounding environment, disturbances of this nature will manifest themselves in what is effectively rigid body motion. Rigid body motion may be removed from the data via software.

Figure 6 shows a composite image of two Flea Point Grey cameras fitted with 35mm lenses and extension tubes, allowing short distance focusing. The cameras are looking through an optical port and are focused at a speckled

tensile specimen that is mounted in our standard tensile test fixture. The fixture resides inside one of our insulated cells, which is temperature controlled to approximately +/- 0.1˚C. In testing, a pre-selected load is applied to the specimen using weights that may be added or removed through use of a remotely controlled support platform. In an initial experiment, we used this system to measure creep strain on an LX-17-1 tensile sample under test conditions of 50˚C and 500 psi stress. The particular combination of load and temperature were chosen to force the sample to fail in a short period of time. The plot shown in Figure 6 is taken from DIC data where the system acquired images at an initial rate of 1 per second for 40 seconds, and switched to 1 image every 2 minutes thereafter. Plotted points are taken from strain averaging over the central region of the specimen. The data shown is reasonable, based on some previous test results that were obtained using estimated effective gage lengths and LVDT measured displacements. DIC provided us with evidence of some problems with non-uniform loading in this test, as well as evidence of the existence of stress concentrations at the base of cones, just below the grip regions of the fixture. This suggested to us a possible need for fixture modification. The DIC measurement technique also allowed post-fracture recovery data to be collected from the shank region of the broken specimen, below the fracture line.

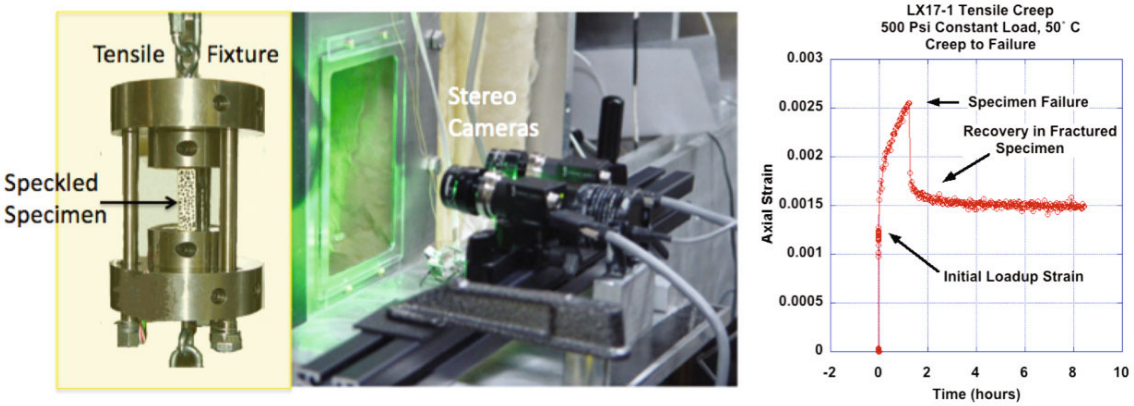

Figure 6 – An illustration of the experimental setup for measuring tensile creep using DIC. Example data from a short-term test where creep resulted in tensile failure is shown at the right. Recovery strain data was measured on a portion of the fractured specimen, post failure.

There is a weakness in this test approach that is shared with many of our DIC strain measurement applications. This weakness is that we are only observing the strain developing at the specimen surface situated at the front of the sample, and that our field of view is limited to less than half of the samples strained area of interest. With the data being acquired in this manner, we cannot average strains from regions symmetrically situated about the sample, and therefore we are unable to compensate for non-uniform sample loading. This is a significant disadvantage, relative to, for example, paired extensometers from which averaged strain data may be extracted. We have been contemplating possible solutions to this particular problem. An obvious solution would be to build test stations that included multiple access ports and additional cameras or camera pairs staged about the sample periphery. This approach would require, among other things, a new test station and changes to our tensile fixture design. Alternately, a system, perhaps mirror based, might be used to bring additional views of the specimen's surface forward and into the cameras' field of view, so that several peripheral views of the sample might be recorded simultaneously. Our thoughts on this approach are not well developed at this time but such an approach may be possible.

Summary

We have been quite successful in applying digital image correlation to a variety of low strain rate measurement applications. DIC is providing us with important new tools and significant improvements in our ability to acquire mechanical property data on plastic bonded explosives. While this technique has some limitations, it is our expectation that, in the future, we will dedicate a substantial portion of our time to improving our knowledge and to expanding our use of this important data-generating capability.

Acknowledgments

We wish to acknowledge the contributions made by Hank Andreski in the area of instrumentation and data acquisition, and to recognize Lisa Lauderbach and Jeff Wardell for their contributions in the area of hardware fabrication and implementation. We also wish to acknowledge Heidi Turner for her thermal expansion measurements on the TMA. This work was performed under the auspices of the U.S. Department of Energy by Lawrence Livermore National Laboratory under Contract DE-AC52-07NA27344.

REFERENCES

[1] Rizzo, H. F.. and Kolb, J. R., .,"Growth of 1,3,5-Triamino 2,4,6Trinitrobenzene (TATB). II. Control of Growth by Use of High Tg Polymeric Binders", UCRL 52662, March 7, 1979.

[2} Cunningham, B. J., Weese, R., Lewis, Harwood, P. and Tran, T. "CTE and Ratchet growth Measurements on LX-17-1 and Constituents", 24th Aging Conference, B.W. Pantex Amarillo, Texas, May 2002.

[3] Gagliardi, F. J., and Cunningham, B. J., "Axial Torsion Testing of Plastic Bonded Explosives to Failure", Annual Experimental Mechanics (SEM) Conference, Albuquerque, New Mexico, June 2-4, 2009.

[4] Gagliardi, F. J., and Cunningham, B. J., "Creep Testing Plastic Bonded Explosives in Uniaxial Compression", SEM 10th Annual International Conference on Experimental and Applied Mechanics, Orlando, Florida, June 2-5, 2008.

[5] Cunningham, B. J., and Gagliardi, F. J., "Confined Creep Testing on Plastic Bonded Explosives", SEM Annual Conference on Experimental Mechanics, , Albuquerque, New Mexico, June 2-4, 2009.

Proceedings of the SEM Annual Conference
June 7-10, 2010 Indianapolis, Indiana USA

Investigation on failure mechanisms of composite structures subjected to 3D state of stresses

D. Leveque, F. Laurin, A. Mavel and N. Carrere
ONERA
Composite Structures and Materials Department
BP72 – 29 avenue de la Division Leclerc – FR-92322 Chatillon Cedex
David.Leveque@onera.fr

J.-M. Laborie, E. Goncalves-Novo and S. Mahdi
AIRBUS Operations SAS
316, route de Bayonne – FR-31060 Toulouse Cedex 9

ABSTRACT

In this project, in cooperation with Airbus-France, an innovative failure approach to predict the rupture of composite structures subjected to complex 3D state of stresses has been proposed [1]. It was first necessary to understand the failure mechanisms occurring in L-angle specimens and to determine intrinsic out-of-plane strengths. The different out-of-plane failure mechanisms in composite laminated structures were identified by an experimental test campaign conducted on composite specimens subjected to different 3D states of stresses with different stacking sequences and thicknesses. This experimental test campaign has been performed on T700GC/M21 material and can be decomposed in three main batches of tests: Four Points Bending (FPB) tests on L-angle specimens, InterLaminar Shear Strength (ILSS) tests on plain laminated coupons, Unfolding Tests (UT) on L-angle specimens to validate the proposed mesoscopic 3D failure criterion. In each case, advanced measurement techniques was used (such as 3D Digital Image Correlation) in addition to standard investigation (strain gauge, LVDT measurements and micrographic analysis) in order to capture the different damage and failure mechanisms occurring during 3D loadings and to validate the FE computation. Due to the complexity of the problem, this study has been performed with a strong connection between experimental data and modeling with finite element analysis.

1. INTRODUCTION

Composite materials are being introduced in primary structures in order to answer to the request of aeronautical companies for lighter, safer and less polluting civil aircrafts. The design of components, such as the centre wing box, the fuselage or the wings, that ensures the structural integrity of the aircraft, necessitates a high degree of confidence into the current strength analysis methods. Composite components containing angles can be found in many locations in current Airbus structures, for example, in the ribs and spars of wings and ailerons, in the centre wing box, in C-profiled floor beams … Moments are applied to these structures that tend to unfold the specimens leading to delamination in the corner radius. This out-of-plane failure mechanism is catastrophic for laminated structures. Thus, the design of composite structures subjected to complex 3D loading still remains a scientific challenge. The aim of this study is to propose a 3D alternative strength analysis method for L-angle specimens subjected to unfolding loading, physically based but matching the requirements of a design office.

This paper deals with the advanced measurement techniques (such as 3D Digital Image Correlation) used in addition to standard investigation (strain gauge and LVDT measurements, micrographic and fractographic analysis) to understand the failure mechanisms occurring in L-angle specimens and to determine intrinsic out-of-plane strengths. Due to the complexity of the problem, a detailed study of the problem has been performed with a strong connection between experimental data and modeling.

The whole experimental work was planned in three main batches of tests:

T. Proulx (ed.), *Application of Imaging Techniques to Mechanics of Materials and Structures, Volume 4*, Conference Proceedings of the Society for Experimental Mechanics Series 14, DOI 10.1007/978-1-4419-9796-8_6, © The Society for Experimental Mechanics, Inc. 2013

- Batch 1: Four Points Bending (FPB) tests on 100/0/0 L-angle specimens have been conducted in order to determine the out-of-plane strength used in the failure criterion. Other tests on L-angles specimens with different thicknesses have been performed in order to extract intrinsic value (independent of the thickness). Moreover, different stacking sequences (50/25/25, 12.5/75/12.5 and 25/50/25) have been studied to determine the influence of the stacking sequence on the through the thickness tensile strength (TTS). Finally, in order to determine the influence of the thickness of the ply on the out-of-plane allowable, additional tests, on specimen with the same total thickness, but different ply thicknesses, have been performed.
- Batch 2: InterLaminar Shear Strength (ILSS) tests on laminates, with different thicknesses and different lay-ups, have been conducted in order to identify an intrinsic out-of-plane shear strength.
- Batch 3: Unfolding Tests (UT) on 100/0/0 L-angle specimens have permitted to validate the new mesoscopic 3D failure criterion for structures subjected to complex 3D loadings. Indeed in these unfolding tests, important out-of-plane tension and out-of-plane shear stresses appear in the radius of corner L-angle specimens. Moreover, other L-angle specimens, with different stacking sequences, have been tested in order to determine the predictive capabilities of the failure approach proposed in this project.

This paper will focus on the identification of the out-of-plane tensile (batch 1) and shear (batch 2) strengths.

2. EXPERIMENTAL WORK

2.1 Specimen details

The experimental test campaign has been performed on a carbon fiber/epoxy matrix T700GC/M21 material (Hexcel Composites), which has been used for current civil and military Airbus aircrafts. This material is considered with two different area weights: 134 g/m² and 268 g/m². This experimental campaign involved the manufacturing of 51 L-angle specimens for the four points bending tests, 42 plate specimens for ILSS tests and 24 L-angle specimens for unfolding tests. On a total of 117 specimens, only 3 specimens are manufactured with an area weight of 134 g/m^2. Some of the specimens are shown at Figure 1 for each different test. In each configuration, 3 specimens are tested for repeatability. In the four points bending test on L-angle specimens, four different symmetric lay-ups, composed with 0°, ±45° and 90° plies are tested in order to cover the whole stacking sequences of L-angle corner used in Airbus-France. In order to study the influence of the total thickness of the specimen on the prediction of the "apparent" out-of-plane strength, three different thicknesses have been chosen for L-angle specimens constituted with 16, 32 or 48 plies.

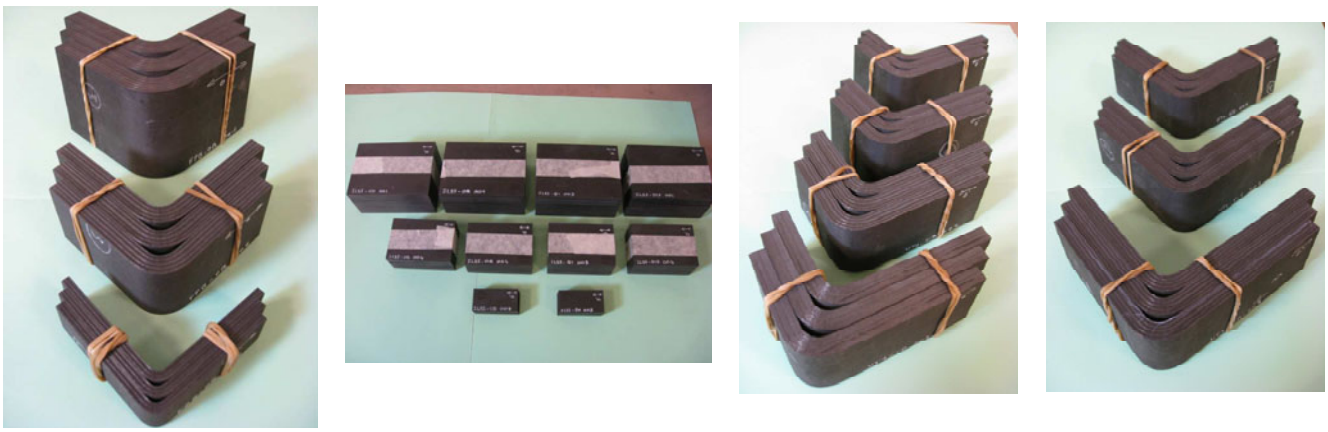

FPB *ILSS* *UT1* *UT2*

Figure 1: View of some manufactured specimens

2.2 Experimental devices

Four points bending tests on 100/0/0 laminate have been planned in order to determine out-of-plane tensile strength σ_{33}^R of the considered composite material. ILSS tests on 100/0/0 laminate have been planned to determine the out-of-plane shear strength τ_{13}^R. Additional four points bending tests and ILSS tests on laminates, with representative stacking sequences used in Airbus-France, have been planned in order to improve the

understanding of the failure mechanism and to propose an innovative 3D failure criterion. Finally, unfolding tests on different laminates have been planned in order to validate the predictions of the onset of delamination for structures subjected to complex 3D loadings. The different test configurations are represented in Figure 2.

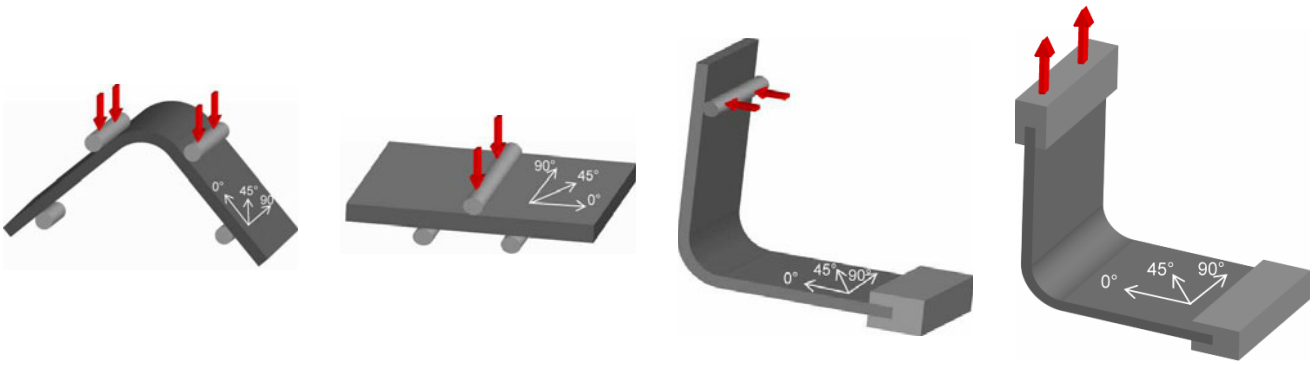

FPB test *ILSS test* *UT1* *UT2*

Figure 2: Different test configurations (0°-ply direction indicated on the specimen)

On each batch of 3 specimens by kind of tests, many measurements techniques are used (not always at the same time but in a complementary manner): LVDT sensor for measuring the deflection under the internal radius of the corner (Figure 3) or under the load span for ILSS tests (Figure 4), 3D Digital Image Correlation (Vic3D system [2]) on one free-edge of the specimen with black and white paint speckle for tracking of the global displacement of the specimen (and comparing it to the LVDT value) and estimation of the out-of-plane strains (Figure 4), longitudinal strain gages bonded on the upper and lower face of the specimen for following the strain in the corner radius (Figure 3), Acoustic Emission for detecting any damage event during the loading (see Figure 4). One specimen is properly polished on a free-edge in order to visualize any defects or damage occurring during the test. By default each specimen free edge is painted in white for global visualization of the damage (see examples at Figures 3 & 4). In each test, the load/machine displacement curve is saved synchronously with the LVDT evolution. For the tests with 3D-DIC and/or strain gages, all the images are stored synchronously with the load and LVDT data. All the specimens are loaded by means of an electromechanical testing machine (Zwick Z150) with a constant cross-head speed of 0.5 mm/min.

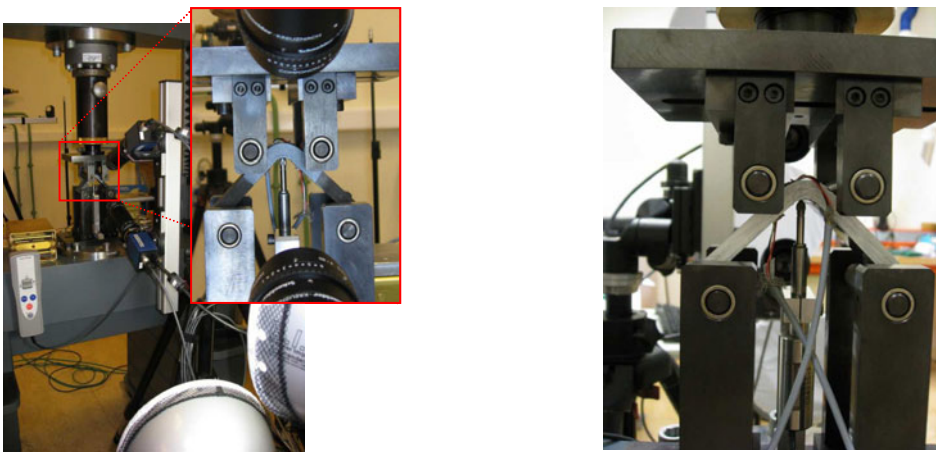

Front view with 3D-DIC measurement *Back view with white painting*

Figure 3: FPB test device with some measurement techniques (LVDT, strain gages and stereo-correlation)

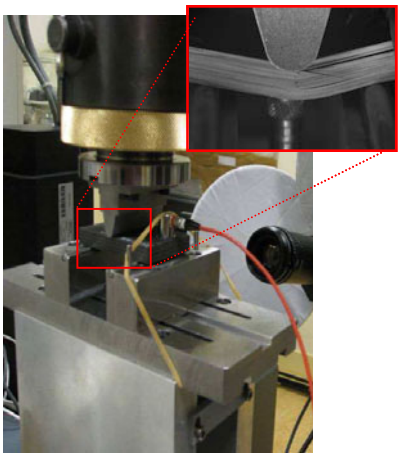

Experimental device for ILSS testing on plain laminated coupons

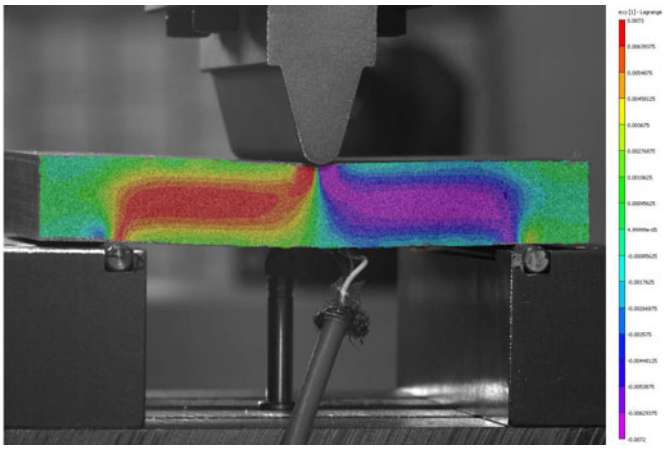

Example of a strain field component (out-of-plane shear) measured by 3D-DIC during ILSS testing on UD laminate

Figure 4: ILSS test device

2.3 Some experimental results on FPB tests

No in-plane damage is detected (no damage evidence by Acoustic Emission tracking) prior the first macro-delamination in the all tested L-angle specimens subjected to four points bending tests except in one case (see below). Considering the maximum load values (load at first crack, i.e. delamination), the mean standard deviation for the three repeated tests is reduced. Moreover, the load/LVDT or testing machine displacements measurements offer a good repeatability between the three repeated tests.

An example of 3D-DIC displacement field measurement is shown at the Figure 5 (U corresponds to the displacement in the loading direction) for a unidirectional (UD) laminate. From this field one can extract a mean value of U in a small zone near the internal radius (discrete points on the load/displacement curve), directly comparable to the displacement measured by the LVDT sensor. In the same manner, we can compare the longitudinal strains measured by the inner/outer gages bonded on the face at a quarter distance of the width from the free-edge and 3D-DIC strains deduced from the displacement field. If the outer responses (face in compression mode) are quite similar, this is not the case for the inner ones. This difference may be due to the position of the inner gage (small radius and effect of bending, even for a small thickness of grid support, modifying the gage response from the real surface to be measured) but also to the position of the zone where the DIC data are extracted (at a small but non negligible distance from the free surface). Of course, it'll be very interesting to compare these data with the results of the FE computations (see next section).

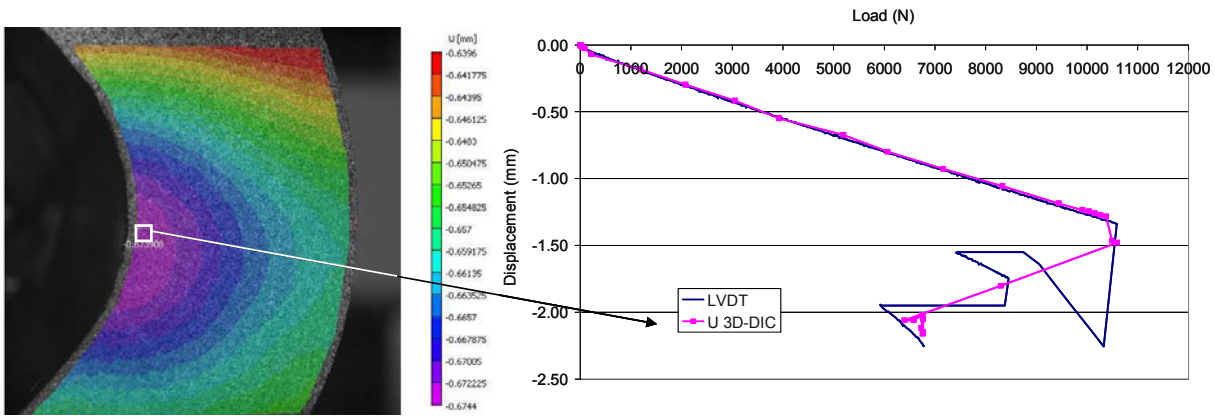

Figure 5: LVDT/3D-DIC displacements comparison for a FPB-UD laminate

The influence of the relative thickness of the plies on out-of-plane strength has been studied by means of FPB tests on quasi-isotropic (QI) laminates with the same intermediate specimen thickness (around 8.4 mm) but four different stacking sequences: $[45_m/90_m/135_m/0_m]_{ns}$ with (m,n) = (4,1), (2,2), (1,4) for the 268 g/m² area weight and (m,n) = (1,8) for the 134 g/m² area weight. It's clear that the relative thickness of the plies impacts the level of load reached at the first crack. For this laminate, the LVDT response and the machine displacement are the same and the results are very similar for the three specimens tested in each configuration. The Figure 6 compares the different load/ LVDT displacement curves for the four different ply-thicknesses. Even if the laminate type and the total thickness are identical, it's quite evident the apparent stiffness cannot be equal considering the specimens are solicited in flexure and, in function of the ply-thickness, the first 0°-ply (making the main flex ure rigidity of the specimen) appears more or less soon in the stacking sequence from the upper surface. It's worth mentioning, independently of a "ply-thickness effect" on the out-of-plane strength, the behavior of the different configurations tested is already different for two reasons. The first one is due to a well-known ply-thickness effect but on the intralaminar damage (i.e. more the ply-thickness is high, sooner transverse cracking will appear) [3,4]. The second reason is due to the manufacture effect due to the use of two different area weights of prepreg tapes: the single-ply thick laminate with the 134 g/m^2 area weight gives a total thickness 6 % smaller than the other QI laminates. The Figure 6 illustrates the ply-thickness effect on intralaminar damage that affects only the fourth-ply thick specimens for which the first damage appearing is transverse cracking in 90° and 45° plies befor e any delamination that is thus adjacent to these first cracks near the lower surface of the specimen, whereas for all the other ply-thicknesses delamination is always the first damage and appears at the same interface around the middle of the laminates.

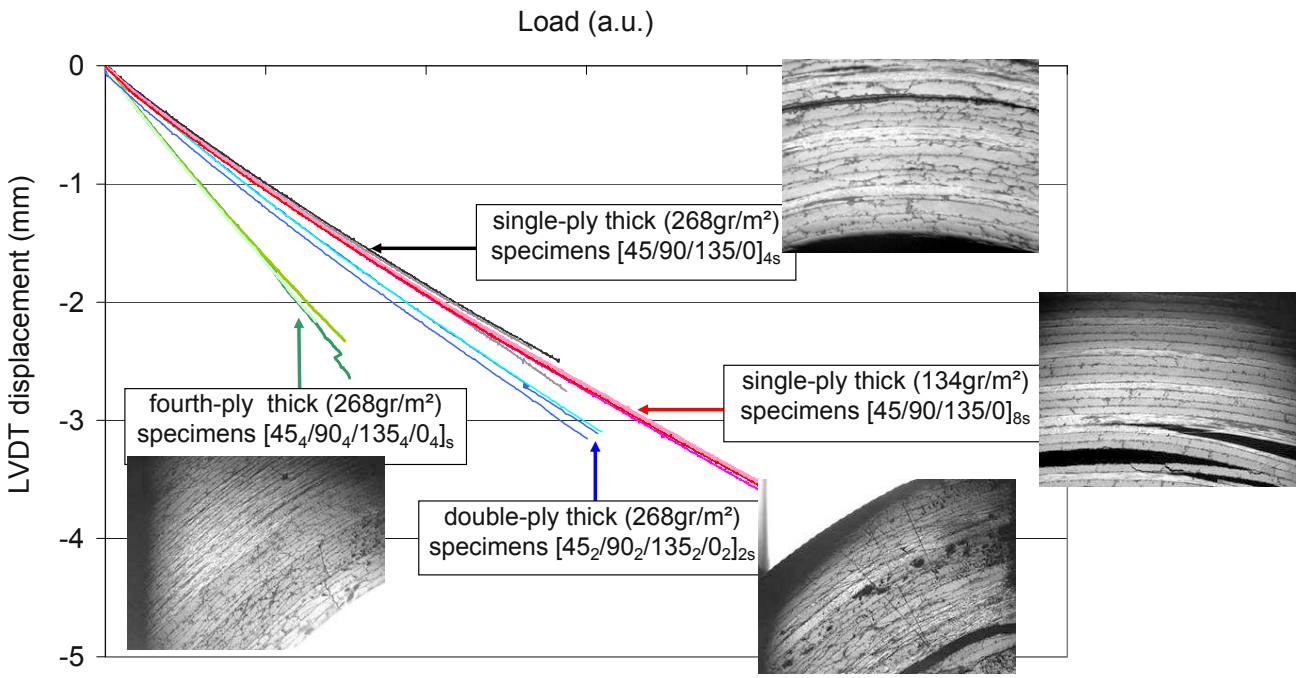

Figure 6: LVDT displacements comparison: effect of ply-thickness on QI specimen's behavior

3. IDENTIFICATION OF THE OUT-OF-PLANE PROPERTIES

3.1 Identification of the out-of-plane tensile strength

Four points bending (FPB) tests on L-angle specimens are currently performed at Airbus to determine the out-of-plane tensile strength. This test is performed on specimens which are representative of some aeronautical components and the determination of the out-of-plane tensile strength depends only on the geometry of the specimen and on the applied loading at failure, in case of the displacement at failure of the structure remains low (< 5 mm) [5]. Finite element (FE) simulations are performed in order to estimate in a correct manner the stress field in the corner radius. These FE simulations have been performed with the code ZeBuLoN (in-house code) in

order to predict the global response of the structure and the final failure of the structure due to delamination in the corner radius. One volume linear element (c3d8) in the thickness of the ply is used. The sizes of the elements are small in the corner radius and under the spans and increases in the legs to reduce the time of computation. This mesh could be important for the thick specimen constituted with 48 plies (around 200,000dof). The UD plies are assumed transversely isotropic with a linear elastic behavior. The elastic properties of the T700GC/M21 UD ply are presented in the Table 1.

E_{11} (MPa)	E_{22} (MPa)	ν_{12}	ν_{23}	G_{12} (MPa)
115000	8400	0.32	0.4	4500

Table 1: Elastic properties on T700GC/M21 (268g/m²) unidirectional ply

Half of the loading spans and of the support spans are meshed with volume linear elements (c3d6). The spans are in steel with the following elastic properties E=210 GPa and ν=0.3. The boundary conditions are reported on Figure 7. The displacement U_y is imposed on the upper faces of the load spans, while the displacement U_y of lower faces of the support spans is fixed. Moreover, three nodes have specific conditions in order to avoid rigid body displacements of the specimens. The contact between the spans and the specimens is taken into account and the friction between the spans and specimen is assumed to be null because of the free rotation of the spans (ball bearing introduced in the experimental device).

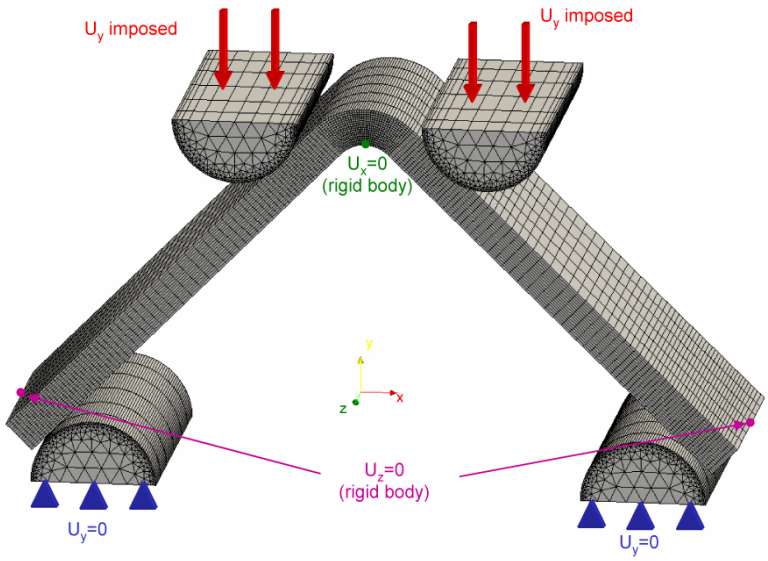

Figure 7: Boundary conditions of the finite element simulations for FPB test on L-angle specimens

The results of the finite element simulations have been compared successfully with different measurements and can be considered as the reference method to predict the stresses state within the corner radius and thus to predict the delamination. For instance, Figure 8 presents the comparison between the predicted strain fields expressed in the global axis and the measured ones on the free-edge of a 100/0/0 thick specimen with digital image correlation (DIC) at 60 % of the failure load. The predicted strain fields are in good agreement with experimental data from a qualitative (shape of the field) and quantitative point of view. The delamination is observed where the out-of-plane normal strain is maximal for this specimen. It is worth mentioning that the predicted load / displacement curve for thick specimens subjected to four points bending tests are in poor agreement with the measurement of the LVDT sensor, probably due to machine compliance effect (this point will be further investigated), while the predicted strains are in good agreement with the measurements of the DIC (Figure 9) and strain gages (Figure 10). On the lower face, the strain gage measures systematically higher values than the ones obtained by DIC.

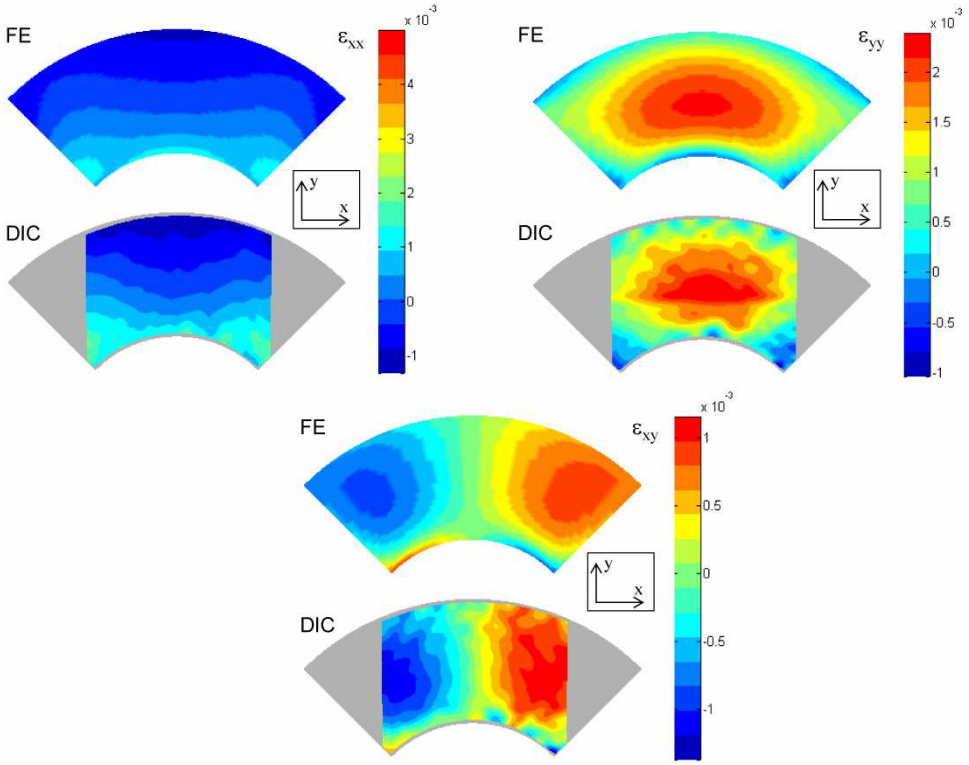

Figure 8: Comparison of the strain fields in the global axis (x,y) measured by 3D-DIC and predicted by FE simulation for a thick 100/0/0 L-angle specimen subjected to FPB test (60 % of failure load)

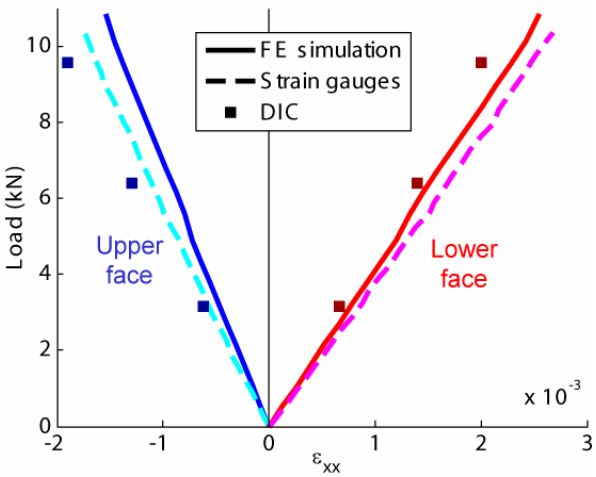

Figure 9: Comparison of the predicted strains on the upper and lower faces with the measured ones for a thick 100/0/0 L-angle specimen subjected to FPB test

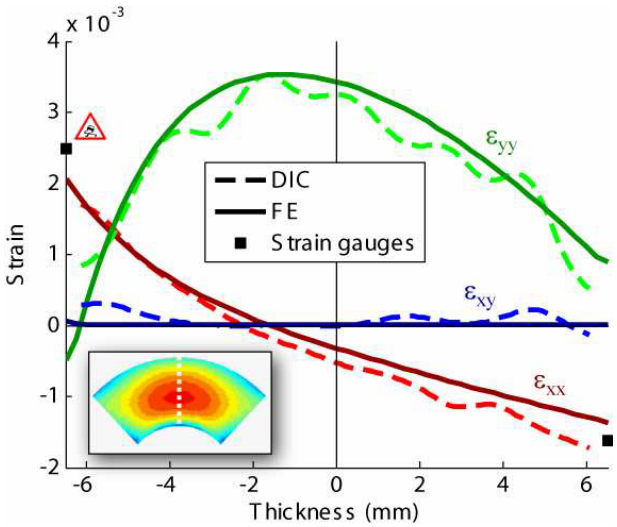

Figure 10: Comparison of the evolution in the thickness of the predicted strains with measured strains for a thick 100/0/0 L-angle specimen (60 % of failure load)

The out-of-plane tensile stresses at failure, determined with finite element simulations on different L-angle specimens subjected to four points loading, are reported in Figure 11. For thin and intermediate specimens, the identified out-of-plane tensile strength seems to be intrinsic to the material because it is independent of the stacking sequences and of the total thickness. Nevertheless, the apparent out-of-plane tensile strength seems to decrease for thick specimens, probably due to a lack of compaction during the manufacturing process of such thick specimens (higher thickness per ply). It is worth mentioning that the results of the intermediate quasi-

isotropic 25/50/25 L-angle specimen are considered as outliners (use of another batch of material). Moreover, the delamination is always observed in the corner radius of the specimens and the localization of the delamination is accurately predicted by finite element simulation, where the out-of-plane stress σ_{33} is maximal, as reported in Figure 12.

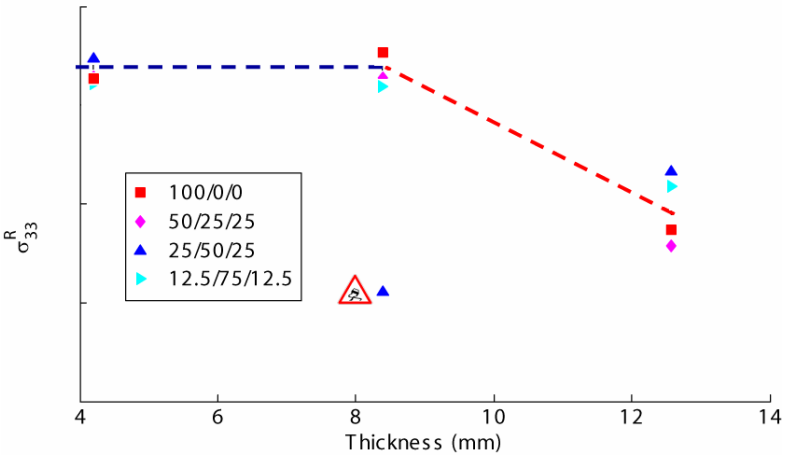

Figure 11: Normalized out-of-plane normal strength determined with FE simulation for L-angle specimens subjected to FPB test

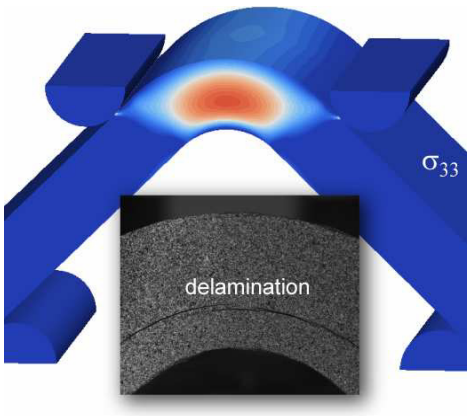

Figure 12: Pattern of delamination observed in thick 100/0/0 L-angle specimen

The influence of the relative thickness of the plies on the out-of-plane tensile strength has been studied by means of four points bending tests on quasi-isotropic 25/50/25 laminates with the same intermediate thickness (around 8.4 mm) but presenting different thicknesses of the plies. Figure 13 shows the determined out-of-plane stress at failure thanks to finite element simulation for the different ply thicknesses. As demonstrated experimentally [3,4,6] for in-plane inter-fiber strengths (transverse tensile strength and in-plane shear strength), the out-of-plane tensile strength seems to be dependent on the thickness of the ply. As proposed in [7,8], a mixed failure criterion is used to predict the evolution of the strength as function of the ply thickness. The main idea consists in assuming that delamination can occur only if the onset of micro-delamination between the plies is reached (modelled with a stress criterion) and if there is enough energy for the coalescence of these micro-cracking (modelled with an energy criterion) leading to the first macroscopic delamination. The proposed mixed failure criterion permits to obtain accurate predictions for the different tested configurations, expect for the thicker plies where in-plane damage is detected prior macro-delamination (see Figure 6).

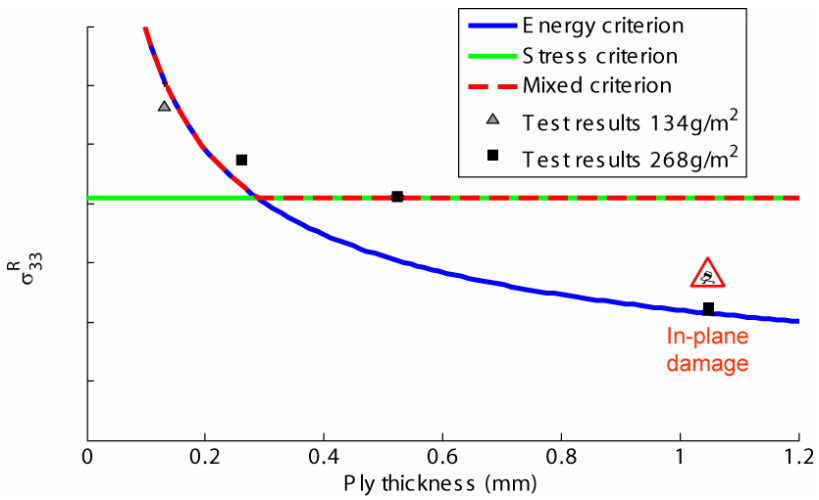

Figure 13: Evolution of the normalized out-of-plane normal stress at failure with finite element simulation for 25/50/25 L-angle specimens subjected to four points bending tests with different ply thicknesses

3.2 Identification of the out-of-plane shear strength

InterLaminar Shear Strength test (ILSS) on 100/0/0 plain laminated coupons are currently performed in Airbus to determine the out-of-plane shear strength τ_{13}^R. The short three points bending test has been chosen because it is rather simple to perform and it has been demonstrated that, by insuring the recommendation of the European norm [9], the determination of the out-of-plane shear strength depends only on the geometry of the specimen and on the applied load at failure. The experimental device is reported in Figure 4. The same four different symmetric lay-ups, as those tested in FPB tests, have been studied with the same three different thicknesses.

The out-of-plane shear stresses τ_{13} at failure, determined with finite element simulations on 100/0/0 specimens presenting three different thicknesses subjected to ILSS test, are reported in Figure 14. The determined out-of-plane shear stress at failure with finite element simulations seems to be quasi-independent to the total thickness. Nevertheless, the analysis of the failure mechanisms for the other lay-ups is very different. The out-of-plane normal stress is negligible in the interest area where the delaminations are initiated. The bands of the out-of-plane shear stress τ_{23} correspond to the location of the delamination, contrary to the bands of the other out-of-plane shear stress τ_{13}. It is also important to notice that, when the out-of-plane shear stress τ_{23} is maximal in the thickness of the specimen, the other out-of-plane shear stress τ_{13} is negligible and reciprocally. Therefore, the failure of multilayered specimens, constituted with 0°, 90° and ±45° plies subjected to ILSS test, cor responds to a pure out-of-plane shear τ_{23} failure mechanism, and can be used to determine the out-of-plane shear strength τ_{23}^R (Figure 15). The out-of-plane shear stress at failure, for a given total thickness, is very similar for the oriented 50/25/25 and the disoriented 12.5/75/12.5 lays-up. Nevertheless, the out-of-plane shear stress at failure for the quasi-isotropic 25/50/25 specimens is always higher than the other laminates. The identified out-of-plane shear stress at failure increases with the total thickness until becoming quasi-constant for intermediate and thick specimens. This “apparent” dependence is probably due to the influence of the indentation of the loading span on the global flexure of the specimen leading to a modification of the determined out-of-plane shear stress at failure by finite element simulation. The influence of the indentation of the loading span on the global flexure of the specimen decreases while the total thickness of the specimen increases.

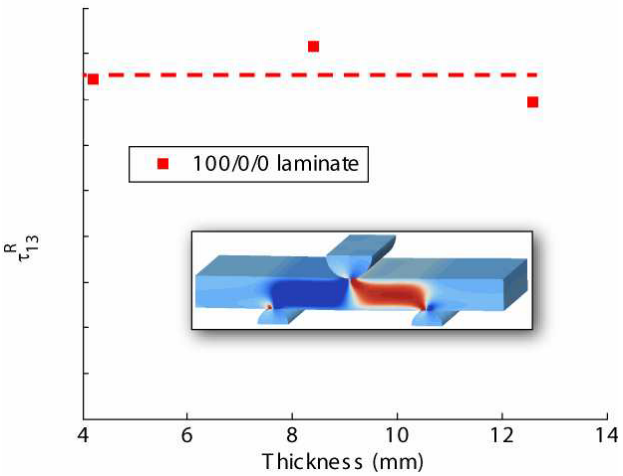

Figure 14: Normalized out-of-plane shear stress at failure (τ_{13}^R) determined with FE simulation for 100/0/0 specimens subjected to ILSS test

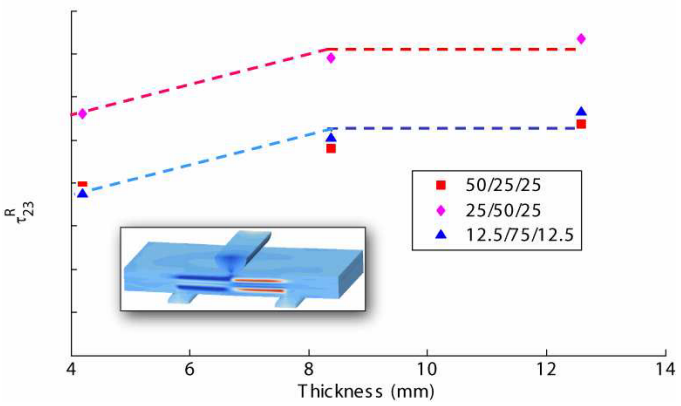

Figure 15: Normalized out-of-plane shear stress at failure (τ_{23}^R) determined with FE simulation for laminated plain specimens subjected to ILSS test

4. CONCLUSIONS AND PERSPECTIVES

In view to propose an innovative failure approach to predict the rupture of composite structures subjected to complex 3D states of stress, an experimental test campaign has been conducted on T700GC/M21 material to understand the failure mechanisms occurring in L-angle specimens and to determine intrinsic out-of-plane strengths. Three kinds of test are under consideration: four points bending tests on L-angle specimens,

interlaminar shear stress tests and unfolding tests on L-angle specimens. For each test, different stacking sequences and thicknesses of the ply have been investigated. For some specimen several advanced measurement techniques have been used (strain gauges and LVDT measurements, 3D Digital Image Correlation, micrographic analysis). All this complementary data have been analyzed via FE computation and analytical models in the frame of this research project.

Four points bending tests on L-angle specimens have been performed in order to identify the out-of-plane tensile strength. It has been demonstrated that this strength is independent of the stacking sequences and of the total thickness of the specimen except for very thick specimens (probably due to a statistical effect on the strength of the loaded interfaces). Moreover, the influence of the ply thickness on this strength has been studied thanks to test on QI specimen presenting the same total thickness but different ply thicknesses. These experimental results seem to demonstrate that the out-of-plane tensile strength is dependent of the thickness of the ply, like the transverse tensile strength and the in-plane shear strength. ILSS tests have also been performed in this project to determine the out-of-plane shear strengths. The ILSS tests performed on 100/0/0 lay-up have permitted to determine the out-of-plane shear strength τ_{13}^{R} and to demonstrate that this strength is quasi-independent to the total thickness. The ILSS tests performed on other lays-up allows identifying the other out-of-plane shear strength τ_{23}^{R} thanks to FE analysis. Finally, the predictions of the strength of L-angle specimens subjected to unfolding tests performed with the proposed failure approach have been compared with the available test results (not discussed here).

Some additional tests have been planned in a next project in order to confirm the influence of the ply thickness on the out-of-plane strengths and to study in details the coupling between the in-plane damage and the out-of-plane strengths.

ACKNOWLEDGMENTS

The authors would like to thank the French Ministry of Defense (DGAC) for the funding of this research project conducted by ONERA and leaded by Airbus France.

REFERENCES

1. Carrere N., Laurin F. and Maire J.-F. "Micromechanical based hybrid mesoscopic 3D approach for non-linear progressive failure analysis of composite structures". *Composites Science and Technology*, accepted, 2009.
2. http://www.correlatedsolutions.com/
3. Nairn J.A., Hu S., Bark J.S., “A critical evaluation of theories for predicting microcracking in composite laminates”. *Journal of Materials Science*, Vol. 28, pp. 5099-5111, 1993.
4. C. Huchette, D. Lévêque, N. Carrère, A multiscale damage model for composite laminate based on numerical and experimental complementary tests, Proc. IUTAM Symposium on *Multiscale modelling of damage and fracture processes in composite materials*, Kazimierz Dolny, Poland, 23-27 Mai 2005.
5. ASTM, "Standard test method for measuring the curved beam strength of a fibre reinforced polymer matrix composite". *Norm D6415/D6415M -06a*, 2006.
6. Chang F.-K. and Chen M.-H. "The In Situ Ply Shear Strength Distributions in Graphite/Epoxy Laminated Composites". *Journal of Composite Materials*, Vol. 21, No. 8, pp. 708-733, 1987.
7. Leguillon D. "Strength or toughness? A criterion for crack onset at a notch". *European Journal of Mechanics - A/Solids*, Vol. 21, No. 1, pp. 61-72, 2002.
8. Huchette C., Lévêque D., Carrère N., "A criterion based on stress and energy for the onset of transverse cracking", *ECCM11*, Rhodes, Greece, May 31-June 3, 2004.
9. DIN, "Détermination de la contrainte de cisaillement interlaminaire apparente - méthode par flexion sur appuis rapprochés". *NormDIN EN 2563*, 1997.

Proceedings of the SEM Annual Conference
June 7-10, 2010 Indianapolis, Indiana USA

Structural damage assessment in fiber reinforced composites using image decomposition

A. S. Patki and E. A. Patterson
Department of Mechanical Engineering, Michigan State University,
2555 Engineering Building, East Lansing, MI-48910

ABSTRACT
Image decomposition techniques such as geometric moment descriptors, Fourier descriptors, wavelet descriptors etc. have been used commercially in the fields of biometrics for finger print, iris matching and face recognition for almost over a decade. Initial test results suggest that these techniques can be used to assess the type and extent of damage in composite panels. The assessment can be performed by comparing the key geometric features in the full-field displacement, strain or stress maps of damaged components with those in the corresponding maps of undamaged components. In this study two shape descriptors viz. Zernike moments and Fourier descriptors will be used to represent full-field maximum principal strain data obtained from digital image correlation for composite specimens with different levels of damage. The advantages and short-comings of these shape descriptors will be discussed together with the possibility of combining Fourier decomposition with Zernike moments to provide a simple index of damage.

INTRODUCTION
In order to effectively decompose full-field strain maps of damaged composite panels, it is essential to identify the appropriate shape descriptors. Geometric and Fourier descriptors are some of the most commonly used shape descriptors in the field of pattern recognition. The first significant account of geometric descriptors was published by Hu [1]. He used a non-linear combination of geometric moments to represent the shape features. He observed that a high order of moments was required for this representation. In order to obtain a unique representation of the shape using low-order geometric moment descriptors Teague [2] introduced Zernike moments which are orthogonal over the domain of a unit circle. These geometric descriptors show invariance to rotation, translation and scaling of the shape feature which make them a versatile tool in the field of shape representation [1, 2]. Since then different moments have been introduced for shape representation and a detailed account of their advantages and disadvantages was published by Teh and Chin [3] in 1988, Prokop and Reeves [4] in 1992 and recently by Zhang [5]. These shape recognition techniques are widely used in the fields of biometrics, medical imagery and topographical recognition and have been recently implemented for mode shape recognition and numerical model updating by Wang et al [6].

Another widely used shape descriptor is the Fourier descriptor evaluated by taking two-dimensional discrete Fourier transforms of images. Fourier descriptors were first introduced by Cosgriff [7] in the 1960's. It was observed that the magnitude of the coefficients of the Fourier transform as well as its phase contained important shape information and could be used as shape descriptors. Fourier descriptors inherit properties such as invariance to geometric transformations and scaling from the theory of Fourier series making them a popular choice for shape description [6].

In this study both the Zernike moment descriptors and Fourier descriptors will be applied to decompose full-field strain maps obtained from damaged composite panels. The motivation behind combining these two widely used shape descriptors will be justified with suitable examples.

T. Proulx (ed.), *Application of Imaging Techniques to Mechanics of Materials and Structures, Volume 4*, Conference Proceedings of the Society for Experimental Mechanics Series 14, DOI 10.1007/978-1-4419-9796-8_7, © The Society for Experimental Mechanics, Inc. 2013

IMAGE DECOMPOSITION

After preparing the images for analysis, different shape description techniques can be applied to condense all the shape information in the image into a set of feature vectors called shape descriptors. These shape descriptors are supposed to have a certain set of desirable properties that qualify them as reliable shape descriptors, i.e.

a) they must be computable efficiently;
b) they should be invariant under rotation, uniform scaling and translation of the map;
c) the shape representation by the descriptors should be unique for each shape; and
d) retrieval of the shape information from the shape descriptors for reconstruction of the image should be easy.

There are many different approaches to shape description and a variety of descriptors have been developed over the years based on template matching, statistical methods, a syntactic approach and artificial neural networks that possess the above properties thus qualifying them as reliable shape descriptors. The concept of shape descriptors is to condense two-dimensional information from surfaces and their boundaries into one or more one-dimensional signals which are more efficient to read and compare. Some common examples of shape descriptors are the centroidal distance function, perimeter of the surface boundary, surface area, circularity of the object, etc. A shape descriptor can be formed from either one of these or a combination of these shape signatures. For representation of full-field strain maps of damaged composite materials three different shape descriptors viz. moment descriptors, Fourier descriptors and wavelet descriptors were selected based on some of their remarkable attributes which will be discussed in further sections.

SPECIMEN, EXPERIMENTAL SETUP AND METHOD

A glass fiber reinforced polymer matrix composite CYCOM® 1004 manufactured by CYTEC Industries Ltd. was used in this study. The composite material was made of nine 0/90° plies containing 5 plies in the primary direction. The thickness of the composite material sheet is 3.5 mm. Tensile tests were carried out on two specimens with dimensions 177.8 mm X 25.4 mm to determine the material properties. One specimen had its principal material direction aligned with the longitudinal direction which was the loading direction while the other was aligned perpendicular to this direction. It was observed that the material properties did not change significantly between the two specimens. Three specimens of dimensions 240 mm X 60 mm were manufactured. One specimen was impacted in a drop-weight testing machine (Dynatup®3500) with enough energy for the tup to penetrate through the specimen leaving it with a central impact hole. The second specimen had a carefully machined hole which was approximately the same size as the hole formed due to impact damage in the first specimen. The third specimen was a virgin specimen without any damage. Aluminum tabs were glued to each side of the composite specimen at the ends to provide a location for gripping the specimen. These metal tabs prevented damage to the composite specimen in the loading grips of the test frame, and provided a uniform and gradual load transfer from the hydraulic grips to the composite specimen. The specimens were spray-painted with a black and white speckle pattern for digital image correlation.

The specimens were loaded in a uniaxial 50,000N MTS servo-hydraulic loading frame. A digital image correlation system *(Q-400 and ISTRA™4D – Dantec Dynamics, Denmark)* was used for recording full-field displacements in the specimens. A single camera was positioned at right angles to the specimen surface to capture images for two-dimensional digital image correlation. Care was taken in obtaining focused and sharp images of the specimen and a ring light was fitted on the camera lens to uniformly illuminate the specimen surface. Images were taken at each load step. Digital image correlation was performed on the captured images to obtain full-field displacement and strain maps. Shape descriptors were evaluated for all three specimens using stand-alone Matlab™ codes developed by the author. Finally the shape descriptors of the full-field strain maps for all three specimens were compared to examine the effectiveness of the proposed image decomposition techniques.

ZERNIKE MOMENTS

Geometric moment descriptors have been proven to be invariant to rotation, scaling and translation; not all of them are orthogonal and some are capable of containing a high degree of redundant information. The orthogonality condition simplifies the reconstruction of the original function using the generated moments by

providing a unique representation. A set of orthogonal complex polynomials, *V* defined over a circular domain of unit radius introduced by Zernike [8] are given as:

$$V_{n,m}(x,y) = V_{n,m}(\rho,\theta) = R_{n,m}e^{im\theta} \tag{1}$$

where, *n* is a non-negative integer which represents the order of the radial polynomial, *m* is an integer subject to the constraint *n*-$|m|$ is even and $|m| \le n$, *(x, y)* are Cartesian coordinates while *(ρ, θ)* are the polar coordinates in the complex plane and $R_{n,m}$ are radial polynomials defined as:

$$R_{n,m}(\rho) = \sum_{s=0}^{\frac{n-|m|}{2}} (-1)^s \frac{(n-s)!}{s!\left(\frac{n+|m|}{2}-2\right)!\left(\frac{n-|m|}{2}+2\right)!}\rho^{n-2s} \tag{2}$$

where, *s* goes from zero to $\frac{n-|m|}{2}$. These radial polynomials satisfy the orthogonal relation [9] i.e. the inner product yields:

$$\left\langle R_{p,q}, R_{n,m}\right\rangle = \int_0^1 R_{p,q}(\rho), R_{n,m}(\rho)\rho d\rho = \frac{1}{2n+2}\delta_{n,p} \tag{3}$$

where, $\delta_{n,p}$ is the kronecker delta which takes the value of zero when n ≠ p and one when n = p. Similarly, using equation (1) and the orthogonal property of the radial polynomials $R_{n,m}$ given by equation (3) we can prove that the Zernike polynomials are orthogonal over the same domain of a unit circle:

$$\left\langle V_{p,q}, V_{n,m}\right\rangle = \frac{\pi}{n+1}\delta_{n,p}\delta_{m,q} \tag{4}$$

The Zernike moment descriptor of an image *I(x, y)* is defined as its projection on the complex orthogonal Zernike polynomial of order *n* and with *m* repetitions and it is given as:

$$Z_{n,m} = \frac{\left\langle I(x,y), V_{n,m}\right\rangle}{\left\langle V_{p,q}, V_{n,m}\right\rangle} \tag{5}$$

Using the result in equation (4) we get:

$$Z_{n,m} = \frac{n+1}{\pi}\iint_{x^2+y^2\le 1} I(x,y)\left[V_{n,m}(x,y)\right]^* dxdy \tag{6}$$

Since the Zernike moments are orthogonal only over a unit circle it is advisable to rewrite equation (6) in polar coordinates over the domain of a unit circle as:

$$Z_{n,m} = \frac{n+1}{\pi}\int_0^{2\pi}\int_0^1 I(\rho,\theta)\left[V_{n,m}(\rho,\theta)\right]^* \rho d\rho d\theta \tag{7}$$

After further simplification the Zernike moments given by equation (7) can be written in terms of real-valued even and odd Zernike polynomials as:

$$Z_{n,m} = \frac{n+1}{\pi}\int_0^{2\pi}\int_0^1 I(\rho,\theta)\,{}^eU_n^m \rho d\rho d\theta - i\left(\frac{n+1}{\pi}\int_0^{2\pi}\int_0^1 I(\rho,\theta)\,{}^oU_n^m \rho d\rho d\theta\right) \tag{8}$$

Where ${}^eU_n^m = R_{n,m}\cos(m\theta)$ are the real valued even Zernike polynomials, and ${}^oU_n^m = R_{n,m}\sin(m\theta)$ are the real valued odd Zernike polynomials which are related to the complex Zernike polynomials by the following relation:

$$V_{n,m} = {}^eU_n^m + i\,{}^oU_n^m \tag{9}$$

Equation (8) is used to decompose a given two-dimensional map, *I(ρ, θ)* into its corresponding Zernike moments, $Z_{n,m}$.

$$Z_{n,m} = {}^{e}Z_{n}^{m} - i\,{}^{o}Z_{n}^{m} \tag{10}$$

One of the requirements for the shape descriptors is its ability to represent the shape uniquely. This means that it should be possible to reconstruct the original image using the shape descriptors. This reconstruction can be performed using:

$$\hat{I}(\rho,\theta) = \sum_{n=0}^{N_{\max}} \sum_{m} R_{n,m} \left[{}^{e}Z_{n}^{m} \cos(m\theta) + {}^{o}Z_{n}^{m} \sin(m\theta) \right] \tag{11}$$

Zernike moments are invariant to rotation, uniform scaling, translation etc. [10] and their ability to uniquely define a given image makes them an ideal choice to represent full-field strain maps obtained from DIC, thermoelasticity and other methods of experimental stress analysis. However Zernike moments are orthogonal only over a circular domain of unit radius. This requirement makes it necessary to map a rectangular image onto a unit circle. This transformation can be easily performed. Zernike moments are sensitive to the geometry of the specimen, e.g. in a specimen with a central hole, the hole acts as a stress concentration and the stresses in the vicinity of the hole form the important feature that needs to be captured by the Zernike moments but the hole is a discontinuity in the shape. The inability of Zernike moments to cope with such discontinuities even with increased maximum order will be illustrated in this section.

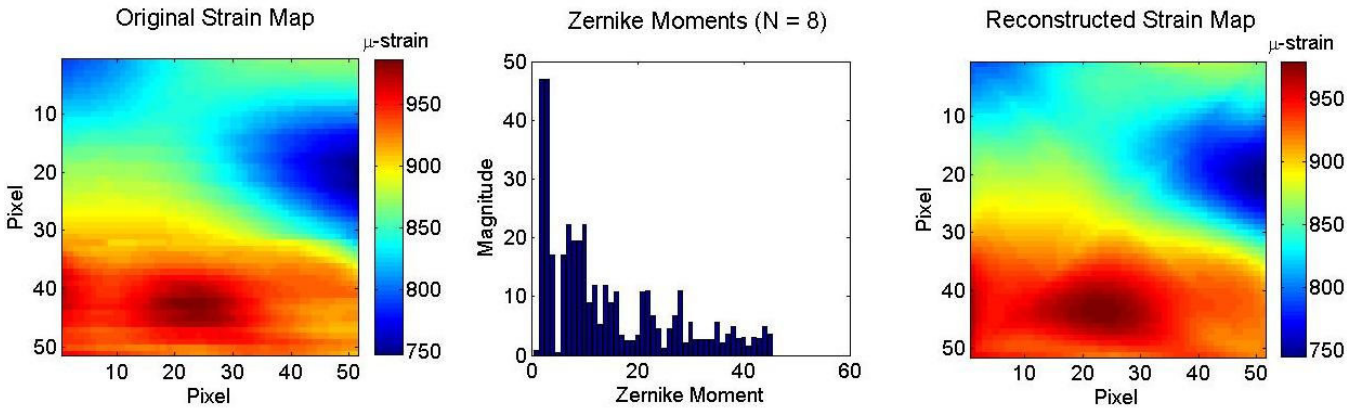

Figure 1: Zernike moments (center) and reconstructed strain map (right) of the original maximum principal strain map obtained from digital image correlation for a virgin composite specimen without any damage.

Figure 1 plots the Zernike moments of the maximum principal strain map for the virgin composite specimen without damage. The maximum order of Zernike moments, N_{max} was 8. It should be noted here that the variation of strain throughout the specimen is less than 200 μ-strain. The reconstructed strain map using the Zernike moments is also plotted in figure 1 and illustrating the ability of Zernike moments to effectively describe this shape the correlation coefficient, ϑ given by equation (12) was evaluated to be unity.

$$\vartheta(\hat{I}, I) = \frac{\iint_{\Omega} (\hat{I} - \bar{\hat{I}})(I - \bar{I}) dA}{\sqrt{\left[\iint_{\Omega} (\hat{I} - \bar{\hat{I}})^2 dA \right] \left[\iint_{\Omega} (I - \bar{I})^2 dA \right]}} \tag{12}$$

where, Ω denotes the internal domain of a unit circle, dA is the infinitesimal area, I is the original image, I is the reconstructed image and

$$\bar{\hat{I}} = \frac{\iint_{\Omega} \hat{I} dA}{\iint_{\Omega} dA} \tag{13}$$

$$\bar{I} = \frac{\iint_{\Omega} I dA}{\iint_{\Omega} dA} \qquad (14)$$

This correlation coefficient provides an indication of the degree of similitude between the original and reconstructed strain maps.

Figure 2.b shows a plot of the Zernike moments for the maximum principal strain map for the composite specimen with a machined hole plotted in Figure 2.a. For this specimen the maximum order of Zernike moments, N_{max} was 20. Two reconstructed images were obtained; one using the first 45 Zernike moments corresponding to N_{max} = 8 plotted in figure 2.c and the other using all the Zernike moments corresponding to N_{max} = 20 plotted in figure 2.d. It can be seen from figure 2.d that even higher order Zernike moments are not capable of accurately representing the sharp discontinuity in the specimen due to the presence of a hole.

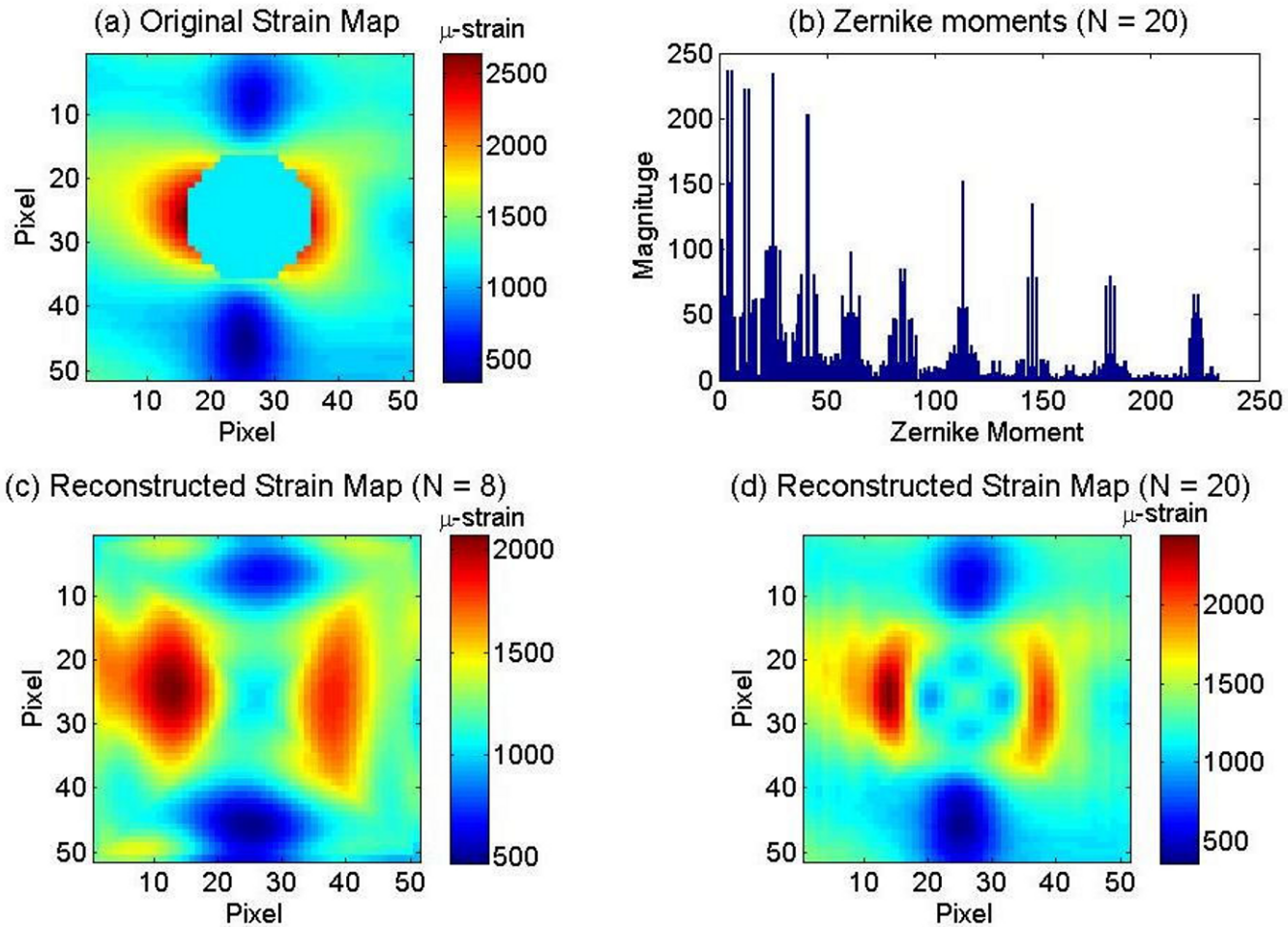

Figure 2: Zernike moments with a maximum order 20 (top right) of the maximum principal strain map obtained from digital image correlation for a composite specimen with machined hole (top left) and the reconstructed strain maps for maximum order of Zernike moments equal to 8 (bottom left) and 20 (bottom right).

The Gram-Schmidt process of arb-Zernike polynomials [10, 11] can be used to eliminate this problem by considering only those polynomials, $V_{n,m}(\rho,\theta)$ that describe the shape in the annular region bounded by the outer

radius of the unit circle and the radius of the hole transformed to the unit circle. This technique requires the identification of the Zernike moments associated with the discontinuity and their elimination from the analysis. This technique can be extended to various geometries, e.g. circular plates with rectangular holes. Though an effective solution, the process can be time consuming and is impractical for composite specimens with irregular, unsymmetrical or unknown damage. In the next section other shape description techniques will be explored to address these shortcomings of Zernike moments.

FOURIER DESCRIPTORS

In general Fourier descriptors are obtained by taking Fourier transforms of a signal, i.e. [12]:

$$D_F(f) = \int_{-\infty}^{\infty} u(t) e^{-i2\pi ft}\, dt \tag{14}$$

In the above case, the signal has the unit of time and the Fourier transform of the signal has the units of frequency, the inverse of time. Equation (14) can be represented in discrete form for computational efficiency as:

$$D_F(\xi) = \sum_{n=0}^{N-1} u(t) e^{-i\frac{2\pi}{N}\xi n} \tag{15}$$

This discrete Fourier transform (DFT) has some useful properties which are relevant to its performance as a good shape descriptor. DFT is invariant in translation while rotation in the spatial domain can be easily accounted for by multiplying each coordinate in the frequency domain with a term $e^{j\alpha}$ where α is the angle of rotation. Scaling of the original signal requires scaling of the DFT with just a simple scalar. The reconstruction of the original signal can be easily obtained by taking an inverse Fourier transform.

The concept of Fourier Descriptors can be extended to two-dimensional images by taking multi-dimensional Fourier transforms. The expression for a two-dimensional discrete Fourier transform is given as [12]:

$$D_F(u,v) = \frac{1}{KL} \sum_{k=0}^{K-1} \sum_{l=0}^{L-1} e^{-i2\pi\left(\frac{\xi k}{K} + \frac{\eta l}{L}\right)} I(k,l) \tag{16}$$

where $\xi=0,\ldots,K-1$, $\eta=0,\ldots,L-1$, (u, v) are coordinates of points in the frequency domain while (k, l) are coordinates of points in the spatial domain. In the case of two-dimensional maps their discrete Fourier transform would have units equal to the reciprocal of the units of area.

The magnitude map of the Fourier transform can be further described using a normalized elliptical vector given by f_{ell},

$$f_{ell} = \begin{Bmatrix} centroid, u \\ centroid, v \\ orientation \\ eccentricity \\ spread \end{Bmatrix} \tag{17}$$

which is constructed from the centroid, orientation, eccentricity and spread of the Fourier descriptors in the frequency domain. A hierarchal clustering algorithm is applied to a set of such elliptical descriptors which based on a predefined threshold segregate the data based on the similarity of the elliptical descriptors [12]. However this technique can prove to be ineffective in case of full-field strain maps of composite specimen due to lack of symmetry and repeatability in the shape. Nevertheless Fourier descriptors are capable of handling discontinuities

in the specimen due to internal geometric features or damage. The possibility of combining discrete Fourier Descriptors with Zernike moments to provide an effective technique of feature recognition will be discussed with results in the next sections.

FOURIER-ZERNIKE DESCRIPTORS

The objective of this study is to perform shape decomposition which is simple to apply as well as interpret. It is easy to decompose a given image with data points of the order of at least 10^3 in terms of only a few hundred Zernike moments which are easy to interpret. However they are incapable of handling sharp discontinuities in the image. On the other hand two-dimensional discrete Fourier transforms provide us with the magnitude of the Fourier coefficients and the phase information both of which can be used as shape descriptors. These Fourier descriptors are of limited value on their own since they are images which are of the same size as the original strain map and hence provide no reduction in the quantity of data. Various techniques have been used to extract useful shape information from these Fourier descriptors [7, 12]; one of which was discussed in the previous section. Many of these shortcomings can be alleviated by combining Fourier transforms and Zernike moments.

The discrete Fourier transform of the strain map for the composite specimen with a hole is a good representation of the original map without any sharp discontinuities. Thus it is proposed that Zernike moments can be obtained for the discrete Fourier transform of the original strain map of the specimen. Since both the Fourier descriptors and the Zernike moments have been demonstrated to have the capability of representing each shape uniquely the Zernike moments of the Fourier descriptor of any strain map should in theory be a unique shape descriptor as well. The Zernike moments of the Fourier descriptor of the shape are named as the Fourier-Zernike moment descriptors. In this case the natural logarithm of the magnitude of the frequency components was used in order to reduce the dynamic range of the Fourier transform that needs to be represented by the Zernike moments.

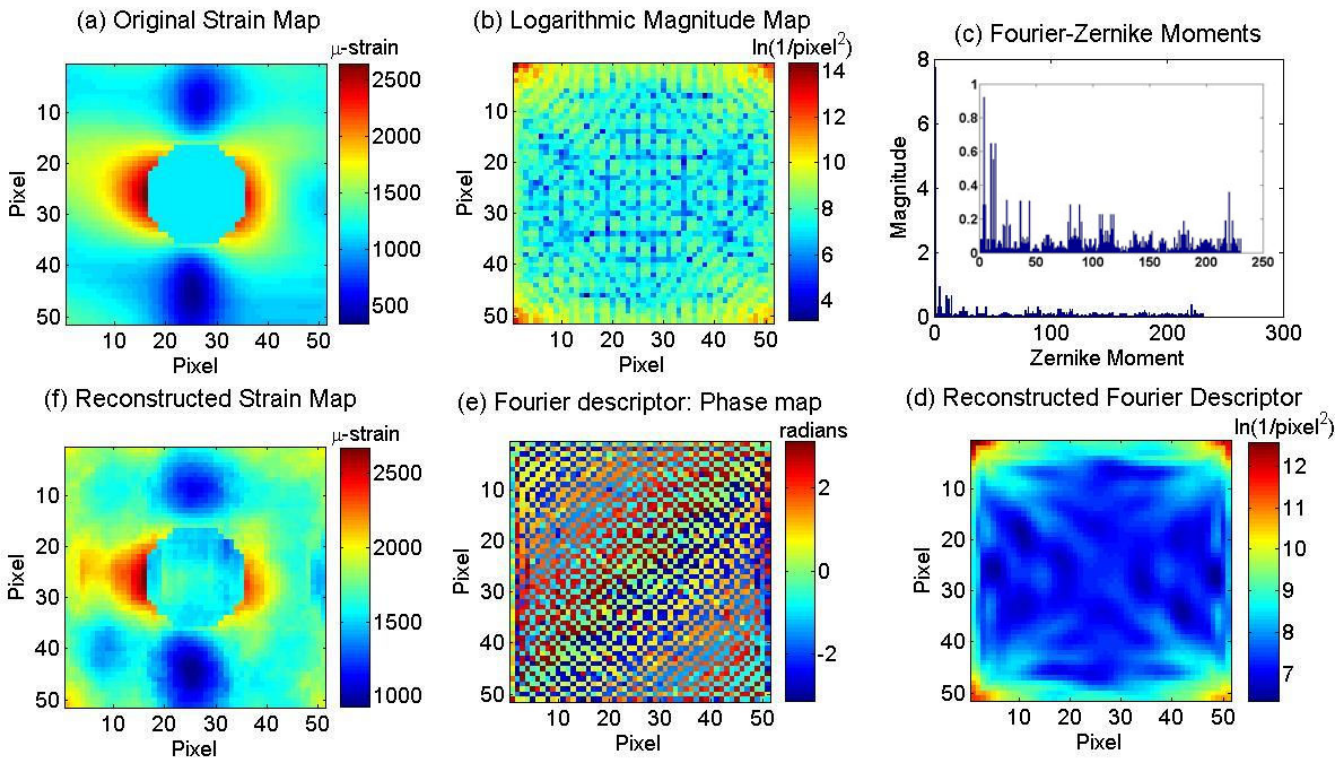

Figure 3: Zernike moments with a maximum order 20 (top right) of the logarithmic magnitude of the frequency component of the discrete Fourier transform (top center) of the original maximum principal strain map obtained from digital image correlation for a composite specimen with a machined hole (top left) and the reconstructed strain map (bottom left) obtained using the reconstructed map of the logarithmic magnitude (bottom right) and original phase map (bottom center) of the frequency component of the discrete Fourier transform.

Figure (3) illustrates results from the method of obtaining Fourier-Zernike moments for the strain map for a composite specimen with a machined hole. First the logarithmic magnitude map shown in figure (3.b) and the wrapped phase data shown in figure (3.e) were found for the strain map in figure (3.a). The Zernike moments were then calculated for the logarithmic magnitude map in figure (3.b) and are plotted in figure (3.c). The inset graphs in figure (3.c) have the lower order moments removed to reveal the detail for the higher order moments. The ability of the Fourier-Zernike moments to uniquely represent the shape of the full-field strain map was verified by attempting to reconstruct the strain map from the corresponding shape descriptors. The Fourier-Zernike moments were used to reconstruct the logarithmic magnitude map plotted in figure (3.d). The reconstructed logarithmic magnitude map and the original wrapped phase data were used to obtain a reconstruction of the strain map plotted in figure (3.f). Comparing the original and reconstructed strain map in figures (3.a) and (3.f) respectively it can be concluded that the Fourier-Zernike moments are capable of uniquely representing full-field strain map and are capable of accounting for the sharp geometric discontinuity in the strain such as in the presence of a hole in the specimen. The closeness of the reconstructed and original strain maps was evaluated in terms of the correlation coefficient, ϑ given by equation (12). The correlation coefficient was calculated to be approximately equal to unity.

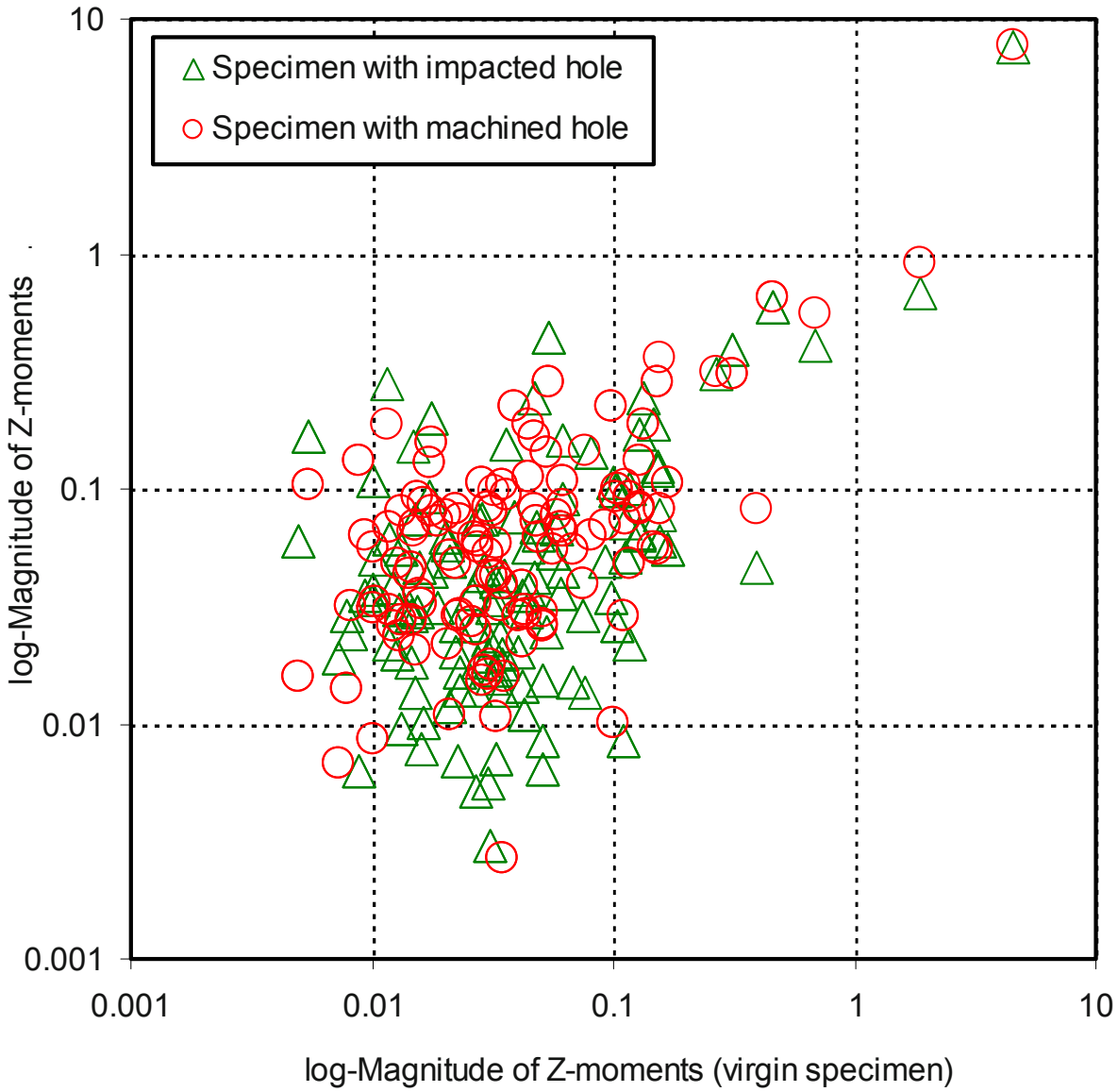

Figure 4: Comparison of Fourier-Zernike moments of the maximum principal strain maps for a composite specimen with a machined hole and a composite specimen with an impacted hole with the maximum order of Zernike moments of N = 20 and plotted as a function of the Fourier-Zernike moments of the maximum principal strain map for a virgin composite specimen.

Fourier-Zernike moments were evaluated for all three specimens. The maximum order of Zernike moments was chosen as 20 giving 231 real valued Zernike moments for each specimen. Once the image was imported into the custom-written Matlab™ code it took approximately 10 minutes to optimize the solution and evaluate the Fourier-Zernike moments for a strain map with a 50 by 50 pixel resolution. To make a comparison, the Fourier-Zernike moments for the two damaged specimens were plotted against those of the virgin specimen on a log-log scale as shown in figure (4). It can be observed from the figure that there is a significant difference between the plots for the composites specimen with a machined hole and that for the composite specimen with an impacted hole. This difference can be attributed to the discrepancy in the strain fields of both the specimen due to the corresponding types of damage mechanisms. The impacted-hole specimen had a considerable amount of delamination surrounding the impact hole while the machined hole was manufactured carefully such that it caused minimal delamination in the composite specimen. Although the graph in figure (4) does not lend itself to quantitative assessment of the differences in the Fourier-Zernike moments of the strain maps for the two composite specimens, it does provide a qualitative comparison.

CONCLUSIONS

A new shape descriptor is introduced which combines the traditional Zernike moments and discrete Fourier transforms. This combined Fourier-Zernike moment descriptor inherits all of the desirable properties of its parent shape descriptors such as rotational, translation and scaling invariance while orthogonal properties of Zernike moments provide unique shape representation capabilities. At the same time the Fourier-Zernike moment descriptors are able to eliminate the shortcomings of both its parent descriptors. The ability of the Fourier-Zernike moments to represent continuous strain maps as well as strain maps with sharp geometric discontinuities and strain raisers with reasonable accuracy has been demonstrated in this paper by testing three composite specimens with different types of damage. These shape descriptors are easy to evaluate with a competitive computational efficiency and more importantly they are comparatively much easier to interpret. All the properties mentioned above make Fourier-Zernike moments an ideal choice to represent full field stress/strain maps of composite panels with unknown level and location of damage. These shape descriptors can also be used for finite element model validation against full-field experimental results. Both of these above mentioned applications of the Fourier-Zernike moment descriptors make them an important tool for damage assessment in the field of experimental mechanics. Future work will concentrate on the decomposition of the phase data of the frequency component of the strain maps and on the development of a quantitative technique for the comparison of different sets of Fourier-Zernike moments.

BIBLIOGRAPHY

1. Hu M K (1962), Visual pattern recognition by moment invariants. *IRE Trans. Inf. Theory*, **IT-8**, 179-187.
2. Teague M R (1980), Image analysis via the general theory of moments. *Optical Society of America*, **70**, 920-930.
3. The C H and Chin R T (1988), On image analysis by the method of moments, *IEEE Transactions on Pattern Analysis and Machine Intelligence*, **10**, 496-513.
4. Prokop R J and Reeves A P (1992), A survey of moment-based techniques for unoccluded object representation and recognition, *Graphical Models Image Processing*, **54**, 438-460.
5. Zhang D and Lu G (2004), Review of shape representation and description techniques, *Pattern Recognition*, **37**, 1-19.
6. Wang W, Mottershead J and Mares C (2009), Mode-shape recognitionand finite element model updating using the Zernike moment descriptors, *Mechanical Systems and Signal Processing*, **23**, 2088-2112.
7. Cosgriff RG (1960), Identification of shape, *Report No. 820-11 of the Ohio State University Research Foundation*.
8. Zernike F (1934), Diffraction theory of the cut procedure and its improved form, the phase contrast method. *Physica 1*, 689.
9. Hew P (1996), Orthogonal functions on the unit disk having invariance in form, *The University of Western Australia*.
10. Mahajan V N (1981), Zernike annular polynomials for imaging systems with annular pupils. *J. Opt. Soc. Am.,* **71(1)**, 75-85.
11. Mallat S (2009), A wavelet tour of signal processing – Sparse Edition. *Elsevier*, New york, USA.
12. Wang W, Mottershead J and Mares C (2009), Vibration mode shape recognition using image processing. *Journal of Sound and Vibration*, **326(3-5)**, 909-938.

Proceedings of the SEM Annual Conference
June 7-10, 2010 Indianapolis, Indiana USA

Finite element Model matching based on optical measurement fields on single shear lap joint

J. S. Dupuy, F. Lachaud, R. Piquet and J. Huet

E-mail address: jean-sebastien-dupuy@isae.fr
Mechanics of structure and Materials Department, ISAE
Clement Ader Institute, University of Toulouse, F-31077 Toulouse, France

Abstract

This paper presents a study of Finite Element Model Matching, based on the use of displacement field measurements. The wealth of information provided by full-field measurement techniques is extremely useful in experimental mechanics, because it is without contact. This study is a three-dimensional mechanical problem. An investigation of the secondary bending on aeronautical structures is presented, especially on the single shear lap joint. First we introduce the optical method and the results of field measurements applied to a tensile test on single-shear lap joint specimen. The experimental technique to determine the displacement field is presented. Afterwards we outline the use of Finite Element Modelling to achieve a correlation between numerical fields and their experimental counterparts. This study is applied to one type of joint; numerical and experimental example is presented: metal/metal lap joints, with one fastener (LGPL type). We describe the matching process. Finally, a parametric study is presented to show the effect of fastener preload clamping and fit clearance between plate hole and shank fastener on the secondary bending.

1. Introduction

Assembling thin walled aircraft structures are often done by means of rivets or shear bolts. Mechanically fastened joints are proven to join metallic and/or composite sheets to the substructure (low transfer joints), quasi mandatory as for as a joint must transfer high inner loads form one thin part to another.

For years, designers have used empirical formulas and experimental macro scale allowables for dimensioning and justification of joint design. A lot of attempts are made today to replace physical tests by numerical tests ([1], [2] and [3]). One target is to come to a better knowledge of joints physical behaviour and parameters effects on their strength.

Several failure modes are observed, governed by many design parameters, manufacturing parameters and of course material parameters. Some of them are due to fastener strength (fastener shear, fastener head bending), most of them to assembled parts strength like net section tension failure, shear out, cleavage, bearing, pull out and fatigue.

A particular phenomenon can be added to these failure modes, the secondary bending (SB) [4], which occurs in structural elements with geometric eccentricities during the loading in tension (Figure 1). Due to these eccentricities, out-of-plane displacements occur leading to local bending. The eccentricities are especially present in single-shear lap joints, but also in plates with increased local thickness. This SB phenomenon is unfavourable for the fatigue properties of a structure [5].

Several investigations on the effect of parameters have been performed, by numerous authors, on fastener type, geometry, stiffness, fit (clearance or interference) and clamping force. Esquillor et al. [6] have studied the several phases of single lap joint behaviour observed during the experimental tests compared with a 3D finite element

T. Proulx (ed.), *Application of Imaging Techniques to Mechanics of Materials and Structures, Volume 4*, Conference Proceedings of the Society for Experimental Mechanics Series 14, DOI 10.1007/978-1-4419-9796-8_8, © The Society for Experimental Mechanics, Inc. 2013

(FE) model, to permit a better understanding of the phenomena. He has underlined a phenomenon which plays a major role on global behaviour and SB curvature: the under-head bending. Studies regarding the influence of different fastener systems and installation parameters, i. e. bolt fit and lateral clamping, were reported by Van der Linden [7]. It was found by J. EKh and al. [8] that the lateral deflection due to tensile loading, in case of two fastener's rows, depends directly on the row spacing. The deformed shapes are similar but a closer study of the curvature reveals that small row spacing tends to generate more severe bending in the plates.

The study presented in this paper relates to a single lap joint described here after. Experiments and a 3D FE model matching have been conducted in parallel in order to study the potential effect of the assembled parts secondary bending on such a joint strength.

Nonlinear finite-element models are developed that predict the SB's deflection of bolted lap joints. Model parameters, such as part discretization, material model selection, sliding interface friction coefficients, and convergence tolerances, are discussed. A better approach for correlation between experimental and numerical tests could allow a good prediction of single lap joint behaviour with threaded or swaged collar fasteners, and to estimate the bearing strength for other cases not mentioned in the MMPDS-01 [9].

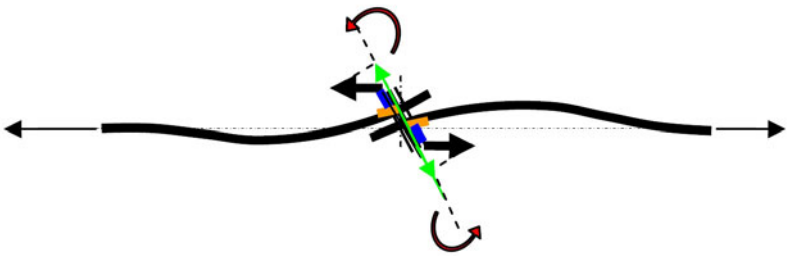

Figure 1 : secondary bending schematic [6]

2. Identification from measurements of mechanical fields

Optical measurement techniques are one of the most appealing methods to estimate two-dimensional displacement fields. Upon loading, the observed surface moves and deforms. By acquiring pictures at different load levels using a Charge-Coupled Device (CCD) camera, it is possible to determine the in-plane and out-of-plane displacement fields by matching different zones of two pictures. The correlation technique used (ARAMIS) is presented.

2.1. Presentation of the method

A method for full field displacement measurement (and strain rate) during a tensile test is introduced on single shear lap joints. The measurements are done by using the ARAMIS three-dimensional image correlation system (GOM Optical Measuring Techniques [10]). The technique relies on 3D image correlation photogrammetric principles providing deformation and full-field strain. This system is based on the digital speckle photography (DSP) technique and allows for contact free measurement. Experimentally, a random pattern with good contrast was applied to the surface of a thin substrate, and the deformation of substrate under load was recorded and evaluated using digital image processing. The principle is to track an applied surface pattern while it is being deformed by taking digital images of the surface at various stages of deformation. Measuring displacements in 3D requires that two cameras are recording the same surface simultaneously. A calibration process permits to establish the precise position of cameras, relative to each other and to the test specimen. Measurement accuracy is affected by several factors, such as the camera positions, lighting variations and stability of the pattern under load. This enables accurate measurements of the deformations in 3D on the specimen surface using photogrammetry.

2.2. Experimental procedure

All specimens were cleaned individually with acetone in order to remove any grease or dust, which could affect the coefficient of friction between plates and to fix the paint. At first, the samples were painted in white on the area to be measured. And afterwards, the specimen was spray-painted using an aerosol can with white mat acrylic paint. The spray button was pressed very gently to produce a high-contrast splash pattern on the area. Therefore, a random speckle pattern was applied on the area to be studied.

Then, the sample was installed in the hydraulic tensile testing machine with hydraulic grips. The ARAMIS 3D system was calibrated and positioned in front of the sample.

During the tensile test, the cameras observe and record the 3D displacement of the bolted area and the corresponding tensile force, at regular time intervals. In addition, the applied tensile force is recorded. The value of the actual force is also assigned to each image pair. Then, the behaviour of the sample during the test can be evaluated and displayed graphically. The deformation of the sample is visible in the captured image series.

In tensile tests of riveted single-shear lap joints, the sample under load starts tilting in z-direction (orthogonal to the plate surface). In this direction, only small displacements are measured.

The specimens are clamped into a static testing machine Instron 8800 series (max 100 kN). Displacement controlled loading at a rate of 1 mm/min was applied. Cross bar displacements, strain gauge measurements and loads were recorded at high frequency and stored in a PC.

Both cameras were positioned to cover as much as possible of the superior plate as indicated in Figure 2 (a). Pictures were taken simultaneously with both cameras at 5 s of intervals. Images were stored on the PC for further post-processing.

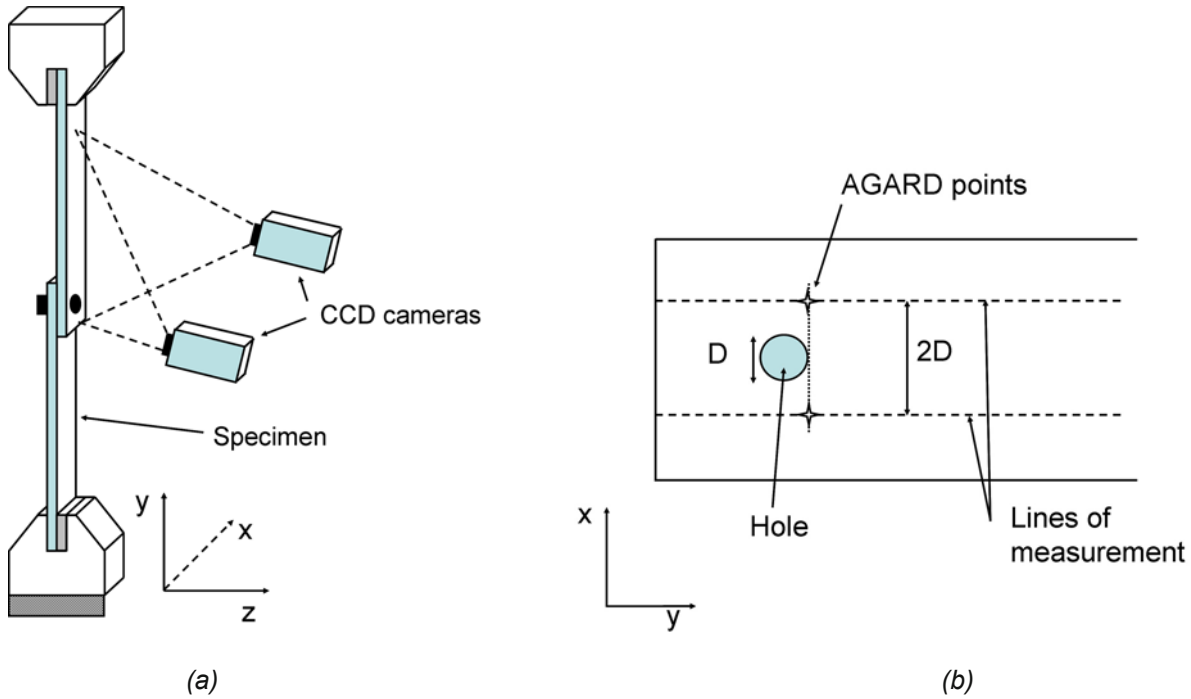

Figure 2 : ARAMIS setup (a) and definition of the lines of z-displacement measurements (b)

The majority of investigations have been experimental; this implies that it is necessary to use a particular standardization for the measurements of the z-displacement. A definition of the location in the transverse direction was proposed [11]; the distance in the transverse direction between the hole center and the point of measurement is equal to the diameter of the hole (shown in Figure 2 (b)). In our case, the measurement was made on the lines passing on the AGARD points and parallel to the edge of the sample, as it's shown on the Figure 2 (b). The Advisory Group for Aerospace Research and Development (AGARD) adopted this definition, as suggested in Ref.[11], in their final report on fatigue rated fastener systems [7]. Investigations by Jarfall [12] showed that the sensitivity of the transverse location was not significant whereas a greater sensitivity could be expected in the longitudinal direction.

2.3. Manufacturing of specimens

Each specimen was assembled from an aluminium alloy 7075-T6 plates using one or two protruding-head fasteners to implement a single overlap joint configuration. The geometry of the plates and the joint configuration

are shown in Figure 3. The fasteners were manufactured from titanium alloy TA6V with a shank diameter of 5/16 inch (7.92 mm), type Lockbolt (LGPL4SP-V). These were installed with a small bolt-hole clearance using swaged-collar in aluminium alloy 2024. The shanks of fasteners are designed in such a way that the part, where the load is applied during the installation, broke off when sufficient pre-load has been applied.

The geometry of the sample, shown in Figure 3, is based on the optional test lap joint specimen configuration of MMPDS-01 [9]. The relatively small thickness was chosen to accentuate three-dimensional effects introduced by the secondary bending, and to be more representative of primary structural joints. And, in order to avoid premature bolt failure and to obtain bearing as the primary mode of failure, a nominal plate thickness of 3 mm was chosen giving a t/D ratio of 0.38, where D equals the nominal diameter of the fastener. The remaining specimen dimensions were derived from this ratio. The grain direction was same for all specimens. Fastener holes were be line drilled perpendicular to the sheet surface with accuracy.

In order to analyse secondary bending and to compare with the finite element (FE) model, the plate was equipped with strain gages as shown in Figure 3.

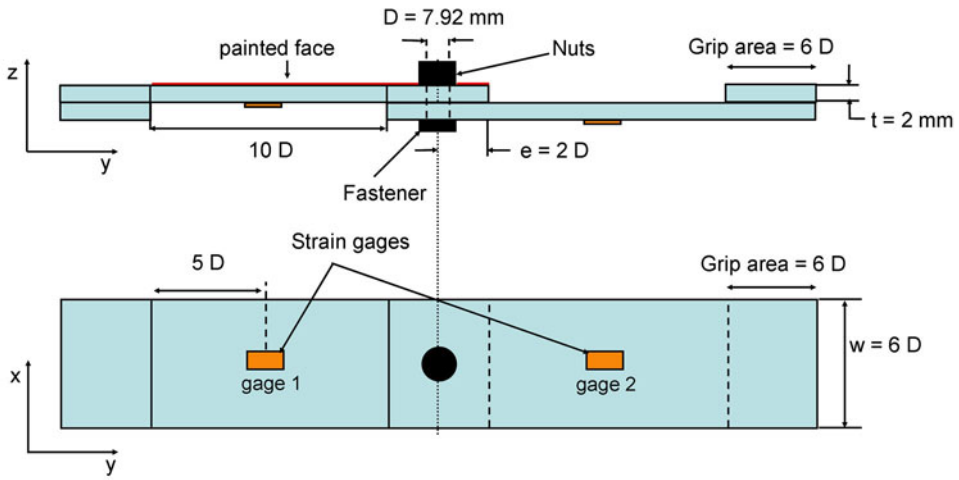

Figure 3 : single-shear lap joint, simple fastener test specimen schematic [9]

2. Finite Elements Analysis

All finite element analyses were achieved with the FE software SAMCEF, version 13.1. The main objective was to process a comparison of the FE model with the experimental results in order to have a predictive model. The study of the curved surface on both sides of the hole implies an orientation of the FEs towards accurate representation of the bending properties. It is found that specimen curvature is equivalent to the secondary bending. Rather than resolving the stresses in the vicinity of the bolt holes, the analysis can be to gear towards the penetration of the fastener's head in the plate during primary bending of the fastener due to the eccentricity of the loading lines.

All physical entities of the real structure are represented in the FE model. Each joint component (i.e., the plates, bolt and nuts) was meshed independently using first order solid elements (with eight-nodes). For the plates, a relatively high mesh density was used in the vicinity of the hole, where high strain gradients exist.

A mesh refinement study was performed, in particular for the effect of mesh size on the curvature of SB, this allowed to reduce errors in the solution. It has been seen that the differences between the models are significant and it was concluded that it is necessary to use a rather fine and regular meshing for the part between the grip area and the fastener. As presented in Figure 4 (a) and (b), two different mesh densities were used in vicinity of the fastener (in the lapped plates) and in the remaining positions. A constant number of six elements is considered in the thickness of plates. This model is chosen as the reference model.

The boundary conditions remain unchanged throughout the analysis. The clamped regions of the sample ends are not considered in the FE models. The sample can be divided in two symmetrical parts from the longitudinal

center line to characterize symmetry boundary conditions for all parts. On one end of sample, the nodes are clamped (displacements in all directions and rotations are blocked) whereas, on the other end, the nodes can move themselves only in longitudinal direction corresponding to direction of load. Each slave node of this end is linked to a master node by rigid elements, to concentrate the load at this point.

In reality, the bolt-hole clearance for the allowable metallic structures is relatively small in aeronautic (less than 0.06 mm), and for this reason, the clearance is considered null in the reference model.

Initially, the fastener head, fastener shank and nut are modelled as one unit with different material properties. The characteristics of materials used for different parts are presented in the Table 1. Metal parts are modelled as isotropic, linear and elastoplastic.

Parts	Materials	Tensile modulus E_T (GPa)	Poisson's ratio	Yield tensile stress F_{ty} (MPa)	Ultimate tensile stress F_{tu} (MPa)
Swaged-collar	Aluminium 2024	71000	0.33	380	480
Shank-fastener	Titanium TA6V	110000	0.31	870	925
Plates	Aluminium 7075 T6	71000	0.33	480	540

Table 1 : material's properties of each part

The preloaded bolt was by specific manner, presented in the Ref.[13]: the bolt is cut perpendicularly to longitudinal axis and a sensor node is introduced between the two parts of the shank. Displacement of this node corresponds to the relative displacement of the two faces. The pre-load of the bolt is introduced by loading this sensor node. The load on the sensor node depends directly upon tightening provided by the fastener manufacturer. Generally, the tightening load is between 40 and 50 percent of the elastic strength of the shank material. The clamping level for the reference model is chosen at 40 percent. The interface between the nut and the shank are not modelled, these are directly joined. In non-linear computation (MECANO) in SAMCEF, it is possible to impose the pre-stress in a first sub-case and to fix the relative displacement for the other sub-cases. The result is shown on the Figure 4 (a).

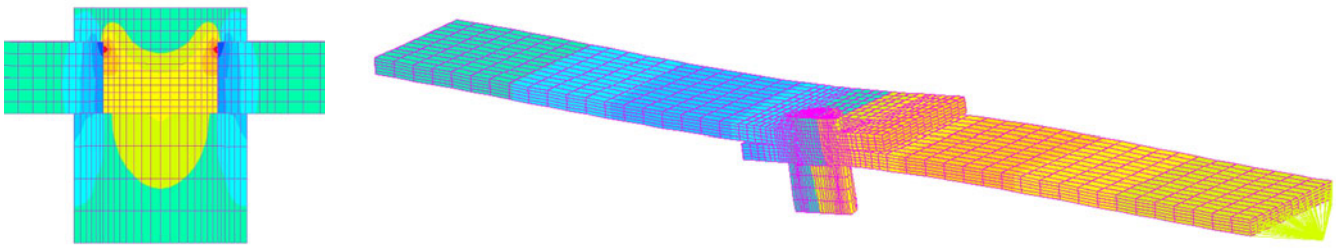

(a) *(b)*

Figure 4 : simulation of bolt preload, stress σ_{33} (a) and secondary bending (z-displacement) on half specimen

For example, in his work, Mc Carthy et al. [5] use orthotropic thermal expansion coefficients on one of the washers. In our study, it is not necessary to introduce a washer between the head of fastener or nut and the plate. The advantage is that no other piece is added on the initial structure, which could modify the analysis.

An important aspect of this work was to model the contact correctly between the different facets. This procedure is conducted by a macro command which writes contact conditions and contact elements between a group of slave facets and a group of master facets. The friction forces are dependent on the normal interaction at each contact surface in the model and are different as a function of materials in contact. We use a Coulomb friction coefficient of 0.15 between the different pieces of FE model. The contact model that allows no penetration of the slave facets into master facets was used to model the normal interaction.

The strain gages are modelled by membrane shell type elements with the same size, positioned on four structure nodes, with zero thickness and weak stiffness, and at correct position along y-axis.

3. Results and discussion

Measured z-displacements (out of plan) from the DSP were collected on measurement lines of the two samples, as indicated in Figure 2 (a). This graph shows an evolution of the z-displacement as a function of the position (y coordinates on the line of measurement upper face of the sample), and represent, in other words, the deflection of SB. In order to enable a better resolution and accurate measurement, the dimension of the considered area are limited (principally along y-axis) to 70x70 mm. By extrapolation, the deflection of SB must be close to 0 for z-displacement at position 0 on y-axis. Raw experimental data from the two measurements are plotted together with the calculated interpolation values for the reference joint configuration in Figure 5 (a). For a same level of load (F≈4500N), the variability between the two tests is low, which permit to represent, accurately, the results using a third order polynomial interpolation with least squares method. Thus, the Figure 5 (a) presents lateral displacements of the top surface of the specimen in vicinity of the bolt as measured experimentally. It is evident that the displacement field varies less transverse direction (x-direction) than in the longitudinal direction (y-direction). This note is in agreement with the work of Jarfall [12]. The Figure 6 (a) reveals that the deflection of the SB along a line through the AGARD points increases with increased applied load. It is easy to localise the position of the fastener on the sample which corresponds to a z-displacement close to 0 and is in correlation with the real position. It should be noted that z-displacement for each curvature remain minimum for the position in y-axis close to 60 mm, and whatever the load level. From z-displacement measurement, we can say that the curvature of SB is maximal in vicinity of y-position 60 mm and is minimal around the fastener.

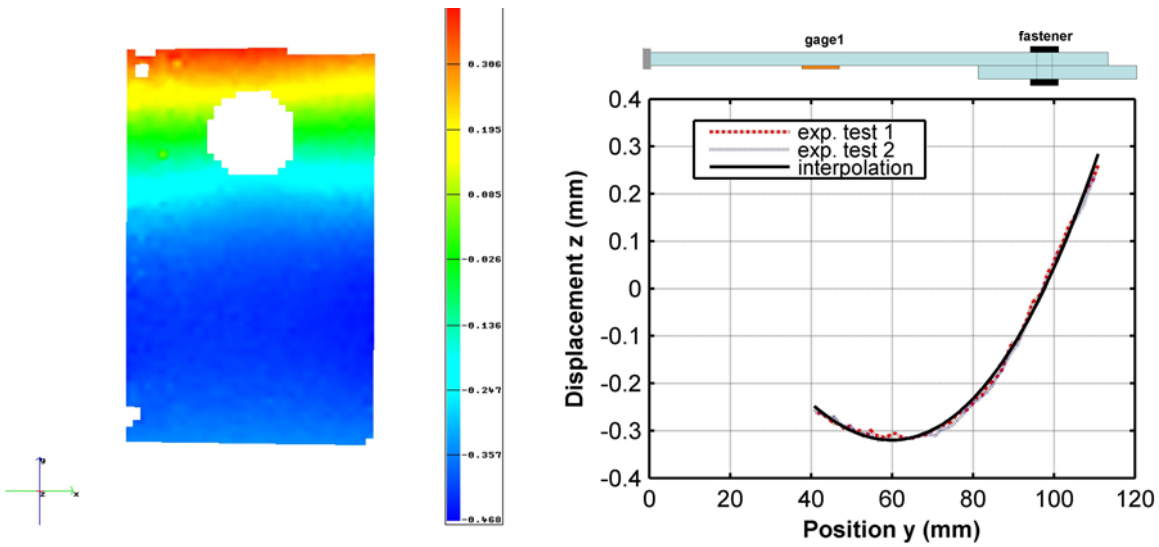

(a) (b)

Figure 5 : (a) z-displacement field on top of the sample in vicinity of the bolt for a load of 8224 N; (b) comparison between two tests: evolution of z-displacement (out of plane) as function of y-position on the specimen for a load of 4500 N

As it is said previously, the mesh fineness is very important out of the overlay zone to represent as faithfully as possible the SB deflection. However, for this model, the convergence is reached and it is not necessary to refine more the mesh. The Figure 6 (b) presents the small effects of meshing on the z-displacement between the reference FE model and a coarser model.

A first comparison is made between experimental and numerical results for a load level approximately 4500 N, as plotted in Figure 7 (a). Values are obtained from the reference FE model and test along the longitudinal line through the AGARD points. First, we notice an apparent difference between experimental and numerical data for z-displacement. Then, by comparing the bending, we remark a slight offset of the minimum displacement, y-position 60 for measurements, and close to the fastener for FE model (at y-position 65). It can be concluded that the model is stiffer than the experiments and this is obviously due to boundary condition hypotheses, for example

the clamping conditions on grip area during the test, the pre-load in the plates exerted by the fastener, or the clearance fit between the hole and the shank of fastener. The graph on the Figure 7 (b) presents the gross stress as function of the numerical and experimental data obtained from two strain gages and shows a significant difference between the two results. This difference confirms that the FE model is slightly stiffer than the real sample.

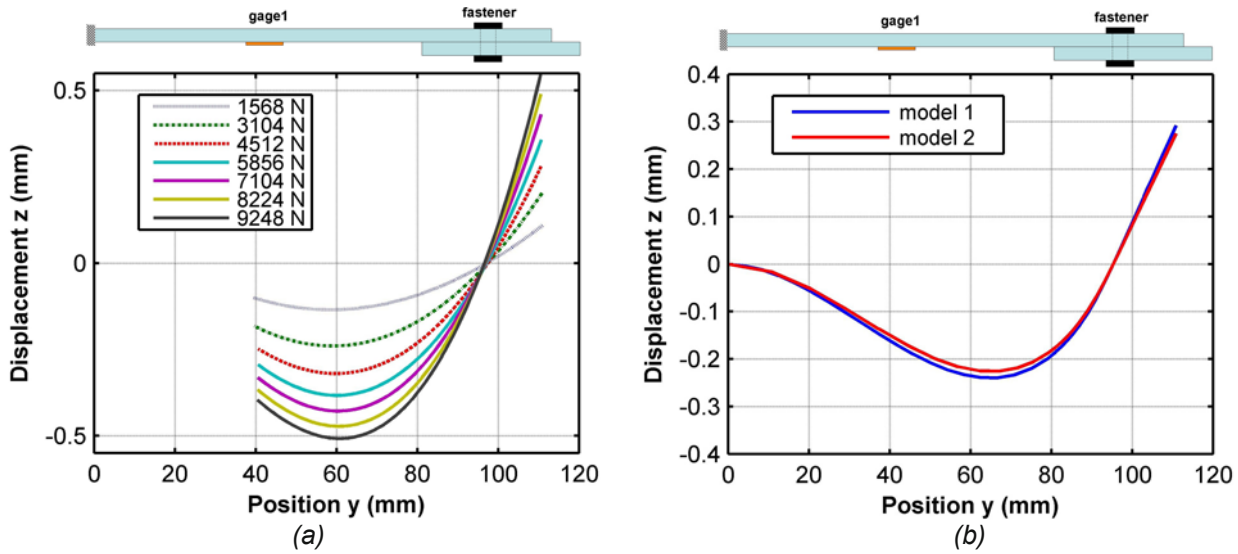

Figure 6 : (a) experimental variation of z-displacement as function of y-position on the sample and the load; (b) comparison between the reference FE model (model 1) and coarser mesh (model 2)

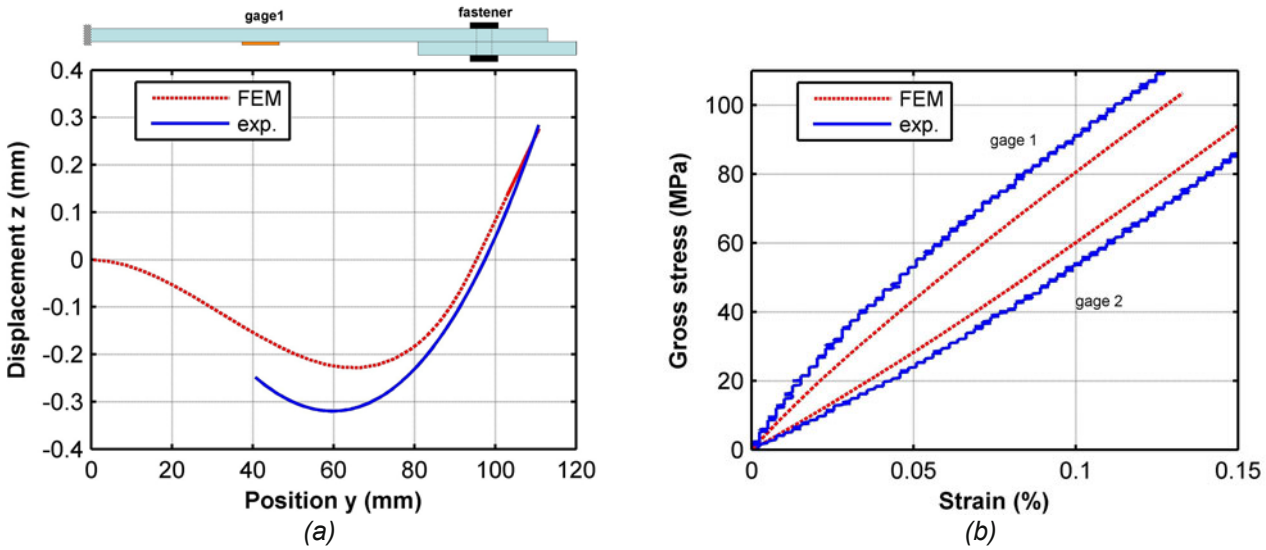

Figure 7 : comparison between numerical and experimental results: (a) SB for a loading F≈4500N and (b) gross stress versus two strain gage results, experimental (blue) and numerical (red)

A parametric study was conducted for the FE model to show the effects of: (i) the clearance fit between the hole and the shank of fastener and (ii) the clamping load exerted by the fastener, on the SB deflection. As shown in Figure 8 (a), the pre-load level applied by the clamping torque of the fastener has less effect on the curvature. In other words, the result is binary and the difference is visible only between the case where the pre-loading by the fastener is zero and the cases where the clamping torque is applied (whatever the torque level). Starikov [14] investigated the influence on SB of the lateral clamping force exerted by the fastener. As in his study, it was found

experimentally that an increased clamping force did not affect the values at the AGARD Point. This result is confirmed numerically by the reference model.

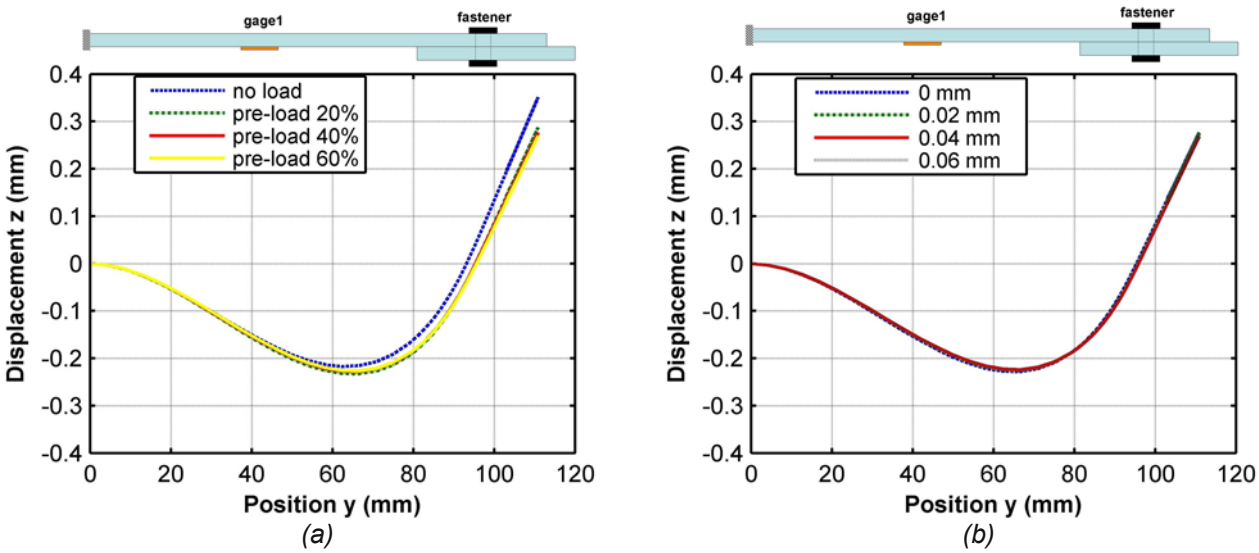

Figure 8 : parametric study: effect of clamping load (pre-load in percent of the yield strength of the shank's material) of fastener (a) and clearance fit (b) on the curvature

A comparison of bending is performed between the reference joint configuration, with no clearance fit, and other joint configurations with a varying fastener fit. The analysis of the graph in Figure 8 (b) reveals that there is no effect of the clearance fit at the deflection but it is easy to remark one weak difference between the case with no clearance fit and the others. The influence of fastener fit on curvature for several joint configurations was reported by Van der Linden [7]. It was found experimentally that curvature was smaller for joints with interference fit than for joints with clearance fit in all cases.

Yet, these parameters have no effect on the displacement magnitude in z-direction. At this stage, we can think that the boundary conditions are originally of bad correlation between measurements and FE model. Indeed, the clamping conditions on grip, modelled in FE, are not representative of the reality because of added pieces on the specimen ends (see grip area in Figure 3).

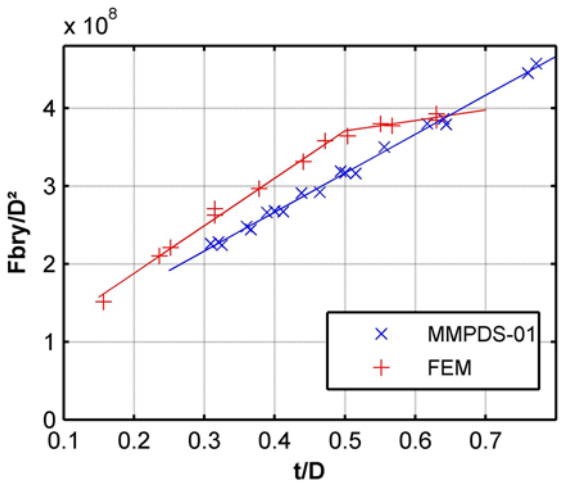

Figure 9 : comparison between numerical predictions (with FEM) and data of MMPDS-01 [9] for one type au single lap joint and one type of fastener

The parametric study shows from the z-displacement that the curvature is small in vicinity of the fastener and is independent of the fastener clamping level and the clearance fit. This analysis attests almost no influence of the SB on local behaviour of the single shear lap joints around the fastener. New analysis based on global behaviour, would be necessary to confirm that SB affect little the specimen strength. Indeed, the failure modes of single shear lap joints are concentred on superposed plate area and are due to high stress near the hole. The effect of the SB on single shear lap joint specimen with only one fastener is negligible on the global behaviour. On the real structure, the influence of the SB may be different depending on the geometry of parts.

The base objective of this study is to give a good prediction of the results of MMPDS-01 [9] from FE models for single shear lap joints. The Figure 9 shows a comparison between the data of MMPDS-01 [9] and results from FE model. F_{bry}, D and t represent respectively the bearing yield load of the joint, the nominal fastener diameter and the plate thickness. In the case of experimental results (MMPDS-01), the measurement was realised on a single lap joint with aluminium alloy Clad 7075 T6 plates, whereas for the FE model, the material used is simply aluminium 7075 T6. An extremely thin sheet of pure aluminium laminated onto each side of an aluminium alloy sheet improves the corrosion resistance with little impairment of strength. For the same thickness of plates, the difference of behaviour between the two materials explains, to some extent, the variation between the two curves (Figure 9). The alloy titanium fasteners (type CSR 925) were used and modelled as presented in this paper. Even if some of errors sources are known, these initial results are encouraging and show that attention should be given to model matching, especially towards plastic behaviour of materials.

4. Conclusion

This paper is based on the lateral displacement fields of the sample surface which was assessed experimentally with optical full field measurement method. This out-of-plan displacement is due to the eccentricities and occurs with local bending as a result. Many parameters, as the boundaries conditions, the clamping load of the fastener or the clearance fit, can be influential and modify the curvature of the SB.

A matching process, for the parameter identification and the model validation, was performed. Thus, the use of Finite Element Modelling from the correlation between numerical fields and their experimental counterparts, allowed understanding the effect of the different parameters on the bending behaviour. In the case of single lap joints, the curvature of SB is not influenced by the clamping level of the single fastener. This study has shown that there have not or not much effects of clearance fit between the hole and the shank, for fit tolerable in aeronautical.

In return, the analysis of the SB deflection has shown that the effect of the boundary conditions is not negligible. Several possibilities are envisaged to improve the matching by decreasing the effect of clamping conditions. The first method is to create a complete model with the clamping. Another method is to increase the length each sides of sample for compensate the effect of clamping (stiffness of clamping). Based on analytical model (fixed-end beam with intermediate moment), an inverse method can give an indication on the added length at the sample.

The FE model that was developed for this study must be enabling to foresee, with a good accuracy, the specific behaviour of single lap joints, in order to find numerically the values, of tables in the MMPDS-01, for many different configurations. Therefore, other new modifications are certainly necessary to approach more closely the real behaviour, and especially the plastic behaviour of the different materials.

References

[1] Bedair O.K., Eastaugh G.F., A numerical model for analysis of riveted splice joints accounting for secondary bending and plates/rivet interaction. Thin-Walled Structures, 45:251-258, 2007.

[2] Schijve J. Campoli G. Monaco A.,Fatigue of structures and secondary bending in structural elements. International Journal of Fatigue, 31:1111-1123, 2009.

[3] Ekh J., Schön J., Gunnar Melin L., Secondary bending in multi fastener, composite-to-aluminium single shear lap joints. Composites Part B: engineering, 36:195-208, 2005.

[4] Dybskiy P.A., Secondary bending in a fuselage lap joint. SEM IX International Congress on Experimental Mechanics; Orlando, USA; 5-8 June 2000. pp. 500-503. 2000.

[5] McCarthy C.T., McCarthy M.A., Stanley W.F., Lawlor V.P., Experiences with modelling friction in composite bolted joints. Journal of Composites Materials, 39:1881, 2005.

[6] Esquillor J., Huet J. and Lachaud F., Modeling of single lap joints with finite element model. XVIth French Mechanics Congress, France, 2005.

[7] Van der Linden H.H., Fatigue rated fastener systems, Technical report AGARD No. 721, National Aerospace Laboratory, NLR, Amsterdam; 1985.

[8] Ekh J., Schön J., Effect of secondary bending on strength prediction of composite, single shear lap joints. Composites Science and Technology, 65:953-965, 2005.

[9] MMPDS-01, Metallic Materials Properties Development and Standardization, U.S. Department of Transportation, Federal Aviation Administration, Office of Aviation Research, Washington, D.C. 20591. 2003

[10] GOM, Mittelweg 7-8, 38106 Braunschweig. ARAMIS 4.7, 2005.

[11] Van der Linden H.H., Determination of secondary bending and load transfer; NLR Memorandum SB-81-083U, 1981.

[12] Jarfall L., Determination of secondary bending and load transfer; Technical report. Saab-Scania, 1982.

[13] Gohorianu G., Interaction between drilling defects and bearing behaviour of carbon/epoxy bolted joints. Thesis, University of Toulouse, 2008.

[14] Starikov R., Mechanically fastened joints: critical testing of single overlap joints. Technical report. Swedish Defence Research Agency; FOI-R-0441-SE, 2002

Proceedings of the SEM Annual Conference
June 7-10, 2010 Indianapolis, Indiana USA

Interaction between a dynamically growing crack with stiff and compliant inclusions using DIC and high-speed photography

Kailash Jajam and Hareesh Tippur
Department of Mechanical Engineering
Auburn University, AL 36849, USA
htippur@eng.auburn.edu

ABSTRACT

In this work, cylindrical inclusions of two different elastic moduli – stiff and compliant relative to the matrix – are examined. The former is a borosilicate glass inclusion whereas the latter is a polyurethane inclusion in an epoxy matrix. The 2D digital image correlation (DIC) technique along with high-speed photography is used to study crack growth behavior as a function of inclusion-matrix interfacial strength and the inclusion location relative to the crack under stress wave loading conditions. An ultra high-speed rotating mirror-type CCD digital camera is used to record random speckle patterns in the crack-inclusion vicinity at rates ranging from 150,000 to 300,000 frames per second. Two sets of images, one set before loading and another set during the fracture events are recorded. The crack tip deformation histories from the time of impact until complete fracture are mapped and fracture parameters are extracted. Different crack propagation patterns in terms of crack speed, crack path and stress intensity factor histories are observed followed by a macroscopic examination of fractured surfaces.

Introduction

Multiphase heterogeneous materials are used in a number of engineering applications. In the last few decades, there has been a great deal of interest in improving the fracture toughness of materials by addition of either stiff or compliant filler particles relative to the matrix [1-5]. In view of this, the focus of the current work is to study failure behavior of such materials by investigating interactions between a dynamically growing matrix crack and a stationary inclusion. Apart from analytical [6, 7] and numerical [8-10] works on this topic, a very limited number of experimental investigations have been reported in the literature. One of the very early experimental efforts in this regard dates back to the photoelastic investigation of crack-inclusion interactions under quasi-static loading conditions by O'Toole and Santare [11]. Recently, Savalia and Tippur [12] performed a quasi-static analysis of crack-inclusion interactions using moiré interferometry. Among the very few dynamic studies in this area, Kitey and Tippur [13] have investigated the dynamic crack growth behavior in the vicinity of an isolated stiff inclusion using coherent gradient sensing (CGS) in conjugation with high-speed photography.

A quick review [14-17] shows that the method of digital image correlation (DIC) has been a popular tool in the field of experimental mechanics lately. Recently, Tippur and his coworkers [18-20] have successfully extended the DIC method dynamically to determine full-field surface displacements in the vicinity of a stationary and a rapidly growing crack. In contrast to other interferometric techniques, DIC is relatively simple and optically less demanding in terms of optical components, light source, vibration isolation and stringent specimen surface preparation requirements. These features of DIC have prompted its use in the current study along with high-speed photography. The objective of this investigation is to examine the interactions between a dynamically propagating crack with stiff and compliant inclusions embedded in an epoxy matrix as a function of inclusion-matrix interfacial strength and inclusion location relative to the initial crack tip. The entire crack tip deformation history from the time of impact to complete fracture is mapped and the instantaneous values of crack extension are then used to calculate crack velocity. The crack tip displacement fields are used to obtain stress intensity factor histories for both pre- and post-crack initiation regimes. This is followed by the examination of fractured surfaces in order to distinguish the effect of inclusion elastic modulus on the toughening mechanisms.

T. Proulx (ed.), *Application of Imaging Techniques to Mechanics of Materials and Structures, Volume 4*, Conference Proceedings of the Society for Experimental Mechanics Series 14, DOI 10.1007/978-1-4419-9796-8_9, © The Society for Experimental Mechanics, Inc. 2013

Experimental Approach

In this work, random speckle patterns on a specimen surface were monitored during a fracture event. The light intensity of these image patterns was recorded at two different states, one before and another after deformation. The corresponding images from deformed and undeformed sets were paired and analyzed separately. During the analysis, a sub-image in an undeformed image was chosen and its location in the corresponding deformed image was identified. Once the location of this sub-image in the deformed image was found, the local displacements of this sub-image could be readily determined. A three-step approach, developed by Kirugulige *et al.* [18] on a MATLAB^{TM} platform, was used to estimate two-dimensional (2D) displacement components. In the first step, initial estimation of in-plane 2D displacements was done by performing a 2D cross-correlation with a peak of the correlation function detected to a sub-pixel accuracy interpolation. This process was repeated for the entire image to obtain full-field in-plane displacements. In the second step, an iterative approach based on nonlinear least-square minimization was used to minimize the 2D cross-correlation function in order to refine the displacement fields obtained in the previous step. Finally, the third step includes smoothing of displacement fields, as the displacements obtained from image correlation represent average values for each sub-image and tend to be noisy; therefore, a smoothing method based on an unbiased optimum smoothing parameter was used for this purpose. Further details of this approach can be found in Refs. [18-20].

Sample Preparation and Geometry

Edge cracked epoxy specimens were prepared by mixing a low viscosity two-part epoxy as a matrix material. Before pouring the mixture to the mold, a cylindrical inclusion of diameter, d=4mm and length equal to the specimen thickness (8.65 mm) was positioned at the center of the mold as shown in Fig. 1. In this study, cylindrical inclusions of two different elastic moduli – stiff and compliant relative to the matrix – were used. The former was a borosilicate glass inclusion whereas the latter was a polyurethane inclusion in an epoxy matrix. A weak inclusion-matrix interface was created by applying a thin layer of grease on both stiff and compliant inclusion cases. In order to achieve a strong inclusion-matrix adhesion, the glass inclusion was treated with silane whereas the polyurethane inclusion surface was roughened using a sand paper. It should be noted here that, traditionally the silane works best at bridging an organic to inorganic interface and because of that polyurethane inclusion was not treated with silane and the roughening of inclusion surface was found to create a strong interface between polyurethane and epoxy. The material was cured at room temperature for about one week. The cured material was then machined into test specimens of dimensions 200 mm x 50 mm x 8.65 mm. An edge notch of 5 mm in length was cut into the sample and the notch tip was sharpened using a razor blade. A random speckle pattern was created on the surface of the sample by spraying a fine mist of black and white paints alternatively. Figure 1 depicts the specimen geometry, dimensions and loading configurations with crack-tip coordinate system and inclusion location with an illustration of random speckle pattern on it.

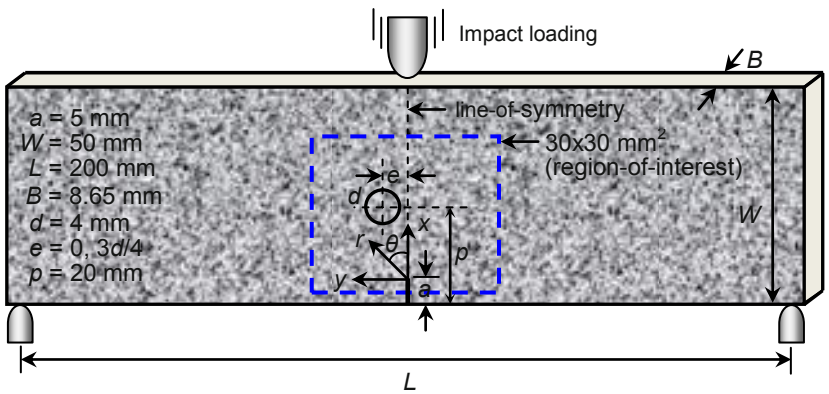

Fig. 1: Specimen geometry and loading configuration.

In Fig. 1, the circle indicates cylindrical inclusion, and its location relative to the crack-tip is defined by two parameters; (p-a) and e. The distance of the inclusion center from the specimen edge with the crack of length a is defined by p. The eccentricity, e, is defined as the distance between the inclusion center and the line-of-symmetry. In the current study, two different eccentricities, e=0, and 3d/4 are considered, and p=20 mm is maintained constant in all experiments.

Experimental Set-up and Testing Procedure

A schematic of the experimental set-up used in this work is shown in Fig. 2. It included a drop tower for impacting the inclusion specimens and a Cordin-550 ultra high-speed digital camera for capturing speckle images during the fracture event. Two high-energy flash lamps, triggered by the camera, were employed to illuminate the sample surface. The digital high-speed camera is capable of recoding images at rates of up to 2 million frames per second on 32 individual 1000x1000 pixel CCD image sensors positioned circumferentially around a rotating mirror which reflects and sweeps light over these sensors. Details about camera performance evaluation and calibration can be found in Refs. [18, 19]. The camera was focused on a 30 x 30 mm^2 region of interest (ROI) in the vicinity of crack-tip and inclusion. Prior to impacting the specimen, a set of 32 images of ROI were recorded at an appropriate framing rate and stored.

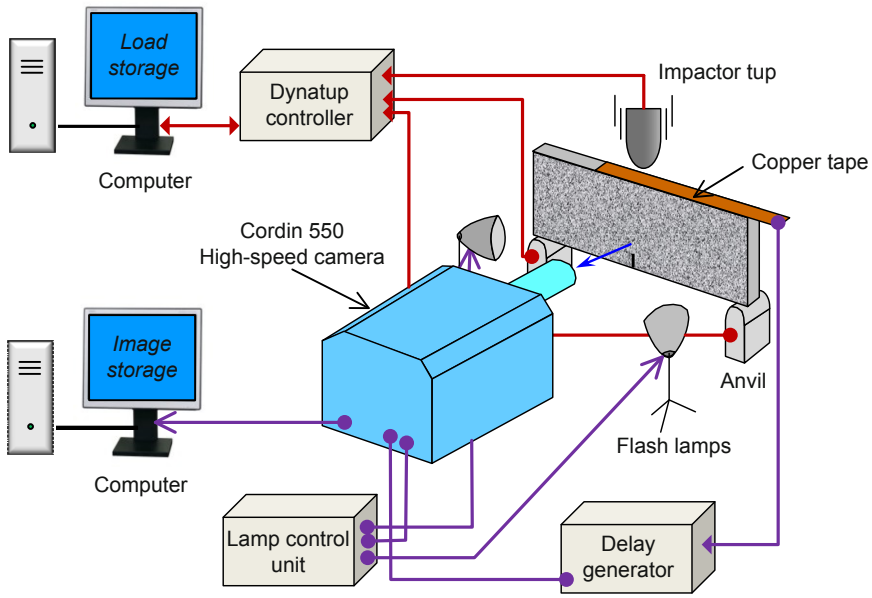

Fig. 2: Schematic of the dynamic experimental setup.

While maintaining all camera settings same, another set of 32 images was captured after the specimen was impacted at a velocity of 5 m/s. In order to capture whole fracture event, the images in the case of glass inclusion specimens were recorded at a framing rate of 300,000 frames per second whereas a framing rate ranging from 150,000 to 250,000 frames per second was used for polyurethane inclusion specimens. A total of 32 images were recorded for each undeformed and deformed sets. In the case of glass inclusion specimens the time interval between successive images was 3.33 micro-seconds whereas for polyurethane inclusion specimens it ranges from 4 to 6.66 micro-seconds. The corresponding two images for each sensor were paired from undeformed and deformed sets and each of these 32 matched pairs was analyzed individually.

Experimental Results

The representative speckle images of 30 x 30 mm^2 ROI for dynamically fractured specimens at various time instances for weakly and strongly bonded glass and polyurethane inclusions at eccentricities, e=0 and, e=3d/4 are shown in Fig. 3. The dotted circle and arrow in speckle images indicate the inclusion location and crack-tip position respectively. In all experiments, crack propagation took place in a dominant mode-I fashion before and after crack interacts with the inclusion. The crack was arrested and reinitiated in the vicinity of inclusion–matrix interface for both weakly bonded glass as well as polyurethane inclusions. In the case of glass inclusion specimens, opposite crack trajectories were observed with crack attraction by the weak interface for e=0 and, crack deflection as a result of strong interface for e=3d/4, whereas for polyurethane inclusion specimens, the crack was completely arrested by the weak inclusion-matrix interface and reinitiated along initial crack path for e=0 and it was partially attracted by strong inclusion-matrix interface for e=3d/4. When comparing strongly bonded glass and polyurethane

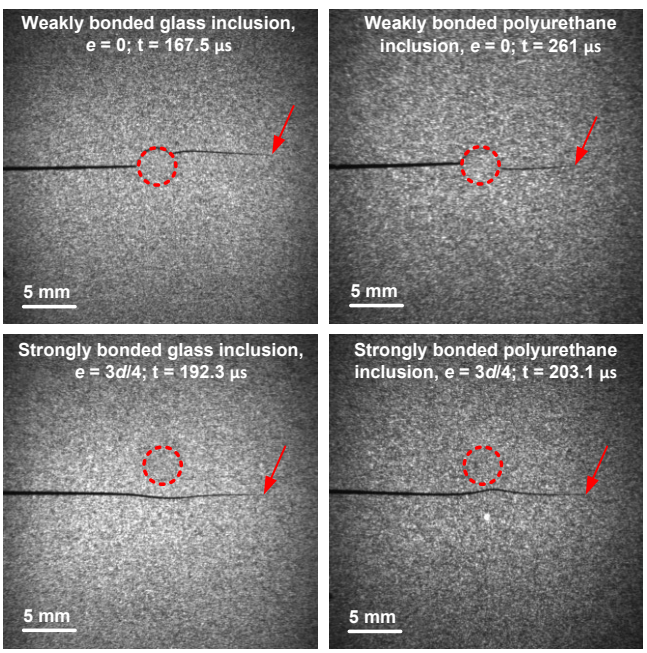

Fig. 3: Speckle images of fractured specimens.

inclusion cases with *e*=3d/4, it is interesting to note that unlike glass inclusion the crack was attracted in the vicinity of polyurethane inclusion-matrix interface.

In this work, displacements fields were obtained as a 34 x 34 matrix of data points for each image pair and subsequently full-field displacement contour plots were generated. A few selected speckle images with corresponding full-field crack-opening displacement, *v* (displacement along *y*-axis) and sliding displacement, *u* (displacement along *x*-axis) for weakly bonded glass inclusion and strongly bonded polyurethane inclusion specimens at eccentricity, *e*=0 can be seen in Fig. 4.

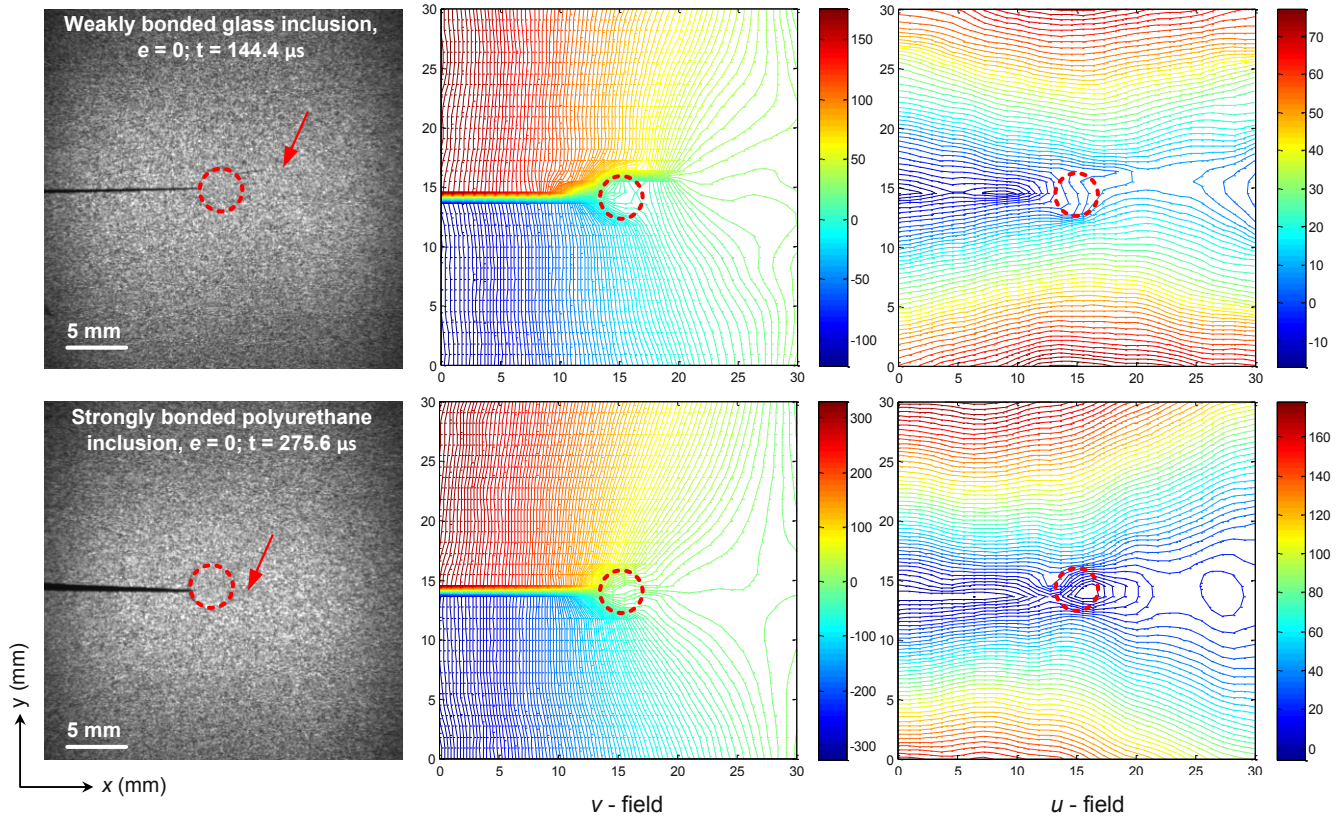

Fig. 4: Crack-opening (*v*-field) and crack-sliding (*u*-field) displacement contours. Dotted circle represents inclusion location and arrow indicates crack-tip position. Color-bars indicate displacement in micrometers.

The instantaneous values of crack extension were measured by locating the crack-tip from the digitized images and crack extension histories were used to calculate crack velocity. The crack velocity histories for specimens with weakly and strongly bonded glass and polyurethane inclusion specimens with eccentricity *e*=0 are plotted in Fig. 5(a) and (b) respectively. Here, t_i indicates the crack initiation time after impact. It should be noted that the time window for polyurethane inclusion specimens is about 60-100 micro-seconds larger than that of glass inclusion specimens as the dynamic fracture events were captured at lower framing rates in the former compared to the latter. The effect of inclusion elastic moduli and inclusion-matrix adhesion/bond strength on crack velocity for glass and polyurethane inclusion specimens with eccentricity, *e*=0 is represented by Fig. 5(a) and (b) respectively. In Fig. 5(a), the symmetrically located glass inclusion shows nearly similar velocity profiles until the crack encounters the inclusion. A sudden drop in velocity can be seen in both weakly and strongly bonded inclusion cases when the crack is arrested at inclusion-matrix interface just before re-initiation. The drop in crack velocity is ~90 m/s and 190 m/s for weakly and strongly bonded inclusions respectively. The re-initiation velocities in weakly and strongly bonded inclusions reach to ~900 and 650 m/s respectively. Fig. 5(b) shows crack growth histories of weakly and strongly bonded polyurethane inclusion specimens. Upon initiation, crack rapidly accelerated and subsequently propagated at relatively steady velocity of ~300 m/s for about 50 micro-seconds and then decelerated when it encountered the compliant inclusion and completely stalled at inclusion-matrix interface for about 50 and 90 micro-seconds for both weakly and strongly bonded inclusions, respectively.

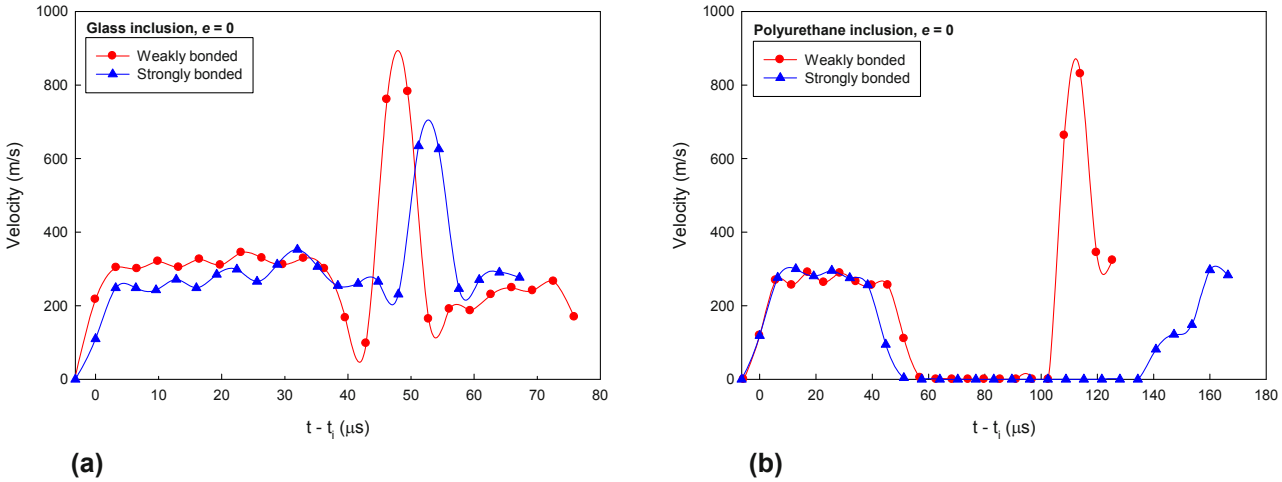

Fig. 5: Crack velocity histories for weakly and strongly bonded inclusions at eccentricity, *e*=0. **(a)** Glass inclusion, **(b)** Polyurethane inclusion

Following this, the crack reinitiated with a velocity of ~700 m/s and accelerated with a maximum velocity of ~850 m/s and subsequently slowed to ~350m/s in the weakly bonded case, on the other hand for strongly bonded one, crack reinitiated at low speed and slowly accelerated to ~300 m/s.

The effect of inclusion elastic moduli and inclusion-matrix adhesion strength on stress intensity factor (SIF) histories for glass and polyurethane inclusion specimens with eccentricity, e=0 is represented by Fig. 6(a) and (b) respectively. Figure 6(a) shows SIF histories of weakly and strongly bonded glass inclusions for eccentricity, *e*=0. The mode-I SIF, K_I at initiation for both specimens is ~1.0 MPa-m$^{1/2}$. Following initiation both specimens show monotonic increase in K_I values before crack encounters the inclusion, with K_I relatively higher for weakly bonded case compared to strongly bonded inclusion case.

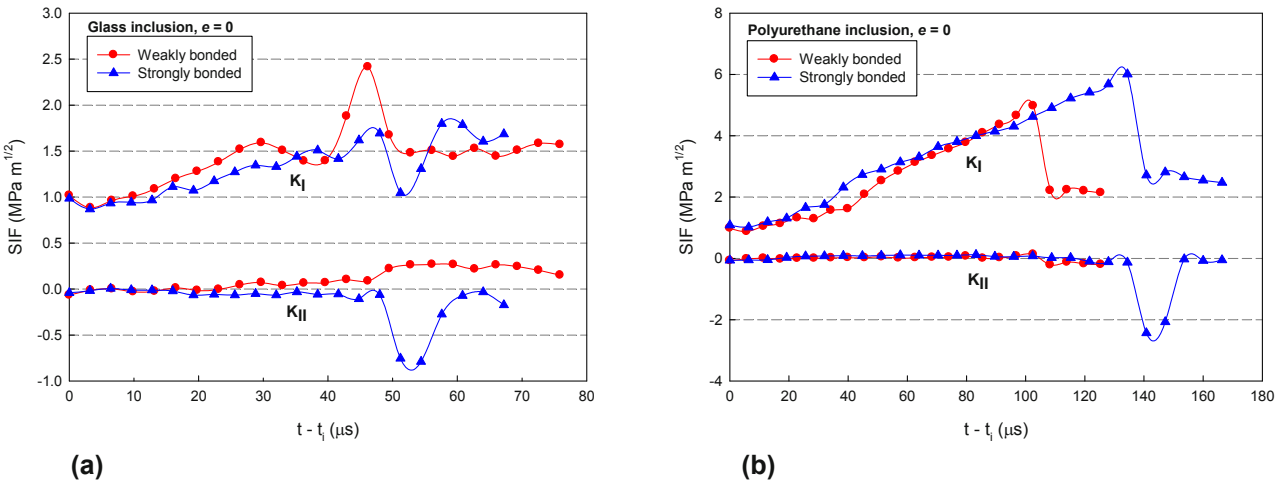

Fig. 6: Stress intensity factor (SIF) histories for weakly and strongly bonded inclusions at eccentricity, *e*=0. **(a)** Glass inclusion, **(b)** Polyurethane inclusion

A small and steady drop in K_I is seen for weakly bonded inclusion followed by an increase to a maximum value of ~2.4 MPa-m$^{1/2}$ when the crack is in the proximity of the inclusion, beyond which K_I drops to ~1.5 MPa-m$^{1/2}$ and continue to remain constant, whereas a large and steep drop in K_I is noticeable for strongly bonded one in the crack-inclusion vicinity. The mode-II SIF, K_{II}, values are close to zero in both cases until the crack tip begin to interact with the inclusion. When the crack is arrested by the weakly bonded inclusion, K_{II} shows a slight increase. This is followed by a monotonic decrease to attain a value close to zero, whereas a steep negative dip is

observed followed a monotonic increase for the strongly bonded case. Figure 6(b) shows SIF histories of weakly and strongly bonded polyurethane inclusion specimens at eccentricity, e=0. The K_I at initiation for both specimens is ~1.0 MPa-m$^{1/2}$ followed by a monotonic increase until it reaches a maximum value of ~5.0 and 6.0 MPa-m$^{1/2}$ for weakly and strongly bonded inclusions respectively and then suddenly drops to ~2.4 and 2.8 MPa-m$^{1/2}$ and beyond which it continues to remain constant. For both bond strengths, K_{II} remains close to zero before crack reaches in the inclusion proximity. When the crack reaches the inclusion vicinity, K_{II} still remains close to zero in the weakly bonded case while it shows a negative dip for strongly bonded one and then again continues to close to zero.

The differences in toughening mechanisms in stiff and compliant inclusion embedded in an epoxy matrix specimens can be explained by examining fracture surfaces. The photographs of the entire x-z plane of dynamically fractured inclusion specimens with eccentricity, e=0 are shown in Fig. 7 with both ligaments of the fractured specimens, one ligament showing the inclusion cavity and the other holding the inclusion. The dotted arrow indicates the direction of crack propagation. Figure 7(a) and (b) depict fractured surface of weakly bonded glass inclusion and strongly bonded polyurethane inclusion specimen. In both cases, the fracture surfaces just before crack reaches inclusion are essentially smooth and shiny indicating brittle crack growth. The polyurethane inclusion is surrounded by a pool of epoxy showing a strong inclusion-matrix bonding and clearly demonstrates that the roughening of polyurethane inclusion was a good choice for creating a strong interface. It is interesting to note that this pool of epoxy material is maximum at initial region just before crack encounters the inclusion and as crack advances it diminishes at other end symmetrically with an angle of 45º with respect to the center of crack front. The fracture surfaces of both ligaments in the case of polyurethane inclusion reveal that a highly transient fracture has occurred after crack leaves the inclusion, showing very rough, highly textured, surfaces containing a large number of river markings, tail lines and deep furrows. On the other hand, the glass inclusion specimen ligaments indicate much lower roughness, fewer tail lines and river-bed morphology. The presence of high concentration of tail lines and higher surface ruggedness in case of polyurethane inclusion specimens suggest greater energy dissipation and accounts for the improved fracture toughness compared to the glass inclusion specimens.

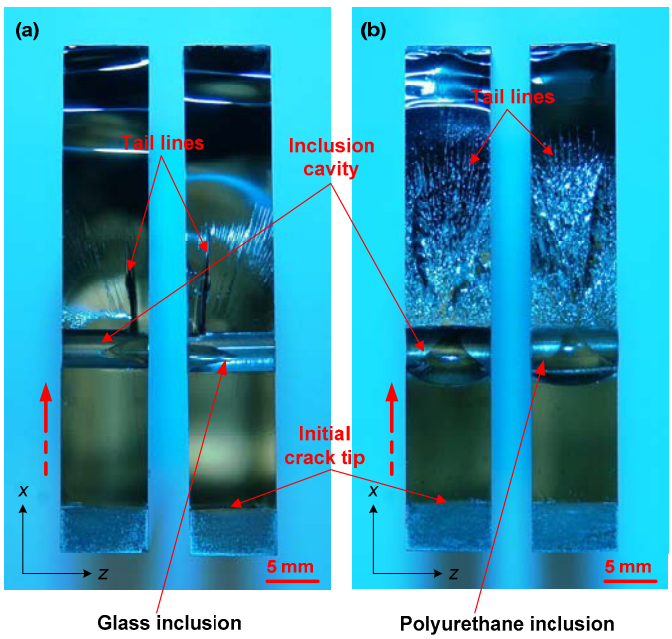

Fig. 7: Macrographs of dynamically fractured specimens. **(a)** Glass inclusion, **(b)** Polyurethane inclusion

Conclusions

The method of digital image correlation combined with high-speed digital photography was successfully employed to study interactions between a dynamically propagating crack with stiff and compliant inclusions. Edge cracked epoxy specimens embedded with cylindrical inclusions of two different elastic moduli – stiff (glass) and compliant (polyurethane) - with weak and strong inclusion-matrix bond strength and located at two different eccentricities, e=0 and 3d/4 with respect to the initial crack path, were prepared and subjected to impact loading. The interactions between a dynamically growing mode-I crack and an isolated stiff/compliant inclusion were recorded. The entire crack tip deformation history form the time of impact to complete fracture of the specimen was mapped. Fractured specimens show different crack trajectories and crack velocities for each inclusion location and inclusion-matrix bond strengths. For weakly bonded inclusion specimens, higher crack velocities were observed for both glass as well as polyurethane inclusions when compared to the strongly bonded ones. The crack was completely stalled for about half the duration needed to complete the fracture of samples in the case of polyurethane inclusion samples. The dynamically propagating crack was attracted and arrested by the weak inclusion interface for both glass and polyurethane inclusion case at e=0 whereas it was being deflected away by the stronger one for glass and attracted by polyurethane inclusion at e=3d/4. The inclusion elastic moduli and inclusion-matrix interfacial strength also affected the mode-I and mode-II SIFs. The polyurethane inclusion

specimens showed much higher fracture toughness for weak and strong bond strengths when compared to the glass inclusion counterparts. The macroscopic analysis of dynamically fractured specimens accounted for the greater crack resistance in polyurethane inclusion specimens compared to the glass inclusion ones.

Acknowledgements

Authors would like to thank National Science Foundation for supporting this research through a grant NSF-CMMI-0653816.

References

[1] Kinloch, A.J., et al., *Deformation and fracture behavior of a rubber-toughened epoxy: 1. Microstructure and fracture studies.* Polymer, 1983. **24**(10): p. 1341-1354.
[2] Kinloch, A.J., M.L. Yuen, and S.D. Jenkins, *Thermoplastic-toughened epoxy polymers.* Journal of Materials Science, 1994. **29**(14): p. 3781-3790.
[3] Evans, A.G., S. Williams, and P.W.R. Beaumont, *On the toughness of particulate filled polymers.* Journal of Materials Science, 1985. **20**(10): p. 3668-3674.
[4] Geisler, B. and F.N. Kelley, *Rubbery and rigid particle toughening of epoxy-resins.* Journal of Applied Polymer Science, 1994. **54**(2): p. 177-189.
[5] Hussain, M., et al., *Fracture behavior and fracture toughness of particulate filled epoxy composites.* Materials Letters, 1996. **27**(1-2): p. 21-25.
[6] Tamate, O., *Effect of a circular inclusion on stresses around a line crack in a sheet under tension.* International Journal of Fracture Mechanics, 1968. **4**(3): p. 257-266.
[7] Erdogan, F., G.D. Gupta, and M. Ratwani, *Interaction between a circular inclusion and an arbitrarily oriented crack.* Journal of Applied Mechanics-Transactions of the Asme, 1974. **41**(4): p. 1007-1013.
[8] Bush, M.B., *The interaction between a crack and a particle cluster.* International Journal of Fracture, 1998. **88**(3): p. 215-232.
[9] Kitey, R., et al., *Modeling of crack growth through particulate clusters in brittle matrix by symmetric-Galerkin boundary element method.* International Journal of Fracture, 2006. **141**(1-2): p. 11-25.
[10] Savalia, P.C., H.V. Tippur, and M.S. Kirugulige, *A numerical study of inclusion-matrix debonding in the presence of a nearby crack.* Engineering Fracture Mechanics, 2008. **75**(5): p. 926-942.
[11] O'Toole, B.J. and M.H. Santare, *Photoelastic investigation of crack-inclusion interaction.* Experimental Mechanics, 1990. **30**(3): p. 253-257.
[12] Savalia, P.C. and H.V. Tippur, *A study of crack-inclusion interactions and matrix-inclusion debonding using Moire interferometry and finite element method.* Experimental Mechanics, 2007. **47**(4): p. 533-547.
[13] Kitey, R. and H.V. Tippur, *Dynamic crack growth past a stiff inclusion: Optical investigation of inclusion eccentricity and inclusion-matrix adhesion strength.* Experimental Mechanics, 2008. **48**(1): p. 37-53.
[14] Peters, W.H. and W.F. Ranson, *Digital imaging techniques in experimental stress-analysis.* Optical Engineering, 1982. **21**(3): p. 427-431.
[15] Sutton, M.A., Wolters W.J., Peters W.H., Ranson W.F., McNeil S.R., *Determination of displacements using an improved digital image correlation method.* Image and Vision Computing, 1983. **1**(3): p. 133-139.
[16] Bruck, H.A., et al., *Digital image correlation using Newton-Raphson method of partial-differential correction.* Experimental Mechanics, 1989. **29**(3): p. 261-267.
[17] Reu, P.L. and T.J. Miller, *The application of high-speed digital image correlation.* Journal of Strain Analysis for Engineering Design, 2008. **43**(8): p. 673-688.
[18] Kirugulige, M.S., H.V. Tippur, and T.S. Denney, *Measurement of transient deformations using digital image correlation method and high-speed photography: application to dynamic fracture.* Applied Optics, 2007. **46**(22): p. 5083-5096.
[19] Kirugulige, M.S. and H.V. Tippur, *Measurement of Fracture Parameters for a Mixed-Mode Crack Driven by Stress Waves using Image Correlation Technique and High-Speed Digital Photography.* Strain, 2009. **45**(2): p. 108-122.
[20] Lee, D., et al., *Experimental Study of Dynamic Crack Growth in Unidirectional Graphite/Epoxy Composites using Digital Image Correlation Method and High-speed Photography.* Journal of Composite Materials, 2009. **43**(19): p. 2081-2108.

Proceedings of the SEM Annual Conference
June 7-10, 2010 Indianapolis, Indiana USA

Electron Micrographic Digital Image Correlation: Method Optimization and Microstructural banding Case Study

J.P.M. Hoefnagels[1*], B.G.Vossen[1], C.C.Tasan[1,2]

[1] Eindhoven University of Technology, Department of Mechanical Engineering,
P.O.Box 513, 5600MB, Eindhoven, The Netherlands
[2] Materials Innovation Institute (M2i),
P.O.Box 5008, 2600GA, Delft, The Netherlands
[*] e-mail: j.p.m.hoefnagels@tue.nl, tel:+31-40-2475894, Fax:+31-40-2447355

ABSTRACT

Segregation-induced microstructural banding is commonly encountered in commercial steels, yet its effect on the global mechanical behavior is disputed in the literature due to the difficulty of designing clean control experiments. This work locally compares the deformation of banded phases with unbanded regions in the same microstructure from in-situ electron micrographs analyzed with (optimized) micrographic digital image correlation. To this end, first, the employed electron micrographic digital image correlation (EMDIC) methodology is optimized in terms of its experimental parameters: specimen surface preparation settings, scanning electron microscopy imaging settings (contrast modes, magnification, resolution, and contrast-brightness), and image correlation settings (facet size and facet step size). Subsequently, the strength of the (optimized) EMDIC methodology is demonstrated on a case study on segregation-induced microstructural banding in steel, in which the influence of the banded phase and its morphology is probed by comparing the mechanical behavior of two carefully chosen, extreme cases of banded microstructures: a microstructure containing a continuous, hard band (the martensitic-ferritic system) and a microstructure containing non-continuous, softer bands (the pearlitic-ferritic system). The obtained micro-scale strain fields yield clear insight into the influence of band structure, morphology and band material properties.

1. INTRODUCTION

Microstructural banding is common in industrial steels and its detrimental effects on fracture toughness is well-known. However, contradictory results exist for its influence ductility [1-5], possibly due to the experimental methodologies commonly employed whereby the global material behavior of a banded microstructure is compared with an unbanded microstructure (produced by a homogenizing heat treatment from the banded material). Such homogenizing heat treatments also change the morphology of inclusions, thereby changing the mechanical behavior of the control specimen and making a clean comparison challenging.

This difficulty is overcome in the present work by *in-situ* micro-scale strain field measurements in the scanning electron microscope (SEM) that enable direct comparison of the banded regions with the unbanded regions in the *same microstructure*, avoiding undesired variations introduced by band-removing heat treatments. This approach enables an in-depth analysis of the influence of the band morphology (thickness, continuity, geometry etc.).

This work presents an optimization study of the electron micrographic digital image correlation (EMDIC) analysis addressing specimen preparation, SEM imaging, and image correlation settings. Subsequently, the strength of the (optimized) EMDIC methodology is demonstrated on a case study on the influence of banded phase and morphology on microstructural banding, investigated using two carefully-chosen limit cases of banded microstructures: a microstructure containing a continuous, hard band (the martensitic-ferritic system) and a microstructure containing non-continuous, softer bands (the pearlitic-ferritic system), with both microstructures processed from the same starting material for optimal comparison. The paper is finalized with the conclusions.

T. Proulx (ed.), *Application of Imaging Techniques to Mechanics of Materials and Structures, Volume 4*, Conference Proceedings of the Society for Experimental Mechanics Series 14, DOI 10.1007/978-1-4419-9796-8_10, © The Society for Experimental Mechanics, Inc. 2013

2. OPTIMIZATION OF THE ELECTRON MICROGRAPHIC DIGITAL IMAGE CORRELATION METHODOLOGY

Utilizing the scanning electron microscope (SEM) micrographs in digital image correlation analysis (with maximum facet correlation) requires the influence of a number of experimental parameters to be assessed. The most critical parameters for this purpose are: (i) the final finish of the specimen surface following metallographic preparation, (ii) SEM imaging settings and (iii) image correlation settings. In this section, the influence of these parameters are investigated using dual-phase 600 steel dogbone shaped tension test samples. For each parameter, SEM images are made at the cross section of a deforming sample and the facet correlation is investigated using Aramis software (GOM GmbH.).

Surface Finish

Following successive grinding and polishing steps, the dual phase steel surface is prepared with different finishes (i.e. electro-etching, chemical etching, chemical over-etching, and combined electro-etching and chemical etching) to reveal the best method in terms of the achieved contrast. Typical results for (a) electro-etching and (b) combined electro-etching and chemical etching are shown in Figure 1. From a comparison of all results, it was found that the best facet tracking is achieved with a combination of electro-etching and chemical etching.

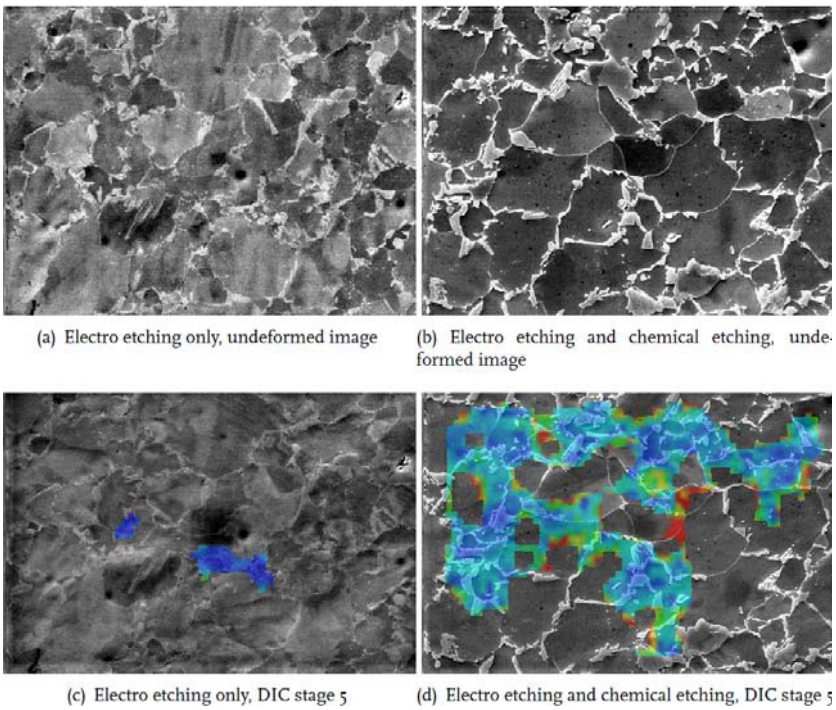

Fig.1. *Influence of specimen surface preparation on correlation quality.*

SEM Imaging Settings

Obviously, the SEM imaging settings such as the contrast mode (i.e. secondary electron mode (SE), backscattering electron mode (BSE), or a mixed mode that combines SE and BSE contrast), magnification, contrast-brightness are as critical as the surface preparation of the specimen to achieve successful facet tracking. For this study, a FEI Quanta 600 scanning electron microscope is used to reveal optimized settings for the dual-phase steel considered. This SEM also allows imaging using the mixed SE–BSE mode, as shown in Fig. 2.

For any microstructure, the most challenging regions to track (using DIC) are those without significant topographic or morphologic differences. In the case of dual phase steel, the ferritic grains present the most difficult regions to correlate. It is seen in Fig. 2a that the SE contrast mode allows for visualization of fine dispersoids which appear in good contrast with the ferritic grains. This contrast is lost to a noticeable degree when BSE contrast is also incorporated in the SE image. Also, the contrast between the martensitic islands and the ferrite grains are more significant under SE contrast. Due to these reasons, pure SE contrast is clearly most suited for EMDIC.

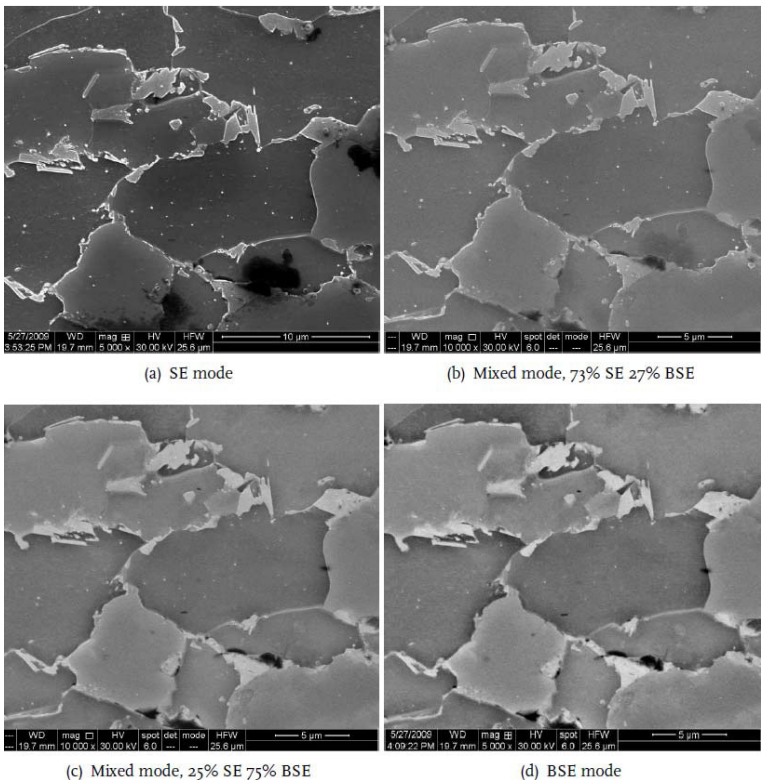

Fig. 2. *Dual phase steel microstructure viewed in different SEM contrast modes.*

Next, the influence of SEM magnification is considered. For *in-situ* experiments, the choice for the level of magnification generally creates a dilemma: either high magnification, hence more details but smaller area of view (which may mean that the investigated microstructural mechanism is not captured, while also small contrast features needed for digital correlation may be lost) or low magnification, hence less details but larger area of view (especially important for capturing randomly occurring events such as damage evolution or fracture). In this work, a third option is investigated, where low magnification but with very high resolution images are captured (12 megapixels), which allows the combination of large area of view with significant level of detail (Fig. 3) at the expense of extended imaging time.

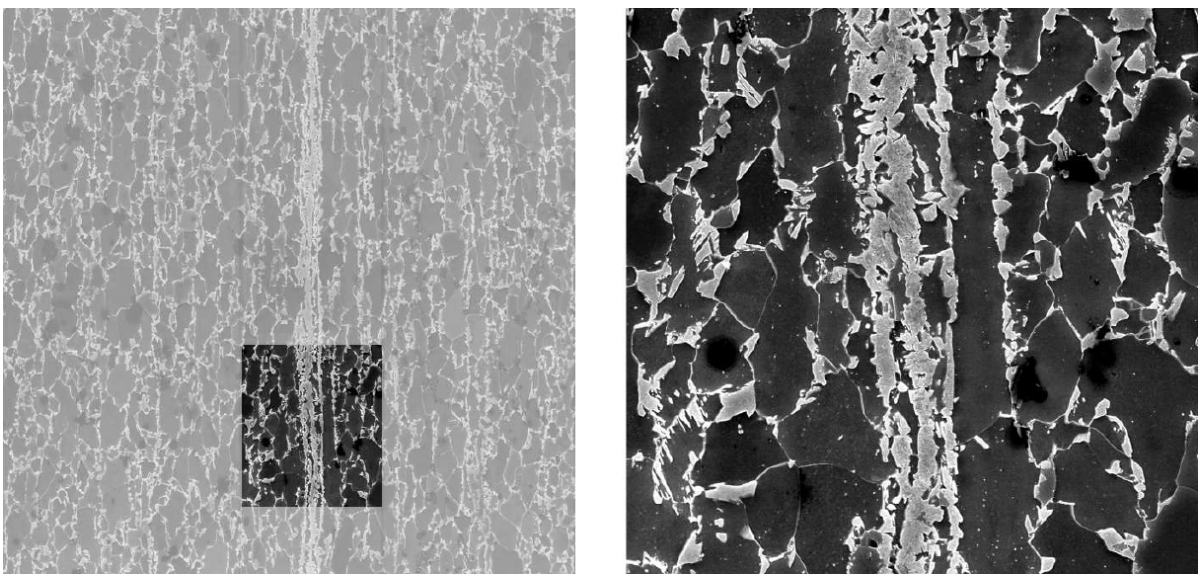

Fig. 3. *Low magnification, high resolution imaging combines large area of view with high details level.*

Finally, the SEM contrast-brightness have been investigated. The main conclusion from this study is that the facet tracking significantly increases with increasing imaging contrast, as shown in Fig. 4. Note that, this may result in final images that are not “visually” ideal, with respect to general SEM practice.

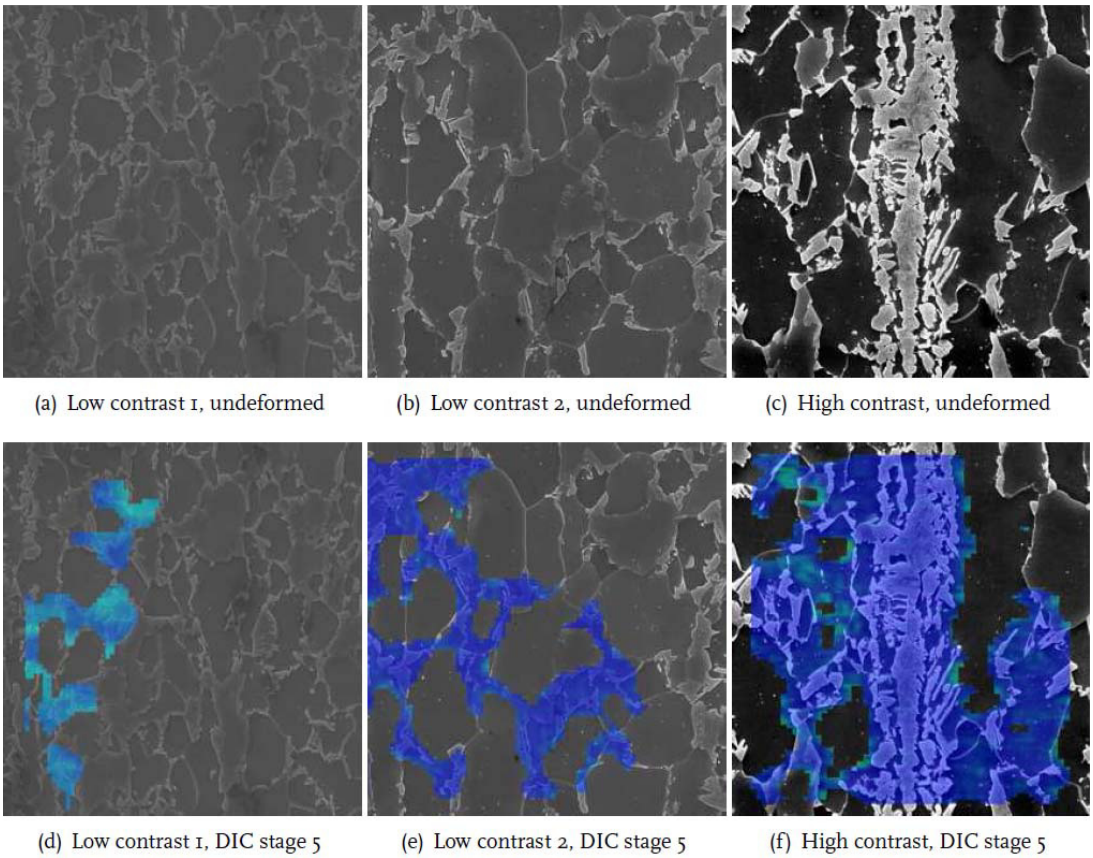

Fig. 4. *Influence of SEM imaging contrast on facet correlation.*

Image Correlation Settings

It was first indentified that the most critical parameters for facet tracking are the facet size and facet step size. To determine the ideal approach in determining these settings, computer generated images with a known strain pattern are used (Fig. 5), as this enables the comparison of the DIC-generated strain patterns for different facet size and facet step size with a well-defined reference case.

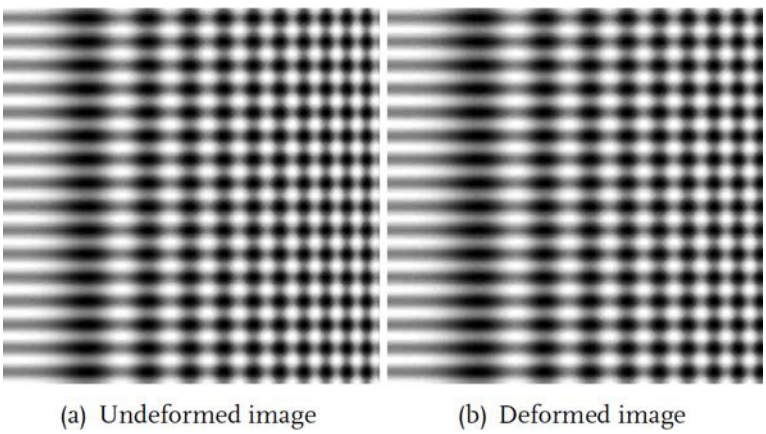

Fig. 5. *Computer generated images with a known strain pattern of* $\varepsilon_x = (4\pi/40)*\cos(2\pi x/50)$.

The results are shown in figures 6, which shows the analytical strain pattern together with the strain patterns calculated from digital image correlation for several settings of facet size and facet step size. Optimum results are obtained using the smallest facet size and the smallest step size possible. In real applications, however, measurement noise and lack of contrast are important limiting factors to the applicable facet and step sizes.

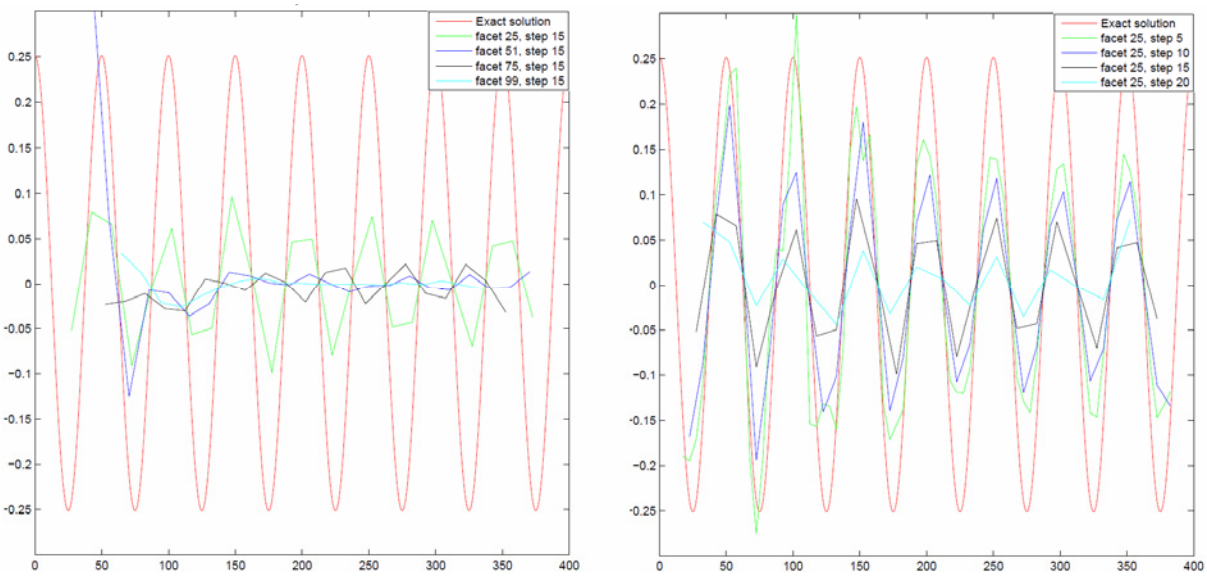

Fig. 6. *Effect of facet size and facet step size analyzed using computer generated images. In the left graph, the facet size is changed between 25 and 100 pixels for a constant facet step size of 15 pixels; in the right graph, the facet step size is changed between 5 and 20 pixels for a constant facet size of 25 pixels.*

3. CASE STUDY: EMDIC ANALYSIS OF MICROSTRUCTURAL BANDING EFFECTS IN STEEL [6]

In-situ uni-axial tensile deformation tests with combined EMDIC micro-scale strain field measurements are carried out for two distinct banded microstructures: 1 mm thick martensitic-ferritic dual-phase steel sheets have a ~5 μm thick martensitic band in the center, and ferritic-pearlitic banded steel (produced by austenizing the (undeformed) dual-phase steel) with a morphologically comparable microstructure but for which the continuous martensite band is replaced by a non-continuous pearlite band. Tensile test samples are cut using electro-discharge machining, while the cross sections are metalographically prepared using successive grinding and mechanical polishing steps, followed by electropolishing and etching with 2 vol. % nital solution, which is the optimum surface preparation procedure deduced from the EMDIC analysis in Section 2. Intermittent tensile tests of these materials are carried out using a Kammrath-Weiss micro-tensile stage, placed in the FEI Quanta 600 scanning electron microscope. Following the optimum SEM imaging setting obtained in Section 2, high resolution, low magnification micrographs in secondary electron contrast mode are captured at successive stages of deformation ($\sim\Delta\varepsilon_{global} \approx 0.03\%$). The gray value histograms of the obtained images were adjusted for maximum overlap, and regions of interest are chosen for local strain field analysis, which is carried out by the Aramis software.

The obtained micro-scale strain field measurements of the martensitic-ferritic steel are shown in Fig. 7 and those of the pearlitic-ferritic steel in Fig. 8, which show distinctly different behaviors. Let us first examine the martensitic-ferritic steel. Early in deformation, the formation of local slip lines within individual ferritic grains is observed. With proceeding deformation, the number of slip lines increases and the strain distribution becomes increasingly heterogeneous as a result of the formation of shear bands. The local strain fields reveal that the ferrite grains experience significant plastic deformation, whereas the martensite islands are strained only elastically at this stage ($\varepsilon_{global} \leq 0.05$). The martensite band, on the other hand, shows local regions of high strain at those positions where it is the thinnest, as marked with white arrows in Fig. 1c and 1d. As can be verified from the micrographs, the martensitic band is severely deformed at these particular regions up to its fracture strain, leading to void nucleation. Careful examination of the complete series of strain maps shows that the intra-granular shear band intercepts the martensitic band exactly at these critical locations, making them the first sites where voids nucleate, while the martensite islands (and the rest of the martensite band) show hardly any deformation or void formation.

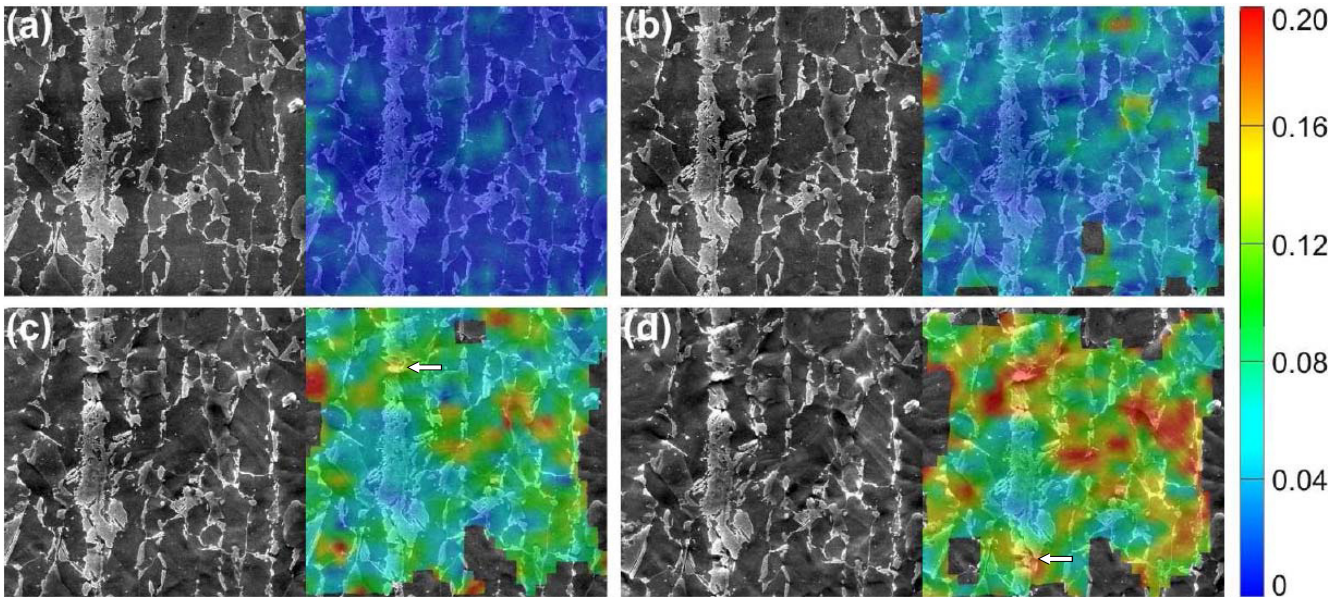

Fig. 7. *EMDIC analysis of martensitic-ferritic dual phase steel with a continuous martensitic band.[6]*

Let us now concentrate on the pearlitic ferritic steel shown in Fig. 8. At the first glance, examination of the micrographs and the strain maps at different stages of deformation reveals similar trends in the deformation as found for DP steel: initially formation of the slip lines in the ferritic grains and then the evolution of the strain distribution from homogeneous to increasingly heterogeneous with increasing deformation. However, more detailed analyses reveals that the first shear band initiates at a discontinuity in the pearlitic band (shown with a white arrow in Fig. 8b). As was confirmed by additional measurements, for the case that the band (morphology) is not continuous, the preferential path for the shear bands is through the gaps in the band. With further deformation, this shear band deforms steadily while the rest of the pearlitic band experiences only a limited amount of deformation (Fig. 8c). Only at much higher global strain, another shear band is developed that percolates through the narrowest section of the pearlitic band (shown with an arrow in Fig. 8d), in the absence of any void nucleation.

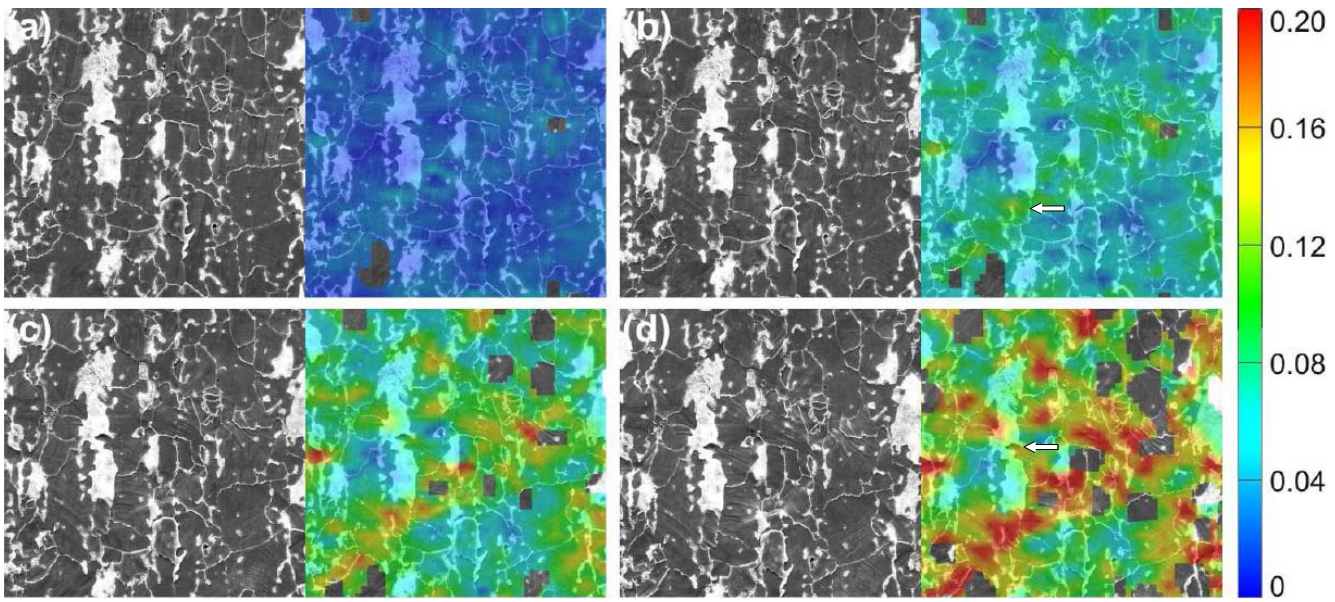

Fig. 8. *EMDIC analysis of pearlitic-ferritic steel with a non-continuous pearlitic band.[6]*

These results of the local analysis on two limit cases of banded structures show that the influence of a banded structure on the global properties (YS, UTS, ductility, etc.) of metals is critically dependent on the morphology of the band, as well as the mechanical behavior of the phase that composes the band. In microstructures where there is a continuous microstructural band, shear bands are forced to develop through the band, therefore they percolate through the narrowest section of the band. This forces the banded phase to deform beyond its plastic limit, especially if there is a significant difference in the ultimate strains of the phases composing the banded microstructure (e.g. the case of martensitic-ferritic dual phase steel). For discontinuous microstructural bands, shear bands naturally cross at the gaps within the band, thereby delaying early damage initiation. Obviously, the strength of the banded phase also plays an important role, e.g. a continuous band of a high fracture strength phase may accommodate high local stresses without damage initiation, whereas a low fracture strength phase may not.

4. CONCLUSIONS

In this work mechanical influences of segregation-induced banding in steels is investigated using in-situ tests coupled with real-time micrographic analysis. The microscopic-mechanical approach taken on board here is a strong tool that can be used for extending the understanding on many complex microstructural mechanisms, especially due the possibility of using the obtained micrographs for digital image correlation analysis to obtain the local strains at the micro-level. To optimize the micrographs for the latter analysis, first study investigated the influence of the critical experimental parameters on facet tracking, i.e. specimen surface preparation settings, scanning electron microscopy imaging settings (contrast modes, magnification, resolution, and contrast-brightness), and image correlation settings (facet size and facet step size). Results show that best correlations are achieved with a combination of electro-etching and chemical etching of the samples surfaces, by acquiring high-contrast, high resolution, low magnification SEM images in (pure) secondary electron contrast mode, and using the smallest facet size and facet step size applicable within limits of measurement noise and lack of contrast. Subsequently, these optimized settings are used for a case study on microstructural banding in steel, which revealed a clear detrimental effect for hard bands with a continuous morphology, thereby demonstrating the strength of the (optimized) EMDIC methodology.

REFERENCES

[1] R.A. Grange, Metall. Mater. Trans. B., 2 (1971) 417.
[2] A.R. Marder, Metall. Trans. A., 13 (1982) 85.
[3] W.A. Spitzig, Metall. Trans. A., 14 (1983) 271.
[4] A.S. Bor, ISIJ. Int., 31 (1991) 1445.
[5] X.L. Cai *et al.*, Metall. Trans. A., 16 (1985) 1405.
[6] C.C. Tasan *et al.*, Scripta Mater. (2010), doi:10.1016/j.scriptamat.2010.02.014.

Proceedings of the SEM Annual Conference
June 7-10, 2010 Indianapolis, Indiana USA

Development of Multi-scale Deformation Measurement System for Solid Materials

T. Arikawa*, G. Murasawa**, T. Koda**, A. Nishioka**, K. Miyata** and S. Yoneyama***

*Graduate Student, Yamagata University, 4-3-16, Jonan, Yonezawa, Yamagata 992-8510, Japan. tws52835@st.yamagata-u.ac.jp
**Department of Mechanical Engineering, Yamagata University, 4-3-16, Jonan, Yonezawa, Yamagata 992-8510, Japan.
***Department of Mechanical Engineering, Aoyama Gakuin University, 5-10-1 Fuchinobe, Sagamihara, Kanagawa 229-8558, Japan.

ABSTRACT

The purpose of this study is to perform Digital Image Correlation (DIC) by using images obtained from Scanning Electron Microscopes (SEM). Firstly, some pictures of SEM at magnifications of 200X and 5000X are taken without moving the specimen, and DIC is performed using by these pictures. From the results, we can see that the errors of small random displacement occur at whole correlation area for 200X and 5000X images, and drift of specimen occurs for 5000X images. However, the errors of small random displacement can be removed by performing the original image processing. About drift, we measure the amount of drift. As a result, it is seen that the amount of drift increases monotonously. Therefore, we try to predict the amount of drift by the proposed original method. Then, the drift can be eliminated from the results of DIC using SEM image.

1. INTRODUCTION

Steel and Aluminum alloys usually show local deformation behavior such as the propagation of Luders band, Portevin Le Chatelier effect and necking. Recently, some researchers began to study about the nucleation and propagation of shear band for some metal materials (Kuroda et al., 2007; Tong et al., 2005; Zhang et al., 2004; Cheong et al., 2006; Tang et al., 2005; Hoc et al., 2001; Louche et al., 2001). Then, macroscopic local deformation behaviors are derived from the minute deformation behavior such as the initiation and progress of slip or twinning deformation. Also, such initiation and progress behaviors are dependent on the force and its direction applied to each grain in polycrystalline. However, the force and its direction, on a grain in polycrystalline for macroscopic applied load, are unknown in general. Huge combinations of them exist in polycrystalline system. It is not practical for us to investigate all of them. On the other hand, it is well known that metal material sheets have texture after cold rolling and annealing. In this time, the crystal orientation on almost grains in polycrystalline becomes the same, and it is something practical for us to investigate the relationship between deformation behavior, crystal orientation and applied stress on a grain in polycrystalline. Also, it is much important to investigate the deformation behavior in a grain around grain boundary, and before or after the initiation of minute deformation.

Digital Image Correlation (DIC) is a powerful technique to evaluate the inhomogeneous deformation behavior. Many researchers have been utilizing DIC for solving the mechanism of something phenomena (Murasawa et al., 2009; Yoneyama et al., 2007). Furthermore, if we apply SEM image to DIC measurement, above mentioned investigation, the relationship between deformation behavior, crystal orientation and applied stress on a grain in polycrystalline, can be available for us.

The purpose of this study is to perform Digital Image Correlation (DIC) by using images obtained from Scanning Electron Microscopes (SEM). Firstly, some pictures of SEM at magnifications of 200X and 5000X are taken without moving the specimen, and DIC is performed using by these pictures. From the results, we can see that the errors of small random displacement occur at whole correlation area for 200X and 5000X images, and drift of specimen

T. Proulx (ed.), *Application of Imaging Techniques to Mechanics of Materials and Structures, Volume 4*, Conference Proceedings of the Society for Experimental Mechanics Series 14, DOI 10.1007/978-1-4419-9796-8_11, © The Society for Experimental Mechanics, Inc. 2013

occurs for 5000X images. However, the errors of small random displacement can be removed by performing the original image processing. About drift, we measure the amount of drift. As a result, it is seen that the amount of drift increases monotonously. Therefore, we try to predict the amount of drift by the proposed original method. Then, the drift can be eliminated from the results of DIC using SEM image.

2. DIGITAL IMAGE CORRELATION

DIC is one of the techniques for measuring the deformation of solid materials by using its images. In this method, the images before and after deformation of solid material are prepared, and the displacement distribution on the surface of material can be measured by comparing the patterns of each area within the image before and after deformation. The details of calculation process are following.

The plane surface of an object is observed usually by a CCD camera with an imaging lens. Then, the images on the surface of the object, one before and another after deformation, are recorded, digitized and stored in a computer as digital images. These images are compared to detect displacements by searching a matched point from one image to another. Here, because it is almost impossible to find the matched point using a single pixel, an area with multiple pixel points (such as 20 × 20 pixels) is used to perform the matching process. This area, usually called subset, has a unique light intensity (gray level) distribution inside the subset itself. It is assumed that this light intensity distribution does not change during deformation. Figure 1 shows the part of the digital images before and after deformation. The displacement of the subset on the image before deformation is found in the image after deformation by searching the area of same light intensity distribution with the subset. Once the location of this subset in the deformed image is found, the displacement of this subset can be determined. In order to perform this process, the surface of the object must have a feature that allows matching the subset. If no feature is observed on the surface of the object, an artificial random pattern must be applied. The above concept is common among other techniques in digital image correlation.

Based on the above basic concept, following function (normalized cross-correlation) is used to match the subset from one image to another.

$$C(x,y,x^*,y^*) = \frac{\sum F(x,y)G(x^*,y^*)}{\sqrt{\sum F(x,y)^2 \sum G(x^*,y^*)^2}} \tag{1}$$

where $F(x,y)$ and $G(x^*,y^*)$ represent the gray levels within the subset of the undeformed and deformed images, and (x,y) and (x^*,y^*) are the coordinates of a point on the subset before and after deformation, respectively. The symbol of the summation represents the sum of the values within the subset. The coordinate (x^*,y^*) after deformation relates to the coordinate (x,y) before deformation. Therefore, displacement components are obtained by searching the best set of the coordinates after deformation (x^*,y^*) which maximize $C(x,y,x^*,y^*)$.

The pixel points within the subset usually locate among the pixels on the deformed image. In addition, the subset can be deformed along with the deformation of the object's surface. In a digital image, gray values exist on discrete pixel points. In order to calculate the correlation on the position among pixel points and to allow the deformation of the subset, therefore, the values of gray level among the pixel points are required.

The simplest approach to obtain the value of gray level among the pixels is a bilinear interpolation. Not only the measurement accuracy but also the time for analysis is obviously dependent on the interpolation method. However, it is noted that the gray level obtained at a fractional pixel point by any interpolation technique is essentially not an actual value but just an interpolated and deduced value. It is observed that continuous light intensity distribution is obtained by interpolation.

The coordinate (x^*,y^*) after deformation relates to the coordinate (x,y) before deformation. Assuming that the displacement gradients are constant throughout the subset, then the coordinate (x^*,y^*) is expressed as

$$\begin{aligned} x^* &= x + u_x + \frac{\partial u_x}{\partial x}\Delta x + \frac{\partial u_x}{\partial y}\Delta y \\ y^* &= y + u_y + \frac{\partial u_y}{\partial x}\Delta x + \frac{\partial u_y}{\partial y}\Delta y \end{aligned} \tag{2}$$

where Δx and Δy are the x and y directional components of the distance from the center of the subset to the point (x,y) respectively. As a result, the subset deforms in the parallelogram as shown in Fig. 2. In this figure, the center point P and the point Q on the undeformed subset move to the points P' and Q' on the deformed subset, respectively. Then, the moving distance from the point P to the point P' is interpreted as the displacement and the position of the point Q' is expressed as Eq. (2). It is noted that the displacement gradients, i.e., the strains are assumed as uniform within the subset. On the other hand, higher order displacement gradients can be used to express complicated deformation of the subset.

The correlation coefficient C in Eq. (1) is the function of the displacement components u_x and u_y, and the displacement gradients $\partial u_x/\partial x$, $\partial u_x/\partial y$, $\partial u_y/\partial x$, $\partial u_y/\partial y$. Therefore, the displacements are determined by searching the best set of the displacements and the displacement gradients, which maximize the correlation coefficient C. At first, the approximate displacements are estimated within the accuracy of one pixel with zero gradients. In this process, gray level interpolation is not needed. After the first estimation, the process varies to search both the displacements and the displacement gradients with gray level interpolation. Here, the following simultaneous equation that is obtained by differentiating Eq. (1) by the displacements and the displacement gradients is solved to find the extreme value of the correlation coefficient.

A numerical technique such as a Newton-Raphson method can be used. In final, the displacements and the displacement gradients are obtained. It is noted that the displacement gradients are simultaneously calculated with the displacements in order to increase the accuracy of the displacements. Therefore, the displacement gradients themselves obtained by above procedure are not accurate to evaluate strains. If the second order displacement gradients are included to evaluate the displacements, the accuracy of first order displacement gradients may be improved.

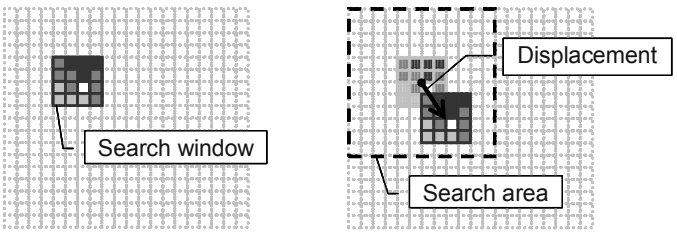

(a) Undeformed image (b) Deformed image

Figure 1 Schematic illustration of the principle of DIC

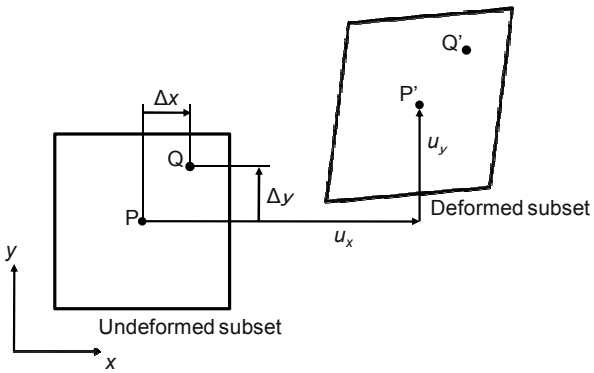

Figure 2 Subset before and after deformation

3. VERIFICATION FOR APPLYING INTACT SEM IMAGE TO DIC MEASUREMENT

A SEM image is drawn from the amount of secondary electrons emitted from the specimen during irradiating electron beam. Then, it is well known that the amount of secondary electrons is unstable due to a little scatter of density and irradiation of electron beam. Therefore, in general, it is suitable for SEM image to observe the object, but not suitable to quantitatively analyze its deformation and so on. Firstly, we investigate the verification for applying intact SEM image to DIC measurement in this section.

3.1 Methods

3.1.1 Specimen and measurements for non-displacement

The specimen used for this experiment is a thin strip of Al-Mg (94.5Al 5.5Mg [wt.%]) plate. The surface of specimen is electrically polished, and the grain boundary is electrically etched.

Tiny-SEM510 (TECHNEX) is used in this experiment. The magnifications used in this experiment are 200X and 5000X. Also, the schematic illustration of a non-displacement measurement is shown in Fig.3. Measurement methods are followings. (1) The specimen is put on the stage in chamber, and it is never moved during experiments. (2) SEM images are taken at a constant interval (1 minute) for 10 minutes. (3) After acquiring some SEM images, DIC is performed by using the obtained images.

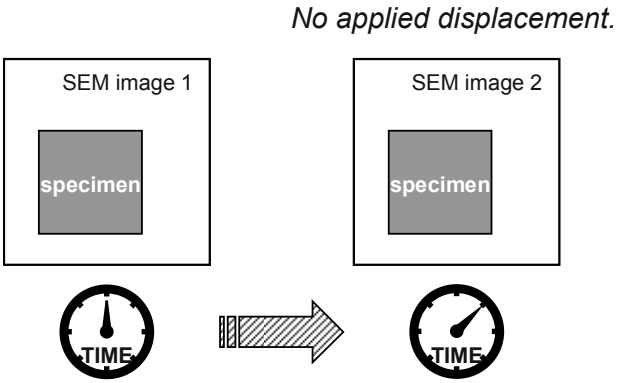

Figure 3 Schematic illustration of non-displacement test

3.2 Results And Discussion

3.2.1 Displacement distribution at magnification 200X

The SEM image used for this experiment is shown in Fig.4. The length per pixel is 0.78 um/pixel in SEM image. In present study, the region surrounded with the black square line in the image is defined as a "correlation region". DIC is performed in correlation region by using the images at 0s and 540s. This displacement distribution should be 0 because specimen is not moved during experiment.

The results of the non-displacement measurement at the magnification 200X are shown in Fig.5. The vertical axis and horizontal axis in Fig.5 reveal the vertical position *y* and the horizontal position *x* as shown in Fig.4. Both units of them are pixel in figure. Also, the color level in figure shows the degree of displacement errors. *u* presents the x-displacement errors and *v* indicates y-displacement errors. Those units are um. From even a cursory examination of Fig. 5, displacements of *u* and *v* are scattered all over the correlation region. But those values are less than about 0.8 um (≒1 pixel). Then, the cause of displacement errors can be assumed as a little scatter of density and irradiation of electron beam. As a result, there exists the random change of gray level in each SEM image. In present study, the change of gray level is defined as "random noise". Furthermore, in the region of the upper part in SEM image, it seems that large displacement errors occurs with 0.8 um or more. The region is located in the upper part of the correlation region in Fig.4. Also, the contrast of gray level in the region is not obvious as compared with other region. In the calculation of displacement, the correlation coefficient of formula (1) can determine the correct displacement by using the surrounding pattern, even if a little random noise occurs. However, large displacement errors occur at the upper part in SEM image. This can be notice that large displacement error may occur in the case of combination of low contrast and random noise in image.

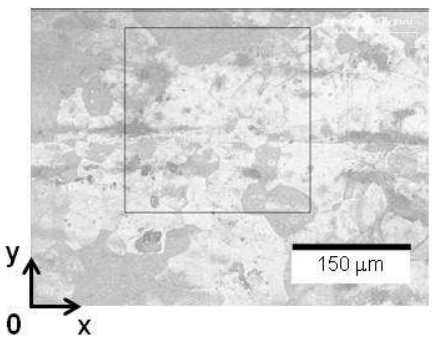

Figure 4 SEM image of an aluminum alloy at 200X. The length per pixel is 0.78 um/pixel

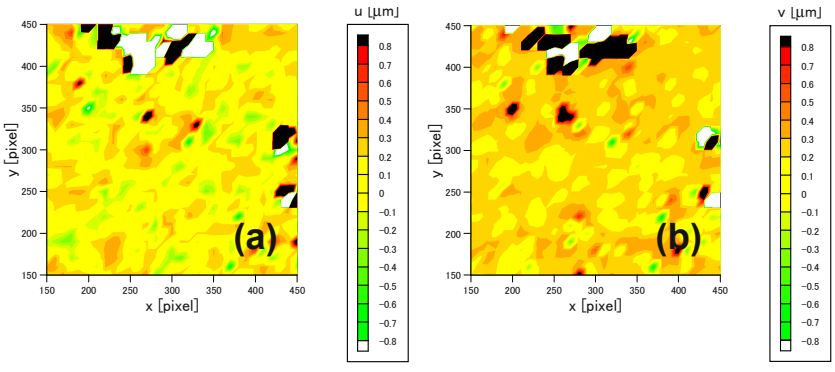

Figure 5 (a) Horizontal and (b) vertical displacement field at 200X obtained from DIC under non-displacement test. The maximum range of displacement is ±0.8 um (≒±1 pixel)

3.2.2 Displacement distribution at magnification 5000X

The SEM image used for this experiment is shown in Fig.6. In this image, there also exists random noise. The length per pixel is 0.025 um/pixel. DIC is performed in correlation region by using the images at 0s and 540s.
The results at the magnification 5000X are shown in Fig.7. From the results, it is seen that the value of displacement errors are much large as compared with the result of 200X, especially in horizontal displacement. The values are about 0.5 um (20 pixel) at the maximum. Furthermore, its displacement errors uniformly occur all over the correlation region. It can be predicted from the fact that SEM image moves along to a direction during experiment. The cause of parallel movement can be assumed as the thermal expansion of stage in chamber. Thus, in present study, the parallel movement of SEM image is defined as "drift". Also, large displacement errors occur in the region of the bottom part in SEM image. This can be the same reason as the result of 200X, large displacement error may occur in the case of combination of low contrast and random noise in image.

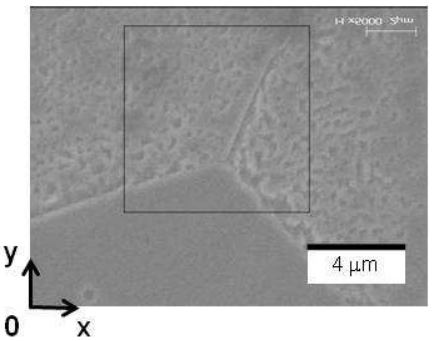

Figure 6 SEM image of an aluminum alloy at 5000X. The length per pixel is 0.025 um/pixel

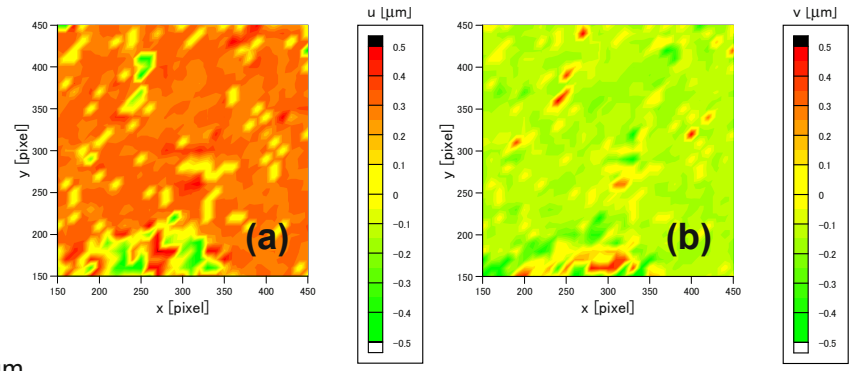

Figure 7 (a) Horizontal and (b) vertical displacement field at 5000X obtained from DIC under non-displacement test. The maximum range of displacement is ±0.5 um (±20 pixel)

4. PROPOSED NOVEL METHOD FOR APPLYING SEM IMAGE TO DIC MEASUREMENT

Above results of non-displacement measurement pointed two problems on performing DIC using SEM images. The first is "random noise" derived from the random change of gray level in each SEM image. The second is "drift" that SEM image moves along to a direction during experiment. In this chapter, we propose the elimination method of random noise and the novel elimination method of drift. Then, applying SEM image, 200X and 5000X, to DIC measurement is tried finally.

4.1 Elimination Method Of Random Noise

Figure 8 shows the schematic illustration of method for eliminating random noise in SEM image. In this method, as shown in Fig.8, the gray levels are averaged at same position of pixel in each SEM image.
In present study, this elimination method of random noise can be automatically performed by in-house software suited on a LabVIEW platform. To begin with, 10 SEM images without movement are taken continuously by using Tiny-sem510. Secondarily, the former 5 SEM images are averaged by using in-house software, then the latter ones are also done. After this processing, we can get 2 averaged SEM images. Thirdly, DIC is performed by the 2 averaged SEM images.
The results are shown in Fig.9. As shown in this figures, we can see that the displacement errors become much small as compared with Fig.5. Furthermore, large displacement errors in the region of the upper part, with 0.8 um or more in Fig.5, becomes small ones with 0.5 um or less. From these results, we can think that the random noises can be disappeared by this technique.
Table 1 shows the average value of displacement errors all over the correlation region with and without random noise. These values are determined from the average value of displacement errors for all pixels of correlation region. From these results, we can see that the displacement errors of *u* and *v* decrease up to 78% and 73%, as compared before image processing with after image processing. Also, present results indicate that the resolution of displacement is about 0.1~0.14 um (100~140 nm) in the magnification 200X.

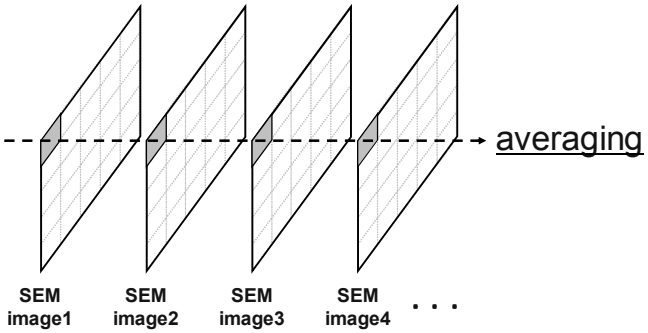

Figure 8 Schematic illustration of method for averaging gray level

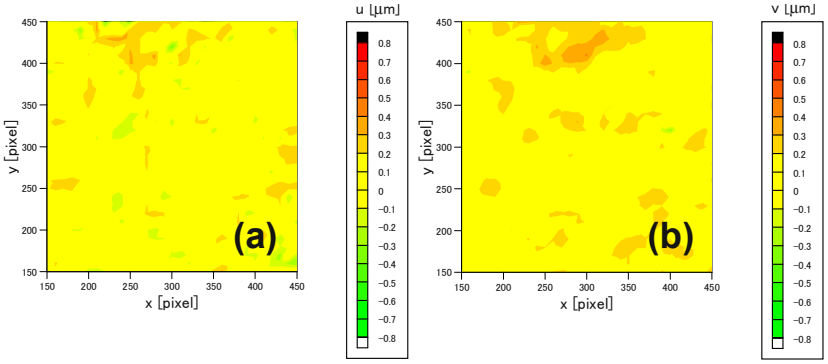

Figure 9 (a) Horizontal and (b) vertical displacement field without random noise at 200X obtained from DIC under non-displacement test. The maximum range of displacement is ±0.5 um (≒±1 pixel)

Table 1 The average absolute value of displacement errors with and without random noise at 200X

Before image processing		After image processing	
u [um]	*v* [um]	*u* [um]	*v* [um]
0.495	0.499	0.108	0.134

4.2 Elimination Method Of Drift

4.2.1 Measurement for the amount of drift during experiments

It can be predicted that SEM image moves along to a direction during experiment. The cause of parallel movement can be assumed as the thermal expansion of stage in chamber. So, we try to measure the amount of drift in chamber from SEM image. The specimen used for measurement is the same as above section. JSM-5410LV (JEOL) is used as SEM so that we can use it for long time. Firstly, SEM images are continuously taken at a constant interval (1 minute) for 1 hour. Secondarily, DIC is performed for each image, such as 1-2, 2-3, 3-4, ••••, 59-60. Thirdly, the median value is determined as a typical displacement for all pixels of correlation region in a result of DIC. This median value is defined as the relative amount of drift during experiment. Then, these results are integrated to acquire the absolute amount of drift during measurement.

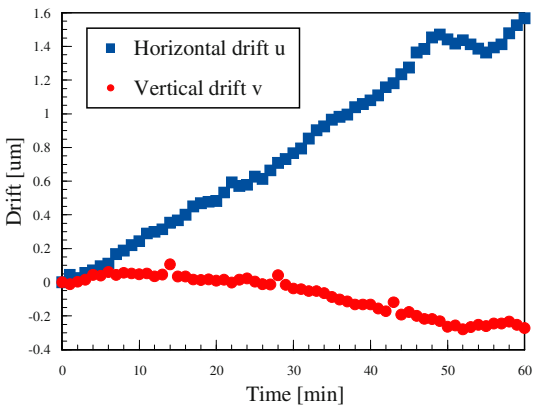

Figure 10 The absolute amount of drift as a function of time at 5000X

Figure 10 shows the absolute amount of drift as a function of time during experiment. The plots of blue square and red circle are horizontal amount of drift u and vertical amount of drift v. From the results, it is seen that the amount of drift increases or decreases monotonously. Then, that does not become equilibrium value during present experiment.

4.2.2 Prediction method of drift during experiment

From Fig.10, the amount of drift increases or decreases monotonously. Therefore, following novel method is proposed to predict the amount of drift during experiment, especially for tensile loading in chamber of SEM. Figure 11 shows the schematic illustration of method for predicting the amount of drift. Multi-step tensile loading is adopted as loading method.

(1) Several SEM images are taken before mechanical loading.
(2) Mechanical loading is applied for specimen.
(3) Several SEM images are taken after mechanical loading.
(4) The amount of drift is calculated for several images before and after mechanical loading as shown in Fig.11(a).
(5) Quadratic approximation is performed for the amount of drift and time curve. Firstly, an arbitrary point x_0 on the amount of drift and time curve is selected, and its before and after points are pointed. Secondarily, these 3 points are approximated by quadratic least squares method. Thirdly, the slope of approximated quadratic curve is obtained at the point x_0. This calculation is conducted at all points on curve. Obtained drift speeds are shown in Fig. 11(b).
(6) Linear approximation is carried out for drift speed-time relation as shown in Fig.11(b).
(7) The amount of drift is predicted by integrating the approximated linear line with respect to time from just before mechanical loading to just after one as shown in Fig.11(b)..
Calculation is automatically conducted for all data by in-house data analysis software suited on a LabVIEW platform.

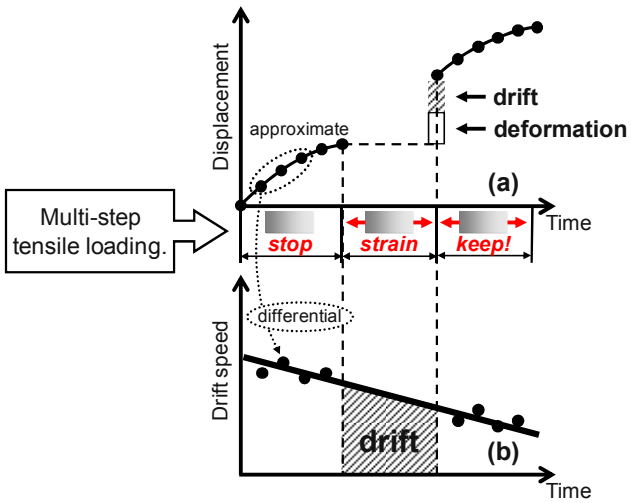

Figure 11 Schematic illustration of method for predicting the amount of drift

4.2.3 Elimination of drift and random noise

SEM images are continuously taken at a constant interval (1 minute) for 1 hour. The SEM image is shown in Fig.12. The length per pixel is 0.04 um/pixel in SEM image. In present section, the prediction interval for the amount of drifts is for 10 minutes from 20 min to 30 min in Fig.10. Also 10 SEM images from 11 min to 20 min are used in order to predict the amount of drift before mechanical loading. 10 SEM images from 30 min to 39 min are used in order to predict the amount of drift after mechanical loading. From the 20 images before and after mechanical loading, the amount of drift is predicted along present method. Furthermore, the amount of drift is eliminated from each images, the 11~20 min images and the 30~39 min images. Then, random noise is also eliminated by using the 11~20 min images and the 30~39 min images. 2 SEM images without drift and random noise can be prepared. After that, DIC is performed to calculate the displacement by using above the 2 SEM images.

Figure 13 shows the results at magnification 5000X by using images with random noise and drift. Also, Fig.14 shows the results at magnification 5000X by using images without random noise and drift. Furthermore, Table 2 shows the average value of displacement errors all over the correlation region with and without random noise and drift. As a result, the displacement errors of *u* and *v* decrease up to 95% and 60%, as compared before image processing with after image processing, respectively. Also, present results indicate that the resolution of displacement is about 0.02~0.03 um (20~30 nm) in the magnification 5000X.

From these results, big improvement can be accomplished for measuring the displacement at the magnification 5000X by applying present method.

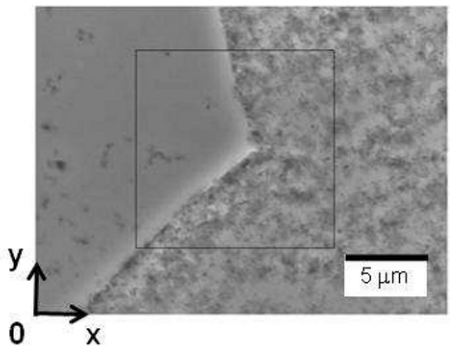

Figure 12 SEM image of an aluminum alloy at 5000X. The length per pixel is 0.04 um/pixel

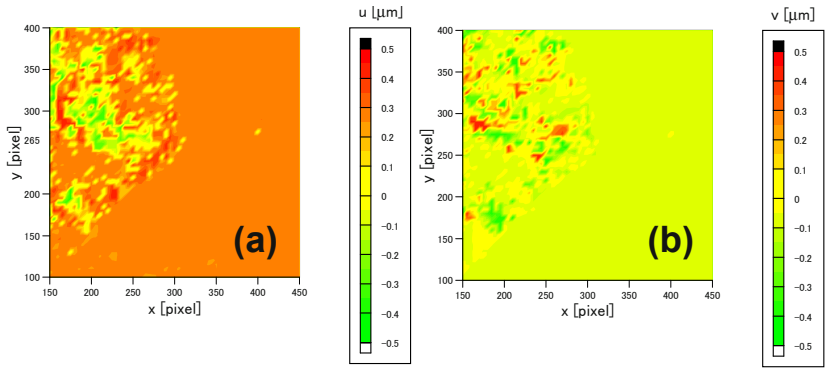

Figure 13 (a) Horizontal and (b) vertical displacement field at 5000X obtained from DIC under non-displacement test. The maximum range of displacement is ±0.5 um (±12.5 pixel)

Table 2 The average absolute value of displacement errors with and without random noise and drift at 5000X

Before image processing		After image processing	
u [um]	*v* [um]	*u* [um]	*v* [um]
0.261	0.070	0.013	0.028

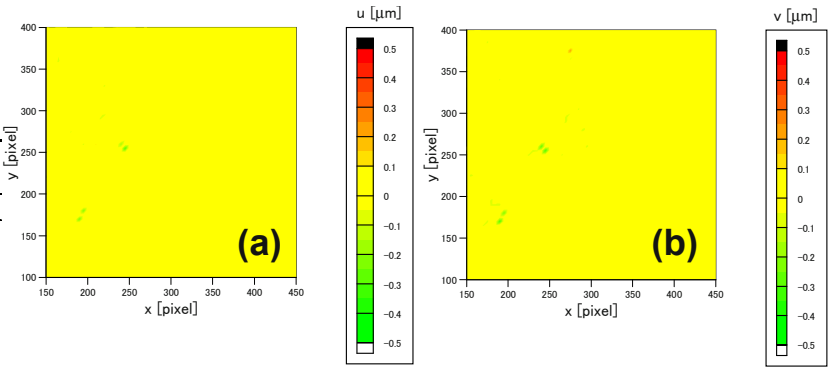

Figure 14 (a) Horizontal and (b) vertical displacement field without random noise and drift at 200X obtained from DIC under non-displacement test. The maximum range of displacement is ± 0.5 um (±12.5 pixel)

5. CONCLUSIONS

In present study, firstly, some pictures of SEM at magnifications of 200X and 5000X are taken without moving the specimen, and DIC is performed using by these pictures. From the results, following conclusions emerge,

(1) The errors of small random displacement occur at whole correlation area for 200X and 5000X images.

(2) The drift of specimen occurs for 5000X images.

The errors of small random displacement can be removed by performing the original image processing. About drift, we try to predict the amount of drift by the proposed original method. Then, the drift can be eliminated from the results of DIC using SEM image. From the results, following conclusions emerge,

(3) By applying present method, big improvement can be accomplished for measuring the displacement at the magni-

fication 5000X. Also, present results indicate that the resolution of displacement is about 0.1~0.14 um (100~140 nm) in the magnification 200X and about 0.02~0.03 um (20~30 nm) in the magnification 5000X.

REFERENCES

Cheong, K.-S. and Busso, E.P., 2006. Effects of lattice misorientations on strain heterogeneities in FCC polycrystals. J. Mech. Phys. Sol. **54**, 671-689.

Hoc, T., Rey, C. and Raphanel, J.L., 2001. Experimental and Numerical Analysis of Localization during Sequential Test for an IF-Ti Steel. Acta mater. **49**, 1835-1846.

Jin, H., Lu, W.Y., and Korellis, J., 2008. Macro-scale Deformation Measurement Using the Digital Image Correlation Technique and Scanning Electron Microscope Imaging. J. Strain Analysis **43**, 719-728.

Kuroda, M. and Tvergaard, V., 2007. Effects of texture on shear band formation in plane strain tension/compression and bending. Int. J. Plasticity **23**, 244-272.

Louche, H. and Chrysochoos, A., 2001. Thermal and dissipative effects accompanying Luders band propagation. Mater. Science and Engineering **A307**, 15-22.

Murasawa et al. Macroscopic stress-strain curve, local strain band behavior and the texture of NiTi thin sheets. Smart Mater Struct (2009) vol. 18 (5) pp. 055003

Murasawa, G., Koushinbou, M., Yoneyama, S., Sakuma, T. and Takashi, M., 2004. Measurement of Inhomogeneous Deformation Behavior Arising in Shape Memory Alloy. Journal of the Society of Materials Science **53**(9), 995-1005.

Sutton, M.A., Li, N., Joy, D.C., Reynolds, A.P. and Li, X., 2007. Scanning Electron Microscopy for Quantitative Small and Large Deformation Measurements Part I: SEM Imaging at Magnifications from 200 to10,000. Experimental Mechanics. **47**, 775-787.

Sutton, M.A., Li, N., Garcia, D., Cornille, N., Orteu, J.J., McNeill, S.R., Schreier, H.W., Li, X. and Reynolds, A.P., 2007. Experimental Mechanics. **47**, 789-804.

Tang, C., Li, Y. and Zeng, K., 2005. Effect of residual shear bands on serrated flow in a metallic glass. Materials Letters **59**, 3325-3329.

Tong, W., Tao, H., Zhang, N. and Hector Jr., L.G., 2005. Time-resolved strain mapping measurements of individual Portevin-Le Chatelier deformation bands. Scripta mater. **53**, 87-92.

Toyooka, S., Madijarova, V. and Kadono, H. 2002. Full-field Dynamic Measurement of PLC Effect in Plastic Deformation of Ai-alloy by DESPI. J. Mechanical Engineers 29-30.

Yoneyama and Morimoto. Accurate displacement measurement by correlation of colored random patterns. Jsme Int J A-Solid M (2003) vol. 46 (2) pp. 178-184

Yoneyama et al. Automatic evaluation of mixed-mode stress intensity factors utilizing digital image correlation. Strain (2006) vol. 42 (1) pp. 21-29

Yoneyama S, Kitagawa A, Iwata S, et al. Bridge deflection measurement using digital image correlation. EXPERIMENTAL TECHNIQUES (2007) vol. 31(1) pp.34-40

Zhang, N. and Tong, W., 2004. An experimental study on grain deformation and interactions in an Al-0.5% Mg multicrystal. Int. J. Plasticity **20**, 523-542.

Proceedings of the SEM Annual Conference
June 7-10, 2010 Indianapolis, Indiana USA

An Integrated Tool for Estimation of Material Model Parameters

Sarbajit Ghosal*, Narasimha Acharya, T. Eric Abrahamson, La Moyne Porter II
SC Solutions, Inc., 1261 Oakmead Pkwy, Sunnyvale, CA 94085

Hubert W. Schreier
Correlated Solutions, Inc.

(*Corresponding author's email: ghosal@scsolutions.com)

ABSTRACT

In this paper, we present results on estimating material model parameters from inverse analysis of full-field deformation data that was obtained with a prototype of a novel integrated tool consisting of a digital image correlation system and software for data analysis and parameter estimation. Such a tool is needed for characterizing the properties of new materials, and for calibrating and validating material models. The stereo microscope-based image analysis system may be used for measurements at temperatures up to 750°C, and field sizes of approximately 1 mm. The Graphical User Interface (GUI)-based parameter estimation tool integrates modules for image data analysis and inverse analysis, and incorporates features for interfacing the tool with commercial finite element (FEM) packages. The GUI, together with a micrograph of the sample, is used to select a subset of the imaged region for analysis, and for specifying sample grain boundaries needed for developing the FEM model. Data analysis includes data averaging to reduce measurement noise, and filtering to correct for rigid body translations and rotations. The inverse analysis module runs the FEM model under experimental loading conditions within its iterative loop, using the downhill simplex method for parameter estimation. The methodology was successfully validated from measurements on a superalloy sample.

1 An Integrated Tool for Full-field Measurements and Model Calibration

In recent years, complex multi-scale material models have been increasingly used in design and analysis for various engineering applications. The scope of these physics-based models is varied, dealing with stress-strain relationships, defect initiation and growth, thermal behavior, fracture mechanics, etc. A primary purpose of attaining predictive capabilities using the material models is to estimate the performance, safety and reliability of the components that are developed using these materials, and operated under a wide range of conditions. The capabilities may be used for lifetime prediction of existing mechanical components, or for predicting the performance limits of components designed with new, engineered materials. However, for these models to be used reliably, they first need to be calibrated and validated.

A formal approach for estimation of material model parameters from experimental data was presented by Johnson *et al.* [1] with the goal of efficient model validation. This approach integrates experiments with a software platform where optimization techniques use FEM models of the sample and the data to estimate model parameters. In a typical experiment, a solid sample is subjected to a sequence of step changes in load conditions. A series of images of the sample's region-of-interest (ROI) is acquired at each load step. The images are then precisely aligned and the evolution of the displacements is calculated from the difference of each of the images relative to a reference image following extensive image analysis [1]. As shown in Figure 1, an iterative inverse analysis is required to estimate the material parameters of the model.

T. Proulx (ed.), *Application of Imaging Techniques to Mechanics of Materials and Structures, Volume 4*, Conference Proceedings of the Society for Experimental Mechanics Series 14, DOI 10.1007/978-1-4419-9796-8_12, © The Society for Experimental Mechanics, Inc. 2013

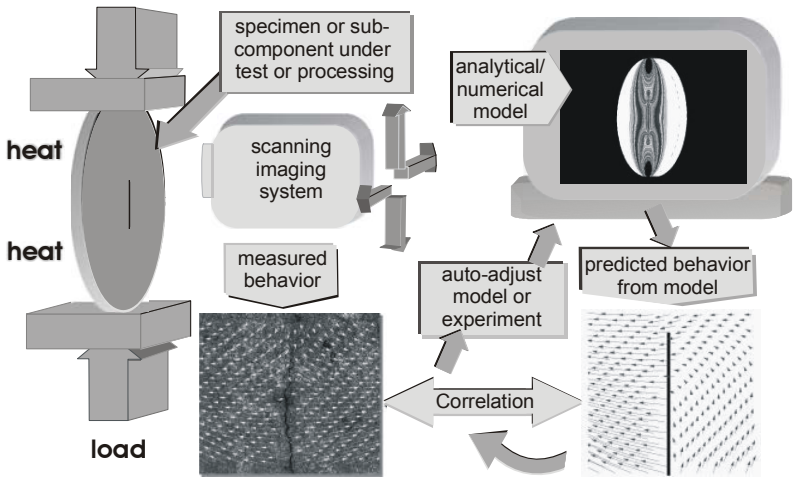

Figure 1: Schematic representing the process material model parameter estimation [1].

We have developed this concept into a novel integrated measurement, analysis, and parameter estimation tool that enables materials engineers and researchers to make deformation measurements of materials at high magnification and at high temperatures, then analyze the data, and run parameter estimation computations using commercial FEM models of the sample in an iterative procedure within the tool. In this section, we give an overview of the tool. The following sections detail results obtained for a material parameter estimation application.

The tool includes a new high-magnification stereo microscope-based Digital Image Correlation (DIC) system (Vic 3D) that can measure deformation up to temperatures of 750°C with sub-micron resolution. DIC is a non-contacting measurement technique widely used in experimental mechanics to acquire full-field deformation measurements [2]–[6]. The technique uses a random dot pattern applied to the test article to track the deformation on the surface (see Figure 2). During the experiment, images are taken at intervals, and digital image correlation is then used to determine the deformation in the image plane. A calibration is performed in order to relate the displacements found in the image plane to object displacements. The calibration permits a three-dimensional reconstruction of the object shape, as well as the determination of the complete, three-dimensional displacement vector field.

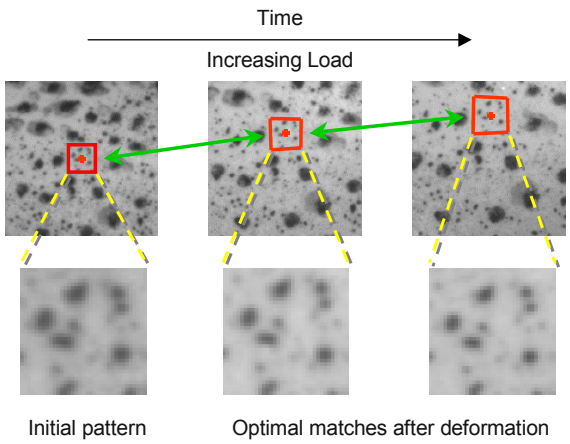

Figure 2: Tracking of object deformation using Digital Image Correlation.

The underlying concept of DIC is the measurement of displacement (and possibly displacement gradients as well as higher-order terms) at a point in an image by considering the gray value pattern in a small neighborhood. Given a second image, the objective of the method is to find the displacements (and possibly higher-order terms) that maximize the similarity between the pattern in the original image neighborhood and a displaced (and possibly deformed) version of the same pattern in the second image. An efficient method to solve this problem is the iterative algorithm proposed originally in [3]. Let θ be a parameter vector that contains the image displacements and possibly higher-order terms. Let f_i denote the gray values in the original image neighborhood, and $g_i(\theta)$

denote the corresponding gray values in the image *after* deformation. An objective function, **E**, is defined and minimized using standard numerical methods to obtain the best parameter estimate, $\hat{\theta}$.

$$\mathbf{E} = \sum_i \left(f_i - g_i(\theta) \right)^2 . \quad (1)$$

The objective function could be based on the sum of the squared differences as shown above, or could use the normalized cross-correlation as well as the zero-mean normalized cross-correlation criteria for improved performance. The resolution capabilities of the DIC method have been shown to be better than 0.01 pixels for displacements with negligible bias [5], [6]. Since the digital image correlation method acquires displacement and strain data over the entire specimen area being imaged, it is ideally suited to measure non-homogeneous deformation fields.

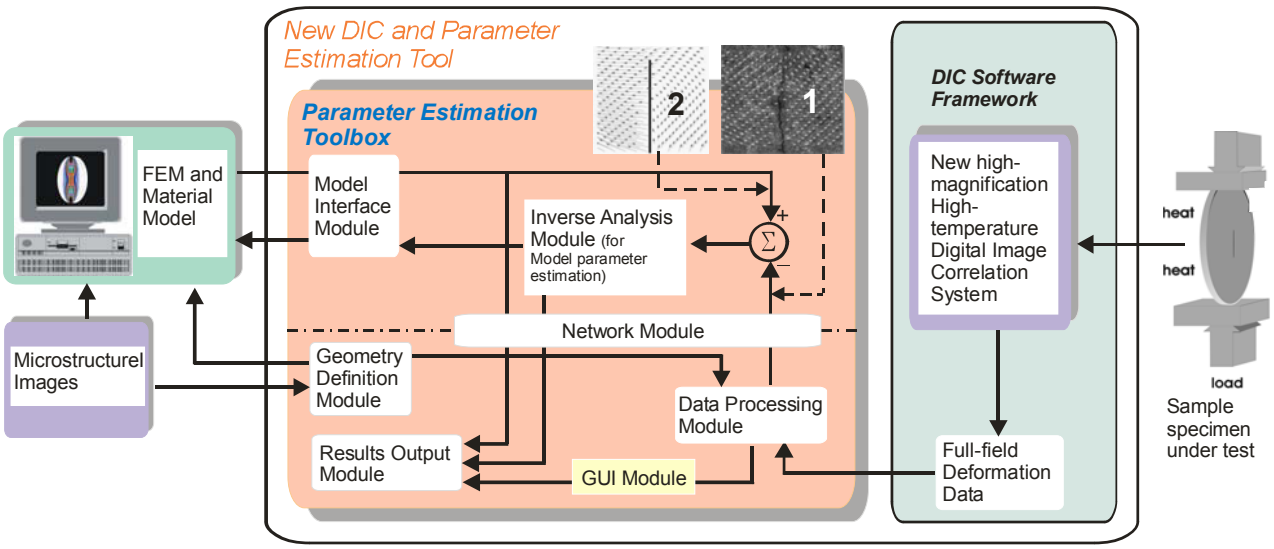

Figure 3: Schematic overview of the tool prototype. The images 1 and 2 show the deformation fields from FEM computations and the DIC data, respectively.

Figure 3 shows a high-level schematic of the integrated tool. The deformation data produced by Vic 3D is an input to the Parameter Estimation Toolbox (PE Tool), which consists of seven functional modules that exchange data (mostly through files) as shown by the arrows in Figure 3, and are related as follows:

- The *Model Interface Module* implements a protocol for exchanging data with the user-created FEM model (using third-party software) of the sample that, in turn, incorporates the material model.
- The *Geometry Definition Module* allows the user to interactively identify the grain boundaries in the form of polygons using a digital image of the microstructure, and also specify regions that the user wishes to exclude from the parameter estimation computations, e.g., if the deformation data in those regions is not sufficiently accurate.
- The *Data Processing Module* performs extensive pre-processing of the data from Vic 3D (including data averaging, transformations, etc.) to allow the user to manage the large amounts of deformation data from Vic 3D.
- The *Inverse Analysis Module* uses optimization algorithms to determine the optimal values of the material model parameters that minimize the difference between the measured and the model-predicted displacements while running the FEM model in an iterative loop.
- The *Results Output Module* incorporates several file manipulation and plotting routines to graphically display results of data analysis and parameter estimation computations.
- The *Graphical User Interface (GUI) Module* serves as the interface to all the other modules, and it integrates the various modules into one user-friendly tool. It enables the user to develop, control, and examine the results of data processing and the parameter estimation process on a Windows desktop.
- The *Network Module* allows the user to optionally perform the computationally-intensive inverse analysis on a different high-performance computer (referred to as target computer) while controlling the task using the GUI Module from the Windows “host” machine. The data and the results being

generated are available to the user for interaction and visualization purposes *via* the GUI. In Figure 3, the dot-dashed line separates the software modules that run on the host and target computers.

The integrated hardware-software tool is innovative in many ways. The high magnification stereo-microscope system permits deformation measurement with sub-micron resolution. The furnace with optical access enables measurements at high temperatures using the stereo microscope. The parameter estimation software has been designed to be modular and can be adapted to various applications easily. For example, the PE Tool can be interfaced with a wide range of commercial FEM packages and various data formats. It can incorporate new optimization techniques, and can use deformation data from multiple sources.

2 Experiment and Data Analysis

As a demonstration of the tool, deformation measurements under tensile loading were performed on a dogbone sample made of single-crystal nickel superalloy. The dogbone dimensions were 50 mm (length) by 8 mm (width, 3 mm in the neck region) by 1.5 mm (thickness), as shown in Figure 4. The rectangular measurement area of dimension 6.5 mm by 2.7 mm was located at the center of the sample on one surface. The Bunge-Euler angles, Φ_1, Ψ and Φ_2, were used to characterize the orientation of the crystal axis of the single-crystal sample. Sequential rotations about the laboratory coordinate axes (or the primary axes of the sample) bring the former into alignment with the principal crystallographic directions. The values of these angles were measured separately as $\Phi_1 = 8.6°$, $\Psi = -3.2°$ and $\Phi_2 = -8.3°$.

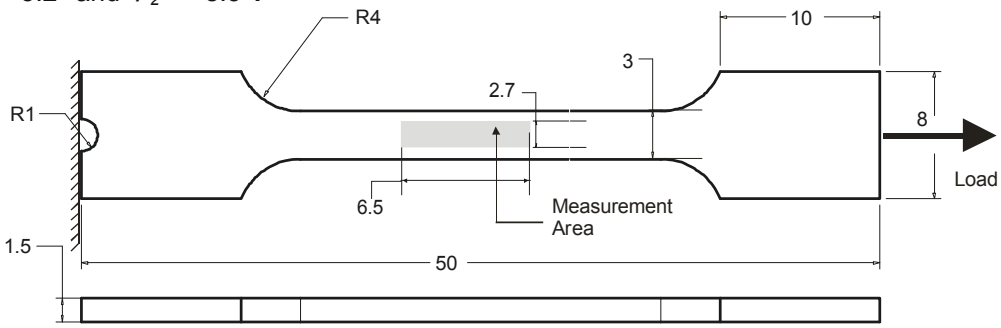

Figure 4: Schematic of the dogbone sample of the single crystal nickel superalloy showing the loading arrangement and measurement area. All dimensions shown are in mm. The schematic is not drawn to scale.

In the experiment conducted at room temperature, 240 image pairs were acquired before specimen failure, resulting in approximately 1.4 GB of image data. Image processing using the Vic-3D stereo image correlation software yielded approximately 60,000 data points per load step. However, for parameter estimation, we need deformation data at each mesh point in the measurement region of the FEM model (as described in Section 3.1). To this end, the DIC data was averaged at each mesh point using an exponential weighting function whose shape is specified by the user. There were 1071 mesh points in the FEM model of the sample, and the deformation at each of these points was obtained by averaging data at about 50–200 data points in the immediate neighborhood. The averaging also reduced the measurement noise significantly, especially for small deformations. The averaged data was then filtered to remove rigid body translation and rotation using the following filter *at each load*:

$$F = \begin{cases} u + u_0 - u_{left\_edge} \\ v + v_0 - \mathrm{mean}(v) \\ \\ \min_{\theta} \left| R(\theta) \begin{bmatrix} u \\ v \end{bmatrix} \right|_{y=0} \end{cases} \tag{2}$$

Here, u_0 and v_0 are the offsets to account for initial deformation measurements with non-zero loading. The third operation is the rotational transformation which corrects the rigid-body rotation. We will refer to the filtered displacement data as u_f, v_f, and w_f. The profiles of v and v_f are shown in Figure 5. In order to use deformation data at *all loads* for *each mesh point*, we computed the best-fit linear fit to the load-displacement graph in the elastic region, and used the slope of this line in our inverse analysis. In the process, we further reduced the effect of measurement noise.

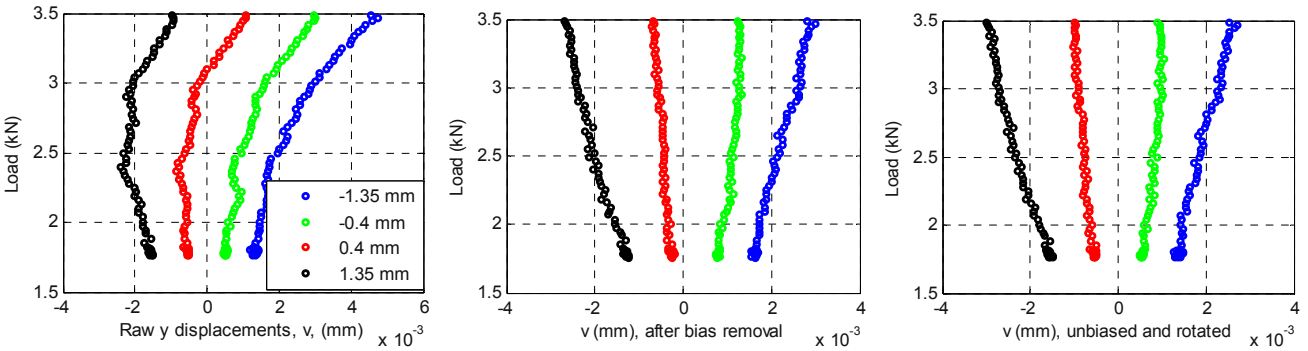

Figure 5: Effect of translation and rotation on load *vs.* elastic *v* data at four points along the vertical centerline of the sample. **Left:** raw data. **Center:** data after the mean value of *v* has been subtracted. **Right:** final filtered data, v_f, after performing rigid body rotation on data from the second figure.

For the plastic deformation data we found that the filtering could not adequately correct the distortions in the y-displacements (v_f) as seen in the set of graphs on the left side of Figure 6, perhaps because of minor twisting and/or bending of the sample due to loading asymmetry that is magnified at higher loads. However, it was found that the *change in the width* of the measurement area, δv, averaged over all the x locations, was less sensitive to small twisting and/or bending of the sample, as shown in Figure 6, and this metric was used for inverse analysis instead of v_f. As described in Section 3.3, the non-linear plastic region was approximated by three linear zones. As in the case of deformation in the *x* direction, we computed the slope of the best linear fit to the graph of the normalized load, *F' vs.* scaled average change in width of the measurement area, $\delta\overline{v}'_o$, which are defined as:

$$F' = \frac{F - F_1}{F_2 - F_1}; \qquad \delta\overline{v}'_o = \left(\delta\overline{v}'\right)_F - \left(\delta\overline{v}'\right)_{F=F_1}. \tag{3}$$

Here, F_1 and F_2 are the loads at the beginning and end of each plastic region. The scaled change in width at any load with the offset, $\left(\delta\overline{v}'\right)_F$, was calculated as:

$$\left(\delta\overline{v}'\right)_F = \frac{(1/n_x)\sum_x\left[\left(v_f\right)_{y=y_{\min}} - \left(v_f\right)_{y=y_{\max}}\right]}{\max\left((1/n_x)\sum_x\left[\left(v_f\right)_{y=y_{\min}} - \left(v_f\right)_{y=y_{\max}}\right]\right)}. \tag{4}$$

Here, n_x is the number of points along the *x* direction at which the change in width was computed (51 in this case). Scaling ensures that the slopes have magnitudes of the order of unity instead of very large values that may be obtained with unscaled loads and changes in width. As before, using the slope of *F' vs.* $\delta\overline{v}'_o$ in inverse analysis enables use of data at all loads at a mesh point, and also reduces the effect of measurement noise.

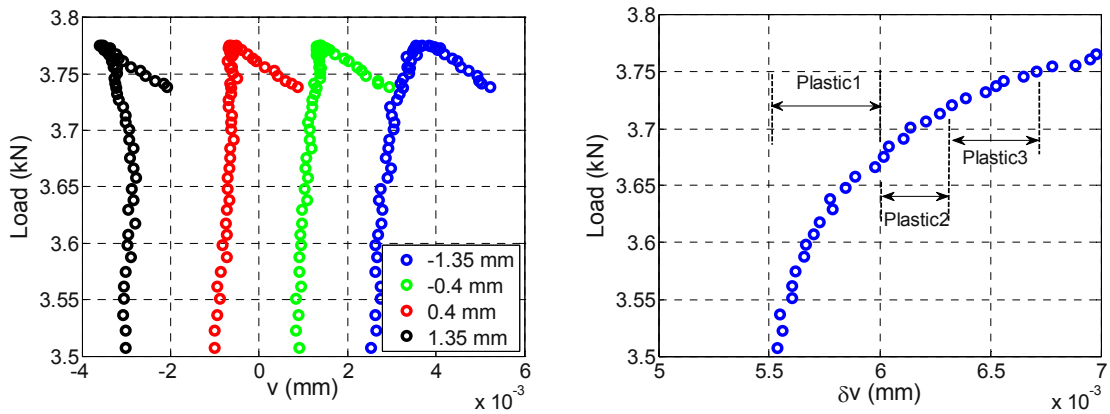

Figure 6: **Left:** Load *vs.* filtered y-displacements, v_f, at x = 0 and four y locations, **Right:** Load *vs.* width change averaged over 51 points along the x axis. Both figures are in the plastic region.

3 Finite Element Analysis and Material Models

3.1 Geometry, Mesh, and Boundary Conditions

We developed a 3D FEM model in ADINA®, a commercial software product, for the dogbone sample. The mesh used consisted primarily of quad bricks, and the total number of mesh points was 9894. The measurement area was meshed separately from the rest of the dogbone with a rectangular grid of 51×21 points along the *x* and *y* axes. This separate meshing was performed to obtain a higher mesh density in the measurement area, as shown in Figure 7. One end of the dogbone was fixed (boundary conditions: fixed *u*, free *v* and *w*) while the other face had force boundary conditions (equal forces at all the nodes on that face that add up to the total applied force, and free *u*). Additionally, *v* and *w* were fixed on the end points of the longitudinal centerline on one surface.

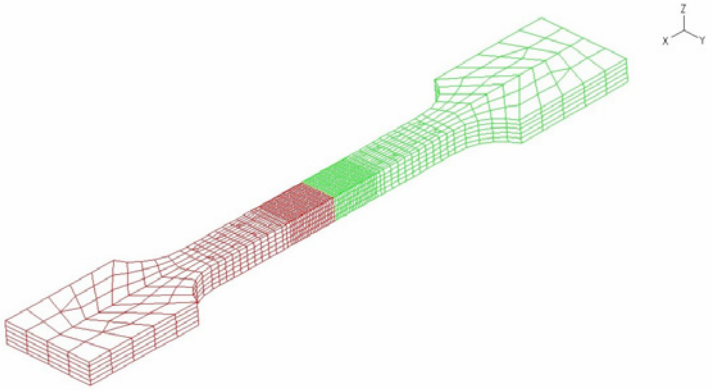

Figure 7: FEM model of dogbone sample (made of the single-crystal superalloy) developed in ADINA®.

3.2 Elastic Region

The single-crystal superalloy has been modeled as a simply orthotropic material, with the following stress-strain relationship in the primary (material) coordinate system [7]:

$$\begin{bmatrix} \vec{\sigma} \\ \vec{\tau} \end{bmatrix} = C_{ij} \begin{bmatrix} \vec{\varepsilon} \\ \vec{\gamma} \end{bmatrix} \tag{5}$$

Here, the elasticity stiffness matrix, *C* is a 6×6 matrix. For *simply* orthotropic materials, only 6 out of the 36 elements are independent*:* $E_1(=E_2)$, E_3, G_{12}, $G_{23}(=G_{13})$, ν_{12}, $\nu_{23}(=\nu_{13})$.

3.3 Plastic Region

The non-linear plastic region was modeled as three piecewise-linear regions, as shown in Figure 8, which displays load *vs. u* that was measured on the single-crystal sample at the center of the measurement region. The three locally-linear regions are marked Plastic1, Plastic 2 and Plastic3, with end-points corresponding to loads of 3.68 kN, 3.72 kN, and 3.75 kN, respectively. The deformation continues to increase with small increases in load, and additional locally linear regions can be identified. However, for purposes of demonstration of the parameter estimation technique, we will restrict ourselves to three zones. We assume that the sample does not undergo creep, *i.e.*, that the strains are only dependent on the load and are time-independent at a given load.

Hill's model was used for yield and a hardening rule was used for deformation in the plastic region. The Hill's yield model has six parameters which are the yield stresses in the directions of the material axes (*1, 2, 3*) and the yield stresses for pure shear in the material planes (*12, 23, 13*), i.e., $\sigma_{Y,1}$, $\sigma_{Y,,2}$, $\sigma_{Y,,3}$, $\sigma_{Y,12}$, $\sigma_{Y,23}$, $\sigma_{Y,13}$, respectively. We used a single universal plasticity modulus, E^u_p for modeling hardening [8]. Effective Poisson ratios along the material axes (denoted by subscripts 1, 2, and 3) were used, and these are related *via* Lankford coefficients, (r_0, r_{45}, r_{90}), and volume conservation [9]. In ADINA®'s implementation of this plasticity model, there are five independent parameters: $\sigma_{Y,1}$, r_0, r_{45}, r_{90}, and E^p_u. Hence, a set of Lankford coefficients is needed for each of the three linear segments that approximate the plastic region. Of course, the relationship to yield stresses *via* the Hill parameters is physically meaningful only for the first linear plastic zone.

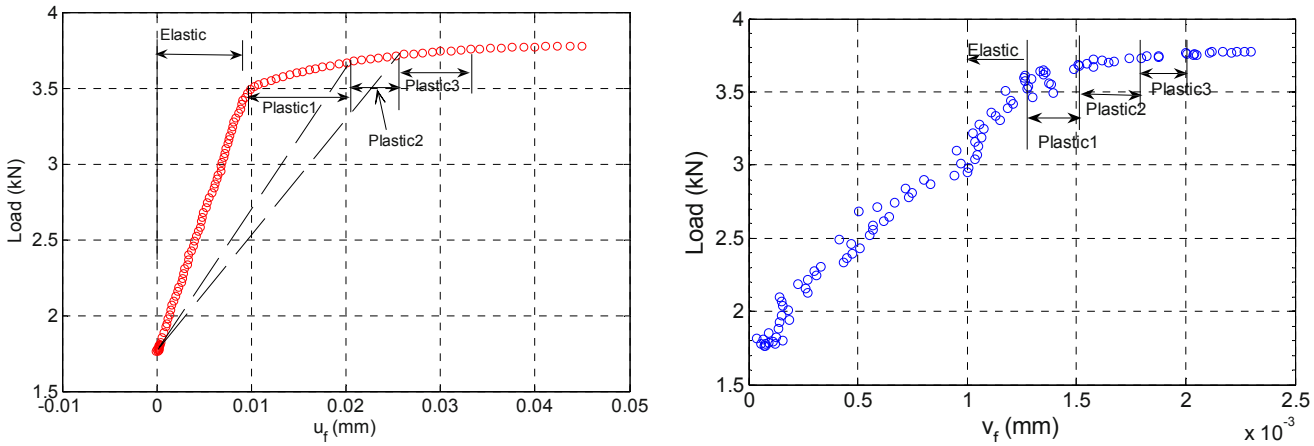

Figure 8: **Left:** Load *vs. u* data at the center of the measurement region for the single-crystal sample. **Right:** Load vs. *v* data at x = 0, y = -1.35 mm for the single-crystal sample.

4 Parameter Estimation for the Elastic Region

In the inverse analysis for parameter estimation, the generalized cost function, *J*, that was used in the optimization computations was defined as the two-norm of the normalized error between the model prediction and the experimental values of *Y*, averaged over the total number of measurement axes (*n*) and FEM models (*m*). Here, *Y* may represent either the (filtered) measured displacements, or the best-fit slope of the load *vs.* displacement graph:

$$J = \frac{1}{m}\sum_{i=1}^{m}\left[\frac{1}{n}\sum_{j=1}^{n}\left\{\sqrt{\frac{1}{N}\sum_{k=1}^{N}W_{i,j,k}\left\|\frac{Y_{E,i,j,k}-Y_{M,i,j,k}}{Y_{E,i,j,k}}\right\|^2}\right\}_j\right]_i . \qquad (6)$$

The subscripts *E* and *M* refer to the experimental data and model results, respectively. The number of good data points (i.e., mesh points where the displacement measurements are sufficiently accurate) in the i^{th} model along the j^{th} axis is $N_{i,j}$. Since we are using only one FEM model, *m* = 1. Also, since we are not using *w* data, *n* = 2. Each data point has a weight $W_{i,j,k}$ that can have any value between 0 and 1.

When we analyzed the sensitivity of the measurements to the material model parameters, it was found that only two of the six parameters in this simply orthotropic model showed sensitivity to the measured displacements, and hence only these two (E_1= E_3, E_2) could be estimated. The reason for this limitation is two-fold. First, since the sample motion in the out-of-plane direction was not very well constrained during the test, the out-of-plane deformation data, *w*, did not contribute meaningful information for parameter estimation. Second, for small values of Bunge-Euler angles, as is the case for this sample (see Section 2), the principal stresses in the material coordinate system, σ_2 and σ_3 have very small magnitudes. Consequently, the dependence of *u* and *v* on material parameters other than E_1 and ν_{12} (through elements of the matrix C_{ij}) is very weak. The situation would be different if the material axes were to be substantially out of alignment with the global coordinate axes, in which case the stress vector would be full, and the measured displacements (consequently, the cost function *J*) would have significant sensitivity to all the material parameters.

Inverse analysis was performed using the downhill simplex method, a robust search algorithm that has been successful in finding the global minimum of various non-linear cost functions, and does not involve slope computations [10]. Table 1 shows the values of the elastic Young modulus along the (*1, 2*) material axes that were obtained after starting from two different sets of trial values that are quite far apart. Figure 9 shows the load *vs.* displacement (v_f) graphs from the FEM model using these optimal parameters and with the data. Good agreement between the model and data is seen in the elastic range. For the other four parameters, we used nominal values for this material of ν_{12} = ν_{13} = 0.39, ν_{23} = 0.3, G_{12} = G_{13} = 100 GPa, G_{23} = 110 GPa. The values of E_1 and E_2 obtained here compares well with the effective modulus of 138.3 GPa in the loading direction calculated from the gross measurements. The optimization computations took approximately half an hour to converge on a

Linux workstation powered by an AMD Opteron 248 running at 2.2 GHz with 12 GB of RAM machine. Almost all of the computation time is used for the cost function computations, i.e., running the ADINA® simulations.

Table 1: Optimal parameters for the elasticity model.

	Run 1		Run 2	
	Initial	**Final**	**Initial**	**Final**
E_1 **(GPa)**	80.0	129.5	180.0	129.5
E_2 **(GPa)**	80.0	141.6	180.0	141.6

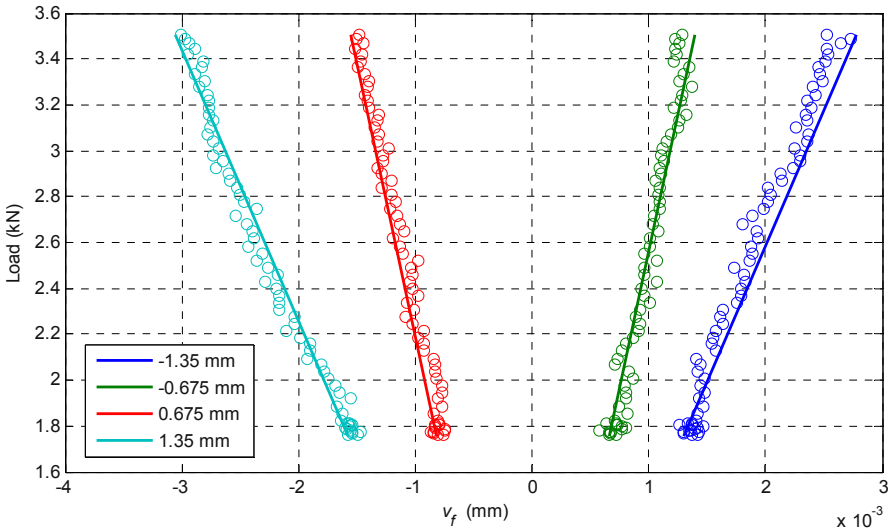

Figure 9: Load *vs.* v_f at four points along centerline (y = 0) in the elastic regime. Circles are experimental data and the straight lines are FEM model results for optimal material parameters.

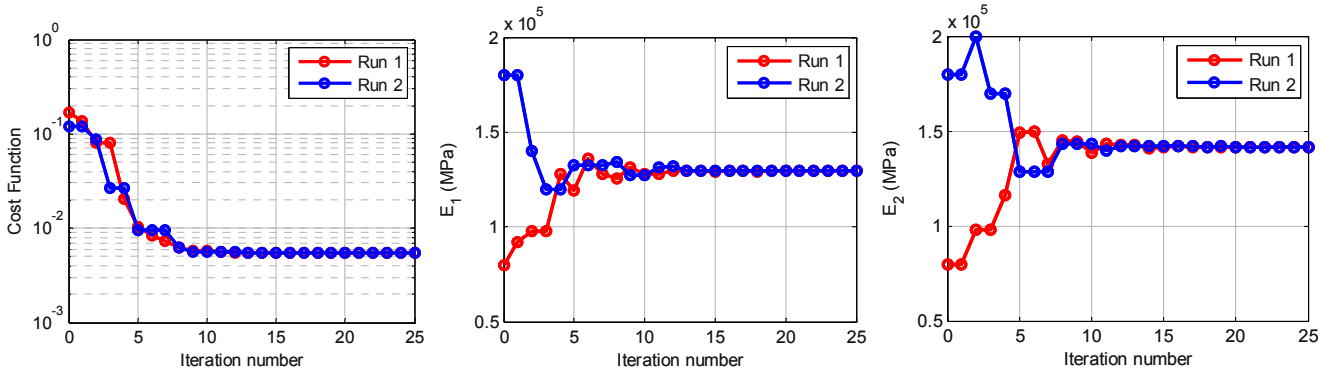

Figure 10: Convergence plots for the estimated material parameters of the single crystal sample, and the associated cost function..

5 Parameter Estimation for the Plastic Region

As stated earlier, we have modeled the plastic region as consisting of three piece-wise linear segments (denoted as Plastic1, Plastic2 and Plastic3 in Figure 8), each with its own universal plasticity modulus and Lankford coefficients. We first estimate the parameters for Plastic1 zone. The elastic properties are specified as the values determined from the elastic analysis of Section 4. In order to implement the model for plastic zones 2 and 3, we assume that the boundary point between zone 1 and 2 is the yield point of a fictitious material with elastic properties, as shown using dotted lines in Figure 8. Next, we estimate the elastic properties of this fictitious material, and the plastic properties (yield stresses, universal plasticity modulus and Lankford coefficients). We discard the elastic properties and the yield stresses and retain the Lankford coefficients and the universal plasticity modulus for the zone Plastic2. This procedure is then repeated for the third plastic zone.

Sensitivity analyses showed that for this single crystal sample under the imposed loading condition, we can estimate only three of the five material model parameters: $\sigma_{Y,1}$, r_0, and the universal plasticity modulus, E^u_p. The other two coefficients were assigned the following values: r_{45} = 0.2 and r_{90} = 0.05. These approximate values were determined from the measured strain ratios in the three directions. The plasticity model involves both the yield stress and hardening behavior model parameters (Lankford coefficients). Consequently, in our linearized (slope-based) approach to the plastic zone, we have to tie down the plasticity slope to the yield point. Therefore, the cost function was modified to incorporate the error in the displacements at the yield load. The cost function, J, was re-defined for the plastic zones as:

$$J = \frac{\sum_{j=1}^{2}\sum_{k=1}^{N}\left\|\frac{Y_{E,j,k}-Y_{M,j,k}}{Y_{E,j,k}}\right\|^2 + 0.25\sum_{k=1}^{N}\left\|\frac{u_{f,E,k}-u_{f,M,k}}{u_{f,E,k}}\right\|^2}{2N}. \quad (7)$$

Here u_f is the filtered x-displacement at yield load. This term has weighting of 0.25 to reduce the potential effect of noise in the u data on the optimization accuracy. The choice of the factor of 0.25 was reached after trying a few other values for the fastest convergence. Y is the best-fit slope to the load-displacement plot. The subscripts j refers to the axis (x or y), k represents the data point number, and E and M refer to experimental data and model results, respectively. The optimization computations took approximately 12 hours to converge for Plastic 1 zone, and 6-7 hours for the other two plastic zones on the AMD Opteron workstation running at 2.2 GHz with 12 GB of RAM.

The optimal parameters for the three plastic zones are shown in Table 2 and Table 3. Figure 11 shows the comparison of the model and data over the entire load range of interest. The figure on the left shows average stress *vs.* strain at two points. The quality of the model fit can be examined more closely in the graphs on the right side of Figure 11 where u_f has been plotted individually for the elastic and the three plastic zones. The fits are very good overall, and the optimization convergence is excellent (see Table 2 andTable 3).

Table 2: Initial and final parameter values for the first plastic zone.

	Run 1		**Run 2**	
	Initial	**Final**	**Initial**	**Final**
E^u_p (GPa)	10.0	13.7	18.0	13.7
$\sigma_{Y,1}$ (GPa)	0.40	0.77	0.80	0.77
r_o	0.2	0.021	0.025	0.021

Table 3: Initial and final parameter values for the second and third plastic zones.

	Plastic Zone 2				**Plastic Zone 3**			
	Run 1		**Run 2**		**Run 1**		**Run 2**	
	Initial	**Final**	**Initial**	**Final**	**Initial**	**Final**	**Initial**	**Final**
E^u_p (GPa)	10.0	6.4	2.5	6.4	7.5	4.74	5.0	4.75
r_o	0.2	0.061	0.25	0.061	0.25	0.064	0.1	0.064

6 Conclusions

We have successfully demonstrated the capability of a new integrated hardware-software tool to measure full-field deformation data and then process the data for use in estimating the sample's material model parameters. The stereo microscope-based DIC system can handle field sizes of about 1 mm and high temperatures up to 750°C. Measurements were made on a single-crystal nickel superalloy sample. The parameter estimation toolbox processed the vast amounts of DIC data that was generated, and interface with ADINA®, a commercial FEM software to run the model in an iterative loop during optimization calculations. The model parameters converged to the same values irrespective of the starting points, and the final values are typical of this material. It was noted that the choice of sample and the quality of the data can have a major impact on the parameter estimation results.

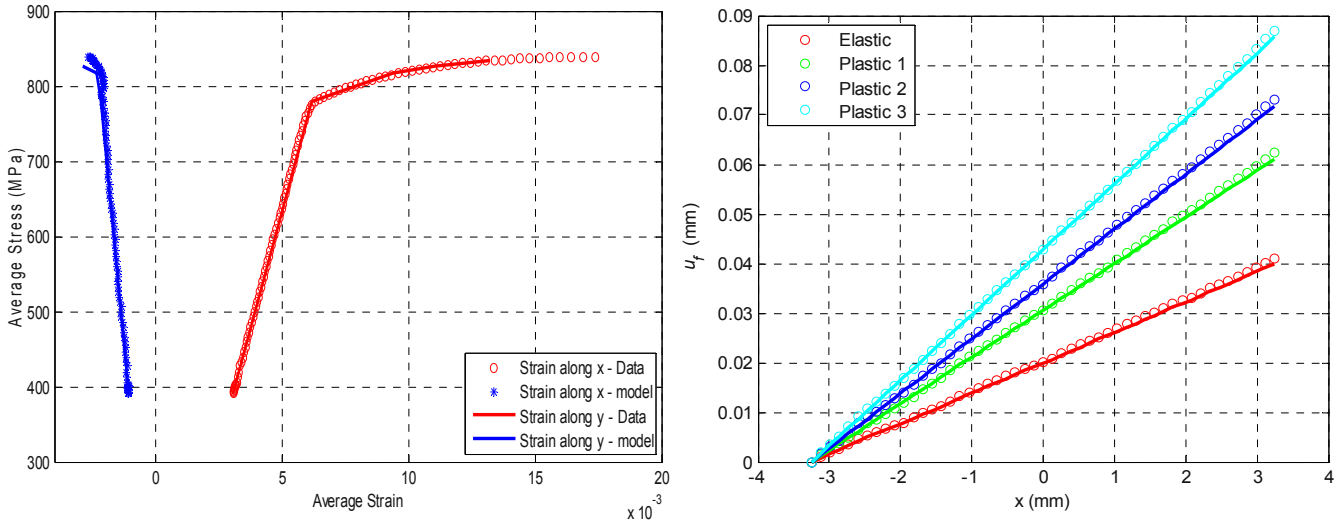

Figure 11: **Left:** Graphs of average stress *vs.* strain in *x* directions (mesh point at (3.25 mm, 0)), and *y* direction (mesh point at (0, 1.35 mm)). Circles are experimental data and the straight lines are FEM model results for optimal material parameters. **Right:** u_f at all points along the x direction for elastic and plastic regions with displacements in each zone shifted to pass through same starting point to allow closer inspection of the match between model and data.

Acknowledgement

This work was funded by the Air Force SBIR Contract # FA8650-05-C-7251. The authors would like to thank Dr. D. A. Johnson, Dr. R. John, Dr. M. J. Shepard, 2nd Lt. S. M. Visalli, and 2nd Lt. S. Haering at AFRL for technical discussions and for program support, as well as Prof. M. A. Sutton and A. P. Reynolds at University of South Carolina, Columbia, SC, and Dr. J. L. Ebert at SC Solutions for their technical suggestions.

References

[1] Johnson, D. A., Porter III, W. J., John, R., "Full-Field Techniques in the Study of Multi-Scale Nonlinear Material Behavior," Proc. SEM Annual Conference, *Experimentation and Modeling at the Nanoscale*, Society for Experimental Mechanics, Charlotte, NC, 2–4 June 2003.

[2] Chu, T. C., Ranson, W. F., Sutton, M. A., Peters, W. H., "Application of Digital Image Correlation Techniques to Experimental Mechanics," *Experimental Mechanics*, 25 (3), pp 232–245, 1985.

[3] Sutton, M. A., Cheng, M., Peters, W. H., Chao, Y. J., and McNeill, S. R., "Application of an Optimized Digital Correlation Method to Planar Deformation Analysis," *Image and Vision Computing*, 4 (3), pp 143-150, 1986.

[4] Helm, J. D., McNeill, S. R., Sutton, M. A., "Improved 3-D Image Correlation for Surface Displacement Measurement," *Optical Engineering* 35 (7), pp. 1911-1920, 1996.

[5] Schreier, H. W., Braasch, J. R., Sutton, M. A., "Systematic Errors in Digital Image Correlation Caused by Intensity Interpolation," *Opt. Eng.*, 39(11), 2000.

[6] Schreier, H. W., Sutton, M. A., "Systematic Errors in Digital Image Correlation Due to Undermatched Subset Shape Functions," *Experimental Mechanics*, 43(2), 2002.

[7] Jones, R. M., *Mechanics of Composite Materials*, 2nd Edition, Taylor and Francis, 1999.

[8] ADINA R&D, *ADINA Theory and Modeling Guide, Volume 1: ADINA Structures and Solids*, p. 278, October 2005.

[9] Lankford, W. T., Snyder, S. C., Bausher, J. A., "New Criteria for Predicting the Press Performance of Deep Drawing Sheets", *Trans. ASM*, 42, 1197–1205, 1950.

[10] Press, W. H., Flannery, B. P., Teukolsky, S. A., Vetterling, W. T., *Numerical Recipes in C, The Art of Scientific Computing*, Cambridge University Press, Second Ed., 1992.

Proceedings of the SEM Annual Conference
June 7-10, 2010 Indianapolis, Indiana USA

Extended DIC to Measure Stress Intensity Factors from AFM-images

S. Roux[1], M. Ciccotti[2] and F. Hild[1]
[1] LMT Cachan, ENS Cachan/CNRS UMR 8535/Univ. Paris 6/PRES UniverSud Paris,
61 Avenue du Président Wilson, 94235 Cachan Cedex, France
stephane.roux@lmt.ens-cachan.fr
2: LCVN, Univ. Montpellier II / CNRS, place Eugène Bataillon
34095 Montpellier Cedex 5, France

ABSTRACT

Subcritical crack propagation in amorphous silica glass can be imaged during propagation with an AFM at different stages of propagation. Digital Image Correlation constitutes an attractive technique to measure the displacement fields relating different topographic images, and from it to estimate quantitatively the stress intensity factor governing the crack velocity. However, the emergence of the crack on the free surface, which is imaged, induces a significant out of plane motion whose magnitude is comparable to the surface roughness. This difficulty calls for an extension of the usual "brightness conservation" allowing for an evolution of the image texture, i.e. surface topography. The high level of AFM-image noise is tackled through integrated DIC, namely, few well chosen kinematic fields are selected to decompose the searched displacement field. The latter are considered because of their mechanical relevance to the problem at play (e.g., rigid body motion, plane stress mode I displacement field, out-of plane singular field) or to compensate for AFM artifacts. The resulting novel DIC algorithm provides directly an evaluation of the stress intensity factor, K_I, without any further post-processing; 10% (resp. 15%) uncertainty on K_I is achieved based on 1 × 1 μm^2 (resp. 200 × 200 nm^2) images.

INTRODUCTION

Digital Image Correlation (DIC) is a technique that allows for the measurement of displacement fields by registering a reference with deformed images, most often optical ones. Introduced a long time ago in the field of solid mechanics [1], this technique has known a very rapid development due to the wide availability of digital imaging devices, and the increasing performance and reliability of the analyses. Its non-intrusive character, its easy deployment and wide versatility are responsible for its remarkably fast dissemination in experimental solid mechanics. Moreover, as it gives access to full field measurement of kinematic fields the further exploitation of these fields for the identification of mechanical properties is an additional motivation for its present success. In particular for cracks, since the pioneering work of Sutton *et al.* [2], recent works [3-5] have shown that stress intensity factors can be estimated very accurately either directly through integrated DIC that incorporates analytic crack fields [3], or through a tailored post-processing of the measured displacement fields [3,4,6].

However, most applications of DIC deal with optical images, and very few with Atomic Force Microscopy (AFM) images. AFM imaging provides invaluable information on the surface topography of any material at the nanometer scale. Over the years, considerable progress has been achieved in developing different acquisition modes that through their sensitivities to specific features of surface interaction forces are able to reveal very rich information. Among the few works devoted to the application of DIC to AFM images, the most advanced published ones concern thin polycrystalline silicon films [7-11]. In particular, the measurement of a uniform strain field from AFM images at different scales down to 1 x 2 μm^2 images [10] allowed for the estimation of elastic properties of polycrystalline silicon used for MEMS. More recently, stress intensity factors were evaluated for cracks propagating in such films [11]. The columnar structure of the samples as well as their geometry leads the authors to analyze a rather large region of interest (typical size of the order of 10-15 μm). Linear elastic fracture

T. Proulx (ed.), *Application of Imaging Techniques to Mechanics of Materials and Structures, Volume 4*, Conference Proceedings of the Society for Experimental Mechanics Series 14, DOI 10.1007/978-1-4419-9796-8_13, © The Society for Experimental Mechanics, Inc. 2013

mechanics and plane elasticity were appropriate to account for the observed displacement field. Stress Intensity Factors (SIFs) were evaluated indirectly based on a comparison with an elastic finite element simulation of the test where the geometry of the crack and most importantly the location of the crack tip were estimated from an AFM image. In a different spirit, a recent study by Xu et al. [12] investigated systematic bias such as drift and distortion of large AFM images (6.4 × 6.4 μm^2) on unstrained samples in order to estimate (and reduce) strain measurement uncertainties. These two sets of studies have demonstrated the feasibility of using DIC on AFM images, mostly for simple strain fields and large scanned regions. The pioneering work of Cho et al. [11] showed that more complex displacement fields could be exploited, although the evaluation of SIFs required a post-processing with a finite-element computational step.

The present paper is aimed at a *direct* determination of stress intensity factors (SIF) through DIC at a much lower scale than previously considered, namely, from 1 × 1 μm^2 down to 200 × 200 nm^2, i.e. about 100 times smaller than in previously reported studies [11], without any recourse to numerical finite-element simulations. This analysis requires overcoming a number of very difficult obstacles:
- As the size of the region of interest is reduced, the noise level of AFM images becomes very strong.
- Images consist in topographic measurements. In contrast with classical speckle patterns, which are simply advected by the displacement field, the topography is affected by out of plane motion of the free surface. In the present study, the typical peak-to-valley roughness of say 1 μm size images is of the order of 3 nm. The out-of-plane displacement difference due to a crack at the critical stress intensity factor will be estimated below as being about 2 nm, and hence cannot be ignored. Thus, the very foundation of DIC, i.e. the conservation of "brightness," has to be revisited and generalized to account for this effect.

EXPERIMENT

The mechanisms of subcritical crack propagation in silicate glasses have been the subject of extensive research (cf. [13,14] for recent reviews). The development of advanced AFM techniques to probe *in-situ* crack propagation or *post-mortem* crack surface morphologies have recently led to explore these mechanisms at their pertinent nanometric scale leading to remarkable observations on plastic crack tip damage [15] revisited by Fett et al. [16], stress-induced ion migration [17] and capillary condensation inside the crack tip cavity [18]. The Double Cleavage Drilled Compression (DCDC) test set-up is particularly convenient for these studies due to its excellent stability and several theoretical modelings were devoted to it [19,20].

In the present experiments, fractures were initiated and propagated in a DCDC set-up at a constant temperature of 23.0 ± 0.5 °C in a leak-proof chamber under a controlled atmosphere composed of pure nitrogen and water vapor at relative humidity 23 ± 1 %. The parallelepipedic DCDC samples (4 × 4 × 40 mm^3, with 10 μm tolerance) of pure fused silica glass (Suprasil 311, Heraeus, Germany) were polished to a RMS roughness of 0.5 nm (for an area of 1 × 1 μm^2). Developments of different patterning techniques through lithography [21] have been reported in order to achieve an image texture which is suitable for DIC. In the sequel, the initial surface was not prepared in any artificial way, and the natural surface roughness (3-4 nm at most) of the glass surface is exploited. A hole of radius R = 500 ± 10 μm was drilled at the specimen center to trigger the initiation of two symmetric fractures of length c as shown in Figure 1. The details of the technique can be found in Refs. [15,18]. After extensive stabilization, all the images presented here were acquired within a two-hour interval, so that crack propagation conditions can be considered as stable at a propagation velocity v = 0.7 ± 0.1 nm/s. For an applied force F = 1844 ± 4 N and an average crack length c = 6145 ± 10 μm, the SIF is estimated to K_I = 0.39 ± 0.02 $MPa.m^{1/2}$ according to Ref. [19]. AFM observations were performed in tapping mode with a D3100 apparatus from Veeco Metrology Inc. (Santa Barbara, CA). Typical topographic and phase images are shown in Figure 2.

PRINCIPLE OF INTEGRATED DIC ANALYSIS

Let us denote by $f(\boldsymbol{x})$ and $g(\boldsymbol{x})$ the topographic images of the reference and deformed states, where $\boldsymbol{x}$ are the coordinates in the observation plane. f and g are the height of the observed surface in nanometers. The generalization of the so-called brightness conservation that relates the two images reads

$$g(\boldsymbol{x}) = f(\boldsymbol{x} + \boldsymbol{u}(\boldsymbol{x})) + v(\boldsymbol{x}) \quad (1)$$

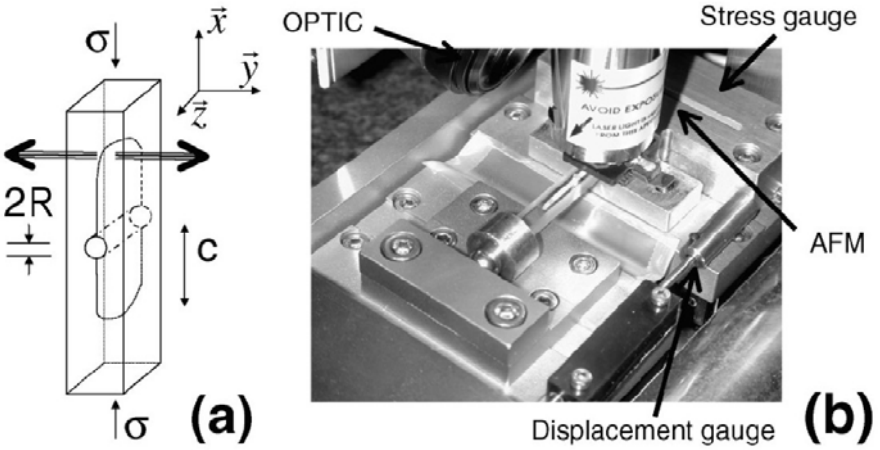

Figure 1: Schematic representation (a) of the sample geometry and (b) of the DCDC experiment set-up.

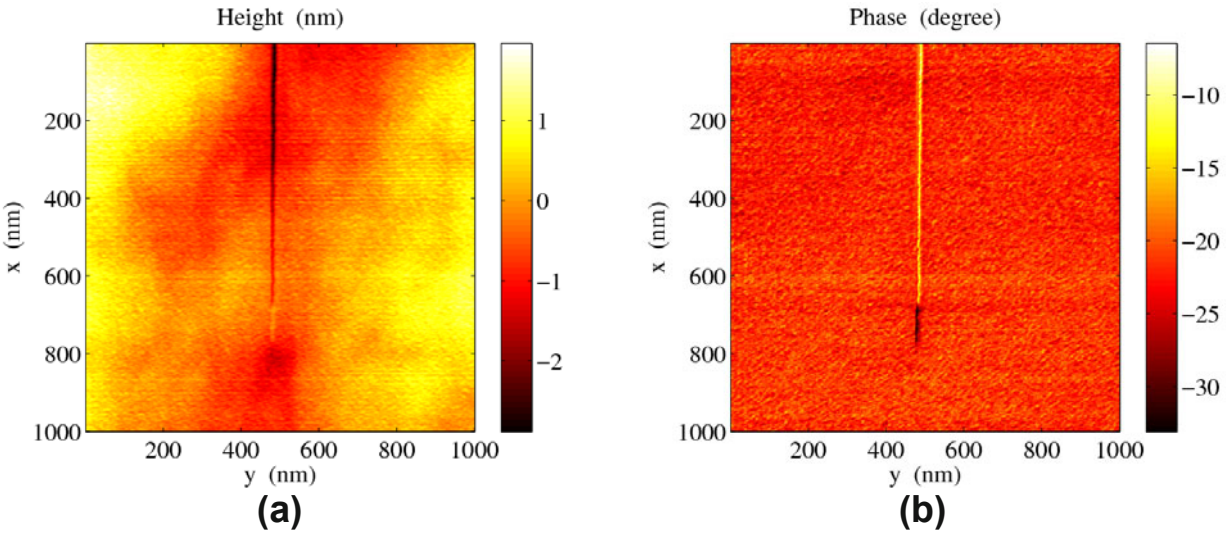

Figure 2: Topographic (a) and phase (b) image of the specimen. The crack is easily seen in particular in the phase image. The black region behind the crack tip corresponds to a capillary water condensate. This feature allows for a precise visualization of the crack tip.

where $\boldsymbol{u}$ (resp. v) denotes the in-plane (resp. out-of-plane) displacement field. In order to develop a robust method, an "Integrated" DIC (IDIC) approach as introduced in Ref. [3] is chosen. The displacement field ($\boldsymbol{u}(\boldsymbol{x})$; $v(\boldsymbol{x})$) is searched for as a combination of a few expected fields $\Phi_n(\boldsymbol{x})$

$$(\boldsymbol{u}(\boldsymbol{x}); v(\boldsymbol{x})) = \sum_n a_n \Phi_n(\boldsymbol{x}) \tag{2}$$

Those fields consist of rigid body motions for $1 \le n \le 6$ (three translations and three rotations). Higher indices $7 \le n \le 10$ are relative to mode I crack displacement fields. The latter fields are well known in either plane stress or plane strain conditions [22], which unfortunately do not strictly apply for a crack front emerging on the free surface of a 3D sample [20]. However, the in-plane component $\boldsymbol{u}(\boldsymbol{x})$ can be well approximated by the plane stress condition. The notation $\boldsymbol{\varphi}(\boldsymbol{x})$ is introduced for such an in-plane displacement field for a crack tip located at the origin, and crack path along the $x_1 < 0$ semi-axis. The displacement field normal to the free surface is not known analytically. The latter, for a unit mode I stress intensity factor, is denoted by $\psi(\boldsymbol{x})$, for the same reference geometry. Because of their different status, the in-plane and out-of-plane displacements will be treated in the sequel as two *independent* fields.

An additional difficulty is that as crack propagation under a constant load is followed, the crack tip is present in both images although at different locations. Let us call $\boldsymbol{x}_0$ and $\boldsymbol{x}_1$ the crack tip positions in f and g respectively. The displacement field to be applied to the reference image thus consists in closing the crack at point $\boldsymbol{x}_0$ and opening it at $\boldsymbol{x}_1$. Thus the 7th and 9th basis field are $\boldsymbol{\varphi}(\boldsymbol{x} - \boldsymbol{x}_0)$ and $\boldsymbol{\varphi}(\boldsymbol{x} - \boldsymbol{x}_1)$ respectively, while the 8th and 10th fields are the out-of-plane components $\psi(\boldsymbol{x} - \boldsymbol{x}_0)$ and $\psi(\boldsymbol{x} - \boldsymbol{x}_1)$ respectively. For steady state propagation under the same stress intensity factor, the following constraints hold

$$a_7 = -\, a_9 \quad \text{and} \quad a_8 = -\, a_{10} \tag{3}$$

Those equalities are enforced using Lagrange multipliers. Thus the problem consists in evaluating the above 10 unknowns, a_n, (8 degrees of freedom) through a weak form of the extended brightness conservation to be minimized

$$\boldsymbol{T} = \iint \left(g(\boldsymbol{x}) - f(\boldsymbol{x} + a_i\, \Phi_i^t(\boldsymbol{x})) - a_j\, \Phi_j^n(\boldsymbol{x})\right)^2 \, \mathrm{d}^2\, \boldsymbol{x} \tag{4}$$

where $\Phi_i^t(\boldsymbol{x})$ and $\Phi_i^n(\boldsymbol{x})$ designate respectively the in-plane and out-of-plane displacements. When suitably normalized (using the pixel size and the elastic properties of the silica glass specimen), the SIF is directly estimated from the a_7 parameter value.

This problem, which is strongly non-linear because of the unknowns appearing as arguments of the function f, has to be solved avoiding local minima trappings. This requires specific strategies. The one chosen here is a multiscale procedure that consists in minimizing the above functional from coarse-grained images down to finer ones [23]. Each minimization is performed through successive linearizations and deformed image correction using a bi-linear subpixel interpolation.

MODE I CRACK OUT-OF-PLANE DISPLACEMENT

One major difficulty is that $\psi(\boldsymbol{x})$ function is unknown. The general problem of the emergence of a crack on a free face is a difficult issue. In the framework of linear elasticity, at the very point of intersection between the crack front and the free surface, *i.e.* the observed "crack tip", a point singularity occurs, whose exponent depends continuously on the angle of the crack front incidence and on Poisson's ratio. A detailed theoretical and numerical study of this effect applied to glass and specifically in the very same DCDC test as the one considered herein can be found in Ref. [20].

It has been argued that the crack front geometry adjusts itself at propagation so that the singularity exponent is the same, 1/2, as for a planar crack front [24]. Thus, as a rough approximation, $\psi_0(\boldsymbol{x}) = |\boldsymbol{x}|^{1/2}$, is first assumed. Although not equal to the actual displacement field, yet it allowed registering both images, with the appropriate in-plane displacement. Once this is achieved, the height difference $\delta z(\boldsymbol{x})$ between the reference and deformed surfaces is extracted ignoring the $\psi_0(\boldsymbol{x})$ contribution (Figure 3a). In the absence of error and noise, this difference should be expressed as $\psi(\boldsymbol{x} - \boldsymbol{x}_0) - \psi(\boldsymbol{x} - \boldsymbol{x}_1)$. A simple algebraic expression for ψ is proposed

$$\psi\,(\boldsymbol{x}) = |\boldsymbol{x}|^{1/2} \sum_n \alpha_n \cos(n\theta/2) \tag{5}$$

where θ is the polar angle of the current point $\boldsymbol{x}$ with respect to the crack tip. Low orders for the parameter $0 \le n \le 2$ are chosen. A least square fit based on the above three parameter algebraic form allows for the identification of α_n parameters as shown in Figure 3b. As shown in Figure 3c, the resulting difference between $\delta z(\boldsymbol{x})$ and the proposed fit shows that most of the coherent displacement field has been captured. This result allows for a direct experimental determination of the out-of-plane displacement field $\psi(\boldsymbol{x})$, which is then used in the DIC analysis. Figure 3d shows the bare $\psi(\boldsymbol{x})$ function that turns out to be in fair agreement with the numerically computed displacement field by Fett et al. [20].

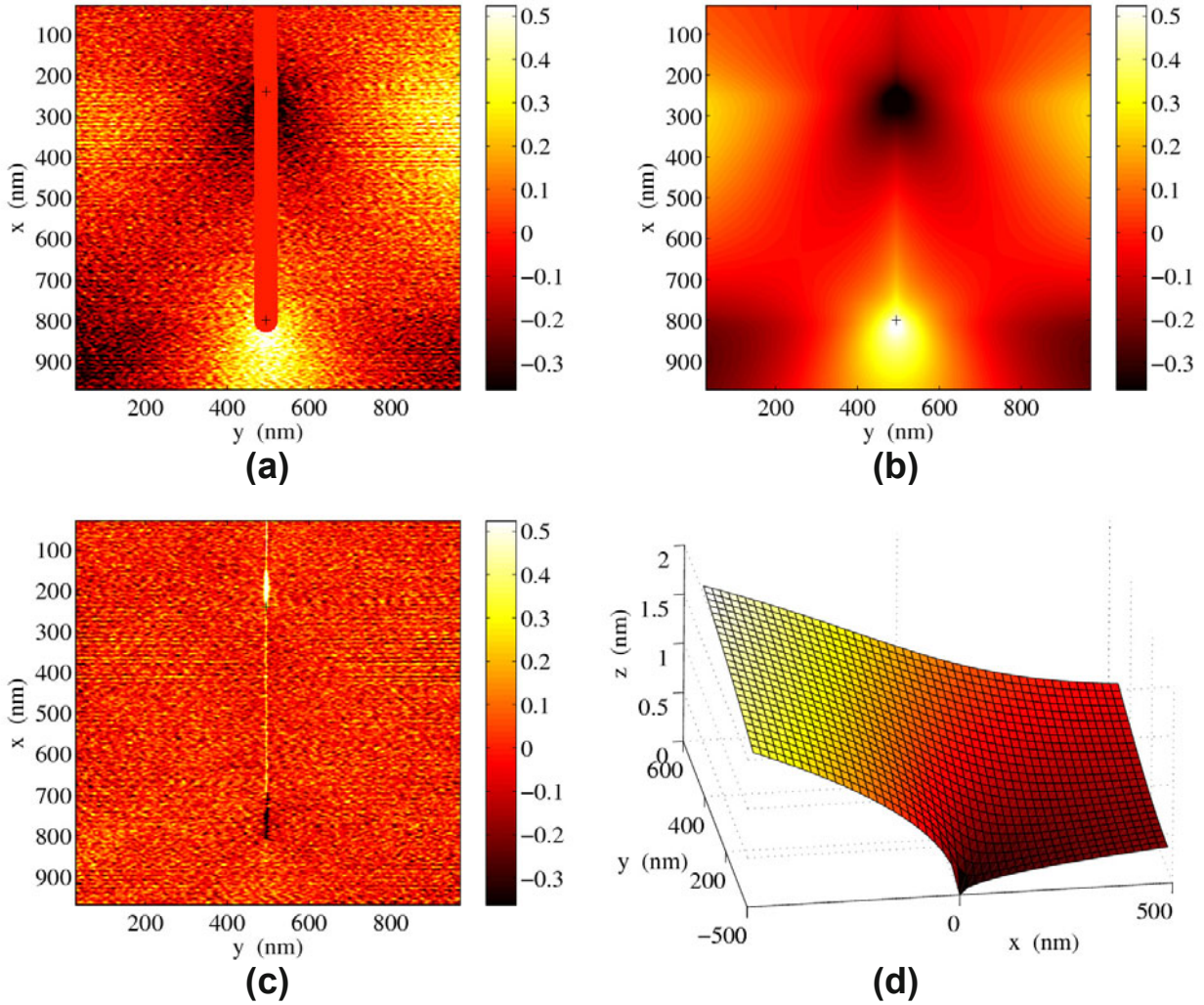

Figure 3: (a) Residual height difference after image registration but no singular out-of plane correction. (b) Fitted form using the three unknowns a_n, the two positions of the crack tip in the deformed and reference images. (c) Difference between the two fields (a) and (b) showing that most of the coherent height difference is well accounted for. (d) Representation of the bare $\psi(\boldsymbol{x})$ field for a crack tip located at the origin, and crack path along $x \leq 0$ and $y = 0$.

ONE MICROMETER SIZE IMAGE ANALYSIS

A series of 5 images of the same 1 × 1 μm^2 zone swept by a crack is first analyzed (cf. Figure 3). The quality of the DIC measurement is evaluated by evaluating the normalized residual, η, *i. e.* the standard deviation of the remaining residual, normalized by the peak-to-valley roughness of the original topographic image. In the present cases, even though the kinematic fields were adjusted with very few parameters, and in spite of the difficulty of comparing two AFM images taken at different instants, the normalized residual η was very stable at about 1.6%, a remarkably low value that gives confidence in the convergence of the procedure. The measured SIF values (assuming a Young's modulus of 72 GPa, and a Poisson's ratio of 0.17) were successively K_I = 0.38, 0.36, 0.44 and 0.38 MPa.m$^{1/2}$. The stability of the four independent measurements gives an *a posteriori* indication on the uncertainty of the toughness measurement, 0.39 ± 0.04 MPa.m$^{1/2}$, which is in excellent agreement with the macroscopic value of 0.39 ± 0.02 MPa.m$^{1/2}$ estimated independently.

200 nm SIZE IMAGE ANALYSIS

Going to the smaller scan size of 200 nm, a number of difficulties arise. First, the precise reposition of the same zone is done within a few tens of nanometers, i.e. a large fraction of the scanned image and such a large offset is more difficult to handle for DIC. This difficulty was taken care of by a prior rough determination of the mean translation by means of the maximum cross-correlation function in subregions avoiding the crack path. Second, the fluctuations in the "slow scan" direction are much more intense than in the fast scan direction (here transverse to the cracks). The reason for this is a small height drift (of the order of angstroms), which in the slow scan direction generates high frequencies that make the computation of image gradient insecure. In order to limit this noise, a low-pass Fourier filtering was applied to the image at the cut-off frequency for which the slow and fast scan power spectra depart from each other. For 200 nm images, although being composed of 512 × 512 pixels, wavelengths below 4 pixels (*i.e.* about 1.5 nm) were filtered out. The resulting filtered images are shown in Figure 4. Another major difficulty comes from uneven step sizes in the slow scan direction. A simple bare eye inspection does reveal that images appear to be either dilated or expanded along the slow scan direction by a significant amount. Similarly, due to inaccuracies in the reposition at the beginning of each new line an artificial simple shear can be introduced. Thus, some additional degrees of freedom in the kinematics are implemented. They correspond to those artifactual deformation modes. Finally, it is worth mentioning that pointing at the crack tips, even from phase images, is quite delicate and does contribute to the final uncertainty.

With those additional procedures, image series could be analyzed successfully, in the sense that the residual, η, could be brought down to 5-6 %. A visual check based on the comparison between reference and corrected deformed images confirms the reliability of the image registration, and hence the robustness of the algorithm, in spite of the significant level of noise in the images. Measurements of the mean strain along the slow-scan direction revealed strains that could be as large as 8 %. Although not limiting for image matching, this effect is prejudicial to the measurement of stress intensity factors, as the "pixel" size enters in the measurement. Fortunately, because of the square root dependence, this implies a 4 % uncertainty on K. In the example shown in Figure 5, the SIF is estimated to be 0.44 MPa.m$^{1/2}$, the axis strain is 1.6 %, and the residual amounts to η = 5.4 %. Ignoring the most strained image pair, the SIF value was estimated in the range $0.37 \leq K \leq 0.46$ MPa.m$^{1/2}$. Varying the size of the analyzed domain, and the cut-off frequency induces only very slight modifications in the SIF estimates. The estimate $K = 0.41 \pm 0.05$ MPa.m$^{1/2}$ is again consistent with the macroscopic determination and the larger scale AFM-DIC estimate. Most of the uncertainty lies in the precise identification of the crack tip location.

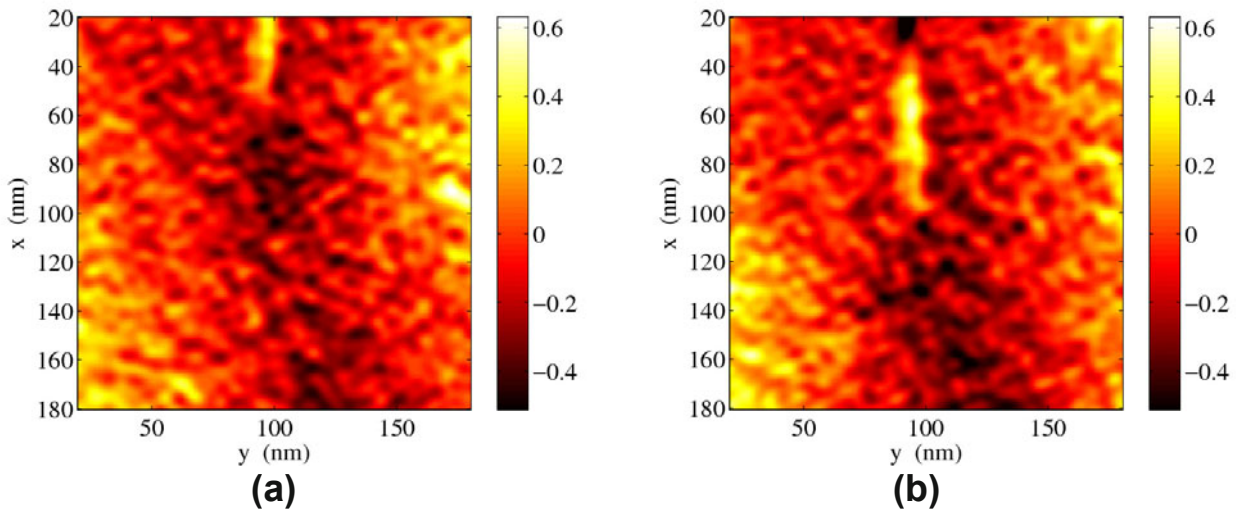

Figure 4: Initial (a) and final (b) topographic AFM images of size 200 nm in between which the crack has progressed by about 50 nm. All units are nm.

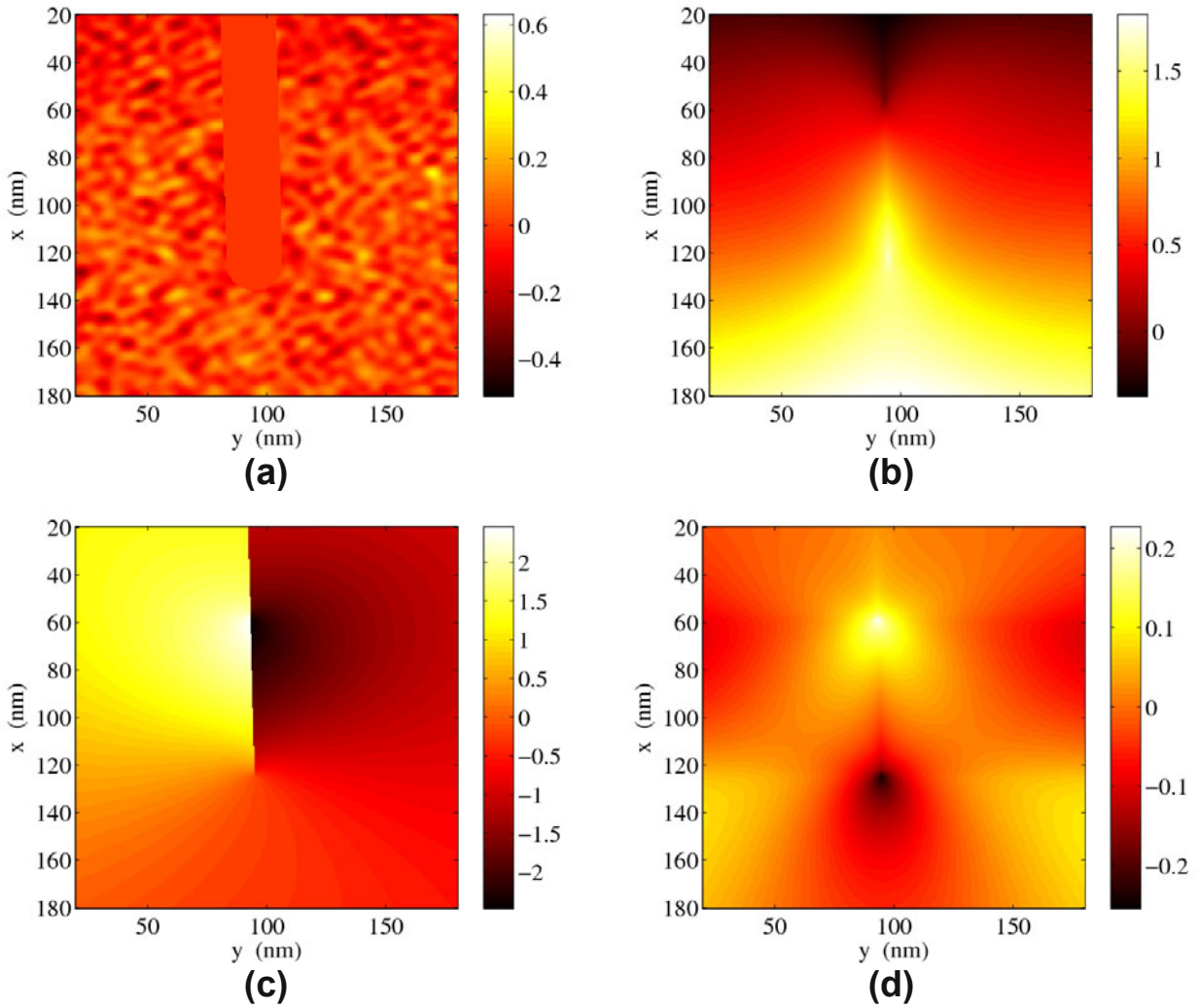

Figure 5: Results of the DIC analysis for 200 nm AFM images. (a) Residual difference after image registration (note that the crack path has been masked). (b), (c) and (d) respectively *x*, *y* and *z* displacement components (in nm) measured from the integrated DIC procedure.

CONCLUSIONS

It has been shown that AFM images of sizes as small as 200 nm wide — about 100 times smaller than the only earlier published AFM DIC study of crack by Cho *et al.* [11] — could be exploited through a suitably extended integrated DIC procedure, leading to a direct measurement of mode I stress intensity factors of a subcritical growing crack. As a side result, the presented procedure provides an experimental evaluation of the out-of-plane displacements at the emergence of the crack front on the observed free surface, which is in good agreement with the numerical study of Fett *et al.* [20].

Based on those quantitative observations, no evidence of a breakdown of linear elastic fracture mechanics — possibly due to micro-damage or plasticity — could be observed even in the immediate vicinity (within 10 nm) of the crack tip.

REFERENCES

[1] M. A. Sutton, W. J. Wolters, W. H. Peters, W.F. Ranson and S. R. McNeill, Image Vis. Comput. 1, 1333-1339, (1983)
[2] M. A. Sutton, J. L. Turner, H. A. Bruck and T. A. Chae, Exp. Mech., 31, 168-177, (1991)
[3] S. Roux and F. Hild, Int. J. Fract. 140, 141-157, (2006)
[4] S. Yoneyama, T. Ogawa and Y. Kowabayashi, Eng. Fract. Mech. 74, 1399-1412, (2007)
[5] S. Roux, J. Réthoré and F. Hild, J. Phys. D: Appl. Phys. 42, 214004, (2009)
[6] J. Réthoré, S. Roux and F. Hild, submitted for publication, (2010)
[7] I. Chasiotis and W. G. Knauss, Exp. Mech. 42, 51-57, (2002)
[8] S. W. Cho, J. F. Cárdenas-Garía and I. Chasiotis, Sens. Actuators A Phys. 120, 163-171, (2005)
[9] S. W. Cho, I. Chasiotis, T. A. Friedman and J. Sullivan, J. Micromech. Microeng. 25, 728-735, (2005)
[10] S. W. Cho and I. Chasiotis, Exp. Mech. 47, 37-49, (2007)
[11] S. W. Cho, K. Jonnalagadda and I. Chasiotis, Fatigue & Fract. Engng. Mat. Struct. 30, 21-31, (2007)
[12] Z.-H. Xu, X.-D. Li, M. A. Sutton and N. Li, Strain Analys. 43, 729-743, (2008)
[13] S. W. Freiman, S. M. Wiederhorn and J. J. Mecholsky, J. Am. Ceram. Soc. 92, 1371-1382, (2009)
[14] M. Ciccotti, J. Phys. D: Appl. Phys. 42, 214006 (2009)
[15] F. Célarié, Ph.D. thesis, Université Montpellier 2, France, (2004)
[16] T. Fett, G. Rizzi, D. Creek, S. Wagner, J.-P. Guin, J.M. López-Cepero and S. M. Wiederhorn, Phys. Rev. B 77, 174110, (2008)
[17] F. Célarié, M. Ciccotti, and C. Marlière, J. Non-Cryst. Solids 353, 51-68 (2007)
[18] A. Grimaldi, M. George, G. Pallares, C. Marlière and M. Ciccotti, Phys. Rev. Lett. 100, 165505, (2008)
[19] G. Pallares, L. Ponson, A. Grimaldi, M. George, G. Prevot, M. Ciccotti, Int. J. Fract. 156, 11-20 (2009)
[20] T. Fett, G. Rizzi, J.P. Guin, J. M. López-Cepero and S. M. Wiederhorn, Eng. Fract. Mech. 76, 921934, (2009)
[21] W. A. Scrivens, Y. Luo, M. A. Sutton, S. A. Collette, M. L. Myrick, P. Miney, P. E. Colavita, A. P. Reynolds and X. Li, Exp. Mech. 47, 63-77, (2007)
[22] M. L. Williams, ASME J. Appl. Mech. 24, 109, (1957)
[23] F. Hild, B. Raka, M. Baudequin, S. Roux and F. Cantelaube, Appl. Optics 41, 6815-6828, (2002)
[24] A. Dimitrov, F.-G. Buchholz, E. Schnack, Comp. Mod. Engng. Sci. 12, 125, (2006)

Proceedings of the SEM Annual Conference
June 7-10, 2010 Indianapolis, Indiana USA

Characterization of a structural adhesive by Digital Image Correlation

D. MORIN[(a,b,c)], G. HAUGOU[(a,b,c)], B. BENNANI[(a,b,c)], F. LAURO[(a,b,c)]

(a) Univ Lille Nord de France, F-59000 Lille, France

(b) UVHC, LAMIH, F-59313 Valenciennes, France

(c) CNRS, FRE 3304, FR-59313 Valenciennes, France

Corresponding author: franck.lauro@univ-valenciennes.fr

ABSTRACT

In the recent years, structural bonding takes an important place in assemblies techniques used for the automotive design. The next step to optimize the use of adhesive in car structures is to realize accurate finite element simulations of behaviour until failure of bonded joints. These kinds of calculations are only possible if fine behaviour and failure models are provided into the finite element software. In these works, tests on bulk adhesive specimens are realized to characterize the mechanical properties. 2D and 3D Digital Image Correlation are used to investigate the behaviour and failure of the shear and tensile specimens.

I) Context

Nowadays structural bonding is widely used in automotive industry. This interest is focused on classical advantages of structural bonding like stress concentration reduction and the possibility of join materials of different nature but also on new applications like:

- improvement of energy management of car structures,
- reduction of number of spotweld.

For these use of bonding a new generation adhesive is designed by chemical industry. This adhesive defined as crash-stable adhesive is based on a classical epoxy matrix toughened by addition of elastomers nodules. The addition of polymer nodules confers to the epoxy matrix new mechanical properties [1] like:

- visco-elasticity,
- visco-plasticity,
- non-isochoric plasticity and damage.

So as to take into account the adhesive in finite element simulation of car structures, fine behaviour and failure model has to be provided. In the literature, the adhesive properties are generally identified on assemblies tests with butt joint and single or double lap joint for tensile and shear properties respectively. Although these tests are

T. Proulx (ed.), *Application of Imaging Techniques to Mechanics of Materials and Structures, Volume 4*, Conference Proceedings of the Society for Experimental Mechanics Series 14, DOI 10.1007/978-1-4419-9796-8_14, © The Society for Experimental Mechanics, Inc. 2013

realized in conditions near those used in industry (same adherent material, thickness, chemical composition of the surface …), the stress fields are always heterogenous inside the bonded joint and the mechanical response is mainly controlled by the adherend properties [2,3]. Like the work of Goglio et al. [4], the properties identification is then performed on bulk adhesive specimen in tension and shear on a wide range of strain rate (from 0.01 to 400 s^{-1}). By using Digital Image Correlation, local information are extracted on these tests and a fine characterization of the adhesive is performed.

II) Experimental set up

a) Specimen preparation

An original forming process is designed so as to obtain plates of pure adhesive. These plates are cured under an heating press so as to control the pressure applied during curing (Figure 1). A water cutting technique is used so as to avoid heating and crack initiation of classical machining technique.

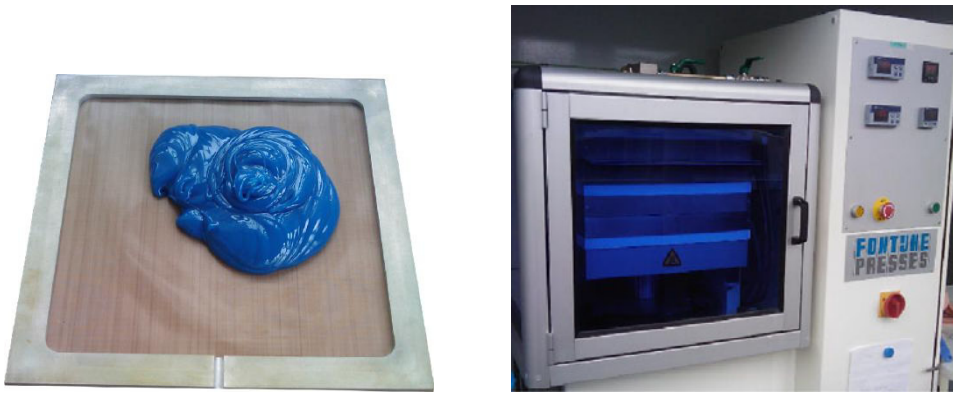

Figure 1: aluminum mould (left) and heating press (right).

b) Loading devices

In order to cover a wide range of strain rates different loading devices are used:

- an electro-mechanical device for the low strain rate range (0.01 to 0.1 s^{-1}),
- a high-speed hydraulic machine for the middle strain rate range (0.1 to 100 s^{-1}),
- a set of pre-stressed Hopkinson bars for the high strain rate range (100 to 400 s^{-1}).

The shear loading is obtained by the Iosipescu test and due to the complexity of the clamping system is only limited to static loading.

c) Geometries

The tensile specimen geometries are extracted from the NF-EN-ISO-527-3 (Figure 2). The effect of the triaxiality stress ratio is studied by realizing test on notched tensile tests. The notched specimens geometries are derived from the normative one (Figure 2).

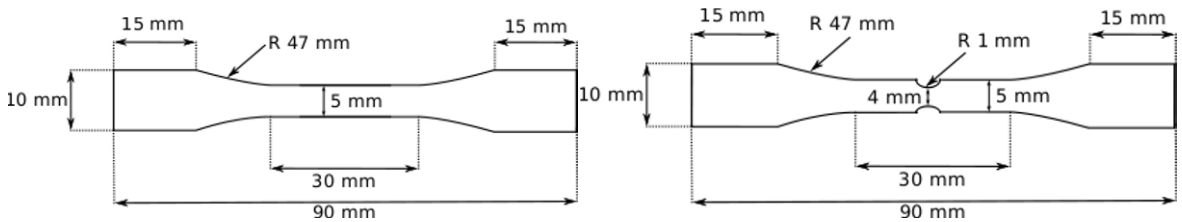

Figure 2: geometry of tensile specimens (left) and notched specimens (right)

The geometry of the shear specimens is extracted from the ASTM-D6539 norm (Figure 3).

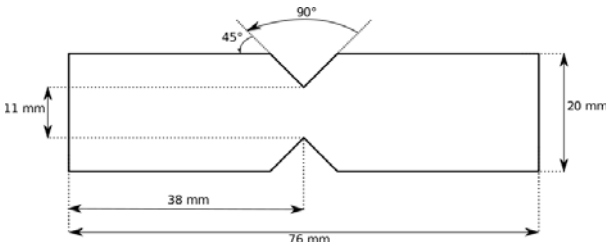

Figure 3: geometry Iosipescu shear specimen

d) Measurement techniques

2D and 3D digital image correlations are used to identify the local strain fields in tensile, notched tensile and shear tests. The strain fields are computed from the measured displacements fields using VIC 2D/3D software. The image sequences are obtained both CCD and CMOS captors:

- 2 CCD captors for the 2D D.I.C. at 10 $f.s^{-1}$ for the low strain rate range,
- 1 CMOS captor for the 2D D.I.C. at 50, 1000, 15000, 37500 f.s-1 for the middle and high strain rate range.

For the D.I.C. calculations, the strains are computed with length scale of 0.3 mm. With this size of scale heterogeneities in strain fields of notched and shear tests can be neglected.

III) Behaviour law

a) Tensile tests

The tensile behaviour laws are extracted using the SEĖ method [5], this technique used the heterogeneities of the strain field to build a 3D behaviour surface in the true strain, true strain rate and true stress space. With this method, the local stress field is computing between each subset of the D.I.C. calculations with the equation 1. In this formula, an hypothesis on the behaviour in the thickness is needed.

$$\sigma_t = \frac{F}{S_0}.e^{-\varepsilon_2}.e^{-\varepsilon_3} \quad \text{(eq. 1)}$$

Where F is the current load in the specimen, S_0 the initial cross section and ε_2 and ε_3 the strains in the cross section.

The transversal isotropy hypothesis which postulates that ε_2 and ε_3 are equal is validated by using 3D D.I.C. measurements on both front and side of tensile specimens as shown in Figure 4. In this Figure a maximum deviation of 300 με is observed between transversal strain of front and side of the specimen.

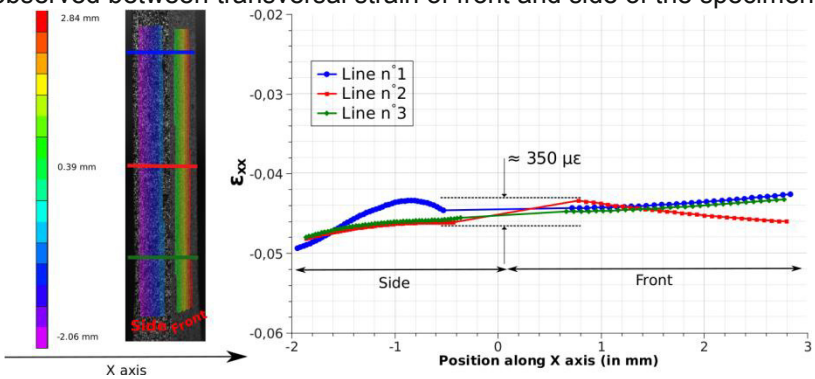

Figure 4: difference between front and side strain.

Figure 5 shows the results in terms of behaviour law, on these curves a high visco-plastic character is highlighted but also softening after a certain amount of plastic strain. This softening is due to the transversal isotropy hypothesis used for the thickness computations, when the behaviour laws are computed with the incompressibility hypothesis (eq. 2) (Figure 6), the softening is not present.

$$\varepsilon_1 + \varepsilon_2 + \varepsilon_3 = 0 \quad \text{(eq. 2)}$$

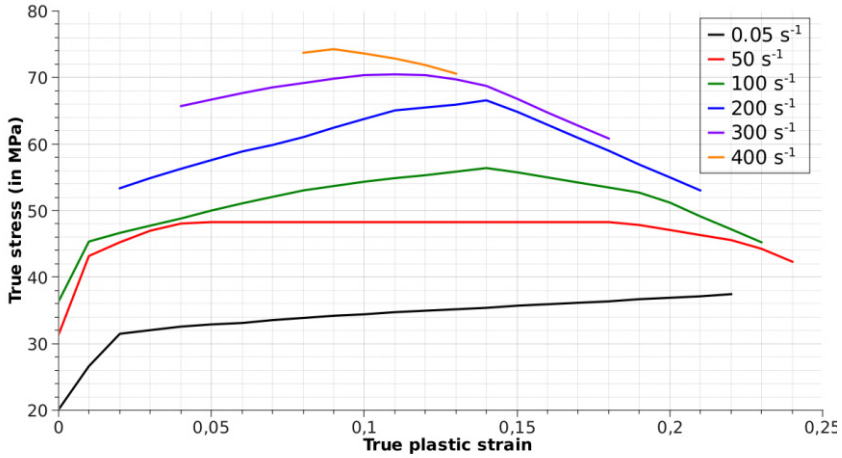

Figure 5: behaviour laws with the transversal isotropy hypothesis.

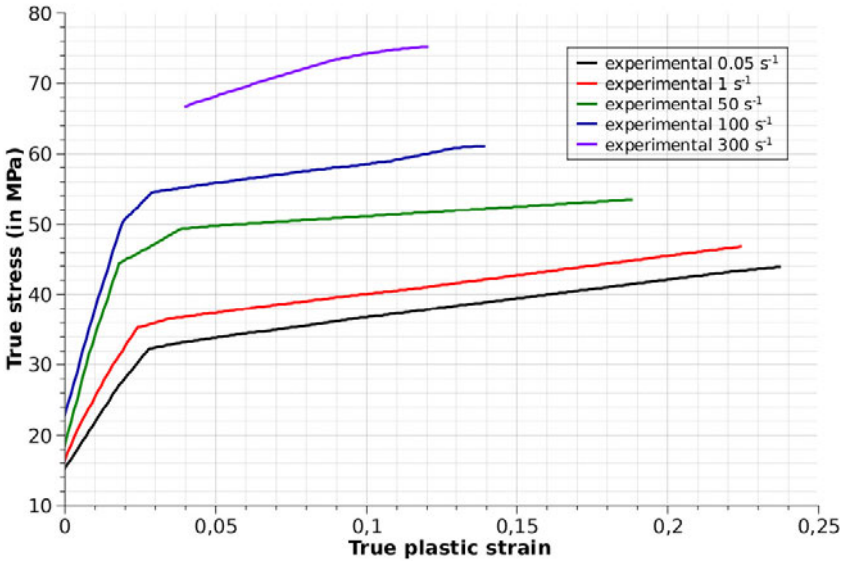

Figure 6: behaviour laws with the incompressibility hypothesis.

b) Shear tests

Before to present results in term of plasticity on the Iosipescu tests, the quality of the shear loading is investigated. This quality is quantified on two levels with the D.I.C. measurements. Firstly, in a shear loading the principal vectors of the diagonalized strain tensor are placed at ±45° of the neutral axis of the specimen. As shown in Figure 7 this requirement is reached. The last requirement is that principal strains have to be of the same magnitude. Figure 8 shows that this requirement is not reached until the failure of the specimen so a confidence interval has to be provided on the behaviour law in shear.

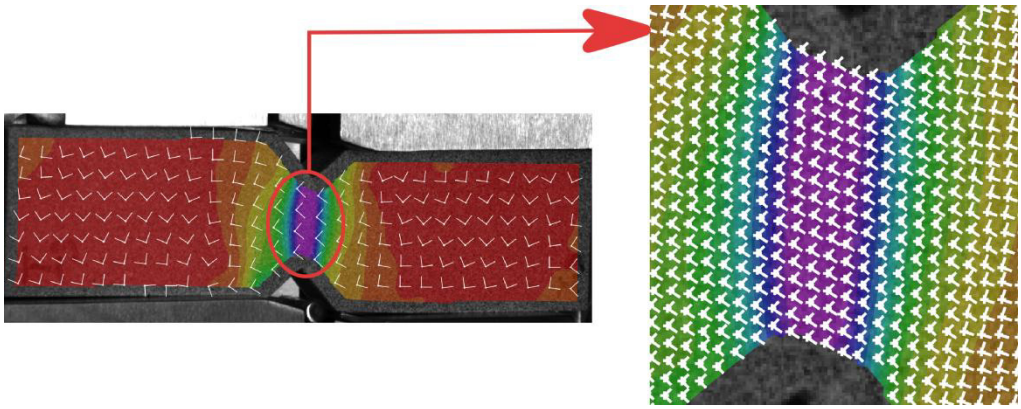

Figure 7: principal vectors of the diagonalized strain tensor.

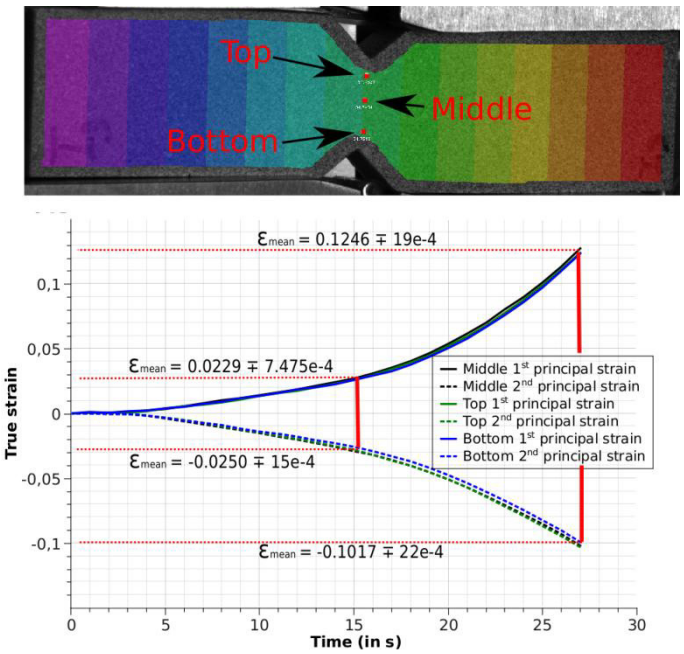

Figure 8: study of the magnitude of the principal strains.

The behaviour law shown in Figure 9 is computed with:

$$\sigma_s = \frac{F}{S_0} \quad \text{(eq. 3)}$$

where F is the current load in the specimen and S_0 the initial cross section.

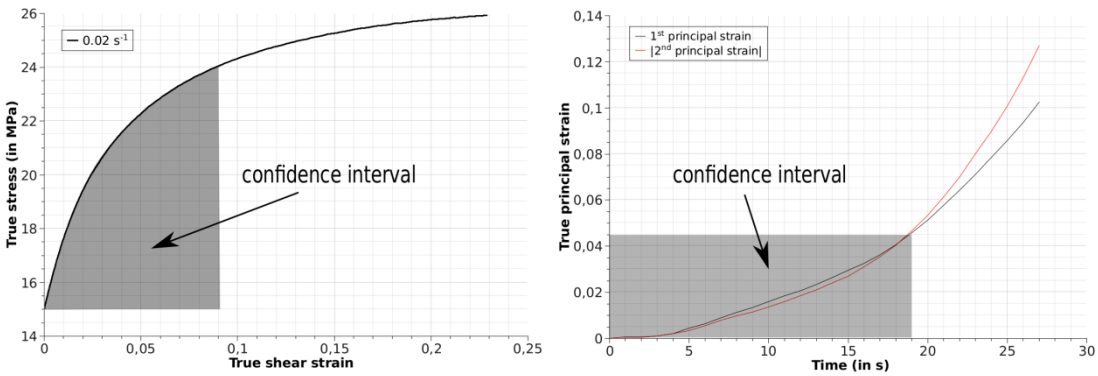

Figure 9: behaviour law in shear and confidence interval.

c) Damage

Damage evolution is investigated using the plastic Poisson ratio extracted with D.I.C. from tensile and notched tensile tests. As shown in Figure 10, the plastic Poisson ratio is never equal to 0.5 which proves that plasticity is not at constant volume moreover plastic Poisson ratio decreases with the increase of longitudinal strain which highlight a damage evolution.

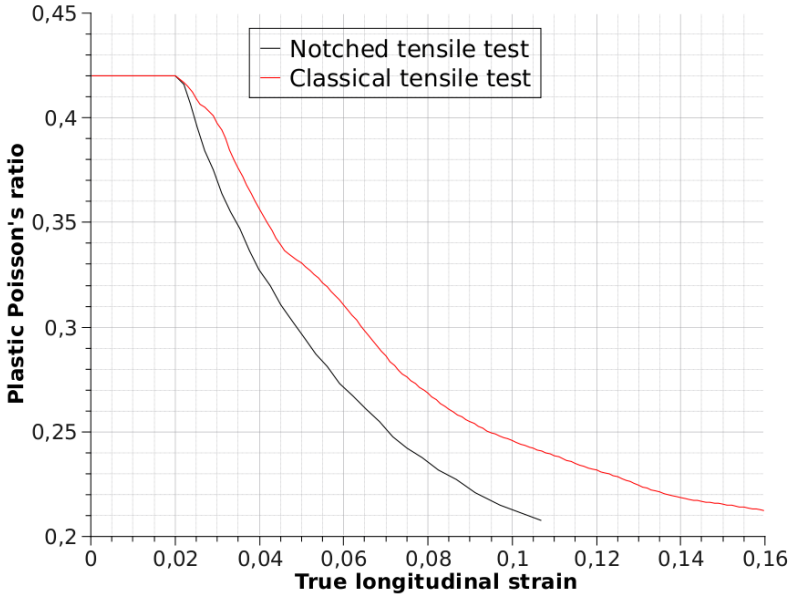

Figure 10: evolution of plastic Poisson ratio.

The damage evolution is extracted from the previous plastic Poisson ratio evolution with equations 4 and 5. The influence of triaxiality stress ratio is highlighted on Figure 11 and can not be neglected in future damage models.

$$\nu_p = (1 - d).\nu \quad \text{(eq. 4)}$$

$$d = 1 - \frac{\nu_p}{\nu} \quad \text{(eq.5)}$$

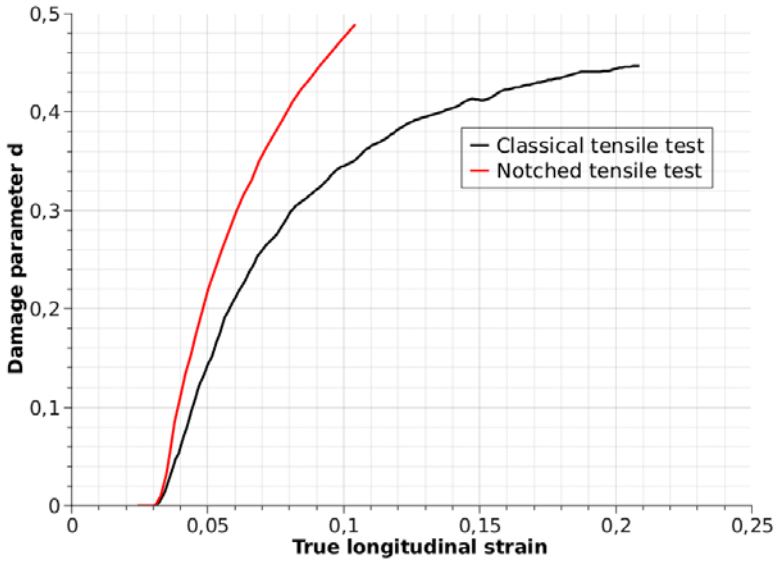

Figure 11: damage evolution.

IV) Failure

a) Tensile and notched tensile tests

The equivalent strain used for the failure characterization is computed following the transversal isotropy hypothesis which leads to a strain tensor of the following form:

$$\bar{\bar{\varepsilon}} = \begin{bmatrix} \varepsilon_{11} & 0 & 0 \\ 0 & \varepsilon_{22} & 0 \\ 0 & 0 & \varepsilon_{22} \end{bmatrix} \quad \text{(eq .6)}$$

and the strain rate is computed using a backward finite difference.

Figure 12 and 13 show the evolution of failure strain in function of strain rate for the tensile and notched tensile tests respectively, in both of case a high strain rate dependency is highlighted. Moreover here again the triaxiality stress ratio has a strong influence on the value and on the evolution of the equivalent failure strain.

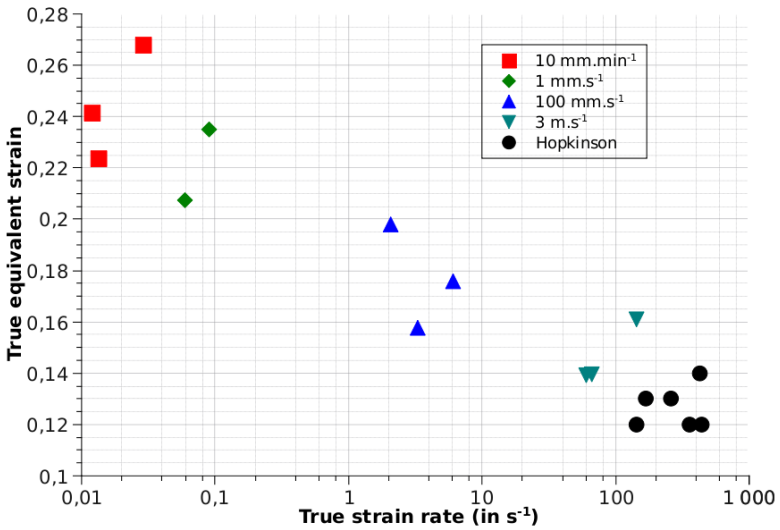

Figure 12: evolution of equivalent failure strain in function of strain rate for the tensile tests.

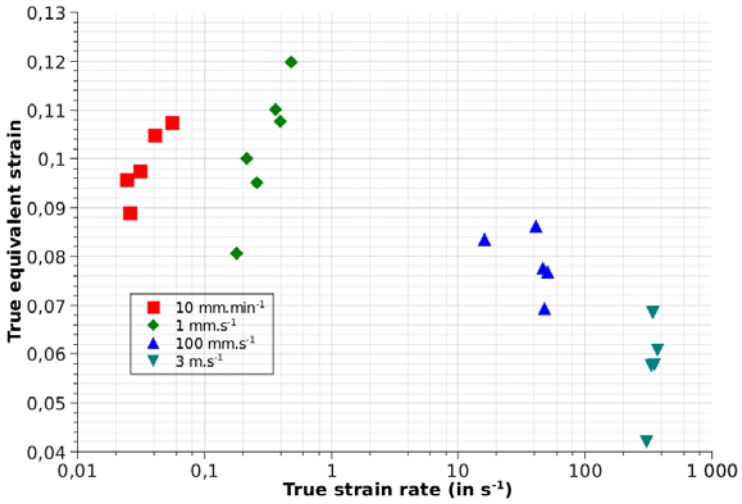

Figure 13: evolution of equivalent failure strain in function of strain rate for the notched tensile tests.

b) Shear tests

For the shear tests, the equivalent strain is computed using the following form of the strain tensor:

$$\bar{\bar{\varepsilon}} = \begin{bmatrix} 0 & \varepsilon_{12} & 0 \\ \varepsilon_{12} & 0 & 0 \\ 0 & 0 & 0 \end{bmatrix} \text{ (eq .7).}$$

The strain rate at failure is also computed by a backward finite difference.
The results in term of equivalent failure strain shown in Figure 14 highlight a high dispersion. This dispersion comes from the initial position of the specimen which is not the same for each test and also the failure phenomenon which is always submitted to a natural dispersion.

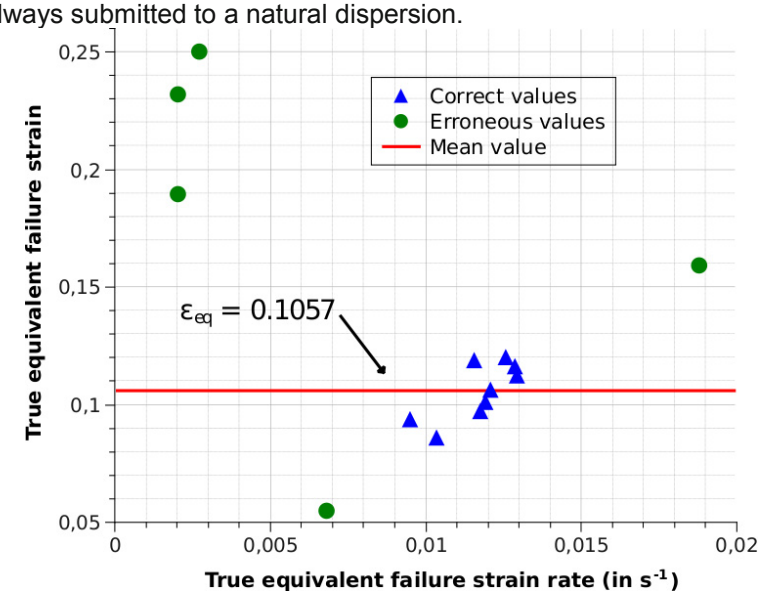

Figure 14: dispersion of equivalent failure strain in shear tests.

V) Conclusions et perspectives

With the increasing use of structural bonding in automotive, fine characterizations of behaviour and failure of structural adhesive are needed. This works brings this fine characterization by the study of tensile, notched tensile tests and shear tests on a wide range of strain rate and using non contact measurement method like 2D and 3D Digital Image Correlation. The SEĖ method is successfully applied on this kind of material and a wide database of true stress / true strain curves at constant strain rate are available to realize the identification of a visco-plastic behaviour model. A fine study of the shear Iosipescu test is realized with 3D D.I.C. and this test is not suitable to obtain pure shear loading until the failure of the specimen. An innovative damage measurement is also realized and the influence of the triaxiality stress ratio is then quantified. The failure of the adhesive is investigated with D.I.C. measurements for different triaxiality stress ratio but also on a wide range of strain rates, this database is available for the identification of a triaxiality stress ratio and strain rate dependent criterion. Finally the results obtained have a high impact on the finite element modeling due to the lack of models which can tackle the previous identified properties.

Acknowledgments

The present research work has been supported by International Campus on Safety and Intermodality in Transportation, the Nord-Pas-de-Calais Region, the European Community, the Regional Delegation for Research and Technology, the Ministry of Higher Education and Research, and the National Center for Scientific Research. The authors gratefully acknowledge the support of these institutions. The authors would like to acknowledge the support of DOW AUTOMOTIVE for the supply of the adhesive.

References

[1] M. Imanaka, Y. Nakamura, A. Nishimura, T. Iida, Fracture toughness of rubber-modified epoxy adhesives: effect of plastic deformability of the matrix phase, Composites Science and technology, 63, 41-51, 2003

[2] A.B. de Morais, A.B. Pereira, J.P. Teixeira, N.C. Cavaleiro, Strength of epoxy adhesive-bonded stainless-steel joints, International journal of adhesion and adhesives, 27, 679-686, 2007

[3] A. Derewonko, J. Godzimirski , K. Kosiuczenko, T. Niezgoda, A. Kiczko, Strength assessment of adhesive-bonded joints, Computational materials science,2007

[4] L. Goglio, L. Peroni, M. Peroni, M. Rossetto, High strain-rate compressive and tension behaviour of an epoxy bi-component adhesive, International journal of adhesion and adhesives, 28, 7, 2008, 329-339

[5] F. Lauro, B. Bennani, D. Morin, A.F. Epee, The SEĖ method for determination of behaviour laws for strain rate dependent material: Application to polymer material, International Journal of Impact Engineering, 37, 6, 715-722, 2010

Proceedings of the SEM Annual Conference
June 7-10, 2010 Indianapolis, Indiana USA

Measurement of Brain Biomechanics in vivo by Magnetic Resonance Imaging

P.V. Bayly, E.H. Clayton, Y. Feng, T. Abney, R. Namani, R.J. Okamoto, G.M. Genin

Department of Mechanical and Biomechanical Engineering, Washington University, Campus Box 1185, St. Louis, MO, USA pvb@me.wustl.edu

ABSTRACT

Computer models of head-brain biomechanics offer enormous potential for improved understanding and prevention of traumatic brain injury (TBI). However existing computer models remain controversial because their predictions have yet to be rigorously compared to measured biomechanical data. The nonlinear, anisotropic, viscoelastic, heterogeneous character of brain tissue, and the intricate connections between the brain and skull, all complicate modeling efforts. In order to make progress toward the goal of accurate simulation of TBI, experimental techniques to address these issues must be developed. In this paper we describe two magnetic resonance (MR) imaging techniques to characterize brain deformation, estimate brain material properties, and illuminate the boundary conditions between brain and skull. *MR tagging* is used to estimate displacement and strain fields in response to rigid-body acceleration of the skull, and *MR elastography* is used to visualize shear wave propagation induced by oscillatory loading at the surface of the skull.

INTRODUCTION

Traumatic brain injury (TBI) is a major health problem in both children and adults; approximately 1.5 million new cases arise each year in the US. Currently over 5 million Americans have disabilities resulting from TBI, incurring costs estimated at $56.3 billion annually [1]. Mild TBI is the most prevalent form of head injury, with over 300,000 concussions/year in the US from sports alone [2]. TBI is an established risk factor for Alzheimer's disease.

The underlying physical process in all TBI is rapid deformation, or strain, of brain tissue [3]. In concussions, mild tissue strain is thought to cause "diffuse mechanically-induced depolarization" of cortical neurons [4]. In severe trauma, diffuse axonal injury (DAI) occurs throughout the white matter of the brain, as axons are stretched beyond a physiological injury threshold [4]. The details of brain deformation in human TBI remain largely unknown, although they have been the subject of much speculation and indirect study. Experimental confirmation has been slowed by the practical difficulty of measuring brain deformation. Holbourn [5] showed that angular acceleration of a model human skull containing gel caused significant shear deformation of the gel. More recently, Margulies et al. [6] and Meaney et al. [7] filmed the motion of grid patterns in gel inside animal and human skulls during imposed angular acceleration. These gel models, however, lacked key features of the true brain and skull anatomy: vasculature, meninges, tissue structure, and cerebrospinal fluid (CSF). Hardy et al. [8] used high-speed (250/sec-1000/sec) bi-planar x-ray imaging to track the displacement of eleven neutral-density radio-opaque markers in the brains of cadavers during impacts. Because of the limited spatial resolution, it was not possible to determine tissue strain [8]. In addition the mechanical properties of cadavers may differ significantly from those of a live subject [9].

An important purpose for experimental measurement of brain deformation is to to validate computer models. Computer models of the brain (for example, [10-13]) offer great potential for studying brain biomechanics, if they are shown to be accurate. For example, simulations could be used to provide estimates of brain deformation during skull accelerations that would be unsafe for human subjects (as in, for example, [14]), or for studies that

T. Proulx (ed.), *Application of Imaging Techniques to Mechanics of Materials and Structures, Volume 4*, Conference Proceedings of the Society for Experimental Mechanics Series 14, DOI 10.1007/978-1-4419-9796-8_15, © The Society for Experimental Mechanics, Inc. 2013

would be costly, difficult, or inconclusive with cadavers or animals. However, accurate computer simulations require accurate information about the brain's material properties, boundary conditions, and tissue connectivity. It is critically important for computer simulations to be verified by comparison to observations.

Tagged MR imaging

MRI "tagging" is a method originally developed to measure deformation of the heart [15]. Harmonic variations of the longitudinal magnetization [16] are imposed on the tissue by applying magnetic field gradients between radiofrequency pulses. The technique causes stripes to appear on the image (Fig. 1). These "tag lines" move with the tissue (Fig. 2) and can be tracked to characterize tissue kinematics [15]. To achieve high temporal resolution, the deformation is repeated multiple times, and a single line of MRI ('k-space') data is acquired each repetition. With this approach we have obtained quantitative measurements of strain in the intact human brain caused by known levels of acceleration [17,18].

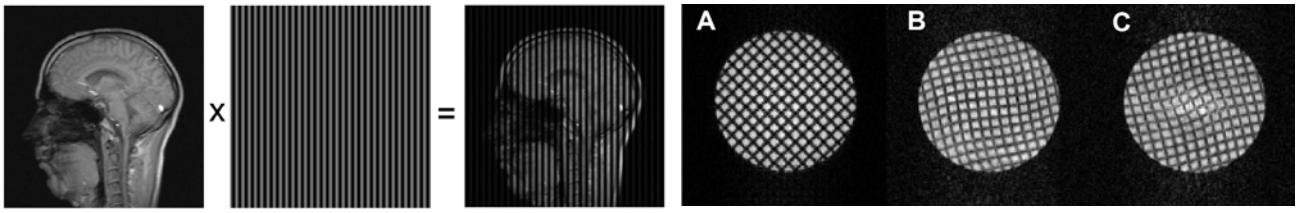

Figure 1: (left) The contrast in a tagged MR image is modulated by a sinusoidal pattern. (right) Tagged MR images of a deforming gel "phantom" show that the tag lines move with material points.

MR Elastography

Shear waves can be observed by MRI if a 'motion-sensitizing' gradient is oscillated in phase with harmonic vibration of the tissue. Muthupillai et al. [19] showed that the images of these waves can be used to estimate the shear modulus of a tissue; this technique was named elastography. The speed and wavelength of propagation depend on stiffness (Fig. 2). While shear wave elastography only provides parameters that govern small deformations, these parameters can be obtained throughout the entire imaging volume as a function of excitation frequency. MR visualization of shear waves provides a valuable tool, not only for estimation of mechanical parameters, but for gaining insight into the complete response of the brain to skull loading.

Recently, MRE studies of the brain have been performed in human subjects [20, 21]. In these studies, harmonic motion was applied to the skull through a vibrating bite bar. Among these studies, estimates of shear modulus vary. McCracken and co-workers [20] used 80 Hz excitation and found shear moduli of 5.3±1.3 kPa for cortical gray matter and 10.7±1.4 kPa for white matter (assumed to be isotropic and locally homogeneous). Sinkus and co-workers [21] used 65 Hz excitation and obtained estimates of shear modulus between 2-3 kPa; they found cortical gray matter *stiffer* than white matter.

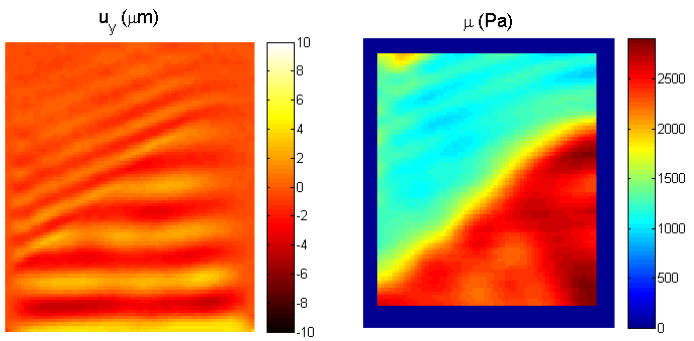

Figure 2: (left) Displacement field due to shear waves induced in a heterogeneous gelatin sample (stiffer in lower right corner than in upper left). (right) Estimated shear modulus obtained by fitting the shear wave equation (Eq. 8) to the measured displacement field.

In this paper we describe the use of tagged MR imaging and MR elastography to probe the mechanical response of the brain to external skull loading. Examples from our recent studies are used to illustrate each approach.

METHODS AND RESULTS

Tagged MR imaging during motion of the skull

A recent study of angular head acceleration illustrates this techique. Adult subjects of average height and weight performed controlled head rotation using a custom, MR-compatible device that imparted a repeatable mild angular acceleration of ~250-300 rad/s^2. These accelerations are about 10% of those experienced during a common athletic activity: heading of a soccer ball [22]. The protocol was reviewed and approved by the Washington University Human Research Protection Office. Tagged MR images were acquired in 3-4 axial planes in each subject. Images of different planes in the same subject were acquired on different days.

The custom MR-compatible head rotator is shown in Fig. 3. The head cylinder, which cradles the subject's head, was designed to fit inside the head coil of a Siemens Sonata MRI scanner (Siemens, Munich, Germany) and rotate freely about a plastic bearing at the back of the device. Rotation was initiated by releasing a latch, which allowed a plastic counterweight to apply torque to the head cylinder. Release of the latch also tripped a fiber optic switch that activated the MRI, initiating the scanning sequence. After approximately 200 ms, the weight impacted a padded stop. The associated mild angular deceleration produced measurable deformation in the subject's brain.

A FLASH2D MR cine sequence was used to collect tagged images of the deforming brain. The sequence had a frame rate of 6 ms and an echo time TE= 2.9 ms. For each nominally identical repetition of the head rotation, a single line of k-space data (192 samples) was collected 90 times; each acquisition was separated by 6 ms. The phase encoding-gradient was incremented after each repetition of motion. In total, 144 rotations of the head were required, leading to a 192x144 data matrix (image) for each of the 90 time points. To superimpose tag lines on the image, immediately after the latch was released, radio-frequency (RF) pulses were applied in combination with magnetic gradients. This sequence causes longitudinal magnetization of spins to vary spatially in a sinusoidal fashion [16], resulting in an image superimposed with an array of light and dark lines. These "tag lines" move with the tissue, and their intersections may be tracked to characterize motion. Images were collected in axial planes at several levels (Fig. 4). The reference plane (0 cm height) passed through the genu and splenium of the corpus callosum. Images were also acquired from parallel planes 2 cm and 4 cm superior to the reference plane, denoted as +2 cm and +4 cm, and 1 cm inferior (-1 cm).

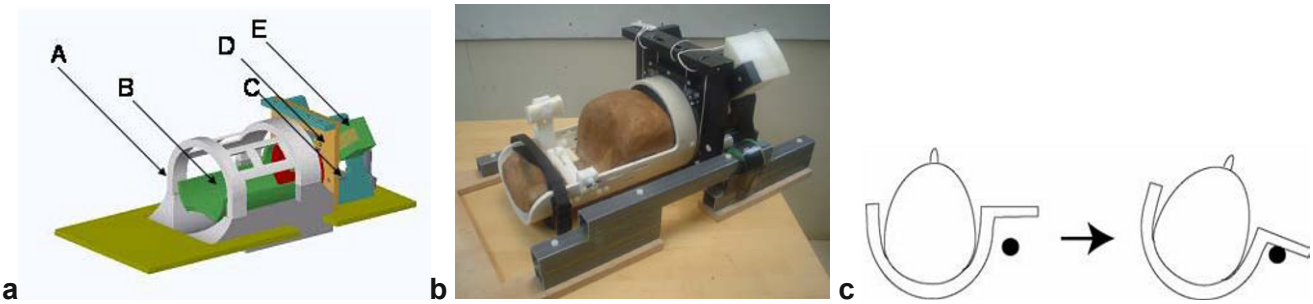

Figure 3: (a) Digital solid model of the device used to constrain head rotation in the MR scanner. (A) The MR head coil (antenna). (B) The rotating head cylinder. (C) The pin used to stop angular rotation. (D) Latch, which is released to initiate motion. (E) Plastic counterweight (600 grams). (b) Photograph of the physical device. (c) The head of the subject was secured inside the head rotator, and the entire assembly translated into the MRI coil for imaging. Upon release of a latch, the head was rotated by the off-axis weight until it was abruptly stopped by a compliant pin. This soft stop provided approximately 250-300 rad/s^2 angular deceleration.

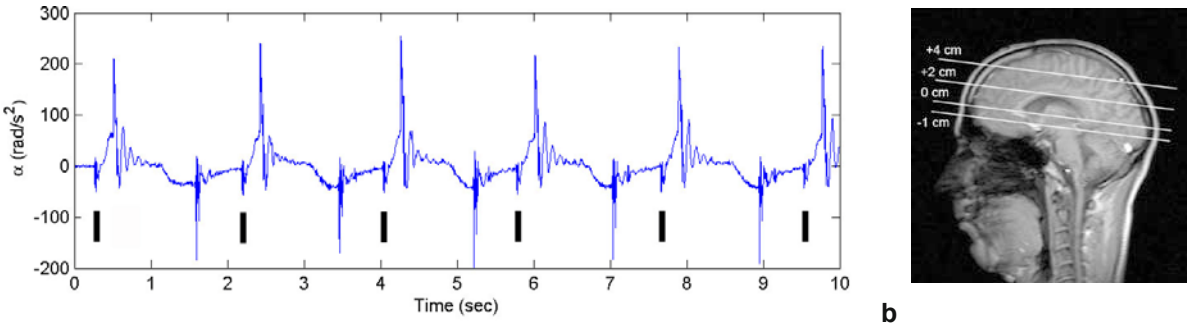

a **b**

Figure 4: (a) Angular acceleration measurements recorded during repeated controlled head rotation (subject S2). Black bars indicate the volunteer-initiated latch release that initiated motion and triggered the scanning sequence; image data were acquired in the subsequent 540 ms. (b) Sagittal image illustrating the axial imaging planes, described with respect to a reference plane passing through the genu and splenium of the corpus callosum.

Analysis of tagged MR images

The analysis of deformation is illustrated in Figure 5. Tag-line intersections were identified and tracked using contours of "harmonic phase" (HARP) (Figures 5b and 5f), via the method developed by Osman et al. [23]. Intersection points in reference (pre-impact) and deformed (post-impact) configurations were registered to one another, and used to generate a common mesh of triangular elements (Figures 5c and 5g). The deformation gradient tensor, **F**, was obtained by fitting the equation:

$$d\mathbf{x}_i = \mathbf{F} d\mathbf{X}_i \; i = 1,2,3\,, \tag{1}$$

where $d\mathbf{X}_i$ is a vector from one triangle vertex to another in the reference configuration, and $d\mathbf{x}_i$ is that same segment in the deformed configuration (Figure 6). A custom algorithm written in MATLAB (Mathworks, Natick, MA) [17] was used to solve for the deformation gradient tensor, **F**. Once **F** was determined from the reference and deformed tagged images, the Lagrangian strain tensor, **E**, was calculated in the Cartesian image coordinate system:

$$\mathbf{E} = \frac{1}{2}\left(\mathbf{F}^T\mathbf{F} - \mathbf{I}\right). \tag{2}$$

Here **I** is the 2nd rank unit tensor, and $\mathbf{F}^T$ denotes the transpose of the deformation gradient tensor.
We studied the planar components [**E**] of the strain tensor **E** in a cylindrical coordinate system with the positive rotation axis ("*z*-axis") in the superior direction:

$$[\mathbf{E}] = \begin{bmatrix} \varepsilon_{rr} & \varepsilon_{r\theta} \\ \varepsilon_{\theta r} & \varepsilon_{\theta\theta} \end{bmatrix} \tag{3}$$

For angular acceleration of the skull, the dominant strain component is radial-circumferential shear, $\varepsilon_{r\theta}$.

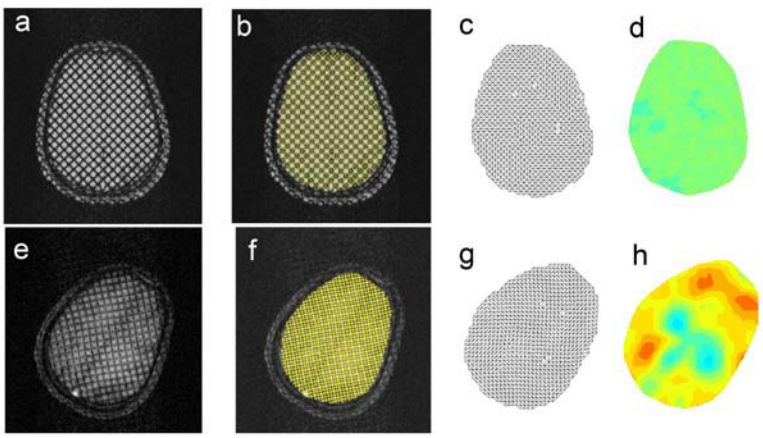

Figure 5. Illustration of strain estimation procedures. Reference image (top, a-d) and deformed images (bottom, e-h). (a, e) Tagged images. (b, f) HARP contours (synthetic tag lines). (c, g) triangular meshes generated from intersection points of HARP contours. (d, h) Radial-circumferential shear strain ($\varepsilon_{r\theta}$) fields.

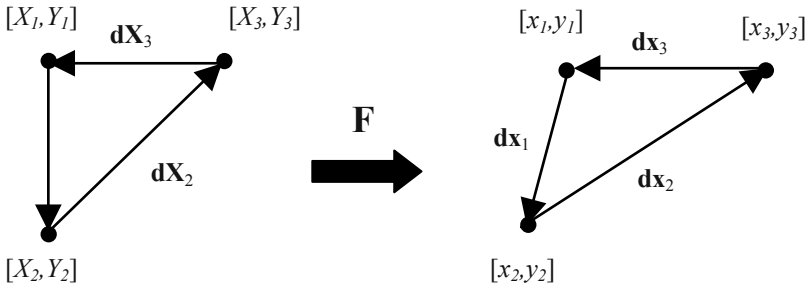

Figure 6: The deformation gradient tensor, **F**, maps each side of the reference triangle into a corresponding side of the deformed triangle (Eq. 1).

Results: Displacement and strain during angular acceleration of the skull

Patterns of deformation are illustrated qualitatively by the reference and deformed grids of tag lines in Fig. 7 (displacements are amplified by a factor of five, for visualization only). Figure 7 illustrates the initial deformation as mobile brain tissue rotates clockwise relative to the skull, which has stopped. Because the brain is tethered to the skull by vessels and membraneous connections at its base and surface, the decelerating torque is transmitted to the brain. Deformation is dominated by radial-circumferential shear.

These changes in shape may be quantified by strain. Shear strain values peak approximately 30-60 ms after initial impact (impact was observed to begin at $t \approx 200$ ms), and then decay. Areas of high shear strain are approximately symmetric about two axes roughly aligned with the medial longitudinal fissure and the central sulcus. Figure 8 shows results from different subjects juxtaposed. Strain fields in subjects S1 and S2 at the +2 cm level are quite similar; both display the symmetries noted above.

Temporal behavior may be characterized by depicting how much of the brain experiences a specific strain level at a given time. This is a measure that is medically relevant, because in more severe impacts high strain is likely to correspond to injury. Figure 9 displays the fraction of the image plane in which radial-circumferential strain exceeds a specified level ε, for ε=0.02, ε=0.04, ε=0.06). The frames of Fig. 9 correspond to the sequences of images in Fig. 8. This representation illustrates the prevalence of small strains (at this level almost 70% of the brain experiences strain > 0.02) but the relative rarity of strains greater than 0.06. Baseline strain estimates before impact (not shown) are very small; strain has dissipated to low levels by 60 ms after impact.

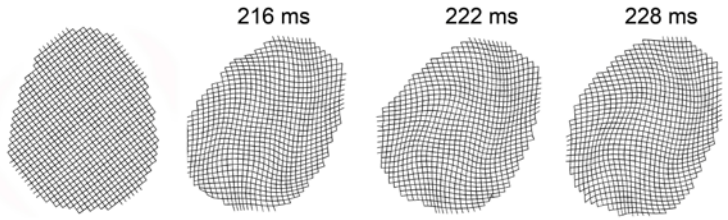

Figure 7: Grids of tag lines (HARP contours) showing “clockwise” shear deformation of the brain relative to the skull in subject S1. Displacements are scaled by a factor of five for visualization.

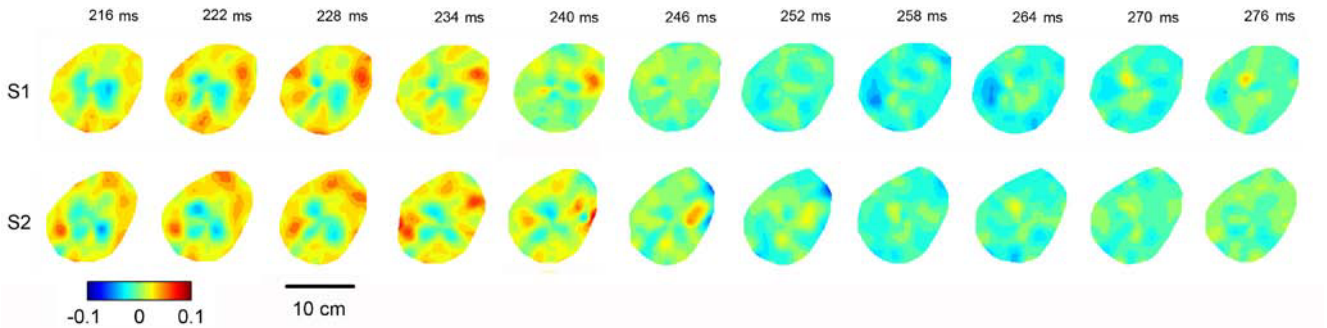

Figure 8: Radial-circumferential shear strain $\varepsilon_{r\theta}$ in the axial plane +2 cm above the corpus callosum in two subjects, S1 and S2. Data are presented chronologically relative to the onset of head rotation (*t*=0ms).

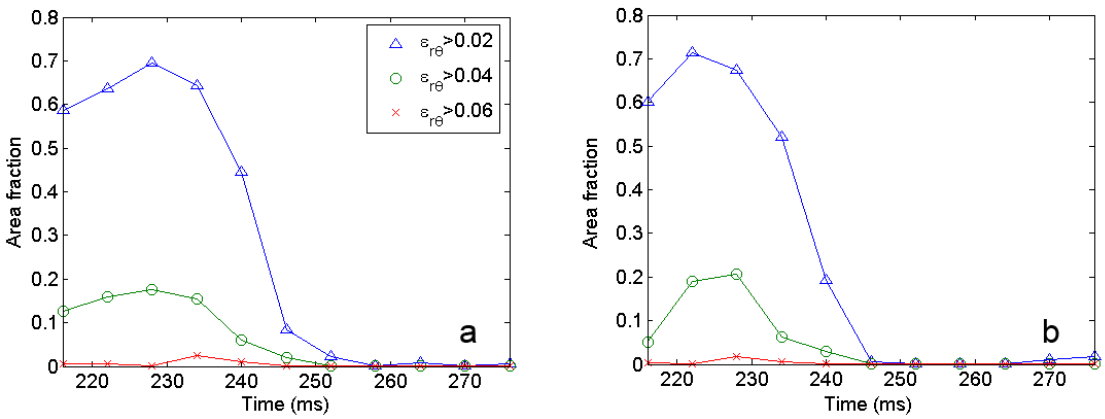

Figure 9: Fraction of image area in which radial-circumferential shear strain $\varepsilon_{r\theta}$ exceeds a specified threshold, ε Data are from the strain fields shown in Fig. 8 (axial plane +2 cm above the reference plane), plotted vs. time after impact. (a) Subject S1. (b) Subject S2.

MR Elastography

Elastography imaging principles: In MRE, oscillating shear displacements caused by harmonic vibration are measured by modulating the gradient field of the MR scanner at the vibration frequency [19]. Application of this sequence leads to images in which phase contrast is developed between vibrating spins, leading to images in which contrast is proportional to displacement (Fig. 2). If oscillating gradients of constant amplitude, frequency, and duration are applied in three orthogonal directions, a vector of motion-induced phase, $\vec{\phi}$, is obtained at each voxel in the image space. The component of oscillatory displacement, $\vec{u}$, of the voxel is proportional to the phase, $\vec{\phi}$, of the tissue spins obtained from elastography images [19]. Following Muthupillai et al. [19] we see that if the position of a spin packet in a 3-D sample is $\vec{r} = \vec{r}_o + \vec{u}$, and $\vec{u} = \vec{u}_o \cos(\omega t - \vec{k} \cdot \vec{r}_o + \theta)$ where $\vec{u}_o$, $\vec{r}_o$, ω, $\vec{k}_o$, and θ are the vibration amplitude, initial position of the spin packet, vibration frequency, spatial frequency vector, and vibration phase respectively, then the component of the phase vector in the direction of the gradient is:

$$\phi_G(\vec{r}_o, \theta) = \gamma \int_0^{2\pi N/\omega} \left(\vec{G} \cdot \vec{r}\right) dt = \frac{\gamma \pi N \left(\vec{G}_o \cdot \vec{u}_o\right)}{\omega} \cos(\theta - \vec{k} \cdot \vec{r}_o) \tag{4}$$

[19], where $\phi_G(\vec{r}_o, \theta)$ is the component of the MR phase vector in the direction of $\vec{G}$; γ is the gyro-magnetic ratio of water, *N* is the number of cycles, $\vec{G} = \vec{G}_o \cos(\omega t)$ is the magnetic field gradient. The expression for displacement can be simplified to $\vec{u}(\vec{r}_o, \theta) = C\vec{\phi}(\vec{r}_o, \theta)$, where *C* is a coefficient of proportionality. Since the gradients are applied in one direction at a time the coefficient of proportionality in the i^{th} direction is

$$C_i = \frac{u_{\max,i}}{\phi_{\max,i}} = \frac{\omega}{\gamma \pi N G_{o,i}} \quad , \tag{5}$$

where $G_{o,i}$ is the gradient amplitude in the i^{th} direction.

Wave propagation and estimation of shear modulus in MRE

For a homogenous, isotropic, linearly elastic material undergoing small strain, the equation governing wave propagation in 3-D is:

$$\rho \frac{\partial^2 \vec{u}}{\partial t^2} = \mu \nabla^2 \vec{u} + (\lambda + \mu) \nabla (\nabla \cdot \vec{u}) . \quad (6)$$

[20], where $\vec{u}$ is the displacement vector, μ is the shear modulus, ρ is the material density, and λ is a Lamé constant. In general, the displacement can be decomposed into transverse, longitudinal, and 'Hodge' components: $\vec{u} = \vec{u}_T + \vec{u}_L + \vec{u}_H$, where $\nabla \cdot \vec{u}_T = 0$, $\nabla \times \vec{u}_L = 0$, and $\nabla \times \vec{u}_H = \nabla \cdot \vec{u}_H = 0$ [16,17]. The transverse, or shear, displacement component $\vec{u}_T$ describes volume-conserving deformation. The transverse displacement is governed by

$$\rho \frac{\partial^2 \vec{u}_T}{\partial t^2} = \mu \nabla^2 \vec{u}_T . \quad (7)$$

If the motion is harmonic with excitation frequency ω

$$\frac{\partial^2 \vec{u}_T}{\partial t^2} = -\omega^2 \vec{u}_T . \quad (8)$$

Equation (4) can then be solved for μ, yielding

$$\mu = \frac{-\rho \omega^2 u_{T,i}}{\nabla^2 u_{T,i}}, \quad i = x, y, z . \quad (9)$$

Since the displacement is simply proportional to phase, $\vec{u} = C\vec{\phi}$, the previous equation can be written as

$$\mu = \frac{-\rho \omega^2 \phi_{T,i}}{\nabla^2 \phi_{T,i}} . \quad (10)$$

For a propagating sinusoidal shear wave, $\vec{u}_T = \tilde{\vec{u}}_T \exp(i(\omega t - \vec{k} \cdot \vec{r}))$, the Laplacian, $\nabla^2 u_{T,i} = -k^2 u_{T,i}$, where k is the magnitude of the spatial frequency vector, $\vec{k}$. Thus Eq. (6) can be written, for a propagating harmonic shear wave, as

$$\mu = \frac{\rho \omega^2}{k^2} . \quad (11)$$

Experimental procedures for MR elastography

Gel samples: The gel phantom for elastography was a 20 mm × 20 mm × 20 mm cube of gelatin prepared and held in a plastic (Delrin™) container. Gelatin (Knox, Camden, NJ) was prepared with 0.0576 g/ml of water. For MRE experiments in gel, the gel was molded inside the custom-built hollow Delrin™ cube. The container was held on a rigid base plate containing a piezoelectric actuator (APA-100, Cedrat), and the actuator tip was placed on a plastic disk on the open surface of the gel. The entire assembly was placed inside a radio-frequency (RF) coil and inserted into the bore of the MRI scanner. The upper surface of gel phantom was vibrated laterally (horizontally) at 400 Hz. Figure 10 shows schematically the actuator-sample assembly and the generation of shear waves.

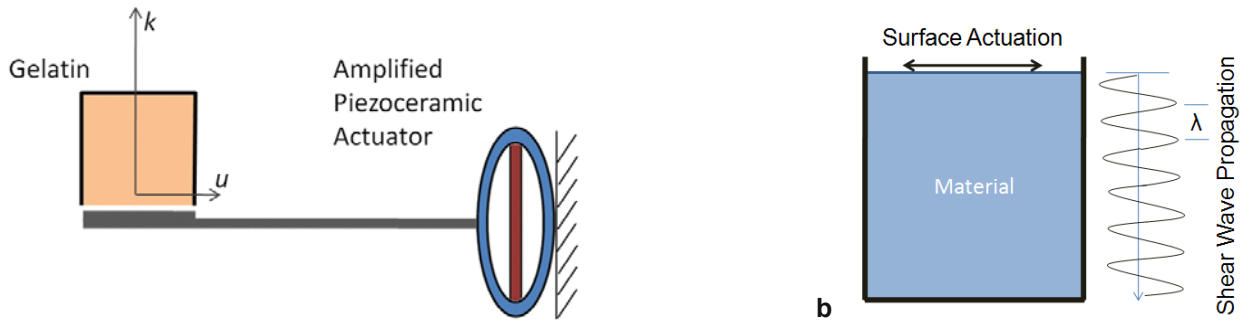

Figure 10: (a) Schematic diagram of the sample and piezoelectric actuator for gel MRE studies; (b) diagram of the wave polarization (displacement) and propagation directions.

MRE imaging procedures: Imaging of gel phantoms was performed on an 11.7T Varian (Palo Alto, CA) INOVA imaging system with high-performance gradient systems (Magnex, Oxford, UK)..A spin-echo multi-slice MRI pulse sequence was modified with motion-sensitizing gradients as described above. Typical MRE acquisition parameters were: repetition time t_r = 1 s; echo time t_e =34 ms; 64 × 64 data matrix; field of view 32 mm × 32 mm; slice thickness of 0.5 mm (voxel size of 0.5 × 0.5 × 0.5 mm). Data were interpolated to 0.25 × 0.25 × 0.25 mm for analysis and presentation. The magnitude of the motion-sensitizing gradient was fixed at 10 Gauss/cm. The sequence was run three times with the motion-sensitizing gradients applied in one of the three different directions: readout (up-down); phase-encode (side-to-side); and slice-select (front-back). For each direction of motion measurement, images were acquired at 8 different temporal points in the excitation cycle by delaying image acquisition by a fraction (1/8, 2/8, 3/8, etc.) of the vibration period.

Because MRE relies on the phase of the MR image data, instead of its magnitude, it is necessary to subtract baseline phase errors so that all phase contrast is due to the periodic motion of the tissue and not due to field inhomogeneity or sampling error. Thus two sets of data were collected for each direction of motion sensitization. In the first data set ("baseline") the sample was imaged using the MRE pulse sequence, but with the actuator turned off. The second data set ("vibration") was collected using the elastography pulse sequence, but with the actuator turned on, exciting mechanical waves in the tissue. By subtracting the phase of the "baseline" phase image from the phase of the "vibration" image, a data set where all of the phase contrast is due to wave motion in the tissue is obtained. The phase of the resulting image is directly proportional to the displacement of the sample in the direction of the applied motion-sensitizing gradient.

Phase wrapping (due to 2π ambiguity in the phase of complex data) is an artifact common to all phase images. Commercial phase unwrapping software (Phase Vision™, Loughborough, UK) was used to unwrap the images. The components of displacement at the excitation frequency were extracted by Fourier transforming the data with respect to time, and retaining the Fourier coefficients corresponding to the excitation frequency.

MRE studies in the mouse

Adult female C57BL6 mice, 12-15 weeks old, weighing approximately 30 g were imaged. Each mouse was anesthetized with isoflurane in air and placed in an MR-compatible holding apparatus which held the animal still and maintained body temperature [24]. Micro-meter amplitude vibrations were applied to the top of the skull by an electromagnetic actuator [24]. Procedures were reviewed by the Washington University Animal Studies Committee and performed in accordance with the Animal Welfare Act and the NIH Guide for the Care and Use of Laboratory Animals.

Imaging of mice was performed on the 11.7T Varian INOVA imaging system with the pulse sequence described above. Typical acquisition parameters were similar to the gel samples except for the following parameters; 64 × 64 data matrix; field of view 16 mm × 16 mm; 15 slices; 0.1 mm gap between slices; slice thickness = 0.4 mm (voxels 0.25 × 0.25 × 0.4 mm). Data were interpolated to 0.125 × 0.125 × 0.25 mm for analysis and presentation. To create waves with short wavelengths relative to the brain dimensions, vibrations were excited at 1200 Hz.

MRE studies in human subjects

Four human subjects, aged 18-29 years-old, were imaged. Experiments were conducted at 1.5T on a MAGNETOM Avanto (Siemens) whole-body clinical scanner in Washington University's Center for Clinical Imaging Research (CCIR) facility. The MRE imaging sequence implemented for this study consists of a specialized gradient-recalled echo (GRE), phase-contrast magnetic resonance imaging sequence with an additional trapezoidal 'motion-encoding' gradient. All procedures were approved by the institutional Human Research Protection Office Internal Review Board to ensure that the rights and welfare of the human research participants were protected.

Motion was transmitted to each subject's skull by affixing two acoustic actuator pads (Resoundant™, Benchmark Industries, Rochester, MN) to the left/right temples with elastic bandages (Fig. 11a). The actuator consists of a stiff rigid plastic hemispherical frame with a flexible membrane stretched across the bowl. Flexible plastic tubing acts as a pressure waveguide, connecting each actuator pad to an active driver outside of the MRI scanner magnetic field. The active driver consists of a voice coil actuator enclosed by cabinet. Pressure waves generated

by the active driver are transmitted through the flexible tubing to the passive pads, causing the pad's flexible membrane to vibrate against the skull.

The actuator pads were configured to transmit a four cycle pressure wave at 45 Hz, synchronized with the MRE imaging sequence. The input excitation amplitude and waveform were quantified by accelerometers attached to the exterior bowl (opposite the pad-subject contact surface) of each pad. A typical MRE image acquisition acceleration time history is shown in Fig. 11b. The motion encoding gradients of the pulse sequence were set to 45 Hz and synchronized with the acoustic actuator. A single 3 mm thick trans-axial image slice was acquired with TR: 133.3 ms, TE: 27.5 ms, flip angle: 25°, and in-plane resolution of 3 mm^2. The imaging sequence was repeated three times to record all displacement components (u, v, and w) relative to a laboratory coordinate system.

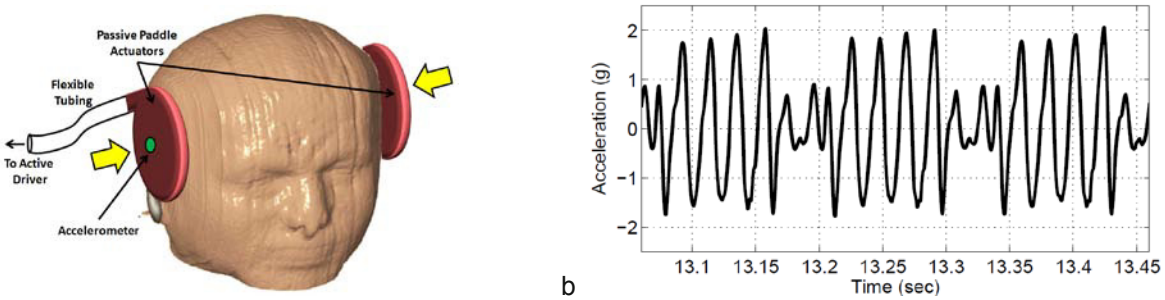

Figure 11: (a) Experimental setup of acoustic pad actuators near left and right temple. Note location of accelerometer shown on right pad. (b) A half-second time history window of the accelerations on the back of the actuator pads; three wave trains of 45Hz four-cycle acceleration are shown.

Elastography results

Shear waves in gel phantoms and mouse brain: Images of shear waves are seen below in Fig. 12. The data sets are dense and comprehensive, containing all three components of displacement throughout the 3-D imaging volume. The periodic motion has been sampled eight times per cycle.

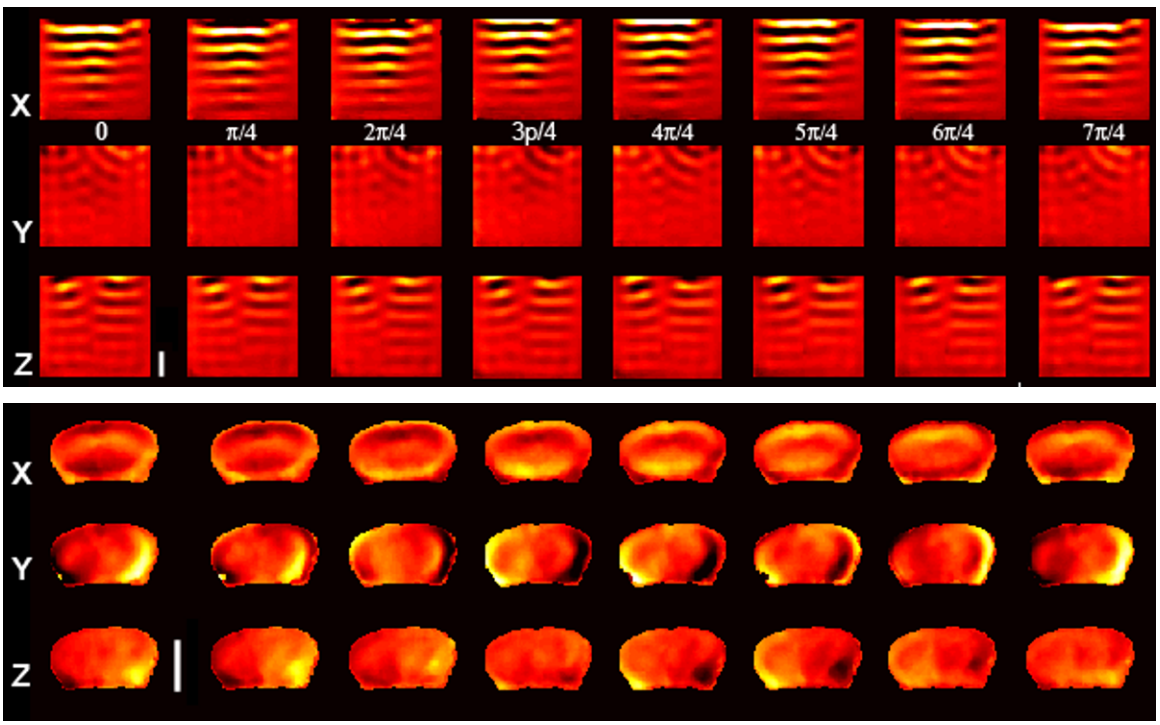

Figure 12: Displacement components of shear waves at 400 Hz in gelatin (top) and at 1200 Hz in mouse brain (bottom). Displacements are obtained at 8 phases of the forcing period. White scale bars are 5 mm.

Observed wavelengths in these materials are consistent with an elastic shear modulus of 1600 Pa in the gelatin at 400 Hz and 12000-15000 Pa for the mouse brain at 1200 Hz. Note that both materials exhibit viscoelastic behaviour in general, so shear modulus is likely to depend on the frequency.

Shear waves in human subjects: Displacement fields in the human brain are presented in Fig. 13. Propagating shear waves were observed at wavelengths of 4-5 cm and propagation speeds of 2-3 m/s. These wavelengths and speeds are consistent with shear motion in a viscoelastic medium with storage modulus 3-5 KPa. Dissipation is apparent by the decay in amplitude as the waves propagate into the interior of the brain. Reflection from interior boundaries (for example, at the falx cerebri between the brain hemispheres) is also apparent. The excitation is almost perfectly symmetric; the brain's response appears laterally anti-symmetric because displacements are positive on one side and negative on the other. Clear differences occur anterior and posterior regions, likely due to the tentorium connection in the rear. These observed patterns are strikingly consistent among all of the subjects studied to date.

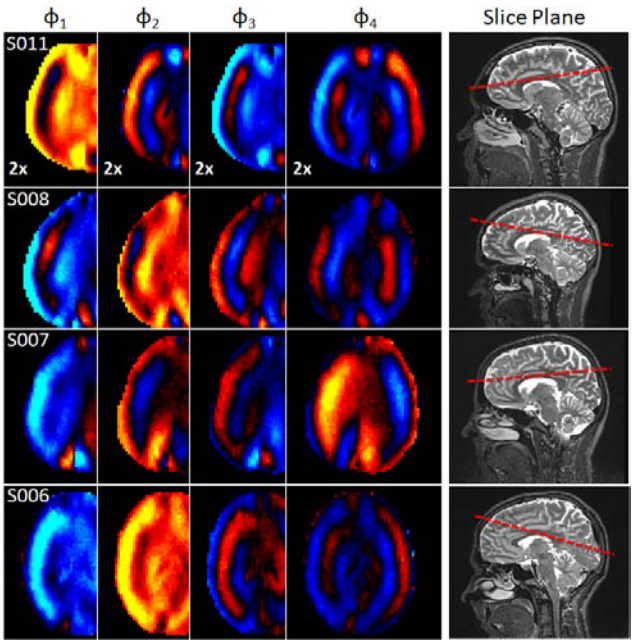

Figure 13: MRE images of displacement (anterior-posterior component) during wave propagation in brain tissue while the skull is subjected to 45Hz, 4-cycle acoustic wave excitation. Data from four human subjects is shown (one per row). Temporal displacement images are shown at four phases (Φ_i) in the excitation cycle; the rightmost image in each row shows the anatomical trans-axial slice plane.

SUMMARY AND DISCUSSION

Tagged MR imaging of displacement and strain due to skull acceleration

Tagged MRI is well-suited to study displacements on the order of millimeters and above in human subjects. For good quality images, the accuracy of displacement estimates is better than the voxel size, but the resolution is probably limited to an order of magnitude fine than the typical 2-3 mm voxel size. This range is adequate for studies of brain motion due to skull acceleration.

The major limitation is that the subject must repeat the acceleration event almost identically until the full image is obtained. This has involved 72-144 repetitions. The modified HARP approach used to determine displacements and strain is quite powerful and has many automated steps, but still requires manual intervention and quality control. A particularly important step is to ensure that the intersection points in the reference and deformed image are correctly matched, or registered.

The motion of the brain also includes a rigid-body rotation component relative to the skull. In the example study described above, the relative brain-skull displacement was not quantified. The motion of the skull presents challenges because the skull contributes little to the overall signal amplitude and is not reliably "tagged". Current work is focusing on characterizing skull motion by sub-pixel image registration and extracting the relative displacements between brain and skull.

MRE for visualization of shear wave motion due to oscillatory pressure loading

MRE allows the measurement of micro-meter level displacements at frequencies from 40-1000 Hz, depending on the technical features of the MRI scanner. This range of displacement and frequency is ideal for visualizing acoustic-frequency shear waves caused by oscillatory skull loading.The magnitude and phase of the observed

displacements and strains can be used to validate computer simulations of blast-induced TBI, and to illuminate fundamental mechanical properties of the skull, brain, and associated intracranial anatomy.

The current results are limited to 45 Hz excitation, only because of the limited number of subjects to date. Higher frequencies would provide shorter wavelengths, and thus higher spatial resolution for estimates of material properties, but dissipation is more pronounced at higher frequencies. Future work will explore the brain's response at other frequencies. Also, the combination of MRE with other imaging modalities will illuminate the effects of anatomy and tissue type on wave propagation.

CONCLUSION

Measurements of displacement and strain can be obtained in human brain tissue, safely and non-invasively, in living subjects by tagged MRI and MR elastography. These measurements can be used to gain insight into the mechanical properties of the brain, and into the response of the brain to loading of the skull.

REFERENCES

[1] Thurman D.. The epidemiology and economics of head trauma. In: Miller L, Hayes R, eds. Head Trauma: Basic, Preclinical, and Clinical Directions. John Wiley and Sons. New York. 2001.

[2] Sosin DM, Sniezek JE, Thurman DJ. Incidence of mild and moderate brain injury in the United States: 1991. Brain Inj.10(1):47-54.1996.

[3] Graham DI, Adams JH, Nicoll JAR, Maxwell WL, and Gennarelli TA. The nature, distribution and causes of traumatic brain injury, Brain Pathology 5:397-406.1995.

[4] Shaw NA. The neurophysiology of concussion, Progress in Neurobiology 67:281-344.2002.

[5] Holbourn, AHS. The mechanics of head injuries, Lancet, 2:438-441. 1943.

[6] Margulies SS, Thibault LE, and Gennarelli TA. Physical model simulations of brain injury in the primate. J Biomech, 23:832-836. 1990.

[7] Meaney DF, Smith DH, Ross DT, Gennarelli TA. Biomechanical analysis of experimental diffuse axonal injury in the miniature pig, J Neurotrauma, 12(4):689-695. 1995.

[8] Hardy WN, Foster CD, Mason MJ, Yang KH, King AI, Tashman S. Investigation of head injury mechanisms using neutral density technology and high-speed biplanar X-ray. Stapp Car Crash Journal 45:337-368. 2001.

[9] Margulies SS and Meaney DF. Brain tissues. In: Handbook of Biomaterial Properties. J. Black and G. Hastings (eds.) Chapman and Hall: London, pp. 70-80. 1998.

[10] Ruan, JS, Khalil T, King AI. Human head dynamic response to side impact by finite element modeling, J Biomech Eng, 113(3):276-283. 1991.

[11] Zhang L,Yang KH, King AI.A proposed injury threshold for mild traumatic brain injury. 126:226-236. 2004.

[12] Kleiven, S. Evaluation of head injury criteria using a finite element model validated against experiments on localized brain motion, intracerebral acceleration, and intracranial pressure. International Journal of Crashworthiness 11:65-79. 2006.

[13] Takhounts EG, Eppinger RH, Campbell JQ, Tannous RE, Power ED, Shook LS. On the development of the SIMon finite element head model. Stapp Car Crash Journal 47:107-33. 2003.

[14] Kleiven S. von Holst H. Consequences of head size following trauma to the human head. Journal of Biomechanics 35:153-60. 2002.

[15] Zerhouni EA, Parish DM, Rogers WJ, Yang A, Shapiro EP. Human heart tagging with MR imaging – a method for noninvasive assessment of myocardial motion. Radiology 169(1):59-63. 1988.

[16] Axel L, Dougherty, L. MR imaging of motion with spatial modulation of magnetization. J Biomech, 171(3):841-845. 1989.

[17] Bayly PV, Cohen TS, Leister EP, Ajo D, Leuthardt EC, Genin GM. Deformation of the human brain induced by mild acceleration. J. Neurotrauma 22(8):845-856. 2005.

[18] Sabet AA., Christoforou E, Zatlin B, Genin GM, Bayly PV. Deformation of the human brain induced by mild angular head acceleration. J Biomech, 41, 307-15. 2008.

[19] Muthupillai R, Lomas DJ, Rossman PJ, Greenleaf JF, Manduca A, Ehman RL. Magnetic resonance elastography by direct visualization of propagating acoustic strain waves. Science 269, 1854–1857. 1995.

[20] McCraccken PJ, Manduca A, Felmlee J, Ehman RL (2005). Mechanical transient-based magnetic resonance elastography. Mag Res Med 53:628-639. 2005.

[21] Sinkus R, Tanter M, Catheline S, Lorenzen J, Kuhl C, Sondermann E, and Fink M. Imaging anisotropic and viscous properties of breast tissue by magnetic resonance elastography. Mag Res Med 53:372-387. 2005.

[22] Naunheim R, Bayly PV, Standeven JW, Neubauer JS, Lewis LM, Genin GM, Linear and angular accelerations during heading of a soccer ball, Med Sci Sports Exer, 35(8):1406-12, 2003.

[23] Osman NF, McVeigh ER, Prince JL. Imaging heart motion using harmonic phase MRI. IEEE Trans Med Imaging, 19(3): 186-202. 2000.

[24] Atay SM, Kroenke C, Sabet A, Bayly PV, Measurement of the dynamic shear modulus of mouse brain tissue *in vivo* by magnetic resonance elastography. Journal of Biomechanical Engineering. 130(2):021013, 2008.

Proceedings of the SEM Annual Conference
June 7-10, 2010 Indianapolis, Indiana USA

Magnetic Resonance Elastography of the Mouse Vitreous Humor *In Vivo*

E.H. Clayton[1], Q. Wang[1], S.K. Song[2], R.J. Okamoto[1], P.V. Bayly[1,3]
[1]Department of Mechanical, Aerospace and Structural Engineering
[2]Biomedical MR Laboratory, Mallinckrodt Institute of Radiology
[3]Department of Biomedical Engineering
Washington University in St. Louis
1 Brookings Drive Campus Box 1185
Saint Louis, MO 63130
clayton@wustl.edu

ABSTRACT

Magnetic resonance elastography (MRE) is a novel experimental technique for estimating the dynamic shear modulus of biological tissue *in vivo* and non-invasively. Propagating acoustic frequency shear waves are launched into biologic tissue via external mechanical actuator and a conventional magnetic resonance imaging (MRI) scanner is used to acquire spatial-temporal measurements of the wave displacement field with micron precision. Local shear modulus estimates are obtained by inverting the equations governing shear wave motion. Changes in tissue pathology may be accompanied by a stark change in tissue elasticity. As a result, MRE has appeal to healthcare practitioners as a non-invasive diagnostic tool. Recently, MRE-based modulus estimates have been obtained in animal liver, brain, and heart [2-7]. Here, for the first time, MRE was used to probe the shear modulus of mouse eye vitreous humor *in vivo* and non-invasively.

INTRODUCTION

Non-invasive measurements of biological tissue stiffness (elastic modulus) can be probed with magnetic resonance elastography (MRE) [1]. To date, many studies have already illustrated the versatility of MRE; *in vivo* stiffness estimates have been obtained on liver, muscle, breast, brain and heart tissue [2-7]. Tissue health or disease is often indicated by its stiffness. Hence, physician palpation, though qualitative, is common practice. When quantitative diagnostics of tissue health are necessary invasive biopsy is often required. However, both diagnostic procedures have limitations. Patient-to-patient variability, skeletal structure, and penetration depth limit the extent of palpation to soft, fatty tissues (e.g., breast and abdominal examinations). Biopsy measurements are highly localized and inflict patient discomfort as well as potentially inducing collateral health risks that vary in severity depending on the anatomy probed. On the other hand, with the continued development of MRE hardware and protocols, regional, non-invasive measures of stiffness are becoming more feasible in many soft tissues.

The eye is one such organ that could possibly benefit from the development of a MRE research protocol. The elasticity of vitreous humor is known to deteriorate with age. Vitreous syneresis is an ocular disease in which pockets of fluid form within in the vitreous matrix and can encumber one's vision. Presently, detecting syneresis is difficult when the fluid pockets are small. An ocular MRE protocol could be used to detect and monitor the onset of vitreous syneresis – perhaps leading to new insight into the disease development. In this pilot study, *in vivo* shear modulus (storage and loss modulus) measurements are taken in the vitreous humor of healthy mice using a non-invasive MR elastography setup. The efficacy of MRE as tool to measure the mechanical properties of vitreous is evaluated.

T. Proulx (ed.), *Application of Imaging Techniques to Mechanics of Materials and Structures, Volume 4*, Conference Proceedings of the Society for Experimental Mechanics Series 14, DOI 10.1007/978-1-4419-9796-8_16, © The Society for Experimental Mechanics, Inc. 2013

METHODS

MRE experiments were conducted with a Varian 4.7 T using a Varian DirectDrive™ small-animal MR scanner. The scanner is built around an Oxford horizontal bore magnet, and is equipped with Magnex high-performance gradients and IEC gradient power amplifiers. Five male C57BL6 mice (Jackson Lab) were studied at three months of age. Mice were initially anesthetized with a single dose of Ketamine (87mg/kg) and Xylazine (13mg/kg). During scans anesthesia was administered continuously via subcutaneous infusion. Body temperature was maintained at 37ºC and respiratory activity was monitored with a small animal heating and monitoring system (SA instruments, NY). All procedures were approved by the institutional Animal Studies Committee in accordance with the NIH Guide on the Care and Use of Animals.

Each mouse was imaged with a custom-built mouse holder for eye imaging. A piezoceramic actuator (APA150M-NM, Cedrat Technologies) was mounted to a Delrin^{TM} angle-section and positioned towards the inferior end of the mouse. A stinger extension with an eye-contacting “shear pad” was attached to the actuator to gently induce propagating shear waves into the eye through the cornea. A transistor-transistor logic (TTL) equipped function generator and low-current voltage amplifier were used to drive the actuator harmonically at 1200 Hz. Motion-encoding gradients were synchronized to actuator vibration to encode an isochromatic phase shift proportional to wave displacements, at four time points, using a custom phase-locked spin echo pulse sequence, cf. Figure 1 [6]. Two sets of motion-encoded data were acquired; one each with positive and negative motion encoding gradient polarity. Eye MRE data was obtained on a single trans-axial slice centered through the optical nerve. The acquired in-plane resolution was 100 x 100 μm^2; through-plane resolution was 150 μm. TR/TE: 1000/27.5 ms and the number of MR motion encoding cycles (N_{MS}) was 5. Motion encoding gradients were sinusoidal with 15 G/cm amplitude. In this study, only through-plane displacements were sensitized, i.e. $u_z(x,y)$.

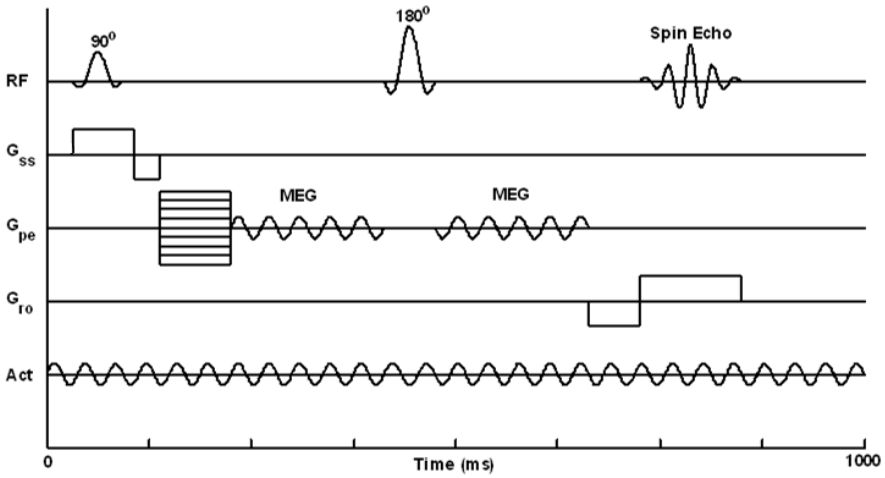

Figure 1: A modified nuclear magnetic resonance (NMR) spin echo pulse sequence for elastography data acquisition is presented above. In addition to RF and magnetic gradient events required for creating a spin echo NMR image, sinusoidal motion encoding gradients (MEG) are placed on each side of the 180° RF pulse and synchronized with the mechanical actuation signal (Act). In this example, a 5-cycle MEG is shown on the phase encode gradient channel (G_{pe}). As a result, NMR phase images can be acquired with contrast proportional to tissue displacements along the G_{pe} axis.

The in-plane voxel dimension was interpolated to 50 x 50 μm^2 to facilitate numerical differentiation. The through-plane voxel dimension remained 150 μm. Motion-sensitized phase contrast images were obtained by complex division of positive and negative polarity phase images. Phase contrast data was converted into displacements, $u_z(x,y,t)$, and the fundamental harmonic coefficient $U_z(x,y,\omega)$ was extracted by Fourier transform along the time dimension; both real and imaginary parts of $U_z(x,y,\omega)$ were retained. $U_z(x,y,\omega)$ were smoothed with a circular 6th-order Butterworth bandpass filter (in: 0.591 mm^{-1}, out: 1.58 mm^{-1}) in the spatial frequency domain. A central difference scheme was used to approximate the Laplacian; $\nabla^2 U_z(x,y,\omega)$.

Inversion of the linear isotropic homogeneous material equation of motion, $(G' + iG'')\nabla^2 U_z(x,y,\omega) = -\rho\omega^2 U_z(x,y,\omega)$, was performed by local least squares fit. For each voxel, the complex modulus was found that minimizes the squared error between this equation and data from a 2-D kernel surrounding that voxel; the residual error of each fit, normalized by the variance in that kernel, was retained to assess "goodness-of-fit" of the linear isotropic homogeneous material model at that location. A normalized residual error (NRE) of zero would indicate a perfect local fit; a residual of 1.0 indicates a poor fit. All modulus approximations were thresholded; if the local model fit yielded an NRE > 0.5 the modulus was discarded and not used in subsequent summary calculations.

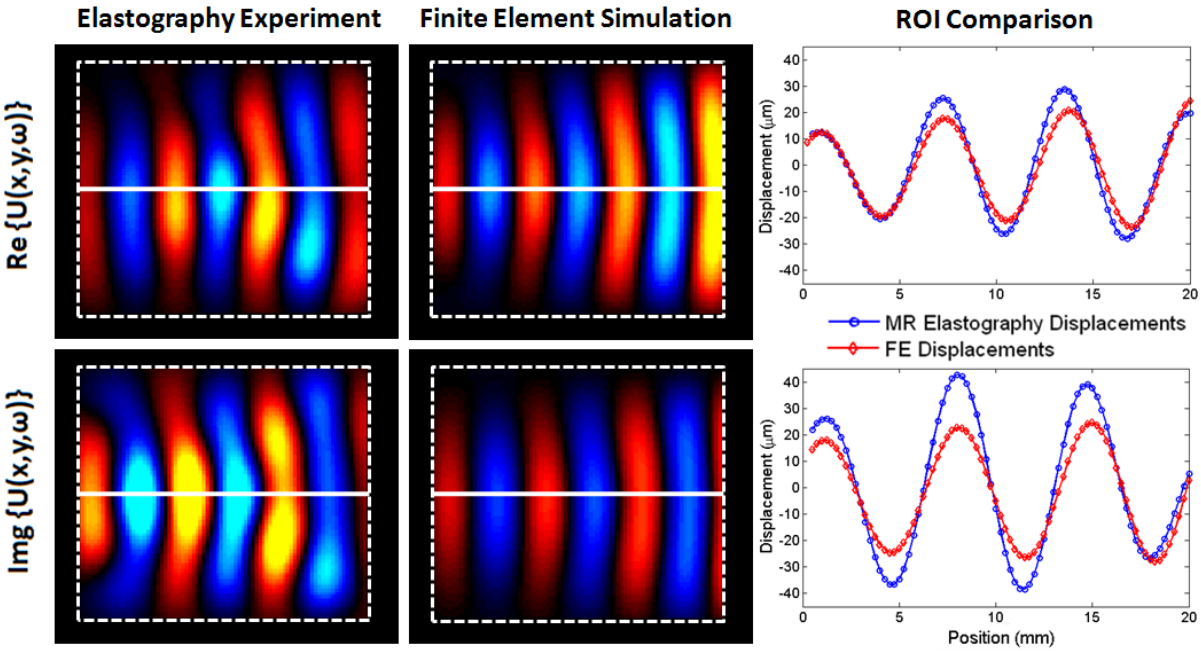

Figure 2: (Left) Displacement fields acquired with a magnetic resonance elastography imaging protocol were inverted to estimate material shear and loss modulus. Shear and loss moduli determined from the MRE experiment were used as input material parameters for a finite element model of the MRE experiment. (Center) Displacement fields obtained by finite element simulations of the MRE experiment are shown. (Right) A direct comparison of MRE and FE displacements along the centerline of the specimen. Agreement between MRE and FE displacement wavelength is excellent.

The complex modulus inversion technique implemented in this study was validated by conducting MRE experiments on a 20 mm x 20 mm x 20 mm cube of biomaterial (Gelatine, Knox). Storage and loss modulus were calculated from spatial-temporal images of a shear wave propagating though the biomaterial at 200 Hz. Figure 2 (left) presents the real and imaginary part of the fundamental displacement harmonic obtained from the MRE imaging protocol. Displacement images were inverted using the described method to estimate the mechanical characteristics of the gelatin; G' = 1.68 kPa and G'' = 0.18 kPa. These material properties were then used as input parameters for a finite element model (COMSOL, Burlington, MA) of the MRE experiment; considering geometry and boundary conditions. Simulated displacement fields are shown in Figure 2 (center). Experimental and simulated wave fields agree well.

RESULTS

Figure 1A,B shows the MRE imaging plane of interest and demarcates key features such as the actuated shear pad location. In Figure 1C unfiltered, uncropped, raw phase contrast data shows good wave penetration into the eye and surrounding tissue via gentle actuation of the cornea. The yellow arrow calls attention to what we believe is a wave reflection off of the retinal surface. A filtered and cropped wave displacement image is shown in Figure 1D. Representative storage (G') and loss (G") modulus maps of mouse vitreous humor were overlaid onto anatomy images in Figure 1E,F. The storage modulus elastogram shows relatively good consistency of the modulus estimates over vitreous region. The mean storage and loss moduli of vitreous for all five mice were 895 +/- 122 Pa and 229 +/- 57 Pa, respectively.

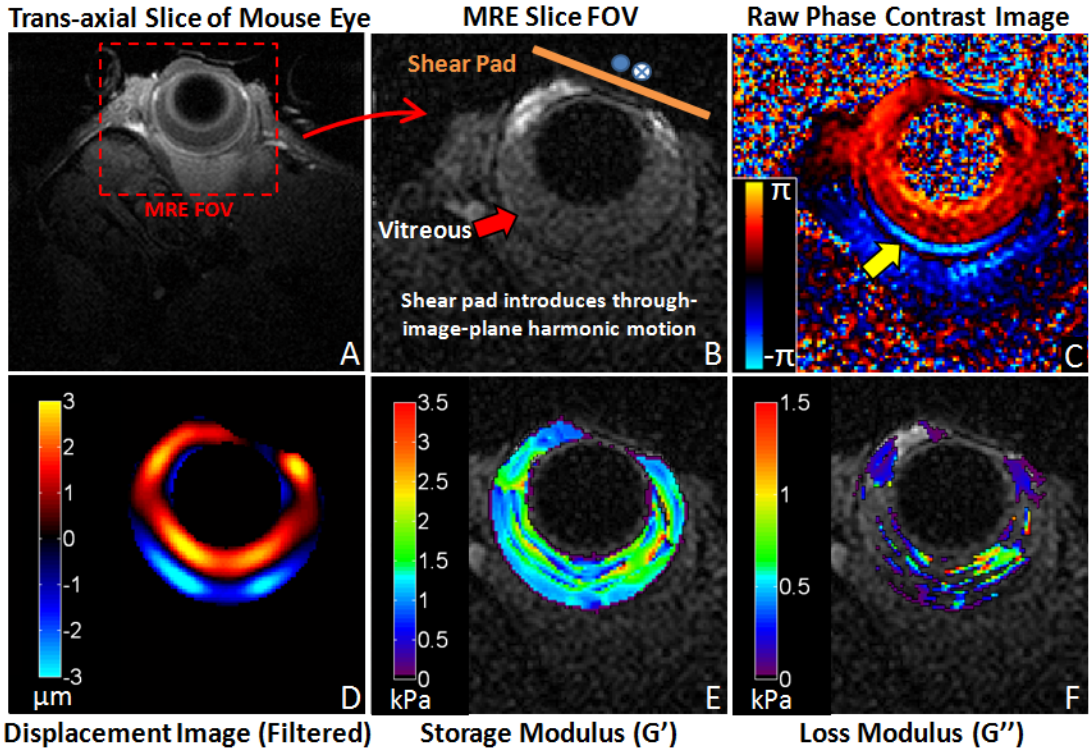

Figure 3: (A) High resolution MRI mouse eye, (B) Image FOV for eye MRE, (C) Raw, unfiltered, phase contrast data showing wave field, (D) Filtered imaginary fundamental harmonic of wave field, (E-F) Storage and loss moduli elastograms.

DISCUSSION AND CONCLUSION

Results indicate that MRE measurement of vitreous humor is feasible in the mouse. Stiffness estimates are plausible; vitreous is significantly softer than mouse brain tissue [6,7]. Storage modulus estimates, within the error limits imposed for this study, are contiguous. Reliable loss modulus estimates are sparse in the vitreous. Future studies will focus on explaining the observed phenomenon. Storage modulus estimates of vitreous could be useful for diagnosis and evaluation of ocular disease.

ACKNOWLEDGEMENTS

The authors acknowledge helpful discussions with Dr. Ying-Bo Shui in the Beebe Laboratory at Washington University in St. Louis School of Medicine, Department of Ophthalmology and Visual Science. Financial support for this research was provided by NIH RO1 NS055951.

REFERENCES

[1] Muthupillai R, Lomas DJ, Rossman PJ, Greenleaf JF, Manduca A, Ehman RL. Magnetic resonance elastography by direct visualization of propagating acoustic strain waves. Science 269, 1854–1857, 1995.

[2] Manduca A., Oliphant TE, Dresner MA, Mahowald JL, Kruse SA, Amromin E, Felmlee JP, Greenleaf JF, Ehman RL. Magnetic resonance elastography: Non-invasive mapping of tissue elasticity. Medical Image Analysis, 5:237–254, 2001.

[3] Sinkus R, Tanter M, Catheline S, Lorenzen J, Kuhl C, Sondermann E, and Fink M. Imaging anisotropic and viscous properties of breast tissue by magnetic resonance elastography. Magnetic Resonance in Medicine 53:372-387, 2005.

[4] Klatt D, Hamhaber U, Asbach P, Braun J, Sack I. Noninvasive assessment of the rheological behavior of human organs using multifrequency MR elastography: a study of brain and liver viscoelasticity. Physics in Medicine and Biology, 52:7281–7294, 2007.

[5] Robert B, Sinkus R, Gennisson JL, Fink M. Application of DENSE-MR-Elastography to the Human Heart. Magnetic Resonance in Medicine, 62(5):1155-63, 2009.

[6] Atay SM, Kroenke C, Sabet A, Bayly PV. Measurement of the dynamic shear modulus of mouse brain tissue in vivo by magnetic resonance elastography. Journal of Biomechanical Engineering. 130(2):021013, 2008.

[7] Clayton EH, Garbow JR, Bayly PV. Frequency Dependence of Mouse Brain Tissue Stiffness Measured in vivo with MR Elastography. Proc. of the Int'l. Society for Magnetic Resonance in Medicine. 633, 2010.

Proceedings of the SEM Annual Conference
June 7-10, 2010 Indianapolis, Indiana USA

Application of the Virtual Fields Method to Magnetic Resonance Elastography data

Prof. F. Pierron[*], Prof. P.V. Bayly[**], Dr R. Namani[**]

[*] Laboratoire de Mécanique et Procédés de Fabrication, Arts et Métiers ParisTech, Rue Saint Dominique, 51006 Châlons-en-Champagne, France
fabrice.pierron@chalons.ensam.fr
[**] Department of Mechanical and Biomechanical Engineering, Washington University, Campus Box 1185, St. Louis, MO, USA pvb@me.wustl.edu

ABSTRACT

This paper deals with the application of the Virtual Fields Method to the identification of the shear modulus of a gel from Magnetic Resonance Elastography data. Volume deformation fields in the cube were recorded at different times during the harmonic loading and the full harmonic response has been reconstructed using Fast Fourier Transform. Strains were then obtained by direct spatial differentiation, without any smoothing. The VFM was then applied with inertial forces balancing out elastic forces, without including the loading force which was not measured here. It has been shown that the choice of the virtual field is critical with such a spatial wave deformation field. A wide range of spatially harmonic virtual fields has been tested at different times within the loading period. The identified shear modulus has been shown to be consistent and to correlate with the value obtained from a simplified approach based on the shear wave solution. This is a feasibility study, it will be extended in the future to heterogeneous materials with a more thorough procedure to build up relevant virtual fields.

INTRODUCTION

In-vivo measurement of the mechanical properties of soft tissues is an important challenge in biomechanics and medicine. There are many underlying applications, such as the early diagnosis of cancerous tumours ([1] for breast cancers, [2] for liver tumours, for instance) or the necessity to know the mechanical response of tissues such as brain to traumatic events such as impact [3].

There are different measurement techniques that can provide in-vivo full-field deformations in such tissues. The most widespread is certainly ultrasonic imaging [4]. In this case, the recorded images before and after deformation (usually static, applied with transducer with force measurement) are processed by cross-correlation algorithms to reconstruct the strain maps. The main problem of this technique is its lack of sensitivity and the fact that an external load has to be applied, which is very inconvenient for deeply buried or inaccessible organs like liver or brain. Nevertheless, the relative ease of operation and low cost make it an attractive technique. A far more accurate way of measuring full volume deformation is Magnetic Resonance Elastography (MRE). This technique, first proposed in [5] relies on the use of a specific input signal ('gradient sensitizing') to a magnetic resonance imaging system which, combined with an harmonic excitation, provides deformation maps at different times within the harmonic response (typically 4 or 8 images). Optical Coherence Tomography (OCT) is also worth mentioning. This technique enables to image through scattering media (transparent or semi-transparent). A correlation algorithm can then be used to extract deformation inside the tissue [6]. A more elaborate version of this, called phase-contrast OCT uses the light phase information to measure displacements within scattering media with a much higher resolution [7]. This has the potential to provide data to extract mechanical properties of tissues such as eye cornea.

T. Proulx (ed.), *Application of Imaging Techniques to Mechanics of Materials and Structures, Volume 4*, Conference Proceedings of the Society for Experimental Mechanics Series 14, DOI 10.1007/978-1-4419-9796-8_17, © The Society for Experimental Mechanics, Inc. 2013

Finally, the problem is to identify the mechanical properties of the tissues from the deformation data. For quasi-static ultrasonic measurements, the main tool used is finite element updating [4,8]. A finite element model of the tissue is built-up and boundary conditions from measurements are used. A cost-function comparing measured with simulated displacements is then minimized to identify the properties. In this case, a force needs to be measured. It should be noted that because of the nearly incompressible behaviour of this type of tissues, a spatially constant value for Poisson's ratio is assumed *a priori* and kept constant through the identification scheme (for instance, 0.45 in [4], 0.4995 in [8]). For dynamic loadings, typical of MRE, it is possible to solve the inverse problem without measuring a force because inertial forces will act as a volume distributed load cell provided that the tissue density is known. The strategy consists in fitting locally the solution of the wave propagation equation to find the shear modulus distribution [3,9]. One of the difficulties however is that the local equilibrium equation (Helmholtz type equation) contains strain derivatives, which are double derivatives of the displacements, hence, very prone to noise. Another difficulty is that since the tissues are nearly incompressible, there is a large contrast between λ and μ (Lamé's coefficients). This means that the trace of the strain tensor (volume variation) is very small compared to the shear components, hence difficult to measure accurately. Nevertheless, since the bulk modulus K is large, the product between K and tr(ε) is not necessarily negligible and cannot be removed from the equation. One way of tackling this is to introduce the curl of the displacement [9] but this requires an extra differentiation.

The objective of the present paper is to investigate the application of the Virtual Fields Method to dynamic deformation obtained on a phantom (gel) using MRE. The Virtual Fields Method has been developed to extract mechanical constitutive equations from full-field deformation data [10]. A first application to biological materials has been published in [11] where the stiffness contrast between a matrix and an inclusion (phantom) was studied, using a piecewise version of the VFM, very similar to the equilibrium gap method in [12]. It has also been recently applied to vibrating plates [13,14] where inertia forces were taken advantage of in the identification process in order to retrieve complex stiffness values. The objective here is to investigate its application to volume deformation data obtained with MRE to see if it could be an alternative to the inversion methods briefly sketched in this introduction.

EXPERIMENTAL SET-UP

Samples

The gel phantom for elastography was a 20 mm × 20 mm × 20 mm cube of gelatine prepared and held in a plastic (Delrin™) container. Gelatin (Knox, Camden, NJ) was prepared with 0.0576 g/ml of water. For MRE experiments in gel, the gel was moulded inside the custom-built hollow Delrin™ cube. The container was held on a rigid base plate containing a piezoelectric actuator (APA-100, Cedrat), and the actuator tip was placed on a plastic disk on the open surface of the gel. The entire assembly was placed inside a radio-frequency (RF) coil and inserted into the bore of the MRI scanner. The upper surface of gel phantom was vibrated laterally (horizontally) at 400 Hz. Figure 1 shows the actuator-sample assembly and its positioning in the magnet bore.

Imaging

Imaging was performed on an 11.7T Varian (Palo Alto, CA) INOVA imaging system with high-performance gradient systems (Magnex, Oxford, UK). A spin-echo multi-slice MRI pulse sequence was modified with motion-sensitizing gradients. The motion-sensitizing gradients cause the nuclear spins to accumulate phase as they oscillate with the gradients. As a result the phase image of the data exhibits contrast proportional to displacement. To maintain symmetry in the spin-echo sequence, half the motion-sensitizing gradients were inserted on each side of the 180º pulse; the two trains of motion sensitizing gradient were separated by an integer number of motion cycles.

Typical MRE acquisition parameters were: repetition time t_r = 1 s; echo time t_e =34 ms; 64 × 64 data matrix; field of view 32 mm × 32 mm; slice thickness of 0.5 mm (voxel size of 0.5 × 0.5 × 0.5 mm). Data were interpolated to 0.25 × 0.25 × 0.25 mm for analysis and presentation. The MRE pulse sequence was used to visualize motion; two, two, four, and eight cycles of the motion-sensitizing gradients were applied on each side of the 180º pulse. The magnitude of the motion-sensitizing gradient was fixed at 10 Gauss/cm. The sequence was run three times with the motion-sensitizing gradients applied in one of the three different directions: readout (up-down); phase-encode (side-to-side); and slice-select (front-back). For each direction of motion measurement, images were

acquired at 8 different temporal points in the excitation cycle by delaying image acquisition by a fraction (1/8, 2/8, 3/8, etc.) of the vibration period. Each set of eight images took approximately 15 minutes to acquire. An additional "baseline" image (see Preprocessing below) acquired with no vibration, took an additional 2 minutes to acquire. Thus to obtain data in all three directions, approximately one hour of imaging time was required.

Preprocessing

Because MRE relies on the phase of the MR image data, instead of its magnitude, it is necessary to subtract baseline phase errors so that all phase contrast is due to the periodic motion of the tissue and not due to field inhomogeneity or sampling errors. Thus two sets of data were collected for each direction of motion sensitization. In the first data set ("baseline") the sample was imaged using the MRE pulse sequence, but with the actuator turned off. The second data set ("vibration") was collected using the elastography pulse sequence, but with the actuator turned on, exciting mechanical waves in the tissue. By subtracting the phase of the "baseline" phase image from the phase of the "vibration" image, a data set where all of the phase contrast is due to wave motion in the tissue is obtained. The phase of the resulting image is directly proportional to the displacement of the sample in the direction of the applied motion-sensitizing gradient.

Phase wrapping (due to 2π ambiguity in the phase of complex data) is an artifact common to all phase images. Commercial phase unwrapping software (Phase Vision™, Loughborough, UK) was used to unwrap the images. The components of displacement at the excitation frequency were extracted by Fourier transforming the data with respect to time, and retaining the Fourier coefficients corresponding to the excitation frequency.

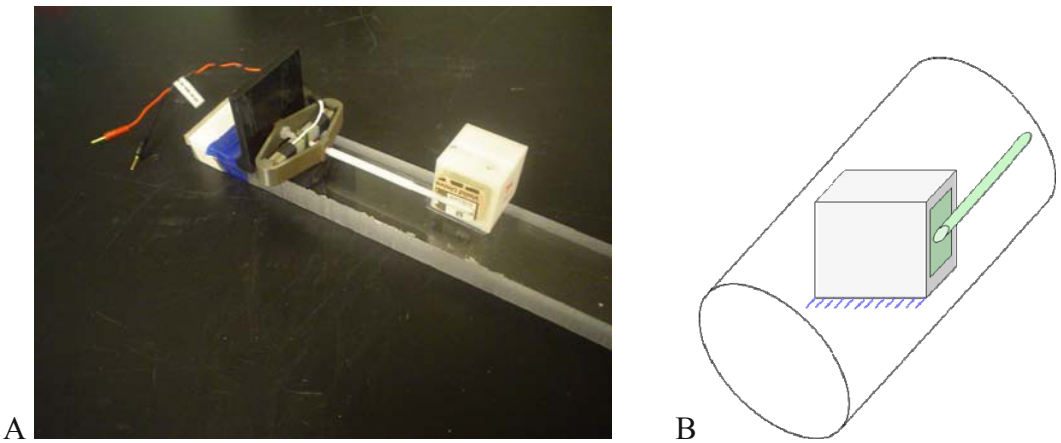

Figure 1 – (A) Photograph of gel sample and piezoelectric actuator for exciting shear waves; (B) Schematic diagram illustrating how the sample is mounted in the bore of the MR scanner.

RESULTS AND ANALYSIS

Results

Fig. 2 shows the U_x displacement in three slices along z (two edges and middle). One can clearly see that the load introduces shear waves in the (x,y) plane. It is interesting to notice that the displacements are very small (a couple of tens of microns at the most) and that there is very little high frequency noise compared to CDD-based measurements. One can also see that the displacements are not uniform throughout z. This is because of the way the load is introduced. Fig. 3 shows four UX plots at z=0 taken at different times during the harmonic loading, t=0 corresponding to the data in phase with the loading. From the 8 images, fast Fourier transform was used to reconstruct amplitude and phase of the three components of the displacements. It should be noted that although the identification procedure could be used for each set of images, the FFT extraction provides a nice extra temporal smoothing.

From the displacement data, strains can be calculated. This was performed here by simple point-to-point finite difference without any spatial smoothing. Slices of ε_{xy} shear strain amplitudes along z are plotted on Fig. 4,

together with slices of the amplitude of the trace of the strain tensor. Such materials are reputed to be incompressible which shows here with much lower values of the trace compared to the shear strain. However, since the test is a shear test, even on a non incompressible material, the shear strains would have been predominant.

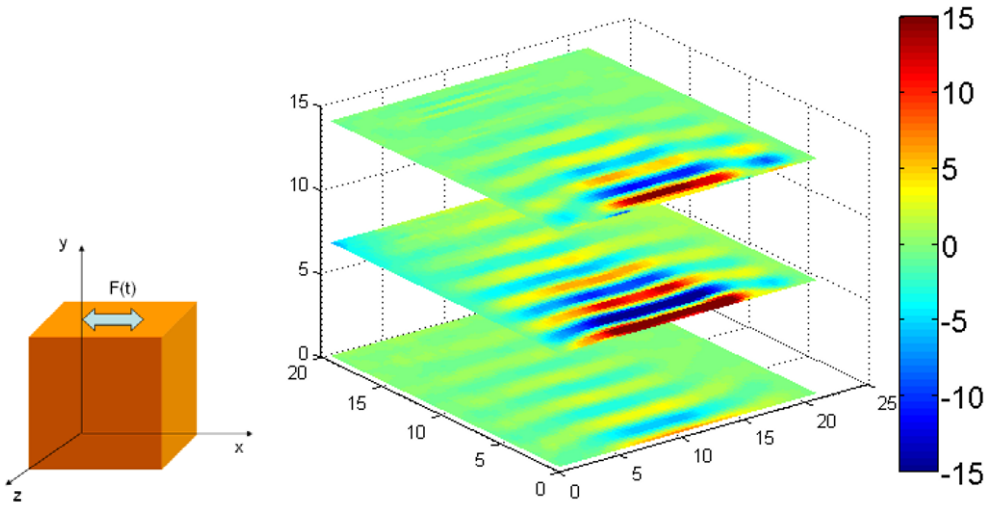

Figure 2 – U_x displacement in three z slices (colorbar in microns), at t=0.

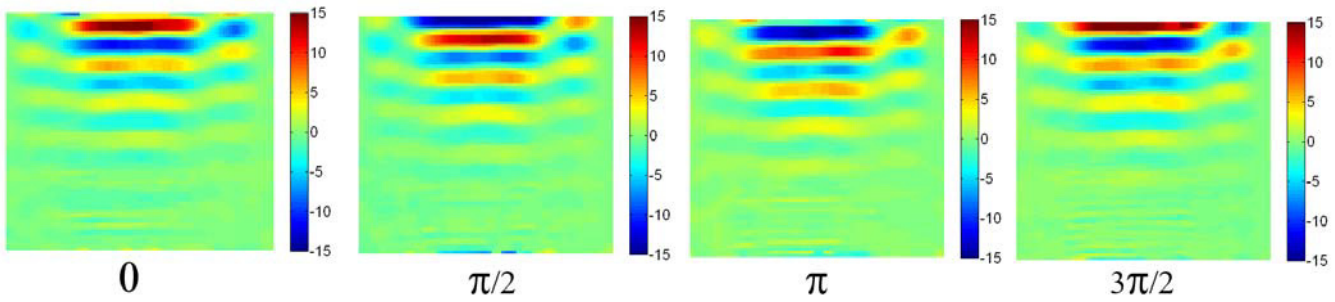

Figure 3 – U_x displacement in the z=0 slice at different times (colorbar in microns)

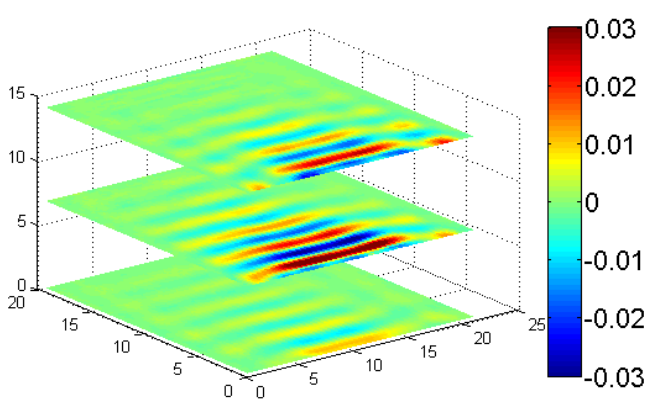

ε_{xy} in three z slices at t=0.

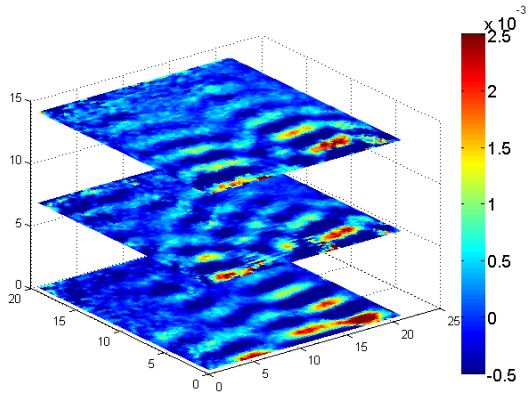

$Tr(\varepsilon)$ in three z slices at t=0.

Figure 4 – Strains in three z slices at t=0.

Analysis

The principle of virtual work writes in general:

$$-\int_V \sigma : \varepsilon^* dV + \int_{\partial V} T.u^* dS = \int_V \rho a.u^* dV \quad (1)$$

where σ is the stress tensor, T the surface density of boundary forces, ρ the density, a the acceleration vector and the star quantities the virtual displacement and strain fields. V is the specimen volume and ∂V its boundary. Assuming a linear elastic constitutive behaviour, one can write:

$$\sigma = \lambda tr(\varepsilon) I + 2\mu\varepsilon \quad (2)$$

where λ and μ are Lamé's coefficients and I the unit tensor. Feeding this into Eq. 1 and assuming the material is homogeneous, one has:

$$-2\mu\int_V \varepsilon : \varepsilon^* dV - \lambda\int_V tr(\varepsilon) tr(\varepsilon^*) dV + \int_{\partial V} T.u^* dS = \int_V \rho a.u^* dV \quad (3)$$

If the material is heterogeneous, the spatial variation of the coefficients needs to be parameterized for the identification (either piecewise constant or continuous with polynomial functions for instance), see [11,15]. In statics, the left hand side term is zero. This means that the load (related to T) needs to be involved in the equation to obtain the stiffnesses. If not, it is possible to select a virtual field so that the virtual work of the external forces is zero but then, the resulting equation will be homogeneous and only a ratio between λ and μ will be obtained (related to Poisson's ratio). In dynamics however, the right hand side term acts as a nice volume distributed load cell if the material density is known, and there is no need to measure the applied load.

Taking into account the harmonic nature of the load and response, the right hand side term can be expressed as a function of the pulsation ω and the displacements. In the present work, the load is unknown so it will be ensured that u* is zero on the top surface were the load is applied. The specimen resting into a plastic cube, there could also potentially be some contact forces at all the boundaries of the specimen but considering the maps in Fig. 2, it seems that nothing much happens at the boundaries except the top one. It should be noted that the analysis has been run with a virtual field zeroing the virtual displacement u_x at all boundaries and the same results as that of the paper were found. For the sake of simplicity, this is not presented here.

Another difficulty arises from the spatial wave shape of the strains. Indeed, if a low spatial frequency virtual field is used, then positive and negative values will tend to cancel out in the spatial average represented by the integrals in Eq. 3. Therefore, a possible virtual field taking all these requirements into account would write:

$$u_x^* = (y - L_y)\sin(\frac{2k\pi}{L_y}y) \;;\; u_y^* = 0 \;;\; u_z^* = 0 \qquad 2\varepsilon_{xy}^* = \sin(\frac{2k\pi}{L_y}y) + \frac{2k\pi}{L_y}(y - L_y)\cos(\frac{2k\pi}{L_y}y) \quad (4)$$

All other components are zero.

where L_y is the specimen length in the y direction and k is a number that has to be selected. With this virtual field, Eq. 3 becomes:

$$-2\mu\int_V \varepsilon_{xy}[\sin(\frac{2k\pi}{L_y}y) + \frac{2k\pi}{L_y}(y - L_y)\cos(\frac{2k\pi}{L_y}y)]dV = -\rho\omega^2\int_V u_x(y - L_y)\sin(\frac{2k\pi}{L_y}y)dV \quad (5)$$

Because of the term y- L_y, there is no contribution in the equation of the load applied at y= L_y, so the virtual work of external forces vanishes. Another very interesting feature is that since only the virtual shear strain in the (x,y)

plane is non zero, μ alone is involved in the equation, so that the problem can be solved without having to worry about the fact that the material is nearly incompressible.

In practice, the integrals of Eq. 5 are calculated by approximating them by discrete sums over all data points as shown below.

$$\int_V \varepsilon_{xy}[\sin(\frac{2k\pi}{L_y}y)+\frac{2k\pi}{L_y}(y-L_y)\cos(\frac{2k\pi}{L_y}y)]dV \approx \sum_{i=1}^{N}\varepsilon_{xy}^{i}[\sin(\frac{2k\pi}{L_y}y^i)+\frac{2k\pi}{L_y}(y^i-L_y)\cos(\frac{2k\pi}{L_y}y^i)]v^i$$
$$\int_V u_x(y-L_y)\sin(\frac{2k\pi}{L_y}y)dV \approx \sum_{i=1}^{N}u_x^i(y^i-L_y)\sin(\frac{2k\pi}{L_y}y^i)v^i \quad (6)$$

where N is the number of data points and v^i the elementary voxel size. If one writes the voxel size as the volume of the cube V divided by N, one can simplify by V and the sums divided by N can be seen as the spatial average of the displacements or strains weighted by some function of the points position (the virtual fields). Finally, one has:

$$-2\mu\left[\overline{\varepsilon_{xy}[\sin(\frac{2k\pi}{L_y}y)+\frac{2k\pi}{L_y}(y-L_y)\cos(\frac{2k\pi}{L_y}y)}\right]=-\rho\omega^2\left[\overline{u_x(y-L_y)\sin(\frac{2k\pi}{L_y}y)}\right]$$
$$\mu=\frac{\rho\omega^2\left[\overline{u_x(y-L_y)\sin(\frac{2k\pi}{L_y}y)}\right]}{2\left[\overline{\varepsilon_{xy}[\sin(\frac{2k\pi}{L_y}y)+\frac{2k\pi}{L_y}(y-L_y)\cos(\frac{2k\pi}{L_y}y)}\right]}=\frac{a}{b} \quad (7)$$

where the upper bar means spatial average. One can see that the identification is direct here, no need for optimization or iteration. The programme has been implemented in Matlab and is composed of a few code lines only.

One particular problem here is the choice of k, which can be interpreted here as a virtual spatial wave number. Indeed, k has to be chosen so that the two terms a and b in Eq. 7 are as high as possible (no cancelling out the positive and negative strains caused by the wave). One way of ensuring this is to choose k to be about 6 since there are about 6 waves along y (as can be seen on Fig. 4.). However, because one has to ensure that u_x is zero at the top surface where the load is applied, the virtual and real waves will not be phased. In order to find an optimal virtual field, the following strategy has been applied. First, a range of k from 5 to 8 has been considered, with increments of 0.05. Then, since Eq. 5 can be applied at any time, it has been applied to eight sets of data shifted in temporal phase by $\pi/16$ (from 0 to 15 $\pi/16$), data reconstructed from the FFT amplitude and phase. The idea is then to browse the data and select identified values of μ corresponding to maximal values of both terms in Eq. 5. It is thought that these values will be the most stable and correspond to the correct identification. An alternative would be to adapt the procedure in [16,17] to find piecewise optimal virtual fields but this is a future objective far beyond the scope of the present paper.

Fig. 5 shows a map of the value of sensitivity defined as the product between a and b. The maximum sensitivity arises around temporal phase $\pi/2$, for a virtual wave number k of around 6.3. Fig. 6 shows a map of identified values of μ. One can see that where the sensitivity is very low (dark blue areas in Fig. 5), the shear modulus is very unstable (highly coloured bands in Fig. 6), highlighting the critical issue of virtual fields selection. Looking at Fig. 6, one can see that the dominant colour is blue, which corresponds to a shear modulus value between 1000 and 2000 Pa. If the average over the whole map is taken, the identified value for μ is 1420 Pa. However, this value is very prone to outliers arising for very low values of a and b. In order to avoid this issue, the average was performed over the data where the sensitivity ab is above a certain threshold. If the maximum value of ab is called max(ab), then one can average the shear modulus values for sensitivity above a certain fraction of max(ab).

Values are reported in Table 1. Between 10% (data averaged over a large part of the map in Fig. 6), and 90% (data averaged over a very small portion of this map), there is only about 3% variation in the value of μ. This provides good confidence in the identification. In order to check this value, it is possible to compare it with the very simple solution provided by the shear wave solution for isotropic homogeneous solids (see[3] for instance):

$$\mu = \rho \chi^2 f^2 \tag{8}$$

where χ is the spatial frequency of the shear wave and f the test frequency. Here, χ is 20 mm divided by 6.5 (about 6 and a half waves along y, as can be seen on Fig. 4), which is 0.0031 m, the frequency is 40 Hz and the density is 1000 kg.m^{-3}. This gives a value of 1540 Pa for μ, which is not far off the results in Table 1. It should be noted however that this simple analysis does not take into account the presence of the other strain components in the data whereas the present approach does. The identified values from Table 1 are therefore thought to be more accurate.

Fraction of max(ab)	10%	20%	40%	60%	70%	80%	90%
Shear modulus (Pa)	1647	1664	1677	1687	1697	1698	1693

Table 1 – Identified values of the shear modulus for different amounts of virtual fields data

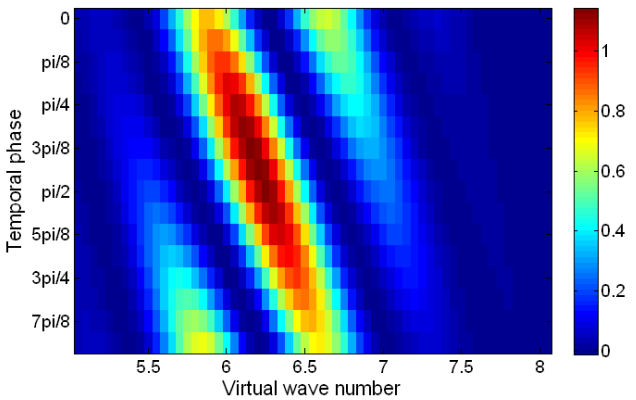

Figure 5 – Map of sensitivity a.b

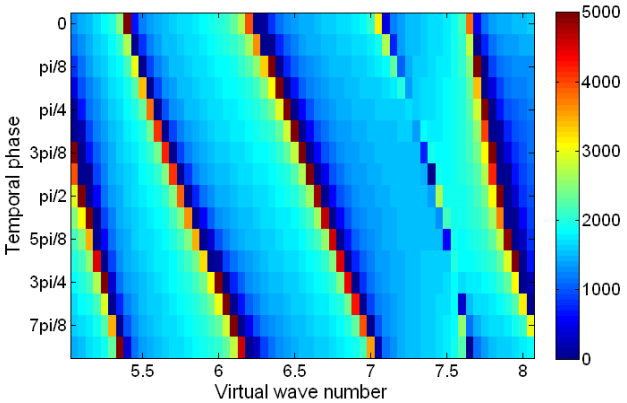

Figure 6 – Map of identified μ (Pa)

CONCLUSION

The present results are preliminary and the objective was to look at the feasibility of using the virtual fields method in this particular case. The results seem consistent and the issue of virtual fields selection has been carefully addressed. Clearly, there is a lot of work to be done to improve the procedure. The main challenge in the future will be to extend it to heterogeneous materials and to apply this to in-vivo tissue deformation measurements. An approach such as in [11] will have to be developed. Also, it would be interesting to try to identify complex stiffnesses such as in [13,14] and maybe to try retrieving the bulk modulus too but for this purpose, some other mechanical test configuration will have to be used to try to induce some bulk strains too.

REFERENCES

[1] Samani A., Zubovits J., Plewes D.B., Elastic moduli of normal and pathological human breast tissues: an inversion-technique-based investigation of 169 samples, *Physics in Medicine and Biology*, 52:1565:1576, 2007.

[2] Venkatesh S.K., Yin M., Glockner J.F., Takahashi N., Araoz P.A., Talwalkar J.A., Ehman R.L., MR elastography of liver tumors: Preliminary results, *American Journal of Roentgenology*, 52(6):1534-1540, 2008.

[3] Atay S., Kroenke C.D., Sabet A., Bayly P.V., Measurement of the dynamic shear modulus of mouse brain tissue in-vivo by magnetic resonance elastography, *Journal of Biomechanical Engineering*, 130:021013 (11 p.), 2008.

[4] Li J., Cui Y., English R.E., Noble J.A., Ultrasound estimation of breast tissue biomechanical properties using a similarity-based non-linear optimization approach, *Journal of Strain Analysis*, 44:363-374, 2009.

[5] Muthupillai R., Lomas D.J., Rossman P.J., Greenleaf J.F., Manduca A., Ehman R.L., Magnetic resonance elastography by direct visualization of propagating acoustic strain waves, *Science*, 269:1854-1857, 1995.

[6] Schmitt J.M., OCT elastography: imaging microscopic deformation and strain of tissue, *Optics Express*, 3:199-211, 1998. http://www.opticsinfobase.org/abstract.cfm?URI=oe-3-6-199

[7] De La Torre-Ibarra M.H., Ruiz P.D., Huntley J.M., Double-shot depth-resolved displacement field measurement using phase-contrast spectral optical coherence tomography, *Optics Express*, 14(21):9643-9656.

[8] Richards M.S., Barbone P.E., Oberai A.A., Quantitative three dimensional elasticity imaging from quasi-static deformation: a phantom study, *Physics in Medicine and Biology*, 54:757-779, 2009.

[9] Sinkus R., Tanter M., Xydeas T., Catheline S., Bercoff J., Fink M., Viscoelastic shear properties of in vivo breast lesions measured by MR elastography, *Magnetic Resonance Imaging*, 23:159-165, 2005.

[10] Grédiac M., Pierron F., Avril S., Toussaint E., The virtual fields method for extracting constitutive parameters from full-field measurements : a review, *Strain: an International Journal for Experimental Mechanics*, vol. 42, pp. 233-253, 2006.

[11] Avril S., Huntley J.M., Pierron F., Steele D.D., 3D heterogeneous stiffness identification using MRI and the virtual fields method, *Experimental Mechanics*, 48(4):479-494, 2008.

[12] Claire D., Hild F., Roux S., A finite element formulation to identify damage fields: The equilibrium gap method *International Journal for Numerical Methods in Engineering*, 61(2):189-208, 2004.

[13] Giraudeau A., Pierron F., Identification of stiffness and damping properties of thin isotropic vibrating plates using the Virtual Fields Method. Theory and simulations, *Journal of Sound and Vibration*, 284(3-5):757-781, 2005.

[14] Giraudeau A., Pierron F., Guo B., An alternative to modal analysis for material stiffness and damping identification from vibrating plates, *Journal of Sound and Vibration*, in press (available online), 2010.

[15] Kim J.H., Pierron F., Wisnom M., Avril S., Local stiffness reduction in impacted composite plates from full-field measurements, *Composites Part A*, 40(12):1961-1974, 2009.

[16] Avril S., Grédiac M., Pierron F., Sensitivity of the virtual fields method to noisy data, *Computational Mechanics*, 34(6):439-452, 2004.

[17] Avril S., Pierron F., General framework for the identification of elastic constitutive parameters from full-field measurements, *International Journal of Solids and Structures*, 44:4978-5002, 2007.

Proceedings of the SEM Annual Conference
June 7-10, 2010 Indianapolis, Indiana USA

Comparison of Dynamic Mechanical Testing and MR Elastography of Biomaterials

[1]E.H. Clayton, R.J. Okamoto[1], K.S. Wilson[2], R. Namani[1], P.V. Bayly[1,2]
[1]Department of Mechanical, Aerospace and Structural Engineering
[2]Department of Biomedical Engineering
Washington University in St. Louis, 1 Brookings Drive Campus Box 1185
Saint Louis, MO 63130
clayton@wustl.edu

ABSTRACT

Magnetic resonance elastography (MRE) is a novel experimental technique for estimating the dynamic shear modulus of biological tissue. MRE can be performed non-invasively, in living subjects. Soft biomaterials are notoriously difficult to characterize, since they are typically nonlinear, anisotropic, viscoelastic, and heterogeneous. The ability of MRE to capture the frequency-dependent response of tissue to small amplitude deformation over a range of frequencies was investigated by careful comparison to two different dynamic mechanical tests; direct shear and unconfined compression. The mechanical properties of a standardized gelatin biomaterial were probed over various loading rates. Results confirm direct correlation between estimates of shear modulus obtained by MRE, dynamic shear, and unconfined compression, but quantitative differences between values obtained by MRE compared to direct mechanical test. These results in gelatin are consistent with reports in agar from other groups [1,2]. Differences may be due to non-idealities inherent in loading of soft, wet, material (in mechanical testing), boundary effects (in MRE), or differences in strain amplitude and strain rate.

INTRODUCTION

Soft biomaterials are notoriously difficult to characterize. They are typically nonlinear, anisotropic, viscoelastic, and heterogeneous. Despite the hurdles material complexities present, there remains fervent interest within the mechanobiology, bioengineering, and clinical healthcare communities to accurately characterize the mechanical properties of biological material. Namely, material characterization tests can shed new light on tissue and organ physiology and the relationships between structure and mechanical function. However, in almost all cases, mechanical tests designed to probe these materials require excised samples. The process of removing and/or preserving a tissue sample often compromises the structural characteristics which researchers aim to measure. Until recently, there were few alternatives to test mechanical tissue properties without compromising tissue integrity.

Magnetic resonance elastography (MRE) is a novel experimental technique for estimating the dynamic shear modulus of biological tissue [1]. MRE utilizes a standard clinical MRI scanner to image micron-amplitude shear waves which propagate deep into tissue from an *ab extra vivo* mechanical actuator. Displacement images are obtained by synchronizing magnetic “motion-sensitizing” gradient events in the MR imaging sequence with the induced tissue vibrations. Elastograms, or images with contrast corresponding to complex shear modulus (storage and loss modulus), are then computed from raw displacement data by fitting the governing equations of

T. Proulx (ed.), *Application of Imaging Techniques to Mechanics of Materials and Structures, Volume 4*, Conference Proceedings of the Society for Experimental Mechanics Series 14, DOI 10.1007/978-1-4419-9796-8_18, © The Society for Experimental Mechanics, Inc. 2013

motion with the shear modulus that provides the closest match to experimental data (i.e., by solving the inverse problem). MRE can be performed non-invasively in living subjects; hence, structural integrity and metabolic state are preserved while material characterization is performed.

MRE is a potentially powerful tool for characterizing soft biomaterials *in vivo*; however, the accuracy of the material properties obtained remains uncertain. In this study, the complex shear modulus of a standardized gelatin biomaterial is estimated (1) using MRE and compared to values obtained by direct measurement of force-displacement relationships in (2) oscillatory shear and (3) unconfined compression tests. The objective of the study is to assess the accuracy of shear modulus estimates obtained by MRE, as well as to determine limiting factors and/or guidelines regarding the use of MRE for *in vivo* characterization of biological tissue.

METHODS

Gelatin Preparation: Commercial gelatin powder (Gelatine, Knox) was mixed with distilled water to create a 5.5% w/w solution. The solution was heated to dissolve the gelatin powder, then poured into molds and allowed to coagulate for 3-18 hours before testing. For MRE, liquid gelatin was poured into a mold with square cavity (20 mm x 20 mm x 20 mm). For dynamics shear and unconfined compression tests, appropriate volumes of liquid gelatin were poured into 100 ml cell culture dishes to create sheets of gelatin approximately 3 mm thick. Test samples were punched from the sheets using a circular punch.

Magnetic Resonance Elastography: Elastography experiments were conducted at 4.7 T using a Varian DirectDrive™ small-animal MR scanner. MRE data were collected using a circularly polarized transmit/receive RF volume coil (Varian). Three gelatin samples were tested in this study. Each gelatin specimen was poured into a Delrin™ cube form measuring approximately 20 mm on a side. After an appropriate cure time, each cube was affixed to a custom-built simple shear setup driven by a MR compatible peizoceramic actuator (APA100-NM, Cedrat Technologies), cf. Figure 1. Gel cubes were slightly over filled so as to develop a gelatin meniscus, ensuring displacement compatibility between the actuated shear pad and the gelatin free surface. A TTL-equipped function generator and low-current voltage amplifier were used to drive the piezoceramic actuator harmonically at 150, 200, 400, and 800 Hz. MR motion-encoding gradients were synchronized with actuator vibration to encode an isochromatic phase shift proportional to tissue displacement, at four time points, using a custom phase-locked spin-echo pulse sequence [3].

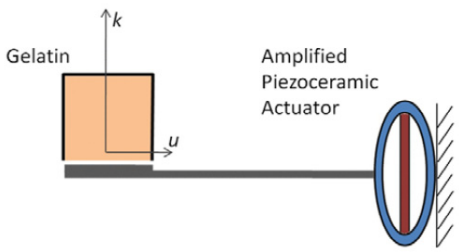

Figure 1: Simple shear setup used to test gelatin cube at 150, 200, 400, and 800 Hz. The shear wave displacement direction is denoted as *u* and the propagation direction as *k*. The trans-axial slice plane is parallel to *k*.

In this study, through-plane, $u_z(x, y, t)$, displacements were acquired. In consideration of boundary effects, a central region of each gelatin sample was imaged with multiple trans-axial slices and the single "best" slice was used for subsequent analysis. The acquired in-plane image resolution was 250 x 250 μm^2 and the slice thickness was 500 μm. TR/TE: 1000/33.2 ms for data at 150 Hz and TR/TE: 1000/27.5 ms for 200-800 Hz data. Since the peak-to-peak displacement of the peizoceramic actuator varies with driving frequency the number of MR motion encoding cycles and the amplitude of the motion encoding gradients were adjusted for each test frequency to ensure measurement sensitivity.

Two sets of motion-encoded data were acquired; one each with positive and negative polarity motion encoding gradients. Motion-sensitized, phase-contrast images were obtained by complex division of positive and negative polarity phase images. Parasitic phase wrapping was removed via commercial software (Phase Vision Ltd, Loughborough, UK). Phase-contrast data were converted into displacements, $u_z(x, y, t)$, by standard methods

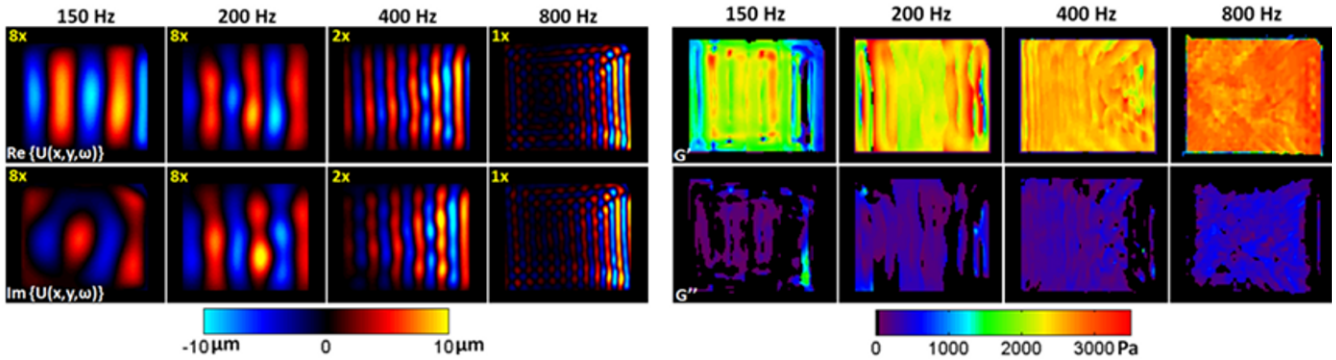

Figure 2: (Left panel) The real and imaginary part of the fundamental displacement harmonic, $U_z(x,y,\omega)$, for each spatial temporal displacement field is shown. Displacement amplitudes have been scaled for each actuation frequency by the number in the top left corner of each field plot. (Right panel) Calculated storage modulus (G') and loss modulus (G") elastograms for each actuation frequency. A 5 x 5 data kernel was used to invert the governing equation of motion, modulus estimates with normalized residual error greater than 0.5 were discarded. Elastograms provide evidence of frequency dependence in gelatin shear modulus.

[1,3]. Viscoelastic material parameters were obtained from the linear elastic isotropic homogeneous material equation of motion by invoking the correspondence principle [4]. Hence, estimates of the storage (*G'*) and loss (*G''*) shear moduli can be obtained as follows,

$$(G' + iG'')\nabla^2 U_z(x,y,\omega) = -\rho\omega^2 U_z(x,y,\omega) \qquad (1)$$

where ω and ρ are the loading frequency (rad/sec), and material density (1000 kg/m^3), respectively. $U_z(x,y,\omega)$ is the fundamental harmonic of the Fourier transform of the displacement field, $u_z(x,y,t)$.

Displacement data were smoothed with a circular, 8th-order Butterworth band-pass filter in the spatial frequency domain. Optimal filter cut-in and out limits were determined empirically for each data set considering the actuation frequency and image signal-to-noise. A central difference scheme was used to approximate the Laplacian of the displacement field. Finally, inversion was performed by a local least-squares fit using a 2-D kernel of data. The residual error of each fit, normalized by the variance in that kernel, was calculated to assess the "goodness-of-fit" of the linear isotropic homogeneous material model at that location. All modulus approximations were thresholded; if the local model fit produced a normalized residual error (NRE) was greater than 0.5, the estimated modulus was discarded.

Real and imaginary components of shear wave fields obtained using our MR imaging sequence are shown in Figure 2 (left panel). These images indicate motion initiating from the shear pad actuator (right boundary) penetrated with sufficient amplitude through the gelatin (to the left boundary) at all driving frequencies. Note that the wavelength decreases as the actuation frequency increases. The peak-to-peak displacement amplitude varies with driving frequency (~0.02 to ~0.16 mm). Storage and loss modulus elastograms for each actuation frequency are shown in Figure 2 (right panel).

Dynamic Shear Test: Circular samples (15.1-15.6 mm dia., *A* = 180-196 mm^2) were punched from the gelatin and the thickness, *h*, of each sample was measured. The samples were placed on a custom-built oscillatory shear testing system. The lower surface of the sample was subjected to small amplitude (~0.03 mm) horizontal oscillations created by a voice coil actuator. The voice coil was excited using a chirp, which sweeps through frequencies from 0 to 200 Hz in 15 seconds. Horizontal displacement, δ, was measured with a capacitance probe. The vertical position of an upper assembly was adjusted with a digital micrometer until a circular platen touched the sample. Shear force on the upper surface, F_s, was measured with two piezoelectric force transducers.

A data acquisition and control system converted displacement and shear force data to a complex transfer function in the frequency domain. The measured shear force was converted into an average shear stress by dividing by the area, *A,* and the horizontal displacement was divided by the sample thickness to obtain the average shear strain, γ . The apparent complex shear modulus, $G_{app}(i\omega)$ was determined as follows:

$$G_{app}(i\omega) = \frac{\tau(i\omega)}{\gamma(i\omega)} = \frac{F_s(i\omega)/A}{\delta(i\omega)/h} = G'_{app} + i\,G''_{app} \tag{1}$$

This method of calculating the complex shear modulus assumes that the shear strain was uniform through the sample thickness. This assumption remains valid only when the sample thickness is much less than the shear wavelength of the material over the range of frequencies tested. For thicker samples, the shear strain was non-uniform through the sample thickness. When the magnitude of shear strain is greater at the upper surface, the magnitude of the measured shear force will also be larger, causing the apparent shear modulus to increase.

Using the wave equation, Berry and Shuck and Advani derived equations to account for apparent increase in shear modulus for cylindrical viscoelastic specimens undergoing torsional shear loading [5,6]. Similar equations for a slab of material constrained from motion on its upper surface while being subjected to a prescribed horizontal displacement of the lower surface, u_0, were derived over a range of frequencies, ω.

The complex displacement, $u(y,t)$, was assumed to be a separable function of y, denoted $u^*(y)$ multiplied by $e^{i\omega t}$. From a force balance in the x-direction, the function $u^*(y)$ must satisfy the ordinary differential equation,

$$G\frac{d^2u^*}{dy^2} + \rho\omega^2 u^* = 0 \tag{2}$$

where G is the complex shear modulus and ρ is the density of the material being tested. The homogeneous solution is:

$$u^*(y) = A_1\cos(qy) + A_2\sin(qy); \quad q^2 = \frac{\rho\omega^2}{G}. \tag{3}$$

Applying the boundary conditions $u^*(0) = u_0$ and $u^*(h) = 0$, the solution for the displacement is:

$$u(y,t) = \left[u_o\left(\cos(qy) - \cot(qh)\sin(qy)\right)\right]\exp(i\omega t) \tag{4}$$

The shear stress on the upper platen ($y = h$) can be found from:

$$\tau_{yx} = G\left.\frac{\partial u}{\partial y}\right|_{y=h} = -Gq\left[u_o\left(\sin(qh) + \cot(qh)\cos(qh)\right)\right]\exp(i\omega t) = -\frac{Gqu_o}{\sin(qh)}\exp(i\omega t) \tag{5}$$

And the apparent modulus can be found by dividing stress by the quantity u_o/h:

$$G_{app} = \frac{-\frac{Gqu_o}{\sin(qh)}\exp(i\omega t)}{u_o/h} = -\frac{Gqh}{\sin(qh)}\exp(i\omega t) \tag{6}$$

If the material is elastic, then G is a real number and τ_{yx} is singular when qh is equal to multiples of π, or when:

$$h = \frac{n\pi}{q} = \frac{n\pi}{\omega}\sqrt{\frac{G}{\rho}} \quad n = 1, 2, \ldots \tag{7}$$

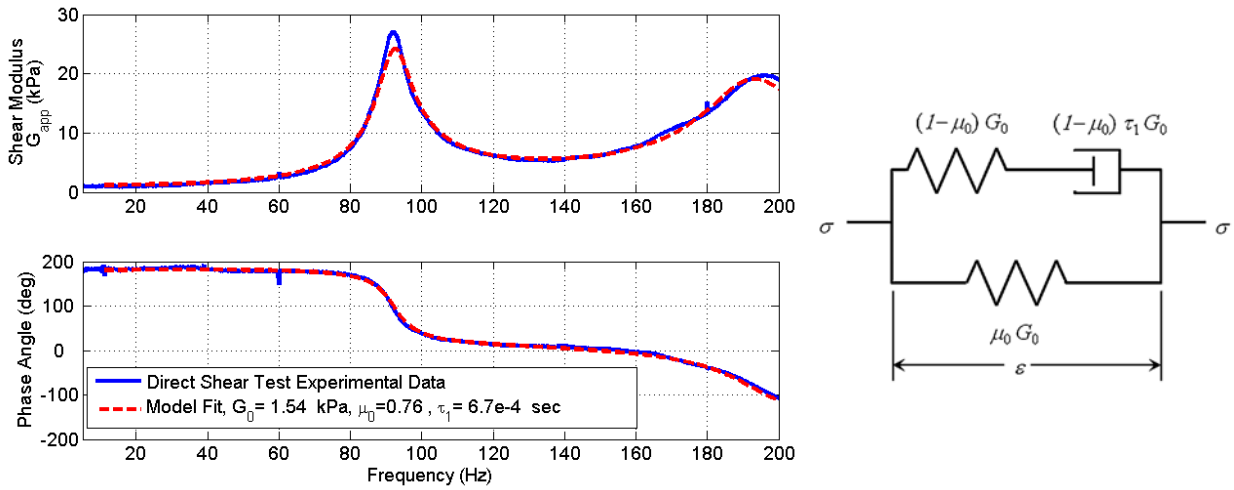

Figure 3: (Right) Standard linear solid model, spring-dashpot representation. (Left) DST data from 0 - 200 Hz is fit to a standard linear solid model to characterize the three unknown parameters, G_0, μ_o, and τ_1.

For a viscoelastic material, $\sin(qh)$, is complex and the maximum magnitude of τ_{yx} is finite. For a given h, the value of ω at which τ_{yx} reaches the maximum will depend upon the specific function G.

In fitting our results, we assume that gelatin can be modeled as a standard linear solid with three parameters, cf. Figure 3 (right); G_0 (high frequency modulus), μ_o (between 0 and 1) and a time constant, τ_1 [7]. At very low frequencies $G = \mu_o G_0$.

From this relationship, the equations for G' and G'' as well as the loss factor, γ, can be derived in terms of the three parameters and the frequency:

$$G = G' + iG'' = G_o \frac{\tau_1^2\omega^2 + \mu_o}{\tau_1^2\omega^2 + 1} + i\left(G_o \frac{\tau_1\,\omega(1-\mu_o)}{\tau_1^2\omega^2 + 1} \right) \tag{7}$$

$$|G| = \frac{G_o\sqrt{\left((\tau_1^2\omega^2)^2 + \mu_o{}^2 + \tau_1^2\omega^2(1+\mu_o{}^2)\right)}}{\tau_1^2\omega^2 + 1} \tag{8}$$

$$\gamma = \tan(G) = \frac{G''}{G'} = \frac{\tau_1\,\omega(1-\mu_o)}{\tau_1^2\omega^2 + \mu_o} \tag{9}$$

To find the values of G_0, μ_o and τ_1 that best fit the experimental data, we minimized the sum-of-squares difference between the model predicted apparent modulus (Eq. 6) and the apparent modulus obtained from the experimental data. The initial fit was done using MATLAB (Mathworks), cf. Figure 3 (left). The best-fit values of G_0, μ_o, and τ_1 were used to predict the values of G' and G'' at the frequencies tested during elastography.

Unconfined Compression Test: A three step displacement controlled, stress relaxation protocol was used for unconfined compression tests. Three gelatin samples, 3.0 mm thick, were cored with a 15.875 mm (0.625") diameter punch and sandwiched between two polished stainless steel plates. The top plate was connected in series to a load cell (Honeywell Sensotech, Model 31, 150g) and a high-precision linear actuator (Model M-227.25, Mercury DC-Motor Controller, Polytech PI). Movement of the top plate was recorded with a non-contact displacement sensor (Model 10001-5MM, Metrix Instrument). Analog voltage measurements were digitized with a commercial data acquisition card (Model USB-9162, National Instruments). Displacement and force time histories were recorded using MATLAB.

The thickness of each gelatin sample was verified by moving the top plate downwards in ~14 micron increments until a 5 mN change in load was observed. From this position the top plate was further moved downwards in ~0.5 micron increments till the change in force was at least ~10 mN. The resulting gap between the top and bottom stainless steel plates was measured with a non-contact optical laser probe (Model LD 1605-10, Micro-Epsilon) and taken to be the sample thickness. The optical probe was calibrated with stainless steel gauge blocks prior to gelatin testing.

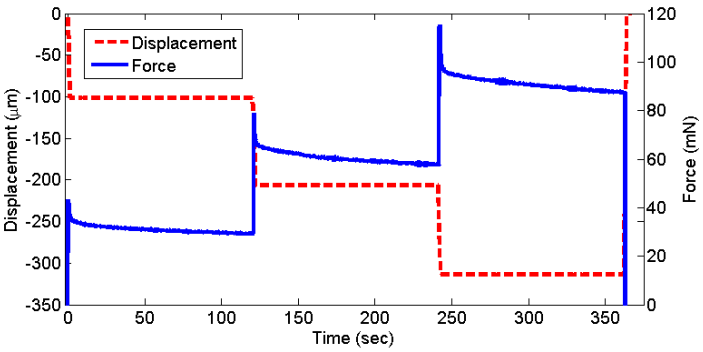

Figure 4: Displacement time history shows the three step stress-relaxation unconfined compression protocol. Spikes in the force time history during specimen compression indicate viscous effects are prevalent, requiring two minutes to subside. The peak and equilibrium force were recorded for each displacement step and used to calculate G_0 and G_∞, respectively.

The unconfined compression test was displacement controlled and implemented a three step stress-relaxation protocol, cf. Figure 4. Each displacement step induced roughly three percent compressive strain and was completed in 0.3 seconds. After each successive step, the sample was permitted to relax for 120 seconds under confinement. At the end of the third hold period the top plate was returned to its initial position, unloading the gel sample. Each cylindrical gelatin sample was coated with canola oil to lubricate the gel-plate boundary, allowing Poisson effects to occur freely during compression.

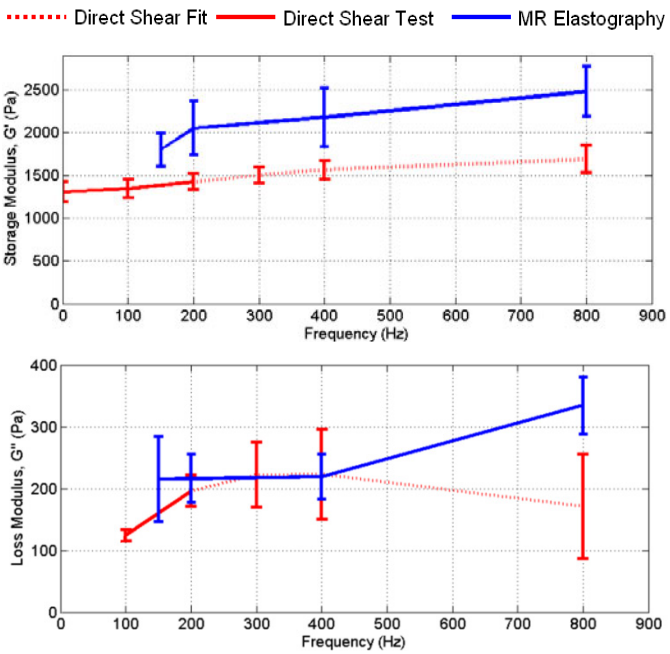

Figure 5: Storage modulus (G') and loss Modulus (G") versus frequency for both direct shear test and MR elastography. Note direct shear test values beyond 200 Hz have been determined by a standard linear solid model fit based on experimental data within 0 - 200 Hz. Error bars represent one standard deviation from the mean calculated value.

The dynamic shear modulus, G_0, was calculated by recording the peak load for each of the three displacement steps. These load-displacement data points were used to calculate the corresponding uniaxial compressive stress and strain based on measurements of pre-test specimen geometry. Stress-strain data were plotted and fit to a straight line. The slope of the best-fit line is equivalent to the dynamic modulus of elasticity. Assuming gelatin exhibits a negligible volume change during compression (e.g. incompressible, $\nu = 0.5$) the dynamic elastic modulus is related to the dynamic shear modulus, G_0, by a factor of one-third. Based on the present unconfined compression test protocol, dynamic shear modulus approximations are valid at 3 Hz loading rate, nominally. The equilibrium shear modulus, G_∞, was approximated following the procedure described for dynamic shear modulus calculation; however, the equilibrium loads obtained at the end of each 120 second relaxation period were used for subsequent calculations instead of peak loads.

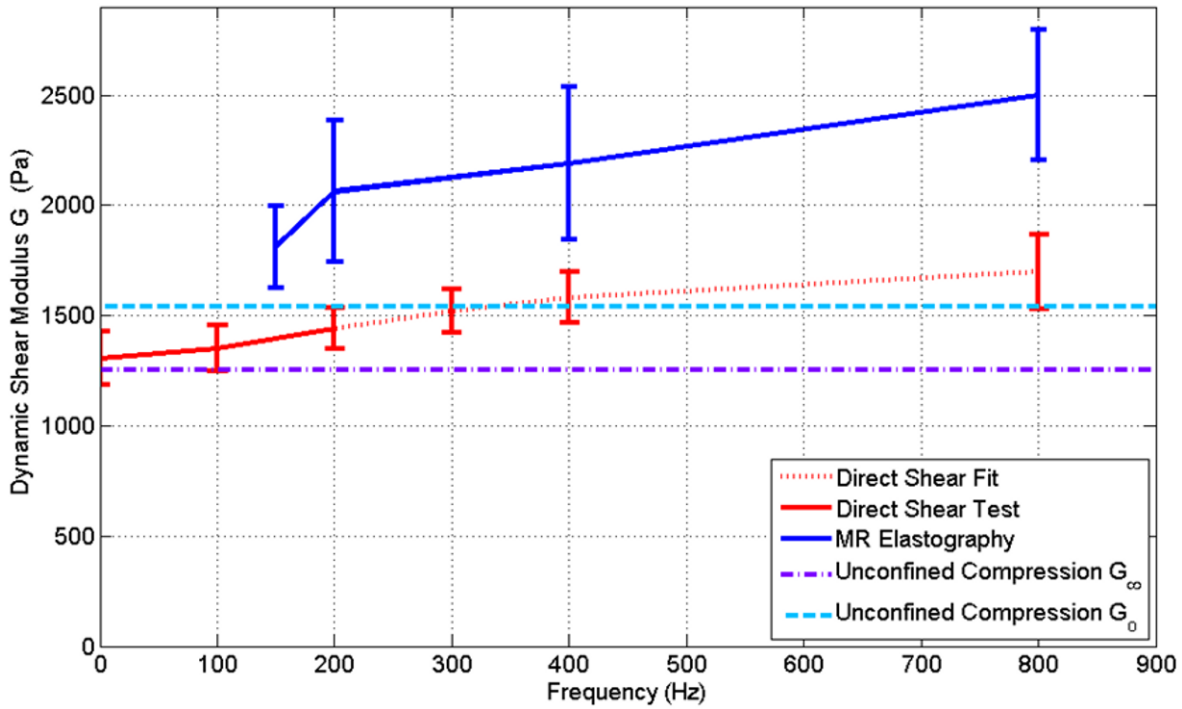

Figure 6: The viscoelastic properties gelatin were quantitatively probed using three different experimental material characterization methods; nuclear magnetic resonance elastography (MRE), direct oscillatory shear testing (DST), and unconfined compression testing (UCT). Estimates of the dynamic shear modulus of gelatin show correlation, but values obtained using MR elastography can be as much as one and a half times those found using DST or UCT.

RESULTS

Storage (*G'*) and loss (*G"*) modulus estimates of gelatin obtained by MR elastography and dynamic shear testing are presented in Figure 5. The dynamic shear modulus, *G*, is the root-sum-square combination of the storage and loss moduli. The dynamic shear modulus for gelatin has been calculated for MR elastography as well as both mechanical material characterization tests and is shown in Figure 6.

DISCUSSION & CONCLUSION

In this study the mechanical response of a soft biomaterial (gelatin) has been characterized by spatial-temporal images of propagating shear wave frequency and wavelength (MRE) as well as by direct mechanical measurement of force-displacement relationships in oscillatory shear and unconfined compression. Estimates of shear modulus obtained by MRE are correlated with, but differ from, estimates obtained by two direct mechanical tests. This result is consistent with others who have aimed to validate MRE using direct mechanical tests [1,2].

The mechanical response of biomaterials, like gelatin, agar, or soft tissue is known to depend on both the frequency and amplitude of loading. The dynamic shear tests and MRE studies reported here have overlapping frequency ranges, so that direct comparison between 150-200 Hz is feasible, and indirect comparison between 200-800 Hz was approximated via a standard linear solid model. Even when the identical frequencies are used, estimates of shear modulus from MRE are approximately 30-45% higher than those from oscillatory shear test. Shear modulus estimates from the oscillatory shear tests at low frequencies are quantitatively consistent with estimates from unconfined compression.

The amplitudes of imposed strain differ between MRE and the direct tests. This is inherent in the techniques: MRE involves micron-amplitude displacements measured by magnetic resonance imaging. Strain amplitude depends on response of the material. In direct mechanical tests, the strain is controlled by the investigator; it is important to apply a large enough strain to produce measurable stresses and forces. An important next step is to systematically investigate the effect of strain amplitude on apparent shear modulus in a single test protocol.

Other possible reasons for the discrepancy include the non-ideal features of both methods. The sample in MRE is, by necessity, held in a closed container. Boundary conditions (almost-rigid walls) may increase the apparent modulus of the gelatin in its container, although this has not been seen in simulations. Oscillatory shear tests require a finite pre-load normal to the surface of the sample, in order to provide a finite frictional load on the surface. In MRE, the modulus is determined at a small number of frequencies over a wide range, up to 800 Hz. The DST method is limited to frequencies less than 200 Hz. Our current DST device is limited to range of displacement amplitudes less than 0.03 mm. As the sample becomes thicker, signal-to-noise is degraded at low frequencies, thus our method provides estimates of the SLS parameters in the range of 10-200 Hz. On the other hand, the lowest frequency that can be used in MRE is a function of the shear modulus and the sample dimensions. MRE samples with larger dimensions could be used in future studies to obtain a greater range of overlap in the test frequencies.

In conclusion, our results indicate that MRE can provide estimates of complex shear modulus in gelatin that approximate estimates obtained by direct mechanical tests, but MRE estimates are consistently 30-45% higher. These results build confidence in the applicability of MRE to characterize soft tissue, but serve as a reminder that results from both tests must be used cautiously, and with explicit caveats, to predict the response of soft tissue under different loading conditions.

ACKNOWLEDGEMENT

Research funding provided by NIH RO1 NS055951.

REFERENCES

[1] Muthupillai R, Lomas DJ, Rossman PJ, Greenleaf JF, Manduca A, Ehman RL. “Magnetic resonance elastography by direct visualization of propagating acoustic strain waves,” Science. 269(5232):1854–1857, 1995.

[2] Ringleb SI, Chen Q, et al. (2005). "Quantitative shear wave magnetic resonance elastography: comparison to a dynamic shear material test," Magn Reson Med **53**(5): 1197-1201.

[3] Atay SM, Kroenke C, Sabet A, Bayly PV, “Measurement of the dynamic shear modulus of mouse brain tissue in vivo by magnetic resonance elastography,” J Biomech Eng. 130(2):021013, 2008.

[4] Flugge W., *Viscoelasticity*. Blaisdell,1967.

[5] Berry DS. (1957). “Stress Propagation in Visco-elastic Bodies.” J Mech Phys Sol. 6(3): 177-185.

[6] Shuck LZ, Advani SH. (1972). “Rheological Response of Human Brain Tissue in Shear,” Trans ASME J Basic Eng. 94(12) 905-911.

[7] Bayly PV, Massouros PG, et al. (2008). "Magnetic Resonance Measurement of Transient Shear Wave Propagation in a Viscoelastic Gel Cylinder." J Mech Phys Solids. 56(5): 2036-2049.

Proceedings of the SEM Annual Conference
June 7-10, 2010 Indianapolis, Indiana USA

Back-directional Gated Spectroscopic Imaging for Nanoscale Deformation Analysis in Bone

Zhengbin Xu, Xuanhao Sun, Jingjing Liu, Qinghai Song, Ozan Akkus, and Young Kim*
Weldon School of Biomedical Engineering, Purdue University, 206 South Martin Jischke Drive, West Lafayette, IN 47906
*Corresponding author: youngkim@purdue.edu

ABSTRACT
Although crack mechanisms in bone have been intensively studied to have a better understanding of bone fracture, exact prefailure damage mechanisms about how cracks or deformations at nanoscales occur still remain unexplored due to technical limitations. In this pilot study, we apply back-directional gated spectroscopic imaging (BGSI) to examine the exact spatial extent of such damage in in-situ mechanical testing of bovine cortical bone. Our imaging approach provides a relatively large field of view, while the wavelength dependence of light elastically backscattered from bone at each pixel can capture structural alterations in a few tens of nanometers. Thus, our imaging method can simultaneously examine various length scales. Using a notched bovine cortical bone wafer, we report that an altered field of a couple of square millimeters forms at the tip of the notch during tensile loading in the transverse orientation, and this field disappears upon unloading. We conducted simple pilot simulations of optical waves in one-dimensional layered media to gain an understanding of the potential mechanisms about the spectral dependence on nanostructure alterations. Our results imply that the bone nanostructure may allow the formation of nanoscale deformation over a relatively large area to prevent microcrack formation or fracture as an energy dissipating mechanism. We further envision that BGSI may facilitate understanding how the nanostructure of bone controls bone characteristics and properties.

A. Introduction

Bone is a biological nanocomposite of a mineral phase (e.g., rigid crystals such as hydroxyapatite crystals) and organic matrix (e.g., mainly collagen protein) [1, 2]. This nanocomposite provides the structural basis for mineralized collagen fibrils as the basic building block of bone. Bone's entire structure is highly complex and hierarchical, containing multiscale features from the nanoscales to the macroscales [1, 2]. The properties of bone at the microscales have been intensively studied for better understanding how bone deforms and fractures in terms of plasticity and toughness [2, 3]. However, prefailure damage and deformation mechanisms in bone still remain relatively unexplored, in part, due to current technical limitations for nondestructively studying its structural properties at nanoscales [4]. In particular, owing to the unique properties of the bone architecture, it is hypothesized that nanoscale deformation can spread out over a large spatial area as a highly effective energy dissipation (i.e. toughening) mechanism [5]. Given that exact prefailure damage mechanisms in bone induced by daily habitual strain and loading still remain unexplored [6], it would be of importance to determine the exact spatial extent of nanoscale deformation, its propagation, and its responsible bone structure. Indeed, although the current characterization methods are highly valuable for investigating various aspects of nanostructures, they do not allow probing deformation and damage at nanoscales over a fairly large area, due to the intrinsic tradeoff between the resolution and the field of view.

In this respect, we have recently developed a spectroscopic imaging system that enables the simultaneous measurement of tissue deformation at nanoscales in a relatively large area (i.e., 15 mm × 15 mm). In the spectroscopic imaging system, back-directional gating suppresses the diffuse light which otherwise deteriorates the image contrast and resolution [7, 8]. Diffuse light suppression allows spectral analyses at single pixels. In addition, spectral quantification captures the nanoscale deformation or prefailure damage at individual pixels, which overcomes the weakness of conventional experimental techniques only providing macroscopic information about tissue deformation. In this study, we applied our imaging system to visualize the prefailure deformation in bone at small strains before any conventional damages, such as microcracks, can be discerned. A heterogeneous deformation field around the notch appears in the spectral image during the tensile loading and

T. Proulx (ed.), *Application of Imaging Techniques to Mechanics of Materials and Structures, Volume 4*, Conference Proceedings of the Society for Experimental Mechanics Series 14, DOI 10.1007/978-1-4419-9796-8_19, © The Society for Experimental Mechanics, Inc. 2013

this deformation field vanished upon unloading. To further gain insight for the potential mechanisms of prefailure deformation and damage, we conducted simple pilot simulations of optical spectral response in one-dimensional multiple layered media. Our results support the idea that our spectroscopic imaging method can allow detailed physical mapping of the prefailure deformation field before crack initiation and that spectral quantification can capture the mechanical deformation at nanoscales.

B. Materials and Methods

1. Back-directional gated spectroscopic imaging setup

For in-situ mechanical testing of bovine cortical bone, we used our newly developed imaging technology, back-directional gated spectroscopic imaging, which is described in details elsewhere [7, 8]. In brief, a highly collimated light beam with the diameter of approximate 15 mm from a Xenon arc lamp is illuminated onto a sample. The backscattered photons from the sample are collected by a beamsplitter. These photons go through a four focal length system which has a small aperture in the center. This small size aperture serves as back-directional gating because it only accepts photons backscattered within a small angular cone and rejects most diffuse light with an oblique angle with respect to the incident light. Because the bone tissue is highly anisotropic such that the light is scattered in the same direction with respect to the incident direction, back-directional gating allows the isolation of light propagation in localized volumes, significantly improving imaging resolution and contrast [8]. A CCD camera (Princeton Instruments, Trenton, NJ) mounted onto an imaging spectrograph (Princeton Instruments) is used to record the spectral response of the sample in the visible spectral range. The 50 μm wide entrance slit of the spectrograph is scanned along the image plane with a step size the same as the width of the slit. A three dimensional data set is then recorded for each sample recording the spectral response at individual pixel (x, y) with a pixel size of 50 μm × 50 μm. In other words, we can obtain scattered intensity as a function of x, y and the wavelength λ in the range of 400 - 700 nm in the area of ~15 mm x 15 mm. In this study, the spectral intensity at each pixel from 500 nm to 700 nm was fitted to a linear line which can account for most of the spectral variance. Thus, we were able to use the absolute value of the spectral slope of the fitted line at each pixel to generate a spectroscopic image.

2. Specimen preparation and mechanical loading setup

We first sectioned block beams from diaphysis of bovine femurs using a precision saw (Buehler Ltd., Lake Bluff, IL). We took samples from locations longitudinal to the bone long axis. A v-shaped notch, approximately half of the sample width, was grinded into the center of the sample using a mill (Series 5400, Sherline, Vista, CA). The orientation of the notch was such that the potential crack forming direction was transverse to the long axis of the femurs. We further sectioned the notched samples into thin wafers and polished them by using polishing paper (Buehler Ltd., Lake Bluff, IL) and a 0.3 μm fine alumina powder. Between each polishing stage, samples were sonicated. The final polished cortical bone sample was approximately 50 mm in length, 4 mm in width and 0.2 mm in thickness as shown in Figure 1.

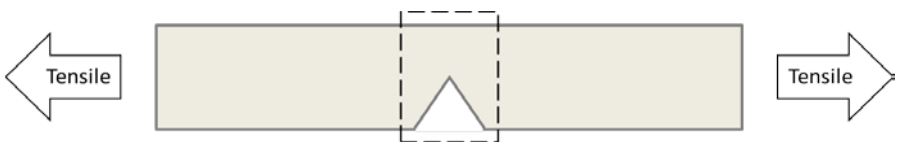

Figure 1. Diagram of the bovine cortical bone sample. The tensile force was introduced on the sample using a specially customized device. The region within the dashed box was the imaged area.

To introduce the tensile force onto the bone sample, we used a miniaturized tensile testing device (Ernest F. Fullam Inc., Latham NY). The device applies the tensile force onto the sample symmetrically, which minimizes the shift of the notch tip during loading. The device was fixed onto the sample stage of the spectroscopic imaging system. A cover slide was placed onto the sample covering the imaged notch area. We acquired three image data sets for each specimen before, during, and after the tensile loading. The tensile force applied on the sample was approximately 22 Newton, while the total displacement of the sample under tensile force was less than 75 μm (sample length between clamps was about 30 mm). No microcracks or other damages were observed at the notch tip upon loading when examined under a high magnification reflectance microscope using a 50X objective. Throughout the entire measurements, the bovine cortical bone was kept under hydrated conditions.

3. Numerical studies of backscattered spectra in one-dimensional layered media

We further conducted pilot numerical stimulations to gain an understanding of physical insight about potential origins of the spectral alterations. We intended to address possible underlying nanoscale deformation mechanisms that are attributable to the changes in the wavelength dependence. We approximated the bone structure to a one-dimensional structure based the following reasons: 1) The transmission and reflection of optical waves from random media consisting of multiple layers can be readily calculated by the transfer matrix method [9]. Indeed, using other numerical methods such as finite element methods and finite-difference time-domain methods, it is practically impossible to simulate the transmission and backscattered signals in three-dimension structures for numerous realizations, especially for a relative large tissue area. 2) In the transverse orientation, the mineralized collagen fibrils are oriented along the longest dimension (i.e. tensile force is applied in the transverse direction). Thus, the optical waves in our experimental configuration propagate perpendicular to the orientation of the mineralized collagen fibrils. 3) In our experiment setup, back-directional gating significantly removes diffuse light, because the high anisotropic property of the bone tissue keeps the light propagation along the direction of the incident light. In addition, the thickness of the specimen and the pixel size are on the order of the transport mean free pathlength of the light l_s^* in the bone (we estimated that l_s^* ~ 100 μm using coherent backscattering measurements). Thus, we have minimal crosstalk between adjacent pixels, indicating that the partial waves propagating approximately one-dimensional path significantly contribute to the image formation.

In our one-dimension structure for the numerical studies, we modeled the bone structure as dielectric multilayers to mimic the mineralized collagen fibrils and the interfibrillar spaces. We randomly stacked 1000 dielectric layers consisting of 500 mineralized collagen fibril layers and 500 interfibrillar layers. We also obtained 1000 realizations by randomly varying the order of each layer to mimic the interaction of the partial waves with the bone tissue in one pixel. We modeled two different possible scenarios: 1) We varied the refractive index of the mineralized collagen fibril layer from 1.55 to 1.65 with a fixed thickness of 100 nm. On the other hand, the thickness and the refractive index of the interfibrillar space were kept constant to be 50 nm and 1.40, respectively. 2) The thickness of the mineralized collagen fibril layer were kept unchanged with its refractive index of 1.61, while we varied the interfibrillar spacing width from 80 nm down to 25 nm with its refractive index of 1.40. In the both cases, the overall refractive index of the numerical samples were approximately close to a measured refractive index of our bone specimen of 1.59 +/- 0.02 at λ = 650 – 830 nm using our Fourier-domain optical coherence tomography system. Using the transfer matrix method, we calculated the backscattered intensity as a function of the wavelength from 400 – 700 nm in each realization and averaged all the realizations to obtain a representative spectral pattern. As a result, the reflectance spectrum can be described by a declining function of the wavelength, which is similar to the experimental data. In this case, a linear fit to the spectrum from 500 to 700 nm can account for the most spectral variance.

C. Results and Discussions

Figure 2 shows representative spectroscopic images of our bovine cortical bone specimen at three different conditions: before, during, and after the loading. Because of the heterogeneous structures of the bone, the spectroscopic image before the loading displays non-uniform and irregular features. Interestingly, the spectroscopic image during loading shows a deformation zone around the tip of the notch. This deformation zone almost vanished upon unloading. As shown in blue areas during loading in Figure 2, in this deformation zone, the backscattered intensity decayed faster over the wavelength with increased values of the spectral slope. Typically, in biological tissue backscattered light spectra have been shown to be sensitive to the subcellular structural alterations [10]. Thus, the deformation zone detected by the spectroscopic image implies that externally applied tensile stresses on the bone tissue can result in changes in the structural alterations at submicron or nanometer levels in the bone structure. Another interesting observation is that this deformation zone is relatively large covering an area of ~1 mm x 1 mm. The results demonstrate that our spectroscopic imaging has the potential to map prefailure deformation during mechanical testing.

To gain physical insight about potential origins of the spectral alterations, we constructed two different configurations of the one-dimension structure. In the first case, we varied the refractive index of the mineralized collagen fibril layer from 1.55 to 1.65, while fixing the thickness of the mineralized collagen fibril and the interfibrillar layers as well as the refractive index of the interfibrillar layers. When the spectral slopes were plotted as a function of the refractive index of the mineralized collagen fibril layer, the spectral slopes linearly decreased with the increase in the refractive index. This result implies that in the prefailure deformation zone, the properties of the mineralized collagen fibrils can be altered by small strains. In the second case, we changed the interfibrillar spacing width from 80 nm down to 25 nm, while other parameters were fixed. When the backscattered spectral slopes were plotted as a function of the spacing width between the mineralized collagen fibrils, as the interfibrillar

spacing width decreased, the spectrum decayed faster within the analyzed range with larger absolute values of the spectral slope. When the bone sample was subjected to the tensile loading, the slope value around the notch dropped approximately 30 percent on average. Based on that the bridging spacing width between the mineralized collagen fibrils is approximately 65 nm at the initial state [11], we estimated that the spacing width decreased approximately 10 nm under the tensile loading. When the tensile force was released, the value of the spectral slope around the notch recovered almost back to the original state, indicating that the spacing width recovered to nearly its initial value. As a potential physical mechanism for these models, the spectral changes might be attributed to the deformation-induced opaque process zone. Our recent study also showed that this deformation zone can be stained by negatively charged fluorescence dyes during loading, which might indicate collagen-mineral debonding [12]. At the nanoscale level, the interfibrillar spacing between the collagen fibrils (i.e., the width of interfibrillar matrix) may decrease when the cortical bone is subjected to tensile loading along the longitudinal axis. These potential mechanisms may also serve as an energy dissipation mechanism (i.e. toughening mechanism) to prevent micro crack formation.

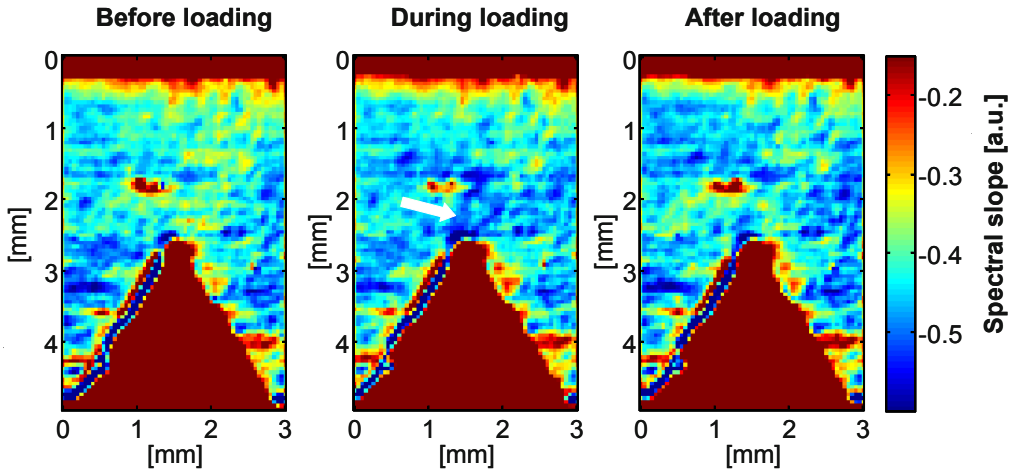

Figure 2. Representative images of bovine cortical bone from back-directional gated spectroscopic imaging system. Images are the spectroscopic images characterized by spectral slopes over the wavelength. A relatively large prefailure deformation zone (indicated by the white arrow) is observed at small strains under tensile loading.

D. Summary

We demonstrated that back-directional gated spectroscopic imaging can be used to visualize and investigate the prefailure deformation in bone tissue. Our imaging method allows the generation of spectroscopic images to sensitively map the heterogeneous nanoscale prefailure deformation of bone over a large area at small strains in in-situ mechanical testing. This prefailure deformation we observed was mostly recovered upon unloading. We proposed possible optical origins for the spectral variation in this deformation field using the transfer matrix method in one-dimensional layered structures.

Acknowledgments

This project was supported in part by a grant from Purdue Research Foundation and the ITRAC internal pilot grant mechanism of the Indiana University Simon Cancer Center.

References

[1] Yerramshetty JS, Lind C, Akkus O. The compositional and physicochemical homogeneity of male femoral cortex increases after the sixth decade. Bone. 39(6):1236-1243. 2006.

[2] Ritchie RO, Buehler MJ, Hansma P. Plasticity and toughness in bone. Physics Today. 62(6):41-47. 2009.

[3] Gurkan UA, Akkus O. The Mechanical Environment of Bone Marrow: A Review. Annals of Biomedical Engineering. 36(12):1978-1991. 2008.

[4] Gupta HS, Zioupos P. Fracture of bone tissue: The 'hows' and the 'whys'. Medical Engineering & Physics. 30(10):1209-1226. 2008.

[5] Tai K, Dao M, Suresh S, Palazoglu A, Ortiz C. Nanoscale heterogeneity promotes energy dissipation in bone. Nature Materials. 6(6):454-462. 2007.

[6] Morgan EF, Yeh OC, Chang WC, Keaveny TW. Nonlinear behavior of trabecular bone at small strains. Journal of Biomechanical Engineering-Transactions of the ASME. 123(1):1-9. 2001.
[7] Xu Z, Liu J, Hong DH, Nguyen VQ, Kim MR, Mohammed SI, Kim YL. Back-directional Gated Spectroscopic Imaging for Diffuse Light Suppression in High Anisotropic Media and Its Preclinical Applications for Microvascular Imaging. IEEE Journal of Selected Topics in Quantum Electronics. in press.
[8] Xu Z, Liu J, Kim YL. Diffuse light suppression of back-directional gating imaging in high anisotropic media. Journal of Biomedical Optics. 14(3):030510. 2009.
[9] Yeh P. Optical waves in layered media. New York: Wiley, 1988.
[10] Roy HK, Kim YL, Wali RK, Liu Y, Koetsier J, Kunte DP, Goldberg MJ, Backman V. Spectral markers in preneoplastic intestinal mucosa: An accurate predictor of tumor risk in the MIN mouse. Cancer Epidemiology Biomarkers & Prevention. 14(7):1639-1645. 2005.
[11] Rosen VB, Hobbs LW, Spector M. The ultrastructure of anorganic bovine bone and selected synthetic hyroxyapatites used as bone graft substitute materials. Biomaterials. 23(3):921-928. 2002.
[12] Sun X, Jeon JH, Blendell J, Akkus O. Visualization of a Phantom Post-Yield Deformation Process in Cortical Bone. Journal of Biomechanics. in press.

Proceedings of the SEM Annual Conference
June 7-10, 2010 Indianapolis, Indiana USA

Instruments to measure human feet using Reverse Engineering techniques

A. Rao[1,*], V. Fontanari[2], I. Cristofolini[1], G. De Monte[3]

[1]Department of Mechanical and Structural Engineering, University of Trento, Via Mesiano 77, 38123, Trento, Italy.

[2]Department of Materials Engineering and Industrial Technologies, University of Trento, Via Mesiano 77, 38100, Trento, Italy.

[3]Department of Psychology, University of Torino, Via Verdi 10, 10124, Torino, Italy.

*Corresponding author:
Andrea Rao
FAX: +39 461 881977
Tel.: +39 461 882457
E-mail address: andrea.rao@ing.unitn.it

ABSTRACT

This study represents a preliminary activity for the biomechanical numerical modeling aimed at the prediction of the human foot behavior and the deformation under different load conditions. It also represents the starting point to develop a scientific approach for the functional mass customization aimed at the optimization of comfort in footwear. Reverse Engineering (RE) methodologies developed for building up the external shape of the human foot are presented and discussed. Aim of this work is to study the problem of the digitalization of human feet under different conditions using three technologies: shape from stereo, from silhouette and from shading. The foot is one of the most difficult human parts to reconstruct taking into account the complex surface and the high curvature. In this article the disadvantage and advantage of each technique are analyzed. In particular tests about reliability and precision of the measure are considered.

T. Proulx (ed.), *Application of Imaging Techniques to Mechanics of Materials and Structures, Volume 4*, Conference Proceedings of the Society for Experimental Mechanics Series 14, DOI 10.1007/978-1-4419-9796-8_20, © The Society for Experimental Mechanics, Inc. 2013

1. INTRODUCTION

Reverse Engineering (RE) of shapes aims to create an appropriate computer representation of existing objects from sets of measured data points. Three-dimensional CAD models are the industry standard communication tool for manufacturing and design. By converting physical parts, through 3D scanning to a CAD format, efficiencies can be realized in areas such as product development, manufacturing technology, enterprise communication, market evaluation and time to market [1]. Classically used in many areas of engineering, in the last years the utility of RE processes found interesting applications in medical sciences and biomechanical related applications [2-8]. There are a lot of different 3D surface digitalization devices, which can be divided into different groups depending on various characteristics, such as, technology (e.g. laser scanning or white light projection), system construction (e.g. fix or on CMM/robot/arm) or type of measurement (e.g. surface scanning or profile scanning) [9]. Certainly all these different 3D surface digitalization technologies have some advantages and disadvantages. This is a reason because a large group of 3D measurement systems is composed of solutions customized for specific applications; the systems are optimized for the acquisition of particular objects and are designed according to the specific task. Some of the most established technology for 3D reconstruction of biological materials in medicine are CT (Computer Tomography) or MRI (Magnetic Resonance Imaging) scanning, these techniques provide with a good precision both surface and internal data of the scanned subject, but they are very expensive and CT scans implicates radiation exposure to the subject and operators. When only external surface information of the subject is required, cheaper alternatives to CT/MRI scans are laser scanning [1], projection of light patterns or combination modelling and image processing technologies. These technologies do not require object contact and have no adverse effects for biological materials. Actually there are several scanners available on market based on these three groups of technologies [9]. Some of these scanners have been specifically developed for the digitalisation of the human foot. The foot is one of the most difficult body parts to be scanned because it has a very complex 3D shape (high curvature surfaces), it is soft and deformable. Nevertheless in the literature many information about foot shapes and foot dimension changes can be found [10-14]. In the last years research related to feet and shoes has gained prominence due to consumers' requirements for better–fitting and more comfortable shoes [14]. Footwear comfort is primarily determinate by the fit between foot and shoe and footwear customers more and more benefit from foot scanners utilise. Previous studies describe in a more or less detailed way the accuracy and repeatability of different foot scanners [13, 15], notwithstanding no direct comparisons of laser, optical pattern recognition or shape from silhouette scanning technologies was found.
The aim of this study is thus to test reliability and precision of three different scanner technologies and discuss their advantages and disadvantages.

2. METHODS

The scanners used for the experiments are based on three technologies: silhouette, laser and multiple stereo vision.
Using an impression casting method (phenolic foam, Podoschiuma, Podartis SRL, Italia) the foot and ankle shapes of one male subject's right foot (size 42) were captured. The level of the impression cast covers the foot up to the lateral malleolus. The negative cast was than filled with resin (Podoform H1000, Podartis SRL, Italia). The 3D scan of the non-modified positive foot cast allows as to have a stable and fixed comparative geometry, avoiding all problems related with scanning real feet (e.g. soft tissue deformation). To gain comparability among all the measurements in whole experiments the foot cast was covered by a socket. The stereo vision scanner needs a socket with markers. This is fundamental for the technologies of multiple stereo vision and for the silhouette. In the stereo vision the markers are not projected on the surfaces but they are directly impressed on socket surfaces. On the contrary in the silhouette scanner the foot cast must be white to increase the contrast with the background.

Figure 1. The scanner used for the experiment: silhouette (left), laser (centre) and multiple stereo vision (right) technologies.

2.1 Silhouette

To test the silhouette method a custom made scanner was built. It was composed by three components: 2 mirrors, 2 cameras and a background in black cotton tissue. The foot cast was placed in the middle and a sequence of five acquisitions was performed. The images acquired were processed by means of the algorithm described by K. Forbes et al. [16]. Thus the output of the instrument was directly a triangular mesh. The foot cast was fixed to a support in the middle of the mirrors and five subsequent scans were performed.

2.2 Laser

The Laser scanner used was the Digipie (Automática y Control Numérico S.L, Inescop, Spain). It is composed by four cameras and four laser line modules on a sliding rail. The distance between the acquired slices was 1.37 mm. The foot cast was hold on the internal support surface of the instrument. In this way each acquired slice creates a transversal section of the foot. Five scans with noise automatic filter and five without it were obtained. The acquired points clouds were processed by the built in software to obtain triangular meshes.

2.3 Multiple stereo vision

The multiple stereo vision scanner tested was the Foot-o-graph (Delta R&S, Italy) [17]. It is composed by 14 cameras grouped in couples triggered synchronously. Each couple measures a part of the foot cast. To test this scanner the white socket was substituted with a socket characterized by colored markers adopted to add a pattern for multiple stereo vision. In any case this socket has the same characteristics of the previous one excepted the coloration. See for details the description in [17]. The output model was represented by a triangular mesh. The foot cast was fixed directly to the frame to permit a stable acquisition. Three series of acquisitions were performed: five scans in one position, five scans after re-worn the socket and finally five scans repositioning the foot cast.

2.4 Data analysis

In order to estimate accuracy, repeatability and validity of scan methods distance analysis were performed in Catia version 5 (Dessault Systemes), dimensional analysis were performed in Rhinoceros version 4 (McNeel) and statistics with Statistica version 9 (StataSoft).

3. Results

The foot cast and the model acquired using silhouette method were too different. The gap in some area was too large. For this reason the silhouette cannot be introduced in the scientific analysis. The analysis carries on using two scanners remained.

The dimensional analysis was performed by Rhinoceros using the bounding box command. This allowed to evaluate the foot cast length and width. Additionally two perimeter sections (transversal and longitudinal) were calculated. These two dimensions were ball girth and foot girth respectively.

The dimension analysis using mesh unfiltered and filter mesh data obtained from laser scanner shows the mean values and standard deviations for length, width, ball girth and foot girth reported in Table 1 and Table 2 respectively.

Table 1. laser scanner dimension analysis using mesh unfiltered data, distance in mm.

	Valid N	Mean	Min	Max	Std.Dev.	Coef.Var.
Length	5	257.7	256.7	258.4	0.8	0.3
Width	5	103.6	103.0	104.1	0.5	0.5
Ball Girth	5	244.7	244.2	245.4	0.4	0.2
Foot Girth	5	603.8	602.6	604.9	0.9	0.2

Table 2. laser scanner dimension analysis using mesh filtered data, distance in mm.

	Valid N	Mean	Min	Max	Std.Dev.	Coef.Var.
Length	5	256.8	255.1	258.3	1.2	0.5
Width	5	104.0	103.0	104.8	0.7	0.7
Ball Girth	5	244.5	244.2	245.1	0.4	0.2
Foot Girth	5	603.3	602.3	603.9	0.6	0.1

Concerning the dimension analysis obtained from stereo vision scanner of series 1, the mean values and standard deviations for length, width, ball girth and foot girth reported in Table 3.

Table 3. stereo vision scanner dimension analysis using mesh series 1, distance in mm.

	Valid N	Mean	Min	Max	Std.Dev.	Coef.Var.
Length	5	254.1	254.1	254.2	0.0	0.0
Width	5	105.9	104.8	106.3	0.7	0.7
Ball Girth	5	254.7	253.3	256.0	1.3	0.5
Foot Girth	5	580.3	552.8	600.8	24.3	4.2

Finally, same parameters obtained by stereo vision scanner of series 3 are shown in Table 4.

Table 4. stereo vision scanner dimension analysis using mesh series 3, distance in mm.

	Valid N	Mean	Min	Max	Std.Dev.	Coef.Var.
Length	5	255.0	254.6	255.2	0.3	0.1
Width	5	103.8	102.7	105.1	1.4	1.1
Ball Girth	5	253.4	252.2	254.0	0.7	0.3
Foot Girth	5	580.1	527.4	599.8	31.5	5.4

The data acquired were then compared in Catia, performing a surface distance analysis. Moreover the dimensions and the geometrical characteristic of the scanned data were compared with a 3D model of the foot cast obtained by a Coordinate Measuring Machine (CMM, Global Image 07.07.07, DEA, Italy). CMM can measure point by point or scanning, and it guarantees an accuracy of 1.7 μm [18] when measuring point by point, and of 3.4 μm [19] when measuring by continuous scan [20]. In this work, surfaces were measured by scanning mode. The precision of the CMM is more than one order magnitude larger than that of scanners.
To align the reference with the models acquired, the best fit alignment of Catia was used. After alignment the foot cast models were trimmed with a reference boundary for standardizing the area of comparison. The trimline was similar to that of commercially available insoles, but in this design, the forefoot section was included. The foot model were trimmed 15 mm horizontally above the weight-bearing plane. These models were also compared in Catia performing distance analysis. This allows to evaluate the differencies between two geometrical entities defined by meshes. In Fig. 2 it is possible to observe of the results of distance analysis considering one laser scanner model (randomly chosen) and the reference. The color of each point was related to the gap between models. The lower and upper worst distances were -1.8 mm and 1.7 mm.

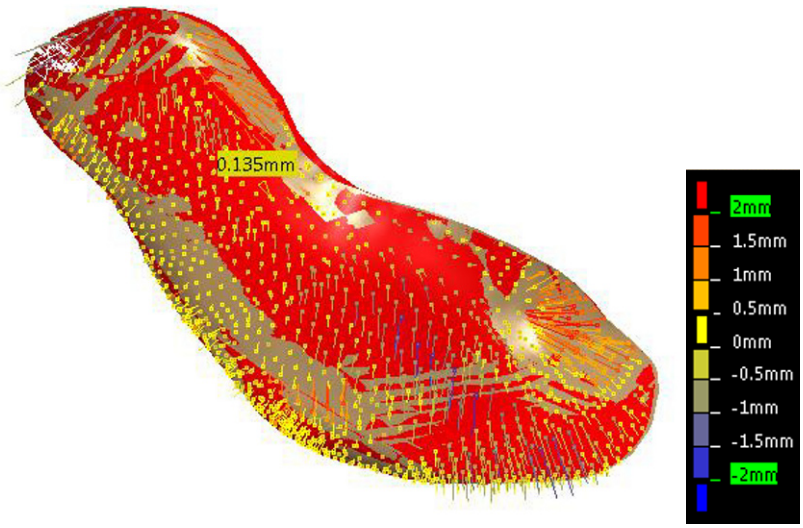

Figure 2. Distance analysis of one laser scanner model and reference model.

The statistical analysis shows (Table 5) the percentage in each single range (e.g. in the gap 0.5-0mm the percentage of model was 32.1%).

Table 5. statistical analysis of the gap between laser scanner and reference model.

Gap		% of model
2	**1.5**	1.0%
1.5	**1**	4.6%
1	**0.5**	6.9%
0.5	**0**	32.1%
0	**-0.5**	33.0%
-0.5	**-1**	17.2%
-1	**-1.5**	4.6%
-1.5	**2**	0.6%

In Fig. 3 it is possible to observe the results of distance analysis considering one laser scanner model and the reference. The lower and upper worst distances were -1.4 mm and 1.6 mm. Table 6. shows the statistical analysis.

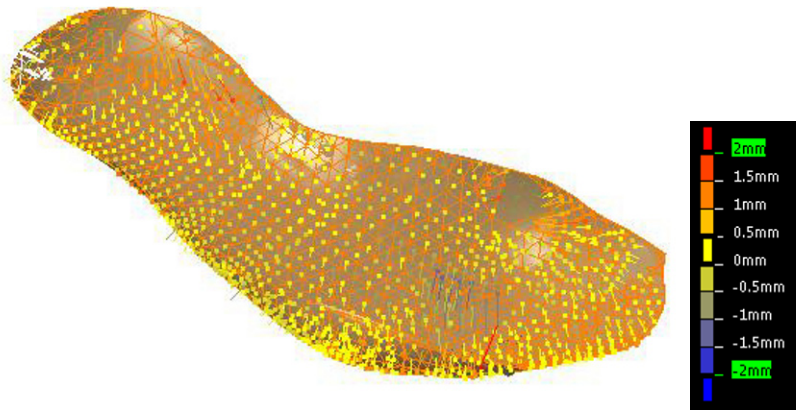

Figure 3. Distance analysis of one stereo vision model and reference model.

Table 6. statistical analysis of the gap between laser scanner and reference model.

Gap		% of model
2	**1.5**	0.1%
1.5	**1**	1.0%
1	**0.5**	11.3%
0.5	**0**	41.4%
0	**-0.5**	41.0%
-0.5	**-1**	4.2%
-1	**-1.5**	1.1%
-1.5	**2**	0.0%

4. Discussion

As pointed out in the results, the foot cast and the model acquired using silhouette method were too different. The incongruence of these data is the reason because they were not considered in the comparison with the laser and the optical technology based scanners. Probably the acquired data (number of Images) were to small in order to have a sufficient detailed 3D reconstruction of the foot cast; however this methodology was unsatisfactory compared with the two others.The results of both laser and multiple stereo vision scanner could be considered good enough to have a detailed 3D reconstruction of the reference foot cast [21]. The existing differences between these two methodologies even though around 2 mm in length allow a good external anatomical description of the foot as required for tailored shoes. The estimated width values were similar in both technologies. Both scanners show a good repeatability and a low coefficient of variation (Table 1, 2, 3, 4). Considering the obtained results, the multiple stereo vision scanner seems to be the better instrument to estimate the foot dimensions. It shows better coefficient of variation (excepted for the foot girth, see Table). This indicates a good repeatability.

The lightly higher coefficient of variation of length estimated from the laser scanner data can be explained through the acquisition step imposed (1.37 mm). As a consequence the maximal error could be 1.37 * 2.

One of the most important advantages of the laser scanner technologies is the possibility to acquire data of one foot from different weight bearing conditions. On the contrary with the stereo vision scanner tested only the unloaded foot condition is possible. The laser scanner time is few seconds. The pulsation and vibration provoked by uncontrolled muscle contractions of real feet could be a noise factor in the measurement.

Instead the laser scanner acquisition time is instantaneous. Moreover one of the disadvantages in the stereo vision system was related to the adoption of the socket. It must be used because it contains the pattern for the image recognition.
The distance analysis of the laser scanner shows large portion of the model characterized by the same average distance (areas visualized in Fig. 4 by the same color), related to alignment difficulties of the automatic filtering routine.

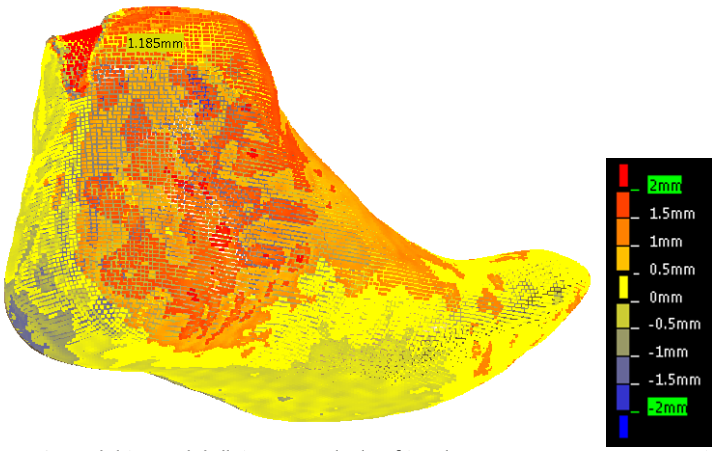

Figure 4. model to model distance analysis of two laser scanner measurements

To avoid alignment problems on both systems a fitting algorithm based on the position of heel and metatarsal head is in development [22]. However in the present work the alignment of the stereo vision data was done with the fitting algorithm included in Catia. Considering the length data of the laser scanner measurement we can observe that it decreases from ~107 of unfiltered data to ~104 mm of the filtered one. This is probably caused by an “aggressive” filter (Fig. 5) that works in a similar way to a low-pass. It decreases significantly the curvature of same zones.

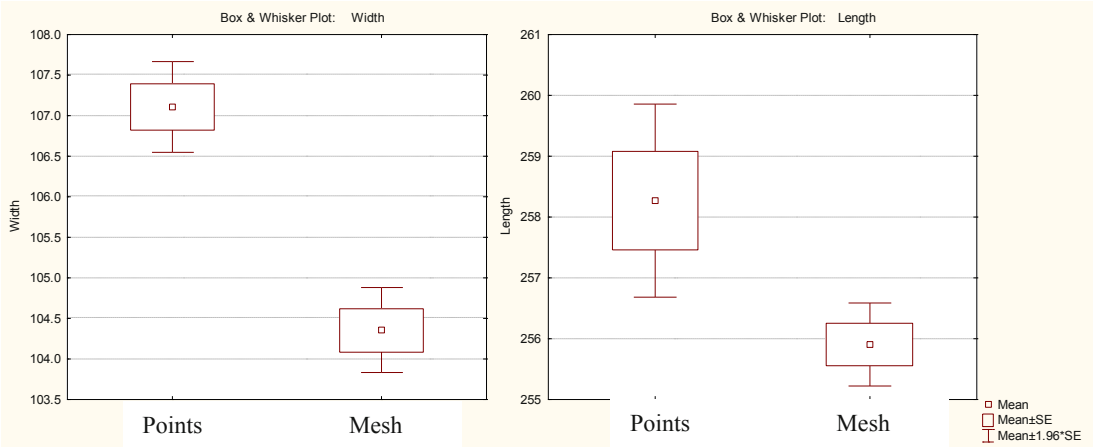

Figure 5. Width (left) and length (right) of points acquired by laser scanner and the mesh filtered.

The points cloud sampling (related to the pattern on the socket) of the stereo vision is lower than that of laser but it cannot be considered a downsampling. Anyway the details obtained still defines a proper 3D representation of the model. However, for further calculation can be an advantage diminishing the number of data.
Concluding the scanners have advantages and disadvantages, notwithstanding both (Foot-o-graph and Digipiè) can be useful for the 3D reconstruction of real feet, as required by the current footwear industry. This consideration is sustained from the fact that the amount of differences found are localized prevalently in length measure and not reflected in other important parameters related to the custom shoes (e.g. width and ball girth). The length discrepancies can be easily managed during the customization of shoes if they are systematic as in our results.

The silhouette technology could support the data acquisition and filtering as pointed in Yemez et al. [23]. All the existing methods can provide unique information and the objective of the future research should be focused in combining laser, stereo and silhouette scanners in fusion techniques.

References

[1] T. Lerch, M. Mac Gillivray, and T. Domina, "3D Laser Scanning: A Model of Multidisciplinary Research," *JTATM,* vol. 5, 2006.

[2] J. Yang and G. Zheng, "Reverse engineering and rapid prototyping technique for restoration of mandibular bone defect" *Sheng Wu Yi Xue Gong Cheng Xue Za Zhi,* vol. 26, pp. 440-2, Apr 2009.

[3] I. Popov and S. O. Onuh, "Reverse engineering of pelvic bone for hip joint replacement," *J Med Eng Technol,* vol. 33, pp. 454-9, 2009.

[4] G. Zhang, J. Yao, X. Wei, F. Pei, and Z. Zhou, "Research on point cloud smoothing in knee joint prosthesis modeling based on reverse engineering" *Sheng Wu Yi Xue Gong Cheng Xue Za Zhi,* vol. 25, pp. 1009-13, 1020, Oct 2008.

[5] Z. L. Tang, X. Wang, and B. Yi, "[Reverse-engineering-based quantitative three-dimensional measurement of facial swelling after administration of Yunnan Baiyao following orthognathic surgery]," *Zhonghua Yi Xue Za Zhi,* vol. 88, pp. 2482-6, Sep 16 2008.

[6] N. Chantarapanich, K. Sitthiseripratip, B. Mahaisavariya, M. Wongcumchang, and P. Siribodhi, "3D geometrical assessment of femoral curvature: a reverse engineering technique," *J Med Assoc Thai,* vol. 91, pp. 1377-81, Sep 2008.

[7] Y. P. Lin, C. T. Wang, and K. R. Dai, "Reverse engineering in CAD model reconstruction of customized artificial joint," *Med Eng Phys,* vol. 27, pp. 189-93, Mar 2005.

[8] B. Mahaisavariya, K. Sitthiseripratip, T. Tongdee, E. L. Bohez, J. Vander Sloten, and P. Oris, "Morphological study of the proximal femur: a new method of geometrical assessment using 3-dimensional reverse engineering," *Med Eng Phys,* vol. 24, pp. 617-22, Nov 2002.

[9] N. D'Apuzzo, "Overview of 3D surface digitalisation technologies in Europe," *Three-Dimentional Image Capture and Applications VI, Proc. of SPIE-IS&T Electronic Imagin, SPIE,* vol. 6056, 2006.

[10] A. Luximon, R. S. Goonetilleke, and M. Zhang, "3D foot shape generation from 2D information," *Ergonomics,* vol. 48, pp. 625-641, 2005.

[11] C. P. Witana, J. Feng, and R. S. Goonetilleke, "Dimensional differences for evaluating the quality of footwear fit," *Ergonomics,* vol. 47, pp. 1301-17, Oct 10 2004.

[12] R. E. Wunderlich and P. R. Cavanagh, "Gender differences in adult foot shape: implications for shoe design," *Med Sci Sports Exerc,* vol. 33, pp. 605-11, Apr 2001.

[13] C. P. Witana, S. Xiong, J. Zhao, and R. S. Goonetilleke, "Foot measurements from three-dimensional scans: A comparison and evaluation of different methods," *International Journal of Industrial Ergonomics,* vol. 36, pp. 789-807, 2006.

[14] S. Xiong, R. S. Goonetilleke, J. Zhao, W. Li, and C. P. Witana, "Foot deformations under different load-bearing conditions and their relationships to stature and body weight," *ANTHROPOLOGICAL SCIENCE,* vol. 117, pp. 77-88, 2009.

[15] R. S. Goonetilleke, C. P. Witana, J. Zhao, and S. Xiong, "The Pluses and Minuses of Obtaining Measurements from Digital Scans," *V.G. Duffy (Ed.): Digital Human Modeling, HCII 2009, LNCS 5620 © Springer-Verlag Berlin Heidelber,* pp. 681-690, 2009.

[16] K. Forbes, F. Nicolls, G. De Jager, A Voigt, "Shape-from-silhouette with two mirrors and an uncalibrated camera", Computer Vision, vol: 3952, pp 165-178, 2006

[17] Cremaschi A., Olivato P., Rao A. “Manufacturing upon knowledge: a new approach to engineering wearable products”, Procedings of Mass Customization & Personalization (MCPC 2007), Boston, 7th-10th October 2007.

[18] ISO 10360-2, 2001. Geometrical Product Specifications (GPS) – Acceptance and reverification tests for coordinate measuring machines (CMM) – Part 2: CMMs used for measuring size

[19] ISO 10360-4, 2000. Geometrical Product Specifications (GPS) – Acceptance and reverification tests for coordinate measuring machines (CMM) – Part 4: CMMs used in scanning measuring mode

[20] http://www.dea.it, accessed November 24th 2009

[21] L. Mundermann, A. Mundermann, A. M. Chaudhari, T. P. Andriacchi, “Conditions that influence the accuracy of anthropometric parameter estimation for human body segments using shape-from-silhouette”, Procedings of Videometrics VIII, San Jose, CA, 18th January 2005

[22] A. Rao, “Ricostruzione della superficie esterna del piede mediante tecnica di stereo visione multipla”, Procedings of AIAS, Torino, 9 th -11 th September 2009

[23] Yemez Y., Wetherilt C.J: A volumetric fusion technique for surface reconstruction from silhouettes and range data, Computer Vision and Image Understanding, Volume: 105, Issue: 1, January, 2007, Pages. 30-41.

Proceedings of the SEM Annual Conference
June 7-10, 2010 Indianapolis, Indiana USA

Characterization of Mechanochemically Active Polymers Using Combined Photoelasticity and Fluorescence Measurements

Sharlotte Kramer[1,2,*], Brett Beiermann[1,2], Douglas Davis[2,3], Nancy Sottos[1,2], Scott White[2,4], and Jeffrey Moore[2,3]
University of Illinois at Urbana-Champaign
[1]Department of Materials Science and Engineering, [2]Beckman Institute,
[3]Department of Chemistry, and [4]Department of Aerospace Engineering
[*] *Corresponding Author*: 405 N. Mathews Ave., Urbana, IL 61801, sbkramer@illinois.edu

Abstract

Force-sensitive molecules, called mechanophores, exhibit a chemical response to mechanical force and can be incorporated into the polymer chains. Mechanically stressing these polymers in turn can activate the mechanophore, producing an advantageous chemical response. We have previously demonstrated activation of a mechanophore called spiropyran, which undergoes a force-induced, 6-π electrocyclic ring-opening reaction accompanied by a color change, in linear polymers in solution via sonication and in bulk solids via tension and compression. Reliable, fully characterized transfer of macroscopic stress on a bulk solid polymer to the mechanophore remains a topic of active research. The premise for mechanical activation in linear polymers is that aligned polymer chains can better transfer mechanical energy to the mechanophore than a randomly oriented chain. We have combined photoelasticity and fluorescence measurements for the same field of view during uniaxial tension experiments of two bulk linear solid spiropyran-linked polymers, elastomeric poly(methyl acrylate) (PMA) and glassy poly(methyl methacrylate) (PMMA), in order to quantify the influence of polymer chain orientation, determined from optical birefringence, on mechanophore activation evident by color change. These experiments elucidate the critical molecular orientation and macroscopic stress level required to activate the mechanophores, which are critical for the design of systems incorporating mechanochemically active polymers.

1 Introduction

Mechanochemical transduction essentially is the energy pathway between mechanical and chemical energies. Nature holds a myriad of systems where mechanical and chemical energies are linked such that mechanical stimuli induce biochemical responses such as hearing, muscle contractions, and force-controlled switching of protein functions [1, 2]. Research in mechanochemical transduction has mainly been in biology and chemistry, but recent interdisciplinary work between chemists, material scientists, and mechanicians has led to mechanochemically active engineering materials [3, 4]. Mechanochemical molecules, called mechanophores, which exhibit a chemical response to mechanical force, can be incorporated into the polymer chains. Mechanically stressing these polymers in turn can activate the mechanophore, producing an advantageous chemical response; yet, reliable, fully characterized transfer of macroscopic stress on a bulk solid polymer to the mechanophore is still a topic of active research. The purpose of the research presented in this paper is to characterize the influence of molecular orientation on mechanophore activation in a bulk solid polymer, under the premise that linearly oriented polymer chains can better transfer mechanical energy to the mechanophore than a randomly oriented chain that will use the energy to entropically deform. In pursuit of this goal, we have developed a new hybrid experimental technique to measure the chain alignment of linear polymers via birefringence measurements from photoelasticity while monitoring the fluorescence of the color-changing mechanophore incorporated into the polymer chains.

To harness the mechanochemical reactions of mechanophores, the bulk polymers must transfer external force efficiently to a small number of specific bonds, so careful design of these polymers is imperative. To aid the study of this global force transfer to local molecules, we chose a mechanophore with easily detectable activation characteristics: spiropyran (SP), which undergoes a force-induced, 6-π electrocyclic ring-opening reaction accompanied by a color

T. Proulx (ed.), *Application of Imaging Techniques to Mechanics of Materials and Structures, Volume 4*, Conference Proceedings of the Society for Experimental Mechanics Series 14, DOI 10.1007/978-1-4419-9796-8_21, © The Society for Experimental Mechanics, Inc. 2013

change. SP has photochromic and thermochromic responses [5] due to a reversible rupture of the spiro carbon-oxygen (C-O) bond (see Figure 1(a)), transforming the colorless spiropyran form, a.k.a "closed-form SP," to the reddish colored merocyanine form, a.k.a "open-form SP," which also exhibits fluorescence when excited by UV and visible green wavelengths of light. Spiropyran has several linking sites for the polymer chains, though not all possible configurations allows for efficient transfer of force across the spiro-junction. The 5' and 8 attachment points were functionalized with α-bromo groups, as shown the top configuration 1 with red labels in Figure 1(b), for subsequent polymerization by either single-electron-transfer living radical polymerization (SET-LRP) or atom transfer radical polymerization (ATRP). These attachment points will allow for good transfer of load to the spiro-junction. Two control configurations can also be prepared that should not activate due to external mechanical forces, but only due localized heating or UV radiation that need to be excluded from mechanical testing. The monofunctional control (configuration 2) has only one polymer chain attachment point, so no significant external forces can be transferred to the SP. The difunctional control (configuration 3) has two polymer attachment points on one side of the spiro-junction, leading to insufficient transfer of load to the spiro-junction. We previously demonstrated mechanophore activation in SP-linked elastomeric poly(methyl acrylate) (PMA) under uniaxial tension, but quantified activation of the mechanophores via optical RGB analysis of optical images acquired during testing [4]; we did not take advantage of the fluorescence of the open-form SP and did not fully characterize the mechanism for efficient activation.

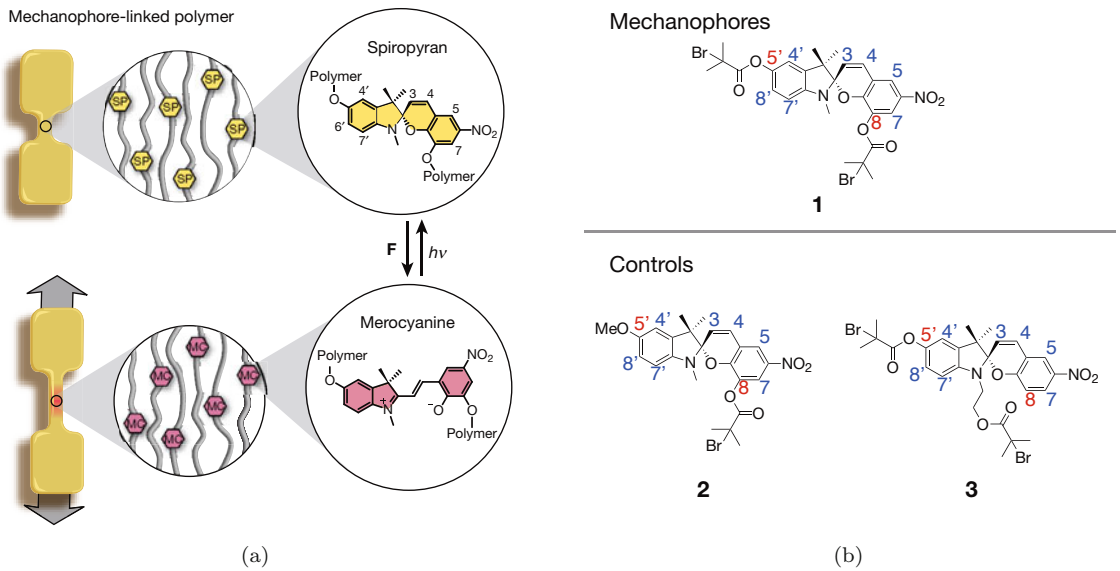

Figure 1: Mechanophore-linked polymers: (a) Schematic of mechanophore-linked polymer dog bone specimens showing the closed-form spiropyran and the open-form spiropyran also known as merocyanine. The closed-form spiropyran linked in PMA and PMMA gives the polymers a slightly yellow tint as opposed to the completely clear plain polymer, but the mechanophore-linked specimens are still translucent. When the spiropyran undergoes 6-π electrocyclic ring-opening reaction by breaking of the spiro-junction, the resulting merocyanine gives the polymer specimen a red color, and the merocyanine also emits red-wavelength fluorescence; (b) Spiropyran has several possible linking sites for the polymer chains labeled in blue and red. These three different configurations lead to linear polymers that are either (i) able to transfer force across the spiro-junction (configuration 1), leading to mechanochemically active polymers, which we call the active form of the mechanophore-linked polymer, or (ii) unable to transfer force to the spiro-junction (configurations 2 and 3), leading to mechanochemically inactive polymers, which we call control mechanophore-linked polymers. [Reprinted by permission from Macmillan Publishers Ltd.: *Nature*, Reference [4], copyright (2009)]

Figure 2 show results from the previous uniaxial testing of PMA-SP-PMA [4]. The active form of the polymer PMA-1-PMA, i.e. PMA with centrally located configuration-1 SP, in Figure 2(a), has a vibrant red color in the gage section after monotonic uniaxial tensile testing as compared to PMA-1-PMA before testing and to the controls PMA-2 and PMA-3-PMA that did not show any activation under the same testing conditions. The uniaxial cyclic

fatigue testing of active PMA-1-PMA and monofunctional control PMA-2 demonstrated significant accumulation of irreversible plastic strain, ϵ_p, as shown in Figure 2(b), but only the active polymer showed a color change. The green intensity in the optical images due to the increasing red color began to decrease at 200% plastic strain in PMA-1-PMA. The accumulation of plastic strain due to uniaxial loading likely leads to increased alignment of the polymer chains to the loading direction, and this also accompanies vibrant color change, i.e. SP activation, in PMA-1-PMA; hence, we postulate that a mechanism for efficient mechanophore activation in these linear polymers is some degree of chain alignment that allows for efficient transfer of global mechanical force across the spiro C-O bond as opposed to entropic deformation of the polymer chain arms.

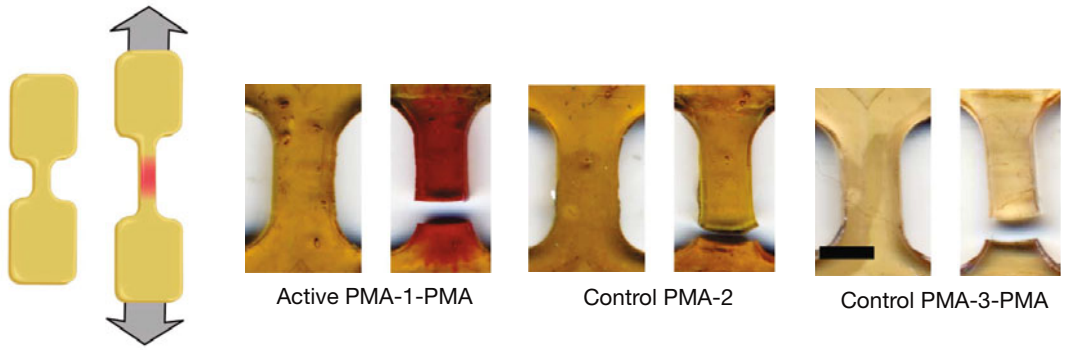

(a)

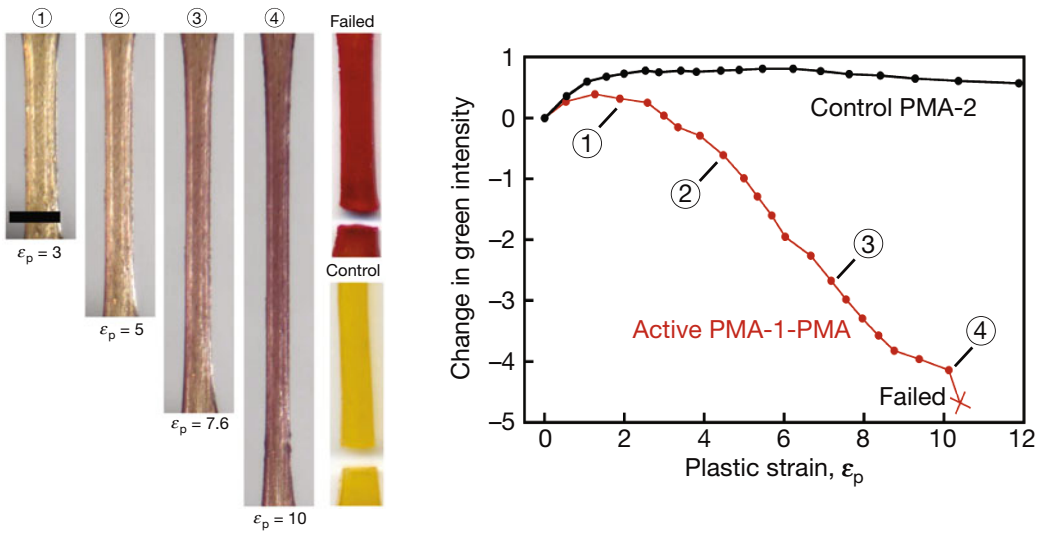

(b)

Figure 2: Uniaxial tensile testing of SP-linked PMA (scale bars are 2 mm): (a) Before (left) and after (right) images for PMA-1-PMA, PMA-2, and PMA-3-PMA under monotonic uniaxial tension, showing mechanical activation of the SP only in the active PMA-1-PMA specimen ; (b) accumulation of irreversible plastic strain when these polymers are under cyclic loading shows vibrant color change in the PMA-1-PMA beginning at $\epsilon_p = 2$ evident by a loss in green intensity, but no color change in the monofunctional control PMA-2 evident by no loss in green intensity [Reprinted by permission from Macmillan Publishers Ltd.: *Nature*, Reference [4], copyright (2009)]

To test this postulation, we have developed a new hybrid experimental method that determines both polymer chain alignment from photoelastic birefringence measurements and activation of spiropyran from fluorescence imaging. This experimental method will be useful not only for the elastomeric PMA-SP-PMA previously studied, but also glassy PMMA-SP-PMMA given its detectable birefringence under uniaxial tension with stretches beyond the yield

point. The challenge with PMMA is to stretch these glassy polymer specimens beyond yield at room temperature without fracture, which has be achieved through plasticizers. Qualitative studies of color change in PMMA-SP-PMMA indicate that activation of the SP occurs beyond the yield point at an elevated temperature (90^oC) below its glass transition temperature (135^oC), so the PMMA-SP-PMMA study will likely involve the drawing regime beyond yield where the chains tend to align.

2 Experimental Methods

2.1 Birefringence due to polymer chain alignment

Photoelasticity is a optomechanical technique that classically determines the difference in principal stresses ($\sigma_1 - \sigma_2$), in transmission mode, for a stress-birefringent (photoelastic) material [6, 7]. The essence of photoelasticity is measuring material optical birefringence, Δn, which can be related to stress via the Stress Optic Law: $\Delta n = n_1 - n_2 = C(\sigma_1 - \sigma_2)$, where C is the relative stress-optic coefficient for a linearly elastic photoelastic material. A photoelastic plate under stress acts as a linear retarder plate for polarized light with linear retardation δ with a fast axis at angle α relative to the x axis, also known as the isoclinic angle. The linear retardation δ called the isochromatic phase is related to Δn in a photoelastic plate by

$$\delta = \frac{\Delta n \lambda}{2\pi h}, \tag{1}$$

where λ is the wavelength of light, and h is the thickness of the plate. The isochromatic phase can be determined by appropriately managing polarization optics before and after the photoelastic material, as will be discussed below.

Without the requirement of knowing the photoelastic constants in the Stress Optic Law, photoelasticity can be utilized purely for the measurement of change in optical birefringence during a mechanical test. In a linear polymer, optical birefringence is related to polymer chain alignment in a uniaxial loading condition by the second moment of the polymer segmental orientational distribution function, also known as the order parameter or Hermans orientation function, S:

$$S = \frac{\Delta n}{\Delta n_o} = \frac{\langle 3\cos^2(\theta) - 1 \rangle}{2}, \tag{2}$$

where θ is the angle of the polymer chains relative to the axis of uniaxial loading, and Δn_o is the intrinsic optical birefringence when all the polymer chains are aligned in the loading direction (i.e. $S = 1$) [8, 9]. Assuming that the intrinsic birefringence Δn_o can be determined from IR spectroscopy [10] or from extrapolation of birefringence data in uniaxial tension experiment, then the average orientation of the polymer chains for a given stretch can be determined.

The experimental setup for photoelasticity used in this study is a circular polariscope with a polarizer with axis at angle ρ, a $\lambda/4$ plate with fast axis at angle ξ, the photoelastic material, another $\lambda/4$ plate with fast axis at angle ϕ, and a final polarizer with axis at angle β as shown in Figure 3. In order to determine the isochromatic phase, several phase shifting methods requiring four to six images [6, 7, 11] are possible, but in a uniaxial tension test where the optical birefringence is assumed to monotonically increase with tensile stretching, simply using the bright-field (I_1) and dark-field (I_2) images are required:

$$I_1 = I_o[1 + \cos(\delta)], \tag{3a}$$

$$I_2 = I_o[1 - \cos(\delta)], \tag{3b}$$

$$\delta = \arccos\left\{\frac{I_1 - I_2}{I_1 + I_2}\right\}, \tag{3c}$$

where I_o is the relative intensity of the light field. Since arccos() gives a range of $[0, \pi)$, the δ in Eq. (3) is "wrapped" and requires unwrapping to retrieve the true possible range of δ, $(-\infty, \infty)$. Knowing that the optical birefringence is monotonically increasing with tensile stretch, the wrapped δ can easily be unwrapped, provided that the change in thickness, h, during the tensile testing is accounted for. Several combinations of polarization optic angles can produce the bright and dark-field images [6, 7, 11]. The angles utilized in this study are given in Table 1.

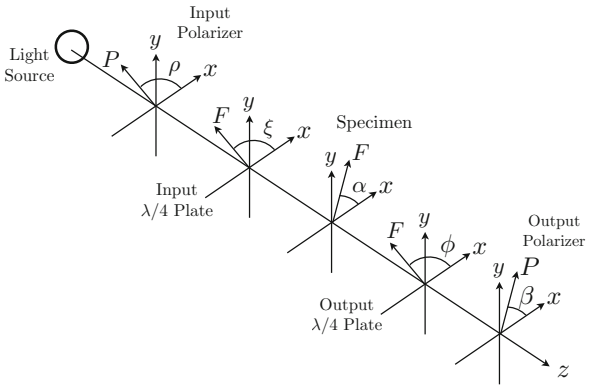

Figure 3: Schematic of circular polariscope with fast axes of optics labeled

Image	Intensity	ρ	γ	ϕ	β
Bright Field	$I_o[1 + cos(\delta)]$	0	$\pi/4$	$\pi/4$	$\pi/2$
Dark Field	$I_o[1 - cos(\delta)]$	0	$\pi/4$	$3\pi/4$	$\pi/2$

Table 1: Circular polariscope configuration for bright and dark-field images (angles refer to fast axis of optics)

2.2 Fluorescence due to mechanophore activation

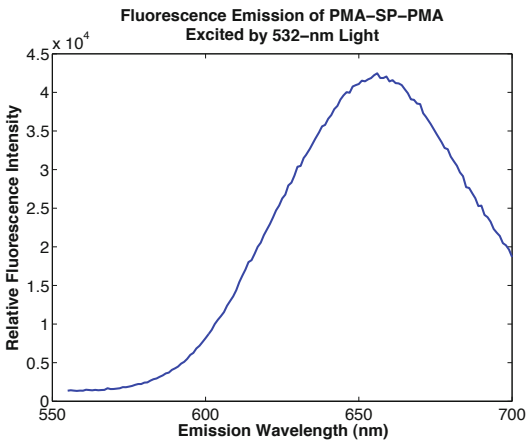

Figure 4: Fluorescence emission spectrum of open-form PMA-1-PMA excited by 532-nm wavelength light, showing emission in the red wavelengths (590-750 nm).

The previous study of SP-linked polymers [4] utilized optical imaging of the specimens during testing to determine the activation of SP from a color change in the specimens (loss of green intensity due in increasing red color). Though this method did prove to demonstrate activation, it did not capitalize on the fluorescence emission of the merocyanine that has shown to be more sensitive than visual color in microscopy imaging of specimens. The basic principle behind fluorescence is the absorption by a molecule of light energy of specific wavelengths that results in a Stokes' shift in the light, which is emitted from the molecule at longer wavelengths. Therefore, emission of these longer wavelengths from a system that is illuminated by the excitation wavelengths requires the presence of these fluorescent molecules. Since SP is only fluorescent in its open merocyanine form when excited by UV light or green wavelengths of visible light and its fluorescent signal is relatively strong, then fluorescence imaging is a natural diagnostic to determine

SP activation in these linear polymers. The fluorescence emission spectrum of open-form PMA-1-PMA excited by 532-nm wavelength light in a fluorimeter is given in Figure 4, showing the strong emission in the red wavelengths (590-750 nm) with a emission peak around 655 nm. An advantage of fluorescence imaging for this hybrid setup is that a single wavelength of green light, which is appropriate for photoelasticity, can also lead to a fluorescent signal appropriate for showing SP activation.

2.3 Hybrid experimental method

Figure 2.3 shows a schematic of the hybrid experimental setup. Green wavelengths of light, which induce red wavelengths of fluorescence emission in SP, is also suitable for photoelasticity. A 532-nm wavelength excitation light was selected for ample fluorescence signal from SP and for compatibility with optics available for photoelasticity. The light source is a 25-mW coherent single-mode polarized 532-nm wavelength diode laser. Since the laser power required for adequate excitation of the SP fluorescence in these specimens may change between polymers, a half-wave plate and polarizer act as power control by rotation of the laser polarization relative to the polarizer. A spatial filter expands the laser beam to 10-mm diameter to provide a large field of view. The first two optics of the circular polariscope, a polarizer and quarter-wave plate, are set to the appropriate optical angles given in Table 1. The transparent specimens are placed symmetrically between the sandwich grips on a custom uniaxial rail table with two actuators that move in opposing directions in the same displacement increments such that the center of the specimen stays in a fixed location. The key to combining these two experimental methods for simultaneous data acquisition is the custom dichroic beamsplitter that reflects the 532-nm wavelength excitation light, preserving its polarization, and transmits >580-nm wavelengths for the fluorescence emission light. Along the reflection arm after the dichroic beamsplitter, a excitation filter that transmits only 532 ± 5-nm light ensures no fluorescent light travels on this optical path. Since the second quarter-wave plate and polarizer are analyzing reflected light, the x Cartesian axes of these optics shown in Figure 3 are rotated by π about their y axes in order to preserve the correct fast-axis and polarization-axis angles given in Table 1. Since the power required for fluorescence is generally higher than that required for photoelasticity, a neutral density filter is placed before the imaging lens and monochromatic CCD camera to reduce the intensity of the photoelastic signal, preventing saturation of the CCD. Along the transmission arm after the dichroic, a long-pass filter, allowing >580-nm wavelengths, further blocks any excitation light. An imaging lens is placed as close to this emission filter as possible to collect as much fluorescence because fluorescence signal emits radially and decreases with distance from the fluorescent molecules. A color CCD camera images the fluorescent signal.

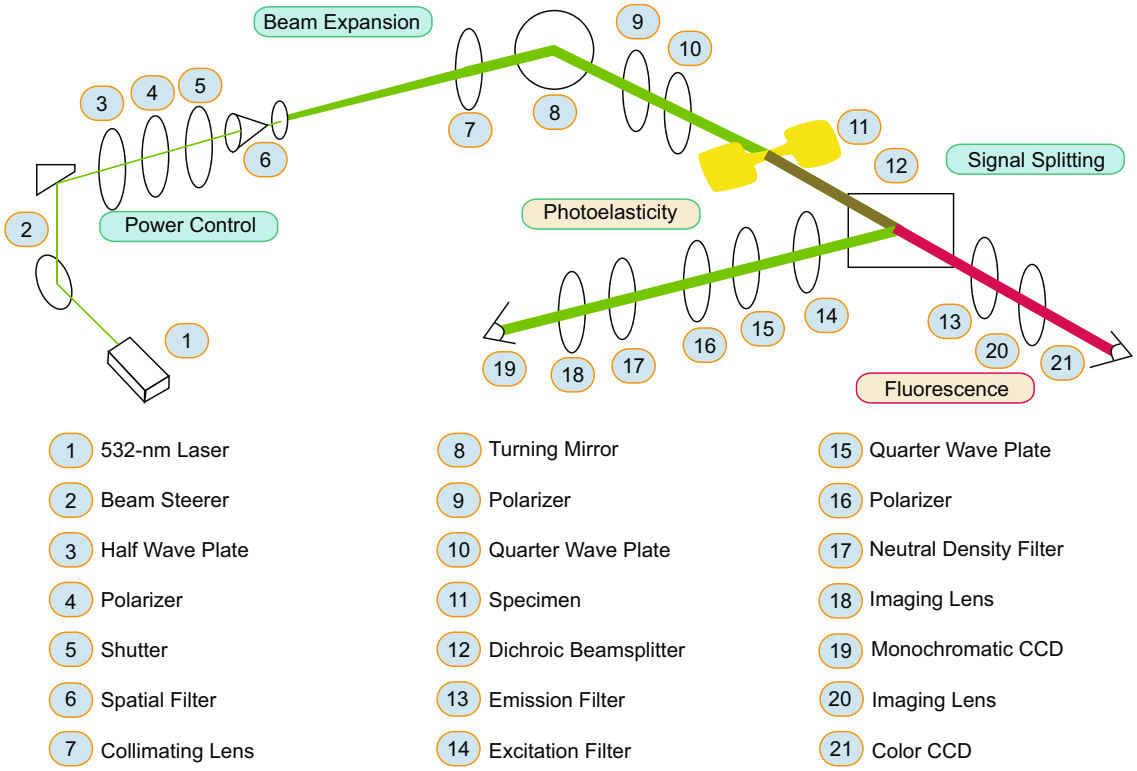

Figure 5: Schematic of Combined Experimental Setup

3 Preliminary Results for PMA-SP-PMA

3.1 Photoelasticity

Initial photoelastic testing of PMA-1-PMA under uniaxial tension demonstrates the determination of birefringence. The dog bone-shaped specimen with initial gage length, L_o, of 6.02 mm, initial thickness, h_o, of 0.67 mm, and initial width, w_o, of 2.18 mm is placed in grips on the custom uniaxial rail table with two actuators. Thus, the center of the specimen can stay in the light beam path and in the camera field of view, useful attributes when studying polymers than can extend to a stretch ratio, $\lambda_s = L/L_o$, over 10 as in the case of PMA. For the test summarized in Figure 6 and 7, the stretch ratio λ_s went to 9.0 before the specimen fractured.

With the circular polariscope described above, bright and dark-field images were taken at displacement increments of $L_o/4$ for λ_s range of [1.0,4.0] and of $L_o/2$ for λ_s range of [4.0,9.0]; these images for λ_s of 1.0, 4.0, and 8.5 are shown in Figure 6. In the field of view, the specimen is being stretched along the x-axis. The monochromatic CCD resolution is 1280×1024. Since these images show a different intensity in the specimen region as opposed to the air around the specimen, PMA-1-PMA has a detectable birefringence, a requirement for photoelasticity.

In this experiment, PMA is assumed to be nearly incompressible, such that $\lambda_s\lambda_w\lambda_h \approx 1$, where $\lambda_w = w/w_o$ and $\lambda_h = h/h_o$ are the stretch ratios in the width and thickness directions. Also, the unconstrained dimensions, w and h, are assumed to undergo the same stretch ratios, i.e. $\lambda_w = \lambda_h$. Measurements of the gage section width, w, from the full-field bright-field images during the test determine λ_w, which in term determines the thickness, $h = \lambda_h h_o = \lambda_w h_o$. As shown in Figure 7(a) for a PMA-1-PMA specimen, the width stretch ratio from the width measurements nearly follows the $\lambda_s^{-0.5}$ behavior expected for incompressible materials.

The specimens can have some imperfections that obscure the transmitted light such that $I_1 + I_2 = 0$; therefore those pixels are excluded from the analysis. Due to these imperfections in the specimen, a point photoelastic measurement

would be prone to high error. The isochromatic phase ideally is uniform in a uniaxial tension test, so an average isochromatic phase is taken from each specimen. Since the stretch ratio is large for these PMA specimens, significant portions of the initial gage section leave the field of view during the course the experiment. To approximately keep the same section of the gage section from which the birefringence is calculated, we first choose a region of the specimen at the largest stretch ratio and consider that the region on interest. The length and width dimensions of the region on interest change with the global length and width stretch ratios such that the initial region on interest has a small length and large width and the final region of interest has the selected large length and small width. The average wrapped and unwrapped isochromatic phase is shown in Figure 7(b) with the standard deviation of the isochromatic phase over the region of interest in the gage section. The wrapped isochromatic phase appears to steadily vary between 0 and π, allowing for easy manual unwrapping of δ. The resulting unwrapped isochromatic phase increases with length stretch ratio. The birefringence calculation from Eq. (1) using the stretch-dependent h in Figure 7(c) shows the increasing birefringence with stretch approaching a plateau value of Δn for larger λ_s. For the sake of brevity, only the birefringence data for PMA-SP-PMA is presented as an example of how photoelasticity can be used to determine birefringence, which can then be converted to polymer chain orientation with further analysis to determine the intrinsic birefringence, Δn_o.

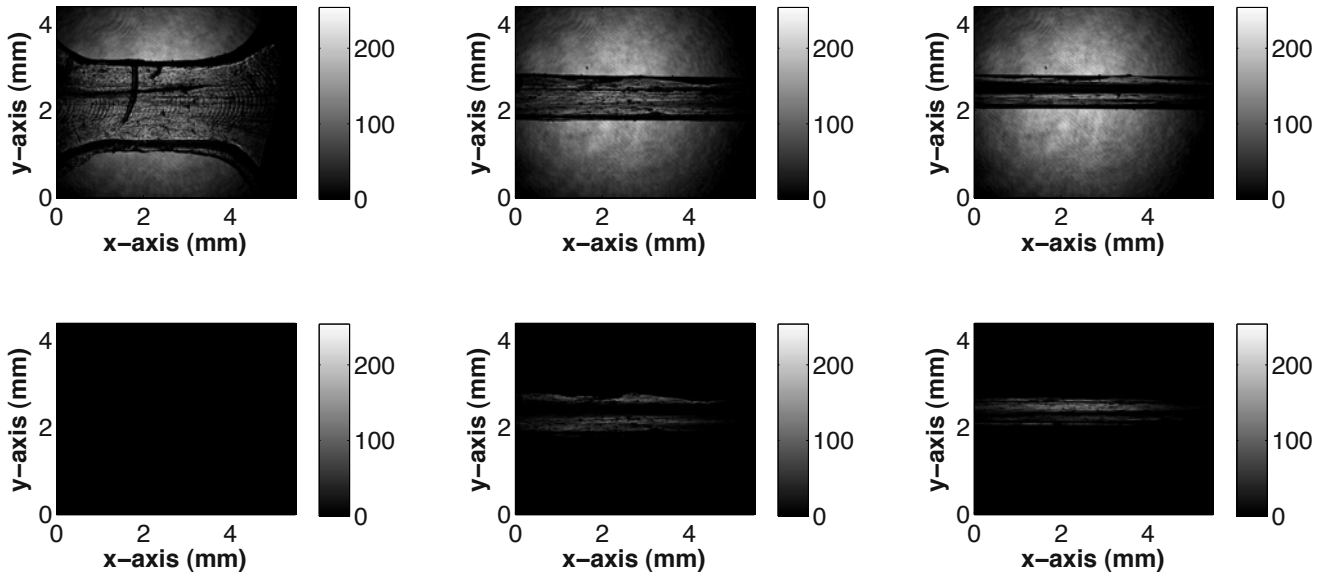

(a) $\lambda_s = 1.0$ (b) $\lambda_s = 4.0$ (c) $\lambda_s = 8.5$

Figure 6: Bright (upper) and dark-field (lower) photoelastic images of active PMA-1-PMA with specimen being stretched along the x-axis.

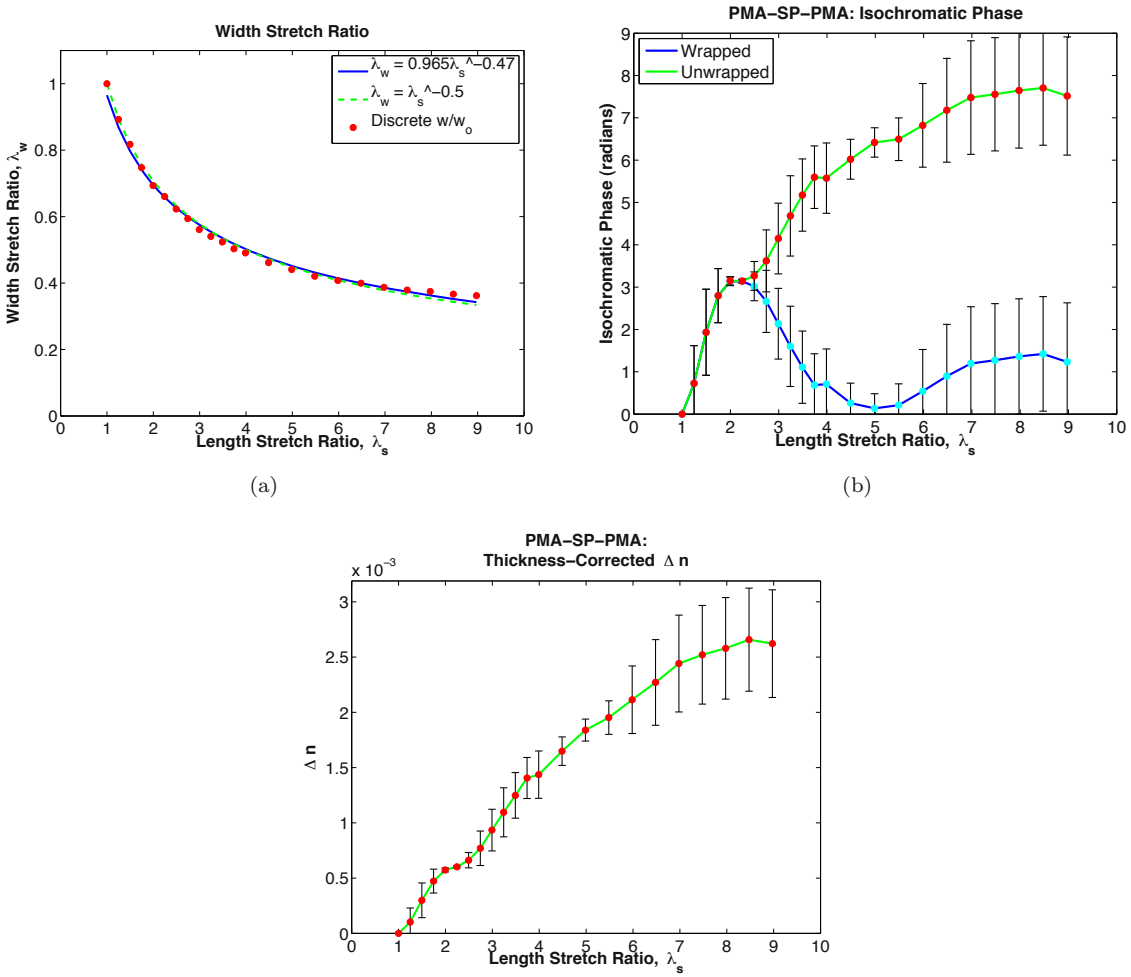

Figure 7: Photoelasticity measurements of active PMA-1-PMA: (a) width stretch ratio close to the incompressible $\lambda_s^{-0.5}$ behavior; (b) the average wrapped and unwrapped isochromatic phase from bright and dark-field image data with error bars showing the standard deviation of the isochromatic phase over the region of interest in the gage section; (c) change in birefringence, accounting for the change in thickness, during the uniaxial tension test approaching a plateau value of Δn for larger λ_s.

3.2 Fluorescence

This experiment requires that the fluorescence be detectable in the hybrid setup with circularly polarized incident light to the specimen. Initial diagnostic experiments confirmed that the fluorescence was detectable for both PMA-1-PMA and PMMA-1-PMMA by full-field imaging. Figure 8 shows the results from one such experiment in PMA-SP-PMA, which is a different specimen than discussed above. This specimen with initial gage length, L_o, of 5.26 mm, initial thickness, h_o, of 0.65 mm, and initial width, w_o, of 1.91 mm underwent uniaxial tensile loading just as the above photoelasticity specimen and was irradiated with the same circularly polarized 532-nm light from the first half of the circular polariscope as above. Unlike in the photoelastic experiment, this specimen was imaged using a color CCD with 1024×768 pixel resolution through a long pass filter that blocks the majority of the 532-nm wavelength ($T_{532} \approx 1\%$) and transmits most of the light above 600 nm ($T_{>600} \approx 90\%$). The particular filter used in this diagnostic test was not meant to block collimated laser light, so some 532-nm light did reach the CCD, hence the vibrant green background in the experimental images in Figure 8. Further improvements will be made to block virtually all of the 532-nm light from the fluorescence arm of the hybrid setup for better quality imaging without risk of saturation on the color CCD; inclusion of the dichroic beamsplitter in combination with a higher quality emission filter will remove the 532-nm light in future experiments with simultaneous image acquisition.

In Figure 8(a), the change in the red intensity on a scale of 0 to 1 is plotted against the length stretch ratio, which went to 16.3 before the specimen fractured in the center of the gage section; these red intensity values were and average of a region of interest in each image determined in the same manner as with the photoelastic data described above. The specimen was stretched first by displacements of $L_o/2$ for λ_s of 1 to 7 and then by increments of $L_o/4$ until fracture. The increase in red intensity indicates increasing number of SP that only fluoresce when opened. In this setup, the only method to open the SP is by global forces on the polymer, so initiation of fluorescence implies some polymer chains are able to transfer the global forces to the their linked SP molecules. In Figure 8(a), the red intensity is at a nominal background level until around $\lambda_s = 7.0$ and then steadily increases until specimen failure. Figure 8(b) - 8(f) show five experimental images, where red intensity is very faint at $\lambda_s = 9.0$, but extremely vibrant by the last displacement increment at $\lambda_s = 16.3$. Figure 8(g) is an optical image of the PMA-SP-PMA showing the vibrant pink color in the gage section due to the opening of the SP; the initial specimen was all optically clear like the grip section before testing. This experiment indicates that the circularly polarized 532-nm wavelength laser light necessary for photoelasticity is able to excite the fluorescence in PMA-SP-PMA and that the fluorescence imaging is able to capture the fluorescence in full field.

4 Conclusions

Mechanochemically active polymers are a new class of bulk polymers that can harness advantageous chemical reactions through mechanical loading, with potential applications such as mechanical sensors or self-healing materials. One hurdle to extensive use of these types of polymers is determining the mechanisms for mechanophore activation. The hybrid experimental method proposed here, combining photoelasticity and fluorescence imaging to study spiropyran linked PMA and PMMA, will quantify the role of polymer chain alignment in mechanophore activation in linear mechanochemically active polymers. The initial diagnostic testing demonstrates that these polymers have detectable birefringence and fluorescence when under uniaxial tensile load. Future experiments where photoelasticity and fluorescence imaging are performed simultaneously for the same specimen should determine the critical chain alignment necessary for mechanophore activation. This understanding will serve as a foundation for designs of future mechanochemically active polymers.

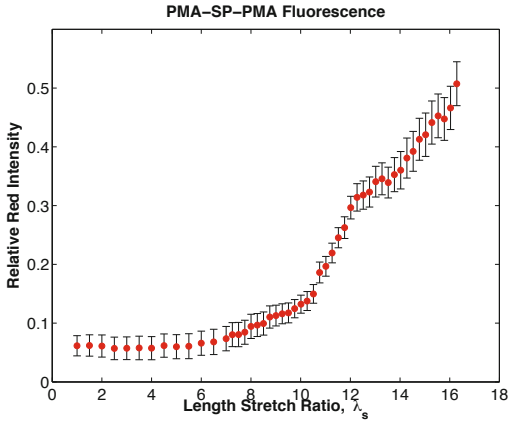

(a)

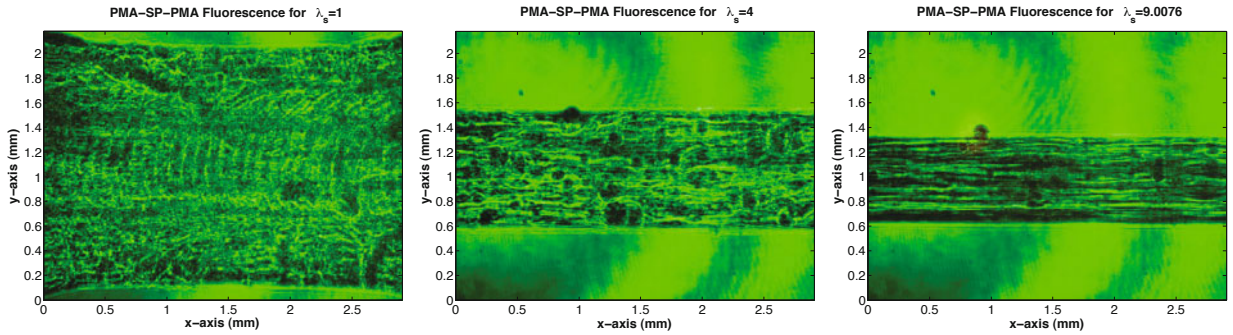

(b) $\lambda_s = 1.0$ (c) $\lambda_s = 4.0$ (d) $\lambda_s = 9.0$

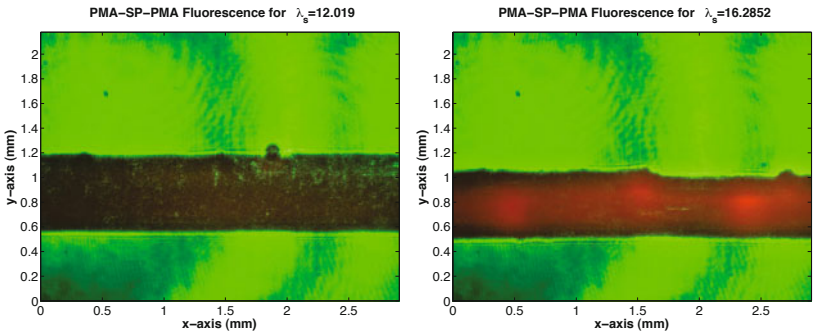

(e) $\lambda_s = 12.0$ (f) $\lambda_s = 16.3$

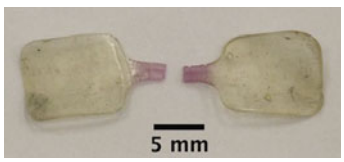

(g)

Figure 8: Fluorescence measurements of active PMA-1-PMA: (a) average change in red intensity over the region of interest vs. length stretch ratio; (b) fluorescence image at $\lambda_s = 1.0$; (c) fluorescence image at $\lambda_s = 4$; (d) fluorescence image at $\lambda_s = 9.0$;(e) fluorescence image at $\lambda_s = 12.0$;(b) fluorescence image at $\lambda_s = 16.3$; (f) optical image of specimen after testing with vibrant color change in the gage section that initially was clear like the grips prior to testing.

Acknowledgments

We gratefully acknowledge the support of the ARO MURI program (grant number W911NF-07-1-0409) for this research.

References

[1] A. S. French, "Mechanotransduction," Annu. Rev. Physiol. **54**, 135–152 (1992).

[2] V. Vogel, "Mechanotransduction involving multimodular proteins: Converting force into biochemical signals," Annu. Rev. Biophys. **35**, 459–488 (2006).

[3] A. Piermattei, S. Karthikeyan, and R. P. Sijbesma, "Activating catalysts with mechanical force," Nature Chemistry **1**, 133–137 (2009).

[4] D. A. Davis, A. Hamilton, J. Yang, L. D. Cremar, D. V. Gough, S. L. Potisek, M. T. Ong, P. V. Braun, T. J. Martinez, S. R. White, J. S. Moore, and N. R. Sottos, "Force-induced activation of covalent bonds in mechanoresponsive polymeric materials," Nature **459**, 68–72 (2009).

[5] V. I. Minkin, "Photo-, thermo-, solvato-, and electrochormic spiroheterocyclic compounds," Chem. Rev. **104**, 2751–2776 (2004).

[6] K. Ramesh, *Springer Handbook of Experimental Solid Mechanics* (Springer-Verlag, 2009), chap. Photoelasticity, pp. 701–742.

[7] E. A. Patterson and Z. F. Wang, "Simultaneous observation of phase-stepped images for automated photoelasticity," J. Strain Anal. Eng. **33**, 1–15 (1998).

[8] R. Wimberger-Friedl, "The assessment of orientation, stress and density distributions in injection molded amorphous polymers by optical techniques," Prog. Polym. **20**, 369–401 (1995).

[9] W. Retting, "Generation and relaxation of the molecular orientation during hot-stretching of amorphour thermoplastics," Colloid Polym. **257**, 689–710 (1979).

[10] A. Uchiyama and T. Yatabe, "Molecular orientation of achromatic polycarbonates containing fluorene side chains by polarized infrared spectroscopy and birefringence analysis," J. Polym. Sci. B **41**, 1554–1562 (2003).

[11] S. L. B. Kramer, M. Mello, G. Ravichandran, and K. Bhattacharya, "Phase shifting full-field interferometric methods for determination of in-plane tensorial stress," Exp. Mech. **49**, 303–315 (2009).

Proceedings of the SEM Annual Conference
June 7-10, 2010 Indianapolis, Indiana USA

ESPI Measurements In the Presence of Large Lateral Displacements

Luke Bingleman and Gary S. Schajer

Dept. Mechanical Engineering, University of British Columbia
Vancouver, Canada, V6T 1Z4. email: schajer@mech.ubc.ca

Abstract

Electronic Speckle Pattern Interferometry (ESPI) provides a sensitive technique for measuring surface deformations. The technique involves comparison of the speckle phase angles within surface images measured before and after material deformation. This phase angle comparison requires that the speckle positions be consistent in all images. A lateral shift between images by just one pixel substantially degrades ESPI measurements, while a shift of two or more pixels typically causes complete decorrelation and compromises the measurement entirely. To prevent such lateral motions, the specimen and the optical system must be rigidly fixed. This requirement typically prevents use of the ESPI method in applications outside laboratories or where it is necessary to remove the specimen from the optical setup between ESPI measurements. Here, Digital Image Correlation (DIC) is used to track speckle motion caused by specimen displacement between ESPI measurements. The measured images can then be mathematically shifted to restore the original speckle locations, thereby recorrelating the ESPI measurements. Examples are presented where ESPI measurements are successfully made with specimen shifts over 60 pixels.

Introduction

Electronic speckle pattern interferometry (ESPI) is an interferometric technique commonly used for surface metrology. Some typical applications include surface deformation measurement [1,2], non-destructive testing [3], and vibration mode shape visualization [4].

In ESPI, light from a coherent laser source is split into two parts, recombined on the specimen surface and then imaged using a digital camera. The resulting interference pattern at the measured surface is modulated by the microscopic roughness of the surface to produce a random pattern of light and dark speckles. The intensity of each speckle depends on the local relative phase of the recombined light beams. The local phase at each pixel can be determined by phase stepping one of the component light beams [5]. The imaged surface is then displaced according to the measurement required, and the new pixel phase angles are then measured. The deformation of the measured surface is then determined from the phase changes at the measured pixels.

The quality of ESPI measurements critically depends on accurate registration of the speckle image sets measured before and after the surface deformation. The speckles are randomly distributed, so neighboring speckles have randomly different local phases [6]. Thus, each speckle within the initial and subsequent image sets must accurately correspond, else random phase differences will appear and create substantial noise in the measurements. A mis-registration of just one or two pixels moves the measurements away from their original speckles, causing decorrelation of the image sets and complete loss of the surface displacement measurement. Thus, ESPI equipment must be rigidly built and used in carefully controlled conditions. This requirement seriously limits the practical application of ESPI measurements, and makes field applications very challenging.

The decorrelation that occurs when speckle images are shifted corrupts but does not destroy the available phase data. When a measured surface moves, the speckle pattern associated with the microscopic roughness on its surface similarly moves [7]. Thus, if the speckle pattern is mathematically returned to its original position, it can be re-correlated with the original speckle image. This concept, suggested by Reu and Hansche [8], is explored in this paper. Digital Image Correlation (DIC) is used to determine the motion of a speckle pattern between successive measurements, and the measured images are then mathematically shifted to return them to their original pixel registration. This process enables useful ESPI measurements to be made under field conditions when individual components are not rigidly fixed. Some components could be removed and imperfectly replaced, etc. This paper explores the speckle correlation technique and shows how it can successfully retrieve useful ESPI measurements with displacements over 60 pixels.

T. Proulx (ed.), *Application of Imaging Techniques to Mechanics of Materials and Structures, Volume 4*, Conference Proceedings of the Society for Experimental Mechanics Series 14, DOI 10.1007/978-1-4419-9796-8_22, © The Society for Experimental Mechanics, Inc. 2013

Proposed ESPI Pixel Recorrelation Method

Figure 1 shows the apparatus used in this study. A beam splitter divides the light from a coherent laser source into two beams, a reference beam and an illumination beam. These beams reflect on mirrors and subsequently combine on the specimen surface to create a speckle pattern such as illustrated in Figure 2.

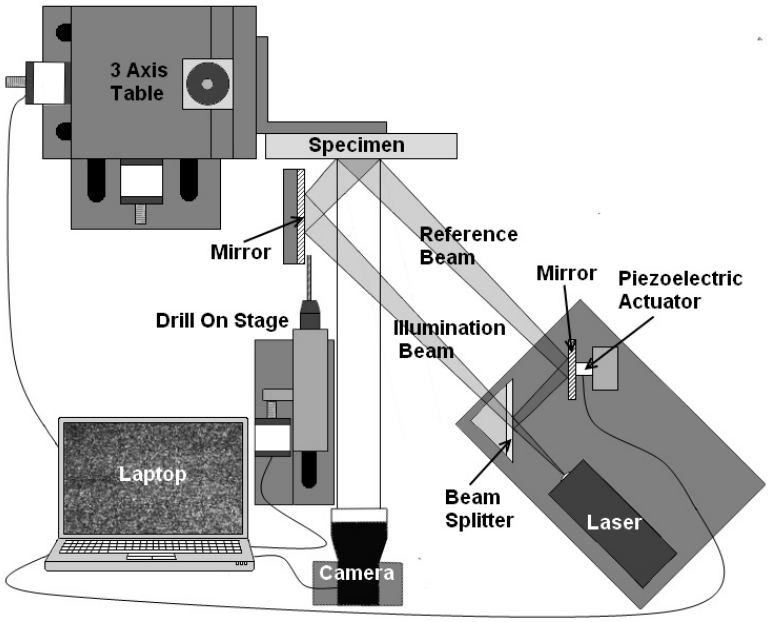

Figure 1. Experimental hole drilling apparatus.

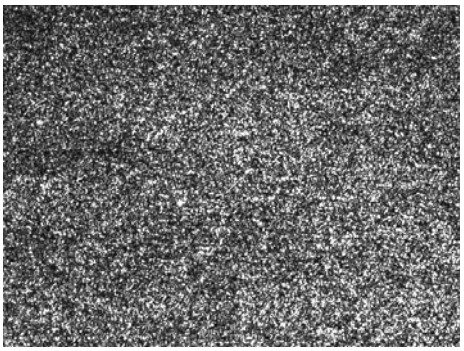

Figure 2. Typical ESPI speckle pattern.

The measured light intensity I at a measured point on the specimen surface depends on the local intensities I_i and I_r and relative phase ϕ of the illumination and reference beams:

$$I = I_i + I_r - 2\sqrt{I_i I_r}\cos\phi \tag{1}$$

The individual beam intensities I_i and I_r are not generally of interest, and Equation (1) can be simplified to:

$$I = A + B\cos\phi \tag{2}$$

where $A = I_i + I_r$ and $B = -2\sqrt{I_i I_r}$.

Motion of the specimen surface alters the relative phase, ϕ. For the optical arrangement shown in Figure 1, ϕ is sensitive to in-plane displacements.

The values of A, B and ϕ can be determined at each pixel by measuring a set of four surface images with the reference beam phase shifted using the piezo-actuator shown in Figure 1 in steps of 90°. The relative phase is [1]:

$$\phi = \frac{I_4 - I_2}{I_1 - I_3} \tag{3}$$

where I_1, I_2, I_3 and I_4 are the light intensities measured at a given pixel within each of the four stepped images. If the measured surface displaces, the motion causes a change in the local relative phase ϕ. This motion can be determined by evaluating the change in relative phases ϕ measured at each pixel before and after the motion.

The local relative phase ϕ varies randomly among adjacent speckles within Figure 2. Thus, to achieve a reliable displacement size evaluation, it is essential that the phase angles measured before and after the motion refer to the same point within each speckle. If there is any mis-registration of the pixels, measurements will refer to different speckles, thereby introducing random noise into the measurements. A mis-registration of more than

one or two pixels introduces noise within the phase angle evaluations greater than π radians, causing decorrelation of the image sets and complete loss of the surface displacement measurement.

In practice, specimen displacements can occur because of optical equipment vibrations and relative motions. To minimize such displacements, the specimen and all optical equipment are typically kept firmly attached to a vibration-isolated optical table. However, it is often needed to work in much less controlled environments or to remove the specimen temporarily to do some other processing. Unfortunately, such non-ideal conditions can introduce serious phase noise or even complete image decorrelation.

The method proposed here aims to address the problem of speckle decorrelation in ESPI measurements caused by specimen motion between measurements. The procedure is based on the observation that the shape of the speckle pattern depends of the microscopic roughness of the specimen surface. When the surface displaces, the pattern of surface roughness moves with the surface, thereby similarly displacing the speckle pattern [7]. The displacement of the speckle pattern can be determined using Digital Image Correlation [9]. This displacement can then be subtracted mathematically to give "corrected" speckle measurements that accurately correspond to the initial speckle measurements, thereby greatly reducing measurement noise.

DIC is a well-established technique for monitoring surface motions [9]. It works by tracking the motion of corresponding features in successive images of the specimen surface. Such features can be the natural texture of the measured surface, or commonly, a random speckle pattern painted on the surface. In its simplest form, DIC involves correlating small areas ("patches") of two measured images and monitoring the correlation coefficient as one patch is shifted relative to the other. The local displacement is determined by finding the patch displacement that gives the maximum correlation. Figure 3 schematically illustrates this process. Interpolation techniques have been developed that can give displacement estimates within 0.02 of a pixel. The quality of the displacement estimate depends on the presence of distinctive features in the measured images and on the patch size. In general, large patch sizes give more accurate displacement evaluations, but require longer computation times and give lower spatial resolution.

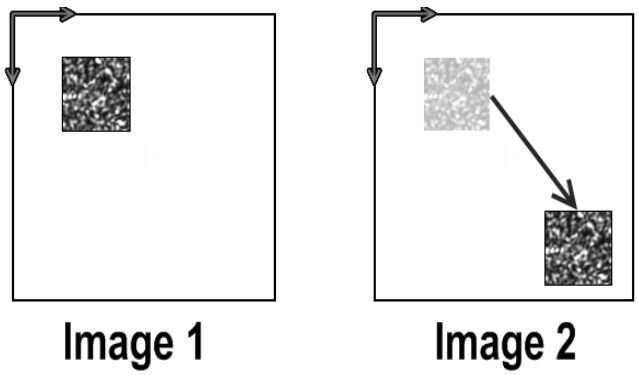

Figure 3. Digital image correlation using patches.

In typical DIC applications, the displacement variation throughout the entire measured area is required. This result is found by successively choosing image patches from within all parts of the measured area. Here, the concern is for bulk motions of the entire image. Thus, it is necessary to use only a small number of patches; at minimum just three are required to evaluate image x and y translations and image rotation. Here, the results from 18 widely spaced patches are used to provide data averaging.

Experimental Apparatus

Figure 1 schematically shows the experimental apparatus used here. Light from a 50mW JDS Uniphase laser, λ = 532nm, was split into two beams that were recombined on the specimen surface using the beam splitter and mirror arrangement shown in the diagram. A piezo-actuator behind one mirror enabled phase stepping of the reference beam. This optical arrangement provided measurement of the specimen displacement parallel to its surface, in the plane of the optical paths. This direction is described as the x-axis. The perpendicular direction within the specimen surface (perpendicular to the plane of Figure 1) is described as the y-axis. The specimen surface was viewed using a Prosilica EC750 camera with a resolution of 640 pixels in the x-direction and 480 pixels in the y-direction. The specimen was 6061 aluminum, mounted to a Daedal 3-axis table to provide controlled displacements. An NSK model EMS-3041 high-speed electric drill, fitted with a 3/32" two-fluted endmill and mounted on a Newport CMA-25CCCL stage was used to drill small holes in the test specimen. This drill was used in some tests to provide surface displacements in the specimen and distinctive ESPI fringe patterns. The equipment was computer controlled using custom software. The entire apparatus was mounted on a vibration-isolated optical table contained within a closed cabinet to minimize thermal disturbances due to air currents.

ESPI Decorrelation

The ESPI equipment shown in Figure 1 was originally constructed for making hole-drilling residual stress measurements [10,11]. This functionality is convenient for this study because it provides a means of creating distinctive ESPI fringe patterns and for evaluating the effectiveness of recorrelating shifted images using DIC. A first set of experiments was done using an aluminum specimen with large residual stresses in the y-direction. The surface was lightly sprayed with matte white paint to give a non-specular reflective surface. An initial set of phase-stepped images was measured to provide a reference phase map. Then, a 2.4mm (3/32") diameter hole was cut into the specimen, causing localized surface deformations. A further set of phase-stepped images was measured, from which the distinctive fringe pattern shown in Figure 4(a) was made by subtracting the reference phase map. The contrast in this image is typical for ESPI measurements, with well-defined fringes within a slightly noisy background. After making the measurements required for Figure 4(a), the specimen was displaced to the right (positive x-direction) by 15μm in the using the 3-axis table. This distance corresponds to approximately 1 pixel in the measured image. A further set of phase-stepped images was measured, from which the original reference phase map was subtracted to give the fringe pattern shown in Figure 4(b). The effect of pixel mis-registration is very evident, with much reduced image contrast and greatly increased background noise. Figure 4(c) shows the fringe pattern obtained after a further 15μm specimen displacement to the right. The narrow vertical line drawn at the right of the image is 2 pixels wide, corresponding to the specimen displacement. This 2-pixel displacement causes complete decorrelation of the images and complete loss of fringe visibility.

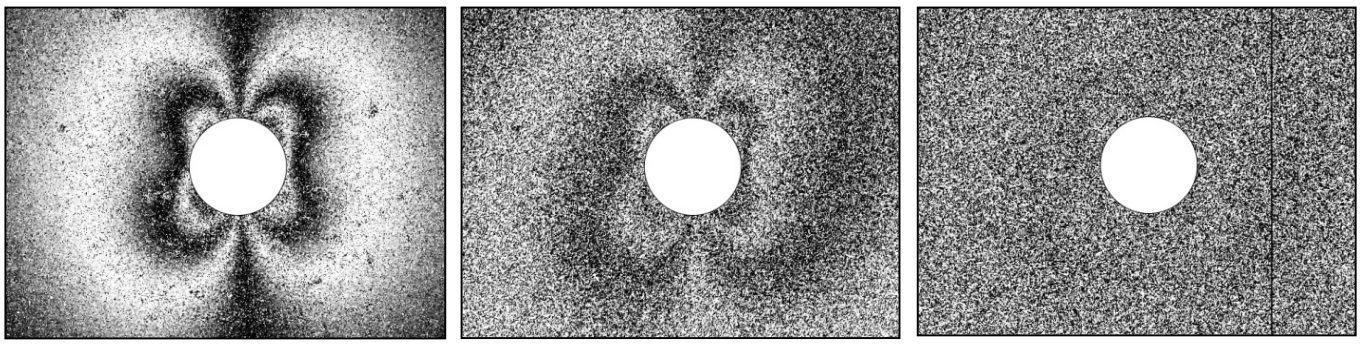

Figure 4. ESPI fringes measured after hole drilling: (a) with no surface displacement, (b) with 15μm (1 pixel) surface displacement, (c) with 30μm (2 pixel) surface displacement.

Phase Independent DIC

Commonly, DIC is used with images of objects that have fixed surface features, either naturally occurring or deliberately applied. These surface features move with the bulk of the object and maintain their shape and optical contrast during the motion. Laser speckles are caused by microscopic surface irregularities, and also move with the bulk of the object [7]. However, the speckles are not "fixed" in the same way as surface features. Their appearance also depends on the optical configuration, particularly the relative phase of the illumination and reference beams. In practice, small thermal fluctuations create drifts in the effective path lengths of these beams, causing slow changes of their relative phase at the specimen surface. At one moment, a speckle could appear bright because the two beams happen to be in phase at that point ($\phi = 0$ in eq. 2). At a later moment, after some drift has occurred, the two beams may be out-of-phase ($\phi = \pi$ in eq. 2), causing the speckle to appear dark. This effect can be seen in practical measurements, where speckle patterns slowly "evolve", with light areas becoming dark, and vice-versa.

The continuous variations in speckle pattern caused by phase drift impair the application of DIC. However, this phase dependence can be mitigated by working with data from all four available ESPI images rather than from just one. In Equation 2, the phase dependent part is the angle ϕ; constants A and B are phase-independent. These represent the mean illumination and the modulation at the given pixel. It is proposed here to do DIC analysis using "images" of A or B instead of the individual measured images. For phase stepping in four equal steps of 90°, A and B can be determined from the intensities I_1, I_2, I_3 and I_4 measured at a given pixel.

$$A = \frac{I_1 + I_2 + I_3 + I_4}{4} \qquad B = \frac{\sqrt{(I_4 - I_2)^2 + (I_3 - I_1)^2}}{2} \tag{4}$$

Statistical tests of DIC capabilities were done on an example specimen mechanically displaced by eighteen 0.1mm increments up to 1.8mm. Sets of four stepped ESPI images were measured after each displacement. For the magnification used, a 0.1mm displacement corresponded to 6.1 pixels. DIC evaluations of the image displacement were done at one hundred 50x50 pixel patches in a 10x10 grid spanning the images. The standard deviations of these DIC evaluations and the average correlation coefficients R^2 within the patches gave indications of the statistical quality of the results.

Figure 5 shows the standard deviation of the DIC displacement estimates vs. amount of image shift. A lower standard deviation indicates less statistical uncertainty and hence greater expected computational precision. In general, the standard deviation increases with image shift, indicating that the speckle pattern does not simply translate, as would happen with images of displaced physical surface features. ESPI speckle patterns from displaced surfaces slowly change due to differences in the illumination at different points in space.

The lowest of the four lines in Figure 5 shows the DIC results using the constant A from Equation 4. The adjacent bold line shows the results from the B image, which are comparable to the A results but deteriorate at higher image shifts. The “Min. Image” and “Max. Image” lines respectively show the minimum and maximum standard deviations observed among the 16 possible combinations of four initial stepped images with four final stepped images. The “Min. Image” results derive from the ESPI images that happen to be in phase, and give results similar to those from the “A” images. However, it is not known in advance which particular ESPI images are in phase. Thus, it would be necessary to test all image combinations to find them, which is not a very practical procedure. The “Max. Image” curve represents case when the chosen images are out of phase, and thus are poorly correlated. The large “Max. Image standard deviations at small image shifts occur because the speckle patterns remain mostly intact in this range, and so adverse relative phase has a large effect. At larger image shifts, the speckle patterns become distorted, and so the additional distortion caused by adverse phase is no longer so influential.

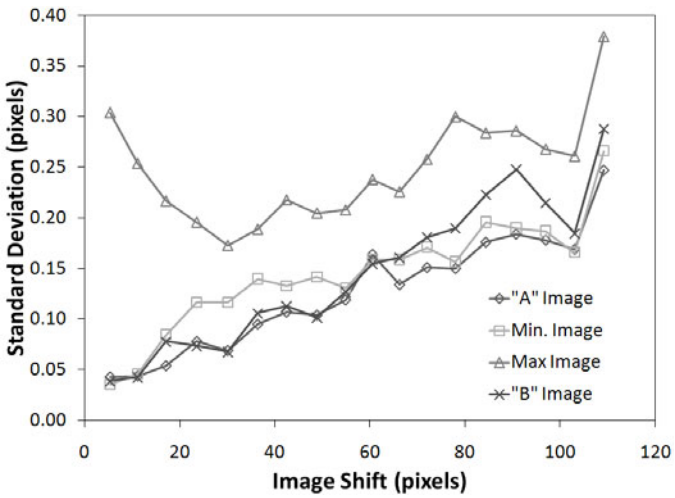

Figure 5. Standard deviation of DIC displacement estimates vs. amount of image shift.

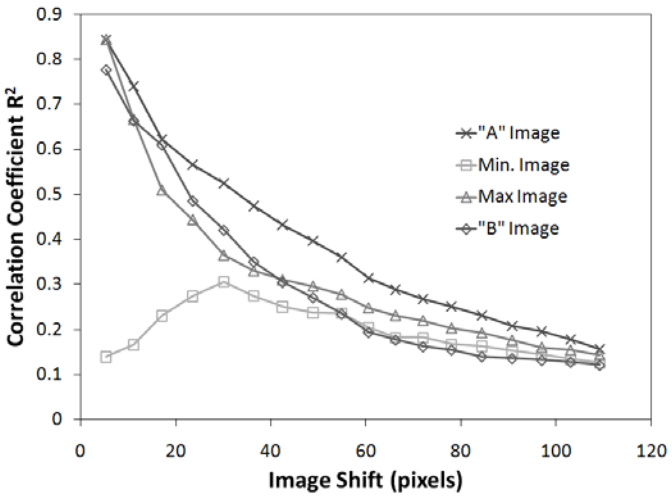

Figure 6. Average correlation coefficient R^2 vs. amount of image shift.

Figure 6 shows the average correlation coefficient R^2 for the same correlation patches as in Figure 5. Higher R^2 is desirable, and thus the trends in Figure 6 support the conclusions from Figure 5. The correlations decrease with amount of image shift, showing the changes in speckle patterns with surface displacement. The R^2 values are much lower than the range 0.95 to 0.99 typically achieved with images of physical surface features. This lower correlation occurs because speckle patterns respond to local changes in illumination as well as to surface displacements. Images “A” in Figure 6 achieve the best (highest) correlation coefficients; images “B” and the raw ESPI images are consistently lower. Thus, based on both Figures 5 and 6, the general use of “A” images for DIC analysis is indicated.

ESPI Recorrelation Using DIC

A further set of experiments was done to explore how well ESPI speckle correlation can be restored by mathematically shifting ESPI images of a displaced plane surface back to their original positions as indicated by DIC. To simplify the procedure, the measurements were done using a plain specimen without any hole drilling.

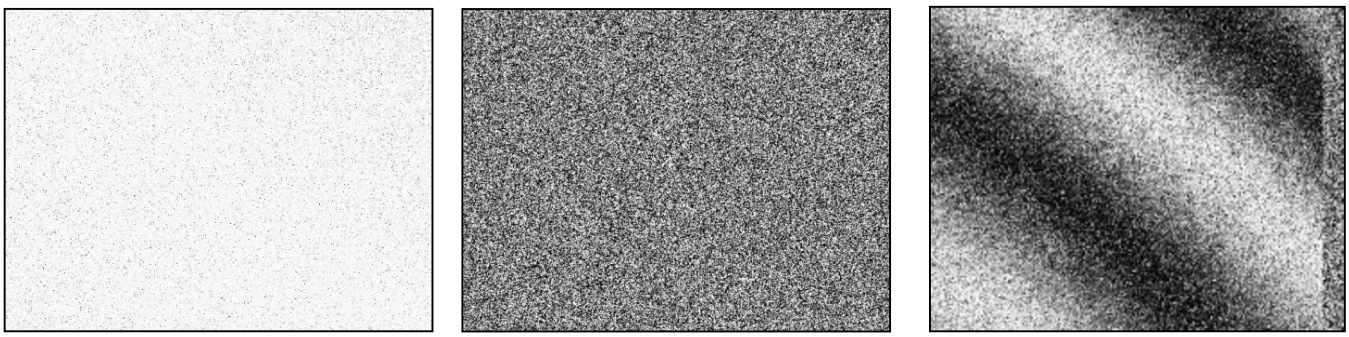

Figure 7. ESPI fringes on an undeformed surface: (a) with no surface displacement, (b) uncorrelated by 0.5mm surface displacement to right, (c) recorrelated after mathematically shifting ESPI images.

Figure 7(a) shows the measured ESPI fringe pattern for the undisplaced plane surface. Here, the second set of phase-stepped images was taken immediately after the reference set, producing a null ESPI fringe pattern with only a small texture due to signal noise. The specimen was then displaced to the right by 0.5mm and a third set of phase-stepped images was measured. The surface displacement caused the complete decorrelation shown in Figure 7(b). Using DIC analysis of the phase-stepped images, the displacement was evaluated as 31.2 pixels. The third set of phase-stepped images was then mathematically shifted 31.2 pixels to the left. Figure 7(c) shows the resulting ESPI fringes. The null fringe pattern seen in Figure 7(a) is successfully restored, but with increased noise and with a diagonal phase variation. The margin on the right side of the image corresponds to the image shift distance. It occurs because no data are available outside the original image to shift into this region.

A linear phase variation similar to that seen in Figure 7(c) was also observed by Reu and Hansche [8]. After some experimentation, it was discovered that this effect is due to asymmetry in the incidence angles of the illumination and reference beams in Figure 1 and the use of diverging illumination and reference beams. This beam divergence causes the wave fronts to be spherical rather than planar. Thus, changes in optical path lengths occur when a surface point displaces laterally. For symmetrical illumination, the optical path length changes are the same throughout the measured image, causing a general phase shift, but no fringes. For unsymmetrical illumination, a phase gradient is created. It may be shown by considering the optical path length changes that the phase difference across the width of the image is:

$$\Delta\phi = \frac{2\pi\, d\, D}{\lambda\, L} \sin(\theta_i + \theta_r)\, \sin(\theta_i - \theta_r) \tag{5}$$

where d is the surface shift distance, D is the surface width within the image, λ is the wavelength of the light source, L is the distance from the focus point of the light source to the illuminated surface, and θ_i and θ_r are the incidence angles of illumination and reference beams respectively. The asymmetry causing the difference between the two incidence angles in the present work was traced to non-perpendicularity of the mirror in Figure 1. This mirror was then adjusted so that the phase gradient artifact was minimized. A preferable adjustment choice would be to use parallel instead of diverging illumination. This would make distance “L” in Equation (5) infinite, and therefore should eliminate the sensitivity to angular asymmetry. This option was not available within the particular optical equipment used here, and so could not be tested.

After mirror adjustment, a further exploration was undertaken using both horizontal and vertical surface displacements. Figure 8 shows the restored ESPI fringe patterns achieved after surface displacements up to 0.8mm (50.4 pixels). Even at the largest displacements, the ESPI fringe patterns are restored with good contrast and tolerable noise. This is a remarkable result for such large displacements. The size of the displacements involved can be seen by the width of the unrestored margins at the edges of the various images. The phase gradient artifact seen in Figure 7(c) has been mostly eliminated.

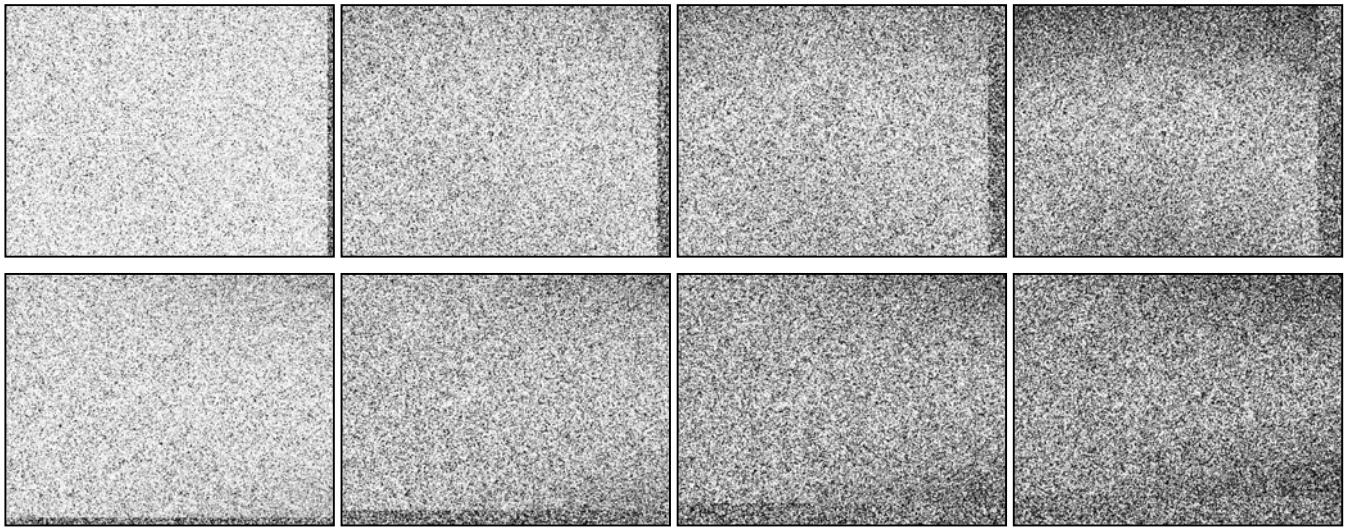

0.2mm (12.9 pixels) 0.4mm (25.5 pixels) 0.6mm (37.6 pixels) 0.8mm (50.4 pixels)

Figure 8. ESPI fringe patterns restored after surface displacement: horizontal displacements in upper row, vertical displacements in lower row.

Example Application

In cases where the absolute phase is desired within a measured ESPI phase map, the phase gradient artifact presents difficulties, and so parallel illumination is essential. However, in many practical applications, the local phase variations within the image are of specific interest, not the absolute phase values. An example of this type is the hole-drilling residual stress measurement illustrated in Figure 4. For this application, the displacements and corresponding phase changes around the hole are the particular interest because the far-field data should diminish to zero. Thus, in this case, it is possible to do a least-squares analysis of the far-field data to find the best-fit bi-linear fit. This result can then be subtracted from the pixel phases to give a zero far field. This technique was applied to the hole-drilling residual stress measurements illustrated in Figure 4. Figure 9(a) reproduces the ESPI fringes measured with no surface displacement, originally shown in Figure 4(a). The specimen was then displaced to the right by 1mm, and new ESPI measurements made. DIC was then applied to the speckle images to determine the image shift (64.5 pixels) and the measured images were mathematically shifted to the left by that amount. Figure 9(b) shows the resulting fringe pattern. The far-field phase gradient was estimated by the least-squares method using pixels chosen far from the central hole, and then subtracted from the fringe pattern. Figure 9(c) shows the phase-corrected ESPI fringes. The resulting fringe pattern is very similar to the undisplaced fringe pattern in Figure 9(a), with the band of uncorrelated data on the right remaining from the image shifting process.

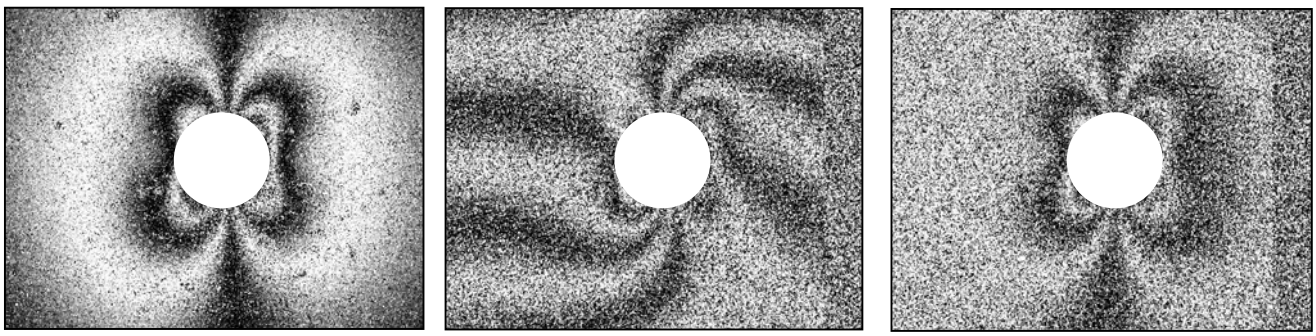

Figure 9. ESPI fringes measured after hole drilling: (a) with no surface displacement, (b) corrected for 1mm surface displacement, (c) after phase gradient subtraction.

As a further test of the utility of the restored ESPI fringes in Figure 10(c), the phase data were applied to their original purpose, the measurement of the in-plane residual stresses σ_x, σ_y and τ_{xy}. Figure 10 shows the results of residual stress calculations using the full-field data [12]. The horizontal lines indicate the stresses calculated from the undisplaced data in Figure 9(a). The three data curves show the stresses calculated from restored data exemplified by Figure 10(c), for a range of specimen displacements is up to 2.5mm in the positive x direction. Figure 10 shows that good residual stress evaluations can be made with specimen displacements up to 1mm (64.5 pixels), and useful but less accurate evaluations can be made with specimen displacement up to 2mm (127.7 pixels). These are substantial displacements compared with the 2.4mm diameter of the drilled hole. The deteriorating stress evaluation capability is caused by the increased noise in the ESPI fringes, as exemplified in Figure 8. The residual stress calculation is fairly tolerant of such noise because it involves substantial averaging of the full-field data.

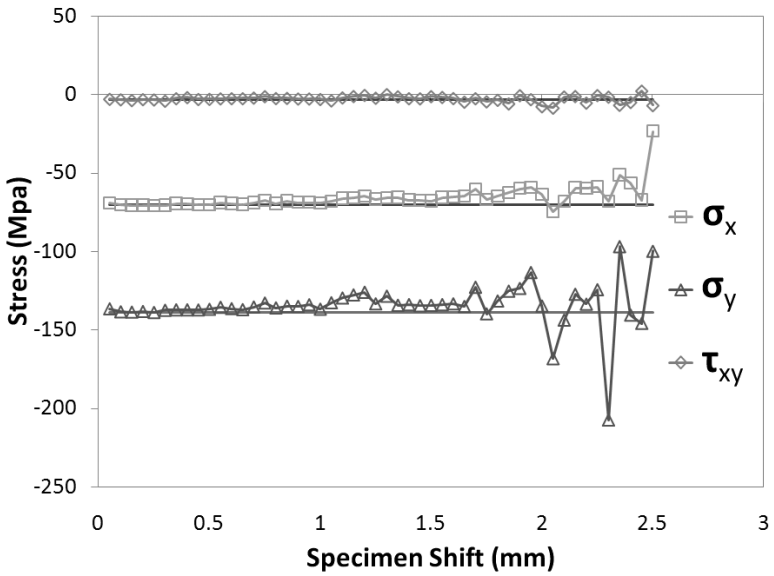

Figure 10. Calculated residual stresses vs. specimen displacement.

Conclusions

In conventional ESPI measurements, gross displacements of the optical equipment or specimen substantially impair the correlation of the initial and subsequent ESPI images and can degrade or entirely destroy the associated phase results. Thus, ESPI measurements are typically done within well-controlled laboratory environments to minimize such displacements. Field applications are feasible, but it is a much more challenging task to get high quality data. The method described here uses Digital Image Correlation to determine the amount of image displacement that may exist between ESPI measurements, then mathematically shifts the images back to their original registration. This process recorrelates the ESPI data and enables effective ESPI measurements to be made, even in the presence of large surface displacements. In conventional measurements, a 2-pixel displacement is sufficient to decorrelate ESPI images. Here, it is shown that displacements over 60 pixels can be reversed mathematically to provide useful ESPI results.

Laser speckle images present significant challenges for Digital Image Correlation. The pattern of laser speckles depends not only on the topology of the measured surface, but also on the illumination conditions, notably the local phase relationship of the illumination and reference beams. As the relative phase changes, speckles change between appearing either bright or dark, thereby confusing the image correlation. This phase dependence can be mitigated by creating phase-independent data for the DIC analysis. Here, the average intensity within a set of phase-stepped images, represented by constant A in Equation 2, was found to be effective.

Local irregularities within the laser light beam cause the speckle pattern to change gradually as it is displaced. Thus, the quality of mathematically restored ESPI phase maps deteriorates with increasing surface

displacement. Phase noise increases, causing increasingly grainy ESPI fringe images. A further phase gradient artifact occurs when the optical setup is not perfectly symmetrical and where the illumination beams are not parallel. Ideally, this artifact should be eliminated by correcting asymmetries or by using parallel illumination beams. However, even without such adjustments, in many cases it is possible to eliminate the phase gradient artifact mathematically. Such correction is demonstrated here where residual stress measurements by the ESPI hole-drilling method were successfully made from data from a surface that had been displaced over 60 pixels.

Acknowledgments

The authors sincerely thank American Stress Technologies, Cheswick, PA, and the Natural Sciences and Engineering Research Council of Canada (NSERC) for their financial support of this research.

References

1. Sirohi, R.S., ed., Speckle Metrology. Dekker, New York, (1993).
2. Shchepinov, V. P. and Pisarev, V. S., Strain and Stress Analysis by Holographic and Speckle Interferometry, Wiley, Chichester, (1996).
3. Erf, R. K., Holographic Nondestructive Testing, Academic Press, (1974).
4. Williams, D. C., ed., Optical Methods in Engineering Metrology, Chapman and Hall, London, (1993).
5. Robinson, D. W. and Reid, G. T. Interferogram Analysis; Digital Fringe Pattern Measurement Techniques, IOP Publishing, Bristol, (1993).
6. Goodman, J. W., Statistical Properties of Laser Speckle Patterns, in: Laser Speckle and Related Phenomena, Dainty, J. C., ed., Springer, New York, (1975).
7. Cloud, G. L., Optical Methods of Engineering Analysis, Cambridge University Press, Cambridge, (1998).
8. Reu, P.L, and Hansche, B.D., Digital Image Correlation combined with Electronic Speckle Pattern Interferometry for 3D Deformation Measurement in Small Samples, Proc. SEM Annual Conference & Exposition, St. Louis, MO, USA, June 4-7, (2006).
9. Sutton, M.A., Digital Image Correlation for Shape and Deformation Measurements, Springer, New York, (2008).
10. An, Y. and Schajer, G.S. Residual Stress Determination Using Cross-Slitting and Dual-Axis ESPI, Experimental Mechanics, Vol. 50, No.2, 169–177, (2010).
11. Steinzig, M., Ponslet, E., Residual Stress Measurement Using the Hole Drilling Method and Laser Speckle Interferometry: Part 1, Experimental Techniques, Vol.27, No.3, 43-46, (2003).
12. Schajer, G.S., Steinzig, M., Full-field Calculation of Hole Drilling Residual Stresses from Electronic Speckle Pattern Interferometry Data, Experimental Mechanics Vol.45, No.6, 526-532, (2005).

Proceedings of the SEM Annual Conference
June 7-10, 2010 Indianapolis, Indiana USA

Micron-scale Residual Stress Measurement using Micro-hole Drilling and Digital Image Correlation

B. Winiarski and P. J. Withers

School of Materials, University of Manchester, Grosvenor Street, M1 7HS, Manchester, UK
b.winiarski@manchester.ac.uk

Abstract

This paper reports a new technique, namely the incremental micro-hole-drilling method (IμHD), for measurement of residual stress profiles as a function of depth. Like its macroscale counterpart, it is applicable to either crystalline or amorphous materials, but at the sub-micron scale. Our method involves micro-hole milling using the focused ion beam (FIB) of a dual beam FEGSEM/FIB microscope. The surface displacements are recorded by digital image correlation of SEM images recorded during milling. The displacement fields recorded around the hole are used to reconstruct the stress profile as a function of depth. In this way residual stresses have been characterised around drilled holes of 4 microns or so, enabling the profiling of the stress variation at the sub-micron scale to a depth of 4 microns. An average -800 MPa $\pm$ 90 MPa was identified approximately 15° to the specimen length and -600MPa$\pm$ 90 MPa perpendicular to it. The new method is used to estimate the stresses in a (peened) surface-severe-plastically-deformed (S^2PD) $Zr_{50}Cu_{40}Al_{10}$ (in atomic percent, at.%) bulk metallic glass.

Keywords: Scanning electron microscopy (SEM), Focused Ion Beam, High magnifications, 2D digital image correlation, Surface decoration methods, Residual stress, Submicron scale

1. Introduction

Residual stresses arise in most materials as a consequence of processing and/or in-service loading. Depending on their sign, magnitude, spatial distribution, and the scale over which they equilibrate, residual stresses can alter the mechanical and functional performance [1]. Consequently their quantification is of great importance across many sectors. Whilst there exists a plethora of techniques for measuring stress at the macroscale, few techniques are available at the micron scale, either laterally or with depth, especially for amorphous materials.

In theory, destructive and semi-destructive techniques based on mechanical relaxation phenomena, such as slitting [2], hole/core drilling [3-5] and curvature methods [6] can be scaled down and applied to smaller structures [7-11] than those to which they have been applied to-date. The advent of dual beam focused ion beam – field emission gun scanning electron microscopes (FIB-FEGSEM) has, in combination with digital image correlation (DIC) analysis, made it possible to make very fine excisions and to record the resulting displacements with high precision. Recently, this has led to a number of micro-scale analogues of the mechanical stress measurement methods. For example, 10 μm deep 10 × 0.5 μm slots have been used to measure the stresses in a amorphous diamond-like carbon coating [8], while stresses have been mapped at the micron scale in bulk metallic glasses using an array of such slots [12]. This method provides a measure of the stress normal to the slot averaged over the slot depth. Depth profiling has been achieved by monitoring beam deflection of micro-cantilevers as they are progressively milled [13]. However, for stress mapping it requires excavation of large micro-cantilevers (length of 100 μm or more). Essentially both methods are based on 1-D analyses allowing only a single component of stress to be determined, with lateral spatial resolutions of many tens of microns.

A FIB microscope is capable of milling holes having diameters of tens of nanometers. Consequently, if the displacement measurement technique can be improved further improvments in the minaturisation of the technique may be possible. The reliability of displacement/strain analysis of DIC-based measurement techniques when applied to FIB-based micro-hole milling strongly depends on the surface contrast. Since image correlation software compares gray-scale maps/patches, it is preferable that the digital images are characterised by random, high contrast features [14, 15]. At the macro-scale this can be achieved by polishing, etching, painting, etc. [16]. However at the micron-scale either the FIB must be used to apply markers (both ion and electron beam assisted deposition of metals e.g. Pt, W, Fe, Co, Au), or other surface decoration methods can be applied [12, 17, 18].

T. Proulx (ed.), *Application of Imaging Techniques to Mechanics of Materials and Structures, Volume 4*, Conference Proceedings of the Society for Experimental Mechanics Series 14, DOI 10.1007/978-1-4419-9796-8_23, © The Society for Experimental Mechanics, Inc. 2013

We demonstrate a new experimental technique, namely the incremental micro-hole-milling method (IμHM), for local measurement of in-depth profiles of principal residual-stresses in either crystalline or amorphous materials. Our incremental method is similar to the microhole drilling method proposed by Vogel et al. [11, 19], but can provide stress-depth profiles. It combines FIB micro-hole milling with two-dimensional (2-D) finite-element analysis (FEA) based on the hole geometry to model the resulting relaxation displacements on the specimen surface, as determined by DIC analysis. This method has the advantages that a) holes can be very compact providing excellent lateral spatial resolution, b) small holes are relatively straightforward to drill, c) it provides the full in-plane stress tensor and d) it is suitable for incremental hole drilling thereby providing good depth resolution. The challenge however is to measure the associated surface displacements which are much smaller than the previously applied techniques mentioned above. Our approach adapts the Unit Pulse Method (UPM) [4, 20] combined with a Thikonov regularisation scheme [21] and uses full-field radial displacement data for each hole-depth increment, from which the associated residual-stress profile is inferred. In this manner the method is appropriate for the estimation of highly non-uniform residual stress distributions and allows for stable residual-stress solution even when the small increments of depth are selected near to, or far from, the material surface. This new method is used to drill 4 μm holes to estimate the residual-stresses profiles with a z-resolution of ~ 200 nm and a lateral resolution of around 10 μm in a surface-severe-plastically-deformed bulk metallic glass (BMG) system.

2. Materials and Methods

2.1. Sample preparation

The Zr-based $Zr_{50}Cu_{40}Al_{10}$ (atm%) BMG was prepared by arc-melting a mixture of pure zirconium, copper, and aluminium melts (purity better then 99.9% by weight) in an argon atmosphere. A tilt-casting method was implemented to cast the alloy to its final rod shape of 60 mm and diameter of 8 mm. The rod sample was cut to a rectangular bar of 3 × 3 × 25 mm^3 and, then, polished using the 600-grit grinding paper.

Subsequently, one side of the specimen was repeatedly bombarded in an argon atmosphere with twenty WC/Co balls, each having a diameter of 1.6 mm, using a Spex 8000 miller in a back-to-force mode with a frequency of 60 Hz. The bombardment process lasted for 180 minutes pausing every 15 minutes. This surface-severe-plastic-deformation (S^2PD) process has a much higher average impact energy than the shot-peening process, thereby generating a severely-deformed near-surface layer in the BMG at room temperature [22].

To enhance the accuracy of the DIC analysis, the specimen surface is decorated with 20 – 30 nm yttria-stabilized-zirconia (YSZ) equi-axed particles precipitated from an ethanol suspension (see Fig. 1), where the surface coverage is about 10%. To minimise any surface charging effects and to 'protect' the surface from Ga^+ implantation, the surface of the specimen was coated with a 22 nm thick carbon film using a Gatan PECS 682 etching-coating system equipped with a Gatan 681.20000 Thickness Meter. This decoration technique allowed us to work at magnifications of 10,000× in FEGSEM mode viewing a surface area of tens of square microns [18].

2.2. Experimental procedure

The two main features that contribute to the accuracy of DIC measurements of surface deformations are the presence of a fine and high-contrast surface texture, and the use of large correlation patch sizes [16, 23]. However, the accuracy of displacement/strain mapping may be significantly impaired if the imaging parameters of the SEM/FIB microscope, namely voltage, current, dwell time, detection of secondary electrons (SE) or back-scattered electrons (BE), secondary ions (SI+), digital image resolution, etc., are suboptimal [24, 25].

A series of FEGSEM imaging trials was performed to find optimal imaging conditions for DIC analysis. The control parameter chosen for minimisation was the uncertainty of the DIC displacement (standard deviation of the displacement (SD_u)) mapped over the whole area of images (here 1015 data points). It was found that an electron beam (e-beam) acceleration voltage of 5 kV, with beam current 0.40 nA, and detection of secondary electrons gives good contrast images with negligible charging of the sample surface. Later, different e-beam dwell times (Dt) (Dt of 1 μs, 3 μs, 10 μs and 30 μs) and image acquisition conditions (image integration over 1, 4, 8 and 16 frames) are analysed. All images were acquired after an auto-brightness/auto-contrast procedure. It was found that an e-beam dwell time of 3 μs and an integration over 8 frames (total image acquisition time = 21.7 s) gave the lowest SD_u equal to 0.0147 pixel for DIC patches of 64×64 pixels overlapped by 75%.

An inherent feature of the FIB-milling process is material redeposition such that the milled walls are not perfectly rectangular, especially when milling deep holes or narrow slits. To limit such effects the FIB-milled hole should be shallow. A diameter to depth ratio less than one is thus well matched to the inherent limitations associated with hole-milling experiments, where the magnitude of the surface relaxations plateau as the contributions of stresses released at greather depths decline rapidly with the hole depth. In order to map the stress profile in a severely plastically peen deformed BMG at the location shown in Figure 1b, we have introduced a micro-hole of 2 μm radius to a depth of 1.8 μm (see Fig. 1a) in 10 depth increments. This was achieved using a focused Ga^+ ion beam of 280 nA accelerated by an electric field of 30 kV.

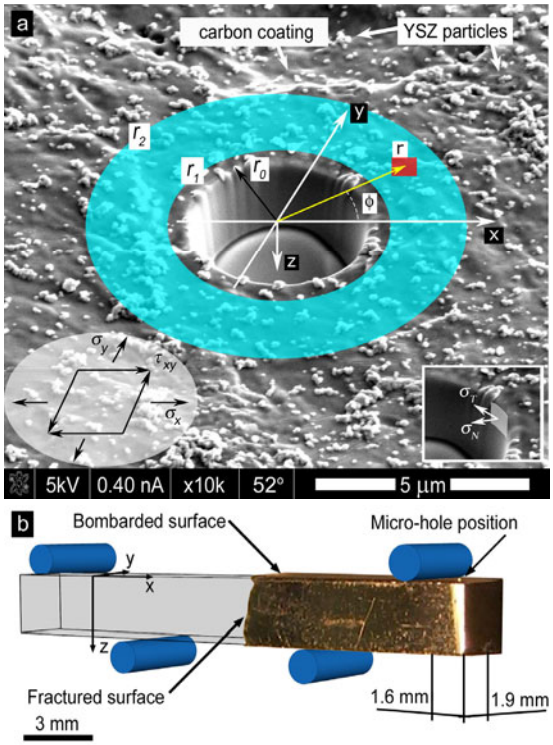

Figure 1. (a) FEGSEM image of the microhole of diameter $d = 4 \pm 0.07$ μm and depth, $z = 1.8 \pm 0.07$ μm; the surface is decorated with YSZ nano-particles and then carbon coated (b) general view showing fatigue test configuration and location of the micro-hole.

The surface displacements due to the stress relaxations were mapped from the FEGSEM images (these are of much higher quality and do little beam damage compared to Ion Beam images) at each increment using DIC software (LaVision DaVis 7.2) (see Fig. 2a). The DIC patches (64×64 pixels overlapped by 75%) covered the whole imaged area apart from the micro-hole and its immediate vicinity (within 0.7 μm), where some excavated material is redeposited. This area experiences the largest surface displacements, however the sputtered material significantly alters the surface contrast (see Fig. 2a) making DIC analysis unreliable there. Since the amplitude of the surface displacements decline rapidly from the hole edge only the region for which the signal-to-noise ratio is larger then 5, is taken into consideration. Accordingly, the analysed region is bounded by inner and outer radii $r_1 = 2.78$ μm ($r_0/r_1 \cong 0.7$) and $r_2 = 4.75$ μm ($r_0/r_2 \cong 0.4$) as shown in Fig. 2b where the maximum principal strains are mapped. It is evident from the surface displacements (Figs. 2c and d) that the state of in-plane compressive stress (since the displacements tend to close the hole) in the vicinlty of the micro-hole is non-uniform and varies harmonically around the hole. The largest compressive stress acts along the sample (x direction). Subsequently we show how these mapped displacements can be converted into stress profiles.

2.3. Stress Reconstruction Method

The analytical solution for the stress-strain state of a cylindrical hole in an isotropic material, where the stresses σ_N, σ_T and angle ϕ are the unknowns, was given by Muskhelishvili, who used the potential function of complex method [26]. Following an argument in [19], the three unknowns (σ_x, σ_y and τ_{xy}) can be determined from Eq. (1) using three values of the relieved displacements (U_I, U_{II} and U_{III}), each measured between two points, which are determined at the intersection of a circle of radius $r > r_0$ and a line crossing the centre of the hole, where the three lines are positioned at $\theta = 0°$, 45° and 90° (see Fig. 2b).

Digital image correlation data allows us to measure up to several hundred data points, therefore the calculation can be repeated for a number of radial ($r_0/r \cong 0.6$, 0.5 and 0.45) and angular ($0° < \theta + \phi < 180°$, $\Delta\phi \cong 5°$) positions. Thus relieved displacements can be expressed compactly in matrix form in terms of radial and angular position, as follows

$$\begin{bmatrix} U_I(r,\phi) \\ U_{II}(r,\phi) \\ U_{III}(r,\phi) \end{bmatrix} = \begin{bmatrix} A(r) & B(r) & 0 \\ A(r) & 0 & 2B(r) \\ A(r) & -B(r) & 0 \end{bmatrix} \begin{bmatrix} P \\ Q \\ T \end{bmatrix} \Rightarrow [U(r,\phi)] = [\Theta(r)][\Pi] \tag{1}$$

$$P = \sigma_x(\phi) + \sigma_y(\phi),\ Q = \sigma_x(\phi) - \sigma_y(\phi) \text{ and } T = 2\tau_{xy}(\phi) \tag{2}$$

where $U_I \cong 2u_N^{(0°+\phi)}$, $U_{II} \cong 2u_N^{(45°+\phi)}$, $U_{III} \cong 2u_N^{(90°+\phi)}$. Stresses $\sigma_x(\phi)$, $\sigma_y(\phi)$ and $\tau_{xy}(\phi)$ are calculated in local rectangular coordinates rotated ϕ degrees in the anti-clockwise direction (see Fig. 1a). Coefficients *A* and *B* are

the cumulative stress relaxation functions (CRFs) (for equi-biaxial and pure shear states of stress) either obtained by FEA[1], or from an experiment where a micro-hole is ion-milled into material with known residual stresses. Separate finite element calculations are required for the coefficients *A* and *B* for various combinations of hole depths and stress locations.

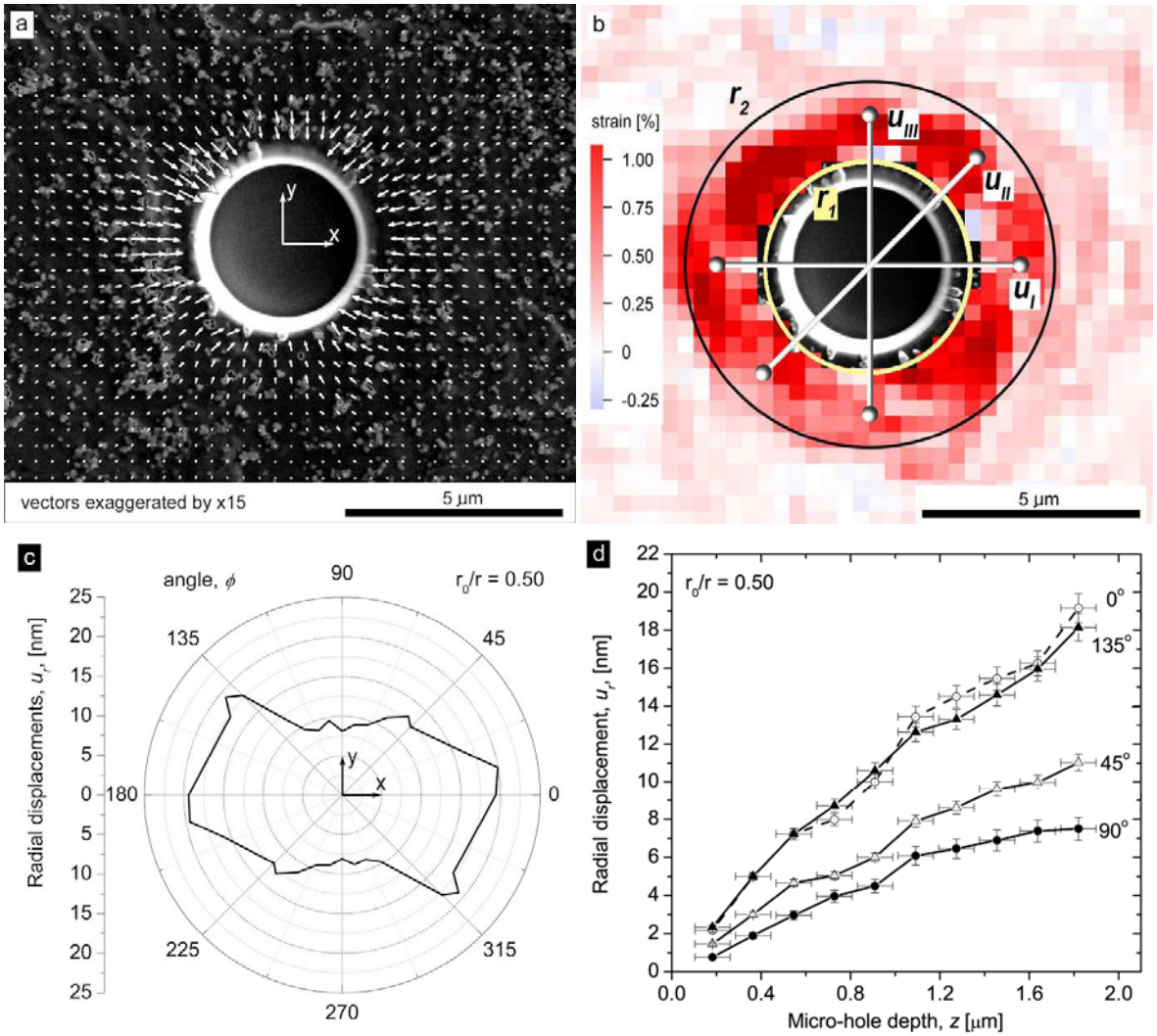

Figure 2. Digital image correlation analysis results for the final increment, $z = 1.8 \pm 0.07$ μm: (a) 2-D displacement vector field (vectors are exaggerated by ×10); (b) 2-D map of the maximum principal strains; (c) radial displacements, u_r, vs. angle, ϕ, measured at distance $r_0/r = 0.5$; (d) radial displacements, u_r, vs. hole depth, z, measured at distance $r_0/r = 0.5$ and angles, $\phi = 0°$, 45°, 90° and 135°.

A superposition argument [6] allowed us to calculate the calibration coefficients in a linear-elastic-isotropic[2] material ($E = 95 \pm$ GPa, and $\nu = 0.37$ [27]) directly using loadings where the reference residual stresses, for which associated deformations have simple trigonometric forms[3], are applied with opposite sign to the curved surface of the micro-hole [5]. The remaining surfaces of the FE models were unstressed. Our FE model was assembled using 8-node (quadratic approximation function) square-shape axisymmetric elements where the size of elements

[1] Abaqus 6.8 package was used.
[2] As a metallic glass material isotropy at this length-scale is justified.
[3] Asymmetric zeroth-harmonic radial displacement (for coefficient *A*) and symmetric second-harmonic radial and circumferential displacement (for coefficient *B*).

in the vicinity[4] of the hole was 1/30th the hole diameter. Equations in matrix form (1) are solved simultaneously for the residual stresses. By transforming the measured stresses into the global coordinates:

$$\begin{bmatrix} \hat{\sigma}_x \\ \hat{\sigma}_y \\ \hat{\tau}_{xy} \end{bmatrix} = \begin{bmatrix} \cos^2\phi & \sin^2\phi & -2\sin\phi\cos\phi \\ \sin^2\phi & \cos^2\phi & 2\sin\phi\cos\phi \\ \sin\phi\cos\phi & -\sin\phi\cos\phi & \cos^2\phi - \sin^2\phi \end{bmatrix} \begin{bmatrix} \sigma_x(\phi) \\ \sigma_y(\phi) \\ \tau_{xy}(\phi) \end{bmatrix} \tag{3}$$

we can estimate the three unknown stresses (σ_x, σ_y and τ_{xy}) by the mean stresses $\left(\overline{\sigma}_x,\ \overline{\sigma}_y,\ \overline{\tau}_{xy}\right)$ acting in the directions x and y (see Fig. 1a). We can extend the methodology presented above to reconstruct the residual-stress depth profiles using the Unit Pulse Method [1]. Equation (1) relates the measured displacements U to the equivalent uniform in-plane residual stress in the first depth-increment. Generalising to k depth-increments we obtain in compact form

$$\begin{bmatrix} U^{(1)} \\ U^{(2)} \\ \vdots \\ U^{(i)} \end{bmatrix} = \begin{bmatrix} \Theta_{11} & 0 & 0 & 0 \\ \Theta_{21} & \Theta_{22} & 0 & 0 \\ \vdots & \vdots & \ddots & 0 \\ \Theta_{i1} & \Theta_{i2} & \cdots & \Theta_{ii} \end{bmatrix} \begin{bmatrix} \Pi^{(1)} \\ \Pi^{(2)} \\ \vdots \\ \Pi^{(i)} \end{bmatrix} \Leftrightarrow \widehat{U}^{(i)} = \widehat{\Theta}_{ij}^{(i)} \widehat{\Pi}^{(i)} \tag{4}$$

where, for the sake of clarity we omitted terms (r) and (r,ϕ), e.g. $U^{(i)} \Leftrightarrow U^{(i)}(r,\phi)$. $U^{(i)}$ is a vector of the displacements components measured by DIC when the hole-depth is h_k; $\Pi^{(j)}$ is a vector of the uniform stress terms $P^{(i)}$, $Q^{(i)}$, $T^{(i)}$ acting in stress layer ΔH_j, lying between depths H_{j-1} and H_j; and $\Theta(h_i, \Delta H_j)$ is a matrix of the incremental calibration functions (ICFs) relating the relieved displacements to the uniform stress terms acting at depth H_j when the hole depth equals h_i. Following argument in [4] and if we know the CRFs obtained from FEA, the ICFs can be determined easily for any number and size of hole-depth increments by simple subtractions. We can obtain the desired solution of the stress variation with depth by inverting Eq. (4). We obtained a tentative solution (the linear operator equations) to Eq. (4) using pseudo-inversion. The three unknown stresses (σ_x, σ_y and τ_{xy}) for each hole-increment can then be estimated by the mean stresses ($\overline{\sigma}_x$, $\overline{\sigma}_y$ and $\overline{\tau}_{xy}$) acting in the directions x and y using similar relationships to Eqs. (2) and (3).

2.4. Regularisation

In practice data are a convolution of measurement noise and 'true data'. The pseudo-inversion algorithm yields stable residual stress solutions if the coefficients of the ICFs matrix are of the same order of magnitude. However, the incremental micron-hole milling processes expressed in mathematical terms using pulse functions produces relatively small matrix entries in the diagonal bands of the ICFs matrix. Thus, the linear operator equations for a large number of increments become numerically ill-conditioned and lead to unstable solutions, giving large oscillations of the residual stress solution with depth. These problems can be suppressed by careful selection of the hole-depths at which the residual stresses are calculated, which usually lead to in-depth stress profiles inferred using a reduced number of data points [28-30].

Alternatively in order to overcome the numerical ill-conditioning, to stabilise residual stress solution and reduce the noise amplification the linear operator equations can be mathematically modified. These equations are usually augumented using different variants of the well-known Thikonov regularisation method [21, 31-34]. This method states the problem of minimizing the square of the Euclidean norm of the residuals of the residual stress solution according to chosen strategy (*a priori* or *a posteriori*) of selecting the regularization parameter α. Since *a priori* methods require the definition of an additional unknown smoothness parameter, ν, [33] we used an *a posteriori* selection criteria following [21]. Within the adopted regularisation scheme we select the regularisation parameter, α, based on an estimate δ_{est}(r) of the measurement noise in the measured data $\widehat{U}^{(i)}$. The parameter α was choosen in such way that the Euclidean norm of regularised solution discrepancy is equal the discrepancy level in the measured data, δ, in our case the discrepancy in displacement measurement. Since the displacements are mapped at several radial positions ($\widehat{\Theta}_{ij}^{(i)}(r), r_0/r$ = 0.6, 0.5 and 0.45), thus the following procedure is repeated for each radial position:

---

[4] The vicinity of the hole is equal 6× the hole diameter in radial and hole depth directions.

(i) Estimate the error norm δ_{est}(r) of measured displacement vector $\overline{U}^{(i)}(r)$, which is given by $\delta_{est}(r) = \left\| \widehat{U}_{rnd}^{(i)} + \widehat{U}_{sys}^{(i)}(r) \right\|$. Here, $\widehat{U}_{rnd}^{(i)}$ is the random error vector obtained by replacing each element in $\overline{U}^{(i)}(r)$ by appropriate random error value from Table 1, and $\widehat{U}_{sys}^{(i)}$ is the systematic error vector obtained by taking the appropriate percentage value from Table 1 of each element in $\overline{U}^{(i)}(r)$. The elements of vector $\overline{U}^{(i)}(r)$ are calculated as follows an average value of four angular positions ϕ = 0, 45, 90 and 135°. The random error is calculated as the standard deviation of DIC displacement of the evaluated sets of 1015 *x* and *y* displacements. Whereas the systematic error is is the scatter in displacement measurement using different patch sizes and different patch overlap (OV): 32×32 pixels OV by 25%, 64×64 pixels OV by 25%, 64×64 pixels OV by 50%, 64×64 pixels OV by 75%; which in this case is ± 4 % of the measured value.

Table 1. Estimated DIC analysis accuracy

Component	Random error	Systematic error
u_N	0.36 nm (0.0147 pixel)	± 4 % of measured value

(ii) Calculate the least-squares solution discrepancy δ_0 for non-bounded problem for each radial positions using $\delta_0(r) = \left\| \widehat{\Theta}_{ij}^{(i)} \widehat{\Pi}^{(i)} - \widehat{U}^{(i)} \right\|$. (iii) Solve for the regularised solution $\widehat{\Pi}_{\alpha}^{(i)}$. Iterate by varying the regularisation parameter α using a bisection algorithm, until $\left\| \widehat{\Theta}_{ij}^{(i)} \widehat{\Pi}_{\alpha}^{(k)} - \widehat{U}^{(i)} \right\| = \delta(r)$. The discrepancy in displacement measurement after regularisation, δ(r), is determined from Eq. (5) following from [21], thus

$$\delta(r) = \begin{cases} \delta_0(r) + 0.25\delta_0(r)\exp(\Delta\delta(r)/0.25\delta_0(r)), & \Delta\delta(r) \le 0 \\ \delta_{est}(r) + 0.25\delta_0(r), & \Delta\delta(r) > 0 \end{cases} \text{ where } \Delta\delta(r) = \delta_{est}(r) - \delta_0(r) \tag{5}$$

The discrepancy in the measured displacements, the least-squares solution discrepancy and the discrepancy in displacement measurement after regularisation for different radial locations (r_0/r = 0.6, 0.5 and 0.45), and for 10 and 5 depth increments are shown in Table 2.

Table 2. The discrepancy of the measurement for different radial locations and depth increments.

	δ_{est}			δ_0			δ		
r_0/r	0.6	0.5	0.45	0.6	0.5	0.45	0.6	0.5	0.45
10 incements	2.38 nm	1.64 nm	1.09 nm	1.62 nm	0.64 nm	0.41 nm	2.78 nm	1.8 nm	1.19 nm
5 increments	1.05 nm	0.55 nm	0.40 nm	0.43 nm	0.10 nm	0.22 nm	1.16 nm	0.48 nm	0.23 nm

3. Uncertainty in Stress Determination

For the IμHM method, uncertainties have five main sources: (a) displacement measurement errors, which include DIC calculation errors, material redeposition and additional residual stresses induced by Ga^+ ions implantation; (b) hole depth measurement errors, which include non-flatness of the bottom of the hole; (c) hole diameter measurement errors, which include tapering of the hole and deviation from roundness; (d) incorrect material constants; (d) hole eccentricity, which include possible focused ion beam drifts. Note that the sources (a) are independent of the stresses that are present. Whereas the sources of uncertainties (b) – (d) are proportional to the residual stresses and varies the ICFs matrix, $\widehat{\Theta}_{ij}^{(i)}$.In this study, following the argument in [28], we include only the sources (a) where the strain perturbations, e.g. $[\delta U^{(i)}]$ (the random error and the systematic error) result in calculated residual stress perturbation, e.g. $[\delta \Pi_{\alpha}^{(i)}]$. Thus, the mean standard deviation (for r_0/r = 0.6, 0.5 and 0.45) in the uncertainty of infered stress is calculated from following equation

$$^{SD}\widehat{\Pi}^{(i)} = \sqrt{\sum_j \left(\left[\left(\widehat{\Theta}_{ij}^{(i)} \right)^T \widehat{\Theta}_{ij}^{(i)} \right]^{-1} \left(\widehat{\Theta}_{ij}^{(i)} \right)^T \delta U^{(i)} \right)^2} \tag{6}$$

The standard deviation for regularised stresses, $^{SD}\widehat{\Pi}_{\alpha}^{(i)}$, is calculated similarly. In this study the stress calculation uncertainty lie within a range of ± 1.64 standard deviations with a probablility of 90%. Equation (6) quantifies the

propagation of uncertainties with the distance from the surface. Physically, following the St. Venant's principle, it demonstrates diminishing efficiency of hole drilling based stress estimation methods to evaluate stresses deep below the surface.

It was shown previously that the UPM can reconstruct highly non-uniform stresses [3, 4]. However, the estimates do not adequately fit the original stress profiles (since stair-like shape of inferred stress profiles), thus an additional source of error potentially exists, namely '*the unit pulse model uncertainty*'. Generally, the unit pulse model error is disproportionate to the number of hole-depth increments. Indeed a similar concept of 'model error' was introduced by Prime & Hill [36] for the series expansion method. It was shown that the uncertainties of measured data and the model uncertainties are two major sources of uncertainties of stress calculations [36].

4. Results

Figure 3a shows the back-calculated unregularised in-plane residual stress components as a function of depth from the deformed surface (the depth resolution of 180 nm), whereas the corresponding results after the regularisation procedure are presented in Figure 3b. The results of estimates with the depth resolution of 360 nm are shown in Figure 4 a and b for unregularised and regularised reconstruction algorithms, respectively. All Figures show probability bounds of 90% for σ_x only (thosef for other stress components are of the same order of magnitude and are thus omitted in the figures for the sake of clarity).

The compressive residual stress component σ_x in the longitudinal direction of the sample (see Fig. 1b) appears to be some 30% higher than the stress component σ_y in the transverse direction. There is some evidence of shear stresses ~120 MPa) such that the principal stresses lie at around 15° to the specimen length.

The recorded longitudindal stress (σ_x) averages to a value around -800 MPa $\pm$ 90 MPa (90% bounds) over the evaluation depth (1.8 µm) and compares to -650 MPa $\pm$ 50 MPa (90% bounds) measured over a depth of 4.1 µm obtained using a FIB microslotting method [12], and to -920 MPa $\pm$ 230 MPa (90% bounds) in [37] obtained by the down-scaled rosette method averaged over a depth of 2 µm.

4. Discussion

Peening of $Zr_{50}Cu_{40}Al_{10}$ BMG results in high compressive residual stresses, especially within the 180 µm deep microstructurally affected layer [12]. Here we have inferred the local in-plane residual stress within the immediate vicinity of the surface as a function of depth for the same BMG sample for which the longitudinal stress was reported in [12] by microslotting averaged over a depth of 4 µm and in [37] by the down-scaled rosette method profiled over a depth of 2 µm.

As expected, unregularised calculation algorithms yield unstable (oscillating) solutions with the uncertainty bounds becoming increasingly wider with distance from the specimen surface, see Figure 3a and 4a. Note that on the contrary to other work [28], the uncertainty propagation analyses considers the more severe case where the displacement measurement errors are not all equal. Therefore, the bounds widen sharply with the depth, in particular for 10 hole-depth increments. Mathematically, this behaviour reflects the distribution of the coefficients in the matrix ICFs, where the diagonal entries are of an order of magnitude smaller then others. Since our method calculates the average values of the stress components the oscillations in results are not pronounced for larger numbers of depth increments (Figure 3a). On the contrary, the down-scaled rosette method in [37] for the unregularised alogorithm gives high amplitude oscillations in the estimates for the same number of depth increments. Besides that, the bounds are more then 3 times further apart than within the current studies.

By reducing of the depth resolution from 180 nm to 360 nm we obtained more accurate results, since the entries in the ICFs matrix are less computationally problematic and the propagated errors are much smaller (Figure 4b vs. Figure 3b). In other words, a lower depth resolution yields less uncertainity in the residual stress estimates.

Regularised algorithms reduced the oscillations in stress estimates and the uncertainty bounds became much closer together (more then 2.5 times smaller then the unregularised stress estimates) and of the same order of magnitude for all depth increments. Mathematically, the regularisation methodology redistributes the entries in the augumented ICFs matrix making them of the same order of magnitude along the diagonal. Thus, the residual stress estimates and uncertainty bounds for the depth resolution of 180 nm and 360 nm are comparable. Therefore '*the unit pulses model uncertainty*' is reduced. The error propagation analysis for the regularised alogorithm of the down-scaled rosette method [37] yielded bounds about 3 times larger than the bounds estimated herein. The down-scaled rosette method tends to overestimate the stress estimates by about 15%.

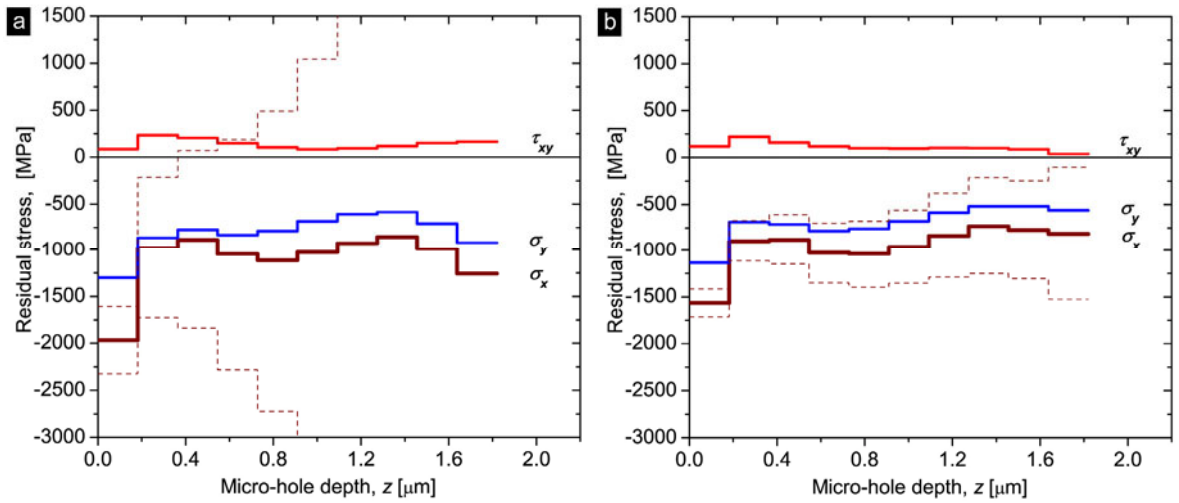

Figure 3. Inferred in-plane residual stresses profiles (σ_x, σ_y and τ_{xy}) as a function of depth from the deformed surface for depth resolution of 180 nm. Dashed lines show probalility bounds of 90% for σ_x. (a) unregularised; (b) regularised.

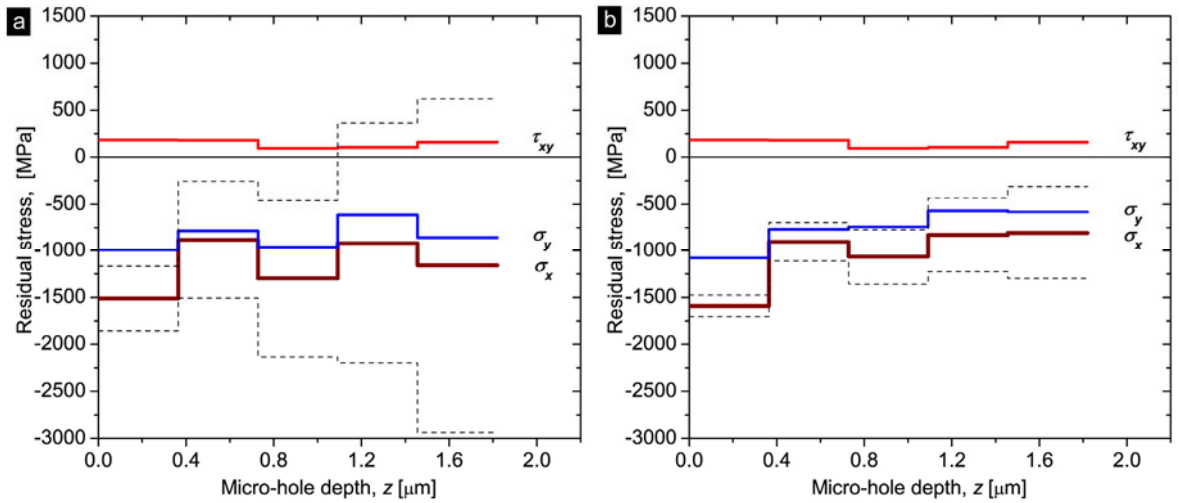

Figure 4. Inferred in-plane residual stresses profiles (σ_x, σ_y and τ_{xy}) as a function of depth from the deformed surface for depth resolution of 360 nm. Dashed lines show probalility bounds of 90% for σ_x. (a) unregularised; (b) regularised

The error analysis for the results estimated from a single depth increment at depth of 1.8 μm yields narrow uncertinity bounds of ±75 MPa. In this case, the incremental micro-hole-drilling method loses its capability of inferring depth profiles of stresses and '*the unit pulse model uncertainty*' will reach its maximum. Qualitatively, in the view of the current studies, we can say that '*the unit pulse model uncertainty*' is disproportionate to the depth resolution and is coupled with unregularised and regularised probalility bounds of residual stress estimates.

The uncertainties in the displacement measurements are relatively large (particularly the systematic error), which result in large uncertainty bounds, even for regularised analysis. Therefore, to achieve consistent and reliable SEM measurements for use with DIC (to reduce the source of errors included in the point (a) in Section 3.), the surface must be characterised by dense, random, high-contrast surface speckle pattern, as discussed and analysed in [18]. Ideally, the random error of displacement mapping should be reduced to below 0.005 pixels and the systematic error should not exceed about 1.5%.

5. Conclusions

In summary, this work presents a new method for mapping in-plane residual or applied stresses incrementally as a function of depth at the micron-scale laterally and sub-micron scale depth-wise.The proposed methodology reconstructs the residual stress distribution from full-field radial displacements. The results obtained agree with residual stresses inferred using the down-scaled rosette method and the microslotting method. By mapping full-field radial displacement we reduced separation of the bounds by about 3 times when comparing with the down-scaled rosette method. The stabilisation approach based on the Thikhonov regularisation efficiently reduced the oscilations in stress estimates and substantially narrowed the bounds of stress estimates (more then 2.5 times). In addition, the regularisation allowed us to increase the depth resolution from 360 nm to 180 nm without significant increase of residual stress estimations uncertainty.

The results of the current work and surface decoration methods developed in [18] point to the scalability of this method to map residual stresses in volumes as small as $1 \times 1 \times 0.2\ \mu m^3$ or less. The potential applications of this technique are wide ranging, including stresses in amorphous thin films, MEMS components and devices, organic electronic devices, nanostructured materials, etc. Though applicable to crystalline materials, for amorphous materials our micro-hole milling method has few competitors.

Acknowledgments

The measurements were made within the Stress and Damage Characterization Unit at the University of Manchester, U.K., supported by the Light Alloys Towards Environmentally Sustainable Transport (LATEST) EPSRC Portfolio Project. We are grateful to P. Liaw (the University of Tennessee, U.S.A.) and Y. Yokoyama (Himeji Institute of Technology, Japan) for provision of the sample; to P. Xiao (the University of Manchester, U.K.) for YSZ nanopowder and A. Gholinia (the University of Manchester, U.K.) for technical and scientific suggestions during the experiment and Dr G.S. Schajer for advice.

References

1. Withers, P.J., *Residual stress and its role in failure.* Reports On Progress In Physics 70(12): p. 2211-2264, 2007.
2. Schajer, G.S. and Prime, M.B., *Residual stress solution extrapolation for the slitting method using equilibrium constraints.* Journal Of Engineering Materials And Technology-Transactions Of The Asme 129(2): p. 227-232, 2007.
3. Schajer, G.S., *Measurement Of Non-Uniform Residual-Stresses Using The Hole-Drilling Method .1. Stress Calculation Procedures.* Journal Of Engineering Materials And Technology-Transactions Of The Asme 110(4): p. 338-343, 1988.
4. Schajer, G.S., *Measurement Of Non-Uniform Residual-Stresses Using The Hole-Drilling Method .2. Practical Application Of The Integral Method.* Journal Of Engineering Materials And Technology-Transactions Of The Asme 110(4): p. 344-349, 1988.
5. McGinnis, M.J., Pessiki, S., and Turker, H., *Application of three-dimensional digital image correlation to the core-drilling method.* Experimental Mechanics 45(4): p. 359-367, 2005.
6. Klein, C.A., *How accurate are Stoney's equation and recent modifications.* Journal Of Applied Physics 88(9): p. 5487-5489, 2000.
7. Sabate, N., et al., *Measurement of residual stress by slot milling with focused ion-beam equipment.* Journal Of Micromechanics And Microengineering 16(2): p. 254-259, 2006.
8. Kang, K.J., et al., *A method for in situ measurement of the residual stress in thin films by using the focused ion beam.* Thin Solid Films 443: p. 71-77, 2003.
9. McCarthy, J., et al., *FIB micromachined submicron thickness cantilevers for the study of thin film properties.* Thin Solid Films 358(1-2): p. 146-151, 2000.
10. Massl, S., Keckes, J., and Pippan, R., *A new cantilever technique reveals spatial distributions of residual stresses in near-surface structures.* Scripta Materialia 59(5): p. 503-506, 2008.
11. Vogel, D., et al. *FIB based measurement of local residual stresses on microsystems*. in *Proceedings of SPIE - The International Society for Optical Engineering* San Diego, CA. 2006.
12. Winiarski, B., et al., *Mapping residual-stress distributions at the micron scale in amorphous materials.* Metallurgical and Materials Transactions A - In Press: p. 1-9, 2009.
13. Massl, S., Keckes, J., and Pippan, R., *A direct method of determining complex depth profiles of residual stresses in thin films on a nanoscale.* Acta Materialia 55(14): p. 4835-4844, 2007.
14. Quinta De Fonseca, J., Mummery, P.M. and Withers, P.J., *Full-field strain mapping by optical correlation of micrographs acquired during deformation.* Journal of Microscopy 218: p. 9-21, 2004.
15. Peters, W.H. and Ranson, W.F., *Digital imaging techniques in experimental stress-analysis.* Optical Engineering 21(3): p. 427-431, 1982.
16. Lecompte, D., et al., *Quality assessment of speckle patterns for digital image correlation.* Optics and Lasers in Engineering 44(11): p. 1132-1145, 2006.

17. van Kouwen, L., Botman, A., and Hagen, C.W., *Focused Electron-Beam-Induced Deposition of 3 nm Dots in a Scanning Electron Microscope.* Nano Letters 9(5): p. 2149-2152, 2009.
18. Winiarski, B., Schajer, G.S. and Withers, P.J., *Surface decoration for improving the accuracy of displacement measurements by Digital Image Correleation in Scanning Electron Microscopy*. to be published in Experimental Mechanics.
19. Vogel, D., et al. *FIB based measurements for material characterization on MEMS structures*. in *Proceedings of SPIE - The International Society for Optical Engineering*, San Diego, CA, 2005.
20. Flaman, M.T. and Herring, J.A., *Comparison of Four Hole-Producing Techniques for the Center-Hole Residual-Stress Measurement Method.* Experimental Techniques 9(8): p. 30-32, 1982.
21. Tjhung, T. and K.Y. Li, *Measurement of in-plane residual stresses varying with depth by the Interferometric Strain/Slope Rosette and incremental hole-drilling.* Journal Of Engineering Materials And Technology-Transactions Of The Asme 125(2): p. 153-162, 2003.
22. Tian, J.W., et al., *A study of the surface severe plastic deformation behaviour of a Zr-based bulk metallic glass (BMG).* Intermetallics 17(11): p. 951-957, 2009.
23. Yaofeng, S. and Pang, J.H.L., *Study of optimal subset size in digital image correlation of speckle pattern images.* Optics and Lasers in Engineering 45(9): p. 967-974, 2007.
24. Jin, H., Lu, W.Y., and Korellis, J., *Micro-scale deformation measurement using the digital image correlation technique and scanning electron microscope imaging.* Journal of Strain Analysis for Engineering Design 43(8): p. 719-728, 2008.
25. Sutton, M.A., et al., *Scanning electron microscopy for quantitative small and large deformation measurements Part I: SEM imaging at magnifications from 200 to 10,000.* Experimental Mechanics 47(6): p. 775-787, 2007.
26. Muskhetishvili, N.L., *Some Basic Problems of the Mathematical Theory of Elasticity*, Leyden, the Netherlands: Noordhoff Groningen, 1977.
27. Pelletier, J.M., Yokoyama, Y. and Inoue, A., *Dynamic mechanical properties in a $Zr_{50}Cu_{40}Al_{10}$ bulk metallic glass.* Materials Transactions 47: p. 1359-1362, 2007.
28. Schajer, G.S. and Altus, E., *Stress calculation error analysis for incremental hole-drilling residual stress measurements.* Journal Of Engineering Materials And Technology-Transactions Of The Asme 118(1): p. 120-126, 1996.
29. Vangi, D., *Data managements for the evaluation of residual-stresses by the incremental hole-drilling method.* Journal of Engineering Materials and Technology - Transactions of the ASME 116(4): p. 561-566, 1994.
30. Zucarrello, B., *Optimal calculation steps for the evaluation of residual stress by the incremental hole-drilling method.* Experimental Mechanics 39(2): p. 117-124, 1999.
31. Tikhonov, A.N. and Arsenin, V.Y., *Solution of Ill-posed problems*, New York: John Wiley & Sons, 1977.
32. Schajer, G.S. and M.B. Prime, *Use of inverse solutions for residual stress measurements.* Journal Of Engineering Materials And Technology-Transactions Of The Asme 128(3): p. 375-382, 2006.
33. Neubauer, A., *On converse and saturation results for Tikhonov regularization of linear ill-posed problems.* Siam Journal on Numerical Analysis 34(2): p. 517-527, 1997.
34. Lamm, P.K. and Elden, L., *Numerical solution of first-kind Volterra equations by sequential Tikhonov regularization.* Siam Journal on Numerical Analysis 34(4): p. 1432-1450, 1997.
35. Beck, J.V., Blackwell, B. and St.Clair Jr., C.R., *Inverse Heat Conduction - Ill-Posed Problems,* New York: Wiley-Interscience, 1985.
36. Prime, M.B. and Hill, M.R., *Uncertainty, model error, and order selection for series-expanded, residual-stress inverse solutions.* Journal Of Engineering Materials And Technology-Transactions Of The Asme 128(2): p. 175-185, 2006.
37. Winiarski, B. and Withers, P.J. *Mapping residual stress profiles at the micron scale using FIB micro-hole drilling*. in *7th BSSM International Conference on Advances in Experimental Mechanics, 7-9 September 2010*. 2010. Liverpool: to be published in Trans Tech Publications.

Proceedings of the SEM Annual Conference
June 7-10, 2010 Indianapolis, Indiana USA

Studying the Effect of Residual Stresses on Fatigue Cracks through Full-field Methods

David A. Johnson*, Dennis J. Buchanan*, and Reji John
Air Force Research Laboratory, AFRL/RXLMN,
Materials and Manufacturing Directorate,
Wright-Patterson Air Force Base, Ohio 45433, USA

*University of Dayton Research Institute
Dayton, Ohio 45469, USA
David.Johnson@udri.udayton.edu

ABSTRACT

In this effort, a corner crack was grown from a notch in a nickel-based superalloy specimen with a shot-peened surface treatment to induce residual stresses. The crack length was less than 200 microns, and the full displacement field near the crack was determined using advanced digital image correlation. The specimen was then annealed at elevated temperatures to reduce or eliminate the residual stresses, and the full displacement field near the crack was again determined. The displacements after annealing were indeed significantly larger than those previous to annealing, demonstrating the reduction in residual stresses. Modeling has been done to determine the approximate level of residual stresses induced and then reduced through annealing. Through this method, the effect of residual stresses on short fatigue cracks can be directly studied.

Further work will be discussed on the effect of temperature on residual stresses, an area of great concern in predicting fatigue lives of components. The degree to which these residual stresses are reduced under service conditions is not well understood, and the approach described here is expected to be extremely useful in determining and predicting this residual-stress reduction, leading to greatly enhanced life prediction where residual stresses are involved.

Introduction

Shot peening is extensively used to impart compressive surface residual stresses in metallic components [1]. The benefits of these residual stresses in increasing fatigue lives are well-documented [2,3]. However, there is some question as to the intensity of these beneficial residuals after extensive time under service conditions. This question is particularly important when considering the beneficial effect of shot peening on nickel-base superalloys, which are typically used where the absolute temperature may be at or near 70% of the melting temperature of the alloy and stresses may approach the yield strength of the material. In addition, the accuracy of predictions of remaining residual stresses also depends on the accuracy of the knowledge of the initial residual-stress conditions. The shot-peening process itself has many parameters, which contribute to the variability of imparted residual stresses, *e.g.*, shot size, hardness, coverage, and angle.

In order to predict fatigue lives with a reasonable degree of fidelity for shot-peened parts, it is vital that the effect of service conditions on residual stresses be better understood. In this effort, a method for studying the effect of shot-peening and the effect of service conditions on shot-peening-induced residual stresses is demonstrated through the determination of their effect on a

T. Proulx (ed.), *Application of Imaging Techniques to Mechanics of Materials and Structures, Volume 4*, Conference Proceedings of the Society for Experimental Mechanics Series 14, DOI 10.1007/978-1-4419-9796-8_24, © The Society for Experimental Mechanics, Inc. 2013

particular mechanism of importance to fatigue-life prediction, the mechanical behavior of the material near a small fatigue crack. This study is accomplished through the use of full-field deformation mapping of this area.

Systems used for the determination of full-field displacements and strains have matured over the past few decades [4-9]. The most common experimental method used for determining displacement fields, and the one that is used in the present work, is known as digital image correlation, or DIC. DIC is accomplished by acquiring a series of images of the same area of a solid's surface while the solid is undergoing deformation. In the present study, the deformation near a small-fatigue crack is studied. Since DIC does not determine the displacement of specific material points, but instead determines the displacement of subsets of pixels in the acquired images, using DIC in situations with displacement discontinuities, especially cracked bodies, is particularly difficult. Therefore, most DIC software requires the user to "mask out" the area near a crack, but this is in many cases the very area of most interest. In the present study, special techniques were used to determine the displacement very near the crack [10, 11]. In addition, most DIC systems are not capable of working at the size scales of interest in this study.

A specialized system was used in the present study, which was developed at the Materials and Manufacturing Directorate, Air Force Research Laboratory. This system is capable of high magnifications, by light optics standards, and it is also capable of a wide variety of magnifications through combinations of various objective and photo-eyepiece lenses. Figure 1 shows the test set-up, which consists of a servo-hydraulic load frame and its controls (outside of area shown), with the specimen mounted in the usual position and a microscope system with a digital camera, which is capable of three-axes movement. Through combinations of various objective and photo-eyepiece lenses, a variety of magnifications are possible.

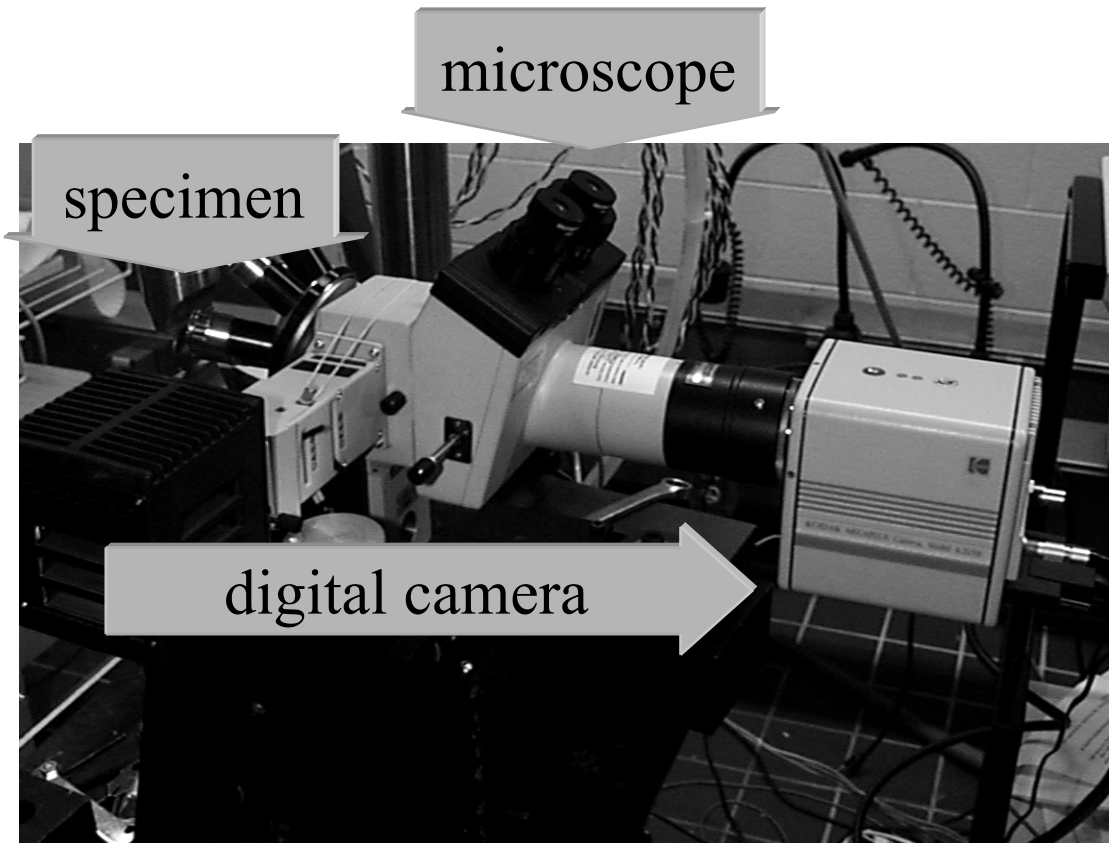

Figure 1 - Test equipment.

Approach and Results

Figure 2 shows the specimen used in the study, which has a corner fatigue crack growing from one of the round notches. There is a starter notch on the corner, which was created through electrical-discharge machining (EDM).

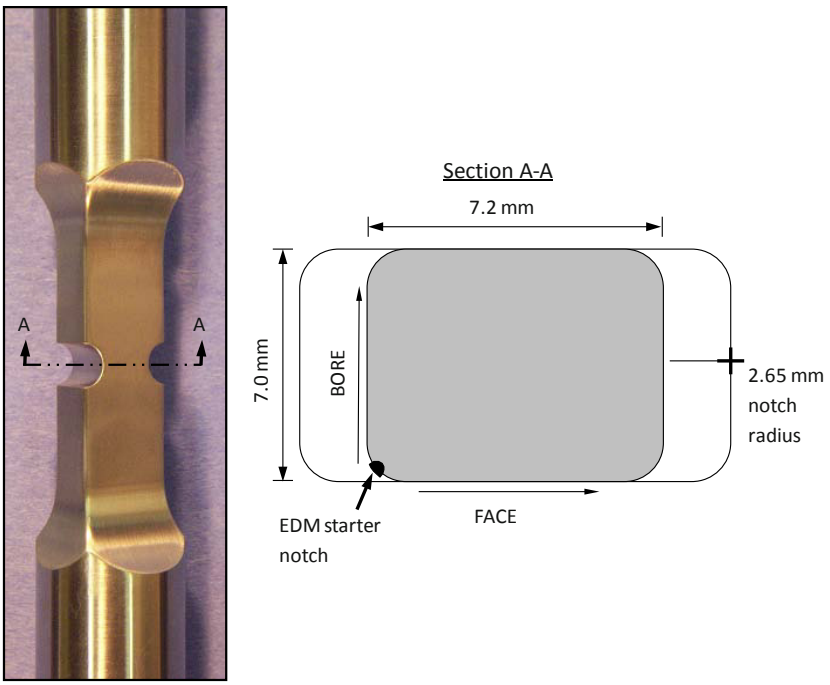

Figure 2 - Image of specimen and machine drawing of specimen geometry in region-of-interest.

The approach taken for this test is as follows. The specimen was shot peened, then a small quarter-circular starter notch was machined into the corner of one of the two larger notches through electrical-discharge machining (EDM), followed by growing a fatigue crack to the length shown. The goal was to minimize the redistribution of residual stresses associated with potential notch yielding and to advance the crack front away from the EDM notch. Figure 3 shows the surface of the specimen near the fatigue crack. At the top of the image, the end of the notch, from which the crack has been grown, can be seen. The test procedure is to acquire a first, reference image, and then acquire images while the specimen is under a series of different load conditions. Care needs to be taken to ensure that each image is spatially matched as closely as possible to the reference image. Because of stretching of the load-train, including the specimen, under load, the microscope is translated to keep the region-of-interest in view and match the reference image spatially. In addition to the motion in the loading direction, there is a limited amount of motion in the transverse in-plane direction. Images are acquired at various load levels in order to study nonlinear behavior.

Figure 4 shows a series of deformation maps, acquired at various load levels, after processing with the specialized DIC algorithms which enable calculations of displacements very near cracks. In each case, the displacement in the loading direction, *v*, and the displacement in the normal to the loading direction, *u*, are shown as surface plots. It should be noted that since the crack is not parallel to either the *x*-axis or *y*-axis (where the *y*-axis is in the loading direction and the *x*-axis is its in-plane normal), the difference in displacement across the displacement discontinuity, or crack, which appears to be a “cliff,” is neither crack-open displacement (COD) nor crack-sliding displacement (CSD), which would need to be measured perpendicular to or parallel, respectively,

to the direction of cracking at each point along the crack. With this caveat, it is still useful to observe this behavior, because it does give a general idea of the level of displacement discontinuity across the crack. It is possible to calculate a "full-field" crack-closure level, by comparing this level to the level which would be predicted by a linear interpolation of the displacements at maximum loading. For example, if the displacement difference across the displacement discontinuity at 50% of maximum load is only 40% of the corresponding difference at maximum load, it indicates that there is crack closure. It is also possible to measure closure across any two points lying on either side of the crack.

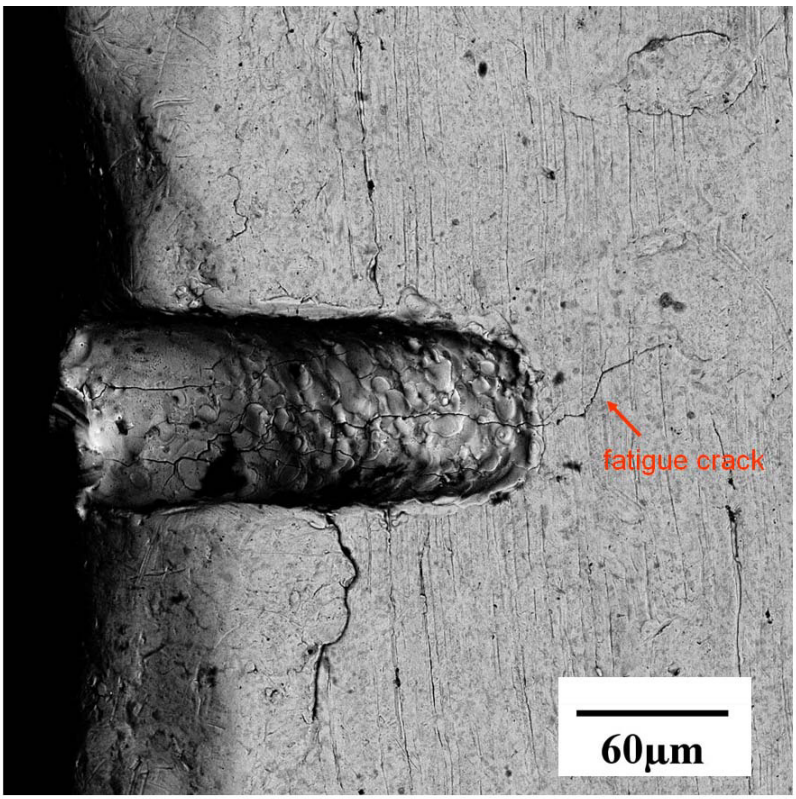

Figure 3 - Small starter notch and fatigue crack.

The purpose of the present study is to compare the deformations determined before a thermal exposure of the specimen to those determined afterwards. It is expected that the residual stresses caused by the shot peening will be reduced through annealing by this thermal exposure, which should result in larger displacements at maximum load. Figure 5 shows that this is indeed the case. For this figure, all displacements are determined at the same maximum load. The top two surface plots show the displacement, *v*, in the loading direction and the displacement, *u*, in the normal to the loading direction before thermal exposure and therefore with the original residual stresses induced by the shot peening. The bottom two surface plots show the corresponding displacements after thermal exposure and therefore with reduced residual stresses. The overall average displacement magnitude of the after-thermal-exposure case is 194% of the average displacement magnitude of the before-thermal-exposure. This is obviously a significant increase, representing a significant reduction of residual stresses caused by the thermal exposure. Through comparison of this information with modeling results, it is possible to estimate the initial surface residual stress and the decrease in residual stress after simulated service conditions.

The great advantage of the method is that it can estimate residual-stress levels and changes by studying one of the most important mechanisms from an engineering perspective affected by

residual stresses, which is crack behavior. By exposing the specimen to various levels of shot peening, thermal exposure, and mechanical loading, it should be possible to study a variety of important issues in the area of residual stress. In addition, it is possible to study the important effect of thermal exposure and mechanical loading on crack-closure levels.

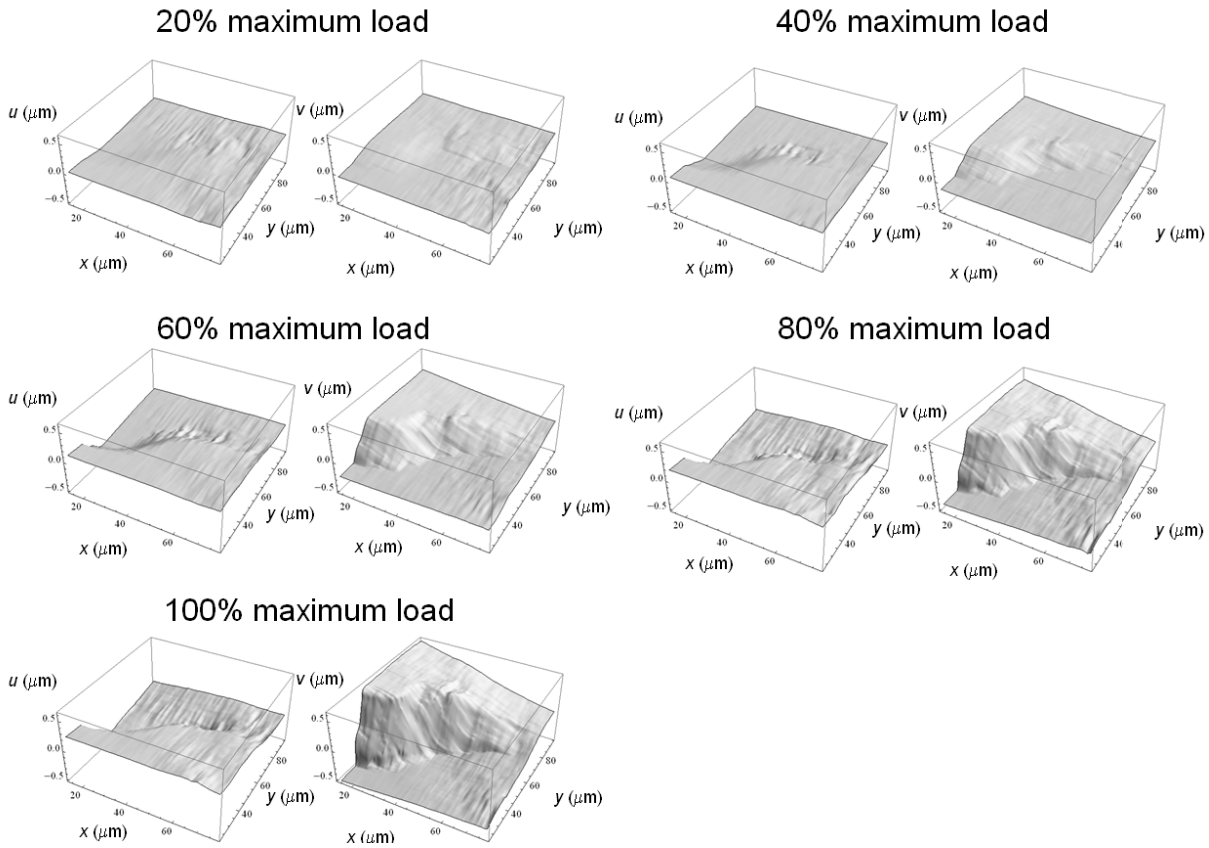

Figure 4 - Deformation maps at various load levels.

Conclusions

The effect of service environment on beneficial induced compressive residual stresses is not well understood. The present study demonstrates a very promising method for quantitatively determining this effect. The great advantage of the method is that it can estimate residual-stress levels and changes by studying one of the most important mechanisms affected by residual stresses, *viz.,* crack behavior. By exposing the specimen to various levels of shot peening or other surface treatments, thermal exposure, and mechanical loading, it should be possible to study a variety of important issues in the areas of residual stress and crack closure. Further work is on-going to correlate these important experimental results with numerical modeling of the specimen and the residual stress state.

Acknowledgment

This work was performed at the Air Force Research Laboratory, Materials and Manufacturing Directorate (AFRL/RXLM), Wright-Patterson Air Force Base, OH. D.A. Johnson and D.J. Buchanan were supported under on-site Contract No. FA8650-04-C-5200. The authors gratefully acknowledge the partial support of Dr. David Stargel of AFOSR under task 2306-6M2AL8.

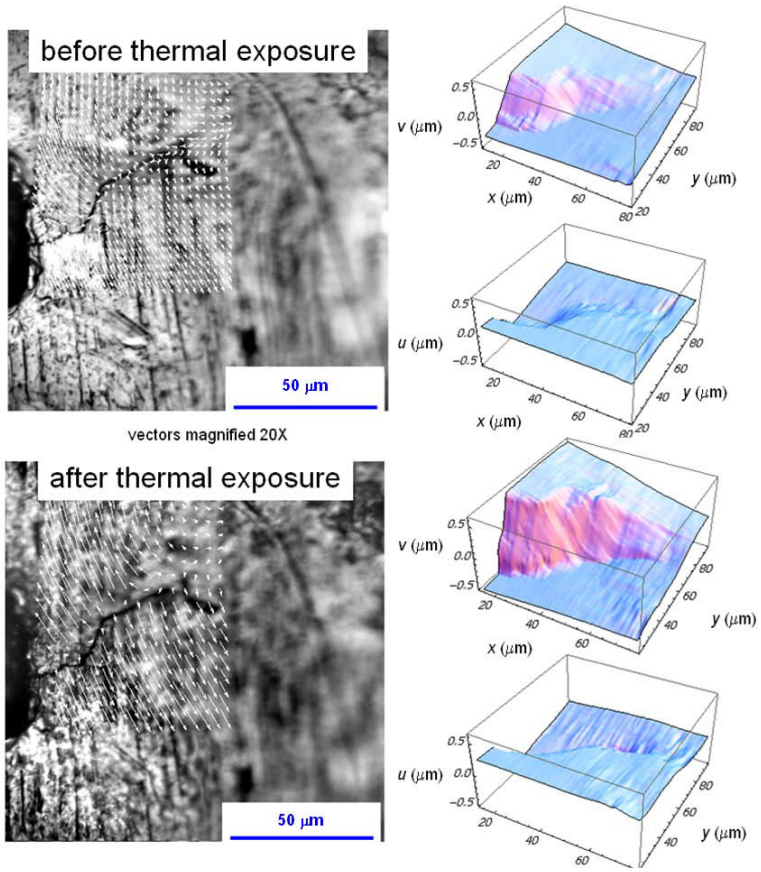

Figure 5 - Comparison of deformation maps before thermal exposure (top) and after thermal exposure (top).

References

1. Almen, J. O., and Black, P. H., *Residual Stresses and Fatigue in Metals*, McGraw-Hill, New York, NY, 1963.
2. Scott, J. A., "The influence of processing and metallurgical factors on fatigue," *Metal Fatigue: Theory and Design*, A. F. Madayag, Ed., John Wiley & Sons, Inc., New York, NY, 1969.
3. Fuchs, H. O., and Stephens, R. I., *Metal Fatigue in Engineering*, John Wiley & Sons, Inc., New York, NY, 1980.
4. Bruck, H.A., S. R. McNeill, and M. A. Sutton, "Digital Image Correlation Using Newton-Raphson Method of Partial Differential Correction," *Experimental Mechanics*, Vol. 29, No. 3, pp. 261-267, 1989.
5. James, M. R., W. L. Morris, and B. N. Cox, "A High Accuracy Automated Strain-field Mapper," *Experimental Mechanics*, Vol. 30, No. 1, pp. 60-67, 1990.
6. Chen, D. J., F. P. Chiang, Y. S. Tan, and H. S. Don, "Digital Speckle-displacement Measurement Using a Complex Spectrum Method," *Applied Optics,* Vol. 32, No. 11, pp. 1829-1849, 1993.
7. Lyons, J. S., J. Liu, and M. A. Sutton, "High-Temperature Deformation Measurements Using Digital-Image Correlation," *Experimental Mechanics,* Vol. 36, No. 1, pp. 64-70, 1996.
8. Sutton, M. A., N. Li, D. C. Joy, A. P. Reynolds, and X. Li, "Scanning Electron Microscopy for Quantitative Small and Large Deformation Measurements Part I: SEM Imaging at Magnifications from 200 to 10,000," *Experimental Mechanics*, Vo. 47, No. 6, pp. 775-787, 2007.

9. Sutton, M. A., N. Li, D. Garcia, N. Cornille, J. J. Orteu, S. R. McNeill, H. W. Schreier, X. Li, and A. P. Reynolds, “Scanning Electron Microscopy for Quantitative Small and Large Deformation Measurements Part II: Experimental Validation for Magnifications from 200 to 10,000,” *Experimental Mechanics*, Vo. 47, No. 6, pp. 789-804, 2007.
10. Johnson, D. A., “The Failure Physics of a Limited-ductility Intermetallic,” Ph.D. Thesis, Harvard University, 2004.
11. Johnson, D. A., “Integrating Experimentation, Modeling, and Visualization through Full-field Methods”, *Proceedings of the SEM Annual Conference and Exposition on Experimental and Applied Mechanics*, 2009.

Proceedings of the SEM Annual Conference
June 7-10, 2010 Indianapolis, Indiana USA

Rapid Imaging Tool for Residual Stress and Defect Quantification in MEMS and PV Applications

Gavin P. Horn, Senior Research Scientist, University of Illinois at Urbana-Champaign
1206 W. Green St. Urbana, IL 61801, ghorn@illinois.edu;
Jon R. Lesniak, President, Stress Photonics, Inc.;
Thomas J. Mackin, Professor, California Polytechnic State University;
Tonio Buonassisi, Assistant Professor, Massachusetts Institute of Technology

ABSTRACT

Performance and reliability of silicon based microelectromechanical systems (MEMS) and photovoltaic (PV) devices are often strongly affected by defects and residual stresses. As a result, both industry and academia need new tools that can rapidly locate and quantify defects. The grey-field photoelastic technique has been shown to improve detection and residual stress quantification of defects in wafer bonded MEMS structures. In the PV industry, the tool has proven capable of detecting high bulk stress in wafers, damage due to wafer cutting, and stresses associated with trapped cracks.

In this paper, we describe the development of an infrared photoelastic tool that captures full-field residual stress images at camera framing rates. This solid state tool, which adapts technology developed for visible light residual stress inspection, reduces the data collection time for residual stress maps from several minutes to a fraction of a second. We demonstrate the tool on canonical samples including a beam in bending and disk in compression to verify stress results and identify the lower limits of detection. We then demonstrate the tool on several industrial applications.

I. INTRODUCTION

The development of commercially successful microelectromechanical systems (MEMS) and photovoltaic (PV) processes and devices are often limited by the presence of defects in the silicon substrates. If failure occurs during processing, significant losses are incurred, including: loss of material, unrecoverable costs from prior processing steps, and machinery downtime during clean up. In other cases, these defects may initiate cracking that leads to premature failure or residual stress states that compromise device performance. As a result, there is a strong need by both industry and academia to develop tools that can rapidly locate and quantify defects. One classic tool of the experimental stress analyst – photoelasticity - has show great promise for detecting high stress defects and quantifying residual stresses. However, the tool has also traditionally suffered from relatively long cycle times that limit its real-time applications.

The discovery that many transparent solids can become doubly-refractive (birefringent) when stressed was made in 1816 by Sir David Brewster [1], a phenomenon that has since become known as the photoelastic effect. Lacking sufficient technology to further this method, significant advances were not made until the early twentieth century [2]. A solid is traditionally labeled transparent if we can see through it with the naked eye. As such, these pioneering works were carried out using visible light. However, nothing in the electromagnetic-field equations indicate that stress-induced birefringence is restricted to this narrow band of wavelengths. In the mid-1950's, Dash experimentally verified birefringence in silicon [3] using infrared light. A few years later, Appel and Pontarelli introduced what is believed to be the first infrared polariscope [4]. Shortly thereafter, Lederhandler published the first images of residual stresses in silicon wafers utilizing an infrared polariscope [5]. Throughout the 60's, 70's, and early 80's interest in IR photoelasticity slowly increased as investigators built many different polariscopes using both plane and circularly polarized light [6-8] and began investigating a wider range of materials. Yamada

T. Proulx (ed.), *Application of Imaging Techniques to Mechanics of Materials and Structures, Volume 4*, Conference Proceedings of the Society for Experimental Mechanics Series 14, DOI 10.1007/978-1-4419-9796-8_25, © The Society for Experimental Mechanics, Inc. 2013

et al [9] and Niitsu [10,11] independently developed two different scanning infrared polariscopes and showed that they could be useful for silicon wafer inspection and process evaluation. The drawback of these systems arises from using a single-point scanning laser source and detector. As such, each wafer must be mounted on a translating stage to allow a series of point wise measurements. Inspection speed is increasing with recent technological advances, but is still a limiting factor. With Yamada's system, the last reported duration for inspecting a 3-inch diameter wafer was *three hours* at a 200 μm spatial resolution [12], which is too slow to be considered an on-line inspection methodology. A commercial implementation of a scanning type infrared polariscope has been brought to market with significant apparent improvements in cycle time, though still requiring several minutes to inspect wafers.

Recent applications of infrared photoelasticity in the PV industry include work from Zheng and Danyluk [13,14] who used full-field phase stepping and fringe multiplication techniques to increases their stress resolution. The trade-offs include increased system complexity and a reduction in spatial resolution. An important contribution of this work is that the angular dependence of the stress-optic coefficient and deviation angle of the maximum shear stress orientations were determined in closed form for in-plane refractive indices in a (100) wafer. When a (100) silicon wafer is inspected in the [001] direction using 1.15μm near-infrared light, the relative stress-optic coefficient can be related to the angle (θ) between the principal stress orientation and the [110] directions by [14],

$$C_{(100)} = (2.66\sin^2 2\theta + 0.71\cos^2 2\theta)*10^{-11}\ Pa^{-1}. \quad (1)$$

Gamboa et al. [15] have also measured thermally induced residual stresses in silicon tubes to be used for photovoltaic energy. Again, a phase shifting routine was utilized to measure sub-fringe order, but it appears that a single point implementation is scanned across the surface to determine stress profiles. Results indicate that the edges of the tube faces showed a substantial increase in residual stress.

The authors have previously developed an infrared grey-field polariscope (IR-GFP) [16] based on the visible light grey field photoelastic technique [17]. This tool has found success in locating trapped particles in bonded MEMS materials at a much higher resolution, and much higher rates, than typical laboratory tools [18]. This is possible because the spatial extent of the measurable residual stress field is significantly larger than the trapped particle or debond [19]. The IR-GFP has also found application in quantifying residual stress concentrations from etched features and surface nanotopography at bond interfaces. In the PV industry, the tool has been applied to determine silicon ribbons with high bulk stress, locate cracks and quantify machining damage [20]. The IR-GFP has an advantage over other previous implementations of the infrared polariscope in that full-field images can be capture in approximately 10 seconds, providing at least an order of magnitude improvement over other IR tools (1600 x 1480 pixels/data points compared to only about 100 data points in 10 seconds utilizing the technique of Yamada). However, the need for a rotating polarizer requires a discrete amount of time between each image capture. While this is acceptable for most laboratory applications, a real-time IR photoelastic stress analysis tool can open the possibilities for on-line process and quality control as well as dynamic process visualization.

Real-time photoelastic stress analysis has only recently been developed for visible light applications. Patterson and Wang [21] pioneered this field, building their "Phase-Stepped Imaged Obtained Simultaneously (PSIOS)" which uses four cameras to collect four phase-stepped images. More recently, Hobbs, Greene, and Patterson present a more compact instrument for capturing four phase stepped images using a single camera [22]. The most successful real-time implementation of photoelasticity is based on the patent of Lesniak and Patterson [23]. The Poleidoscope provides the same images as the PSIOS with a more efficient and elegant optical arrangement [24]. However, a real-time full-field infrared polariscope has not been developed to this point. In this paper, we will present an infrared implementation of the Poleidoscope and provide several applications of the tool.

II. INFRARED POLEIDOSCOPE PROTOTYPE

The infrared Poliedoscope is based on the theory of grey-field photoelasticity developed by Lesniak [17]. Circularly polarized light is projected onto a test sample by placing a condenser lens, polarizer, and quarter waveplate in front of an IR light source. For these experiments a quartz tungsten bulb was used as the IR source. Silicon, one of the most important electronic and structural materials in the MEMS, IC, and PV industries, is a stress birefringent material, meaning that light propagating along the slow axis of the sample is retarded by a phase lag, Δ, with respect to light propagating along the fast axis as given by

$$\Delta = 2\pi C d(\sigma_1 - \sigma_2)/\lambda, \quad (2)$$

where, d is the material thickness, λ is the wavelength of light, C is the stress optic coefficient of the material, and σ_1 and σ_2 are the first and second principal stresses. If there is no stress in the sample, then the transmitted light retains its circular polarization. However, in the presence of stress, this selective optical retardation changes the

circularly polarized light to become elliptically polarized in proportion to the stress state. The magnitude of the ellipticity of the light and the orientation of the ellipse provide enough information to determine the magnitude and orientation of the stress state in the sample.

While the IR-GFP utilized a continuously rotating analyzer and video analysis approach to determine the geometry of the transmitted light ellipse, inspection of the geometry of elliptical light indicates that only four stationary polarizer positions are required to adequately fully characterize the ellipticity of transmitted light (Figure 1). A judicious choice of polarizer orientation of (1) 0°, (2) +45°, (3) 90°, and (4) -45° simplifies data acquisition. Light amplitude is proportional to the elliptical dimensions at each of these polarizer positions. The difference between images 1 and 3 is utilized to characterize shear stress on the 0° plane, while the difference between images 2 and 4 renders shear stress on the 45° plane. These differences are normalized by the average intensity of all images to eliminate spurious lighting effects.

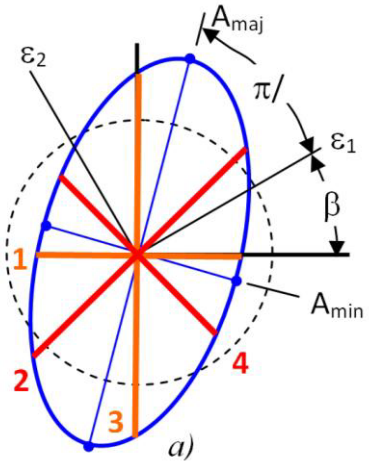

Figure 1. Elliptical light analyzed via four stationary polarizers.

To implement this scheme, four identical images of a single object are made using a specially ground objective lens that refracts a single object image to four distinct focal points at the same focal distance where the CCD detector is located. Four polarizers, oriented at 0°, ±45°, and 90°, are attached to the back of the lens to replace the rotating polarizer. The CCD detector array is then parsed in software where the individual quadrants are subtracted and normalized as detailed in the previous section. The prototype IR-Poleidoscope system is shown in Figure 2.

Figure 2. Phase III prototype optical system inspecting silicon disk in compression sample.

III. CANONICAL EXPERIMENTS

Prior to applying to IR-Poleidoscope to problems of commercial interest, two simple geometries with well know stress solutions are studied. A silicon beam in four point bending and circular sample in compression are imaged while the load is being dynamically applied. Several frames are extracted from the beam in bending example to provide comparison with well known theory. Sample loading is provided by an Instron Mini 44 screw driven loadframe at a constant crosshead speed of 42 μm/sec, while the IR-P system is collecting data at 15 frames per second.

III.1. Dynamic Four-Point Bend Stress Measurements

A sample IR-Poleidoscope image of a double side polished single crystal silicon beam in four point bending (inner span of 15.9 mm, outer span of 31.8 mm, beam height 4.8 mm) is shown in Figure 3 at an applied load of 6.5 N. At this low load, the maximum bending stress is only approximately 12 MPa. The coloration of the image shows tensile stresses in red shades, while compressive stresses appear in blue. The neutral axis at the center of the beam appears in a near black shade In Figure 3, the field of view includes the load application points, which are expected to display high Hertzian contact stresses. Samples that are loaded to failure always break at the load points. The central region between the inner span of the beam has a uniform, linear stress distribution expected for a beam in bending.

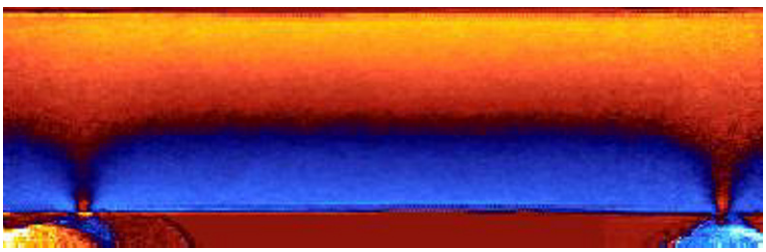

Figure 3. IR-Poleidoscope Shear 45 image of a four point bend specimen (P=6.5 N)

Figure 4 provides a comparison betweem theory and the experimental results for applied loads of 2.5 and 6.5N. The experimental points represent a linescan through the middle of the constant moment portion of the beam, with no data smoothing or averaging across the length of the beam. Data is collected from the center of the constant moment section of the beam in order to eliminate any effect of the bending fixture contact points . Over most of the beam height, the experimental response is linear and compares quite well with theory. The IR-Poliedoscope is calibrated via equation (1), for the stress-optic coefficient of silicon. Figure 4 shows that very low stresses can be resolved with this technique, even for very thin double side polished silicon wafers. The maximum stresses for the lowest load experiment are only 5 MPa and are easily resolved. For both cases, the data are not obscured by noise and follow a linear trend with little scatter, even near the neutral axis of the beam, indicating a much lower stress sensitivity on the order of 500 kPa.

Figure 5 highlights several frames from a video, captured during the dynamic loading experiment, showing the sample throughout loading. The first few images show the incredible sensitivity of the device, where noticeable changes in the signal occur with crosshead displacements less than 0.5 μm (Figure 5b). As a comparison, the second half fringe does not appear until almost two orders of magnitude larger displacement (Figure 5j).

Subfringe sensitivity allows low stress resolution, even for dynamic loading. This capability is important for analysis of silicon and III-V semiconductor devices that may operate at high temperature where the critical resolved shear stress is expected to be on the order of 1 MPa. The high speed data collection indicates that it is possible to collect dynamic stress information from silicon, which would allow in-situ analysis of a thermal cycle. The data collection rate is also rapid enough to inspect thin film depostion processes in-situ, allowing process and quality control for these common and critical processing steps.

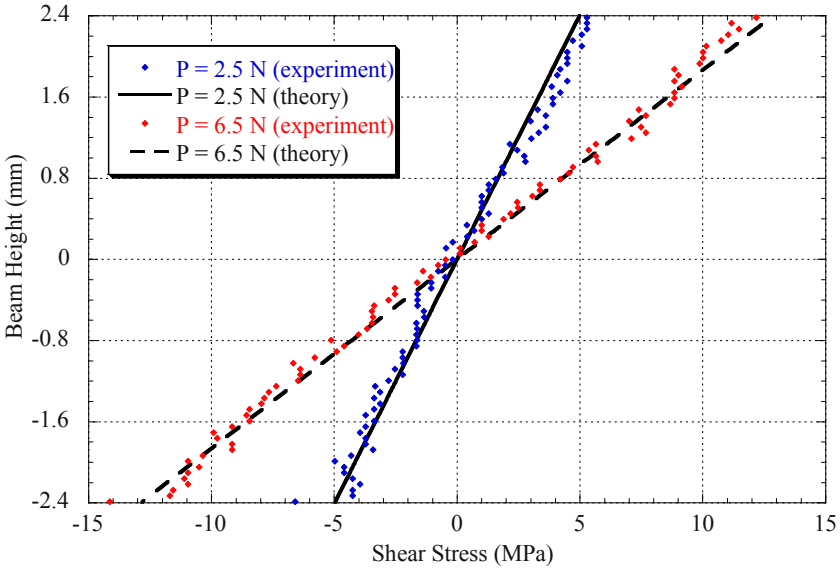

Figure 4. Comparison of theory and experimental results from the four point bend experiments for two different applied loads.

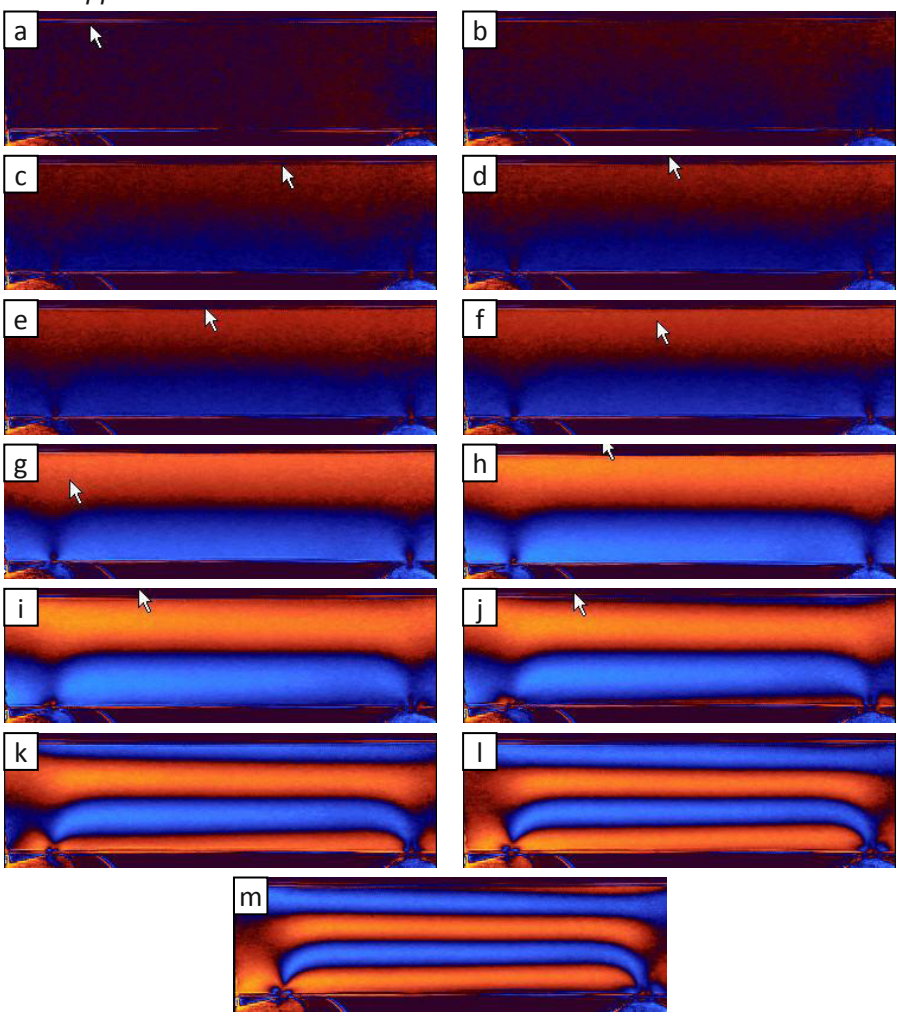

Figure 5. Dynamic imaging of four-point bend test in silicon at a loading rate of 42 μm/sec this series of images was captured over approximately one second.

III.2. Dynamic Disk in Compression Experiments

Sample data for a disk in compression is shown in Figure 6, again collected at a framing rate of 15 frames/second with a cross head speed of 42 μm/sec. The image again shows the symmetric portion of the shear stress about both the x- and y-axes, in accord with the theoretically predicted stress distribution. Noticeable contact stresses are apparent at the loading points for loads much less than 1 N. As the cross head begins translation, the load points quickly show multiple fringes, while the central region, commonly used for photoelastic calibration, exhibits subfringe stress distribution until large loads are applied.

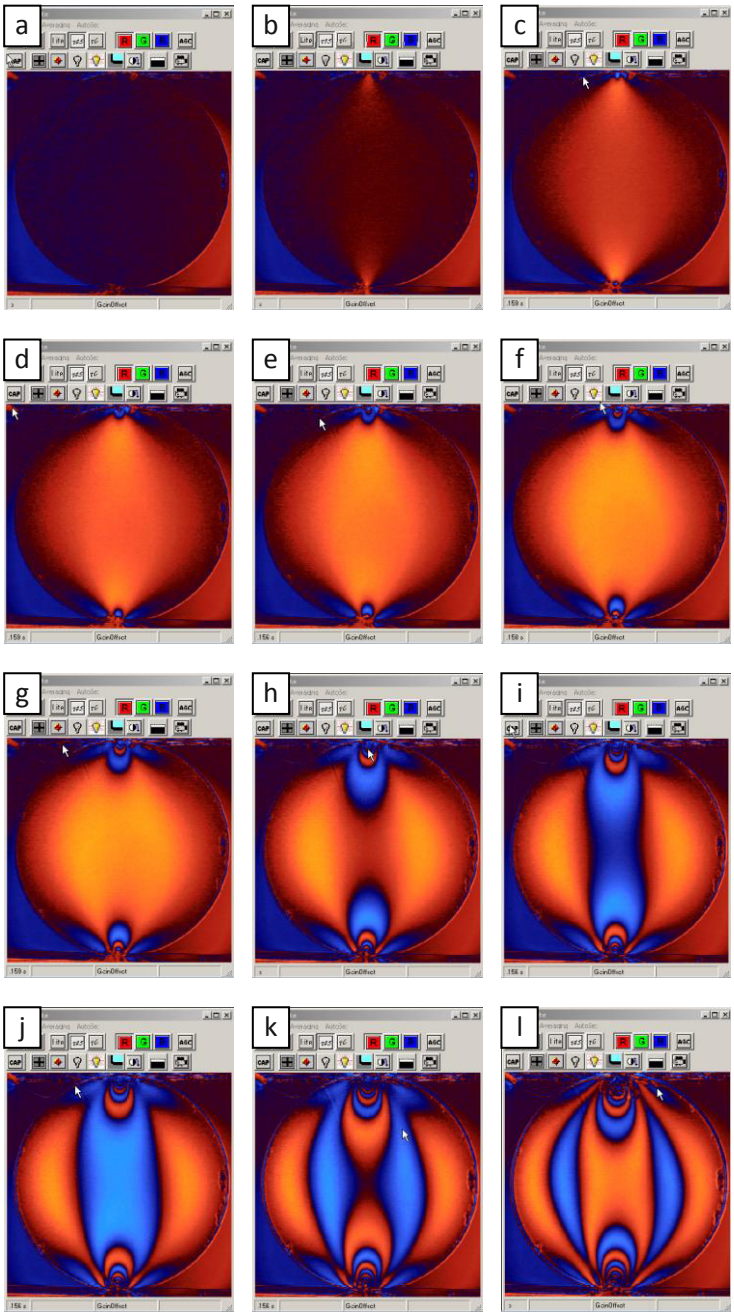

Figure 6. Dynamic imaging of four point bend test in silicon; at a loading rate of 42 μm/sec this series of images was captured over approximately two and a half seconds.

IV. APPLICATION EXPERIMENTS

IV.1. Defective wafer inspection

As silicon wafers used for MEMS and IC applications increase to 300 mm in diameter and beyond and those for PV applications decrease in thickness to less than 100μm, they become increasingly fragile and susceptible to the buildup of stresses during manufacture. Residual stresses accumulate during the growth, sawing - and for some applications through lapping/grinding, etching, and polishing operations - before the wafer has even begun the processing stages. Cracks may be generated throughout processing, which can render the wafer unusable in subsequent manufacturing processes. If failure does not occur at some stage in wafer production, it may initiate in the course of subsequent processing stages should these cracks remain undetected. By using an on-line imaging system to inspect the wafer throughout production, residual stress and cracking problems can be located before adding significant value to the wafer.

Figure 7 shows a series of IR-Poleidoscope images from a silicon wafer with an embedded crack. This 1 mm thick, 200 mm diameter wafer is in the as-sawn condition and other similar wafers experienced catastrophic failure during polishing. The approach that had been previously used to locate pre-existing cracks that might lead to failure was to illuminate the surface with a flashlight at oblique incidence. The crack is only a few centimeters long, and is quite difficult to see, even at high magnification with this approach especially in such a large wafer with a diffuse as sawn finish. However, the stress patterns generated by the crack are immediately visible in the IR-Poleidoscope images due to the large stress concentration of the crack tip as well as the contact stresses that often appear in the crack wake. The series of images shown in Figure 7 are for a wafer mounted on a rotating stage with data capture at camera framing rates; the crack enters the field of view from the top of the image and propagates through the screen. The varying background "color" is due to changes in background residual stress throughout the wafer itself.

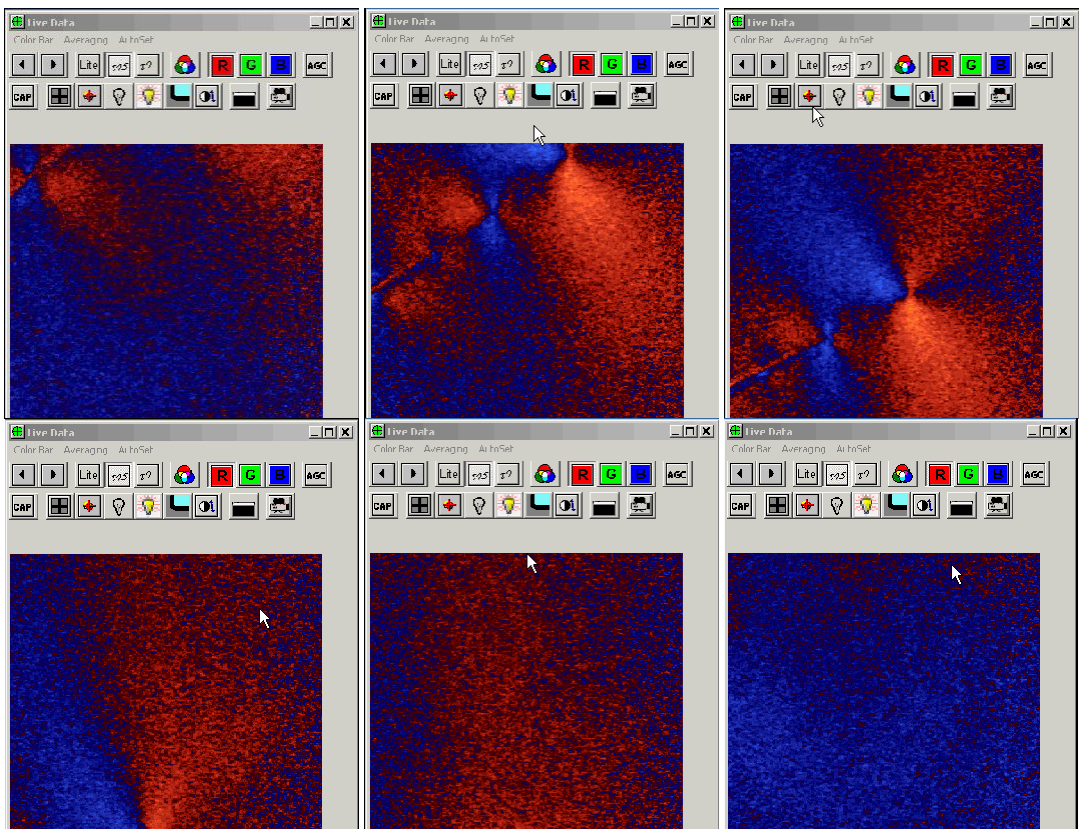

Figure 7. Dynamic imaging of a thick, rough silicon wafer with an embedded crack rotating through the field of view on a turntable.

By employing broad-field illumination and array based detectors, as opposed to a laser source and a single photodetector, specimens with very rough surfaces can be inspected quickly and conveniently from the earliest

stage of production through metallization. Furthermore, a higher wafer throughput can be achieved; making 100 percent on-line inspection at frame rates up to 15 frames per second a distinct possibility.

IV.2. Bonded semiconductor inspection

As mentioned previously, the IR-GFP system has been shown to locate trapped particles in bonded semiconductor devices at a lower magnification than typical IR transmission tools as a result of the large spatial extent over which the residual stress field is visible. The residual shear stress field appears as "bow-tie" pattern, with four lobes of alternating high and low shear stress regions that is expected from a radially symmetric normal stress field. Figure 8 shows an IR-Poleidoscope generated shear stress image from a microfluidic device with a nicely formed "bow-tie" pattern at the known location of the trapped particle ("B"). This particle is very near the intersection of two microfulidic channels. Regions outside of the defect location display an intensity level near the zero baseline. Again, this data is captured at camera framing speeds allowing very rapid inspection of the entire MEMS device on an undiced wafer.

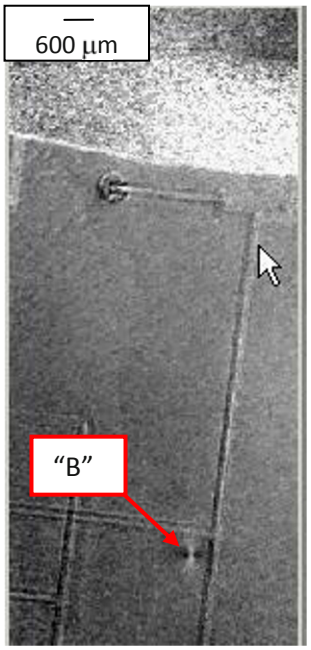

Figure 8. Shear 0 stress image of the adhesively bonded microfluidic device with a trapped particle imaged using the Phase II IR-GFP prototype.

V. SUMMARY

In summary, we demonstrated a rapid method for infrared photoelastic stress analysis that is applicable to on-line inspection of silicon-based materials. As silicon has become one of the most important structural and electronic materials for the MEMS, IC, and PV industries, the tool can significantly impact quality and process control in a range of industries. The IR-Poliedoscope has been shown to have a high sensitivity for stresses even in thin silicon wafers, yet is capable of inspecting wafers with rough surface finish, such as as-sawn substrates.

ACKNOWLEDGEMENTS

This material is based upon work supported by the National Science Foundation under Grant No. 0450604.

REFERENCES

1. Brewster, D., "On the communication of the structure of doubly refracting crystals to glass, muriate of soda, fluor spar, and other substances by mechanical compression and dilatation", *Philosophical Transactions of the Royal Society*,156-178, 1816.
2. Coker, E.G., Filon, L.N.G., *A Treatise on Photoelasticity*, 1st ed., Cambridge University Press, Cambridge, 1931.
3. Dash, W.C. "Birefringence in Silicon", *Physical Review*, **98**, 1536, 1955.
4. Appel, A.V., Pontarelli, D.A., "Infrared Polariscope for Photoelastic Measurement of Semiconductors", *Applied Optics*, **4**(11), 1475-1478, 1965.

5. Lederhandler, S.R., "Infrared Studies of Birefringence in Silicon", *Journal of Applied Physics*, **30** (11), 1631-1638, 1959.
6. Cloud, G.L and Pindera, J.T., "Techniques in Infrared Photoelasticity", *Experimental Mechanics*, **8** (5), 193-201, 1968.
7. DeNicola, R.O., Tauber, R.N., "Effect of Growth Parameters on the Residual Stress and Dislocation Density of Czochralski-Grown Silicon Crystals", *Journal of Applied Physics*, **42** (11), 4262-4269, 1971.
8. Redner, S., "Infrared Photoelasticity," *Strain*, **15** (2), 58-60, 1979.
9. Fukuzawa, M., Yamada, M.**,** "Photoelastic characterization of Si wafers by scanning infrared polariscope", *Journal of Crystal Growth*, **229**, 22-25, 2001.
10. Niitsu, Y., Ichinose, K., Ikegami, K.., "Micro-stress measurement by laser photoelasticity", *Mechanics and Materials for Electronic Packaging, ASME AMD* **187**, 29-35, 1994.
11. Niitsu, Y., Gomi, K., "Stress measurement in Si-wafer using polarizer infrared laser photoelasticity", *Mechanics and Materials for Electronic Packaging, ASME AMD,* **187**, 37-40, 1994.
12. Yamada, M., Ito, K., Fukuzawa, M., "Residual strain as a measure of wafer quality in indium phosphide crystals", *1997 International Conference on Indium Phosphide and Related Materials IEEE,* 1997, p.209-212.
13. Zheng, T., Danyluk, S., "Measurement of Residual Stresses in Silicon with NIR Photoelasticity", *Proceedings of the SEM Annual Conference*, 658-661, 2001.
14. Zheng, T., Danyluk, S., "Study of stresses in thin silicon wafer with near-infrared phase stepping photoelasticity", *Journal of Materials Research*, **17**(1), 36-42, 2002.
15. Gamboa, R.M., Brito, M.C., Serra, J.M., Maia Alves, J.*, "*Silicon tubes by a closed molten zone: a characterization study", *Solar Energy Materials and Solar Cells*, **72**(1-4), 173-181, 2002.
16. Horn, G., Lesniak, J., Mackin, T. and Boyce, B, "The Infrared Grey-Field Polariscope: A tool for rapid stress analysis in microelectronic materials and devices", *Review of Scientific Instruments*, **76** (4), 45108-1-10, 2005.
17. Lesniak, J. R. "Full Field Photoelastic Stress Analysis". *U. S. Patent #6,055,053,* April 25, 2000.
18. Horn, G. P., Mackin, T. J., Lesniak, J., "Trapped Particle Detection in Bonded Semiconductors Using Gray-Field Photoelastic Imaging," *Experimental Mechanics*, **45** (5), 457-466, 2005.
19. Horn, G., Johnson, H. T., Mackin, T. J., Lesniak, J. R. "Quantitative Model-Based Interpretation of Experimentally Measured Nanoscale Stress Sources at Wafer Bonded Interfaces", *ECS Transactions*, **3**(6), 227-238, 2006.
20. Buonassisi, T., Reitsma, S. Sweeney, R. Pickett, M.D. Huang, W. Lesniak, J., and Spencer M.L. **"**Evolution of stresses in wafer bulks and edges during industrial solar cell processing" *Proc. 22nd European Photovoltaic Solar Energy Conference and Exhibition*, Milan, Italy, 2007.
21. Patterson, E.A., Wang, Z.F., "Simultaneous Observation of Phase-Stepped Images for Automated Photoelasticity", *Journal of Strain Analysis*, **33** (5), 400, 1998.
22. Hobbs, J.W., Greene, R.J., Patterson, E.A., "A novel instrument for Transient Photoelasticity", *Experimental Mechanics*, **43**(4), 403-409, 2003.
23. Lesniak, J.R., Patterson, E.A., *U.S Patent # 6,441,972*, August 27, 2002.
24. Lesniak, J., Zhang, S.J., Patterson, E.A., "Design and Evaluation of the Poleidoscope: A Novel Digital Polariscope", *Experimental Mechanics*, **44**(2), 128-135, 2004.

Proceedings of the SEM Annual Conference
June 7-10, 2010 Indianapolis, Indiana USA

Surface Decoration for Improving the Accuracy of Displacement Measurements by Digital Image Correlation in SEM

B. Winiarski[1], G. S. Schajer[2] and P. J. Withers[1]

[1] School of Materials, University of Manchester, Manchester, M1 7HS, UK
[2] Dept. Mechanical Engineering, University of British Columbia, Vancouver, Canada

Abstract

In-situ straining experiments and residual stress evaluations by micromachining require accurate measurement of the surface displacement. These can be conveniently achieved by Digital Image Correlation (DIC). Three surface decoration techniques are presented to enhance surface deformation and residual stress measurement capabilities on micron-scale samples within a Scanning Electron Microscope – Focused Ion Beam (SEM-FIB) instrument. They involve the use of yttria-stabilized-zirconia nano particles applied chemically, nano platinum dots applied using FIB, and Focused Electron Beam (FEB) assisted deposition. The three decoration techniques create distinctive, random surface features that can be used with Digital Image Correlation to provide full field maps of surface displacements at high magnifications. A series of experiments using a FEGSEM / FIB demonstrated the effectiveness of the three surface decoration techniques for FEGSEM imaging at magnifications from 2,000× to 60,000×. The resolution of the image correlation is substantially enhanced by the surface decoration, with displacement standard deviations reduced to the 0.005 − 0.03 pixel range, depending on the patch size used. The implications for displacement measurement at the micro- and nanoscale are discussed and some examples shown.

Keywords: Scanning electron microscopy, Focused Ion Beam, High magnifications, 2D digital image correlation, Surface decoration methods, Residual stress, Submicron scale

1. Introduction

Recent innovations in micro-engineering have made it practical to fabricate structures and components having features in the nanometer range [1]. However, the typical methods for mechanical assessment such as strain gauges, optical non-contact methods [2], [3] etc., cannot be readily applied at this scale. One means of measuring displacement that works well in the nanometer range is Digital Image Correlation (DIC) of high-magnification image sequences from a Scanning Electron Microscope (SEM) [4-14]. The technique may be applied, for example, to monitor in situ straining experiments, or to assess residual stresses by monitoring surface relaxations on micro-machining.

Scanning electron microscopes (SEM) can provide high quality digital images over a broad range of magnifications from 30× to 10,000×. Further, new dual-beam Field-Emission Gun Scanning Electron Microscope − Focused Ion Beam (FEGSEM−FIB) instruments can provide high quality imaging at large magnifications, with resolution of features less than 5nm in size, while allowing precise milling using an ion beam. In addition, they can deposit metals by both ion and electron beam assisted deposition [15-17]. In some cases, scanning ion-beam images can have advantages over SEM images [18].

DIC analysis uses measurements of a visible pattern on the surface of a specimen to track the surface deformation. It evaluates the local surface displacement by comparing corresponding areas in digital images taken before and after deformation. The three main features that contribute to the accuracy of DIC measurements of surface deformations are the presence of a fine and high-contrast surface texture with distinctive features, the use of large correlation patch sizes [10, 19], and the stability of the imaging conditions [12, 13]. Under favourable conditions with a scanning electron microscope, DIC can provide full-field evaluations of the local surface displacements at the microscopic scale with an accuracy of ± 0.015 pixels, equivalent to 0.4 nm at magnification of 5,000× [11, 20, 21].

Often, the grains, inclusions, second phase particles, surface scratches, etc, provide suitable random, high-contrast features suitable for effective DIC. However, in many cases, the natural surface often lacks surface features of the appropriate size or optical contrast, causing the DIC to work poorly, or not at all. In such cases, an artificial surface pattern with appropriate characteristics must be applied. The process of doing this is called surface decoration.

T. Proulx (ed.), *Application of Imaging Techniques to Mechanics of Materials and Structures, Volume 4*, Conference Proceedings of the Society for Experimental Mechanics Series 14, DOI 10.1007/978-1-4419-9796-8_26, © The Society for Experimental Mechanics, Inc. 2013

At the macro-scale, surface decoration is typically done by spray-painting, grinding, etching, etc. [2, 22]. These decoration methods work well at the magnifications up to 1000× available with conventional optical microscopes. At the higher magnifications required to view nanometer scale features with scanning electron microscopes, more specialized surface decoration methods are required for effective DIC. Some decoration techniques used to create feature sizes larger then 100 nm are chemical and physical deposition, air brushing micro size particles (SiC, diamond), deposition of fluorescent nanoparticles, microcontact printing, UV photolithography and gold coatings [14, 23, 24]. However, most of these techniques require very large (compared to feature size) plane surfaces.

Surface decoration can also be applied very locally (approx. $< 15 \times 15\ \mu m^2$) using Focused Ion Beam (FIB) assisted sputtering of metallic films in the pattern of a randomly structured bitmap [20]. However, a possible drawback of a FIB is that it may damage the surface, or alter the stress distribution near the surface due to the implantation of Ga^+ ions. The use of a Focused Electron Beam (FEB) instead of a Focused Ion Beam [15], avoids these concerns. Since the typical FEB spot size (~0.2 nm) is smaller than FIB spot size (~5 nm), FEB assisted deposition also has the advantage of being able to create decoration patterns with smaller feature sizes [25]. However, the FEB method requires a significantly greater time (> 4× longer) than the FIB method to deposit a similar volume of material for the decoration pattern.

This paper explores the use of three surface decoration techniques: yttria-stabilized-zirconia (YSZ) nano particles of size ~ 20 nm applied chemically, nano platinum dots of size > 30 nm applied in a pre-defined random pattern using a FIB, and nano platinum dots of size > 15nm applied using FEB deposition. DIC analyses of the original and decorated surfaces are done to indicate the performance of the image correlations with the various surface treatments. The analysis involves an exploration of the effects of SEM image magnification in the range 2,000× to 60,000×, decoration feature size and DIC patch size.

2. Materials and Methods

2.1. Sample without surface decoration

A 316L stainless steel plate was cut into a rectangular bar (3 × 3 × 25 mm) by wire electron discharge machining (EDM). After machining the sample was mechanically polished using 1200-grit sandpaper and rinsed in ethanol. Later, an AJA ATC2000 radio-frequency magnetron sputtering system was used to deposit a Zr-based metallic-glass film of about 200 nm thickness on the 316L substrate. The working pressure and power during sputtering were 3×10^{-3} Torr and 100 W, respectively. The sputtering target was a commercial-grade alloy of $Zr_{47}Cu_{31}Al_{13}Ni_9$ (in atomic %). This created a microscopically smooth surface with few distinctive features. Subsequently, Agar silver paint was used to attach the specimen to the standard aluminium pin stub of diameter of 12.5 mm. Finally, a Gatan PECS 682 precise etching-coating system equipped with a Gatan 681.20000 Film Thickness Monitor was used to sputter a 24 nm thick carbon film on half of the specimen surface prior the FEGSEM imaging. The carbon target was blasted by a broad argon ion beam (10 kV, 550 µA each gun) in a vacuum of about 2×10^{-5} Torr. This carbon coating eliminated surface charging effects on the amorphous Zr surface.

2.2. Sample with YSZ nano particles

The second half of the Zr film surface was then decorated with Yttria Stabilised Zirconium (YSZ) particles (PI-KEM Ltd., Shropshire, England) of size 20 – 30 nm, precipitated from 40% aqueous ethanol suspension (~ 10 mg/cm^3) and dried at room temperature. An ultrasonic bath was used for 15 minutes to break up large YSZ-particle agglomerates in the suspension prior to application. The decoration procedure was applied in a series of steps: (a) the ethanol suspension of YSZ particles was applied on the as-received surface using a laboratory borosilicate glass micropipette and then dried; (b) the decorated surface was examined using FEGSEM mode of the dual beam microscope; (c) the decorated surface was coated with carbon film of thickness of 4 nm using the Gatan PECS system. The steps (a) − (c) were then repeated two times, where the thickness of the final carbon coating was 14 nm. Each time the ethanol suspension was kept in the ultrasonic bath for 5 minutes. This procedure produced ~20% surface coverage and good separation of nanoparticles, see Figs. 4c and d. The coverage of the surface with YSZ particles could be controlled by changing the particle density in the liquid or by changing the number of steps of the decoration procedure. Carbon coating plays a dual role; removing surface charging effects on the amorphous surface and charging of YSZ particles, as well as attaching the particles to the surface.

2.3. Sample with nano Pt dots

A dual beam FEI xT Nova NanoLab 600i FEGSEM/FIB microscope was used to sputter a pattern of nano Pt dots on the specimen surface. An FEI gas injection system and a standard molecular gas precursor for Pt deposition, $(CH_3)_3Pt(CpCH_3)$, were used. Before deposition, the sample was allowed to stabilise inside the vacuum chamber for more than 12 hours. A pseudo-random nano Pt dot pattern was mapped onto the carbon-coated surface using the 1024 × 844 pixel bitmap shown in Fig.1. This pattern was prepared using Adobe Photoshop software, starting from FEGSEM images of a surface decorated with YSZ nano particles. The original image was digitized at a gray-scale threshold of 128/255. Later, the pattern was augmented manually to add dots to some locally depleted areas. The bitmap shown in Fig. 1a has 20 % coverage and contains 5305 dots, and the bitmap shown in Fig.1b has 12 % coverage and contains 2321 dots.

2.3.1. Sample with FIB assisted nano Pt dots

The FIB imaging and patterning (Pt deposition) mode was used with magnification 3,500× and Wd = 16.5 mm, where the focused Ga^+ ion beam of spot size ~ 5 nm and current of 28 pA was accelerated by electric field of 30 kV. The sputtering area was set to 23.3 × 20 μm^2 with Pt deposition thickness of 14 nm. This setting required 328 seconds of deposition time giving a deposition rate of 0.02μm^3/s.

2.3.2. Sample with FEB assisted nano Pt dots

The FEB patterning mode was used with magnification 15,000× and Wd = 4.85 mm, where the focused Ga^+ ion beam of spot size < 1.4 nm, current 58 pA and voltage 15 kV. The sputtering area was set to 5.43 × 4.66 μm^2 with Pt deposition thickness of 100 nm. This setting required 574 seconds of deposition time, giving a deposition rate of 0.0044 μm^3/s.

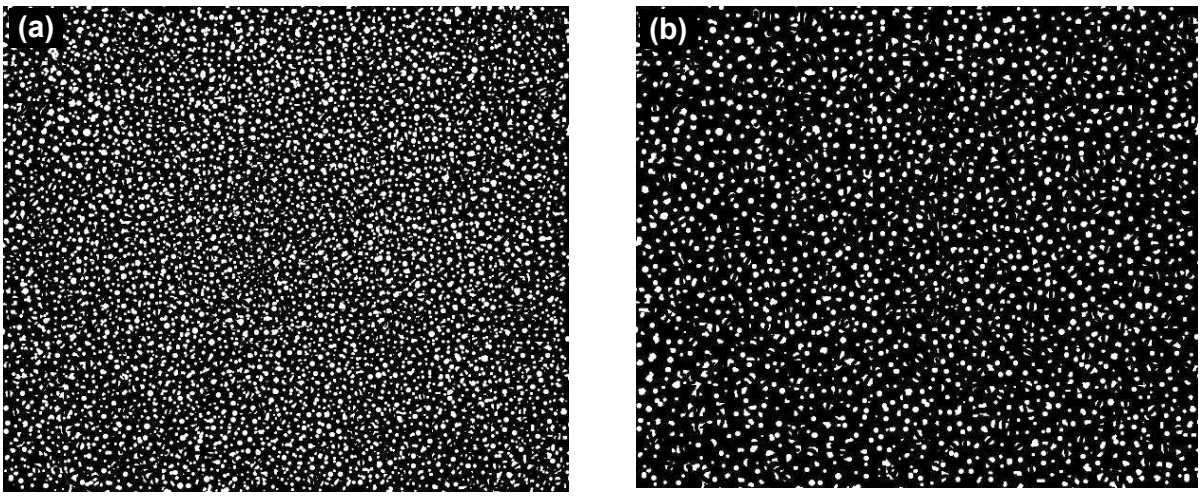

Figure 1. Predefined binary bit maps of resolution of 1024 × 844 pixels used for Pt sputtering: (a) binary bit map with 20 % coverage, (b) binary bit map with 12 % coverage.

2.4. FEGSEM imaging

To achieve consistent and reliable SEM measurements for use with DIC, it is important to choose appropriate imaging conditions, namely voltage, current, dwell time, detection of secondary electrons (SE) or back-scattered electrons (BE), secondary ions (SI^+), digital image resolution, etc. Therefore, a preliminary series of FEGSEM imaging experiments was performed to identify the best instrument settings for good DIC. The control parameter was the standard deviation of the DIC-indicated displacement (SD_u) within the image area. It was found that an e-beam acceleration voltage of 5 kV, with beam current 0.40 nA, aperture 30 µm, spot size < 1.4 nm and detection of secondary electrons gives good contrast images with negligible charging of the sample surface. Usually, the BE signal gave better contrast then the SE signal for a given material, with a working distance of about 10 mm [26]. The surface of the sample was placed in the coincidence point of both beams, giving working distances of 4.85 mm and 15.6 mm for the e-beam and ion-beams, respectively. In this study, images acquired using back-scattered electrons gave lower contrast then the SE signal. Later, different e-beam dwell times (Dt = 1 µs, 3 µs, 10 µs and 30 µs) and image acquisition conditions (image integration from 1, 4, 8 and 16 e-beam scans) are analysed. All images were acquired

after an auto-brightness/auto-contrast procedure. It was found that an e-beam dwell time of 3 µs and integration of 8 frames (total image acquisition time = 21.7 s) yielded the lowest SD_u.

2.5. Digital Image Correlation

Typically, DIC is used with images measured by visible-light digital cameras [4-9]. Here, the dual beam FEGSEM-FIBa FEGSEM is used to record the images. The 2-D DIC method involves making two successive images of the target surface, taken before and after the deformation of interest. The image correlation proceeds by selecting a local area of pixels called a "patch" within the first image, and then locating the corresponding patch position within the second image based on the position of maximum correlation. Interpolation techniques allow the relative position of corresponding patches to be determined to within 0.02 or less of a pixel spacing [6, 13]. The displacement resolution depends on the patch size; typically larger patches give finer resolution, but require much greater computation time.

Here 100 patch locations arranged in a regular 10×10 grid over the initial image were examined. The *x* and *y* displacements at each of the patches was estimated using custom DIC software. The precision of the DIC displacement results was estimated from the standard deviations of the evaluated sets of 100 *x* and *y* displacements. All these evaluations were repeated using square patches 12×12, 17×17, 25×25, 35×35, 50×50, 70×70 and 100×100; each containing approx. double the pixels of the preceding patch size.

2.6. Image Acquisition for DIC

A common measurement procedure was used for each of the four samples used in this study. In turn, each sample was mounted on a mechanized translate/rotation. An initial FEGSEM image was taken of the sample surface. The sample was then rotated by 52° and rotated back to its nominal original position. Small mechanical imperfections in the mechanized stage caused sub-micron discrepancies in the final position of the sample, corresponding to several pixels at the high magnifications used for imaging. A second FEGSEM image was then taken of the sample surface to provide data for the DIC calculations. The time interval between image acquisitions was about 60 s. These measurements were repeated for image magnifications 2,000×; 3,500×; 5,000×; 8,000×; 15,000×, 25,000×, 40,000× and 60,000× for each sample, where corresponding spatial resolution for each pixel was 62.5 nm, 35.7 nm, 25 nm, 15.6 nm, 8.3 nm, 5 nm, 3.1 nm and 2 nm, respectively.

3. Results

Figure 2 shows the standard deviations of the DIC estimates of the *x* and *y* displacements for the nano YSZ particle specimen. Images of sufficient quality to enable DIC estimates of surface displacement with a standard deviation < 0.02 pixels can be achieved by integrating multiple (8) frames scanned with dwell times in the micro-second range. These findings parallel those obtained elsewhere [13].

Figure 3 shows representative images for the four samples used in this study. Without decoration few discernable features are seen; by contrast the YSZ nano particles provide a distinctive and sharply defined surface pattern as do the FIB and FEB (at approximately twice the magnification) assisted Pt dots although less sharply defined at large magnifications. The high-magnification image (h) shows that the edges of the Pt dots are not perfectly sharp, but have a gradient of brightness at their edges. This causes the image to appear slightly blurred. Figure 4 shows the standard deviations of the DIC estimates of *y*-direction displacement for the four sample surfaces for a range of normalized patch sizes. The results in for *x*-direction displacements are similar. The standard deviations are based on the DIC displacement estimates from 100 patches; the corresponding absolute displacements are in the range 0 – 10 pixels.

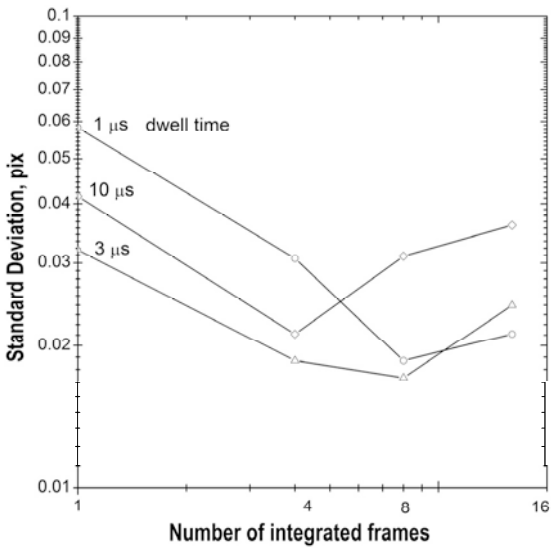

Figure 2. Standard deviation of the DIC displacement estimate vs. number of integrated frames for FEGSEM images for nano YSZ particles and magnification of 8,000×, for patch size 35×35 pixels and spacing 24 pixels.

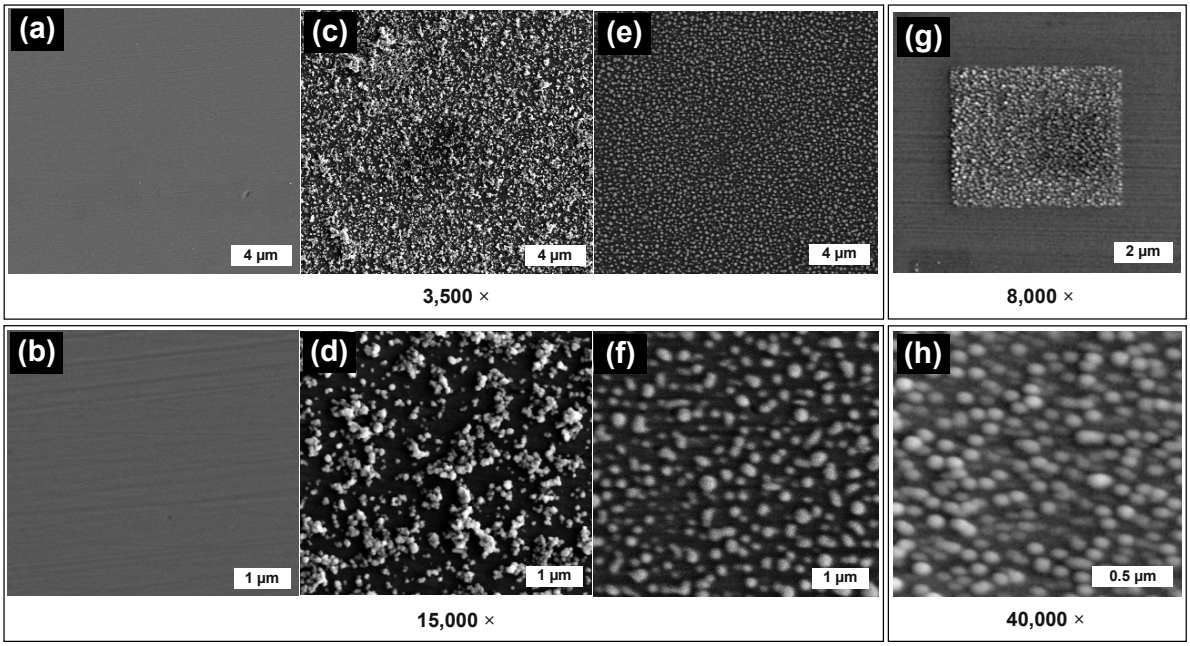

Figure 3. Low and high magnification FEGSEM images of the four samples. (a) and (b) undecorated, (c) and (d) YSZ nano particles, (e) and (f) FIB assisted Pt nano dots at 20% coverage, (g) and (h) FEB assisted Pt nano dots at 12% coverage.

In Figure 4, the patch sizes have been normalized relative to image magnification. This is done because the precision of DIC results depends on the number of distinct features contained within the correlation patch used. The more features there are within the patch, the greater the amount of data available for the correlation and the greater the resulting correlation precision. Thus, normalization by the image magnification eliminates the computational factors and focuses the results on the effect of the various surface decorations.

4. Discussion

Figure 4 shows the standard deviations for the various decoration methods. In all cases the standard deviation is approximately inversely proportional to normalized patch size (gradient = – 1 on a log-log graph). For the untreated surface, Figure 4a, the greater the image magnification, the lower the DIC standard deviation. This occurs because the higher magnifications tend to reveal more surface detail and therefore more features for the DIC to exploit. Nevertheless the scaricity of features mean that the DIC correlation coefficients are very low for all the curves in Figure 4a, with typical R^2 values in the range 0.2 – 0.5. Consequently, the trends of the various curves in Figure 4a are irregular, with several jumps and overlaps. The DIC standard deviation varies within the range 0.06 – 5 pixels, with a typical value around 0.3 pixels. This level of precision compares poorly with the 0.02 pixel standard deviations typically quoted for DIC estimates.

The graph for the YSZ nano particles show the same trend as above, but with much lower standard deviations, since the nano particles create a distinctive patterns of features on the sample surface suitable for DIC analysis. The standard deviations reported in Figure 4b are in range 0.004 – 1 pixels, with a typical value around 0.02 pixels. These values are approximately 10 times smaller than for the smooth surface (Figure 4a), with R^2 values in the range 0.95 – 0.995.

The FIB assisted Pt nano dots (Fig 4c) also provide effective surface decoration. As can be seen from Figures 3e and 3f, the edges of the Pt nano dots are not as sharp as for the YSZ nano particles, and so they provide less distinct features for the DIC analysis. Consequently, the standard deviations are increased, and lie within the range 0.004 – 1 pixels, with a typical value around 0.03 pixels. The corresponding DIC correlation coefficients, R^2 are in the range 0.90 – 0.98.

To take advantage of the smaller spot size associated with the FEB assisted Pt nano dots (~ 0.2 nm compared with ~ 5 nm for the FIB), these measurements were made using a finer resolution dot pattern viewed at a higher magnification. Figure 4d shows that the FEB assisted Pt nano dots provide effective

high-resolution decoration giving comparable, or better, standard deviations to the FIB technique. However, when lower spatial resolutions are appropriate, the FIB technique has the advantage of requiring much less beam time.

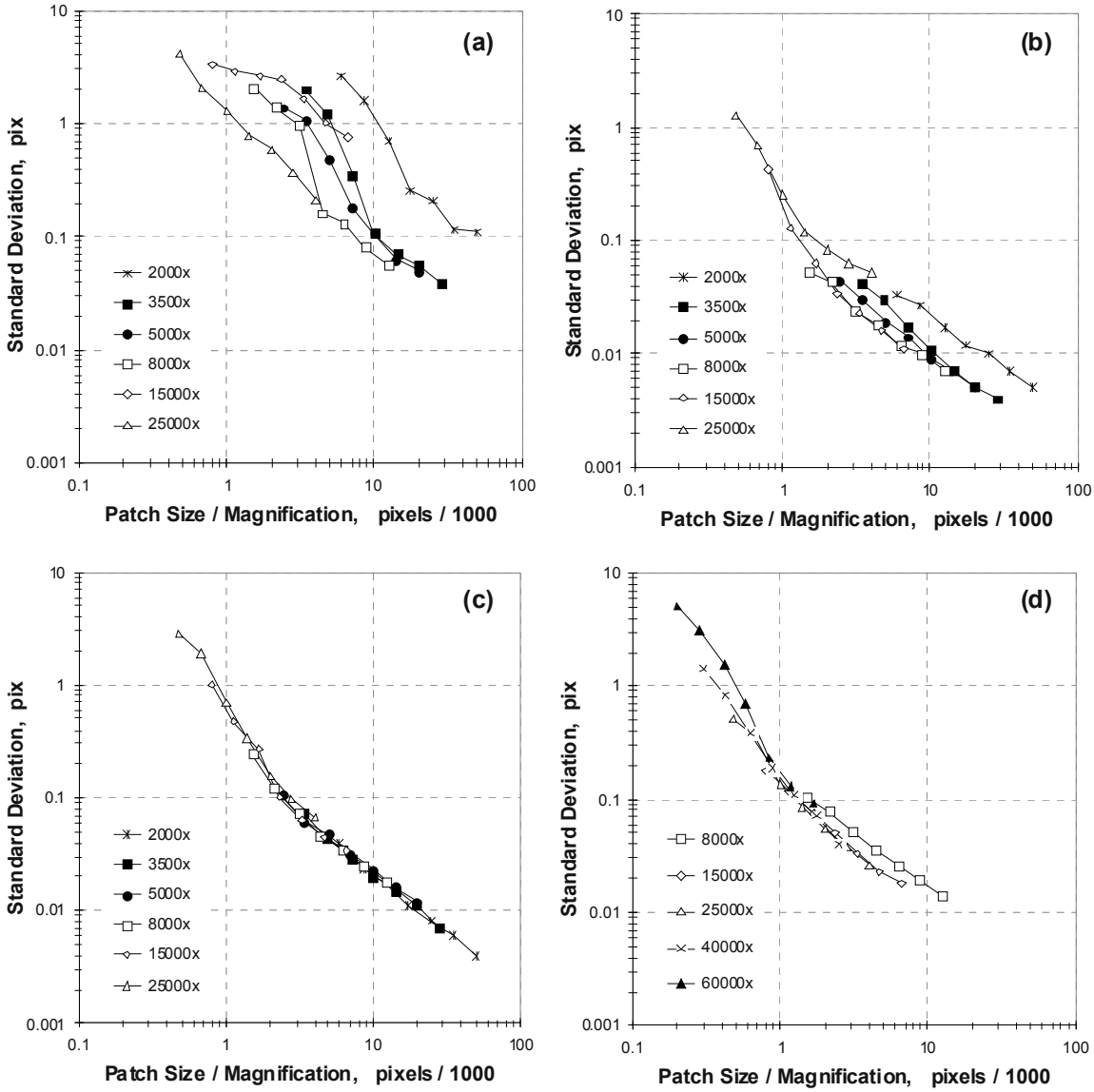

Figure 4. Standard deviation of the DIC displacement estimate vs. normalized patch size. (a) undecorated, (b) YSZ nano particles, (c) FIB assisted Pt nano dots (20% coverage), (d) FEB assisted Pt nano dots (12% coverage).

Figure 5 shows some practical examples of application of the decoration techniques for evaluation of residual stress profiles as a function of depth from laser peened (a and b) and shot peened (c) surfaces of bulk metallic glasses (BMG) by FIB micromachining, i.e., the microslitting method [27] and the microhole drilling [28]. The surfaces of as-cast BMGs have very smooth and lustrous outer appearance with few surface features at micron scale, causing the standard deviation of DIC displacement estimates to be large, around 0.5 pixels. By deposition of nano platinium dots using FIB, the standard deviation was reduced to 0.017 pixels (128×128 pixel patches) and surface displacements used for stress analysis ranged from 0.1 to 0.3 pixels, in Figure 5b, were accurately recovered. In Figure 5c, YSZ nano particles were used to decorate a shot peened surface of Zr-based BMG. Here, typical standard deviation of displacement estimates for the undecorated surface was about 0.25 pixels, whereas for the decorated surface the standard deviation was reduced to 0.014 pixels (64×64 pixel patches). The absolute surface displacements used for stress analysis ranged from 0.4 to 1.2 pixels (in Figure 5c).

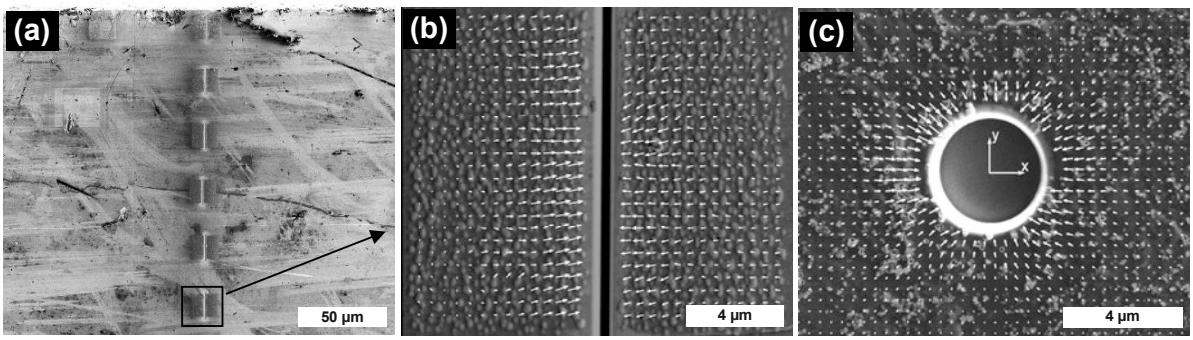

Figure 5. Practical examples of application of the decoration techniques for evaluation residual stresses in laser peened and shot peened BMGs by FIB micromachining. (a) a series of micro slots introduced on a side surface down from a top laser peened surface of Vit-105 BMG and (b) surface displacements recovered FIB microslitting (arrows are exaggerated by 100×); the surface is decorated with nano platinum dots applied using FIB [27]; (c) surface displacements recovered after FIB microhole drilling (arrows are exaggerated by 15×); the surface is decorated with YSZ nano nano particles [28].

5. Conclusions

Experiments and practical applications confirm that surface decoration can greatly improve DIC capabilities within FEGSEM images, particularly when the native specimen surface is smooth with few distinctive features. The three decoration techniques proposed have complementary characteristics.

The YSZ nano particle technique does not require a FIB and their interaction with the surface of the substrate is minimal. The resulting decorated specimen can be measured within a conventional SEM. The decoration has distinctive features when imaged at high magnifications, and gives excellent DIC results. Surface displacements can typically be resolved to within 0.02 of a pixel, reducing below 0.01 of a pixel when using large correlation patches. However, the particle application technique is time consuming and is not easily adaptable to different scales. Furthermore, a random and uniformly dense pattern can be achieved only on relatively large (millimetre scale) plane surfaces.

Conversely, the FIB and FEB assisted and Pt nano dot techniques are very adaptable and controllable. The dots can be laid down at a range of scales and can be precisely placed at specific locations to fit the needs of the desired measurements. However, the dots have less sharp edges than the YSZ nano particles, and generally give slightly less accurate, although still very satisfactory DIC results. Surface displacements can typically be resolved to within 0.03 of a pixel, again reducing below 0.01 of a pixel when using large correlation patches.

As the target feature size decreases, the Pt nano dots become less distinct and they tend to become blurred. With the FIB equipment used in this study, the smallest practical feature size is around 35 nm and 25 nm, for FIB and FEB respectively. Pt nano dots are less easily applied than YSZ nano particles, and require the use of a FIB. A possible drawback of the FIB assisted deposition method is that it may introduce significant surface stresses; the FEB method does not have this characteristic. The FEB assisted deposition technique is also useful for measurements requiring smaller feature size, ~25 nm, but has the disadvantage or requiring relatively long beam times (more than 4× longer).

Acknowledgments

The measurements were made within the Stress and Damage Characterization Unit at the University of Manchester, U.K., supported by the Light Alloys Towards Environmentally Sustainable Transport (LATEST) EPSRC Portfolio Project. We are grateful to P. Liaw (the University of Tennessee, U.S.A.) and Y. Yokoyama (Himeji Institute of Technology, Japan) for provision of the sample; to P. Xiao (the University of Manchester, U.K.) for YSZ nanopowder and A. Gholinia (the University of Manchester, U.K.) for technical and scientific suggestions during the experiment. Author GSS was supported by a grant from the Natural Sciences and Engineering Research Council of Canada (NSERC).

References

1. Bhushan, B. (ed.), *Springer Handbook of Nanotechnology*. 2004, Berlin: Springer-Verlag.
2. Rastogi, P.K., *Photomechanics*. 2000, Berlin, London: Springer.
3. Sirkis, J.S. and Lim, T.J., *Displacement and strain-measurement with automated grid methods.* Experimetal Mechanics 31(4): p. 382-388, 1991.
4. Peters, W.H. and Ranson, W.F., *Digital imaging techniques in experimental stress-analysis*. Optical Engineering 21(3): p. 427-431, 1982.
5. Peters, W.H., et al., Application of digital correlation methods to rigid body mechanics. Optical Engineering 22(6): p. 738-742, 1983.
6. Quinta De Fonseca, J., Mummery, P.M., Withers, P.J., *Full-field strain mapping by optical correlation of micrographs acquired during deformation.* Journal of Microscopy 218: p. 9-21, 2004.
7. McGinnis, M.J., S. Pessiki and Turker, H., *Application of three-dimensional digital image correlation to the core-drilling method.* Experimental Mechanics 45(4): p. 359-367, 2005.
8. Birgisson, B., et al., *An optical strain measurement system for asphalt mixtures.* Materials and Structures/Materiaux et Constructions 42(4): p. 427-441, 2009.
9. Niendorf, T., et al., *Monitoring the fatigue-induced damage evolution in ultrafine-grained interstitial-free steel utilizing digital image correlation.* Materials Science and Engineering A 517(1-2): p. 225-234, 2009.
10. Yaofeng, S. and Pang, J.H.L., *Study of optimal subset size in digital image correlation of speckle pattern images.* Optics and Lasers in Engineering 45(9): p. 967-974, 2007.
11. Winiarski, B., at al., *Mapping residual-stress distributions at the micron scale in amorphous materials.* Metallurgical and Materials Transactions A - In Press: p. 1-9, 2009.
12. Jin, H., Lu, W.Y., and Korellis, J., *Micro-scale deformation measurement using the digital image correlation technique and scanning electron microscope imaging.* Journal of Strain Analysis for Engineering Design 43(8): p. 719-728, 2008.
13. Sutton, M.A., et al., *Scanning electron microscopy for quantitative small and large deformation measurements Part I: SEM imaging at magnifications from 200 to 10,000.* Experimental Mechanics 47(6): p. 775-787, 2007.
14. Scrivens, W.A., et al., *Development of patterns for digital image correlation measurements at reduced length scales.* Experimental Mechanics 47(1): p. 63-77, 2007.
15. Utke, I., Hoffmann, P. and Melngailis, J., *Gas-assisted focused electron beam and ion beam processing and fabrication.* Journal of Vacuum Science & Technology B 26(4): p. 1197-1276, 2008.
16. Langford, R.M., et al., *Focused ion beam micro- and nanoengineering.* MRS Bulletin 32(5): p. 417-423, 2007.
17. Giannuzzi, L.A. and Stevie, F.A. (eds.), *Introduction to Focused Ion Beam*, New York: Springer, p.53-63, 2005.
18. Tellez, H., et al., *Focused ion beam imaging of laser ablation sub-surface effects on layered materials.* Applied Surface Science 255(5): p. 2265-2269, 2008.
19. Lecompte, D., et al., *Quality assessment of speckle patterns for digital image correlation.* Optics and Lasers in Engineering 44(11): p. 1132-1145, 2006.
20. Sabate, N., et al., *FIB-based technique for stress characterisation on thin films for reliability purposes.* Microelectronic Engineering 84(5-8): p. 1783-1787, 2007.
21. Kang, K.J., at al., *A method for in situ measurement of the residual stress in thin films by using the focused ion beam.* Thin Solid Films 443: p. 71-77, 2003.
22. Sun, Z., Lyons, J.S. and McNeill, S.R., *Measuring Microscopic Deformations with Digital Image Correlation.* Optics and Lasers in Engineering 27(4): p. 409-428, 1997**.**
23. Collette, S.A., et al., *Development of patterns for nanoscale strain measurements: I. Fabrication of imprinted Au webs for polymeric materials.* Nanotechnology 15(12): p. 1812-1817, 2004.
24. Berfield, T.A., et al., *Micro-and nanoscale deformation measurement of surface and internal planes via digital image correlation.* Experimental Mechanics 47(1): p. 51-62, 2007.
25. van Kouwen, L., Botman, A. and Hagen, C.W., *Focused Electron-Beam-Induced Deposition of 3 nm Dots in a Scanning Electron Microscope.* Nano Letters 9(5): p. 2149-2152, 2009.
26. Sutton, Sutton, M.A., et al., *Scanning electron microscopy for quantitative small and large deformation measurements Part II: Experimental validation for magnifications from 200 to 10,000.* Experimental Mechanics 47(6): p. 789-804, 2007.
27. Winiarski, B., Wang, G., Liaw, P.K. and Withers, P.J., *Mapping residual stress distributions in laser peened Vit-105 BMG using the FIB micro-slitting method.* unpublished work.
28. Winiarski, B. and Withers, P.J. *Mapping residual stress profiles at the micron scale using FIB micro-hole drilling*. in *7th BSSM International Conference on Advances in Experimental Mechanics, 7-9 September 2010*. Liverpool: to be published in Trans Tech Publications 2010.

Proceedings of the SEM Annual Conference
June 7-10, 2010 Indianapolis, Indiana USA

Heat source estimations to study the localized behaviour of superelastic NiTi shape memory alloys

H. Louche[(1)], D. Favier[(2)], L. Orgéas[(2)], V. Delobelle[(2)], P. Schlosser[(2)]
[1] Université de Savoie / SYMME
BP 80439, 74944 Annecy le Vieux cedex, France
herve.louche@univ-savoie.fr
[2] Université de Grenoble/CNRS
3S-R, BP 53, 38041 Grenoble Cedex 09, France
denis.favier@hmg.inpg.fr, laurent.orgeas@hmg.inpg.fr

ABSTRACT
Full field measurements (thermal and kinematics) are powerful techniques to study the thermomechanical behaviour of materials. This communication presents coupled full field measurements conducted on NiTi SMAs during tensile tests. Temperature fields are used to estimate the heat sources associated with the stress induced phase transformations. A spatio temporal synchronisation between the thermal and kinematics fields allows to express the thermal or heat source fields in the reference (undeformed) configuration. Finally, a temporal integration of the heat sources for each material point gives the evolution of the heat induced by the phase transformation. Examples of such measurements are given in this communication.

INTRODUCTION
Superelastic polycrystalline NiTi Shape Memory Alloys (SMA) are increasingly used for biomedical applications (stents, catheters, implants…) [1]. The superelasticity is a quasi-reversible deformation associated with a stress-induced martensitic (SIM) transformation, a first order reversible solid-solid phase change. It is now well-established that superelastic tension tests on polycrystalline NiTi SMA plates, wires or tubes often exhibits localized Lüders-like deformation modes [1,2]. The localization has been studied using qualitative optical observations [1-3], multiple extensometers [4] and full-field temperature measurements [5,6].

Temperature measurements obtained by infrared thermography was previously used in [6] to estimate the heat sources during the homogeneous stages of a tensile test on NiTi tubes. Such heat power, linked to the local latent heat of the transformation, brought new information on the mechanism involved during these stages. When the transformation is localized the method to estimate localized heat sources is different; see [7] for thin sheets and [8] for thin tubes. Simultaneous measurements of kinematics fields (displacements, strain), obtained with Digital Image Correlation (DIC) applied to visible images recorded during the test, can improve the method and deliver new information [9]. The objective of this communication is to present what can bring such coupled full field observations in the case of tensile tests of NiTi plate samples.

MATERIAL AND EXPERIMENTAL SETUP
The material used was a commercial NiTi alloy produced in China by the company PeierTech with a composition of Ti-50.6 at.% Ni. As received, the material was solution treated for 1 h at 1023 K and aged at 773 K for 30 min. The resulting DSC is shown in Fig. 1.

T. Proulx (ed.), *Application of Imaging Techniques to Mechanics of Materials and Structures, Volume 4*, Conference Proceedings of the Society for Experimental Mechanics Series 14, DOI 10.1007/978-1-4419-9796-8_27, © The Society for Experimental Mechanics, Inc. 2013

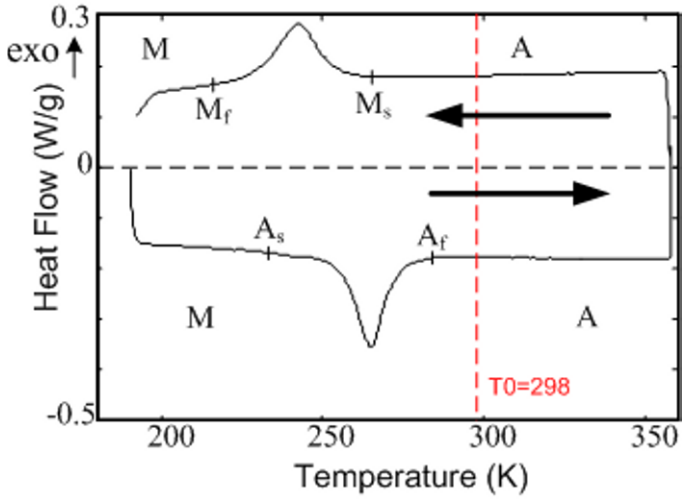

Figure 1: DSC measurements

Temperature and displacement fields were simultaneously measured on the sheet surface. A fast multidetector infrared camera (CEDIP Jade III MW, 14 bit, 320x240 pixels, thermal resolution *20 mK*) was used to measure the temperature field *T(M, t)* of spatial points *M* of spatial coordinate $\vec{x}$ at current time *t*. The displacement field $\vec{u}(M,t)$ on the sample surface was obtained using a digital visible camera (Hamamatsu, 12 bit, 1280x1024 pixels) and a DIC processing software (7D software, [10]).

The sample surface was coated with high emissivity black paint with a white texture on top. As shown in [9], such a coating is compatible with both the infrared and visible observations and its remissibility is very close from that of a black body. The optical axis of the visible camera was normal to this surface and the infrared camera was slightly oriented with an angle of 15° to the normal direction. As the thermal radiation of a black body is not influenced by a misorientation of the camera lower than 45°, our setup allows to measure quantitatively temperature and temperature variation fields.

A mean nominal axial strain was measured from the displacement fields using the relative displacement Δl of two material points A and B located at both extremities of a gauge length l_0=58 mm which is the initial distance between these two points.

EXAMPLE OF RESULTS

Figure 2 shows a typical result obtained during a quasi static loading. It presents the axial component of the Green-Lagrange strain E_{xx}, the temperature variation θ and the heat source *s* fields, at four different times marked in Figure 2a. A constant thermal conductivity was assumed with the arbitrary choice $k=k_M$, where k_M is the martensite thermal conductivity.

In order to have a global view during the loading, a spatiotemporal representation of these fields is plotted in Figure 3. It represents the temporal evolution along an axial profile of the Green-Lagrange axial strain E_{xx}, the temperature variation θ and the heat sources s_M. The grey dot line and the black continuous line superimposed represent the temporal evolution of the nominal stress and of the nominal axial strain ε, respectively .

Temporal integration of the heat sources in each material point gives the evolution of the heat induced by the phase transformation.

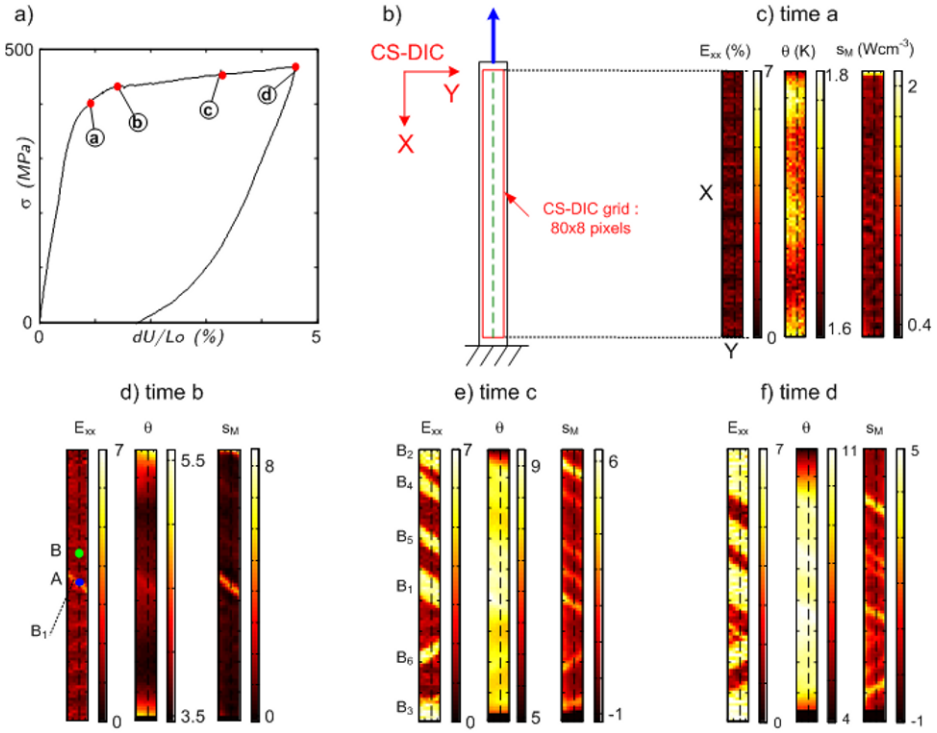

Figure 2: Axial strain, temperature variation and heat sources fields at several times, plotted in reference DIC coordinate system (CS-DIC). a) Nominal stress strain curve and position of the selected times during loading. b) Scheme of the area corresponding to CS-DIC. c) Green Lagrange axial strain $E_{xx}(X,Y,t)$, temperature variation $\theta(X,Y,t)$ and heat sources $s_M(X,Y,t)$ fields at the same time a, indicated in the first Figure. d) to f) same fields at times b, c, d.

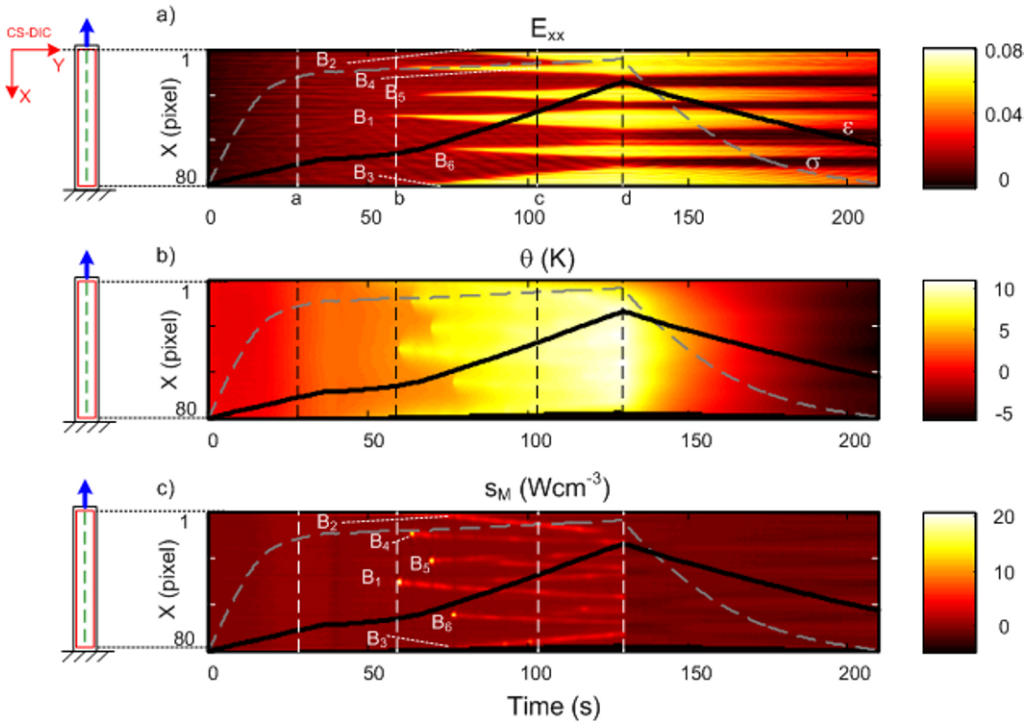

Figure 3: Spatiotemporal representation along the tensile axis, indicated by the green dot line of fixed Y_0 coordinate in the left schemes, of: a) the Green Lagrange axial strain $E_{xx}(X,Y_0,t)$, b) the temperature variation $\theta(X,Y_0,t)$ and c) the heat sources $s_M(X,Y_0,t)$. The two curves super imposed are the nominal stress σ and the local axial strain ε. Refer to Figure 2a to get their amplitude values.

REFERENCES

[1] Miyazaki, S., Imai, T., Otsuka, K. and Suzuki, Y. Lüders-like deformation observed in the transformation pseudoelasticity of a NiTi alloy /Scripta Metall/. 15, 853-56, 1981.
[2] Sun, Q.P. and Li, Z.Q. (2002) The initiation and growth of macroscopic martensite band in nano-grained NiTi microtube under tension. /Int. J. of Plast/, 18, 1481-1498.
[3] Brinson, C.L., Schmidt, I. and Lammering, R., Stress-induced transformation behaviour of polycristalline NiTi shape memory alloy : micro and macromechanical investigations via in situ optical microscopy, /J. Mech. Phys. Solids/, 52, 1549-1571, 2004.
[4] Orgéas, L. and Favier D. Stress-induced martensitic transformation of a NiTi alloy in isothermal shear, tension, and compression, /Acta Mater./, 46 (15) :5579-5591, 1998.
[5] Shaw, J.A., Kyriakides, S. On the nucleation and propagation of phase transformation fronts in a NiTi alloy. /Acta Mater/. 45, 683-700, 1997.
[6] D. Favier , H. Louche, P. Schlosser, L. Orgéas, P. Vacher and L. Debove, Homogeneous and heterogeneous deformation mechanisms in an austenitic polycrystalline Ti-50.8 at% Ni thin tube under tension. Investigation via temperature and strain fields measurement, *Acta Mater.*, 55, 16, 5310-5322, 2007.
[7] A. Chrysochoos and H. Louche, “An infrared image processing to analyse the calorific effects accompanying strain localisation,” Int J Eng Sci, vol. 38, pp. 1759–1788, Nov. 2000.
[8] P. Schlosser, H. Louche, D. Favier and L. Orgéas, Image processing to estimate the heat sources related to phase transformations during tensile tests of NiTi tubes, *Strain*, Vol 43, 3, 260-271, 2007.
[9] P Schlosser, Infuence of thermal and mechanical aspects on deformation behaviour of NiTi alloys. PhD thesis, Université Joseph Fourier, Grenoble, France, 2008.
[10] P. Vacher, S. Dumoulin, and F. Morestin, “Bidimensional deformation measurement us-ing digital images,” Proc. Instn Mech. Engrs, vol. 213, C, pp. 811–817, 1999.

Proceedings of the SEM Annual Conference
June 7-10, 2010 Indianapolis, Indiana USA

On The Martensitic Transformation In SMA Under High Strain Rates

D. Saletti[1] , S. Pattofatto[1] , H. Zhao[1]
[1] LMT Cachan, ENS Cachan/CNRS UMR 8535/Univ. Paris 6/PRES UniverSud Paris, 61 Avenue du Président Wilson, 94235 Cachan Cedex, France
saletti@lmt.ens-cachan.fr

ABSTRACT
Shape memory alloys (SMA) have specific properties that are mainly due to the martensitic transformation occurring in the material when mechanical or thermal loadings are applied. To study the effect of strain rate on the transformation occurring on an NiTi SMA different tests were performed at different strain rates in the range of 0,001 /s to 15 /s. For the dynamic tensile tests, a Split Hopkinson Tensile Bar set-up was used with a fast camera recording at 45'000 fps used to measure the extension rate of the martensitic phase region in the specimen. For quasi-static tests, an additional infrared thermography measurement was used. A superimposition of DIC and IR measurements in time and space can be done during quasi-static tests and the results show that the temperature peak, as expected follows the transformation front. As a consequence of the former validation of the DIC procedure, the velocity of the transformation front at high strain rate is deduced from space-time figures. As a conclusion, in the range of strain rates investigated in this paper, no strain rate sensitivity is observed for dynamics of extension of the transformation region.

INTRODUCTION

Due to two of their specific properties, namely superelasticity and the shape memory effect, shape memory alloys (SMA) have a great potential of applications in a lot of innovative technologies. In particular, the NiTi-based SMAs are widely used as biomaterials (to manufacture stents for heart artery for instance) or in mechanical applications such as in the automotive industry, household appliances, and many other everyday goods.

In such SMA, two phases can be found, separately or combined. The transformation from a phase to the other is triggered when the material is undergoing variation of temperature or mechanical loadings, or both. By analogy with steel, the transformation, the mother phase and the daughter phase are respectively called martensitic transformation, austenite phase and martensite phase. In the case of SMA, martensitic transformation is reversible. Superelastic properties of the SMA are shown on a stress-strain curve, which is decomposed in three parts: first the elastic response of the material in a full austenite phase, then generally a plateau where martensitic transformation is occurring and propagating, which is visible through imaging techniques [1, 2], and finally the homogeneous elastic response of the material in a full-martensitic phase.
Studies have already been done on the influence of strain rate on the macroscopic behavior of the SMA [3]. The higher the strain rate, the more the slope of the plateau part of the stress-strain curve rises. This can be found in compression as well as in tension, despite the asymmetry between the two modes of loading. Assumptions have been made to explain the change in high strain rate response [4] and refer to the adiabatic regime at the transformation front, preventing the austenite phase from transforming unless the level of stress is raised.

In this paper the effect of strain rate on the martensitic transformation in tension on a NiTi SMA is studied. Different tests were performed at different strain rates in the range of 10^{-4} to 15 s^{-1}, extending the range of observations of the investigations previously done by [5]. Methods were used to measure the velocity of the extension of the martensitic phase in the specimen: digital image correlation (DIC) techniques and infrared thermography (IR, during the quasi-static tensile tests only).

T. Proulx (ed.), *Application of Imaging Techniques to Mechanics of Materials and Structures, Volume 4*, Conference Proceedings of the Society for Experimental Mechanics Series 14, DOI 10.1007/978-1-4419-9796-8_28, © The Society for Experimental Mechanics, Inc. 2013

EXPERIMENTAL TECHNIQUES

The measurement techniques employed in this study were different depending on the strain rate applied. For the 1.67 x 10^{-4} s^{-1} strain rate, a classical electromechanical INSTRON machine was used associated with a reflex camera recording at 0.25 frames per second (fps) and an IR thermography device. For the 1.67 x 10^{-2} s^{-1} strain rate, the same machine was used but with a fast camera recording at 125 fps. For the 16 s^{-1} strain rate that corresponds to the dynamic tensile test, a Split Hopkinson Tensile Bar (SHTB) set-up was used with a fast camera recording at 45'000 fps.

Specimen characteristics

Specimen is a NiTi plate shape which dimensions are 60 x 3 x 1.2 mm. It was used for the whole of the experiments. Tensile tests were performed at three different strain rate ranges and at room temperature, clearly above the characteristic A_f temperature so that for the stress-free condition the specimen is in full austenite state. For all experiments the specimen is fixed between two tabs that can further be screwed (i) in the bars for dynamic tensile experiment, (ii) in a clamping system for static experiments. This allows to be more confident in the comparison of experimental results obtained with different devices.

In order to plot a behavior curve of the material, a simple tension experiment was performed on the same specimen, after the experimental series of dynamic and static tests presented on the following article being completed. Experiment was conducted on an electro-mechanical testing machine at a prescribed velocity of 0.01 mm/s. Nominal stress-strain curve is shown in figure 1. Three domains appear on the curve :

- elastic tension in the initial austenite for strains up to 0.01,
- a stress plateau associated to the superelastic domain of interest, corresponding to the stress-induced martensitic (SIM) transformation for strains up to 0.06. The stress at the beginning of the SIM transformation is called the transition stress. An unloading-reloading cycle has been done in the superelastic domain in order to show that the reverse transformation is effectively reversible,
- elastic tension in the supposed "fully" martensitic specimen. The notion of "fully martensitic" refers in fact to the end of the SIM transformation process even if it has been documented that in fact all austenite has not been transformed [6]. In this experiment, maximal strain is under 0.08 and there is no evidence of plastic deformation during tension.

It can be noticed that two serrations are visible at the beginning of the superelastic domain. This phenomenon is due to the heterogeneity of the martensitic transformation and to the apparition of the martensitic zone.

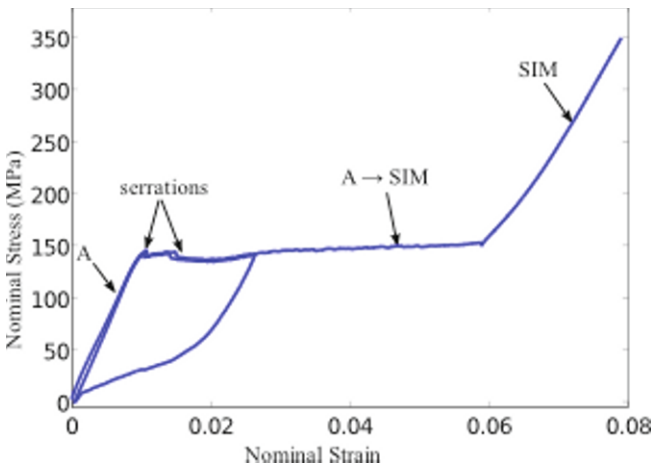

Figure 1 Static strain-stress curve at nominal strain rate of 1.67 x 10^{-4} s^{-1} at room temperature.

Measurement of dynamic nominal stress-strain curve

Tension experiments at moderate impact velocity around 1 m/s are performed on a tensile Hopkinson bar device. The moderate impact velocity allows to test the specimen in a dynamic regime for which pseudoelasticity still exists. At an initial impact velocity of 1 m/s, the strain rate is about 15 s^{-1}. The Hopkinson bar allows to obtain an accurate measurement of forces and velocities on both sides of the specimen and subsequent deformation energy. So strains and displacements are given both by the Hopkinson bars and the optical digital image correlation (DIC) method applied to images acquired by the fast camera as explained in a further section.

The device used in this study is a Split Hopkinson Tensile Bar (SHTB). It is composed of two bars called the input and the output bars, made of maraging steel. The specimen equipped with its end tabs is tightly screwed at the

end of each bar. The tabs that are used to fix the specimen on the bars are manufactured in the same material of the bars and designed so as to minimize any mass effect by matching the same acoustic impedance as the bars. The experiment consists in creating a tensile longitudinal wave in the input bar, called the incident pulse, that propagates towards the specimen. When this pulse reaches the specimen, one part is reflected in the input bar while another part is transmitted by the sample to the output bar. Measurement of strain histories in several locations of the bars with strain gauges allows to determine force and particle velocity at both faces of the specimen ([7],[8]). This set-up is schematically presented in figure 2, along with its dimensions. The incident pulse is obtained by sudden release of an initial elastic energy that is stored in the length L between points A and B of the input bar ([9]). The duration of the tension experiment being related to the length L and the base material of the bars, the test duration is in this case around 1500 μs. The initial stored energy depends on the initial load N_0 that is prescribed and controls the subsequent strain and strain rate applied to the specimen. To perform a test at an initial velocity of 1 m/s, a initial load of 1.5 kN is applied.

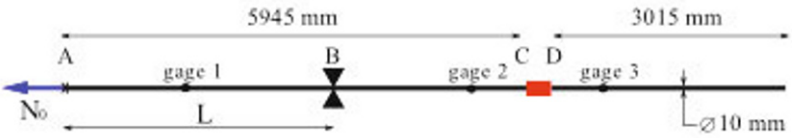

Figure 2 Split Hopkinson Tensile Bar dimensions.

Measurements of the heterogeneity of axial strain
As mentioned in the introduction, pseudoelasticity in the NiTi alloy is due to a martensitic transformation that leads to a heterogeneous strain state in a tensile specimen, observation that is documented for static loadings.

In order to follow this phenomenon at a tension velocity of 1 m/s, complementary measurements are conducted. Displacement and subsequent axial strain path along the specimen are calculated by digital image correlation (DIC) ([10,11]). Moreover, since martensitic transformation is exothermic, infrared thermography (IRT) measurements are also a good mean to measure indirectly the location of the ongoing transformation. Optical and thermal measurements are obtained simultaneously on the same thin specimen, on two opposite sides that are supposed to have the same thermo-mechanical response.

IRT pictures were acquired using an infrared camera (Jade CEDIP) with a resolution of 320 x 240 pixels. For every test, the frame period is 25 fps, the integration time to acquire a picture is 310 μs and the spatial resolution is 0.27 mm/pixel. All the experiments were performed at a room temperature (around 300 K). A thin layer of carbon black powder was deposited on the surface in order to make its emissivity higher and more homogeneous. Moreover, in order to improve the signal to noise ratio, and in particular to prevent effects of perturbative reflections, the optical path between the lens and the surface of the specimen was sheltered by a "tunnel cover" which inner surface was covered with black paint. For the quasi-static tests, IRT measurements are given in addition to DIC measurements and used as a validation of the DIC technique for the measurement of transforming regions in the specimen. IRT thermography was not tried during dynamic tensile tests and this will be a part of a further study.

ANALYSIS OF THE PROPAGATION VELOCITY OF THE MARTENSITIC TRANSFORMATION ON THE QUASI-STATIC CASES

A first analysis of DIC results allows to give qualitative information on the phenomena taking place during the tests. Figure 3, resulting from a quasi-static tensile test at 0.01 mm/s, shows two different strain zones: a 2% strain zone (supposed to be the austenitic phase) and a 6% strain zone (supposed to be the stress-induced martensitic phase). An enlargement of the SIM region can be observed.

In order to show more clearly the growing rate of transformed region, space-time figures are plotted. Such a space-time figure is given in figure 4(a). It is obtained as the time-evolution of the mean longitudinal strain along the deformed specimen. This mean is done over the whole width of the specimen. This was considered, contrary to the choice of a single line without meaning procedure, in order to smooth the results but it induces quantitative errors locally if the transformation front is not perpendicular to the axis of the specimen. This is supposed to be negligible and does not contradict the results on growth rate that is the point of this paper because the angle between the localized bands and the direction of the tensile loading is supposed to be constant in time ([5]).

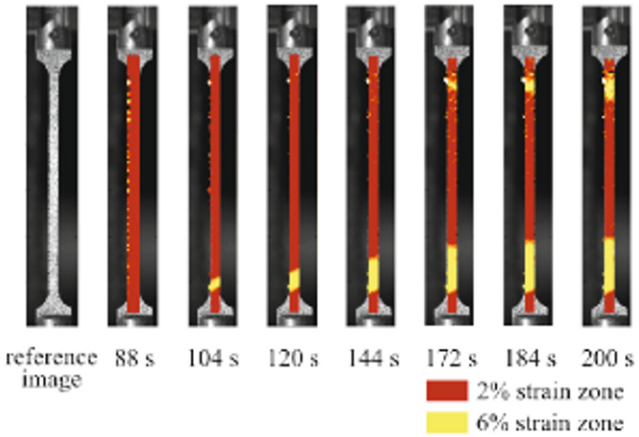

Figure 3 Strain maps for quasi-static tensile test performed at 0.01 mm/s.

The observation of figure 4(a) shows at a first stage a growth of a first transformed area initiated at the lower side of the specimen. Then, at a time of around 160 s, a second transformed region appears at the upper side of the specimen. Longitudinal strain rate can also be obtained by time derivation (here a backward single time step is used). The result for the 0.01 mm/s tensile test is given in figure (b). One can observe that (i) the maximum of strain rate is obviously located at the supposed transformation front, (ii) that two transformations fronts are moving, in opposite directions in this case, (iii) that anywhere else the tranformation fronts, strain rate is almost zero confirming that macrosopic strain rate is due to localized phenomena only. One can noticed that the transformation region seems to have a thickness which doesn't exist in reality. The discretization of the map and the display mode used in MATLAB© cause this effect.

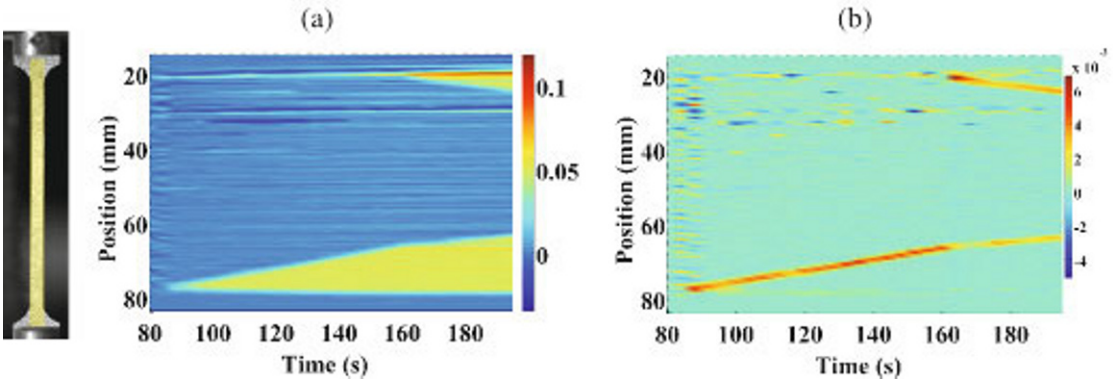

Figure 4 Quasi-static tensile test at 0.01 mm/s. (a) Mean longitudinal strain along the specimen versus time. (b) Mean longitudinal strain rate (/s) along the specimen versus time.

Until now it has been assumed that there were two different regions in the specimen, respectively associated to a austenitic zone and a martensitic zone. This assumption has to be validated. To do this, IR thermography was used. The martensitic transformation is known to be exothermic (and the inverse transformation endothermic). So, in order to validate the fact that the two zones are effectively related to austenite and martensite, IRT measurement is valuable. Figure 5(a) shows the tempreature/DL field on the specimen surface during a quasi-static tensile test at 0.01 mm/s at a given instant T. A localized exothermic process is clearly visible at the lower part of the specimen, revealing a heating phenomenon that is with no doubt the consequence of the martensitic transformation. In the same way as for DIC results, a space-time figure of the results is proposed. Figure 5(b) shows the time-evolution of mean temperature/DL alog the axis of the specimen. This figure is built in the manner of DIC figure in order to allow a direct comparison of the two approaches.

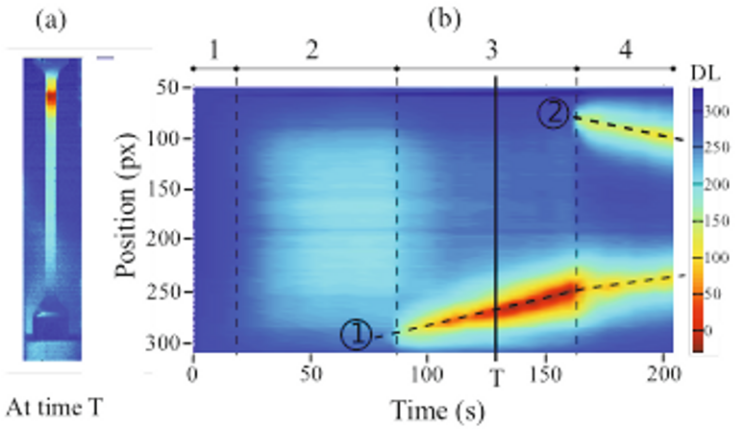

Figure 5 (a) Mean variation of temperature evolution along the specimen at date T. (b) Mean variation of temperature evolution along the specimen. - Quasi-static tensile test at 0.01 mm/s.

MEASUREMENT OF THE EFFECT OF PRESCRIBED VELOCITY ON THE SIM GROWTH RATE

Now that the transformed zone is clearly identified using DIC computations, it is possible to evaluate the evolution of the length of martensite over time during tensile tests. Tests at higher range of strain rate were performed in addition of the 0.01 mm/s quasi-static test, as it was mentioned previously. DIC computations were performed for both the case at 1 mm/s and 1 m/s. Similar maps as the one display on figure 4 were built.

Measuring the extension rate can be achieved by choosing a criterion that determines which part of the map can be considered as transformed if its strain was superior to 0.04. This technique is quiet close to the one used in [12] except that here a strain field is used, not only gauges signals at located points of the specimen. Using a routine, it is possible to measure, at each step of the time of the test, the length of stress-induced martensite. By plotting this length on a curve in time, the slope appears to be the velocity of extension of the transformed area. The results are given in the table 1. Here, for each expected prescribed velocities, the enlargement velocity is given and the ratio between these two values is computed.

Expected Prescribed Velocity	Measured Prescribed Velocity	**Enlargement Velocity**	**Ratio**
0.01 mm/s	0.01 mm/s	0.187 mm/s	18.7
1 mm/s	0.76 mm/s	12.5 mm/s	16.5
1000 mm/s	1100 mm/s	19300 mm/s	17.5

Table 1 Measure and comparison of the enlargement velocity

The ratio between measured prescribed velocity of the specimen and enlargement velocity of the transformed area can be considered as quite constant. This proportionality between these two quantities was found in [4] for strain rate applied from 4 x 10^{-5} s^{-1} to 4 x 10^{-2} s^{-1}. So, this study brings complementary results to these observations.

RESULTS AND CONCLUSION

Specific measurement techniques have been implemented in order to analyze the influence of nominal strain rate on the growth rate of the SIM region in a NiTi specimen. Hopkinson bar measurement technique, DIC applied to quasi-static and dynamic experiment, and IR thermography for static experiments only give accurate and relevant results. After synchronizing DIC and IR measurements in time and space for static experiments, a superimposition can be done and results show that the temperature peak, as expected, follows the transformation front. Finally, the velocity of the propagation front is measured and we show that it depends linearly on the prescribed velocity. As a conclusion, in the range of strain rates investigated in this paper, no strain rate sensitivity is observed in the martensitic transformation.

[1] Pieczyska E.A., Gadaj S.P., Nowacki W.K., Tobushi H., *Phase-transformation fronts evolution for stress- and strain- controlled tension tests in TiNi shape memory alloy*, Experimental Mechanics 46(4), 531-542 (2006)
[2] Murasawa G., Yoneyama S., Saluma T., *Nucleation, Bifurcation and propagation of local deformation arising in NiTi shape memory alloy*, Smart Mat. And Struct. 16, 160-167 (2007)
[3] Nemat-Nasser S., Choi J.Y., *Strain rate dependence of deformation mechanisms in a Ni-Ti-Cr shape memory alloy*, Acta Materialia 53(2), 449-454 (2005)
[4] Shaw J.A., Kyriakides S., *Thermomechanicals aspects of NiTi*, Journal of the Mechanics and Physics of Solids 43(8), 1243-1281 (1995)
[5] Shaw J.A., Kyriakides S., *On the nucleation and propagation of phase transformation fronts in a NiTi alloy*, Acta Materialia 45 (2), 683-700 (1997)
[6] Brinson L.C., Schmidt I., Lammering R., *Stress-induced transformation behavior of a polycrystalline NiTi shape memory alloy : micro and macromechanical investigations via in situ optical microscopy*, Journal of the Mechanics and Physics of Solids 52(7), 1549-1571 (2004)
[7] Davies E.D.H., Hunter S.C*, The dynamic compression testing of solids by the method of the split Hopkinson pressure bar*, Journal of the Mechanics and Physics of Solids 11(3), 55-179 (1963)
[8] Zhao H., Gary G., *A new method for the separation of waves. Application to the SHPB technique for an unlimited duration of measurement,* Journal of the Mechanics and Physics of Solids 45(7), 1185-1202 (1997)
[9] Staab G.H., Gilat A., *A direct tension split Hopkinson bar for high rate*, Experimental Mechanics 31(3), 232-235 (1991)
[10] Besnard G., Hild F., Roux S*., "Finite-element" displacement fields analysis from digital images : Application to Portevin-le Châtelier bands*, Experimental Mechanics 46(6), 789-803 (2006)
[11] Elnasri I., Pattofatto S., Zhao H., Tsitsiris H., Hild F., Girard Y., *Shock enhancement of cellular structures under impact loading: Part I experiments*, Journal of the Mechanics and Physics of Solids 55(12), 2652-2671 (2007)
[12] Niemczura J., Ravi-Chandar K., *Experimental investigation on macroscopic domain formation and evolution in polycrystalline NiTi microtubing under mechanical force*, Journal of the Mechanics and Physics of Solids 54(10), 2136-2161 (2006)

Proceedings of the SEM Annual Conference
June 7-10, 2010 Indianapolis, Indiana USA

Pseudoelastic Shape Memory Alloy Cables

Benjamin Reedlunn, John Shaw, and Samantha Daly
University of Michigan
Departments of Mechanical and Aerospace Engineering
Ann Arbor, MI, USA
breedlun@umich.edu, jashaw@umich.edu, samdaly@umich.edu

Introduction

Conventional structural cables (wire ropes) are composed of steel wires helically wound into strands that are then wound around a core. Cables made from shape memory alloy (SMA) wires are a new structural element with promising properties for a broad range of applications. Among the many potential advantages of this form are increased bending flexibility for spooling/packaging, better fatigue performance, energy absorption and damping, reduced thermal lag, redundancy, and significant design flexibility. Currently there are few studies of SMA cables in the literature. This paper describes exploratory thermomechanical experiments that were performed on two commercially available cable designs.

Specimens and Experimental Setup

Both cables designs tested are made of NiTi wires (pseudoelastic at room temperature) and are shown in Figure 1: a 7x7x0.279 mm cable (7 strands, 7 wires per strand, 0.279 mm diameter wires) and a 1x27x0.229 mm cable (1 strand, 27 wires, 0.229 mm diameter wires). Displacement-controlled uniaxial tensile experiments were performed in room temperature air. As depicted in Figure 2, the load (P) and the displacement of the crosshead (δ) were measured. The torque M_z caused by not allowing the end of the cable to rotate was also measured, but is not reported here. A laser extensometer measured the displacement δ_e between two laser tags placed a distance of L_e apart on the specimen (typically, L_e=75mm to 80mm). The axial stress is reported as P/A_0, where $A_0=n\pi d^2/4$, n is the number of wires, and d is the diameter of a single wire. The axial strain is reported as δ_e/L_e. Two 5 megapixel CCDs were fixed at an angle of 20 degrees relative to one another and used to capture digital images of the specimen, which was painted white with black speckles covering its surface. The images were post processed using Digital Image Correlation (DIC) software (Vic-3D, Correlated Solutions) to calculate the three dimensional strain field on the surface of the specimen. In addition, an infrared (IR) camera (Inframetrics ThermaCam SC1000) measured the specimen's temperature field during each experiment.

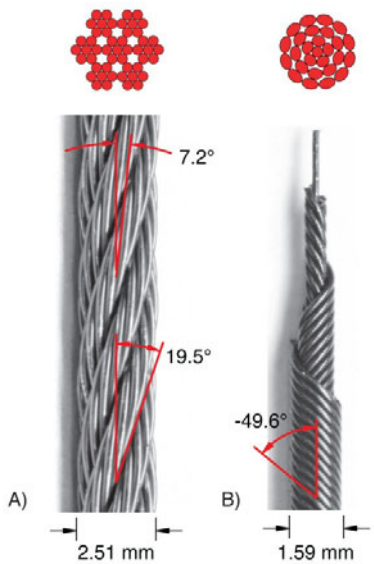

Figure 1: Cable designs characterized: A) 7x7x0.279mm, B) 1x27x0.229mm with inner layers exposed

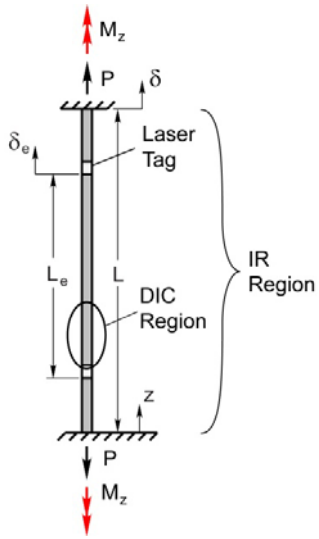

Figure 2: Cable free body diagram with nomenclature

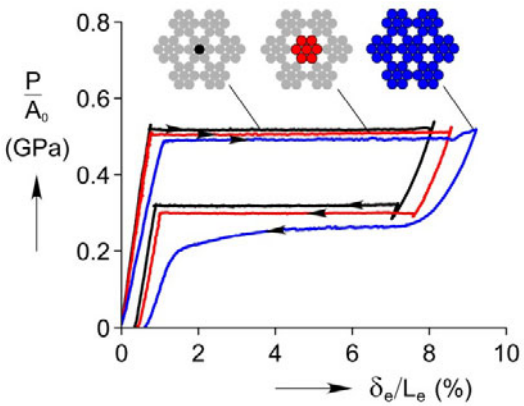

Figure 3: Mechanical behavior of 7x7x0.279mm cable components: core wire, 1x7 core strand, and 7x7 cable

T. Proulx (ed.), *Application of Imaging Techniques to Mechanics of Materials and Structures, Volume 4*, Conference Proceedings of the Society for Experimental Mechanics Series 14, DOI 10.1007/978-1-4419-9796-8_29, © The Society for Experimental Mechanics, Inc. 2013

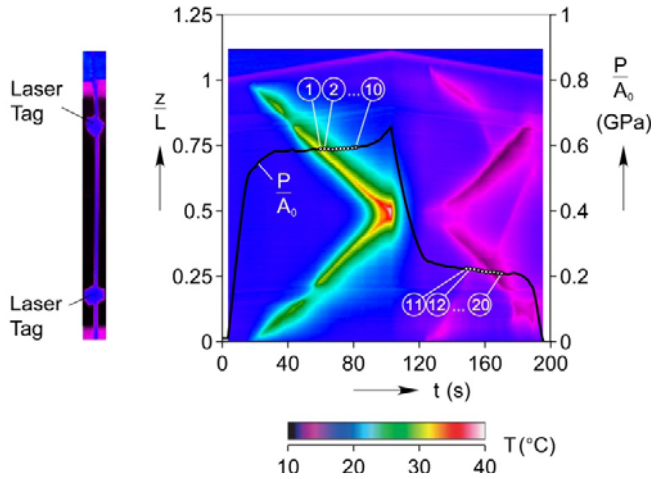

Figure 4: Temperature field and stress histories for a 1x7 core strand

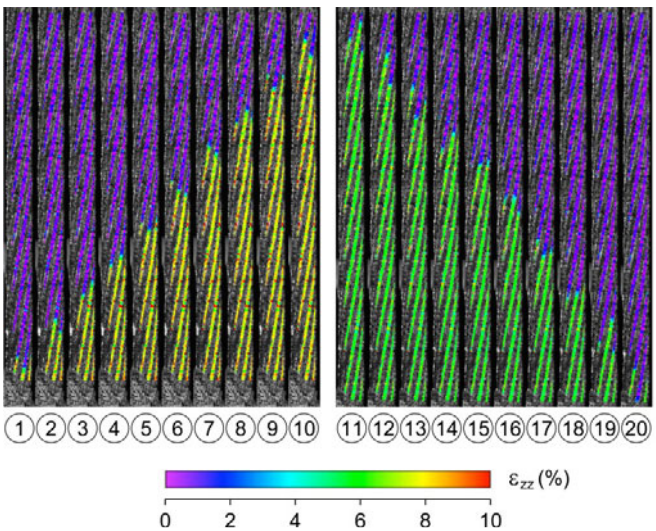

Figure 5: 1x7 core strand axial strain field image sequence of the lower 1/3 of gage length

Results

Figure 3 depicts the mechanical response of three components of the 7x7x0.279mm cable at a strain rate of 10^{-5} 1/s. Due to the shallow helix angles of 7.2° and 19.5° (Fig 1), the core strand and full cable act similar to that of NiTi wires loaded in parallel. At 10^{-5} 1/s and at higher strain rates, the tensile force roughly scaled with the number of wires.

The phase transformation fronts in the 7x7x0.279mm cable also behave similarly to NiTi wires loaded in parallel [1]. The temperature field history for 1x7 core strand strained at 10^{-3} 1/s is plotted in Figure 4. This plot was generated from a sequence of IR images of the specimen (an example image is to the left of the plot), cropped to one pixel wide, and stacked side by side. During loading, the latent heat of transformation illuminates two fronts propagating from the top and bottom grips, which coalesce in the middle of the gage length. The reverse is seen during unloading, along with what may be the core wire transforming independently of the outer wires. The balloon labels in Figure 4 correspond to the axial strain field images in Figure 5. From the DIC derived axial strain, we can clearly see the transformation front propagate up (images 1-10) and down (images 11-20) through the lower third of the gage length.

In contrast, the 1x27x0.229mm cable exhibits significantly altered behavior to wires loaded in parallel. Each additional layer trades off stress for enhanced strain recovery, similar to a spring (Fig 6). To support this, the core wire, 1x6, 1x15, and 1x27 cable broke in the grips at 11.2%, 16.4%, 29.2%, and 39.3% strain. Although not shown here, 1x6, 1x15, and 1x27 cable exhibited diffuse transformation fronts. This de-localization of the transformation fronts led to highly reduced strain rate sensitivity, and less shakedown with successive cycling.

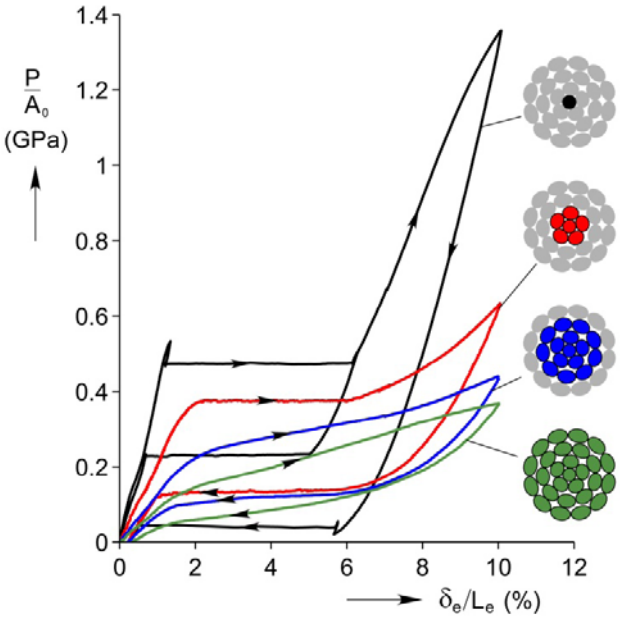

Figure 6: Mechanical response of 1x27x0.229mm cable layers: core wire, 1x6, 1x15, and full 1x27 cable

Conclusions

The 7x7x0.279mm cable should appeal to designers who desire the unique properties of SMA wires, but need the higher force, convenient packaging, and spooling capability of a cable form. The 1x27x0.279mm cable experiment demonstrates how an SMA cable can be designed to exchange force for increased displacement, and minimize potentially undesirable transformation fronts.

Acknowledgments

We gratefully acknowledge the financial support for this work, provided by the National Science Foundation and General Motors. The authors also wish to thank Fort Wayne Metals Research for providing material specimens at no cost.

References

[1] Iadicola, M. A., Shaw, J. A. "Rate and thermal sensitivities of unstable transformation behavior in a shape memory alloy," *Int. J. of Plasticity*, Vol. 20 (2004), pp. 577-605

Proceedings of the SEM Annual Conference
June 7-10, 2010 Indianapolis, Indiana USA

Investigating an aluminum multi-crystal with full-field measurement techniques

C. Badulescu [a], M. Grédiac [a], J.-D. Mathias [b], X. Balandraud [a], H. Haddadi [c], H.-S. Tran [c]

[a] Clermont Université
Université Blaise Pascal & IFMA, EA 3867, Laboratoire de Mécanique et Ingénieries
BP 10448, F-63000 Clermont-Ferrand, France

[b] Laboratoire d'Ingénierie pour les Systèmes Complexes, CEMAGREF, Campus des Cézeaux
24 avenue des Landais - BP 50085, 63172 Aubière Cedex, France

[c] Laboratoire des Propriétés Mécaniques et Thermodynamique des Matériaux.
CNRS UPR 9001, Institut Galilée Université Paris 13, avenue Jean-Baptiste Clément
93430 Villetaneuse, France

ABSTRACT

This paper deals with the analysis of the mechanical response of an aluminium multi-crystal specimen subjected to a tensile load. Two different techniques are used for this purpose: the grid method to obtain strain maps and infrared thermography to deduce heat source distributions from temperature fields. Significant differences between the grains in terms of mechanical response are observed. Experimental results are compared to numerical results obtained with a suitable FE package. A good agreement is observed apart from very localized phenomena occurring near the boundaries of the grains which are not predicted by the FE model.

INTRODUCTION

The development of the plastic strain in coarse-grained aluminum multi-crystals has been a subject of research for many years. One of the main reasons is the fact that phenomena that occur within the grains can be observed more easily than in materials exhibiting smaller grains, thus allowing thorough investigations or comparisons with results provided by a crystal plasticity finite element model for instance [1]. Experimental techniques used for this purpose are generally EBSD that enables the determination of crystallographic orientation maps and digital image correlation that provides displacements at some points regularly spaced on the surface of the specimen. Infrared (IR) thermography has also proved to be an efficient tool for detecting small temperature changes on the surface of multi-crystal specimens subjected to a tensile test, thus allowing the determination of heat source distributions related to mechanical dissipation [2].

The aim of the current work is to analyse the response of a multi-crystal aluminum specimen subjected to a tensile test using two different full-field measurement techniques: the grid method and thermography. These techniques are complementary since they provide strain and temperature maps, respectively. These maps can be determined at different steps of the load, thus allowing us to analyse the evolution of these quantities while applied stress increases. These two techniques are described in the first part of the paper. Some typical strain maps obtained are then shown and compared with their numerical counterparts obtained with a suitable FE package. Temperature maps are finally used to obtain heat source maps and to deduce stored energy when plasticity occurs.

T. Proulx (ed.), *Application of Imaging Techniques to Mechanics of Materials and Structures, Volume 4*, Conference Proceedings of the Society for Experimental Mechanics Series 14, DOI 10.1007/978-1-4419-9796-8_30, © The Society for Experimental Mechanics, Inc. 2013

FULL-FIELD MEASUREMENT TECHNIQUES USED

Grid method

The grid method consists first in depositing a crossed grid on the surface under investigation in order to track the evolution of the grid as loading increases and to deduce the 2D strain fields. The grid is deposited using the procedure described in [3]. The pitch of the grid is equal to 0.2 mm along the two directions. Processing images of grids classically provides phase evolution maps of this periodical marking. This phase evolution is then unwrapped and becomes directly proportional to the displacement [4]. Recently, it has been shown that the metrological performance of this technique could be significantly improved (especially for small strain measurements) by getting rid of grid marking defects which unavoidably occur when grids are printed on their support [5][6]. In particular, a very good compromise is obtained between resolution in strain and spatial resolution. Typically, the resolution is strain is 10^{-4} for a spatial resolution equal to 30 pixels. In addition, calculations are performed pixelwise, thus allowing to detect very localized phenomena. In the current case, a 12-bit/1040x1376 pixel SENSICAM camera connected to its companion software CamWare is employed. The small strain maps are obtained directly from the images of the grids taken by the camera, without differentiating displacement maps. Full details on small strain calculation can be found in [5][6] for unidirectional and crossed grids, respectively.

Since large strains must be measured in the current work, the in-plane Green-Lagrange strain tensor **E** is calculated. In practice, small strain increments are measured using the procedure described in [6]. The Hencky strain tensor **H** is then deduced by adding these small strain increments. The Green-Lagrange **E** is finally deduced using the following relationship between **E** and **H**

$$\mathbf{H} = \frac{1}{2}\ln(\mathbf{I} + 2\mathbf{E}) \tag{1}$$

where **I** is the second order unit tensor.

Temperature and heat source field determination with an infrared camera

Very small temperature changes on the surface of the specimen under load (painted in black to increase thermal emissivity) are detected since the Noise Equivalent Temperature Difference (NETD) of the camera used in this study (a Cedip Jade III-MWIR featuring a 240x320 IR sensor matrix) is nearly 20 mK. For the thermomechanical analysis of materials, temperature change is however not really the relevant information since it is the consequence of various phenomena among which the heat sources due to plasticity, as noted in [7] in a similar context. Hence heat sources must be determined from these temperature fields using a suitable strategy whose main steps are as follows.

The temperature evolution is governed by the bi-dimensional version of the heat diffusion equation, which is suitable for thin flat specimens [7]

$$\rho C\left(\frac{d\theta}{dt} + \frac{\theta}{\tau}\right) - k\Delta\theta = s \tag{2}$$

where □is the temperature variation with respect to a reference temperature measured just before the beginning of the test, s(x, y, t) is the heat source field produced by the material itself, ρ is the mass per unit volume, C the specific heat and k the thermal conductivity of the material, which is assumed to be isotropic, τ a time constant

characterizing the heat exchange with ambient air by convection. This latter quantity is determined experimentally during a simple return to room temperature. In the current study where plasticity occurs, source s can be split in two terms

$$s = d - \alpha T \, tr(\dot{\sigma}) \tag{3}$$

where d is the mechanical dissipation due to plasticity (this quantity is always positive) and $-\alpha T \, tr(\dot{\sigma})$ is the thermoelastic coupling term. α is the coefficient of thermal expansion of the constitutive material, T the temperature in Kelvin and σ the Cauchy stress tensor.

In practice the sought quantity is d, which is obtained by calculating the other terms of Equation (2) from the temperature maps. $d\theta/dt$ is merely obtained by numerical time differentiation, the frequency of temperature acquisition being significant (147 Hz for the present experiments). It is more difficult to calculate the Laplacien term $\Delta\theta$ because of the small number of pixels (compared to the number of pixels of the CCD camera) and because second-order derivatives must be found from data which are unavoidably noisy. Temperature maps are therefore first smoothed using polynomials, the degree of which being thoroughly adjusted when the load level increases. $tr(\sigma)$ is deduced from the stress field assuming that it is uniaxial, its amplitude being equal to the ratio between applied force and cross-section of the specimen. It has been checked through FE simulations that this assumption was reasonable.

The energy stored in the material because of plasticity is the difference between the total strain energy, the elastic strain energy and the energy related to the mechanical dissipation, all these terms being calculated with the above quantities. The amount of stored energy is often characterized through the Taylor-Quiney coefficient defined as the ratio between the mechanical dissipation and the rate of the anelastic strain energy, the latter quantity being the difference between the total deformation energy and the elastic deformation energy [8].

SPECIMEN PREPARATION AND TESTING CONDITIONS

Specimen preparation

The multi-crystal specimen is obtained from a commercial purity aluminium sheet which undergoes two thermal treatments and one mechanical test in the following order: 1- heating at 550°C for 2 hours to erase load history by annealing + moderate recrystallization; 2- tensile test up to 2 % global strain; 3- heating at 550 ◦C for 24 hours to obtain an abnormal growth of a few crystals. About twenty large grains of centimetric size have been eventually obtained (see Figure 1). Seven of these grains are considered in the gauge section of the specimen. The two largest faces A and B shown on the same figure were used to measure strains and temperature maps, respectively..It must be noted that displacement fields are employed to map the temperature fields in the initial configuration to be able to study the evolution of temperatures and heat sources at the same material points.

Testing conditions

The loading rate is a trade-off between two opposite constraints: the cross-head speed must be as low as possible to be able to average some sets of consecutive images captured while the specimen deforms in order to reduce noise in the CCD sensor, especially for small strains; the cross-head speed must be as high as possible to be able to detect significant heat sources because of the high thermal diffusivity $k/\rho C$ of aluminum. In addition, the whole test is captured with a maximum number of 330 optical images because of the buffer size of the optical camera. Some preliminary tests have shown that the best compromise was to drive the test in force and not in displacement. The load rate is equal to 85 N/s. Such a choice leads the specimen to deform at a smaller rate at the beginning of the test, when the apparent stiffness of the specimen is the highest, thus enabling us to average consecutive pictures. Then, the apparent stiffness decreases since plasticity occurs. The strain rate increases, thus limiting the number of images which can be averaged without significantly impairing the measurement resolution. As the strain rate significantly increases when plasticity starts, temperature changes due to strong heat source production are detected by the IR camera.

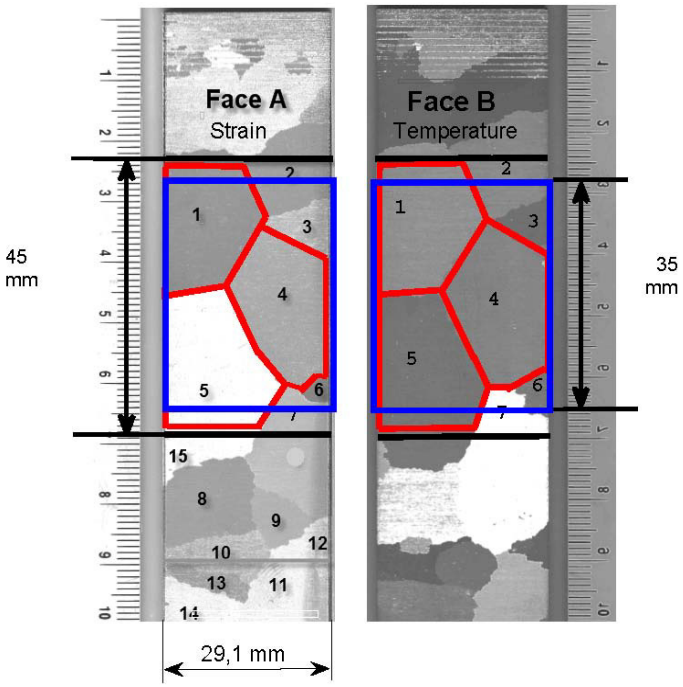

Figure 1. Dimension and gauge section of the multi-crystal specimen

TYPICAL RESULTS AND DISCUSSION

Strain maps. Comparison with FE results

The evolution of the three in-plane strain components has been measured during the test. Note however that the grid was unable to sustain a longitudinal strain greater than 18%: it began to debond at this strain level. Figure 2 shows typical strain maps measured at 73% of the failure load.

The contour of the grains can be clearly distinguished thanks to the strain level which is notably different from one grain to each other because of the orientation of the grain which changes from one grain to each other. It is also worth noting that some grains are subjected to nearly homogeneous states of strain whereas the state of strain becomes heterogeneous in some other ones. In particular, significant localizations can be observed between some grains, along their boundary. They are certainly due to the fact that the boundary between adjacent grains must adapt very different states of strain from one grain to each other in this case. It must be pointed out that such very thin bands can be detected only thanks to the fact that strain is calculated at each pixel of the pictures.

Figure 3 shows the strain maps calculated with a suitable in-house FE package suitable for crystalline plasticity [9] based on the Anan model [10]. The orientation of all the grains was determined by Laüe set-up and OrientExpress software [11] beforehand to construct a FE model as close as possible to reality. Typical constitutive parameters for aluminum are chosen as input parameters for the calculations. As may be clearly seen in Figure 3, calculated and measured strain maps are in very good agreement. Both the distribution and the amplitude of the measured strains match their calculated counterparts. Some localized differences can also be noted especially along the boundary between some grains. This is probably due to the fact that boundaries are modelled with portions of planes whereas the actual boundary shapes can be more complicated in reality. Some other differences have

been noted, especially at the beginning of the test. For instance, strain bands were measured near the free border of some grains, this phenomenon being not predicted by the FE model.

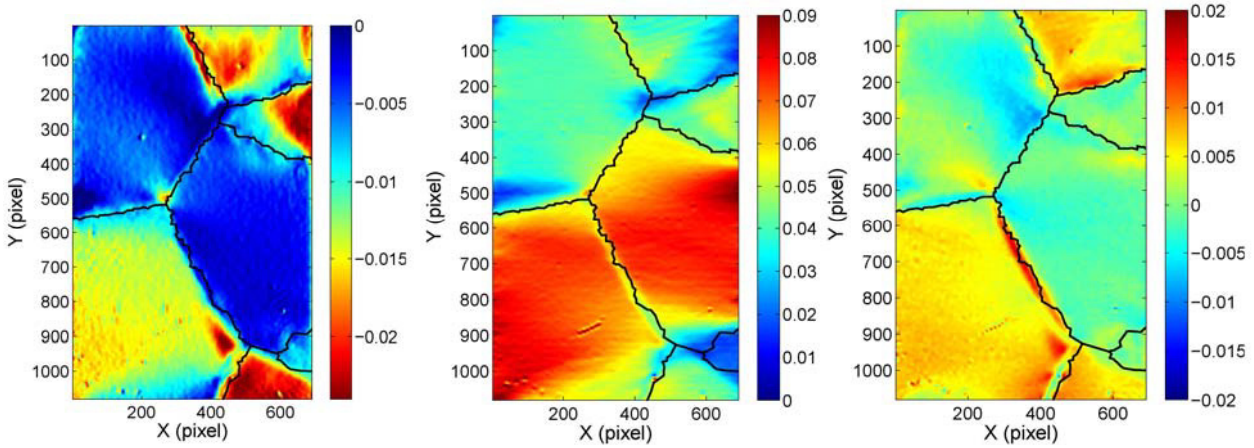

a- Transverse strain b- Longitudinal strain c- Shear strain

Figure 2. Typical strain maps measured at 73% of the failure load

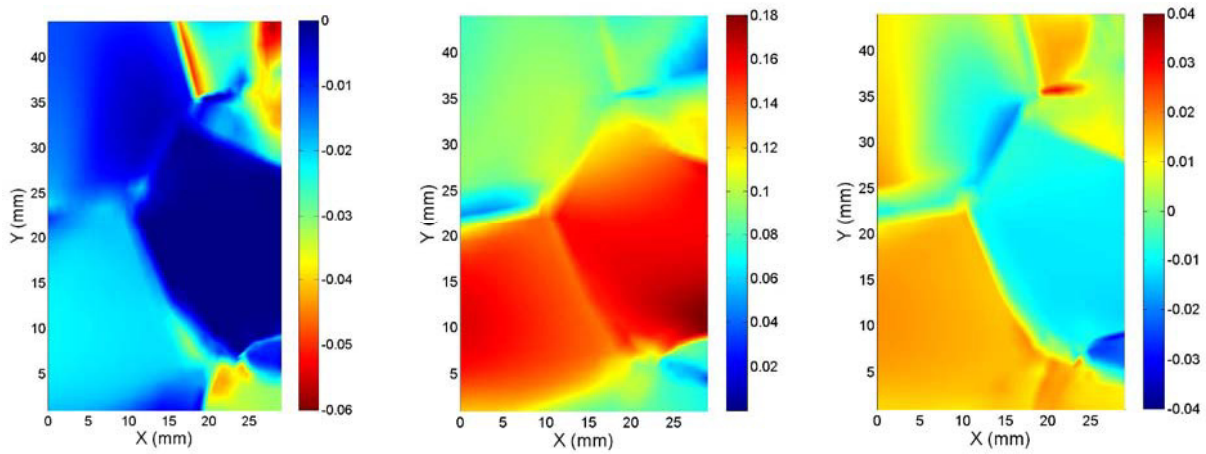

a- Transverse strain b- Longitudinal strain c- Shear strain

Figure 3. Typical strain maps calculated at 73% of the failure load

Thanks to the measurements of the two cameras, the energy balance enables us to obtain the evolution of the different energies defined above. Quantities are averaged over the grains and gives energy densities. Figure 4 shows typical evolutions of different energy densities calculated in a particular grain (grain 4). As expected, the total strain energy density increases from t=10s onward, which corresponds to the beginning of the plastic response of the specimen. These energy densities enable us to calculate the Taylor-Quiney coefficient in the grains. Interestingly, this coefficient evolves linearly from 0 to 0.4 during the first part of the anelastic response of the specimen. It reaches nearly 0.8 at the end of the test. Such an evolution is in good agreement with results found in other studies, but the originality is to measure it at the grain level in the current study whereas only average values (over the whole gauge section) are generally given.

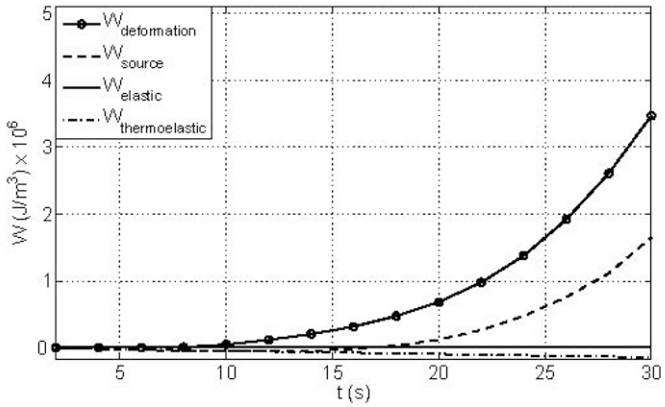

Figure 4. Energy densities measured during the test in grain 4

CONCLUSION

The grid method and infrared thermography have been combined to investigate the mechanical response of a multi-crystal aluminum specimen subjected to a tensile test. Measured and calculated strain maps which have been obtained are in good agreement. They show some significant differences from one grain to each other in terms of mechanical response. These differences are due to the orientation of the grains which evolves from one grain to each other. Some differences were also detected between the two types of maps, especially along some grain boundaries. Displacements have also been also used to map the heat source fields in the initial configuration. Heat source and strain maps enable us to calculate different energy densities at the grain level and to deduce the Taylor-Quiney coefficient evolution. Identifying constitutive parameters by processing such full-field measurement with suitable numerical strategies will be the next step of this study.

REFERENCES

[1] Zhang N., Tong. W., An experimental study on grain deformation and interactions in an Al-0.5 Mg multi-crystal, International Journal of Plasticity, 20: 523-542, 2004

[2] Louche. H., Tabourot, L., Experimental energetic balance associated to the deformation of an aluminium multi-crystal and monocrystal sheet, Materials Science Forum, 467-470: 1395-1400, 2004

[3] Piro J.L., Grédiac M., Producing and transferring low-spatial-frequency grids for measuring displacement fields with moiré and grid methods, Experimental Techniques, 28(4), 23-26, 2004

[4] Surrel Y., Fringe Analysis, in Photomechanics, Topics Appli. Phys. 77, P.K. Rastogi, 55-102, 2000,

[5] Badulescu C., Grédiac M., Mathias J.-D., Roux D., A procedure for accurate one-dimensional strain measurement using the grid method, Experimental Mechanics, 49(6), 841-854, 2009

[6] Badulescu C., Grédiac M., Mathias J.-D., Investigation of the grid method for accurate in-plane strain measurement, Measurement Science and Technology, 20(9), 2009

[7] Chrysochoos A., Louche H., An infrared image processing to analyse the calorific effects accompanying strain localisation, International Journal of Engineering Science, 38: 1759-1788, 2000

[8] Taylor G. I., Quiney H., The latent energy remaining in a metal after cold working, Proceedings of the Royal Society, 28(4): 323-333, 1934

[9] Salahouelhadj A., Haddadi H., Estimation of the Size of the RVE for Isotropic Copper Polycrystals by Using Elastic-Plastic Finite Element Homogenisation, Computational Material Science, accepted, 2010

[10] Anand L., Single-crystal elasto-viscoplasticity: application to texture evolution in polycrystalline metals at large strains, Computer Methods in Applied Mechanics and Engineering, 193(48-51), 5349-5383, 2004

[11] Laugier J., Rolland G., Emeriau J., Dispositif d'orientation rapide de cristaux par la méthode de Laue,

J. Appl. Cryst. 22, 431-434, 1989

Proceedings of the SEM Annual Conference
June 7-10, 2010 Indianapolis, Indiana USA

One-shot thermal *and* kinematic field measurements: Infra-Red Image Correlation

A. Maynadier[1] , M. Poncelet[2] , K. Lavernhe-Taillard[1] , and S. Roux[1]
[1] LMT Cachan, ENS Cachan/CNRS UMR 8535/Univ. Paris 6/PRES UniverSud Paris, 61 Avenue du Président Wilson, 94235 Cachan Cedex, France
anne.maynadier@lmt.ens-cachan.fr
[2] CEA Saclay, DEN-DANS/DMN/SRMA/LC2M, 91191 Gif sur Yvette Cedex, France

ABSTRACT
Strain localization phenomena occur in many materials in different forms, such as PLC & Lüders' bands or Shape Memory Alloy stress-driven martensitic phase transformation. The development of kinematic and thermal full-field measurement techniques, like Digital Image Correlation (DIC) and Infra-Red (IR) thermography helps understanding these tricky phenomena and allows for the identification of such material behaviors. When such kinematic and thermal measurements are coupled, they even offer a full thermo-mechanical characterisation. Unfortunately the space and time association of both fields remains a major difficulty (antagonist surface texture requirements, imaging devices having different pixel number and acquisition rate...). To get round this problem, the present paper introduces a much simpler experimental approach: a novel extended DIC technique applied to a single set of IR images gives access to both displacement and temperature fields decomposed over the same discretization. A first application is performed, where the strain localization due to the phase transformation of a NiTi SMA and its associated thermal dissipation are jointly measured.

INTRODUCTION

Identification of the constitutive laws of solids prone to localization (Portevin-Le Chatelier phenomena, Lüders' bands, Shape Memory Alloys, metallic glasses, semi-brittle materials,...) represents a formidable challenge, in particular on the experimental side. Global strain measurements – because of their averaging nature – and local ones – because of their limited sampling capabilities – betray the inherent complexity of the actual strain field, and hence cannot be trusted. Full-field measurements have the unique advantage of offering a global and yet spatially resolved picture of the strain field, (down to a specific resolution). In the following, the considered full field kinematic analysis will be restricted to Digital Image Correlation (DIC).

Moreover, in most cases, strain localization gives rise to a significant thermal dissipation, which calls for thermal or calorimetric measurements to have a more complete characterization of the phenomena at play. Thermography from Infra-Red (IR) camera again provides a global and spatially resolved field measurement from which dissipation can be inferred.

Jointly, these two field measurements open an avenue to the identification of a full thermo-mechanical description of the material behavior. However, one major difficulty is that these two techniques require different (or even contradictory) surface texture properties: high emissivity homogenous coating for a constitutive measure of temperature using IR camera and a sufficiently contrasted speckle-pattern for DIC. Moreover, these two techniques require also different imaging devices having each their own specific optics, pixel number and acquisition rate. Solutions have been proposed by different groups exploiting clever experimental set-ups, like measurement on both faces of flat sample [1], with proper space and time association of both thermal and mechanical fields. Other groups [2] worked on specimen preparation to perform temperature and displacement measurement on the same face; they however still use two different imaging devices and consequently still need space and time association of the obtained fields that may constitute a spurious loss of information. Another

T. Proulx (ed.), *Application of Imaging Techniques to Mechanics of Materials and Structures, Volume 4*, Conference Proceedings of the Society for Experimental Mechanics Series 14, DOI 10.1007/978-1-4419-9796-8_31, © The Society for Experimental Mechanics, Inc. 2013

solution was proposed by [3] by using two visible and near IR cameras and a projected speckle-pattern. The main limitation is that only the out-of-plane displacement and thermal field can be obtained at the same place.

The present paper aims at introducing a much simpler experimental approach which consists in an extended DIC technique applied to a single set of images from an IR camera. In order to be able to follow the displacements field an original speckle-pattern with sufficient contrast in the IR images was developed. This peculiar sample preparation and experimental set-up is described in the first part of this paper. Then, to solve the thermal problem caused by the non homogenous emissivity, a temperature calibration using a cooling test is presented. After this preliminary step, we introduce the equations of the IR image correlation, providing both displacements and temperature fields decomposed on the same Q4 elements basis. This new approach is finally applied to tensile tests on a Nickel-Titanium Shape Memory Alloy (SMA) well known to present martensitic transformation bands with severe inhomogeneous strains and thermal dissipation [4,5].

CONTRASTED INFRA-RED IMAGES: SPECIMEN PREPARATION AND EXPERIMENTAL SETUP

In our case, the specimen consists in a thin bone sample with sufficient surface with respect to imaging device. As well as the speckle-pattern contrast is of crucial interest to determine the displacements in DIC, this technique main challenge is firstly to obtain a sufficiently contrasted speckle-pattern for the IR imaging device. Since the contrast is linked to emissivity, we decided to cover our sample surface with strong differences of emissivity.

The retained principle is the following: sample surface underwent an electrochemical polishing, inducing a very poor emissivity. Then, the gauge zone surface is covered with an heterogeneous coating of high emissivity black paint, the non-painted zones reflecting a low temperature surrounding called black body witch can be a real black body or any other device at a constant known cold temperature with high emissivity coating. Hence, schematically, the black spots emit IR radiations representative of the sample temperature, whereas the unpainted part reflects the black body low temperature. Consequently (as shown in Figure 1 (a)), sufficient gray contrast on IR images is obtained to follow the displacements and in the meantime an image of temperature is visible in black painted zones.

From a practical point of view, the chosen experimental setup consists in an IR camera, tilted with a low angle from the specimen face normal, and a black body, also tilted with a low angle, reflecting in the specimen face Figure 1 (b). For validation purposes, an IR mirror is placed behind the specimen for this first test, so that the reflexion of the uniformly coated back face of the specimen is visible in Figure 1 (a).

With this set-up, we may follow the in-plane displacement of the sample thanks to sharp contrast, but due to emissivity variations on the surface, prior calibration of temperature measurement is required.

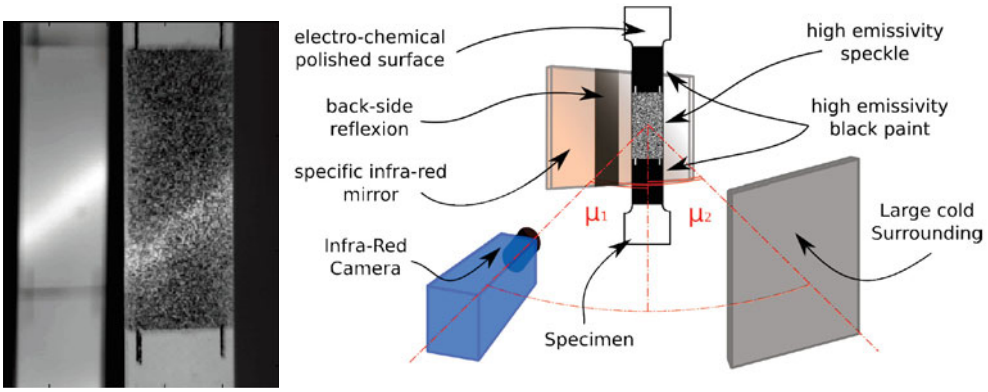

(a) (b)

Figure 1 (a) Typical IR image during the experiment: the speckled front face of the sample and (in the present case) the reflexion of the back face with uniform high-emissivity coating to verify the temperature measurement on the front face; (b) complete set-up shown schematically.

TEMPERATURE CALIBRATION VIA COOLING TEST

To calibrate temperature measurement on our emissivity contrasted sample, we perform a cooling test on this sample with his own speckle-pattern and in the same environment and position as for the real test : testing machine, grips, IR camera and black-body (at the same low temperature).

In order to provide a validation of the calibration procedure, the back face of the sample, covered with a black uniform high emissivity coating, is reflected in a specific IR mirror in order to see both sample faces on the same camera image. Considering that the temperature is uniform across the thickness of the sample, the back face allows one to evaluate the temperature field that can be compared with the temperature calculated from the front face. The reflection of the mirror has been preliminary qualified by using the same imaging set up on a sample whose both faces were covered with a uniform high emissivity coating. Physical reference marks are drawn on each face to permit registration of both temperature fields.

As in any other IR measurement, the translation of the camera gray levels (Digital Levels or DL) into Celsius degree (°C) temperature for a unit emissivity necessitates a prior calibration over the relevant range of temperature. Rather than using the built-in correspondence provided with the camera, a standard calibration has been performed using a reference black body over the temperature interval 5-60 °C.

This correspondence can be used directly on a surface with an emissivity close to unity, and the final calibration step is to evaluate variation of the DL with the local sample temperature for the image of the speckled specimen face in the specific set-up. The unloaded specimen cooling naturally from 60 °C down to ambient temperature is imaged with the IR camera. The final (homogeneous) temperature is $T_0 \approx 26$ °C. It is noticed that the observed image $f(x,T(x))$ (where f is the DL value at pixel x) at all times and temperatures obey the following relation

$$f\left(x,T(x)\right) = \theta + \left((T-\theta)/(T_0-\theta)\right) f\left(x,T_0\right) \tag{1}$$

The temperature θ can be understood as that of the black body. Indeed, if the sample was brought to the same temperature as the reflecting black body, the surface would appear as uniform, irrespective of its local emissivity. Thus, a single reference image of the surface at the reference temperature T_0 is sufficient to appreciate quantitatively the rendering of the surface for any temperature. In the above equation, all temperatures are expressed in DL, and the calibrated correspondence is used to express it in Celsius degrees. From a best fit of the above relation over the entire cooling period provides an independent measurement of θ = 5.37 °C, consistent with the imposed value.

INFRA-RED IMAGE CORRELATION EQUATIONS

Now that the image texture evolution with temperature is known, it can be exploited in order to generalize the standard brightness conservation principle which is at the basis of DIC. The issue is now to retrieve both the displacement field $u(x)$ and temperature field $T(x)$ from the registration of an observed IR image, $g(x)$ under thermo-mechanical loading and a reference one (which we choose to be $f(x,T_0)$), exploiting the following relation

$$g(x) = f\left(x + u(x), T(x + u(x))\right) \tag{2}$$

So that, both unknown fields T and u are obtained from the minimization of the following functional

$$\Re = \int \left[g(x) - \theta - \left((T(x+u(x)) - \theta)/(T_0 - \theta)\right) f\left(x + u(x), T_0\right) \right]^2 dx \tag{3}$$

We have implemented the global DIC approach introduced in Ref. [6]. Both temperature and displacement field are decomposed over Q4 finite element shape functions (bilinear variation over square shaped elements). The algorithm proceeds through successive linearizations of the bracketed expression in the following functional around the current determination of the $(T,\mathbf{u})$ fields down to convergence. A multi-scale algorithm is implemented to allow for large scale displacements without secondary minima trapping, and achieve a quick and robust solution [7].

APPLICATION: STRAIN AND TEMPERATURE LOCALIZATION IN SMA

Specific behavior of NiTi

NiTi based SMA are perfect candidates to evaluate this new method. Their specific behavior is due to a martensitic phase transformation – austenite at high temperature / martensite at low temperature – which can be activated either by mechanical loading or temperature variations. The superelastic behavior for instance is observed during mechanical loading in the austenite phase: after an "elastic" behavior, the stress-strain curve presents a plateau corresponding to austenite → martensite transformation.

These phenomena are well-known [8,4] to be accompanied by strain localization, essentially on NiTi samples of various shapes (flat bone-shaped, thin tubes, wires) loaded in tension. The localization patterns generally form bands for flat samples [9] and helices for thin tubes [10-14], inclined at a 55 degree angle with the tension direction. The nucleation of multiple or a single band(s) and their propagation are sensitive to the imposed global strain rate [5]. The von Mises equivalent strain into bands was observed to be of the order of 3.5 % whereas the equivalent strain outside the bands remains lower than 1.5 % [9]. At the same time, the sample global temperature elevation may reach typical values of 20 °C, due to transformation latent heat, while heterogenety magnitude is about 8 °C due to localization. These values obviously depend although on the specimen geometry and environment [15].

Experimental procedure

The experimental method presented above is applied to tensile tests on a NiTi SMA. The material of composition Ti-Ni 55.4 wt% (commercial name SE508) was produced by Nitinol Devices and Components (Fremont, California, USA). Samples were formed by Nitifrance (Lury-sur-Arnon, France). The forming consists in a cold-rolling followed by a heat treatment of 2 minutes at 480 °C in salt bath. Samples have a rectangular section of 20 x 2 mm^2 and a gauge zone length of 120 mm.

The transformation temperature of the alloy were estimated using Differential Scanning Calorimetry (DSC) measurement: austenite start A_s = 3 °C, austenite finish A_f = 30 °C, martensite start M_s = 30 °C and martensite finish M_f = 0 °C. No trace of rhombohedral phase (R-phase) is observed for this specific forming and heat treatment.

Test is performed on MTS hydraulic testing machine (capacity 100 kN). Loading force and global displacement are measured. Loading is displacement controlled, with rate set to 2 mm/min and a maximum displacement value of 10 mm. The test is performed at ambient temperature (25 °C), the material being consequently initially in the austenitic state. These values were chosen to be consistent with previous test results, performed on similar samples [16].

Because of the machine and the type of grip that are used, the sample has to be thermally isolated from the external heat sources, namely the surface of contact between the specimen and the hydraulics grips and the hydraulic actuator has to be considered. We interpose insulating plastic sheets between the specimen and the grips. Because of the significant applied tension forces, these insulants may give rise to a small amount of slip between the jaws and the specimen head.

An IR camera, Jade III produced by CEDIP®, allows us to obtain images with an acquisition frequency of 100 Hz and an integration time of 930 μs and spatial resolution 5.5 pixel/mm^2. In the present experiment, the physical size of a pixel is about 210 μm.

Results and interpretation

The obtained global stress – global strain curve is given in Figure 2. Global strain means here actuator displacement relative to the initial length of the sample. The observed plateau is specific to superelastic behavior, *i.e.* stress induces austenite to martensite transformation. Such materials, prone to localization usually display a plateau behavior which should not be confused with the actual local constitutive law.

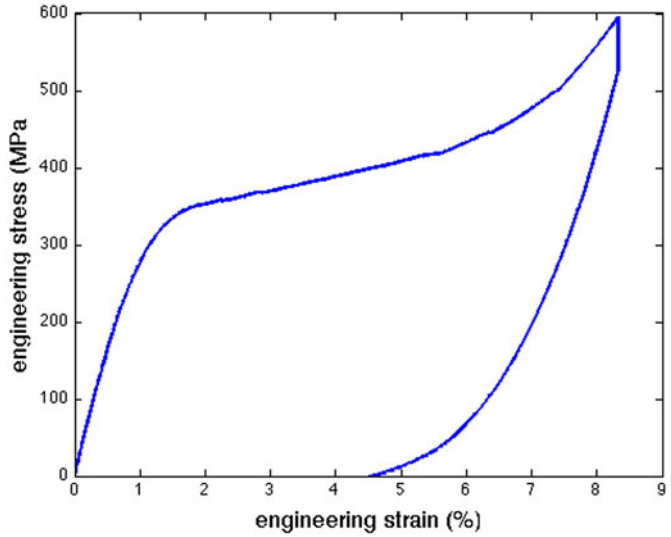

Figure 2 Stress-strain curve for the analyzed test.

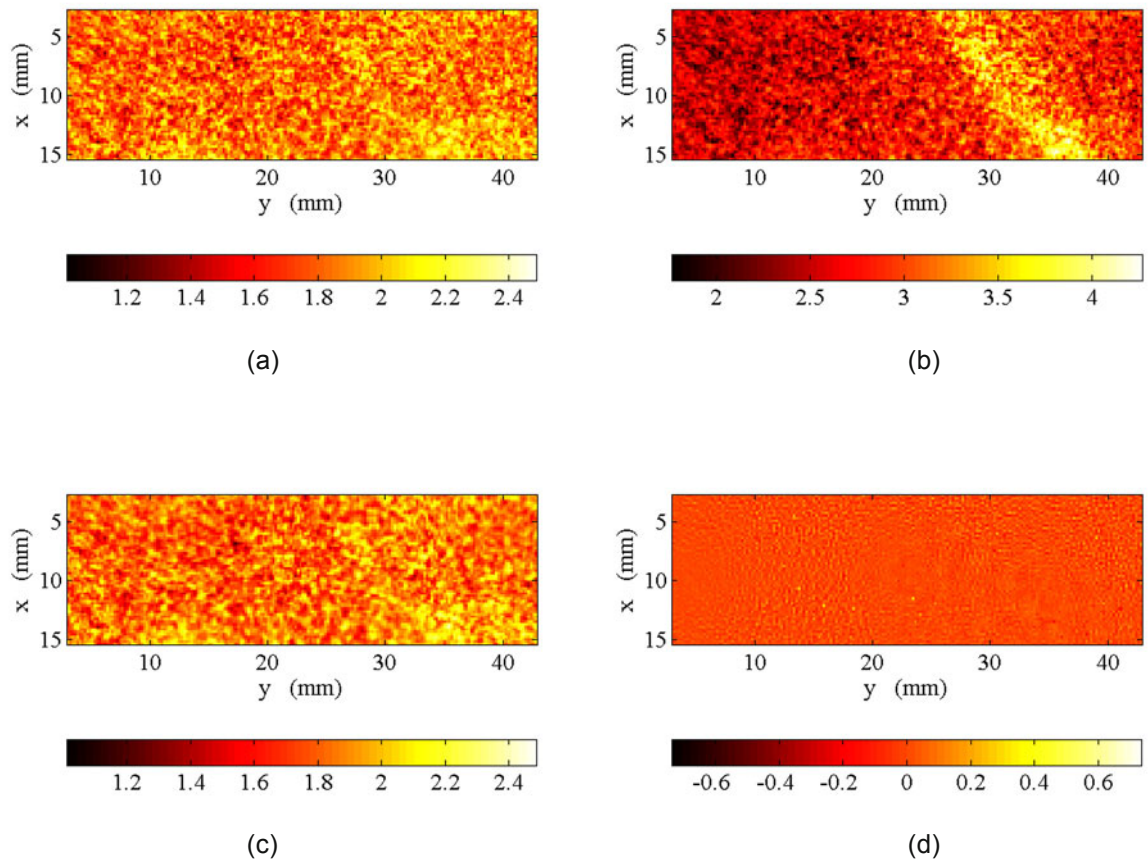

Figure 3 (a) Reference and (b) deformed images. The corrected deformed image and its difference with the reference, (or the residual), are shown respectively in (c) and (d).

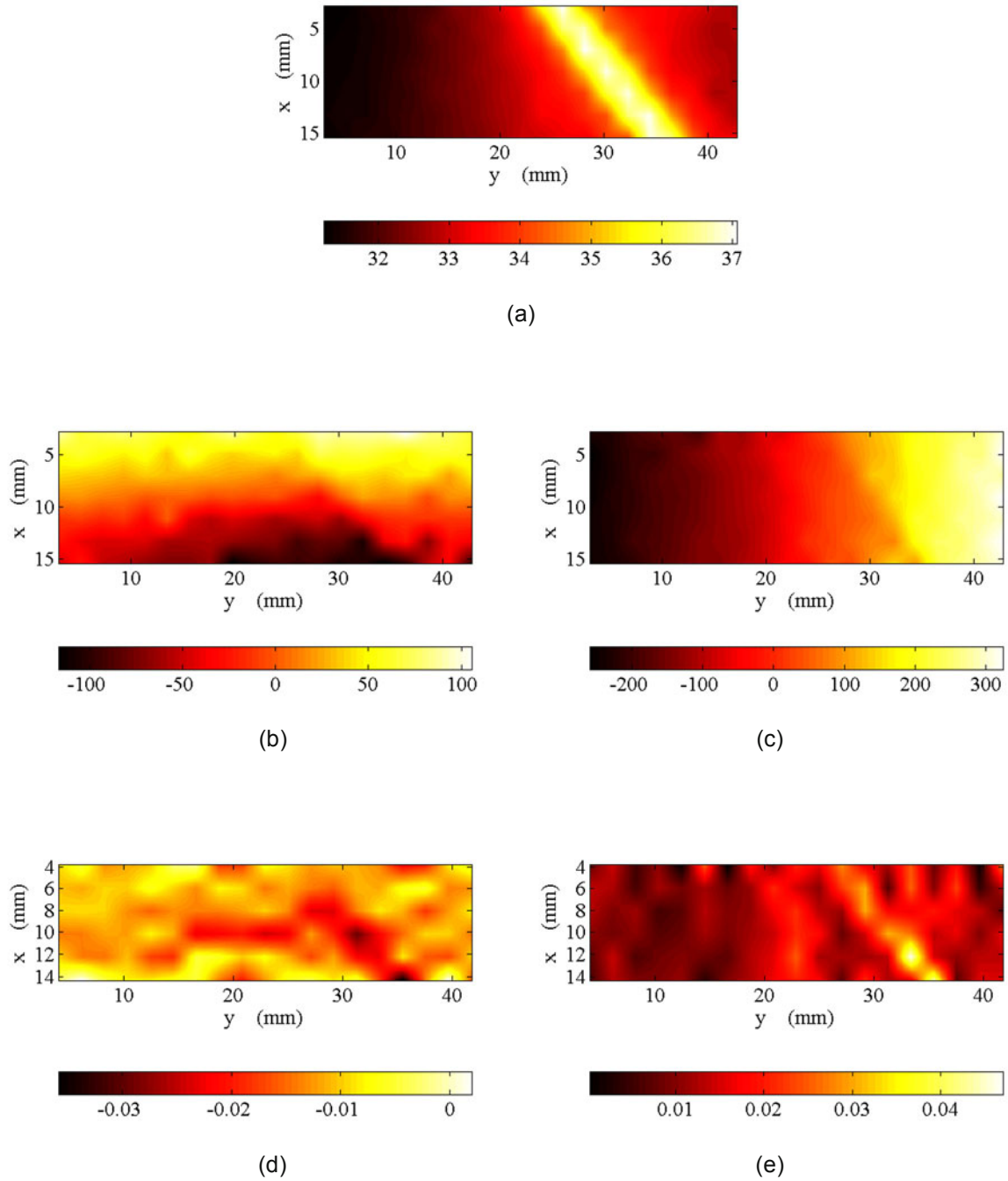

Figure 4 (a) Temperature field in Celsius degrees. (b) Transverse and (c) longitudinal displacements in micrometers. (d) and (e) show respectively the transverse (ε_{xx}) and longitudinal ε_{yy}) strain fields.

In the sequel we report on the analysis of a single IR image taken (no time averaging) in the plateau regime at the onset of the first visible shear band, at about 2.5 % engineering strain. The size of the element was chosen to be 10 pixels (about 2 mm) wide. Larger elements smear out the shear band over a larger region, whereas smaller ones display a significant amount of fluctuations.

Figure 3 shows (a) the region of interest of the reference image (prior to loading, after cooling period) as imaged with the IR camera and (b) a similar region of the specimen under load at the onset of the first localization band. In (c), image (b) corrected by the measured displacement field and effect of temperature elevation is to be compared with (a). The difference between this corrected image and the reference one is shown in (d) with the same gray level dynamics as the reference image. The uniformity of this difference signals a successful registration of the images. It is to be emphasized that the obvious temperature rise along the transformation band in (b) is mostly erased after the correction (c).

The temperature field obtained from the generalized DIC procedure outlined above are shown in Figure 4 (a). The temperature field has been converted to Celsius degrees. The estimated temperature rise within the shear band is about 5 °C above that of the bulk, which is itself roughly 5 °C higher than the initial temperature at this stage of loading (a higher final temperature is reached at the end of loading). The displacement field is shown in (b) and (c) after removal of the mean rigid body motion. The shear band appears markedly on both components of the displacement. Strains are more sensitive to noise, especially for small element sizes (since the number of pixels contributing to the determination of the displacement decreases). Nevertheless both the transverse and axial strains shown in (d) and (e) clearly reveal the presence of a shear band. The order of magnitude of the measured strain both inside and outside the band is in good agreement with previously published values on a similar NiTi material.

CONCLUSION

A joint measurement of the kinematic and temperature fields stemming from an extended Digital Image Correlation technique has been presented. Although the present study reported on a single image, the entire time development of the sample deformation and the intermittency of shear banding is accessible. Similar spatial resolution to conventional global DIC can be reached, albeit an additional (temperature) field is estimated. One of the advantages of the present procedure, in addition to the greatly simplified experimental test set-up, is the fact that the relevant thermo-mechanical fields are directly evaluated onto a finite element mesh, and hence the interface with numerical simulations aiming at identification does not involve any unwanted loss of accuracy in unnecessary projection steps for the comparison.

[1] Chrysochoos A., Berthel B., Latourte F., Galtier G., Pagano S., Wattrisse B., *Local energy analysis of high-cycle fatigue using digital image correlation and infrared thermography*, Journal of Strain Analysis for Engineering Design, 43, 411-421 (2008)
[2] Bodelot L., Sabatier L., Charkaluk E., Dufrénoy P., *Experimental setup for fully coupled kinematic and thermal measurements at the microstructure scale of an AISI 316L steel*, Material Science and Engineering, A 501, 52-60 (2009)
[3] Orteu J.J., Rotrou Y., Sentenac T., Robert L., *An innovative method for 3-D shape, strain and temperature full-field measurement using a single type of camera : principle and preliminary results*, Experimental Mechanics 48(2), 163-179 (2008)
[4] Sittner P., Liu Y., Novak V., *On the origin of Luders-like deformation of NiTi shape memory alloys*, Journal of the Mechanics and Physics of Solids 53, 1719-1746 (2005)
[5] Pieczyska E.A., Gadaj S.P., Nowacki W.K., Tobushi H., *Phase-transformation fronts evolution for stress- and strain- controlled tension tests in TiNi shape memory alloy*, Experimental Mechanics 46(4), 531-542 (2006)
[6] Besnard G., Hild F., Roux S*., "Finite-element" displacement fields analysis from digital images : Application to Portevin-le Châtelier bands*, Experimental Mechanics 46(6), 789-803 (2006)
[7] Hild F., Raka B., Baudequin M., Roux S., Cantelaube F., *Multiscale displacement field measurements of compressed mineral-wool samples by digital image correlation,* Appl. Optics 41, 6815-6828 (2002)
[8] Sun Q.P., Zhong Z., *An inclusion theory for the propagation of martensite band in NiTi shape memory alloy wires under tension*, International Journal of Plasticity 16, 1169-1187 (2000)
[9] Daly S., Ravichandran G., Bhattacharya K., *Stress-Induced Martensitic Phase Transformation In Thin Sheets Of Nitinol*, Acta Materialia 55(10), 3593-3600 (2007)
[10] Sun Q.P., Li Z.Q., *Phase transformation in superelastic NiTi polycrystalline micro-tubes under tension and torsion from localization to homogeneous déformation*, International Journal of Solids and Structures 39, 3797-3809 (2002)
[11] Feng P., Sun Q.P., *Experimental investigation on macroscopic domain formation and evolution in polycrystalline NiTi microtubing under mechanical force*, Journal of the Mechanics and Physics of Solids 54, 1568-1603 (2006)
[12] Favier D., Louche H., Schlosser P., Orgéas L., Vacher P., Debove L., *Homogeneous and heterogeneous deformation mechanisms in an austenitic polycrystalline Ti–50.8 at.% Ni thin tube under tension. Investigation via temperature and strain fields measurements,* Acta Materialia 55, 5310-5322 (2007)
[13] Schlosser P., Louche H., Favier D., Orgéas L., *Image processing to estimate the heat sources related to phase transformations during tensile tests of NiTi tubes*, Strain 43, 260-271 (2007)
[14] Schlosser P., Favier D., Louche H., Orgéas L., *Experimental characterization of NiTi SMAs thermomechanical behaviour using temperature and strain full-field measurements*, Advances in Science and Technology, 59, 140-149 (2008)
[15] Gadaj S.P., Nowacki W.K., Pieczyska E.A., *Temperature evolution in deformed shape memory alloy*, Infrared Physics and Technology 43, 151-155 (2002)
[16] Lavernhe-Taillard K., Maynadier A., Poncelet M., Benallal A., *Caractérisation thermo-mécanique et modélisation des bandes de transformation dans un alliage à mémoire de forme*, Proceeding of 19ème Congrès Français de Mécanique, Marseille, France, (2009)

Proceedings of the SEM Annual Conference
June 7-10, 2010 Indianapolis, Indiana USA

Investigating the thermo-mechanical behavior of clutch facing materials using image processing techniques

Yicheng Peter Pan PhD Candidate
Leonardo Batista Ito Graduate assistant
Tsuchin Philip Chu Professor
Peter Filip Professor
Department of Mechanical Engineering and Energy Process
College of Engineering, Southern Illinois University Carbondale
1230 Lincoln Drive Carbondale, Illinois 62901
Email : Panyicheng@gmail.com

ABSTRACT

The purpose of this paper is to investigate the thermo-mechanical behavior of clutch facing materials using image processing techniques. Infrared thermography and digital image correlation were used to analyze the mechanical behavior of clutch facing material under tensile loads. For specimens under tension loads, Infrared thermography clearly showed the thermo-elastic coupling as well as thermal dissipations due to the microcracking state of damaged clutch facing specimens. During an up to failure tensile test, localized thermal effects were observed at the macro-crack location before it appeared. Strain fields at the surface of specimens under tensile loadings were determined using the digital image correlation (DIC) technique. These experiments showed that the strain fields early became inhomogeneous. Strains concentrated in multiple localization zones which highlighted the role of the fibers in transmitting the internal forces.

1. INTRODUCTION

A clutch is a mechanism for transmitting rotation, which can be engaged and disengaged. Clutches are useful in devices that have two rotating shafts. In these devices, one shaft is typically driven by a motor or pulley, and the other shaft drives another device. The clutch connects the two shafts so that they can either be locked together and spin at the same speed (engaged), or be decoupled and spin at different speeds (disengaged) [1]. Fig. 1 shows a schematic representation of the clutch system in a vehicle [2].

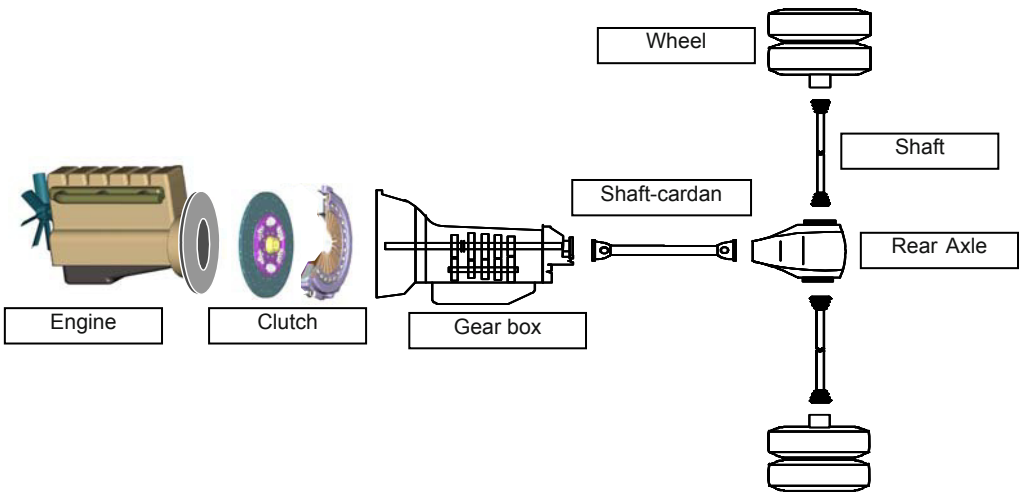

Figure 1: Schematic representation of the clutch system in a vehicle

T. Proulx (ed.), *Application of Imaging Techniques to Mechanics of Materials and Structures, Volume 4*, Conference Proceedings of the Society for Experimental Mechanics Series 14, DOI 10.1007/978-1-4419-9796-8_32, © The Society for Experimental Mechanics, Inc. 2013

In a car the clutch is operated by the left-most pedal using hydraulics or a cable connection from the pedal to the clutch mechanism. No pressure on the pedal means that the clutch plates are engaged (driving), while pressing the pedal disengages the clutch plates, allowing the driver to shift gears [1].

The most common types of friction materials for dry clutch systems are polymeric composite materials. A basic formulation of a polymeric friction material has several components categorized as binders, cure agents, fibers and fillers (inert and functional) [3]. These composites are manufactured in the most common case according to the scatter wound process. A yarn is impregnated in a mixture and then preformed. The preform is molded, cured and grinded to finished dimensions [4]. Fig. 2 summarizes the whole process:

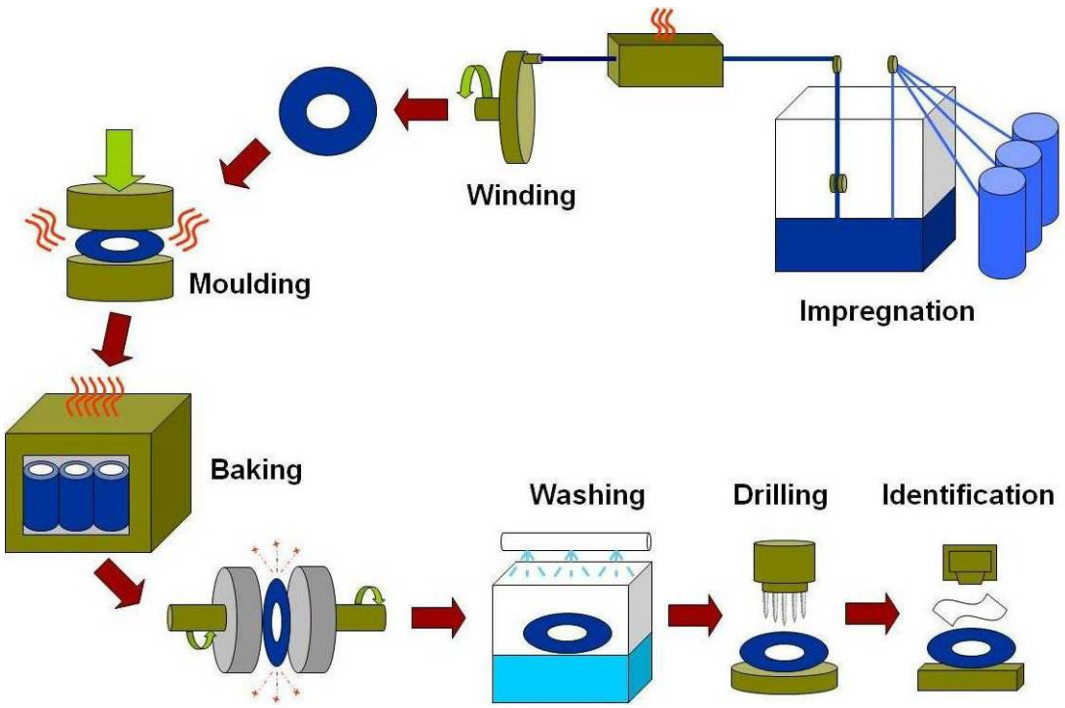

Figure 2: Typical multi-step process to produce clutch facings

Friction materials for dry clutch systems have to fulfill several requirements in order to give a proper performance to the clutch system. Commonly, they have to present a stable coefficient of friction in different conditions (fading resistance), high burst resistance against centrifugal forces, comfort to the driver (no judder), low density for a lower inertia, high thermal resistance, good durability (wear resistance), geometrical resistance, low cost and be environmental friendly. In general, the thermal and mechanical properties of clutch facing are essentially functions of the clutch facing material formulation and the manufacturing process. It is relevant to seek then for analytic formulas and simple tools to relate changes in the structure quantitatively to changes in the effective properties in order to achieve design optimization. In other words, optimized thermal and mechanical properties of clutch facing require new experimental tools allowing more accurate investigation to be performed. However no studies have ever tried to analyze the mechanical behavior of clutch facing specimens. Therefore, this study aims to present some applications of image processing methods for analyzing the thermo-mechanical behavior of clutch facing materials. Infrared thermography and digital image correlation were used for various clutch facing specimens under tensile loadings. Experimental setups are described in next section. Section3 present thermal effects observed under tensile loading, section 4 deals with strain fields recorded during tensile tests.

2. EXPERIMENTAL SETUP

2.1 Tensile testing

An Instron testing machine of 15 KN capacity in the Center for Advanced Friction Studies of Southern Illinois University at Carbondale (SIUC) was used for tensile testing. Instron Station Manager Software was used to manually control the system and the test parameters. The tensile tests were performed according to ASTM D3039M-08 and D5766M-07 standards [5-6]. The standard head displacement rate is 2mm/min. All specimens

were used to conduct the tensile test experiments in a laboratory air environment at room temperature. Figure 3 shows photos of the actual experiment setup at SIUC.

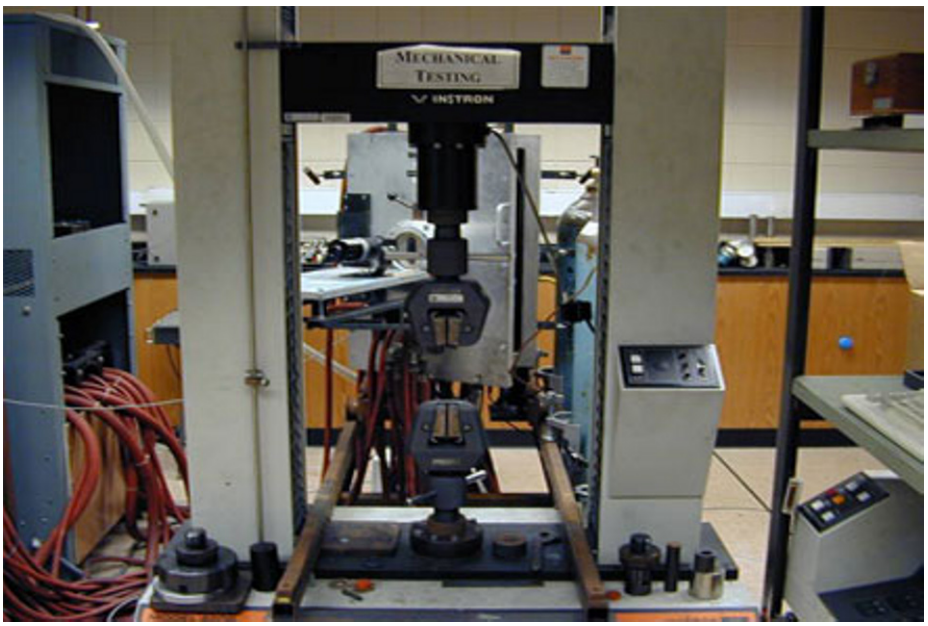

Figure 3: Experimental setup for tensile testing

2.2 Infrared thermal imaging

The equipment used in the experiments conducted at SIUC was the MikroSpecRT IR Camera with a resolution of 0.06°C at 30°C, a measurement accuracy of + 2°C of reading, and 320 x 240 dpi. The thermal image infrared camera unit incorporated a black and white or (grayscale) image viewing screen as well as a colored viewing screen for more refined and sharper imaging. The infrared camera was linked to a Dell Latitude D820 computer, which used the MicroSpecRT software that came with the IR camera. This software allowed for even further rendering and processing of the images. The software could record in real time and create video recordings or take snap shots as the sample was tested. Figure 4 shows photos of the actual experiment setup of IR camera and digital camera.

Figure 4: Experimental setup for infrared thermal imaging

2.3 Digital image correlation

Digital image correlation method is an experimental mechanics technique for displacement and strain mapping. It makes use of two image data sets, typically in the form of a speckle pattern, to extract deformation profiles from small changes in the images. Both local as well as global strain and displacement mapping is possible. For the digital image correlation technique, a digital camera Nikon 5700 Coolpix is used in association with the testing machine and IR camera previously mentioned (see Figure 4). The camera acquires 2560X1920 pixels images of the observed face of the specimen. The acquisition rate is one image per1 KN. Before the test, a speckle pattern is created on the observed face by spraying white paint and black paint. Speckle pattern is very important for digital image correlation analysis. Speckle spot should be uniform size and random spray on surface. The testing sample include 4 and 4 with open-holes specimens were subjected to fatigue tests. The samples with spray painted pattern are show in Figure 5.

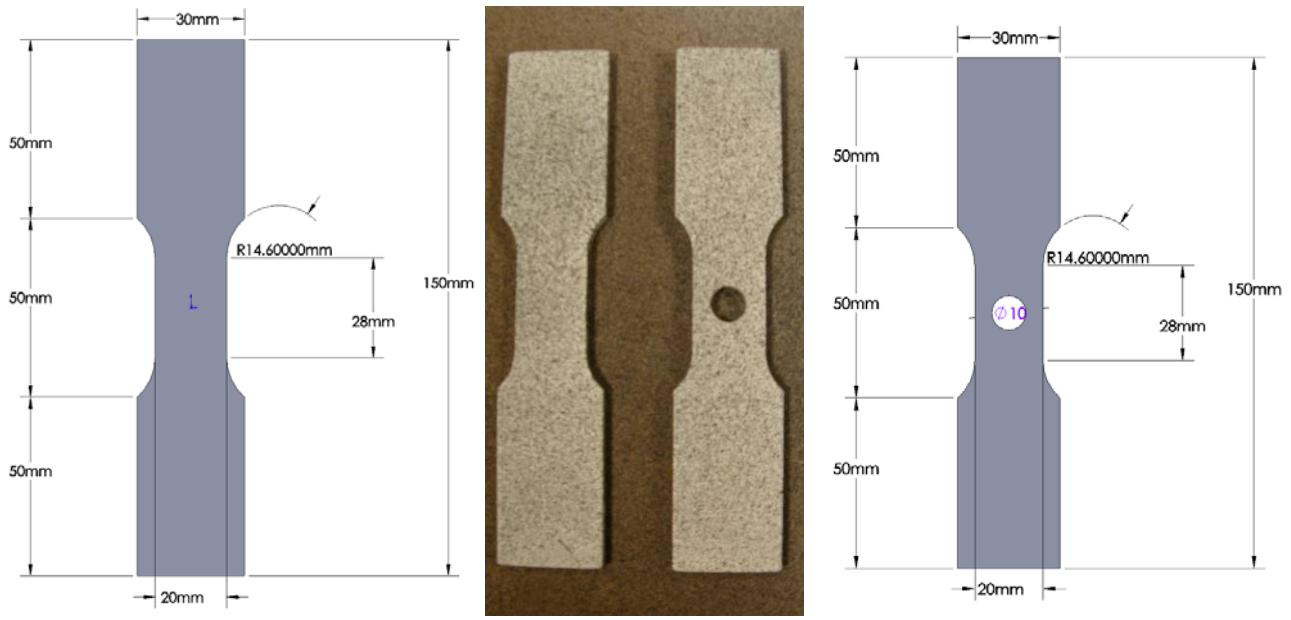

Figure 5: Samples with spray painted pattern

3. THERMAL EFFECTS OF DAMAGE AND CRACKING

From macroscopic effects of damage mainly consist in a decrease of stiffness and strength of the material. But in a microscopic point of view, it relates to the apparition of micro-cracks, which become more and more numerous and connected together. When material plastic deforms, friction occurs between the edges of the cracks. Thermal dissipation due to these frictional forces generated irreversible temperature increases in the sample [7]. In this paper, two examples of thermal records were presented for showing that the significant thermal effects related to damage. First, the thermal observation of a clutch facing specimen during an up to failure tensile test was presented. Then, this study presents the thermal observations of a clutch facing with open-hole specimen during an up to failure tensile test. Tensile test were performed up to failure clutch facing specimens. The sample dimensions are described in Figure 5.

Figure 6 shows the time variation of the tensile stress and thermal images of the surfaces at different times of the test. The maximum tensile stress is about 70 Mpa. These pictures show an overall warning up of the specimen due to thermo-elastic coupling. On image at 81 seconds, the first discernible localized thermal features appear and increase up at lower right area. These first thermal effects correspond to the beginning of the softening domain. The second thermal effects were happened on image at 115 seconds. At this moment, the tensile stress is about 65 Mpa. Form time at 117 to 130 seconds, the temperature variations homogenize. Form time at 135 seconds onwards, temperature increase and localize again up for third and four discernible localized thermal features. The thermal images are obtained from the MicroSpecRT software which depict the area of the fracture.

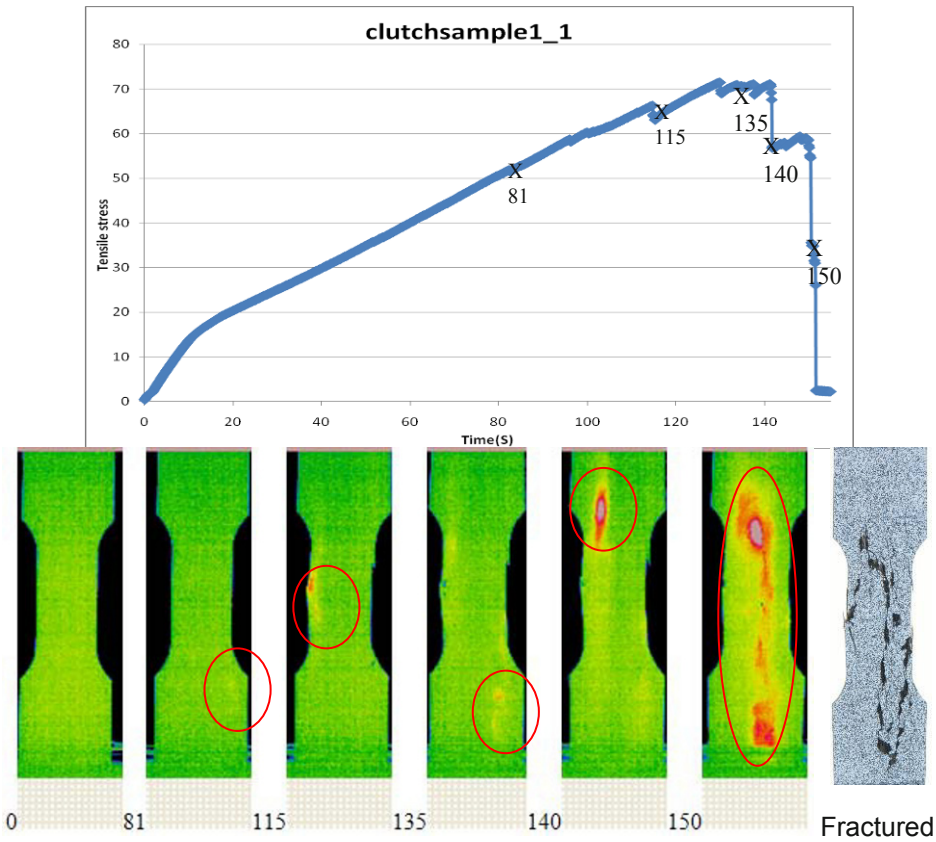

Figure 6: Time variation of the stress during an up to failure tensile test performed on specimen

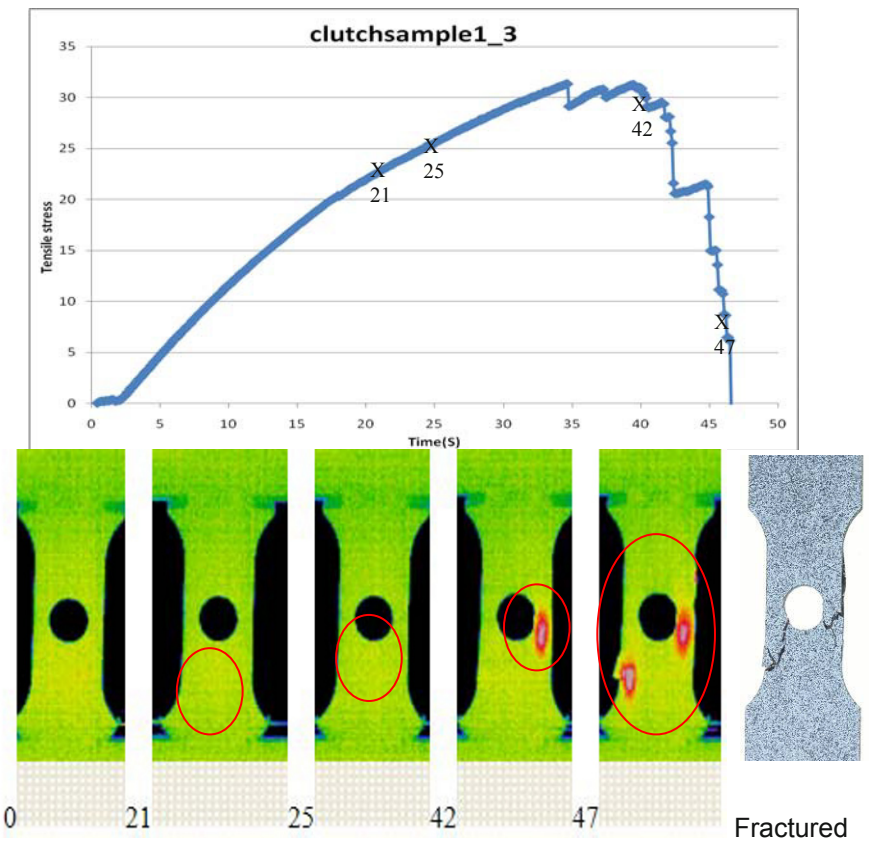

Figure 7: Time variation of the stress during an up to failure tensile test performed on open-hole specimen

Figure 7 shows the time variation of the tensile stress and thermal images of the surfaces at different times of the open-hole specimen test. In the same way, these pictures show the thermo-elastic coupling of the open-hole specimen. It can be supposed that the first thermal effects occurred form time at 21 to 24 seconds that are due to the initiation of cracks at lower center area. On image at 25 seconds, the second discernible localized thermal features appear and increase up at lower open-hole area. The third thermal effects were happened at left open-hole area on image at 42 seconds. At this moment, the tensile stress is about 30 Mpa. Before these third thermal effects, the temperature variations of the initiation of cracks are too small to recognize. The general warming of the open-hole specimen between time at 42 and 47 seconds can be attributed to thermal dissipation due to a distributed state of the damage. The overall temperature immediately decreased due to the stress release expect in the failure zone due to friction between crack edges.

4. STRAIN FIELD MEASUREMENT DURING TENSILE TEST

Digital image correlation of speckle patterns has been used extensively to measure displacement components and deformation gradients of an object surface due to deformation over three decades. The pictures of the specimen during tensile test were obtained at regular intervals. Rapidcorrelator 1.0 software was used to analyze the displacement and strain change. Rapidcorrelator gives the displacement values from which the engineering strains are calculated. After DIC analysis, the U displacement, V displacement, du/dx, du/dy, dv/dx, dv/dy, normal stain (xx), normal stain (yy), shear strain (xy), principal stain (XX) and principal stain (YY) were obtained. In this paper, two examples of DIC were presented for showing the strain field measurement during tensile test. First, the normal strain field observation of a clutch facing specimen at various loading states (from 0-7KN) during tensile test was presented. Then, this study presents the displacement field observations of a clutch facing with open-hole specimen at various loading states (from 0-3KN) during tensile test. Figure 8 and 9 show the normal strain fields at various loading of the test. For clarity reasons color scale is different for each loading. These experiments data showed that the strain fields early became inhomogeneous after loading. Strains concentrated in multiple localization zones which emphasized the role of the fibers in transmitting the internal forces. An open-hole sample of displacement contours are shown in the figure 10 respectively. Again, the color scale of each image is different for demonstration reasons. The pseudo colored strain and displacement contour maps indicate the area of maximum strain and displacement. Thereby predicting crack initiation in the sample. Thus the weaker section of the sample can be detected from the strain contours.

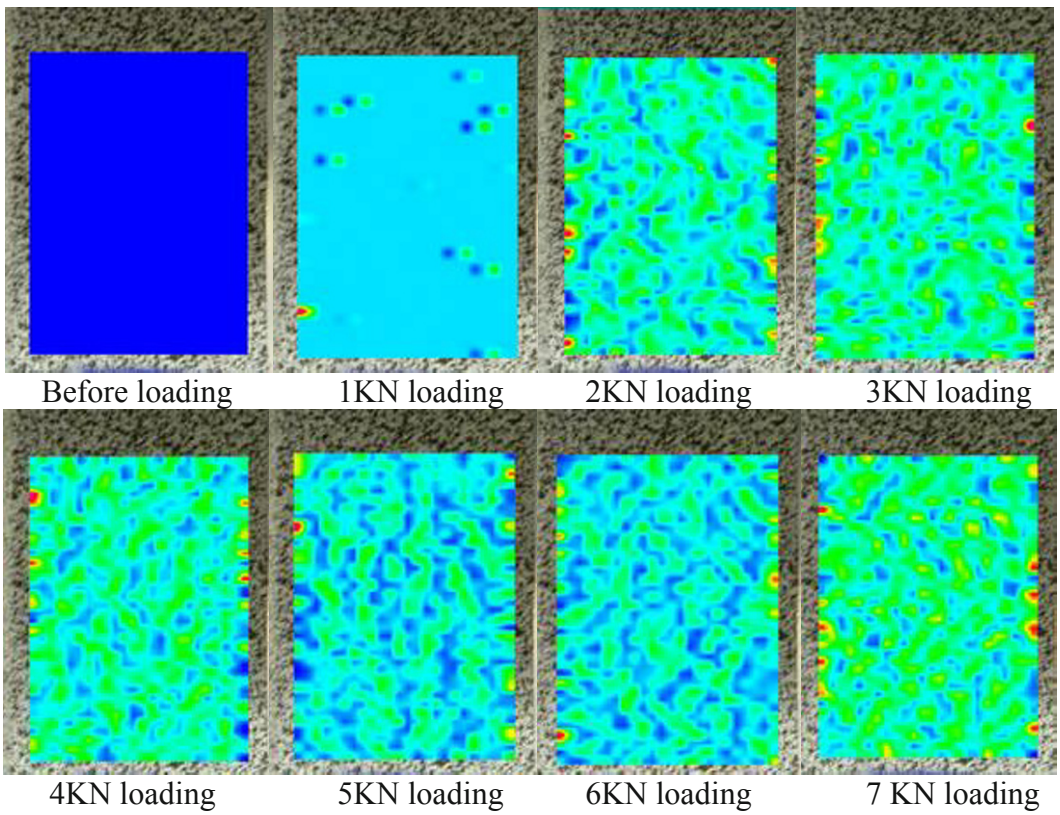

Figure 8: The normal strain (ε_{xx}) during an tensile test performed on specimen

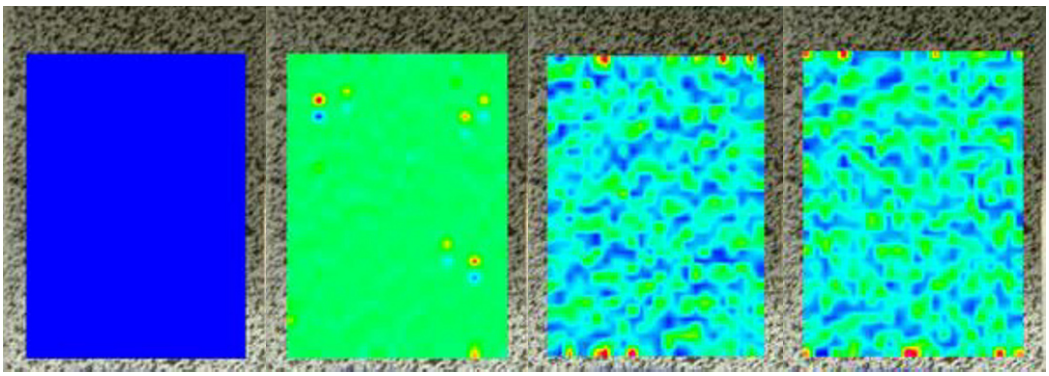

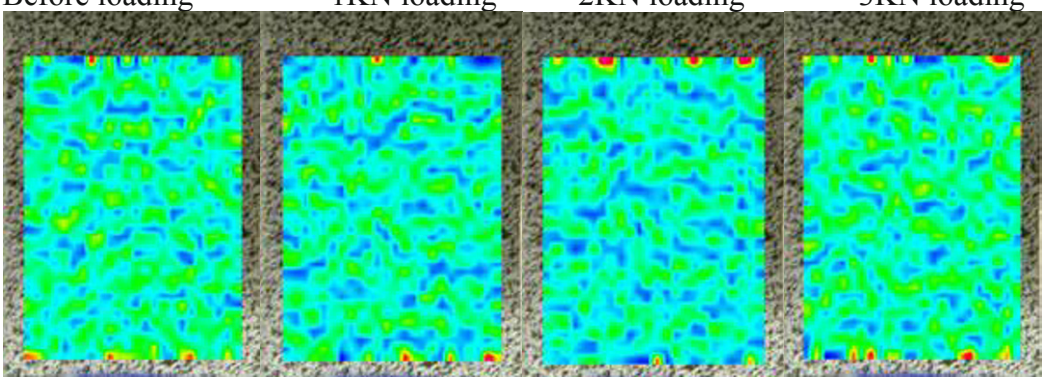

Figure 9: The normal strain (ε_{yy}) during an tensile test performed on specimen

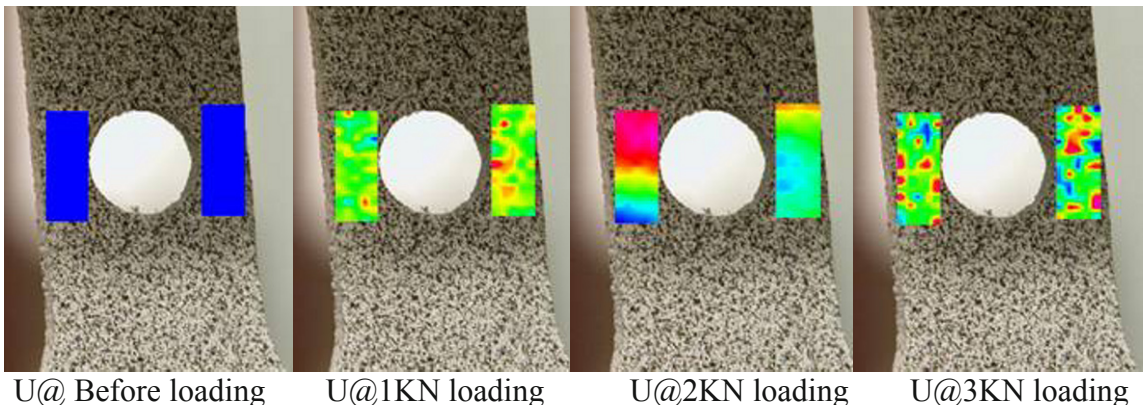

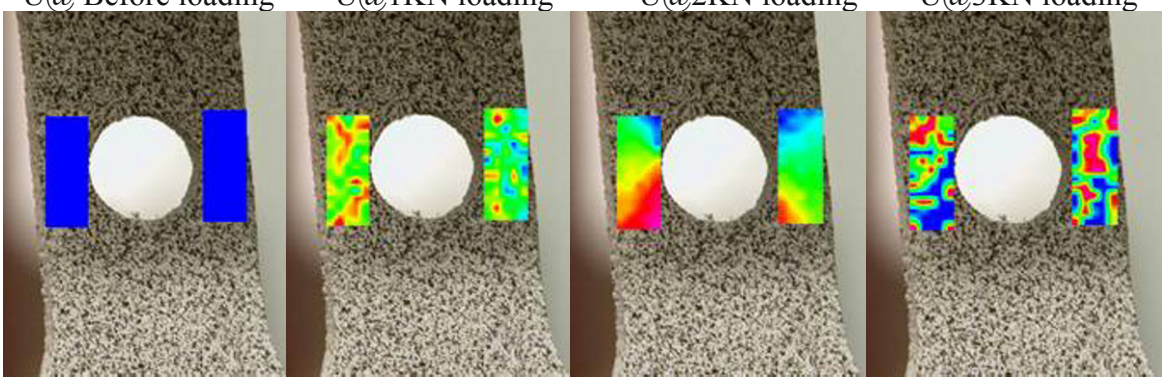

Figure 10: The displacement during a tensile test performed on open-hole specimen

5. CONCLUSION

Some applications of infrared thermography and digital image correlation to the analysis of the behavior of clutch facing have been presented. Infrared thermography allowed to accurately measure the thermo-elastic effect for clutch facing. During an up to failure test, Infrared thermal images showed localized thermal manifestations superimposed on the overall warming due to the thermo-elastic coupling. This localized thermal effect related to damage was observed before the stress peak was reached and increased until failure occurred. Digital image correlation method proved to be an efficient way to determine stain and displacement fields in a clutch facing specimens under tensile loading. Especially, the strain localization effect was observed by using this method. The infrared thermography and digital image correlation methods presented in this paper are effectively to improve the knowledge of the behavior of clutch facings. With the use of these methods, it is a helpful for finding the optimal material formulation and the manufacturing process parameters.

Acknowledgements

The Authors are grateful to Mr. Poh-Wah Lee and Taylor Chance, Southern Illinois University at Carbondale, for the assistance in tensile tests.

References

[1] Clutch. In Wikipedia. Retrieved February 8, 2010, from http://en.wikipedia.org/wiki/Clutch.

[2] Gregori, I., Zanotto, P., and Haertel, W., 2005, “Determination of the Relationship Between Bench and Vehicle Tests of Clutch Friction Facings by Means of Reliability and DOE Techniques”, SAE 2005 World Congress .

[3] Bijwe, J., Kumar, M., Gurunath, P.V., Desplanques, Y., and Degallaix, G., 2008, “Optimization of Brass Contents for Best Combination of Tribo-Performance and Thermal Conductivity of Non-Asbestos Organic (NAO) Friction Composites”, Wear, 265, pp. 699-712.

[4] Khamlichi, A., Bezzazi, M., and Parron Vera, M. A., 2003, “Optimizing the Thermal Properties of Clutch Facings”, Journal of Materials Processing Technology, 142, pp. 634-642

[5] ASTM Standard D3039M-08, 2008, Standard Test Method for Tensile Properties of Polymer Matrix Composite Materials, ASTM International, West Conshohocken, PA, 2003, DOI: 10.1520/E1461-07, www.astm.org.

[6] ASTM Standard D5766M, 2007, Standard Test Method for Open-Hole Tensile Strength of Polymer Matrix Composites Laminates, ASTM International, West Conshohocken, PA, 2003, DOI: 10.1520/E1461-07, , www.astm.org.

[7] Huon, V., Cousin, B., Wattrisse, B., Maisonneuve,O., 2009,”Investigating the thermo-mechanical behavior of cementitious materials using image processing techniques”, Cement and Concrete Research v 39, pp. 529-536

Proceedings of the SEM Annual Conference
June 7-10, 2010 Indianapolis, Indiana USA

Vibration Excitation Methods Applied to Digital Shearography and ESPI

Dirk Findeis, Jasson Gryzagoridis and Leovigildo Mahon Gerona
Department of Mechanical Engineering
University of Cape Town, Private Bag, Rondebosch, 7700
South Africa
Phone: +27 21 650 3670
Fax: +27 21 650 3240
E-mail: dirk.findeis@uct.ac.za

Abstract

Digital Shearography (DS) and Electronic Speckle Pattern Interferometry (ESPI) are laser based optical interference techniques used amongst other to inspect materials and manufactured components for defects. DS captures the rate of surface displacement and ESPI the displacement of an object in response to an applied stress. There are a number of ways to stress the object during the inspection process, the most common being the use of thermal heating or vacuum and pressure chambers. These forms cause whole field object responses, which generate the equivalent fringe patterns. Within these fringe patterns fringe anomalies revealing the presence of a defect are sometimes masked due to the object's whole field displacement. As an alternative stressing technique, this paper investigates the use of vibration excitation methods. The intention with this approach is that the friction produced in an object's defect area generates localised thermal gradients which in turn should be revealed in the produced fringe pattern.

This paper describes the above mentioned inspection techniques and examines the results obtained using Digital Shearography and ESPI when applied to selected samples. In particular the results obtained using vibration excitation are compared with results obtained using thermal stressing techniques, which ultimately attempts to determine the suitability of vibration excitation methods to inspect objects for defects.

Introduction

Composite materials are nowadays used in many different applications and products. When used in critical applications, such as the space and aircraft industry, the integrity of the manufactured components has to be verified at regular intervals. Non destructive testing techniques are commonly used for this purpose and include dye penetrants, X-Ray, Ultrasound, Eddy Current and Optical Inspection methods [1]. Two inspection techniques which fall into the category of Optical Non Destructive Testing techniques are Digital Shearography (DS) and Electronic Speckle Pattern Interferometry (ESPI). It has been shown that these techniques are particularly suited for the inspection of Carbon and Fibreglass based composite for defects, the likes of which include delaminations, debonds and cracks [2].

Theory

Digital Shearography is an optical interference technique and is based on the recording of speckle images, created when two light waves interfere with one another. In order for this to occur, the light waves have to be monochromatic, which is why single mode lasers are employed to illuminate the object being inspected. A video camera is used to view the object through a shearing device. The shearing device is often a proprietary design, but a conventional Michelson Interferometer, as indicated in Figure 1 below, can be used to illustrate the process. The laser light reflected off the object is split into two by the beamsplitter and directed onto mirrors M1 and M2. By tilting mirror M1 either horizontally or vertically, the reflected images can be misaligned, or sheared with respect to each other when recombined at the beamsplitter surface. The video lens then focuses the sheared image onto the CCD. At the CCD plane the recombined lightwaves interfere with each other and produce a speckle pattern which can be captured and digitized using a PC.

T. Proulx (ed.), *Application of Imaging Techniques to Mechanics of Materials and Structures, Volume 4*, Conference Proceedings of the Society for Experimental Mechanics Series 14, DOI 10.1007/978-1-4419-9796-8_33, © The Society for Experimental Mechanics, Inc. 2013

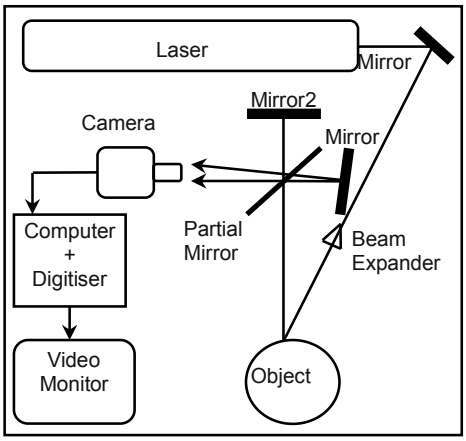

Figure 1. Typical Shearography set-up

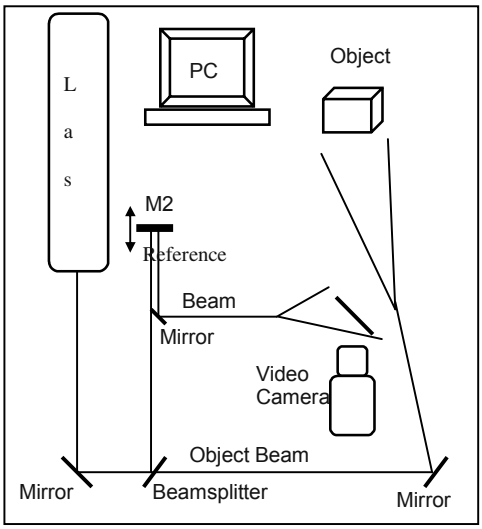

Figure 2. Typical ESPI Set-up

ESPI is also an optical interference technique and, as with Digital Shearography, requires a monochromatic laser light to illuminate the object. The technique however differs from the above in that the laser beam is split into 2 beams, namely the object beam and the reference beam. The object beam is directed onto the object and the reflection off the object is captured via a camera. Before the laser light reflecting off the object is focused onto the CCD, the reference beam is recombined with the object beam, causing the two to interfere and produce a speckle pattern. This process is illustrated in Figure 2 above.

When the object is stressed its surface deforms. This causes the beam path length of the laser light reflecting off the surface to change. With ESPI, only the object beam path length is affected, and as a result of the change in the phase of the laser light, the speckle pattern of the combined reference and object beams alters, directly proportional to the displacement of the surface of the object [3]. For Digital Shearography, both of the recombined beams alter in length and phase and thus only the relative change of the two causes the speckle pattern to alter. Digital Shearography therefore records the rate of displacement of the object [4] As these techniques are so sensitive to the induced displacements, the magnitude of the applied stress is very small, making it a truly non destructive inspection technique. By comparing the speckle pattern of the initial surface geometry with the surface geometry of the object after stressing, areas of correlation and de-correlation are determined and mapped. The resultant information is presented in the form of a fringe pattern image. For Digital Shearography each fringe represents a contour of constant displacement rate as indicated in Equation 1 below [5]and for ESPI each fringe a level of constant displacement as indicated in Equation 2 below [6].

$$\Delta\phi = \frac{4\pi}{\lambda}\left(\frac{\partial d}{\partial x}\right)S \qquad (1)$$

where: $\Delta\phi$ = correlation phase,
$d/\partial x$ = rate of displacement,
S = magnitude of shear,
λ = wavelength of the laser light,

$$d = \frac{n\lambda}{[\cos\alpha + \cos\beta]} \qquad (2)$$

where: d = out of plane displacement of the object due to the applied stress,
α = angle between the camera viewing angle and normal to the object,
β = angle between the object beam direction and normal top the object,
λ = wavelength of the laser beam,
n = no of fringes counted.

There are many ways to stress an object. Typical methods used are based on pressure, thermal or mechanical applications. Another method which can be used is vibratory excitation. With this method the vibratory energy is coupled and transferred to the object and converted to thermal energy due to frictional effects at the location of a defect. The thermal coefficient of expansion of the material in turn causes the object to deform in the region of the defect and thus produce a displacement field which can be captured.

As described above, ESPI and Digital Shearography produce intensity based fringe patterns. In order to determine the object's displacement or rate of displacement, the modulation of the laser phase due to the applied stress needs to be determined as well. This can be achieved using a technique called phase stepping. With this technique, the phase of one of the interfering wavefronts is altered by predetermined amounts during the image capturing stage. For Digital Shearography this would be achieved by moving Mirror2 in Figure 1 and for ESPI, by moving mirror M2 in Figure 2. For a 4 image configuration, the beam path length is increased by a quarter of a wavelength ($\pi/2$) between each of four images captured before and again after the object has been stressed. The intensities of the images can be represented in equation 4 as follows [7].

$$I_i(x,y) = I_B(x,y) + I_{MP}(x,y)\cos(\theta(x,y) + i \cdot \pi/2) \tag{3}$$

$$\phi(x,y) = \arctan\left(\frac{I_3(x,y) - I_1(x,y)}{I_4(x,y) - I_2(x,y)}\right) \tag{4}$$

$$\beta(x,y) = \phi_a(x,y) - \phi_b(x,y) \tag{5}$$

where i = 1,2,3,4
$\phi_a(x,y)$ = phase distribution after stressing,
$\phi_b(x,y)$ = phase distribution before stressing

In order to apply ESPI using UCT's purpose built Digital Shearography system, a modified form of the ESPI configuration was employed. With the modified configuration, the laser light emitted by the unit is directed onto the object to be illuminated as well as a flat plate, placed next to the object to be inspected. The adjustable mirror in the shearing configuration is then tilted such that the illuminated plate overlaps the object when the two images reflected off the two mirrors in the shearing device are recombined in the camera CCD plane. In this way the beam path of the shearing device acts as the object beam and the second beam path acts as the reference beam. When the object is then stressed, the beam path length from the laser to the object surface and then to the CCD plane changes, but the beam path length from the laser to the plate and then to the CCD plane doesn't. The change in phase and speckle pattern is due to the change in the object surface only and the fringe patterns produced depict the magnitude of the object surface displacement. This applies to both the intensity based fringe pattern as well as the Phase stepped fringe pattern.

Results

In order to investigate the use of vibration excitation for the NDT of composite materials an electro-magnetic vibration generator, manufactured by Frederiksen was purchased. The unit had a limiting current of 1A and could operate at frequencies ranging from 0.1 Hz to 5 kHz. The unit was connected to a function generator in order to control the frequency of the sine wave output, as well as the amplitude of the signal.

Three samples were prepared for this investigation. The first was a section cut from a composite helicopter rotor blade which consisted of a shaped Nomex honeycomb core of varying thickness, covered with carbon fiber skins. The section was prepared with 9 external round defects all applied on the surface facing away from the viewing side. i.e. invisible to the naked eye from the inspection side. The second prepared sample was a 20mm thick sandwich honeycomb consisting of a Nomex core and carbon fiber inner and outer skin. In this sample 4 holes were drilled, all to a depth of 5mm, but with different diameters varying from 5 mm to 20mm. With this sample it was intended to determine whether the size of a defect had an influence on the fringe density when using vibration excitation methods. The third sample was again prepared from a section of the helicopter rotor blade. For this test, the outer skin was removed and three internal debonds created. This was achieved by fixing three square brass plates onto the inside of the removed skin and then rebonding the skin onto the Nomex core. The three samples can be seen in Figure 3 below.

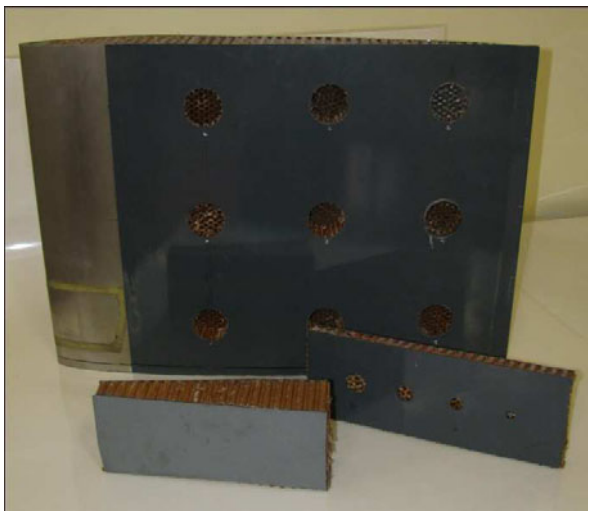

Figure 3. Composite test samples

All inspections were carried out on the laboratory vibration isolation table, using a Helium Neon laser and a selection of optics, as shown in Figure 4 below. The samples were placed on the table and clamped where needed. The vibration generator was positioned such that the probe tip was placed in contact with the object surface. The base plate was then weighted down to prevent shifting of the generator. For thermal heating, an infrared lamp placed sufficiently far from the test piece and connected to a timer was used to stress the samples. A typical application of both methods of stressing can be seen in Figure 5 below.

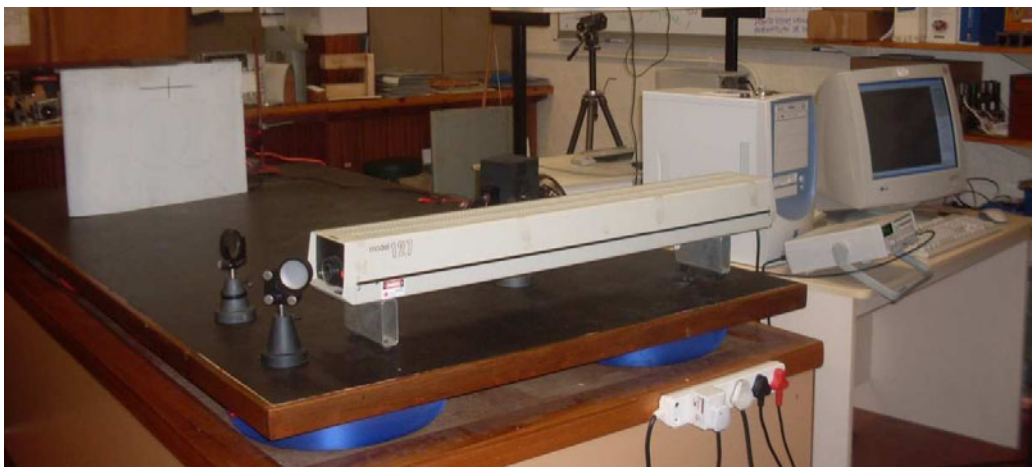

Figure 4. Laboratory inspection setup

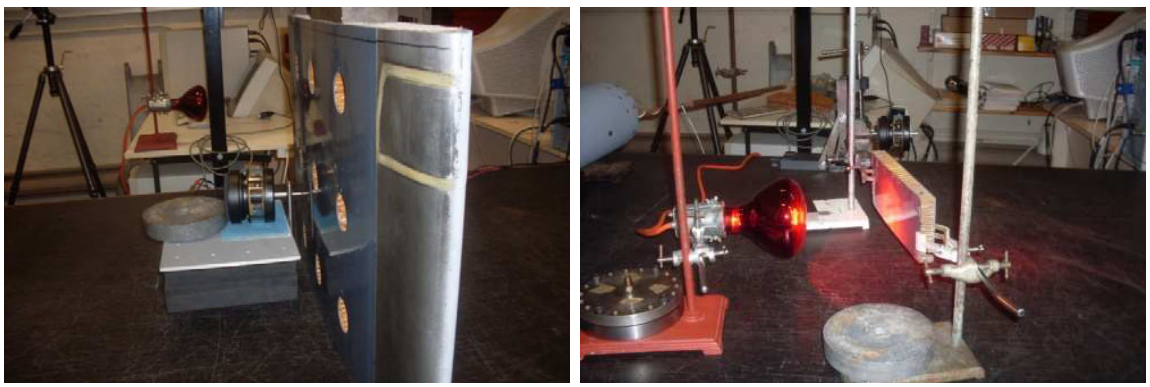

Figure 5. Vibration generator and heating lamp applied to inspection samples.

The first sample to be inspected was the 9 hole helicopter section sample. As a reference image, a separate inspection of the test piece was made by using thermal heating for 5 seconds during the inspection process. The result of this inspection using Digital Shearography is depicted in Figure 6 below. The results clearly reveal the location of the defects via the familiar double bulls-eye or butterfly fringe pattern. Three of the locations are not clearly seen due to the magnitude of the applied shear, but their presence is clearly visible. The variation in fringe density also indicates the severity of the defect, as all man-made defects were not the same. In addition the sample was exposed to vibratory excitation along the length of the section as well as perpendicular to the section. Both directions yielded results and it was thus decided to focus on the perpendicular direction only, as depicted in Figure 4 above. The results of the Digital Shearography based inspection is depicted in Figure 7 below. From simple observation it is clear that the use of a vibration generator also reveals the presence of all 9 defects. It must be noted that the application of the vibratory energy was in the order of 5 minutes and the results were captured only after the generator had been switched off, i.e. during the cooling process. The vertical fringes covering the whole sample in Figure 6 also shows a displacement gradient across the whole helicopter section. This phenomenon cannot be seen in the result in Figure 7, which indicates a uniform energy distribution within the bulk of the sample which is intact. It is only the cross-section anomalies, namely the defects, which reveal a variation in energy levels and thus displacement gradients.

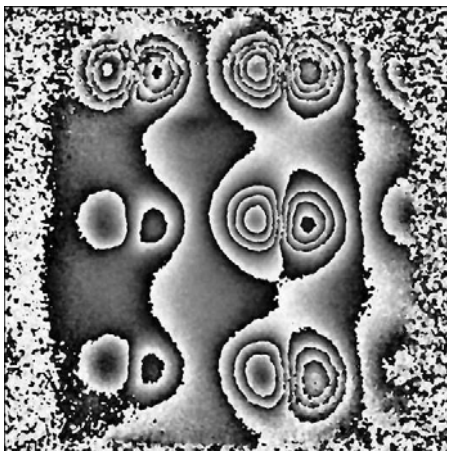

Figure 6. Digital Shearography result using thermal stressing

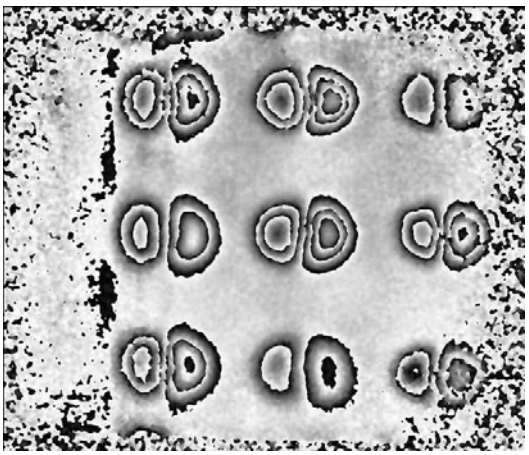

Figure 7. Digital Shearography result using vibratory stressing

.

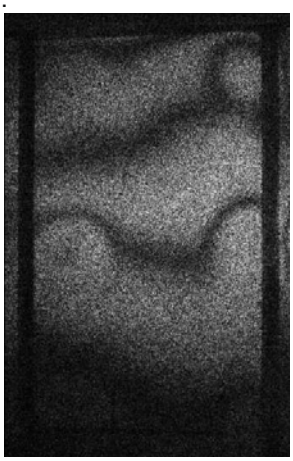

Figure 8.Intensity based ESPI result using vibratory stressing.

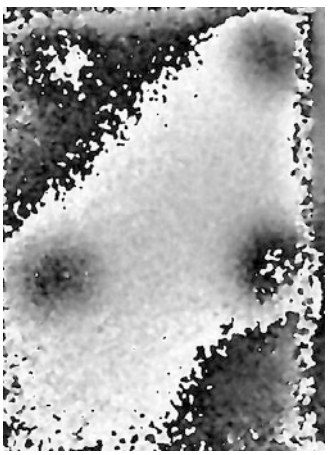

Figure 9.Phase stepped ESPI result using vibratory stressing.

The results using the modified ESPI configuration are reproduced in Figure 8 and 9 above. Here it was not possible to inspect the entire section at once as the amount of tilt was not sufficient to overlap the reference surface over the entire helicopter section. Figure 8 is the result obtained from the intensity based inspection and

Figure 9 from the phase stepped method. It is immediately apparent that the fringes here differ from the shearography fringes in that singular circular fringes are formed, revealing the presence of a defect. In both images the upper 4 defects can be identified and located. Of the lower 2 defects only one can be detected with certainty. The angled horizontal fringes in the images indicate that wholescale object motion was also recorded, a phenomena which Digital Shearography is relatively immune to. It must also be noted that in order to obtain these images the vibration generator was applied twice as long, when compared with the Digital Shearography tests.

The second sample to be inspected was suspended in space using two retort stands, as seen in Figure 5. Here again both the thermal heating and the vibration generator were used to inspect the test piece for the manufactured defects. The results are depicted in Figures 10 – 12 below.

Figure 10. 20mm sample with 5mm deep defects. Phase stepped result, thermal heating

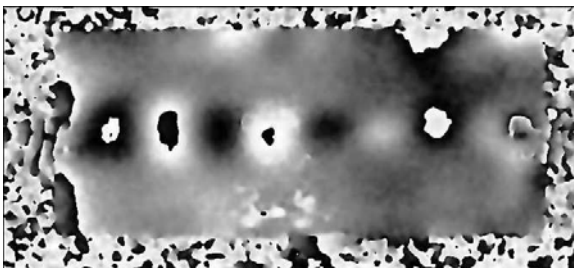

Figure 11. 20 mm sample and 5mm deep defects. Phase stepped result, vibration stress.

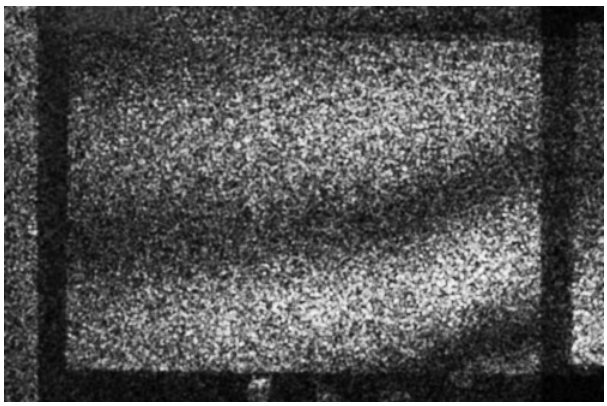

Figure 12.20mm sample with 5 mm deep defects. ESPI result, vibration stress

Figure 10 shows the results obtained using thermal loading during the Digital Shearography inspection. The defects are clearly visible and the increase in defect severity due to the increase in hole diameter size from right to left is also evidenced by the corresponding increase in number of fringes. Figure 11 is the result obtained using the vibration generator. Here as well all four defects have been located, but there is no clear indication of an increase in fringe severity in the number of fringes recorded, but rather in the increase in size of the generated fringes. Comparing Figures 10 and 11, it is again clear that there are negligible global fringes when using vibratory stressing method, unlike in the results obtained from the thermal stressing inspection. With the support of Figure 11 it can be seen that there also are some unwanted defects, most probably lack of skin bond along the top edge and left vertical edge of the sample. Figure 12 depicts the EPSI inspection result using the vibration generator. Unfortunately there are no fringe anomalies to indicate the presence of the defects.

The results of the final sample that was inspected using Digital Shearography are shown in Figures 13 and 14. For this inspection the sample was placed on a metal support and weighed down with a weight placed on top. The results from the ESPI investigation which is the intensity based fringe pattern is shown in Figure 15.

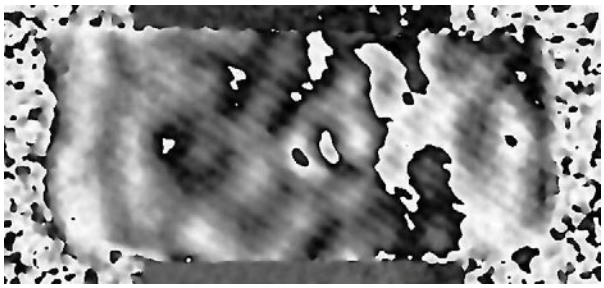

Figure 13. Brass insert defects, Phase stepped Digital Shearography, thermal heating.

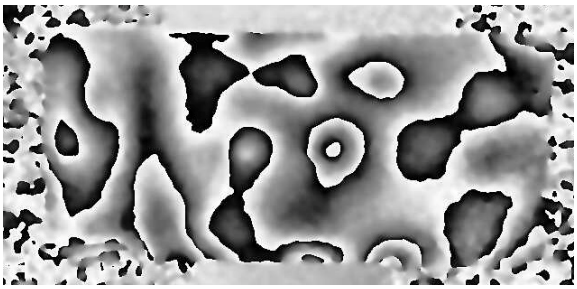

Figure 14. Brass insert defects. Phase stepped Digital Shearography, vibration stressing.

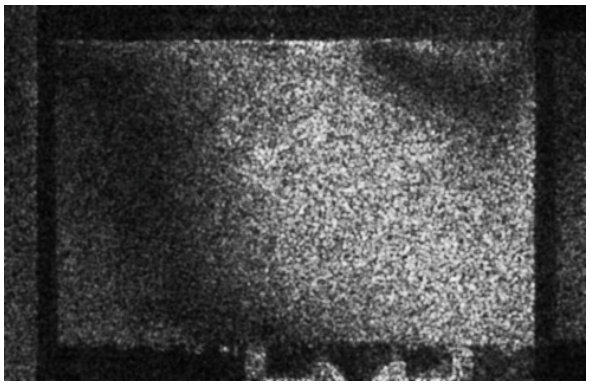

Figure 15. Brass insert defects. Intensity ESPI, vibration stressing.

In Figure 13, the location of the brass inserts can be seen in the fringe pattern. Although not as clear as in the two previous samples, their locations can be observed horizontally along the central length of the sample. The Digital Shearography vibration results in Figure 14 only detect the central brass insert, and not the 2 outer inserts. The irregular fringes in both of the fringe formation results also indicate that there are other irregularities present in the prepared sample. This most probably is due to the varying thickness of the glue that was applied when the skin was rebonded to the surface. Although some fringe irregularities exist in the ESPI vibration result in Figure 15, there unfortunately is no clear evidence of the presence of the brass inserts. What is apparent is the overall movement of the sample during the inspection capturing process, this can be seen via the diagonal fringes covering the sample surface.

Conclusion

The above results indicate that both thermal and vibratory stressing methods can be used to inspect composite components for defects..The thermal stressing technique was able to reveal all man-made defects in the prepared samples. Vibration stressing used in conjunction with Digital Shearography was able to detect most of the defects, with the exception of the two brass inserts.

The results obtained using vibration excitation coupled to ESPI was found to be inferior to the equivalent Digital Shearography results. The fringe anomalies for the 9 defects test section were significantly less in the ESPI results, and the inspections of the 20mm composite plate and the brass insert composite test piece yielded no detectable defects in the recorded fringe patterns.

When comparing the Digital Shearography results for thermal and vibration stressing, the results indicate that the vibration stressing technique does not create stress variations across the object. With thermal stressing on the other hand, uneven thermal loading can create temperature gradients across the object surface, which result in an uneven displacement gradient map across the object surface.

References

1. Stanley R K, Moore P O, Mcintire P, *Nondestructive Testing Handbook, 2nd Ed*, American Society for Nondestructive Testing,1995.

2. Moser E, ”Shearography NDT of Aerospace Structures”, Proc DGZfP International Symposium on NDT in Aerospace, Dec 3-5,Fuerth, Germany, p 174, 2008.

3. Claud G, Optical Methods in Experimental Mechanics, Part 8, Experimental Techniques, Sept/Oct 2003,pp 15-18, 2003.

4. Hung YY, ”Shearography: a new optical method for strain measurement and non-destructive testing”, Opt. Eng. 21 (3), pp 391-395, 1982.

5. Venkatraman B, Jayakumar T, Kalyanasundaram, P, and Raj, B, “NDE Methodologies for Examination of Tail Rotor Blades of Helicopters,” *Proc.15th World Conference on Non-Destructive Testing,* Roma 15-21 October,2000.

6. Jones R, Wykes C, *Holographic and Speckle Interferometry, 2nd Ed*. Cambridge University Press, 1989.

7. Findeis D, Gryzagoridis J, Matlali M, “Phase Stepping Shearography and Electronic Speckle Pattern Interferometry***”,*** *Proceedings 3rd US-Japan Symposium on Advancing Capabilities and Applications in NDE*, Maui, 20-24 June. 2005.

Proceedings of the SEM Annual Conference
June 7-10, 2010 Indianapolis, Indiana USA

Experimental Studies of Phase Transformation in Shape Memory Alloys

Kyubum Kim, Sam Daly*
Department of Mechanical Engineering, The University of Michigan, Ann Arbor, MI 48109
** Corresponding author: samdaly@umich.edu*

ABSTRACT

This research incorporates an experimental study of stress-induced martensitic phase transformation in the shape memory alloy Nickel-Titanium. The rich local thermo-mechanical interactions that underlie the solid-to-solid state phase transformation between the cubic austenite phase and the monoclinic martensite phase are examined via Digital Image Correlation (to obtain local strain fields) and infrared imaging (to obtain corresponding local thermal fields). Although other methods have been used to explore phase transformation in shape memory alloys, this methodology is unique in providing a quantitative estimate of the strain inside the area of martensitic transformation, as well as direct correlations of local strain and temperature fields. Using this combined methodology, we are able to quantify the complex local interactions between released/absorbed latent heat and the extent of transformation, and explore the characteristics of the phase fronts (velocity, width, etc) and the evolution of martensitic volume fraction. There is also evidence of a remarkable cyclic strain memory on the microscale.

EXPERIMENTAL METHODOLOGY

Polycrystalline sheets of Nitinol with an alloy composition of 55.5 wt% Nickel and 45.5 wt% Titanium were cold-rolled by the supplier (NDC, Johnson and Johnson) into a continuous flat strip nominally 50x600 mm long. The specimens were processed to have an A_f = -2°C in order to ensure that they were fully austenitic when unloaded and that stress-induced martensite occurred upon loading. The grain size in the rolled sheet was on the order of 35 nm, as determined by X-ray diffraction using a Rigaku Rotating Anode X-Ray Diffractometer and Jade software.

Dog-bone shaped tensile specimens were extracted from sheet by electrical discharge machining, parallel to the rolling direction (RD) and with the specimen dimensions shown in Figure 1. Full-field characterization of the nucleation and propagation of phase fronts was obtained by three-dimensional Digital Image Correlation (DIC). DIC is an optical method of measuring displacements, and thus Lagrangian strains, on the surface of a sample by tracking a highly anisotropic, high contrast pattern on the sample surface. In these experiments, the pattern was applied by airbrushing a uniform, thin coat of solid white titanium oxide on the surface, followed by a speckle pattern of carbon black. Patterning was applied with an Iwata Custom Micron B airbrush gun. The tests were performed on a 45-kip (200 kN) Instron uniaxial electromechanical testing machine with a custom LabView-based data acquisition system. Three-dimensional DIC (Correlated Solutions) was used to image surface deformation on the specimen and simultaneous infrared imaging (Inframetrics ThermaCam SC1000) measured the surface thermal fields. Two 5-megapixel cameras (Point Grey GRAS-50S5C) were used to image the specimen,

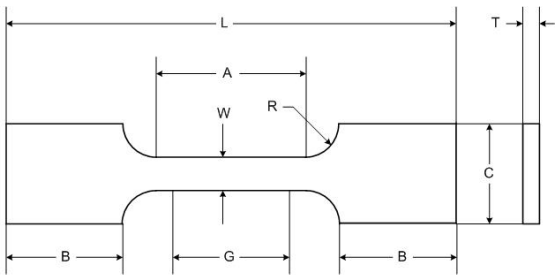

Dimension

	mm
G – Gage length	12.5 ± 0.025
W – Width	3.125 ± 0.0625
T – Thickness	0.254
R – Radius of fillet	5
L – Over-all length	50
A – Length of reduced section	15
B – Length of grip section	12.5
C – Width of grip section	12.5

Figure 1: Tensile specimen geometry.

T. Proulx (ed.), *Application of Imaging Techniques to Mechanics of Materials and Structures, Volume 4*, Conference Proceedings of the Society for Experimental Mechanics Series 14, DOI 10.1007/978-1-4419-9796-8_34, © The Society for Experimental Mechanics, Inc. 2013

and high shutter speed and light diffuser boxes were employed to improve pattern quality. The samples were tested at $\dot{\varepsilon} = 10^{-4}\, s^{-1}$ in zero-to-tension cycling under a ramp profile in displacement control. Samples started in the as-received state and were cycled fifty times. Pattern and rigid body (translation and rotation) baseline testing were performed to evaluate the accuracy of the setup. Using this setup, real-time three-dimensional deformation fields were obtained for the evaluation of the spatial development of inhomogeneity and phase transformation fronts.

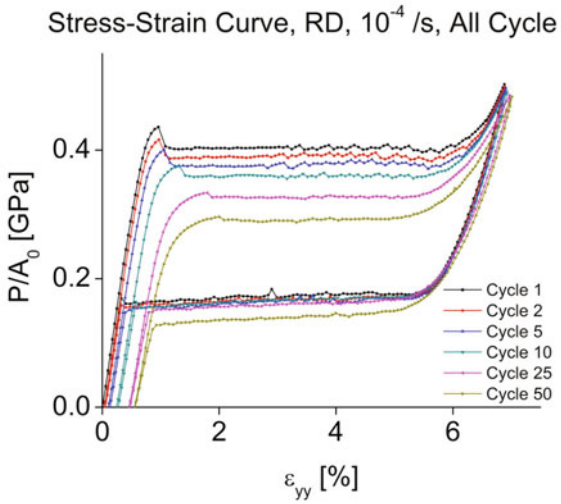

Figure 2: Stress-strain curves under hard cyclic loading obtained using digital image correlation

RESULTS AND DISCUSSION

Macroscopic stress-strain curves for cycles 1, 2, 5, 10, 25 and 50 under a displacement-controlled strain rate of 10^{-4} s^{-1} are shown in Figure 2. Snapshots of the specimen were taken after each displacement increment, and sample position and strain distributions were computed. Each data point on these curves represents a spatial average of the full-field Lagrangian strain map obtained by three-dimensional digital image correlation plotted against the nominal stress applied to the specimen by the tester at the same point in time.

As the cycle number increases, the number of nucleation sites increases and the delineation of the phase fronts degrades. There clearly exists a tendency for the phase fronts to have positional memory with microscale resolution in both the loading (A⇒M) and the unloading (M⇒A) cycles. We expect that the irreversible slip occurring with each cycle would preclude exact repeatability of phase transformation patterns. However, the degree of positional memory for the bands was very strong. The axial strain during stress-induced martensitic transformation, near the midpoint of the A⇒M loading cycle, is compared in Figure 3 for varying cycle number. Note that the nucleation site of the phase front can change location, as in cycle 1 to 2, but the quality of the phase front morphology is strikingly similar.

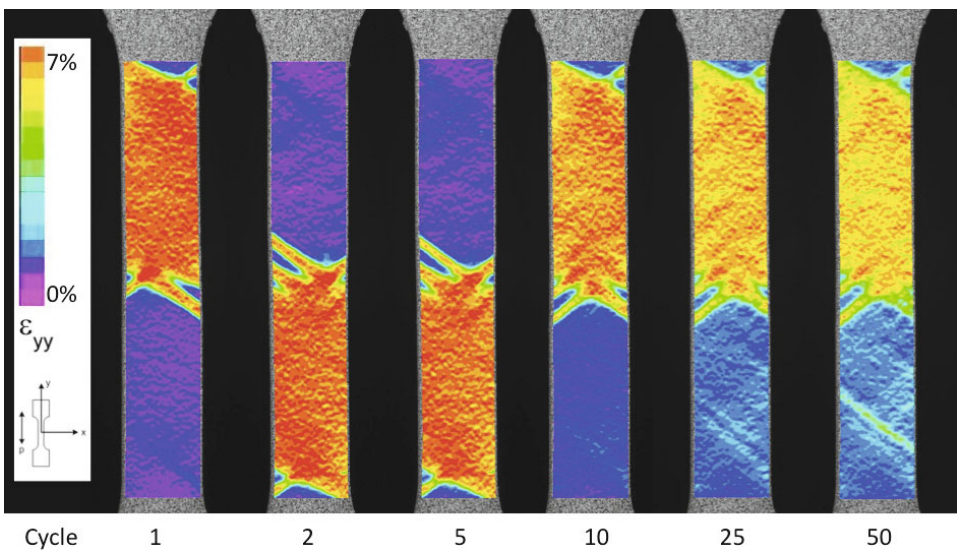

Figure 3: Pattern fidelity during stress-induced martensitic transformation in the SMA Nickel-Titanium under hard cyclic loading (see pdf for color version).

CONCLUSIONS

In this research, we have used three-dimensional digital image correlation to examine the cyclic transformation behavior of Nickel-Titanium subjected to quasi-static, uniaxial, zero-to-tension loading. We observe strain localization and macroscopic cycling characteristics consistent with other researchers, and have been able to examine the full-field, real-time development of stress-induced martensitic transformation in terms of Lagrangian strain. We find that the number of nucleation sites increases and the delineation of the phase fronts decreases with increasing cycle number. However, although the transformation becomes more homogeneous during cycling, there is a remarkable amount of pattern fidelity. Future work will examine the characteristics of individual phase fronts and their interaction as a function of strain rate and loading range, including the effect of mean stress.

ACKNOWLEDGEMENTS

The authors gratefully acknowledge the University of Michigan and the Horace J. Rackham School of Graduate Studies for the start-up funding that allowed the initiation of this work. The authors would like to thank Mr. Benjamin Reedlunn for his experimental assistance.

Proceedings of the SEM Annual Conference
June 7-10, 2010 Indianapolis, Indiana USA

Sources of systematic errors in the determination of heterogeneous strain fields obtained via DIC

P. Lava[1], S. Cooreman[1], S. Coppieters[1] and D. Debruyne[1,2]

[1]Catholic University College Ghent , Association K.U. Leuven
Department of Mechanical Engineering, Gebroeders Desmetstraat 1, B-9000 Gent
pascal.lava@kahosl.be

[2]Department MTM, Katholieke Universiteit Leuven,
Kasteelpark Arenberg 44, B-3001 Leuven (Heverlee)

ABSTRACT

The determination of strain fields based on displacement fields obtained via DIC is subjected to several errors that originate from various sources. In this contribution, we focus on a triplet of these when substantial plastic deformation of the specimen is probed. First, attention is paid to errors that can be directly attributed to the derivation of the strain fields, e.g. the strain-window size and the strain-window interpolation order. Next, we focus on errors that arise from different implementations of the DIC technique. In particular, we investigate the influence of the shape function, the interpolation order and the subset size on the derived strains. A dynamic shape function criterion is developed that increases the transformation order according to the degree of heterogeneity. It is shown that the impact of the subset size on the derived strains persists, despite the fact that it is embodied in the noise of the displacement fields and should largely evaporate during the smoothing procedure. Finally, we study the impact of a non-perpendicular alignment of the camera on a planar specimen. To this purpose, we make a mutual comparison of 2D results obtained via a perpendicular and a non-perpendicular CCD, and a 3D evaluation of the stereo setup. In addition, we estimate the impact of a rectification of the images obtained via the non-perpendicular alignment.

1 Introduction

Optical full-field measurement methods such as Digital Image Correlation (DIC) are currently extensively applied to study the deformation characteristics of a wide range of materials [1, 2, 3]. Started back in the early eighties, DIC yields displacement fields with subpixel accuracy. Traditionally, these are obtained via the so-called subset-based method as described in [4, 5, 6]. These displacement fields contain all the information needed to calculate the normal strain and shear components. Obviously, an excellent control on the accuracy and precision of the obtained DIC results is a clear prerequisite before one can embark on e.g. the identification of material parameters via inverse methodology.

In the past, extensive studies have been dedicated to the validation of DIC displacement fields. Few attention, however, has been paid on the determination of the specific accuracy and precision of the derived strains. In this contribution, we focus on realistic situations with large heterogeneous deformation regions and the impact of the DIC implementations on the derived strains. We compute sub-pixel displacement fields via our inhouse software platforms ”MatchID” [7]. Next, we smooth the obtained displacements via a so-called strain-window method [8]. Indeed, it has been shown that a preliminary smoothing of the estimated displacement fields yields strain derivations with increased accuracy [9, 10, 11, 12].

In order to validate our strain predictions, a similar procedure is adopted as outlined in Refs.[7, 8], focussing on a realistic uni-axial tensile test on a perforated tensile specimen, which results in substantial plastic deformation. A reference image is numerically deformed by imposing finite element (FE) displacement fields corresponding to various load steps. These are obtained by the commercial software package $Abaqus$[13]. Accordingly, we can

T. Proulx (ed.), *Application of Imaging Techniques to Mechanics of Materials and Structures, Volume 4*, Conference Proceedings of the Society for Experimental Mechanics Series 14, DOI 10.1007/978-1-4419-9796-8_35, © The Society for Experimental Mechanics, Inc. 2013

validate our strain predictions by comparing them to the well-known strain fields at the Gauss points. In particular, we investigate the influence of the subset shape function, the interpolation order and the subset size. The impact of these should be minor due to the smoothing procedure applied on the displacement fields. Next, we pay attention to errors that can be directly attributed to the derivation of the strain fields, e.g. the strain-window size and interpolation order. Finally, we study the impact of a non-perpendicular alignment of the camera in a 2D-DIC setup on the derived strain fields. To this purpose, the numerically deformed images corresponding to large plastic strains are numerically rotated for various Euler yaw and pitch angles. Accordingly, we can make a mutual comparison of strain fields obtained in a simulated perpendicular, non-perpendicular and stereo setup on a planar specimen at high plastic deformation. The stereo results are computed with our recently developed inhouse software platform "MatchID 3D" and were validated by commercial software packages.

The outline of this article is as follows. In Sec. 2 we present the formalism for strain derivations. Our results are included in Sec. 3. We conclude in Sec. 4.

2 Formalism

The DIC sub-pixel displacement fields contain all the information needed to calculate the in-plane normal strain and shear components ϵ_{xx}, ϵ_{yy} and ϵ_{xy}. This calculation involves the determination of the so-called deformation gradient matrix $\mathbf{F}$, describing the relative spatial position of two neighbouring particles after deformation in terms of their relative material position before deformation:

$$\mathbf{F} = \frac{\partial \mathbf{x}}{\partial \mathbf{x_0}} = \mathbf{I} + \frac{\partial \mathbf{u}}{\partial \mathbf{x_0}} \, , \tag{1}$$

where $\mathbf{x_0}$ $(\mathbf{x})$ refers to the initial undeformed (current deformed) Cartesian coordinates and $\mathbf{u} = \mathbf{x} - \mathbf{x_0}$ is the displacement vector. Expressing the deformation gradient matrix in terms of the horizontal (x-direction) and vertical (y-direction) displacement components u and v yields

$$\mathbf{F} = \begin{bmatrix} 1 + \frac{\partial u}{\partial x} & \frac{\partial u}{\partial y} \\ \frac{\partial v}{\partial x} & 1 + \frac{\partial v}{\partial y} \end{bmatrix} . \tag{2}$$

The determination of the strain tensor in e.g. the logarithmic Euler-Almansi convention $\epsilon^{\ln EA}$ is now straightforward:

$$\epsilon^{\ln EA} = \ln(\mathbf{V}) = \ln(\sqrt{\mathbf{F}\mathbf{F}^{\mathbf{T}}}) \, , \tag{3}$$

with $\mathbf{V}$ the so-called left stretch tensor obtained via the Cauchy theorem of polar decomposition.

The deformation gradient in Eq. (2) contains derivatives, which are approximated by differentials. These can be directly calculated using the Levenberg-Marquardt optimization routine in the DIC algorithm [7]. Further on it will be shown that substantial variations in the obtained results indicate that they cannot be directly used as reliable strain measurements. Alternatively, strains can be computed by a numerical differentiation of the DIC determined displacement fields. Since noice tends to get magnified by numerical differentiation, however, strains need to be calculated with some care. In general, in order to improve the strain calculation with increased accuracy, one first smooths the estimated displacement fields before starting the differentiation process. This has resulted in the development of a number of techniques, relying e.g. on finite element smoothing [9, 11]. In this work, we adopt a similar smoothing procedure as outlined in Refs.[10, 12] by finding an analytical expression of a surface, which, in a least squares sense, approximates the experimental displacement values in a selected region.

We first select a square "strain window" containing $N \times N$ discrete displacement data points in the vicinity of the point of interest (x_0, y_0). Then, we analytically approximate the displacements by making use of bilinear (Q4) or biquadratic (Q9) Lagrange polynomials that are commonly used as finite element shape functions:

$$\begin{aligned} u^{Q4}(x_0, y_0) &= a_u + b_u x_0 + c_u y_0 + d_u x_0 y_0 \\ v^{Q4}(x_0, y_0) &= a_v + b_v x_0 + c_v y_0 + d_v x_0 y_0 \, , \end{aligned} \tag{4}$$

and

$$\begin{aligned} u^{Q9}(x_0, y_0) &= u^{Q4}(x_0, y_0) + e_u x_0^2 + f_u y_0^2 + g_u x_0^2 y_0 + h_u x_0 y_0^2 + i_u x_0^2 y_0^2 \\ v^{Q9}(x_0, y_0) &= v^{Q4}(x_0, y_0) + e_v x_0^2 + f_v y_0^2 + g_v x_0^2 y_0 + h_v x_0 y_0^2 + i_v x_0^2 y_0^2 \, . \end{aligned} \tag{5}$$

The bilinear expressions allow the deformation of the square strain-window region into an irregular quadrangle, whereas the biquadratic transformation additionally accounts for quadratic deformations. The parameter sets $(a_u, ..., i_u)$ and $(a_v, ..., i_v)$ are determined by minimizing a least squares cost function

$$C = \sum_{i=1}^{P} (u_i - u_i^{DIC}) \, , \tag{6}$$

with P the number of data points inside the strain window and u_i (u_i^{DIC}) the fitted (DIC) displacement components at those datapoints. A Gauss-Newton algorithm is adopted to minimize Eq. (6).

Once the polynomial coefficients entering Eqs. (4,5) are determined, the (Q4) deformation gradient $\mathbf{F}$ of Eq. (2) can be easily derived as

$$\mathbf{F^{Q4}} = \begin{bmatrix} 1 + b_u + d_u y_0 & c_u + d_u x_0 \\ b_v + d_v y_0 & 1 + c_v + d_v x_0 \end{bmatrix} \tag{7}$$

A similar expression can be obtained for the biquadratic case.

It is important to remark that the pixel dimensions of this strain window also depend on the step size chosen in the correlation algorithm. Indeed, if e.g. a step size of 5 pixels is used an experimental displacement value is only available every 5 pixels in both horizontal and vertical direction. Accordingly, a $N \times N$ strain window results in a smoothing area with actual pixel width and height of $[(N-1) \times$ step size $] + 1$.

Finally, we note that close to the specimen boundaries or discontinuity areas, the strain window may contain less than N^2 data points. This data reduction is reasonable as long as the number of points well exceeds the number of unknown parameters entering Eqs.(4,5).

3 Results

Finite element theory, as adopted in the commercial software $Abaqus$ [13], allows us to simulate and analyse realistic plastic deformation in specimens of arbitrary shapes. We adopt a similar procedure as outlined in Refs. [7, 8], using numerically deformed images that were obtained by imposing finite element displacement fields on an undeformed image yielding plastic deformation of the specimen. In particular, we simulate an uni-axial tensile test on a perforated tensile specimen. This has a thickness of 1 mm in the simulation and a plastic hardening behaviour is assumed in accordance to tests on $SS304$ sheet metal: $\sigma_{eff} = 1533(0.033 + \epsilon_{eff})^{0.48}$. The FE calculation yields well-known displacement fields at the nodal points and strain values at the Gauss points of the finite elements. The average generated elements have a size of approximately 3×3 pixels. Next, the nodal displacements are used to numerically deform a random speckle pattern representing an undeformed state.

The strain values at the Gauss points allow us to estimate the errors of the strain results obtained by DIC calculations. To this purpose, we calculate the absolute mean value and the standard deviation σ of the measured differences $\Delta\epsilon = \epsilon_{imp} - \epsilon_{DIC}$ displayed in those figures at various values of maximum equivalent plastic strain. It is important to note that these quantities do not reflect the absolute accuracy of DIC with respect to strain derivations. Rather, they provide us with an indication of the impact of different implementations of the correlation and strain algorithms. Next, we remark that all the following results, except for the parameter under study, are obtained with the following standard settings: ASSD correlation coefficient, affine transformation, bicubic interpolation, a subset size of 13×13 and a step size of 3 for DIC and a strain window of 9×9 with bilinear polynomial order for the strain derivations. These previous DIC correlation settings were chosen since they turned out to be the optimum ones for displacement measurements for the particular speckle pattern under study [7].

In Fig. 1, the mean error and corresponding standard deviations are displayed for different dimensions of the strain window. The test reveals that a direct calculation of the strain fields using the displacement gradients obtained via the Levenberg-Marquardt algorithm in the correlation process yields questionable results. This indeed shows that they cannot be directly used as reliable strain measurements. Next, since variations up to 500 μstrain are noticed, it is crucial to make a conscious choice about the smoothing area pixel dimensions. A strain window of 5×5 data points appears to be the optimum choice when the complete specimen is considered. Since a step size of 3 was used, this corresponds to an actual smoothing area of 13×13. Lower restrictions are imposed since in the case of too small smoothing areas noise will substantially corrupt the derived strains. Larger strain windows, on the other hand, will induce a reasonable reduction of information since they are not able to describe large heterogeneous deformations when combined with lower order polynomials. For homogeneous deformations, however, one expects that a large strain window can still be approximated by a linear plane. To that purpose, distinction should be made

between regions of homogeneous and heterogeneous deformation. In Ref.[8] it is shown that the fact that accuracy and precision are inversely proportional to the strain-window size can be mainly attributed to the heterogeneous regions of the deformation process. Reducing its size, however, may reintroduce the noise originating from the displacement fields. Accordingly, the question arises if we can avoid this noise reintroduction by keeping the strain window substantially large and invoking higher order polynomials for the heterogeneous deformation description. To that purpose, in Fig. 2 we study the impact of the polynomial order on the mean error and standard deviation for a strain window with small and large dimensions. The accuracy and precision are much higher when a biquadratic polynomial is applied to the largest strain window. Indeed, the normal strain components receive a better description up to 500 and 2000 μstrain, respectively. The impact on the small strain window results, however, is minor.

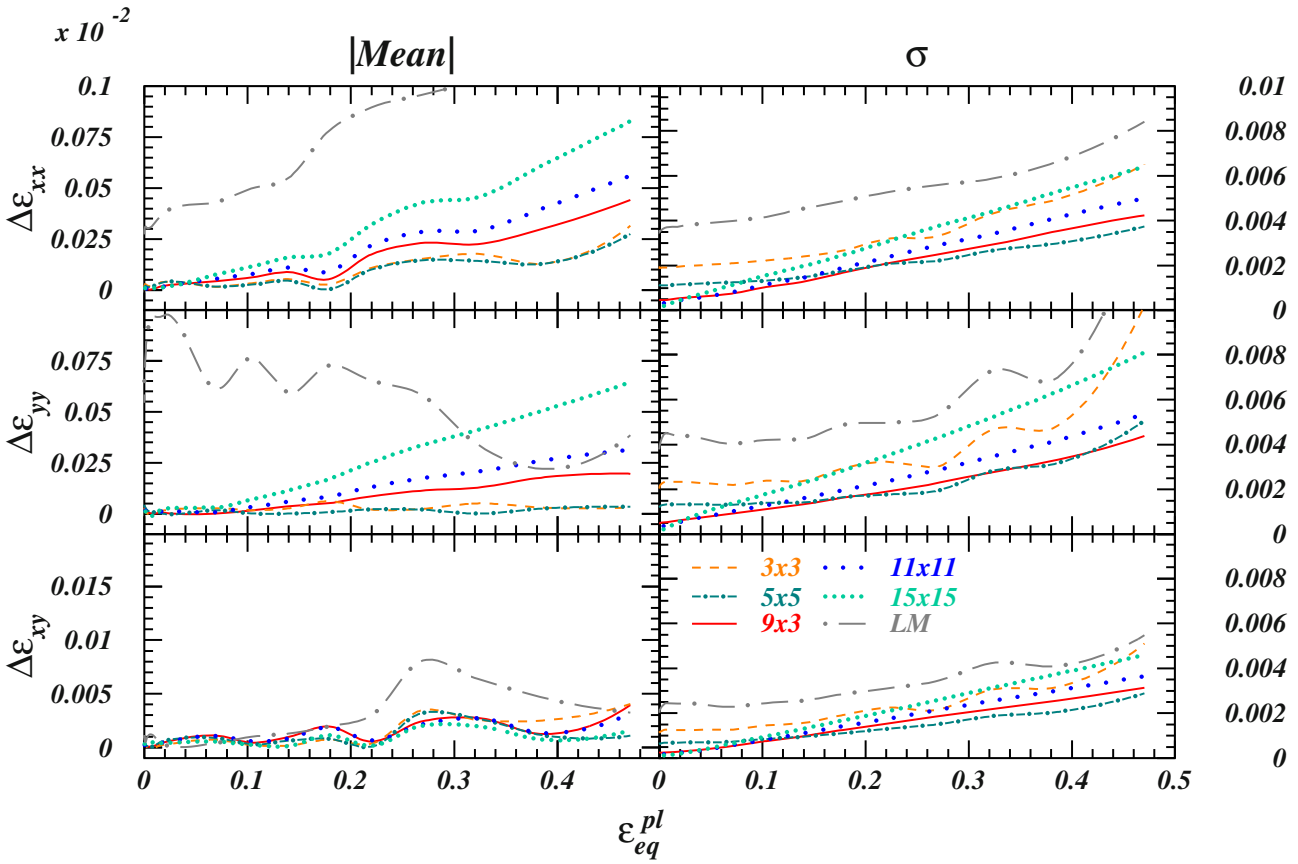

Figure 1: Impact of the strain-window size on the mean systematic errors (left panels) and standard deviations (right panels) for the in-plane strain components of the uni-axial tensile test with a central hole as a function of the maximum ϵ_{eq}^{pl}. The solid, dashed, dot-dashed, long-dotted and dotted lines represent a strain window of 9×9, 3×3, 5×5, 11×11 and 15×15 data points respectively. The long-dot dashed line shows the results of a direct calculation of the strain fields using the displacement gradients obtained via the Levenberg-Marquardt algorithm in the correlation process.

Next, we investigate the influence on the strain components of three quantities that are crucial in the determination of the displacement fields [7]: the order of the subset shape function, the interpolation order and the subset size. Their impact on the mean errors and standard derivations is displayed in Figs. 3,4 and 5, respectively we display the impact of the subset shape function on the mean errors and standard deviations. In Ref. [7] it was concluded that homogeneous displacement fields are better described with an affine subset shape function, whereas a quadratic transformation yields the highest accuracy for the heterogeneous regions. To that purpose, we developed a "dynamic" transformation that switches between affine and quadratic according to the degree of deformation. Since these DIC factors are all embodied in the noise of the displacement fields one expects their impact to evaporate to a large extent by the smoothing procedure. As can be inferred, this is indeed the case for the subset shape function

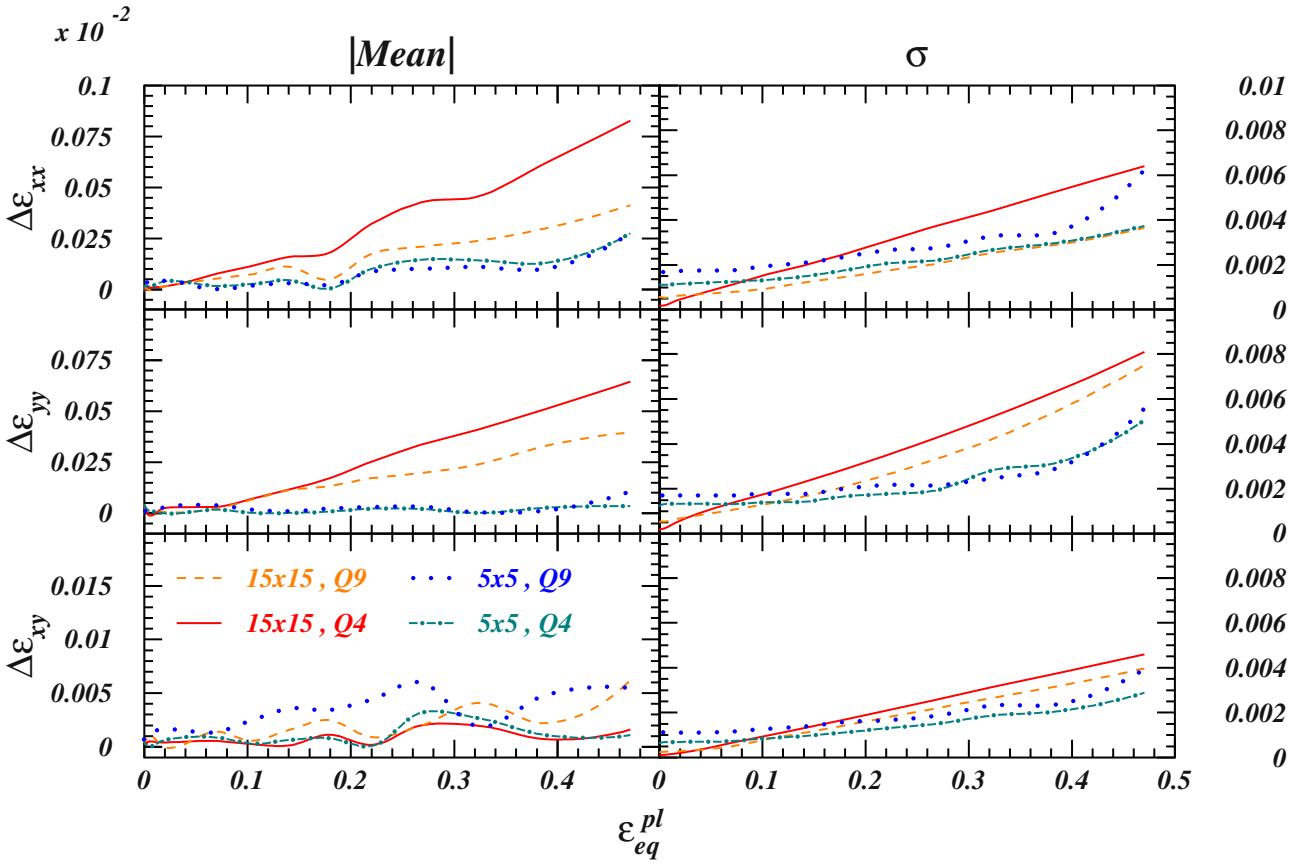

Figure 2: Mean systematic errors (left panels) and standard deviation (right panels) on the in-plane strain components as a function of the maximum ϵ_{eq}^{pl}. The solid lines represent the results of a strain window of 15×15 with bilinear polynomial order, whereas the dashed lines correspond to a quadratic fitting procedure. The dotted and dot-dashed lines correspond to a strain window of 5×5 with bilinear and quadratic polynomial order respectively.

and the interpolation order. The impact of the subset size, however, remains substantial, yielding variations up to 300 μstrain. Accordingly, it is very important to be cautious about the subset size. The conclusions are identical as the ones established for the displacement fields in Ref.[7]: a lower limit for the subset size is governed by the granularity of the speckle pattern, whereas too large subsets are no longer able to describe large heterogeneous deformations.

Finally, we study the impact of a non-perpendicular alignment of the camera in a 2D-DIC setup on the derived strain fields. The effect of out-of-plane motion on 2D correlation measurements was the subject of investigation in Refs. [14, 15]. The focus, however, was on rigid body displacements. In addition, an experimental setup was adopted to estimate errors related to a non-parallel alignment of the image plane and the specimen. In this contribution, we study this impact in the case of large heterogeneous deformation on a purely numerical basis. We emphasize, however, that a planar specimen is considered with no out-of-plane deformations, since the probed strains are well below necking. The procedure is as follows. First, the reference and numerically deformed images corresponding to large plastic strains are numerically rotated for various Euler yaw and pitch angles as displayed in Fig. 6. As such, we can make a mutual comparison of strain fields obtained in a (simulated) 2D DIC setup corresponding to cameras with an optical axis perpendicular and non-perpendicular to the specimen plane. In order to study the impact of a 3D stereo setup on the specimen, we consider the original and rotated images as taken by camera 1 and 2, respectively. A stereo setup, however, urges the input of intrinsic and extrinsic camera parameters. To this purpose, an identical rotation procedure is adopted to a calibration pattern. Next, the fictive camera parameters are estimated in a bundle-adjustment calibration procedure, with the Euler angles fixed to the imposed values. The object distance for all forthcoming results corresponds to $Z \approx 612mm$. For clarity, in Fig. 7

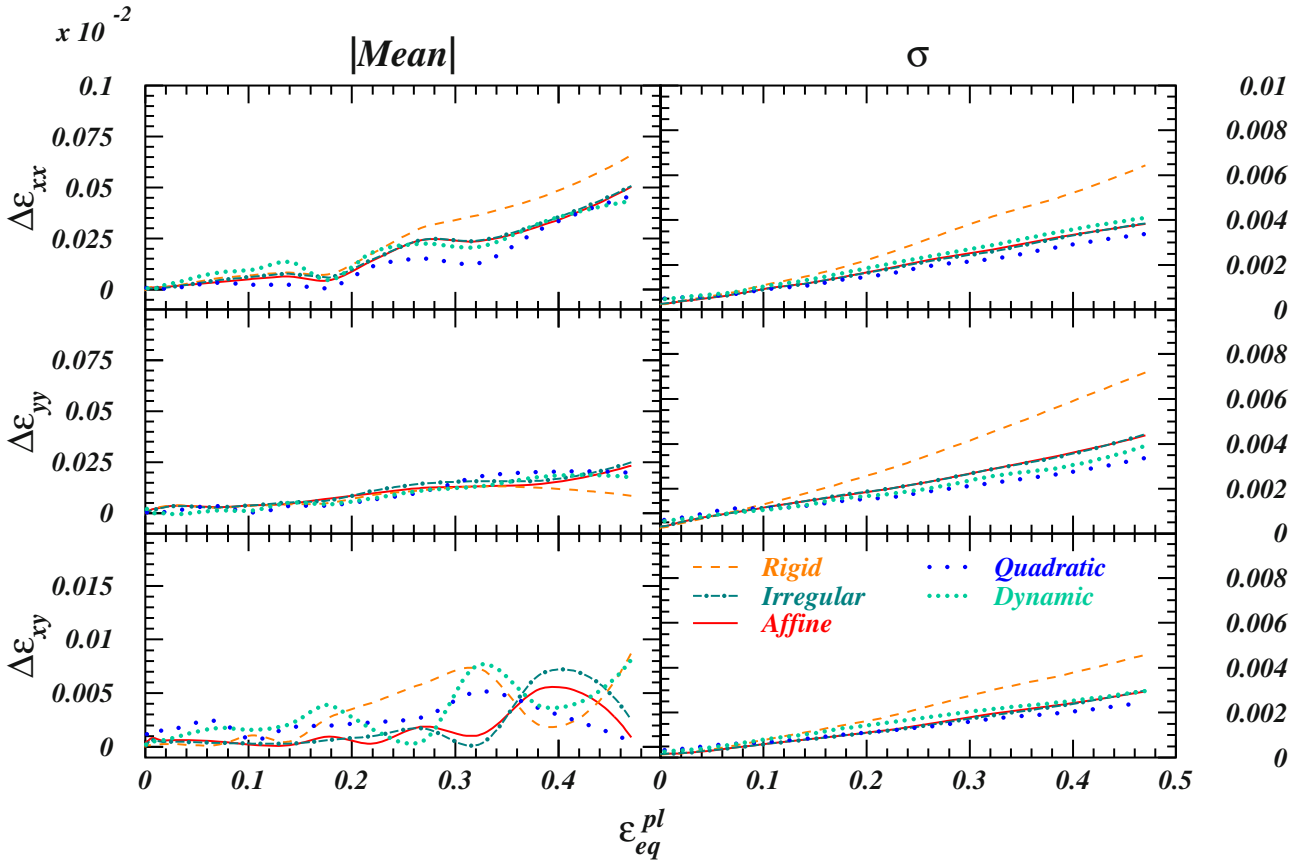

Figure 3: Influence of the order of the subset shape function on the mean systematic errors (left panels) and standard deviations (right panels) for the in-plane strain components of the uni-axial tensile test with a central hole as a function of the maximum ϵ_{eq}^{pl}. The dashed, solid, dot-dashed and long-dotted lines represent the results of rigid,affine, irregular and quadratic transformations respectively. The dotted lines correspond to the calculations adopting a subset shape function with dynamic order.

the strain components are displayed at an equivalent plastic strain of $\epsilon_{eq}^{pl} = 0.3$. The out-of-plane and stereo results correspond to an Euler pitch angle of $30°$.

In Fig. 8 the mean error and corresponding standard deviations are displayed for various Euler pitch angles at an equivalent plastic strain of $\epsilon_{eq}^{pl} = 0.3$. Similar conclusions can be drawn for various Euler yaw angles. As can be inferred, the errors related to a 2D DIC non-perpendicular setup gain in importance when larger Euler pitch angles are probed. The stereo setup accuracy is better, except for ϵ_{yy}. The improvements are small, however, due to the complexity of a regular stereo DIC algorithm. Indeed, this latter involves three 2D DIC correlation runs and a precise determination of the camera parameters. Finally, we rectify the strain fields obtained via the non-perpendicular setup with the obtained camera parameters. It is clear that this induces a major improvement in both precision and accuracy. Work on this is in progress [16].

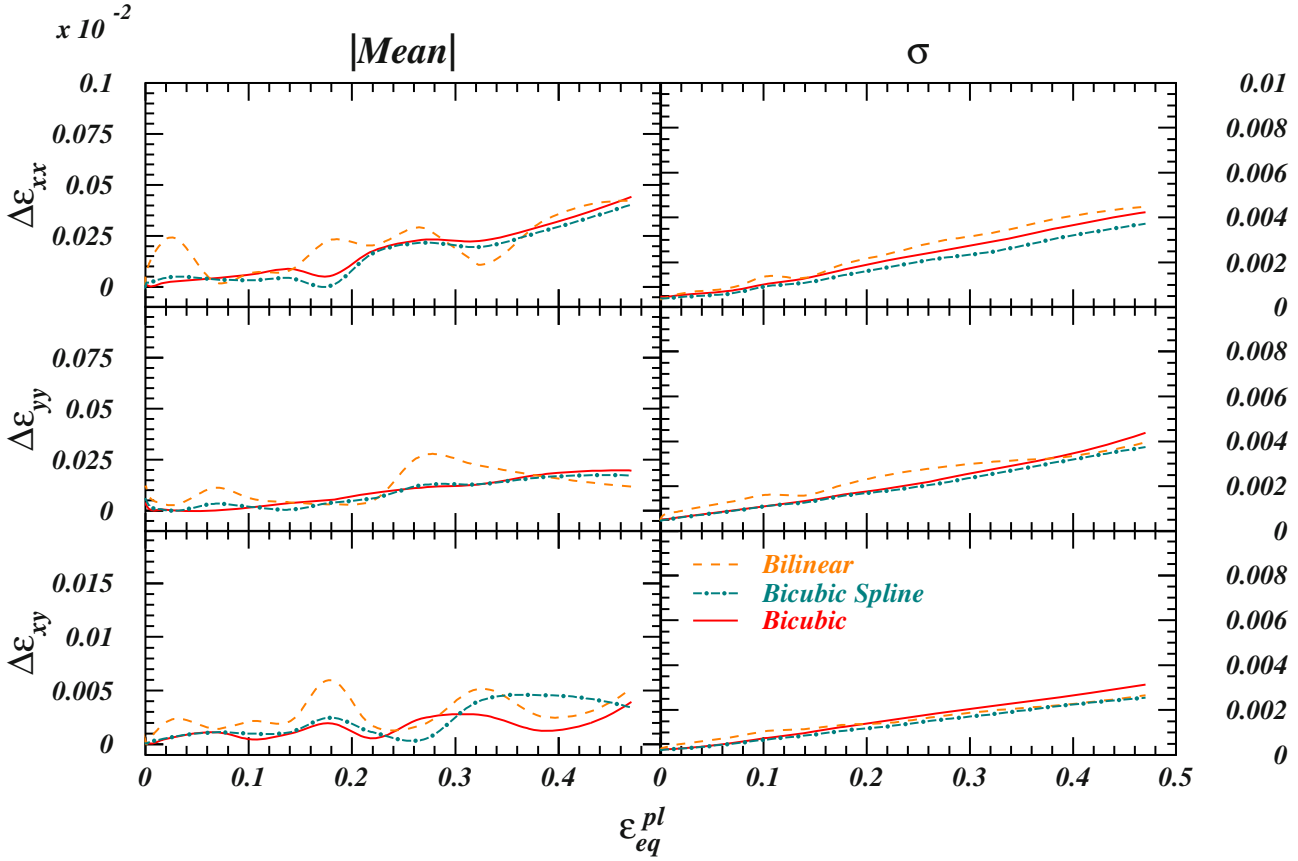

Figure 4: Influence of the interpolation order on the mean systematic errors (left panels) and standard deviations (right panels) as a function of the maximum ϵ_{eq}^{pl}. The solid, dashed and dot-dashed lines correspond to a bicubic, bilinear and bicubic spline interpolation sheme respectively.

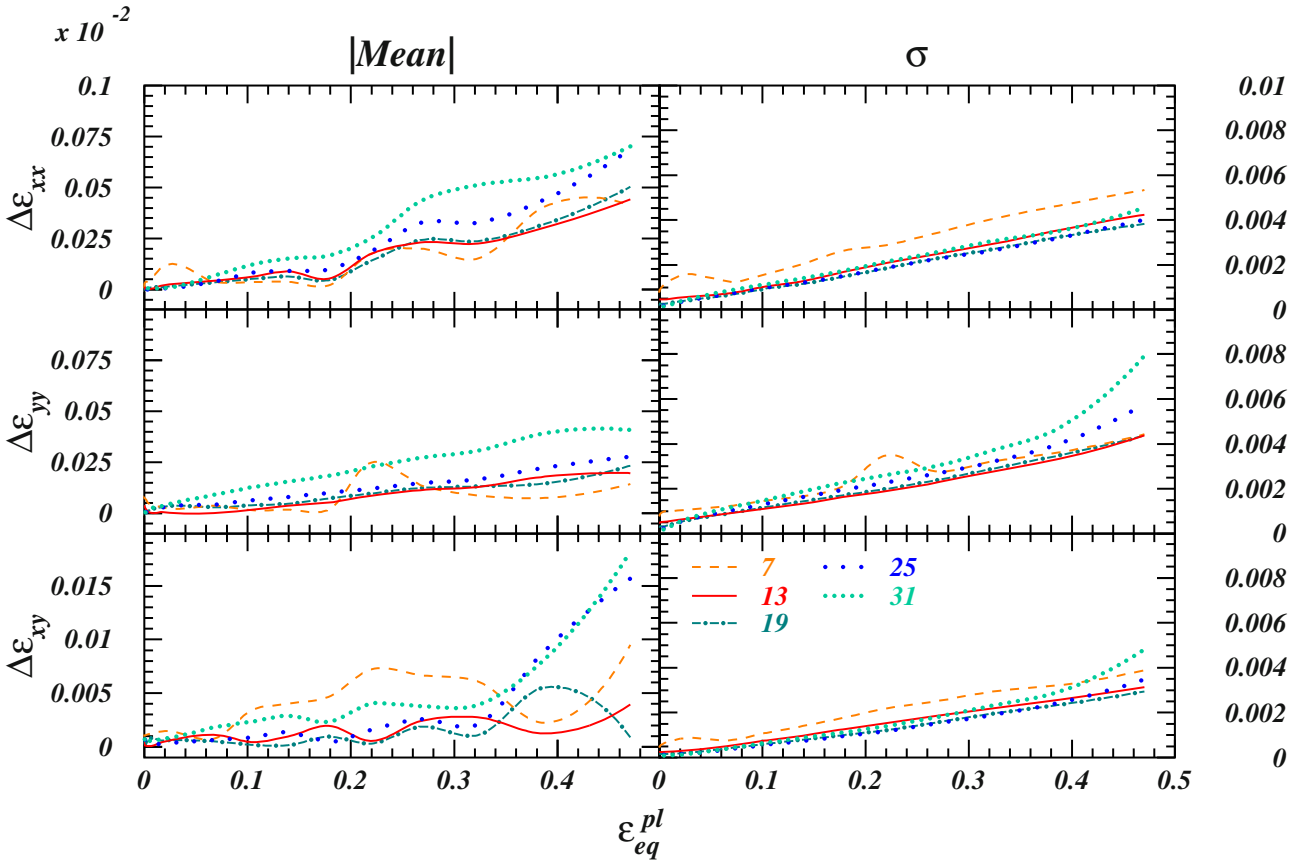

Figure 5: Impact of the subset size on the mean systematic errors (left panels) and standard deviations (right panels) for the in-plane strain components of the uni-axial tensile test with a central hole as a function of the maximum ϵ_{eq}^{pl}. The solid, dashed, dot-dashed, long-dotted and dotted lines represent a subset size of 13×13, 7×7, 19×19, 25×25 and 31×31 pixels respectively.

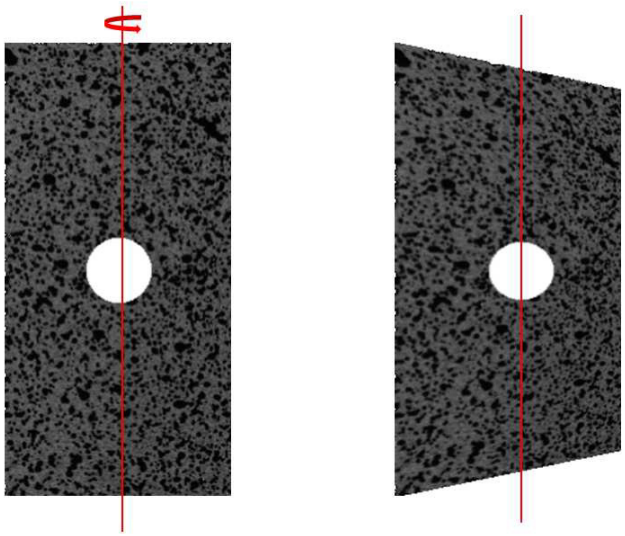

Figure 6: Rotation of the reference speckle pattern corresponding to an Euler pitch angle of 30°.

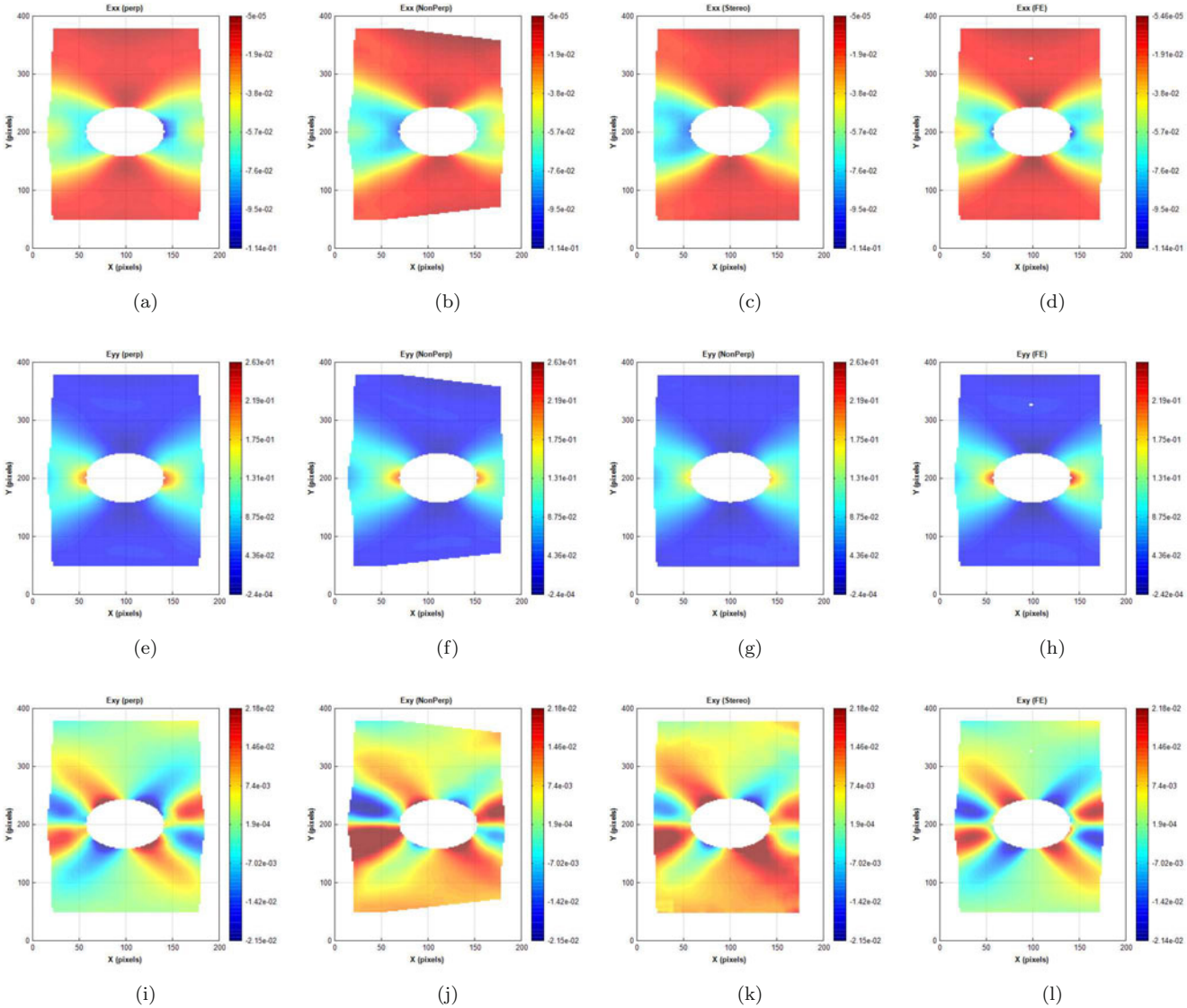

Figure 7: Plots of the in-plane strain components for the uni-axial tensile test with a central hole at an equivalent plastic strain of $\epsilon_{eq}^{pl} = 0.3$. From left to right are displayed: 2D DIC perpendicular optical axis, 2D DIC out-of-plane corresponding to an Euler pitch angle of 30°, 3D DIC stereo setup and the FE imposed strain fields.

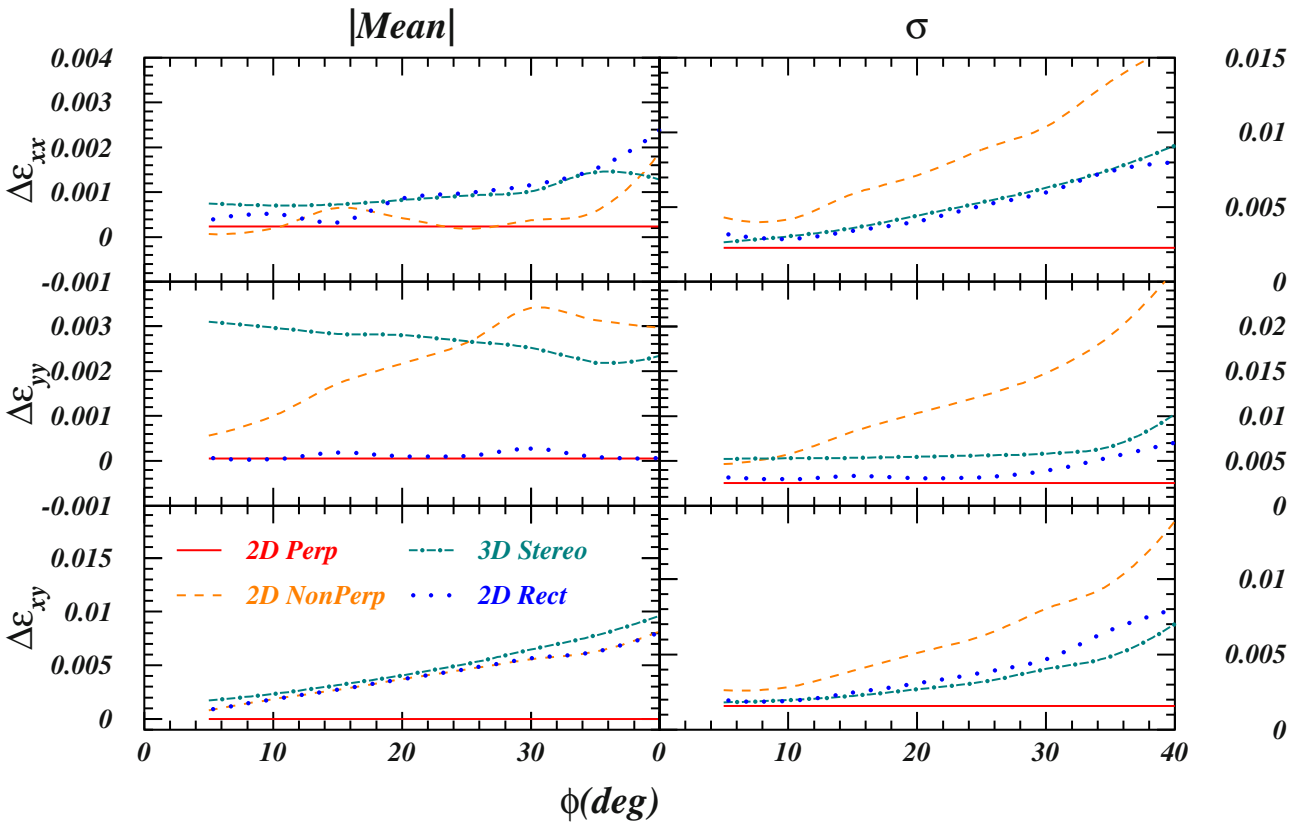

Figure 8: Impact of out-of-plane displacements on the mean error and corresponding standard deviations for various Euler pitch angles at an equivalent plastic strain of $\epsilon_{eq}^{pl} = 0.3$. The solid, dashed, dot-dashed and dotted lines correspond to a 2D perpendicular setup, a 2D non-perpendicular setup, a 3D stereo setup and a 2D non-perpendicular rectified setup, respectively

4 Conclusions

In this contribution, we have estimated systematic errors that arise in the calculation of strain fields based on displacement fields obtained by DIC. In particular, attention is paid to the measurement of large plastic deformation fields in heterogeneous specimens. To this purpose, we numerically deformed a speckle pattern according to displacement fields resulting from finite element simulations of an uni-axial tensile test on a perforated tensile specimen. A comparison of the imposed strain fields at the Gauss points to the calculated DIC strain fields allows us to estimate the systematic errors. In particular, we investigate the influence of the shape function, the interpolation order and the subset size on the derived strains. In addition, we pay attention to errors that can be directly attributed to the derivation of the strain fields, e.g. the strain window size and the strain window interpolation order. It is shown that the impact of the subset size on the derived strains persists, despite the fact that it is embodied in the noise of the displacement fields and should largely evaporate during the smoothing procedure.

In addition, we study the impact of a non-perpendicular alignment of the camera on a planar specimen. To this purpose, a mutual comparison is made of 2D results obtained via a perpendicular and a non-perpendicular CCD, and a 3D evaluation of the stereo setup.

References

[1] Cooreman S, Lecompte D, Sol H, Vantomme J, Debruyne D, Identification of the mechanical material behaviour through inverse modelling and DIC, Experimental Mechanics 48 (2008) 421-433.

[2] Lecompte D, Cooreman S, Coppieters S, Vantomme J, Sol H, Debruyne D, DIC-based plastic material identification: comparison between uni-axial and bi-axial tensile testing, European Journal of Computational Mechanics (2009) in press.

[3] Van Paepegem W, Shulev AA, Roussev IR, De Pauw S, Degrieck J, Sainov VC, Study of the deformation characteristics of window security film by digital image correlation techniques, Optics and Lasers in Engineering 47 (2009) 390-397.

[4] Sutton MA, Wolters WJ, Peters WH, Ranson WF, McNeill SR, Determination of displacements using an improved digital correlation method, Image and Vision Computing 1 (1983) 133-139.

[5] Chu TC, Ranson WF, Sutton MA, Applications of digital image correlation techniques to experimental mechanics, Experimental Mechanics 25 (1985) 232-244.

[6] Bruck HA, McNeill SR, Sutton MA, Peters WH, Digital image correlation using Newton-Raphson method of partial differential correction, Experimental Mechanics 29 (1989) 261-267.

[7] Lava P, Cooreman S, Coppieters S, De Strycker M, Debruyne D, Assessment of measuring errors in DIC using deformation fields generated by plastic FEA, Optics and Lasers in Engineering 47 (2009) 747-753.

[8] Lava P, Cooreman S, Debruyne D, Study of systematic errors in strain fields obtained via DIC using heterogeneous deformation generated by plastic FEA, Optics and Lasers in Engineering 48 (2010) 457-468.

[9] Sutton MA, Turner JL, Bruck HA, Chae TA, full-field representation of discretely sampled surface deformation for displacement and strain analysis, Experimental Mechanics 31 (1991) 168-177.

[10] Wattrisse B, Chrysochoos A, Muracciole J-M, Nemoz-Gaillard, Analysis of strain localization during tensile tests by digital image correlation, Experimental Mechanics 41 (2001) 29-39.

[11] Meng LB, Jin GC, Yao XF, Application of iteration and finite element smoothing technique for displacement and strain measurement of digital speckle correlation, Optics and Lasers in Engineering 45 (2007) 57-63.

[12] Pan B, Asundi A, Xie H, Gao J, Digital image correlation using iterative least squares and pointwise least squares for displacement field and strain field measurements, Optics and Lasers in Engineering 47 (2009) 865-874.

[13] Abaqus, Theory Manual, Version 6.7, 2007.

[14] Sutton MA, Yan JH, Tiwari V, Scheier HW, Orteu JJ, The effect of out-of-plane motion on 2D and 3D digital image correlation measurements, Optics and Lasers in Engineering 46 (2008) 746-757.

[15] Haddadi H, Belhabib S, Use of rigid-body motion for the investigation and estimation of the measurement errors related to digital image correlation technique, Optics and Lasers in Engineering 46 (2008) 185-196.

[16] Lava P, Debruyne D, in progress.

Proceedings of the SEM Annual Conference
June 7-10, 2010 Indianapolis, Indiana USA

Dynamic Response of Curved Beams Using 3D Digital Image Correlation

Adam K. Parks, Aerospace Structures Engineer, Structural Sciences Center, Air Vehicles Directorate, Air Force Research Laboratory, Wright-Patterson AFB, OH 45433
Email address: adam.parks.2@us.af.mil

Thomas G. Eason, Senior Aerospace Structures Engineer, Structural Sciences Center, Air Vehicles Directorate, Air Force Research Laboratory, Wright-Patterson AFB, OH 45433
Email address: thomas.eason@wpafb.af.mil

Jorge Abanto-Bueno, Assistant Professor, Department of Mechanical Engineering, Bradley University, 1501 West Bradley Ave., Peoria, IL, 61625
Email address: jabanto@bradley.edu

ABSTRACT

In this investigation the vibration response of a clamped-clamped steel curved beam is studied experimentally using the non-contact, full-field 3D digital image correlation (DIC) technique. The effect on the boundary conditions of the clamping torque as well as the procedure used to fasten the beam to the testing apparatus was clearly established from measurements of the three-dimensional displacement field. Swept sine tests were performed at 1 g of base excitation and over a frequency range of 20 – 500 Hz. Resonance was qualitatively identified at frequency ranges 75 – 85 Hz, 120 – 138 Hz and 240 – 265 Hz. Swept sine tests were carried out at a rate of 0.2 Hz/s over these three frequency ranges to measure the distribution of the out-of-plane displacement of the beam mid-plane over its entire length. 1024x1024-pixel images were taken at a rate of 2000 fps at frequency 76, 126 and 253 Hz and analyzed using 3D DIC. The results show three different bending modes at these frequencies.

INTRODUCTION

An integral understating of the vibration response of curved beams is of great importance to design more reliable structures in automotive and aerospace applications. Hence, a number of analytical and numerical studies have been performed in this subject. Yamaki and Mori [1] solved analytically the beam equation by combining the Galerkin and the harmonic balance method; and Yamaki et al. [2] experimentally using two non-contacting gap-sensors to measure the displacement of the beam a discrete locations. Significant discrepancies between both approaches were found. Abou-Rayan et al. [3] used a parametric approach to study the free and forced vibration of buckled beam. Afaneh and Ibrahim [4] studied the nonlinear response of a buckled beam subjected to sinusoidal excitation using the multiple scale method, numerical simulation and experiments. Strain gages were used to measure the deformation of the beam. Emam and Nayfeh [5] investigated the nonlinear response of a clamped-clamped buckled beam using the Galerkin procedure to discretize the governing integral-partial-differential equation and associated boundary conditions. With the development of powerful computers, researches have focused on using finite element methods (FEM) to study the nonlinear behavior of curved beams under complex boundary and loading conditions [6 – 8]. Unfortunately, little emphasis has been placed on validating these models through experimental work.

Recently, the Department of Defense has taken a renewed interest in hypersonic flight research. One of the main phases of this comprehensive research is to develop highly accurate simulation capabilities to predict the

T. Proulx (ed.), *Application of Imaging Techniques to Mechanics of Materials and Structures, Volume 4*, Conference Proceedings of the Society for Experimental Mechanics Series 14, DOI 10.1007/978-1-4419-9796-8_36, © The Society for Experimental Mechanics, Inc. 2013

response of aircraft structures subjected to extreme environments which comprise simultaneous mechanical, thermal and acoustic loading. Several projects have been dedicated to address these concerns [9 – 12] from the simulation point of view and develop simplified models to reduce demand of computational resources without losing accuracy. From the experimental mechanics point of view, this requires the use of a full-field technique to provide enough information (i.e., boundary conditions, displacement and strain distribution) about the response of the structure under investigation to generate an accurate FEM model (i.e., boundary conditions, displacement and strain distribution). The main goal of this investigation is to establish the non-contact, full-field 3D digital image correlation technique as a validation tool for simplified FEM models. Specifically, in this investigation this technique is used to measure the in- and out-of-plane displacement field of a shallowly curved, thin beam when excited at resonance. The groundwork laid in this paper will address and advance the knowledge concerning with the full-field mechanical response of these structures which will be used later to validate reduced-order models.

Digital Image Correlation

Digital Image Correlation (DIC) is a non-contact, optical technique that measures the full-field deformation displacement and displacement gradient distribution generated on the surface of body due to external loading. Initially, this technique was used to measure in-plane deformation fields. A classical 2D DIC set-up includes a source of uniform white light and a high-resolution computer-controlled camera to record in real-time, at a pre-defined frame rate, images of the in-plane deformation of the surface of the structure under investigation. Both the displacement and displacement gradient distributions are measured by correlating the position of a series of small but statistically distinctive regions between two images taken at different times during the deformation of the body. Typically one of the images represents the undeformed state of the body. In addition, the surface of the body must exhibit a natural or artificially-created stochastic speckled pattern to accurately measure the evolution of the deformation fields. When the surface out-of-plane displacement field is also needed to fully understand the mechanical behavior of the structure, both experimental set-up and software must be modified to also measure this displacement component using the digital image correlation technique (3D DIC). In this case, two cameras record the deformation of the surface of interest from two different directions. Unlike 2D DIC systems, 3D DIC systems require calibration of the cameras to generate a complete model of the system by defining both its intrinsic parameters (i.e., focal length of the lenses, principle point of the lenses, radial and tangential distortions of the lenses) and extrinsic parameters (i.e., translation vector and rotation matrix). The overall performance of the 3D DIC system strongly depends on the accuracy of the camera calibration. Details of the theoretical foundation of this technique can be found in the literature [13 – 15]

EXPERIMENTAL

Test Article

The test article is a thin curved beam with uniform rectangular cross-section made out of AISI steel 1008. The curvature of the beam was formed by cold working. Two 7.376mm-diameter holes, 19.050mm apart, were drilled at each end of the beam to allow fastening the beam to a C-shape clamping fixture. Table 1 shows the geometric properties of the testing article. Prior to the experiments, a random speckled pattern was carefully generated on the surface of the beam to measure the in- and out-of-plane displacement field. Opaque white and flat black water-based paint was used for this purpose. The mass of the beam before and after applying the random pattern was measured to be 21.34 g and 21.40 g, respectively, resulting in a mass increase of 0.28% which was deemed to be negligible in effecting the mechanical response of the test article.

Table 1. Curved Beam Geometric and Physical Properties

Property	Measured/Calculated Value
Length, *L* (mm)	381.30
Width, *b* (mm)	12.70
Depth, *d* (mm)	0.50
Radius of Curvature, *R* (mm)	3048

Cross-sectional Area, A (mm^2)	6.35
Area moment of Inertia, I (mm^4)	0.1324
Radius of gyration, r (mm)	0.1443
Curvature-to-depth ratio, R/d	6096
Centroidal Axis Eccentricity, e (μm)	6.841
Young's modulus, E (GPa)	200
Density, ρ (kg/m^3)	7850
$\sqrt{\frac{EI}{\rho AL^4}}$ (rad/s)	0.1585

Experimental Apparatus

Fig. 1(a) shows a picture of the experimental set-up. It consists of the test article that is fastened to a C-shape clamping fixture which is, in turn, fixed to the base excitation source. A 3D DIC system completes the experimental set-up. A close-up of the clamping fixture and the test article is shown in Fig. 1(b). The clamping fixture is the most critical component of the testing apparatus. Its main function is to avoid axial beam slippage providing realistic fixed boundary conditions and thus enabling meaningful comparison between experimental data and analytical/numerical models. Researchers have developed different designs for the clamping fixture whose details can be found in [1, 16, and 17]. In this investigation, the clamping fixture developed in [1] to test straight beams was modified by adding two complementing wedged plates, whose mating surfaces were machined to have the same curvature as the beam as shown in Fig. 1(c). The material used to fabricate the whole fixture is black anodized AISI steel 1018 providing enough mass to minimize feedback to shaker without limiting the excitation capabilities of the shaker. The ends of the beam were firmly fixed between the plates by two 6.35mm diameter steel bolts. Uniform base excitation was provided using an MB Dynamics electromechanical shaker (model C10E) with a maximum output force of about 5337 N and maximum acceleration of 68 g's over the frequency range 5 – 3000 Hz. The shaker was controlled using Puma, a Spectral Dynamics software package, through a MB Dynamics M-Series power amplifier. A PCB Piezotronics accelerometer (model 353C22) was attached to the shaker head and used as the feedback sensor to the controller. The sensitivity of the accelerometer is 9.509 mV/g. Signal from the accelerometer was also recorded by an independent data acquisition system (HP 3566A). The 3D DIC system includes two Photron, high speed 12-bit CMOS cameras (model Fastcam SA3 120K). Each camera has an onboard 4GB memory that allows recording a total of 2726, 1024x1024 full pixel resolution images at 2000 fps (1.36 s). The cameras were placed on a tripod and fixed approximately 676mm away from the closest point on the test fixture. The cameras were angled at 14.2° with respect to the normal vector of the center of the beam so that the whole surface of the beam was visible to both cameras simultaneously. The cameras were also focused to 0.5m with an aperture of 22mm on 28mm Nikon lenses. At this set-up, each pixel captured by the camera corresponded to a square with an approximate area of 0.09 mm^2. The cameras and the data acquisition system were simultaneously started using a TTL trigger. In order to minimize the heat generated by halogen lamps typically used in DIC system, two Banner white, high-intensity LED area lights (24 VDC) were used instead.

3D DIC Calibration

In this investigation digital image correlation was performed using ARAMIS, a commercial 3D DIC software develop by Trilion Quality Systems. As mentioned previously, a 3D DIC system must undergo a calibration process to fully define the system parameters. These parameters are then used to perform the displacement and strain measurements. ARAMIS uses a calibration plate that has an array of white dots on a black background. The selection of the calibration plate depends on both the position of the cameras with respect to the testing and the lenses used. A series of pictures are captured by each camera at 13 different orientations of the calibration plate with respect to the cameras. The calibration defines the position of the cameras relative to one another and determines a "measuring volume" that permits accurate measurements when the specimen deforms inside this volume. The measuring volume for this study was 315mm x 325mm x 325mm with a deviation of 0.015 pixels.

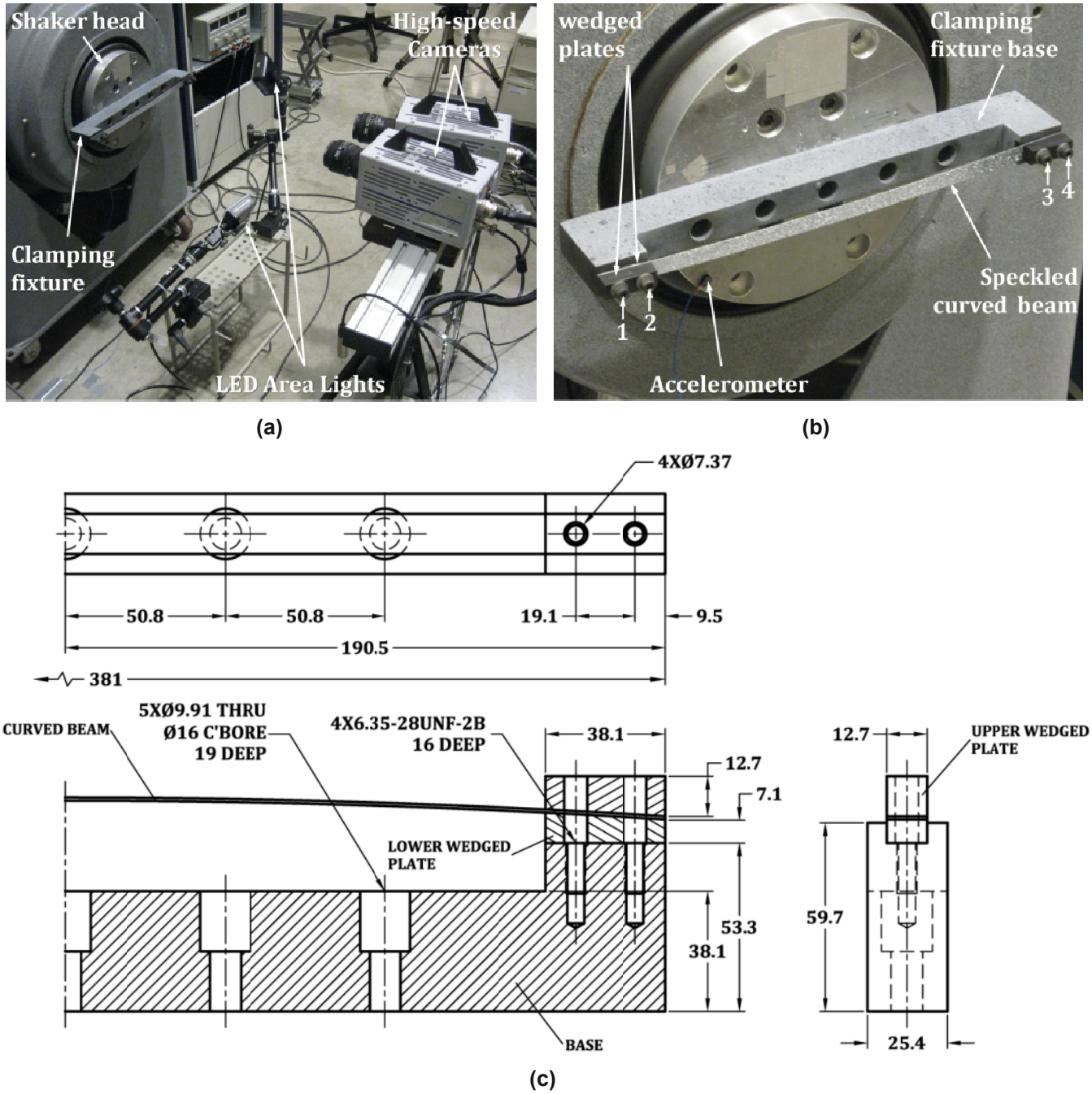

Figure 1: (a) Experimental set-up, **(b)** close-up of the clamping fixture, and **(c)** dimensioned assembly views of the clamping fixture (units: mm)

RESULTS AND DISCUSSION

Boundary Conditions

The vibration response of a body will depend on the state of the structure prior to applying any external loading (i.e., the boundary conditions). Therefore knowledge of the actual boundary conditions is crucial when developing a FEM model to simulate the response of the structure. The clamping fixture used in this investigation was designed to have both ends of the beam fixed while minimizing axial slipping during the experiment. However, preliminary measurements of the out-of-plane displacement at the midpoint of the curved beam using a Polytec

laser vibrometer (model PSV-400) resulted in inconsistent values for the same external loading. These findings led us to believe that the approach used to fasten the beam to the clamping fixture caused these anomalies. Two variables needed to be considered: the clamping torque and the sequence order followed to tighten the four bolts. A series of experiments were carried out to determine the effect of these two variables. Four sequences, 2-3-1-4, 1-4-2-3, 2-4-1-3, and 1-3-2-4 (the assigned number to each bolt is shown in Fig. 1(b), were used to tighten the bolts. Torques of 6.8, 7.9 and 9.0 N-m was used to tighten the beam at each sequence (7.9 N-m is the recommended clamping torque). Before applying these torques, the bolts were tightened by hand following the corresponding sequence. The displacement field over the whole surface of the beam was measured using ARAMIS 3D DIC. The hand-tight state was used as the reference state in the DIC measurements (i.e., undeformed state). Fig. 2 shows the three components of the measured displacement over the whole of the length beam at three positions along its width for the four tightening sequences under consideration (clamping torque: 7.9 N-m). Figs. 2(a) and (b) show typical images captured with the left and right cameras, respectively. The coordinate system used in the DIC measurements (X and Y axis defines the surface of the beam) and the three Sections used to create the plots in Figs. 2(c) – (f). Section 1 is at the mid-plane of the beam and Sections 0 and 2 are about 3.5mm above and below this plane, respectively. From these plots, it is clear that the manner how the beam is clamped will create initial displacements that will change the curvature of the beam and need to be considered when using in subsequent numerical simulations. There were not observed any significant differences in the displacement when the beam was either under- or over-clamped.

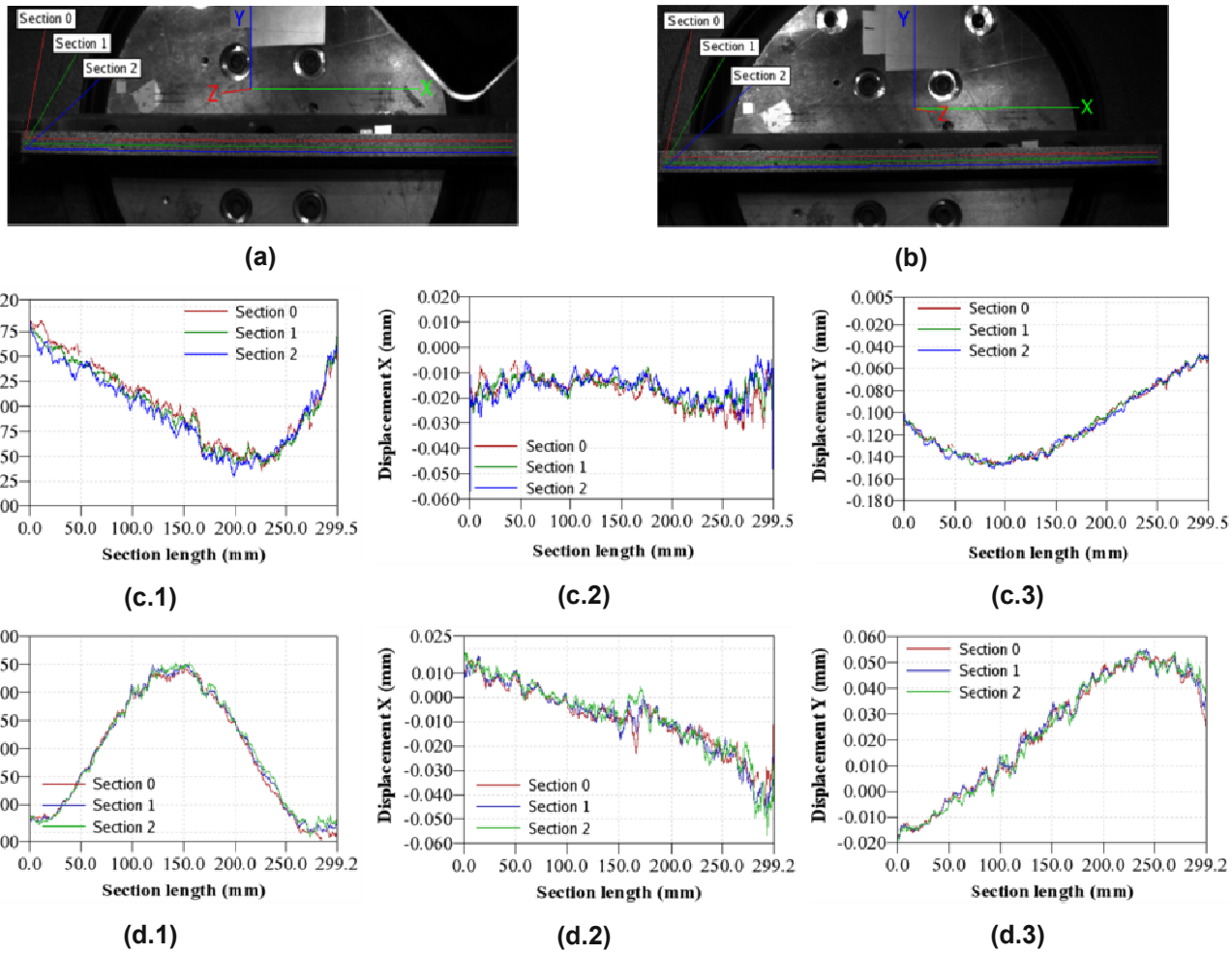

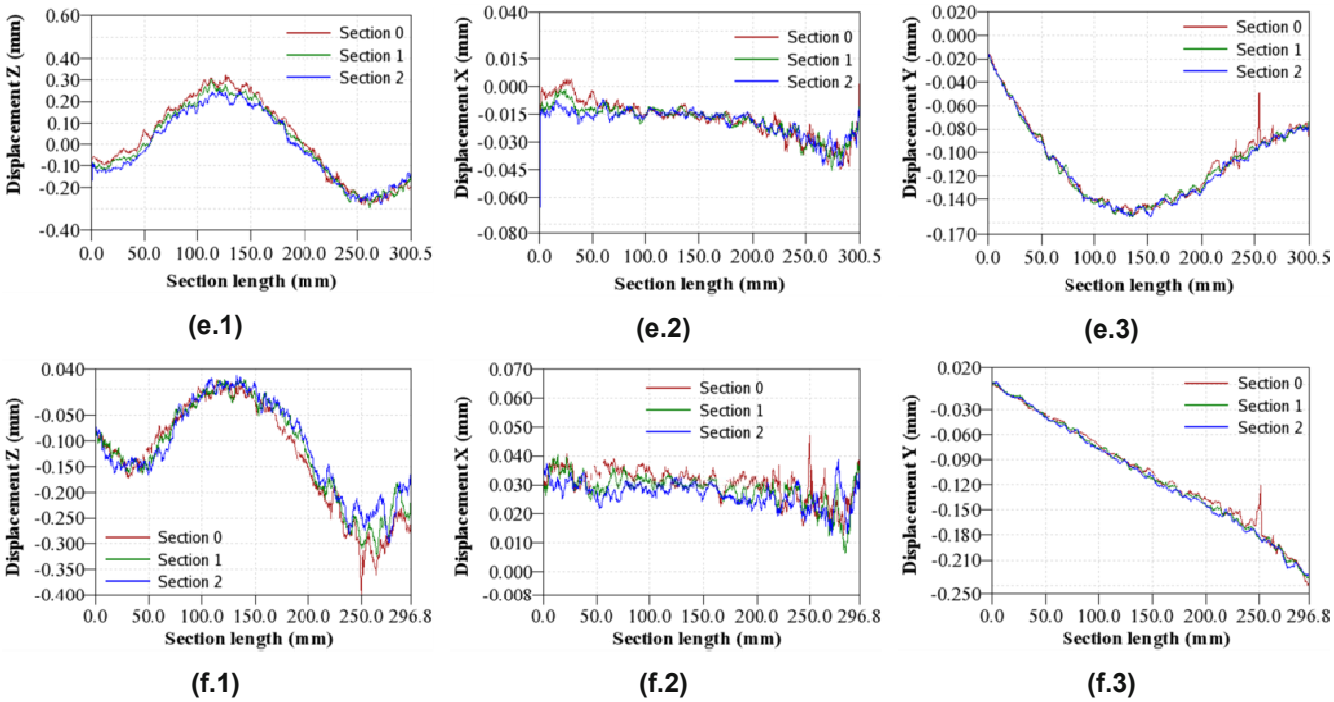

Figure 2: Measured initial displacement due clamping sequences (clamping torque: 7.9 N-m, 3D DIC facet size: 15x15 pixels): **(a)** and **(b)** pictures of the whole beam capture by the camera positioned on the left and right, respectively, **(c.#)** clamping sequence 2-3-1-4, **(d.#)** clamping sequence 1-4-2-3, **(e.#)** clamping sequence 2-4-1-3, and **(f.#)** clamping sequence 1-3-2-4 (**#**=1,2,3 identifies the displacement along the Z, X and Y direction, respectively.)

Out-of-Plane Displacement at Resonance

As mentioned previously, the two CMOS cameras used in this investigation are capable of recording only 1.36 s at a time at 2000 fps (full resolution). Since the frequency range of interest in this investigation was 20 – 500 Hz, it was not possible to carry out a single experiment to cover the whole range. In consequence a swept sine test was carried out over the frequency range at a sweep rate of 20 Hz/s to locate the resonance frequencies of the curved beam. The base excitation in this experiment was 1 g. It was qualitatively determined that the beam resonates at three well defined ranges: 75 – 85 Hz, 120 – 138 Hz, and 240 – 265 Hz. Swept sine tests were repeated over each of three ranges to identify the bending modes of the beam. The sweep rate used in these experiments was 0.2 Hz/s. Full-resolution images of the whole beam were captured at 2000 fps at frequency 76, 126 and 253 Hz. An additional experiment was carried out to record images at 26 Hz (a non-resonant state). All these images were analyzed using ARAMIS 3D DIC. The measured out-of-plane displacement of the mid-plane of the beam (Section 1 in Figs. 2(a) and (b)) over its entire length is shown Figs. 3(a) – 3(d), which corresponds to frequency 26, 76, 126 and 253 Hz, respectively. Very distinct responses can be observed at each frequency. At the non-resonant state (i.e., 26 Hz, Fig. 3(a)), the beam moves at unison with the head of the shaker (rigid body motion). At 76 Hz, only about ¾ of the beam oscillates (left side in Fig. 3(b)) and mostly towards the concave side of the beam. At 126 Hz (Fig. 3.(c)), a central region of about 150mm exhibit large out-of-plane displacement towards the convex side of the beam, while both ends of the beam move in the opposite direction. The central region undergoes larger displacements. On the other hand, at 253 Hz (Fig. 3(d)), the central has been shortened to about 50mm and the extremes of the beam experience larger displacements in the concave direction. From Figs. 3(c) and 3(d), it can be see that the behavior is slightly skew-symmetric. This could be effect of the initial displacement generated while fastening the beam to the clamping fixture. In all the experiments, the tightening sequence used was 2-3-1-4 (see Fig. 2(c)).

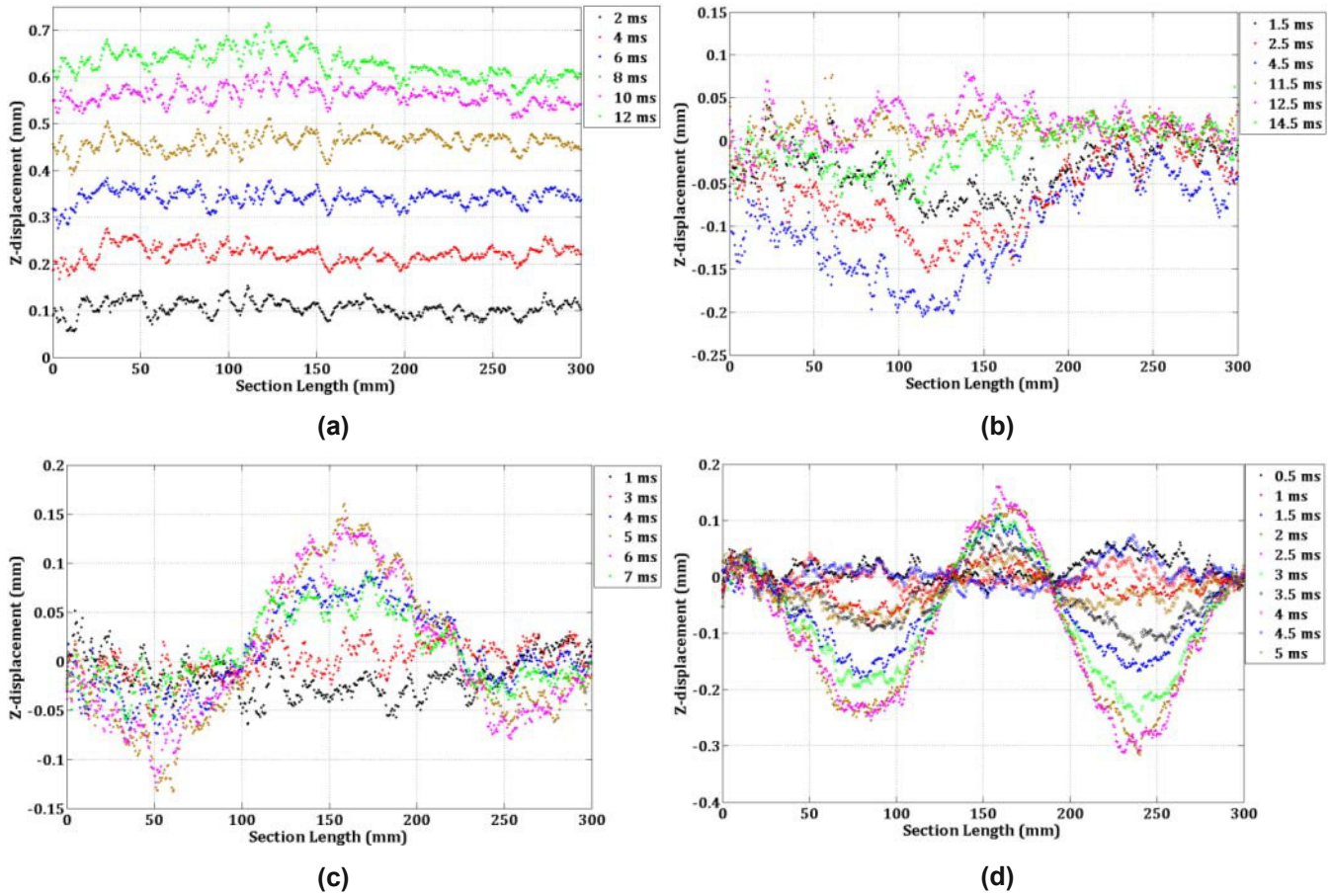

Figure 3: Measured out-of-plane displacement at the mid-plane of the curved beam (Section 1) due to 1 g base excitation at **(a)** 26 Hz, **(b)** 76 Hz, **(c)** 126 Hz, and **(d)** 253 Hz.

CONCLUSIONS

Through the use of two cameras, the 3D DIC technique was successfully employed to obtain a full-field measurement of in- and out-of-plane displacements of a curved beam under clamped-clamped conditions. It was demonstrate that the procedure of fastening the beam to a clamping fixture, regardless of the bolt tightening sequence, will alter the initial conditions of the beam. Knowledge of these initial conditions is critical to develop a FEM model that will be to predict the response of a structure subjected to any source of vibration. We were able to differentiate rigid body motion (non-resonant condition) and bending modes (resonance) of a curved beam over the frequency range of 20 – 500 Hz.

This work has laid the groundwork for using 3D digital image correlation as a complementing and reliable technique to develop and validate numerical models more accurately.

ACKNOWLEDGEMENTS

The authors gratefully acknowledged the Structural Sciences Center in the Air Vehicles Directorate of the Air Force Research Laboratory for supporting this investigation as well as providing the test equipment and facilities.

REFERENCES

[1] Yamaki N, Mori A (1980) Non-linear vibrations of a clamped beam with initial deflection and initial axial displacement, Part I: Theory, Journal of Sound and Vibration 71: 333 – 346.

[2] Yamaki N, Otomo K, Mori A (1980) Non-linear vibrations of a clamped beam with initial deflection and axial displacement, Part II: Experiment, Journal of Sound and Vibration 71: 347 – 360.
[3] Abou-Rayan AM, Nayfeh AH, Mook DT, Nayfeh MA (1993) Nonlinear response of a parametrically excited buckled beam, Nonlinear Dynamics 4: 499 – 525.
[4] Afaneh AA, Ibrahim RA (1993) Nonlinear response of an initially buckled beam with 1:1 internal resonance to sinusoidal excitation, Nonlinear Dynamics 4: 547 – 571.
[5] Emam SA, Nayfeh AH (2004) On the linear dynamics of a buckled beam subjected to a primary-resonance excitation, Nonlinear Dynamics 35: 1 – 17.
[6] Yang F, Sedaghati R, Esmailzadeh E (2008) Free in-plane vibration of general curved beams using finite element method, Journal of Sound and Vibration 318: 850 – 867.
[7] Zulli D, Alaggio R, Benedettini F (2009) Non-linear dynamics of curved beams. Part 2, numerical analysis and experiments, International Journal of Non-Linear Mechanics 44: 630 – 643.
[8] Turner TL, Patel HD (2007) Analysis of SMA hybrid composite structures in MSC.Nastran and ABAQUS, Journal of Intelligent Material Systems and Structures 18: 435-447.
[9] Gordon RW, Hollkamp JJ, Spottswood SM (2003) Nonlinear response of a clamped-clamped beam to random base excitation, Proceedings Eighth International Conference on Recent Advances in Structural Dynamics.
[10] Hollkamp JJ, Gordon RW, Spottswood SM (2003) Nonlinear sonic fatigue response prediction from finite element modal models: A comparison with experiments, Proceedings 44th AIAA/ASME/ASCE/AHS/ASC Structures, Structural Dynamics, and Materials Conference.
[11] Spottswood SM, Hollkamp JJ, Eason TG (2008) On the use of reduced-order models for shallow curved beams under combined loading, Proceedings 49th AIAA/ASME/ASCE/AHS/ASC Structures, Structural Dynamics, and Materials Conference
[12] Wang XQ, Mignolet MP, Spottswood SM, Eason TG (2009) Nonlinear reduced order modeling of curved beams: A comparison of methods, Proceedings 50th AIAA/ASME/ASCE/AHS/ASC Structures, Structural Dynamics, and Materials Conference.
[13] Sutton MA, Mingqi C, Peters WH, Chao YJ, McNeill SR (1986) Application of an optimized digital image correlation to planar deformation analysis, Image and Vision Computing 4: 143-150.
[14] Luo PF, Chao YJ, Sutton MA, Peters III WH (1993) Accurate measurement of three-dimensional deformation in deformable and rigid bodies using Computer Vision, Experimental Mechanics 33: 123 – 132.
[15] Sutton MA, McNeill SR, Helm YD, Chao YJ (2000) Advances in two-dimensional and three-dimensional computer vision, Photomechanics: 323 – 372.
[16] Lacarbonara W (1997) A theoretical and experimental investigation of nonlinear vibrations of buckled beams, Master Thesis, Virginia Polytechnic Institute and State University.
[17] Kreider W, Nayfeh AH (1998) Experimental investigation of single-mode responses in a fixed-fixed buckled beam, Nonlinear Dynamics 15: 155 – 177.

Proceedings of the SEM Annual Conference
June 7-10, 2010 Indianapolis, Indiana USA

Application of High Speed Digital Image Correlation for Vibration Mode Shape Analysis

Thorsten Siebert[1], Matt J. Crompton[2]

[1]Dantec Dynamics GmbH,Kässbohrerstr. 18, D-89077 Ulm, Germany
Thorsten.Siebert@Dantecdynamics.com

[2]Dantec Dynamics Inc., 200 Wiliams Dr., Ramsey, NJ 07446, USA

ABSTRACT

Digital speckle correlation techniques have been successfully proven to be an accurate displacement analysis tool for a wide range of applications. With the use of two cameras, three dimensional measurements of contours and displacements can be carried out.

With rapid new developments in the field of digital imaging and computer technology, the capability of this technique is increasing, opening further applications in the fields of material testing, fracture mechanics and vibration analysis. The high resolution of the deformation measurements in space and time can accurately determines the absolute position and displacements of objects, even if they display high amplitudes and large rigid body movements. The absolute resolution depends on the field of view and is scalable. Calibration of the optical setup is a crucial point which will be discussed in detail. Examples are described including the analysis of a harmonic vibration and transient events from real industrial applications showing the interaction of large accelerations and complex rigid body motions.

INTRODUCTION

In recent years optical full-field measuring techniques are increasingly being used in research and industry as development and design tools for improved characterization of materials and components. Besides moiré and interferometer based techniques the digital image correlation method is widely used for full-field and three dimensional displacement measurements [1-4].

Digital Image Correlation (DIC) is a full-field image analysis method, based on grey value digital images, that allows determination of the contour and surface displacements of an object under load in three dimensions. Due to rapid new developments of high resolution digital cameras and computer technology, the applications for these measurement methods have broadened. Since the system determines the absolute position and displacement of the object in space, deformation measurements with very high resolution are possible even under the presence of large deformation amplitudes and macroscopic rigid body movements.

T. Proulx (ed.), *Application of Imaging Techniques to Mechanics of Materials and Structures, Volume 4*, Conference Proceedings of the Society for Experimental Mechanics Series 14, DOI 10.1007/978-1-4419-9796-8_37, © The Society for Experimental Mechanics, Inc. 2013

The displacement resolution depends on the field of view (typically down to 10^{-5} of the field of view) and therefore is scalable, e.g. a few µm for an A4 paper size field of view depending on the number of pixels used. The measurable displacement range for this configuration is from µm up to several cm.

Out of the contour and displacement measurement, the image correlation technique provides material parameters far into the range of plastic deformation. Further data analysis tools allow the determination of the location and the amplitude of the maximum strain, the global strain distribution and behavior of crack growth. Analyzing the temporal displacement by using e.g. Fourier analysis can give information about modal shape and vibration amplitudes. Since this method is based on series of images it can be applied to many different time scales from a few Hz range up to several 100 kHz range.

PRINCIPLES OF DIGITAL IMAGE CORRELATION

Two imaging sensors, looking from different positions at an object, similar to human vision, provide enough information to perceive the object as three dimensional. Using a stereoscopic camera setup (figure 1, left), each object point is focused on a specific pixel in the image plane of the respective camera.

With the knowledge of the imaging parameters for each camera (intrinsic parameters: focal length, principle point and distortion parameters) and the orientations of the two cameras with respect to each other (extrinsic parameters: rotation matrix and translation vector), the position of each object point in three dimensions can be calculated.

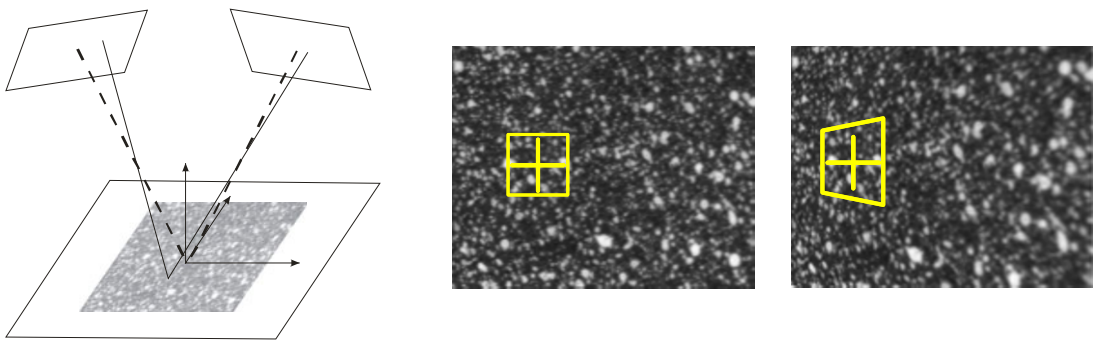

Fig. 1. Principle of stereoscopic setup (left) and grey value pattern in different images on the camera.

Using a stochastic intensity pattern on the object's surface, the position of each surface point in the two images can be identified by applying a correlation algorithm. By using this correlation algorithm, a matching accuracy of the original and the transformed facet of better than 0.01 pixel can be achieved [5].

The stochastic pattern can be applied easily with a colored spray paint, printing or other transfer methods. The size and distribution does influence the achievable resolution. An investigation about an optimum pattern and evaluation parameters can be found e.g. at Lecompte et al [6].

CALIBRATION

The process of determining the projection parameters (intrinsic and extrinsic imaging parameters) is described as the calibration process. Images of a target with a known accurate pattern are recorded with both cameras simultaneously. The system displays in real-time the tracking of target markers and automatically acquires a sequence of images of the target positioned at different angles. From this sequence of images the projection parameter of the whole system, with additional distortion parameter, is calculated based on the pinhole model. The quality of the measurement is directly related to the accuracy of the projection parameters and by simplifying the calibration process and providing quality feedback in this process, accurate measurements can be assured. Typically eight images are sufficient to calculate all calibration parameters accurately.

ACQUISITION

Depending on the type of camera which is used for the image acquisition, several parameters and adjustments of the cameras can be made, e.g. exposure time, frame rate, brightness, contrast and area of interest. Typically a series of a few up to several hundreds of images are acquired and saved during the experiment. The acquisition can be started manually or fully automatically using various types of triggering. These images, combined with the projection parameters, are the base for the evaluation.

EVALUATION

By applying the correlation algorithm, the position of all object points can be identified in the image from both cameras. Using the projection parameters of the system, the 3-dimensional coordinates for each object point can be calculated leading to a 3-dimensional contour of the object.

Following the changes of the grey value pattern for each camera along the loading steps, the surface displacements of the object are calculated. The matching accuracy of the correlation algorithm resulting in a displacement resolution down to 1/100 000 of the field of view for a MegaPixel CCD camera. For an A4 paper size this gives a resolution in displacement of down to 3-4 µm. [5-8]

APPLICATIONS

Digital image correlation opens a wide range of potential applications. Since this technique is based on the analysis of a series of grey value images, deformation and strain analysis of static as well as of dynamic events can be performed. In the dynamic applications different types of excitation are used: a single frequency or a frequency sweep excitation, a shock excitation using a shock event and the use of noise excitation. A comparison between measurements using DIC, accelerometers, strain gauges and simulation have been successfully carried out on measurements of a bending beam using different excitation types [8, 9].

In the following we present three dynamic applications: a vibration analysis of a membrane, an impact test and an excitation of a circuit board using white noise.

VIBRATION OF A MEMBRANE

During this experiment the vibration of a rubber membrane in front of a loudspeaker, which is excited close to a resonance frequency, was investigated. The size of the evaluated area is about 300 x 260 mm^2. The used rubber material has a porous surface, which gives a statistical grey value distribution, thus no extra preparation of the surface was necessary. A white colour was used to increase the amount of diffusely reflected light. The loudspeaker was excited at 59.9 Hz where a membrane was vibrating in resonance.

For image acquisition, high-speed cameras with 1280 x 1024 pixels resolution where used. The maximum frame rate at full resolution of these cameras is 1000Hz, for this measurement the frame rate was reduced to 625Hz. In figure 2 the setup including the high-speed cameras and the loudspeaker, is shown.

Fig. 2. Experimental setup with high-speed cameras, calibration target, loudspeaker and frequency generator for vibration measurement.

The image acquisition was started previous to the excitation of the loudspeaker. For the evaluation 150 images corresponding to 0.25 seconds of testing were processed.

The results of the measurement are displayed as a 3-dimensional model. On the surface of the object's model different data can be mapped in order to display the full field information. The different data are contour information (e.g. distances to Best-Fit plane), displacements (e.g. absolute X-, Y- or Z-deformation) or strains (e.g. principal strains). Figure 5 shows the full field display of the out of plane deformation of the membrane at the maximum elongation during the vibration. The colours represent the amplitudes of displacements. In the lower part of the graphic a spatial profile along the horizontal direction is displayed.

The maximum amplitude in this measurement is about 4 mm. The centre point and the circular area around the centre are vibrating out of phase. In order to get more detailed information the displacements of a marked centre point versus time is shown (figure 3). The evaluated series of images covers about 14 cycles of vibration. As it can be seen from the curve, it takes only 1 to 2 excitation cycles until the system is vibrating in a stable and stationary mode.

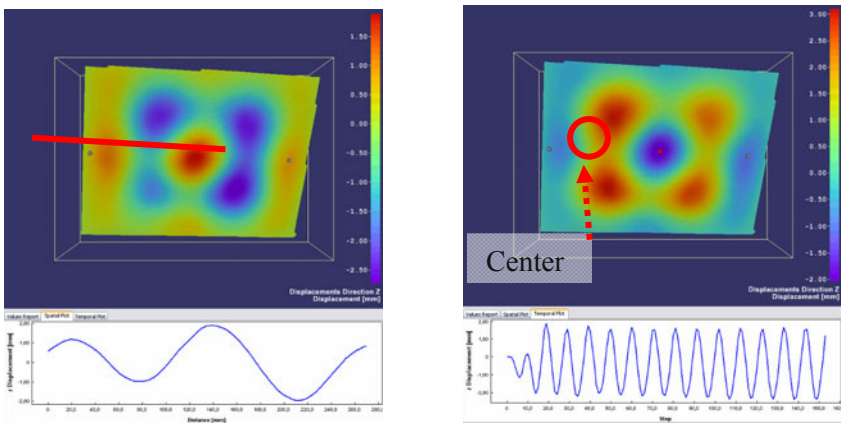

Fig. 3. Full field out-of-plane deformation of the membrane at maximum deflection of the centre (top left and top right). Spatial profile along a horizontal line (bottom left) and temporal plot of the displacement of the centre point (bottom right).

For the next measurement the frequency of excitation was set to another resonance at 36.5 Hz. Figure 4 shows the amplitude of vibration of the centre point and of a point in the lower left corner. The point in the centre vibrates with amplitude of about 5 mm symmetrically in the positive and negative direction. At the corner point the membrane is fixed on the housing of the loudspeaker, thus this point moves only in the positive direction. The amplitude is just about 0.05 mm. This example demonstrates the dynamic range, which can be covered with a single full field measurement.

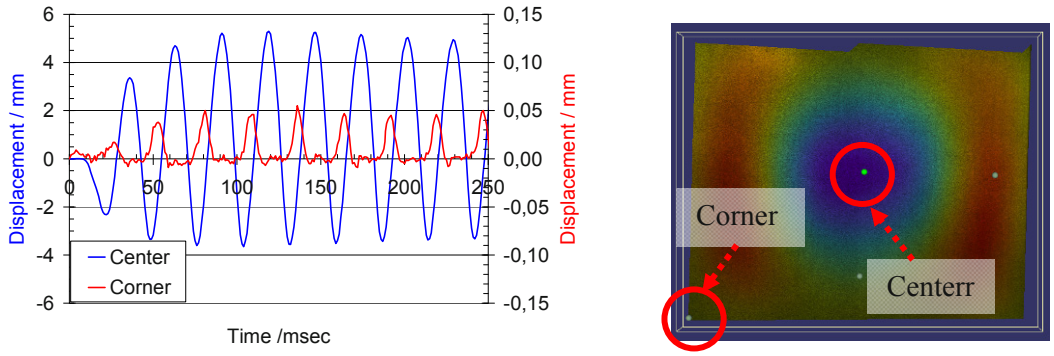

Fig. 4. Out-of plane displacement of points in the centre and in the corner over time.

IMPACT TESTING

Besides harmonic events the technique of image correlation is suitable to analyze transient events. A phone drop test is an example of a transient impact test. The phone was dropped from a height of 1m onto a steel plate. The measurement was performed using high speed cameras running at a frame rate of 5 kHz. The setup of the cameras and the drop testing stand are shown in figure 5.

Fig. 5. Setup for the phone drop test (left: high speed cameras; right: test stand).

As well as the frame rate for each experiment the exposure time is another important parameter. The exposure time should be short enough in order to avoid motion blurring and freeze the image of the moving object. In this case an exposure time of 5 µs was used.

The acquisition of images was started by using an optical trigger. A series of about 400 images corresponding to a time sequence of 0.08 seconds was evaluated. Displacement data from the displacement of opposite corners of the phone was extracted first. From the plot of vertical velocity (Figure 6) it can be observed that first the lower right corner of the phone hits the ground. This impact generates an additional acceleration before the upper right corner hits the ground. The velocity of the upper corner increases by about 50% after the first impact. The maximum acceleration is therefore shown to be when the second impact occurs.

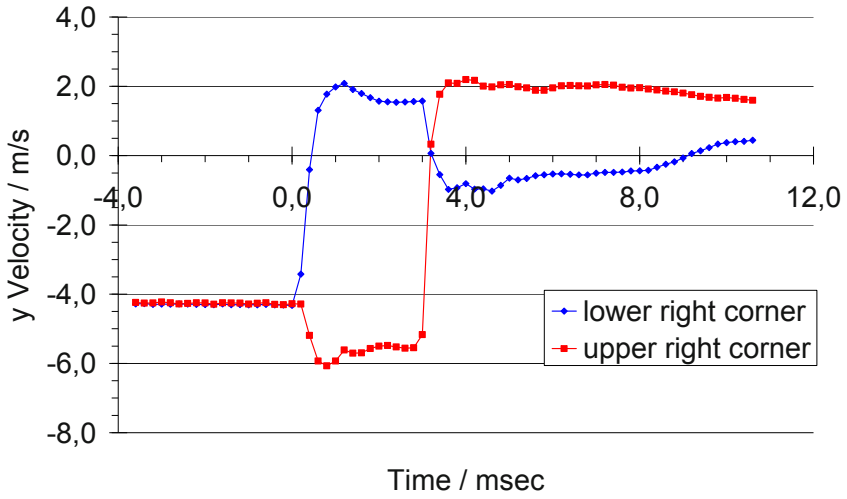

Fig. 6. Velocity of two points as a function of time

In addition to point data, the full-field behaviour of the object can also be analyzed. In this case the out-of plane displacement due to the impact was investigated. The out-of plane displacement just after the second impact is shown in figure 7. Here the most dominant mode shape of the vibration can be observed. The maximum amplitude of vibration is in the order of 0.35 mm.

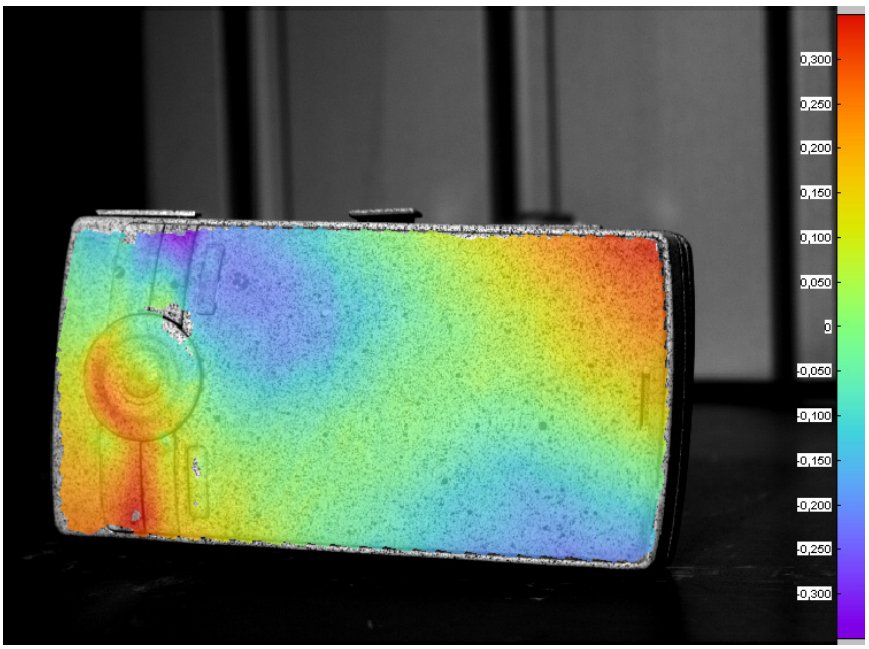

Fig. 7. Out-of plane displacement due to the second impact

NOISE EXCITATION

A circuit board was mounted on a shaker in a horizontal position. In an area of about 65 x 30 mm the movement of the circuit board was recorded at 2 kHz frame rate. The shaker was driven using white noise in a frequency range between 200 and 1 kHz. In Fig. 8 the image of one camera is showing the area under investigation and the full-field result as well as the displacement of a single point over time. The displacement of the point is in the range of ca. 40 µm.

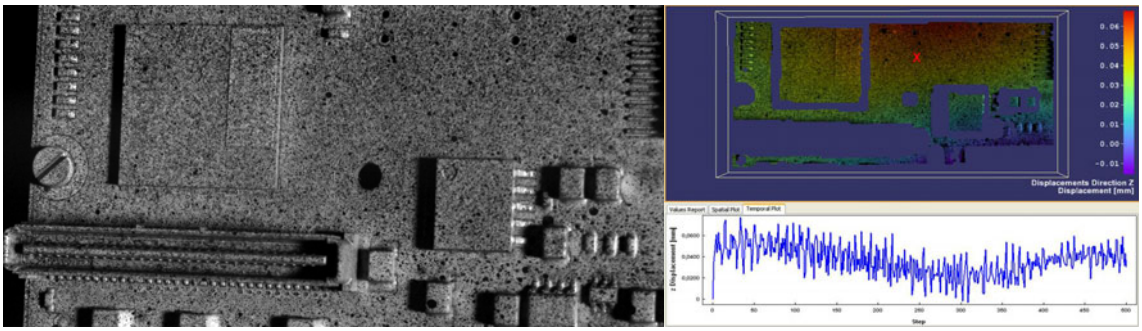

Fig. 8. Field of view (left), full-field displacement at one measurement step (right top) and displacement of marked point (cross) over measurement steps (right bottom).

By applying a frequency analysis at different points the main frequencies of the object can be determined. In this case an accelerometer indicates a main frequency at about 770 Hz. This frequency was found mainly in the centre of the board where the accelerometer was placed and no elements are located. The reconstruction of the mode shape at this frequency is shown in Fig. 9. The amplitude is in the range of 10 µm with a smooth shape which does not show areas of critical stressing of the board.

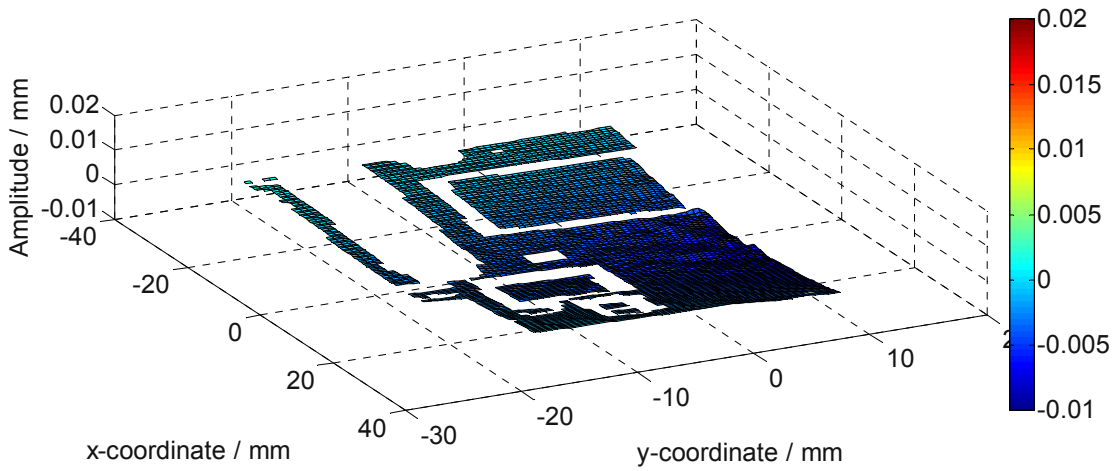

Fig. 9. Reconstructed mode shape at 770 Hz

A frequency analysis at a point close to the longitudinal connector showed another peak at about 535 Hz. The reconstructed mode shape is shown in Fig. 10. The amplitude of about 20 µm doubles the amplitude at 770 Hz. The shape of this mode generates also gradients of displacement and strain in an area of the connector and small electronic elements on the board. This frequency at 535 Hz will lead to higher chance of failure than other frequencies.

The application of this full-field method in combination with a frequency analysis allows the identification and reconstruction of the different mode shapes. This gives quantitative information about the behavior and damage of the sample at different frequencies.

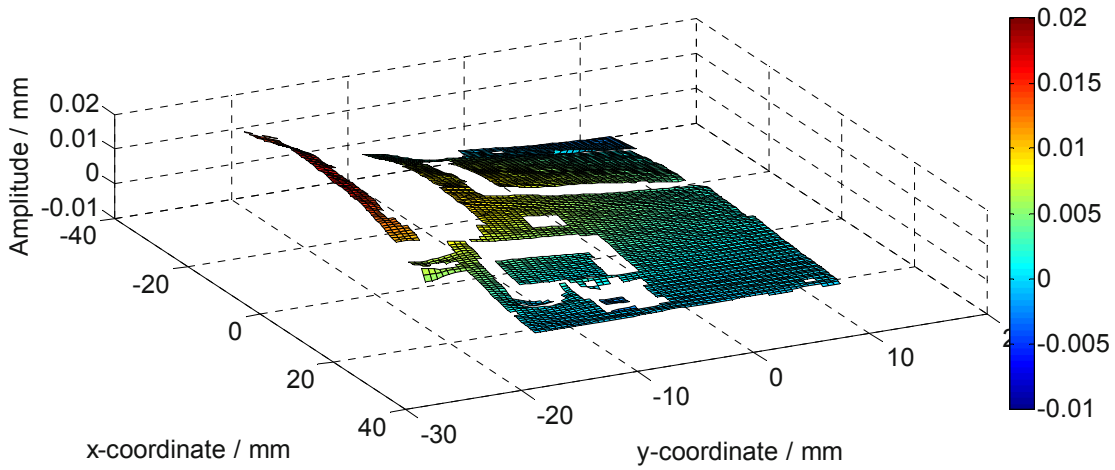

Fig. 10. Reconstructed mode shape at 535 Hz

CONCLUSION

This paper shows recent developments and applications of digital image correlation. Improvements in the calibration process make the system significantly easier to use by decreasing calibration time and enhancing the reliability and quality of the results. Due to the modular concept of the hardware and the software this system can be used for a wide range of applications. Based on a full field method, this technique allows the determination of displacement amplitudes and vibration phases with high spatial and temporal resolution and within a large dynamic range. Amplitudes from m to µm and frequencies up to several tens of kHz could be covered, giving rise to applications of dynamic displacement and dynamic strain measurements. The use of high speed cameras offers the chance of measuring full field deformation and strain fields for harmonic as well as transient events. Applications of harmonic vibration, impact phenomenon and noise excitation were shown, where accurate full field measurements of displacements have been demonstrated. From these measurements different mode shapes can be extracted and displayed.

REFERENCES

[1] Sutton M.A., McNeil S.R., Helm J.D., Chao Y.J, “Advances in 2-D and 3-D computer vision for shape and deformation measurements”, in Photomechanics, P.K. Rastogi, Ed. Topics in Applied Physics, 77, 323-372, Springer Verlag, New York (2000)

[2] Mguil-Touchal S., Morestin F., Brunet M., “Various Experimental Applications of Digital Image Correlation Method”, CMEM 97, Rhodes, May, 45-58

[3] Winter D., “Optische Verschiebungsmessungen nach dem Objektrasterprinzip mit Hilfe eines flächenorientierten Ansatzes“, Dissertation in der Fakultät Maschinenbau und Elektronik an der Universität Braunschweig, 1993

[4] Sutton M.A., Orteu J-J., Schreier H.W., „Image Correlation for Shape, Motion and Deformation Measurements”, Springer Science+Business Media, LLC, ISBN 978-0-387-78746-6 (2009)

[5] Becker T, Splitthof K., Siebert T., Kletting P., “Error estimations of 3D digital image correlation measurements”, Speckle06, SPIE Vol. 6341, 63410F, (2006)

[6] Lecompte D., Sol H, Vantomme J, Habraken A., “Analysis of speckle patterns for deformation measurements by digital image correlation”, Speckle06, SPIE Vol. 6341, 63410E, (2006)

[7] Schmidt T., Tyson J., Galanulis K., Revilock D., Melis M., “Full-field dynamic deformation and strain measurements using high-speed digital cameras”, 26th International Congress on High-Speed Photography and Photonics, SPIE Vol. 5580, 174-185, (2005)

[8] Siebert T., Becker T., Splitthof K., Neumann I., Krupka R., „High-speed digital image correlation: Error estimations and applications”, Optical Engineering, 46(5):051004 (2007)

[9] Neumann, I., „Schwingungsmessungen in der Umweltsimulation mit einem Bildkorrelationsmesssystem“, Diploma Thesis, Hochschule Ravensburg-Weingarten, Germany, 2006

Proceedings of the SEM Annual Conference
June 7-10, 2010 Indianapolis, Indiana USA

Experimental validation of equations for 2D DIC uncertainty quantification

Phillip L. Reu[1*] and Timothy J. Miller[1]
[1]Sandia National Laboratories, PO Box 5800, Albuquerque, NM 87185

ABSTRACT

Uncertainty quantification (UQ) equations have been derived for predicting matching uncertainty in two-dimensional image correlation *a priori*. These equations include terms that represent the image noise and image contrast. Researchers at the University of South Carolina have extended previous 1D work to calculate matching errors in 2D. These 2D equations have been coded into a Sandia National Laboratories UQ software package to predict the uncertainty for DIC images. This paper presents those equations and the resulting error surfaces for trial speckle images. Comparison of the UQ results with experimentally subpixel-shifted images is also discussed.

Keywords: High-speed imaging, digital image correlation, uncertainty quantification

1. INTRODUCTION

Digital image correlation (DIC) is becoming a standard method for making quantitative full-field measurements of displacement and strain. Consequently, understanding the effects of the experimental parameters on the quality of the resulting measurement is critical. To do this, an uncertainty quantification (UQ) study was undertaken with the University of South Carolina. The results for 2D DIC can be found in an article by Wang and Sutton [1]. The equations in this paper reveal important criterion for what makes a good speckle image, and allow one to quantitatively investigate how to improve DIC imaging. For most heterogeneous patterns, the 1D story is completely adequate; but for certain patterns, it would not correctly predict the errors, for instance in images where the speckle patterns have a strong directionality. To overcome this shortcoming, the equations were extended to predict the full 2D error surface.

This paper will briefly introduce the 2D error equations and the predictions made using the Sandia UQ software for a few different images. The 2D error effects are demonstrated using some particularly questionable images that highlight the effects of poor gradient uniformity. A method of experimentally creating exact subpixel shifted images is also presented using numerical binning of ultra-high resolution digital cameras. The experimental results are then compared with the UQ software predictions for a more typical speckle pattern.

2. 2D UNCERTAINTY QUANTIFICATION

2.1. 2D interpolation for intensity pattern reconstruction

A thorough development of the equations provided here is presented in a paper by Wang and Sutton [1]. In this paper, only the final uncertainty equations are given in their matrix form for 2D UQ. In brief, image correlation takes the intensity of an original image, $I(x_{i,j})$, and a translated image, $T(x_{i,j})$, and using a minimization criterion finds the translation, $\boldsymbol{t}$, of the subset at pixel locations $x_{i,j}$. The minimization function used for this analysis was the squared-sum of differences (SSD). The translation in the 2D sense is composed of u and v translations in the x- and y-directions respectively. The subset pixel indexes, i, and j, run from 0 to the subset size, N. The gradients of the translated image, $\nabla T_x(\xi_{i,j})_0$ and $\nabla T_y(\xi_{i,j})_0$, are a mathematical representation of the contrast in the x- and y-directions. The $\xi_{i,j}$ term is the measured position in the deformed image. The translation is calculated on a subpixel sense, τ, via an interpolation function, $h(x_{i,j})$. For this paper, a cubic polynomial function is analyzed. The image noise is assumed to be Gaussian with a zero mean, Noise(σ,0). The calculated translation will have two errors associated with it, a bias error, E(t), and a variance, Var(t).

* plreu@sandia.gov

T. Proulx (ed.), *Application of Imaging Techniques to Mechanics of Materials and Structures, Volume 4*, Conference Proceedings of the Society for Experimental Mechanics Series 14, DOI 10.1007/978-1-4419-9796-8_38, © The Society for Experimental Mechanics, Inc. 2013

$$E(t) \cong \begin{bmatrix} u_0 \\ v_0 \end{bmatrix} + M \cdot \begin{bmatrix} \left\{ \sum_{i=1}^{N} \sum_{j=1}^{N} \left(-h(\mathbf{x}_{ij}) \cdot \nabla T_x((\boldsymbol{\xi}_{ij})_0) \right) \right\} + f_x(\boldsymbol{\tau}) \cdot N^2 \cdot \sigma^2 \\ \left\{ \sum_{i=1}^{N} \sum_{j=1}^{N} \left(-h(\mathbf{x}_{ij}) \cdot \nabla T_y((\boldsymbol{\xi}_{ij})_0) \right) \right\} + f_y(\boldsymbol{\tau}) \cdot N^2 \cdot \sigma^2 \end{bmatrix} \tag{2.1}$$

where

$$M = \begin{bmatrix} \sum_{i=1}^{N} \sum_{j=1}^{N} \left[\nabla T_x((\boldsymbol{\xi}_{ij})_0) \right]^2 & \sum_{i=1}^{N} \sum_{j=1}^{N} \left[\nabla T_x((\boldsymbol{\xi}_{ij})_0) \cdot \nabla T_y((\boldsymbol{\xi}_{ij})_0) \right] \\ \sum_{i=1}^{N} \sum_{j=1}^{N} \left[\nabla T_x((\boldsymbol{\xi}_{ij})_0) \cdot \nabla T_y((\boldsymbol{\xi}_{ij})_0) \right] & \sum_{i=1}^{N} \sum_{j=1}^{N} \left[\nabla T_y((\boldsymbol{\xi}_{ij})_0) \right]^2 \end{bmatrix}^{-1}$$

$$f_x(\boldsymbol{\tau}) = (-1.2234\omega_x - 3.6470\omega_y{}^2\omega_x)$$

$$f_y(\boldsymbol{\tau}) = (-1.2234\omega_y - 3.6470\omega_x{}^2\omega_y)$$

$$\omega_x = \tau_x - 0.5$$

$$\omega_y = \tau_y - 0.5$$

$$Var(t) = 2\sigma^2 \cdot \begin{bmatrix} \sum_{i=1}^{N} \sum_{j=1}^{N} \left[\nabla T_x((\boldsymbol{\xi}_{ij})_0) \right]^2 & \sum_{i=1}^{N} \sum_{j=1}^{N} \left[\nabla T_x((\boldsymbol{\xi}_{ij})_0) \cdot \nabla T_y((\boldsymbol{\xi}_{ij})_0) \right] \\ \sum_{i=1}^{N} \sum_{j=1}^{N} \left[\nabla T_x((\boldsymbol{\xi}_{ij})_0) \cdot \nabla T_y((\boldsymbol{\xi}_{ij})_0) \right] & \sum_{i=1}^{N} \sum_{j=1}^{N} \left[\nabla T_y((\boldsymbol{\xi}_{ij})_0) \right]^2 \end{bmatrix}^{-1} \tag{2.2}$$

The left portion of the expectation equation shown in Equation (2.1), is the *bias interpolation* term due to its dependence on the interpolation function $h(x_{i,j})$. The right half of Equation (2.1) is the *bias noise* term, depending upon both image noise σ and the interpolation method. Equation (2.2) is the variance of the measurement error, which can be reduced by increasing intensity contrast or reducing intensity pattern noise.

2.2. Discussion of the bias and variance results

The interpolation bias shown in Eq (2.1) has no bias at integer or ½-pixel translations. The bias error is generally sinusoidal in shape and in agreement with the results of Schreier [2]. The noise bias term has the largest bias at the integer pixels locations, and none at the ½-pixel point. Both terms are illustrated separately for a typical image with two different noise levels in Figure 1. As shown in Eq (2.2), variance is added to each measurement, with the additive variance term being independent of the amount of subpixel or integer shift.

A number of conclusions can be drawn by inspecting Equations (2.1) and (2.2). First, the choice of subset shape function will affect the amount of bias in the results via $h(x_{i,j})$. It has been shown [1, 4, 5] that higher order shape functions will decrease bias errors at the expense of longer computation times. The other defining characteristic of the bias is its dependence on the image gradients, which is the intensity gradient of the image, and appears in the equations as the sum of the squares of the intensity gradient. For any given set of images, this criterion can be used to determine the optimum subset size.

The intensity gradient is only partially in the experimenter's control and depends greatly on the type of testing being conducted. Typically in laboratory testing, time is available to optimize lighting and speckle pattern to increase the gradients. This is done by having a large number of counts between the black and white speckle values. Contrast optimization is often the most difficult aspect for the experimentalist, particularly in non-ideal settings. This is often true in high and ultra-high speed imaging, where adequate lighting is typically the issue, and

in micro- and nano-imaging where appropriate speckle patterning combined with the SEM imaging can have low contrast. In such cases, *a priori* calculation of the bias and variance is now possible. This is of immediate use for 2D correlation, where the errors are directly applicable.

As shown in Equation (2.1) and (2.2) measurement variance involves the Gaussian pixel noise σ and the intensity gradients. Intensity noise is typically affected by detector quality and detector gain used during imaging. Again, for quasi-static testing and good illumination, pixel intensity pattern noise is typically very small. If further decreases in the effect of noise are desired, averaging of a number of images will decrease the noise. In practical applications, minimizing the camera gain and providing adequate illumination, is the simplest means of decreasing the noise level. That is, the higher the camera gain, the noisier the images.

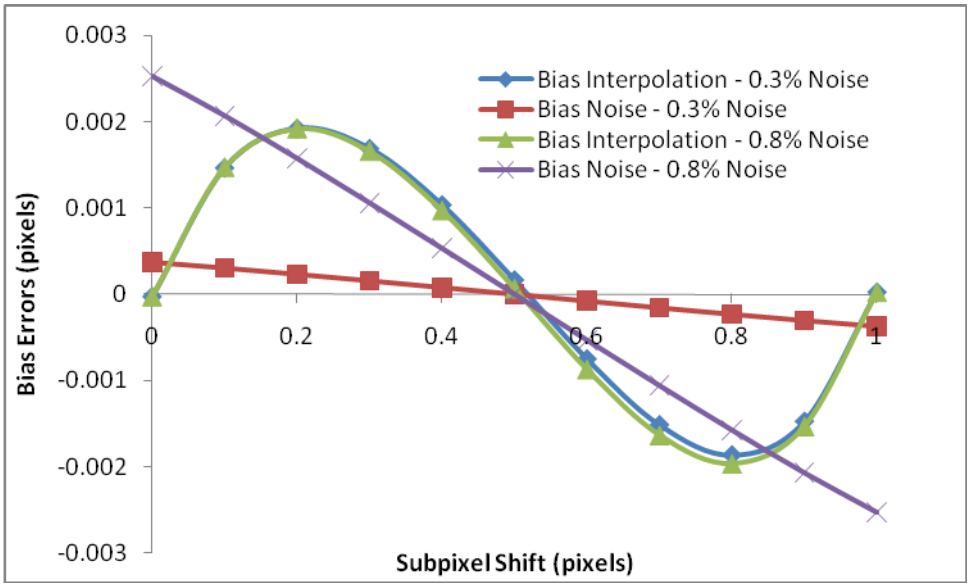

Figure 1. Illustration of Bias Interpolation and Bias Noise terms for two different noise levels

3. 2D NUMERICAL SIMULATION RESULTS

3.1. Error surfaces for heterogeneous patterns

Speckle patterns were used in the UQ software to predict the 2D error surfaces for both the bias noise and bias interpolation. A typical high-contrast pattern was analyzed and the results are shown Figure 2. The bias errors in both directions show the expected sinusoidal shape for all subpixel shifts. The bias noise is also shown in the figure and is a plane passing through zero. Because this is a good pattern with little noise, the interpolation error dominates the error results, with a value of approximately 0.002 pixels relative to the noise bias of 0.0004 pixels. As the noise level increases or the gradients decrease, the noise term will become more dominant. This is illustrated in Figure 3 with the same speckle image as analyzed in Figure 2, but with more noise. The low-noise image had 0.3% noise and the high-noise image had 1.8% noise. For direct comparison to experimental results, as will be described in Section 4, the “total error” should be compared, which is the summation of the noise and interpolation biases in both the *x*- and *y*-directions.

3.2. Error surfaces for patterns with homogeneous patterns

The importance of 2D error analysis is likely to be more important when using speckle patterns that lack a random pattern. A good example, although extreme, would be a pattern with lines. This was analyzed in the UQ software for a line pattern at 45 degrees from the horizontal. This case is particularly interesting because the 1D analysis would find small errors with this case, but the 2D analysis properly determines that in certain directions correlation errors would be high. That is the gradients in both perpendicular directions look good. However, when considering the 45 degree case along the lines, there are no gradients and matching would not be possible. This was analyzed with the 2D UQ software and the results are shown in Figure 4. Looking at the results, the minimum error is seen in the direction perpendicular to the lines and the largest errors are in the direction of the lines. The horizontal errors are somewhere in-between. Why the errors are large in certain directions is more evident when the gradients are inspected (see Figure 4).

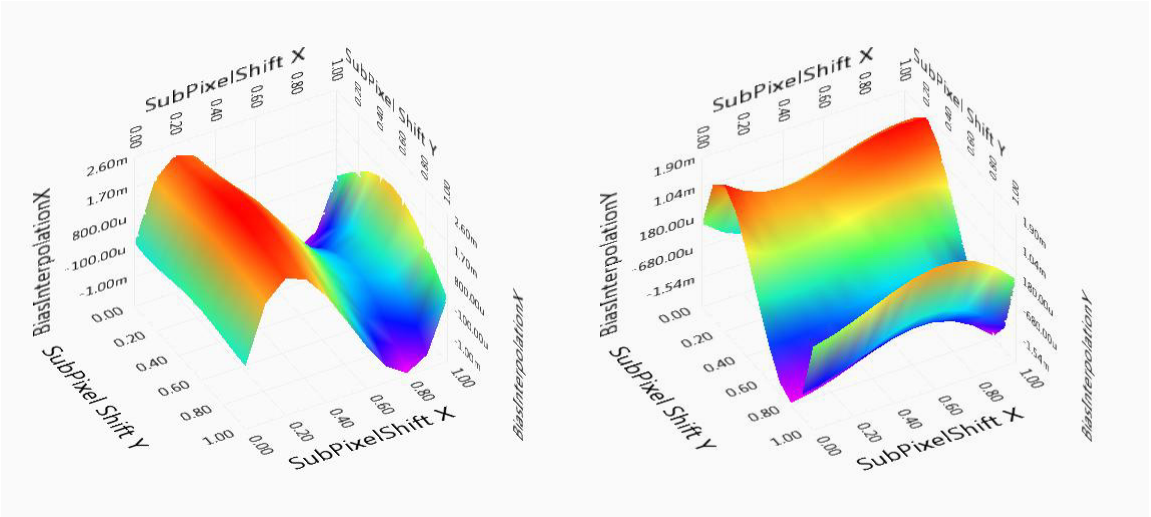

Bias Interpolation X

Bias Interpolation Y

Bias Noise X

Bias Noise Y

Total Error

High Contrast Speckle Pattern

Figure 2. Bias error surfaces for a high-contrast and low-noise image. Bias interpolation and bias noise errors are shown for both the *x*- and *y*-directions. The total error is the sum of all of the above errors. Also shown is the speckle pattern analyzed.

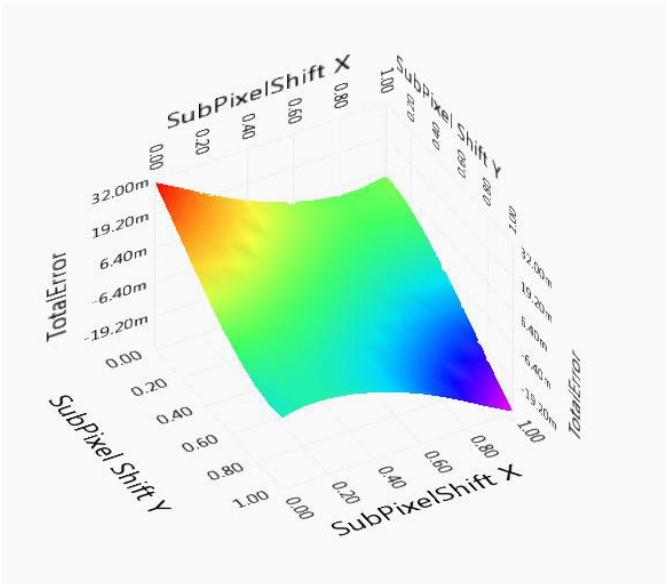

Figure 3. Total error for a high-contrast image with noise showing the tilted total error surface.

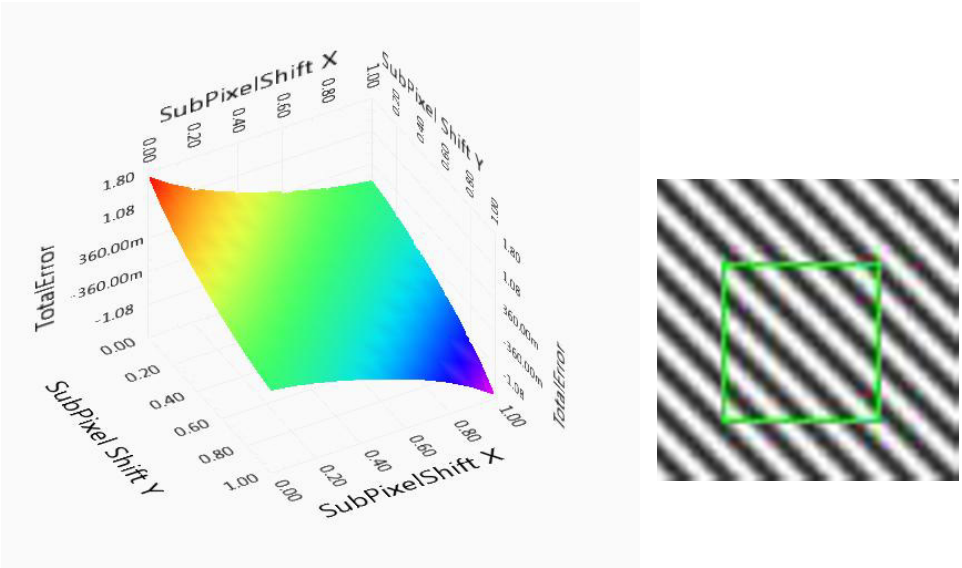

Figure 4. 2D error analysis for a 45-degree line pattern. The total error is shown on the left and indicates that in the direction of the lines, the error is maximum and in the direction perpendicular to the lines the error is minimum. The gradient lines and subset are shown on the right.

4. EXPERIMENTAL VERIFICATION

4.1. Prosilica 2D experimental setup

Perfectly subpixel-shifted experimental images were created using an ultra-high resolution digital camera combined with a “numerical binning” procedure as will be described below. The camera and speckle pattern for this method are both held stationary on the optical table, and the shifting is created by a decimation scheme that varies the starting row or column of the binning. The experimental setup can be seen in Figure 5.

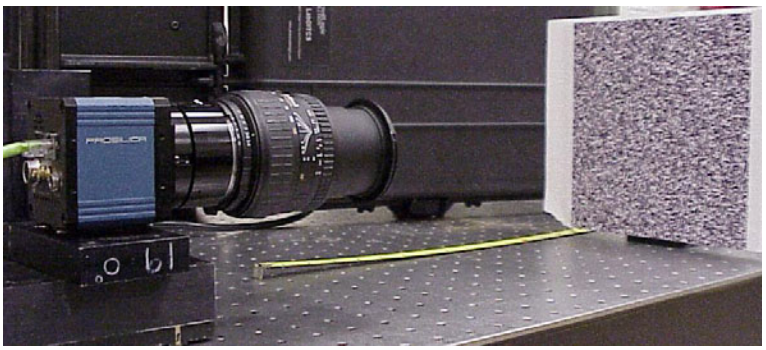

Figure 5. Prosilica camera experimental setup.

The camera, a 16-Megapixel Prosilica GE4900, was used for imaging the speckle pattern. This camera uses a Kodak KAI-16000 sensor. This high-resolution sensor uses micro-lenses to maintain an approximately 100% fill factor. The original image is 4872×3248 pixels. The images are then decimated by a factor of 10 to yield a smaller image that has a resolution of 487×324. The speckle pattern quality can be varied by changing the pattern printed on the paper and attached to the glass plate. The noise in the image can be controlled using the gain of the camera and controlling the lighting. Rather than pure decimation, which would exacerbate any aliasing issues, a method of "virtual binning" was used that numerically averages groups of 10 pixels together to create a single pixel. This is identical to the hardware method of binning where typically two pixels (or 2×2 pixels) are combined electronically to create a single larger pixel. The method of numerical binning is illustrated with a typical speckle image in Figure 6. An array of 4×4 super-pixels, containing an array of 10×10 physical pixels, is shown. Those 10 pixels are then averaged together to yield a single pixel in the decimated image. The large speckles in the original image can be seen in the figure and are approximately 50 pixels in size and yield properly sized speckles in the binned image. That is, speckles that are on the order of 5 pixels, and are unaliased. A subpixel shift is created by changing the start row or column of the binning. With a binning size of 10 as illustrated here, a shift of 0.1 pixels in the binned image is created for each row/column shift in the original image. A purely horizontal or vertical shifting, or combinations of these, can be created. The subpixel shifted images used in the following analysis were all created using this method. Of course, a different number of physical pixels could be combined to create different shift amounts, but would also change the final resolution of the image. Ten was chosen here to give a good compromise between final binned image size and subpixel shift step size.

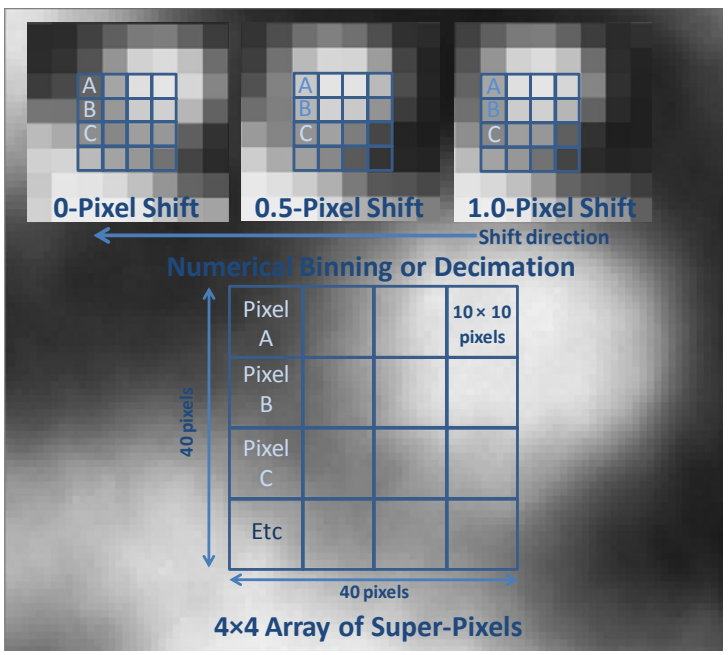

Figure 6. Illustration of numerical binning of a super-pixel. Inset shows a subpixel shift of 0, 0.5 and 1.0 pixels.

4.2. Prosilica 2D experimental results

The Prosilica images were shifted in 0.1-pixel increments in both directions from 0 to 1 pixels. This yielded 121 images to be analyzed in Vic2D. The resulting experimental error curve shown on the left of Figure 7 is the known error. The static noise images from this series are then analyzed using the UQ software to create the predicted error surface on the right of Figure 7. The general shape is correct with the UQ software slightly under predicting the total error. Ongoing research is being conducted to determine why the UQ software is under predicting the errors and to rectify the situation.

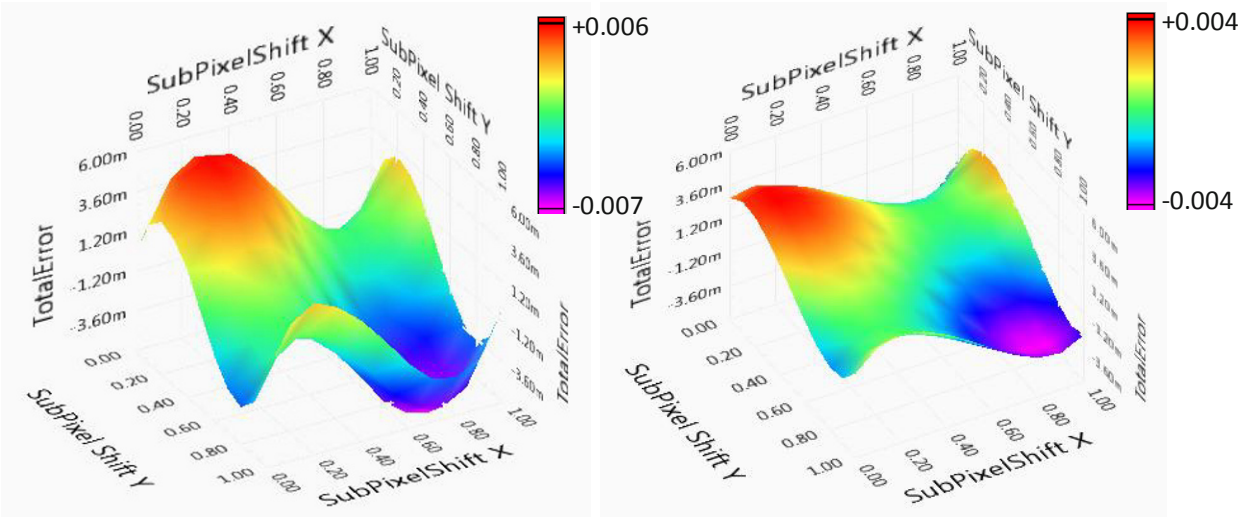

Known Error Predicted Error

Figure 7. DIC Software error surface for a high contrast low noise image. Known error on the left and UQ prediction on the right.

5. CONCLUSIONS

5.1. Summary of 2D results

The bias and variance equations presented here allow an *a priori* assessment of the 2D errors in image correlation. This is important because very often the image quality can vary from test-to-test, and day-to-day and will invalidate any previous attempts to estimate the uncertainty via strain gages or translation tests. The equations can also be used for:

1. Optimizing the subset size of any given analysis,
2. Evaluating speckle pattern and lighting quality for optimal accuracy, and
3. Error estimation for 2D DIC.

In future work the 2D matching errors will be utilized to assess the full uncertainty of 3D DIC. This can be done by propagating the error through the 3D triangulation process. Ultimately this will yield an error sphere in 3D space defining the accuracy of the measurement.

ACKNOWLEDGEMENTS

We would like to thank Prof. Mike Sutton and Dr. Hubert Schreier for many fruitful discussions on these results and their interpretation. This acknowledgement does not however, imply their complete agreement or endorsement of the interpretation of the results.

Sandia is a multiprogram laboratory operated by Sandia Corporation, a Lockheed Martin Company, for the United States Department of Energy under contract DE-AC04-94AL85000.

6. REFERENCES

1. Wang, Y.Q., et al., *Quantitative Error Assessment in Pattern Matching: Effects of Intensity Pattern Noise, Interpolation, Strain and Image Contrast on Motion Measurements.* Strain, 2009. **45**(2): p. 160-178.
2. Schreier, H.W. and M.A. Sutton, *Systematic errors in digital image correlation due to undermatched subset shape functions.* Experimental Mechanics, 2002. **42**(3): p. 303-310.

Proceedings of the SEM Annual Conference
June 7-10, 2010 Indianapolis, Indiana USA

High Performance Digital Volume Correlation

Mark Gates[a*], John Lambros[b], Michael T. Heath[a]
[a] Department of Computer Science, University of Illinois, Urbana, IL 61801
[*] Email: mrgates2@illinois.edu
[b] Department of Aerospace Engineering, University of Illinois, Urbana, IL 61801

ABSTRACT

We develop an improved 3D digital volume correlation (DVC) technique to measure displacement and strain fields throughout the interior of a material. Our eventual goal is to perform DVC with resolution comparable to that achieved in 2D DIC, with a correlation time that is commensurate with the image acquisition time. This would represent a significant improvement over the current state-of-the art available in the literature. Using an X-ray micro-CT scanner, we can resolve features at the 5 micron scale, generating 3D images with up to 8 billion voxels. We compute twelve degrees-of-freedom at each correlation point and utilize tricubic spline interpolation to achieve high accuracy. For DVC, the volume of data, number of correlation points and work to solve each correlation point grow cubically. We therefore employ parallel computing to handle this tremendous increase in computational and memory requirements. We demonstrate the application of DVC using an artificial deformation of actual PDMS samples with embedded particles forming an internal pattern.

1 Introduction

The development of three dimensional (3D) digital volume correlation (DVC), coupled with 3D imaging techniques such as X-ray CT scanners and confocal microscopy, has enabled the measurement of full 3D displacement and strain fields throughout the interior of a material undergoing motion or deformation. DVC is an extension of 2D digital image correlation (DIC), which measures in-plane surface displacements only. DVC is also distinct from 3D DIC, which uses stereo 2D images to measure both in-plane and out-of-plane displacements but only on the surface of a material. In contrast, DVC measures 3D displacements *inside* a material.

Bay et al. [1] first developed DVC using three translation degrees-of-freedom (DOFs), meaning that the three displacements at each correlation point were measured, and C^1 tricubic interpolation. Smith et al. [13] extended this by adding three rotational DOFs, assuming strains are negligible, while Franck et al. [5] added three axial strain DOFs, assuming rotation and shear strain are negligible. Germaneau et al. [6] computed DVC with twelve DOFs, measuring the three displacements and their first derivatives at each correlation point, using less expensive trilinear interpolation. Verhulp et al. [14] also used twelve DOFs, but with tricubic interpolation. Most studies to date have reported computing a relatively modest number of correlation points, 5500 or fewer, except Lenoir et al. [8], who computed more than 60,000 points using three DOFs and trilinear interpolation.

Our eventual goal is to perform DVC with resolution comparable to that achieved in 2D DIC, with a correlation time that is commensurate with the image acquisition time. Here we describe the steps we have taken in improving DVC with an eye to fulfilling this goal, although it has not been completely fulfilled yet. Due to the vastly increased volume of data associated with an undeformed and a deformed image, DVC requires substantially more computation and storage than DIC to achieve similar resolution. A typical grid of correlation points in 2D might be 40×40 to 100×100, so comparable 40^3 to 100^3 resolution in 3D requires

T. Proulx (ed.), *Application of Imaging Techniques to Mechanics of Materials and Structures, Volume 4*, Conference Proceedings of the Society for Experimental Mechanics Series 14, DOI 10.1007/978-1-4419-9796-8_39, © The Society for Experimental Mechanics, Inc. 2013

a grid with 64,000 to 1,000,000 points. The volume of data increases from a few megabytes for 2D DIC to a few gigabytes for 3D DVC, which we handle with careful memory management. To scale to large problem sizes, we utilize parallel computing. To achieve good accuracy, we minimize twelve DOFs and use C^2 tricubic spline interpolation. We also improve the speed of the correlation process by optimizing the spline evaluation.

2 Problem Statement

The problem statement follows the formulation of Bay et al. [1], which in itself is a 3D generalization of the 2D DIC problem formulation of Chu et al. [2]. We define a grid of correlation points in the reference image, at which we measure the deformation, with a 3D subset surrounding each point. Let $\mathbf{p} = [\ p_x \quad p_y \quad p_z\ ]$ be a correlation point in the reference image, $f(\mathbf{x})$ be the subset centered at $\mathbf{p}$ in the reference image, $g(\hat{\mathbf{x}})$ be the corresponding subset in deformed image, and

$$\mathbf{u} = \left[\ u \ \ \frac{\partial u}{\partial x} \ \ \frac{\partial u}{\partial y} \ \ \frac{\partial u}{\partial z} \ \ v \ \ \frac{\partial v}{\partial x} \ \ \frac{\partial v}{\partial y} \ \ \frac{\partial v}{\partial z} \ \ w \ \ \frac{\partial w}{\partial x} \ \ \frac{\partial w}{\partial y} \ \ \frac{\partial w}{\partial z}\ \right]^T \tag{1}$$

be the twelve displacement and derivative degrees-of-freedom to be determined at that point. Let $\mathbf{x} = [\ x \quad y \quad z\ ]$ be a point in the reference subset, and $\hat{\mathbf{x}} = [\ \hat{x} \quad \hat{y} \quad \hat{z}\ ]$ be the corresponding point in the deformed subset, related by

$$\hat{x} = x + u + \frac{\partial u}{\partial x}\Delta x + \frac{\partial u}{\partial y}\Delta y + \frac{\partial u}{\partial z}\Delta z, \tag{2}$$

$$\hat{y} = y + v + \frac{\partial v}{\partial x}\Delta x + \frac{\partial v}{\partial y}\Delta y + \frac{\partial v}{\partial z}\Delta z, \tag{3}$$

$$\hat{z} = z + w + \frac{\partial w}{\partial x}\Delta x + \frac{\partial w}{\partial y}\Delta y + \frac{\partial w}{\partial z}\Delta z, \tag{4}$$

with the offsets from $\mathbf{x}$ to $\mathbf{p}$ given by $\Delta x = x - p_x$, $\Delta y = y - p_y$, and $\Delta z = z - p_z$. The correlation function is computed as a summation over all points $\mathbf{x}$ in the subset. We use the least squares correlation function

$$c(\mathbf{u}) = \frac{\sum_{\mathbf{x}}(f(\mathbf{x}) - g(\hat{\mathbf{x}}))^2}{\sum_{\mathbf{x}} f(\mathbf{x})^2} = \frac{\|f - g\|^2}{\|f\|^2}. \tag{5}$$

For each correlation point, we seek the best possible match between the subsets f and g by finding the deformation $\mathbf{u}$ that minimizes the correlation function $c(\mathbf{u})$.

To determine $\mathbf{u}$, we first perform a coarse search to find an initial guess, which we then use for a minimization algorithm such as Newton's method or BFGS. The points $\hat{\mathbf{x}}$ in the deformed image will not have integer values, thus requiring some form of interpolation between voxels to evaluate $g(\hat{\mathbf{x}})$. We use cubic spline interpolation.

3 Experimental Setup

Generating 3D data sets of internal contrast in materials can be done using techniques such as X-ray CT scanning or confocal microscopy. To faithfully duplicate realistic imaging conditions, we use images acquired through CT scanning. However, as the issue here is the development of DVC methodologies that can fulfill our goals, we use *artificial* deformations of real images to develop and verify our codes. Thus no in situ loading has been done.

We manufacture PDMS (polydimethylsiloxane, commonly known as silicone rubber) samples with embedded silica particles of size 50–250 μm to form a random pattern suitable for DVC. To generate 3D scans, we use a Skyscan 1172A MicroCT scanner, which has a maximum resolution of 5 μm, generating a $4000 \times 4000 \times 2300$ voxel image. For results here, we scan samples at the medium resolution of 10 μm and $2000 \times 2000 \times 900$ voxels.

For baseline tests, we take two consecutive scans, using the same settings and without moving or deforming the sample. Ideally, the displacement field computed by DVC for a pair of baseline images is 0 everywhere, but mechanical perturbations in the scanner may introduce rigid body motion, and scanner noise also affects the results. Baseline DVC tests provide us with a quantitative measure of these two effects.

Tests with strain inducing deformations are generated artificially based on a particular 3D elastic solution. We apply the artificial deformation to one of the two baseline images by computing the analytical displacement field at every voxel and evaluating it using MATLAB's interp3 interpolation function [9]. By performing DVC between the artificially deformed image and using the second baseline image as undeformed, we include the effects of noise in our tests.

4 Interpolation

The core computation of DVC is evaluating the correlation function and its derivatives, which in turn requires interpolating $g(\hat{\mathbf{x}})$ between voxels. We use cubic spline interpolation [3, 4, 11], since in 2D, C^2 bicubic splines have been shown to give superior results to C^1 bicubic interpolation and bilinear interpolation [12]. Here we summarize the different schemes for evaluating splines, comparing their computational complexity and memory requirements, both of which are especially important in 3D DVC.

A cubic spline $\phi(x)$ is a piecewise polynomial of degree three that is C^2 continuous. Three different sets of basis functions are commonly used for splines: the monomial basis, Hermite basis, and B-spline basis. Which basis is most efficient depends on the particular computer hardware, including the size of caches and relative speed of floating point computations to memory bandwidth. Let $x_0, \ldots, x_n$ be knots with associated data $f_0, \ldots, f_n$. For $x \in [x_i, x_{i+1})$, let $\tilde{x} = (x - x_i)/(x_{i+1} - x_i)$ be the local coordinate.

For the monomial basis, each interval is represented separately as

$$\phi(x) = \alpha_0 + \alpha_1 \tilde{x} + \alpha_2 \tilde{x}^2 + \alpha_3 \tilde{x}^3, \tag{6}$$

with coefficients $\alpha_0, \ldots, \alpha_3$. The monomial basis requires the least computation of the spline representations, but also the most memory. Using the monomial basis, a spline with $n+1$ knots in each dimension requires $4n$ coefficients in 1D, $16n^2$ coefficients in 2D, and $64n^3$ coefficients in 3D.

With the Hermite basis, the spline coefficients are simply the function and derivative values at each node,

$$\phi(x) = f_i h_{00}(\tilde{x}) + f_i' h_{01}(\tilde{x}) + f_{i+1} h_{10}(\tilde{x}) + f_{i+1}' h_{11}(\tilde{x}) \tag{7}$$

where

$$h_{00}(x) = 2x^3 - 3x^2 + 1, \qquad h_{01}(x) = x^3 - 2x^2 + x,$$
$$h_{10}(x) = -2x^3 + 3x^2, \qquad h_{11}(x) = x^3 - x^2.$$

Each interval shares function and derivative values with neighboring intervals, so it requires fewer total coefficients than the monomial basis, $2(n+1)$ in 1D, $4(n+1)^2$ in 2D, and $8(n+1)^3$ in 3D.

Each cubic B-spline basis function has support over four intervals and is C^2 continuous across the entire domain. Using the B-spline basis requires the least number of coefficients, $n+3$ in 1D, $(n+3)^2$ in 2D, and $(n+3)^3$ in 3D. However, computing the basis functions is more expensive than computing the Hermite basis functions. The spline is evaluated as

$$\phi(x) = \sum_{r=i-3}^{i} c_r N_{r,4}(x), \tag{8}$$

3D spline	3 DOF			6 DOF			12 DOF			memory
	flops	time	model	flops	time	model	flops	time	model	
monomial basis	126	153	127	127	135	127	129	148	127	62500 KB
Hermite basis	147	54	33	160	60	34	186	82	38	8291 KB
B-spline basis	147	**31**	20	175	**38**	24	231	**59**	31	1163 KB

Table 1: Floating-point operations (flops) per spline evaluation, time to evaluate all points in subset, theoretical model time, and memory requirements for various spline representations of 50^3 subset. Assumes knots are evenly spaced at integer locations. Times in msec on 1.25 GHz PowerPC G4.

with coefficients c_r and B-spline basis functions defined recursively by

$$N_{i,d+1}(x) = \frac{x - x_i}{x_{i+d} - x_i} N_{i,d}(x) + \frac{x_{i+d+1} - x}{x_{i+d+1} - x_{i+1}} N_{i+1,d}(x) \quad \text{for } d > 1,$$
$$N_{i,1}(x) = \begin{cases} 1, & \text{if } x \in [x_i, x_{i+1}), \\ 0, & \text{otherwise.} \end{cases} \tag{9}$$

We substantially optimize this formula by assuming data at fixed width voxels, so the denominators can all be pre-computed.

For multiple dimensions, we use a tensor product of 1D splines. We summarize the relative complexity and speed of the various 3D spline representations in table 1 for the case of three DOF (i.e., displacements only), six DOF (displacements and normal strains) and twelve DOF (displacements and first derivatives). For three DOF, the basis functions are evaluated at the same point within every voxel, so can be evaluated just once at the beginning. For six DOF, the grid of points is axis-aligned; along a grid line parallel to the x axis, the y and z basis functions are constant, so can be evaluated just once per grid line. These optimizations are reflected in the reduced complexity and faster times for three DOF and six DOF variants.

The smaller memory requirements of the B-spline basis cause it to be faster on this processor than the Hermite basis, despite doing more computation. Evaluation using the monomial basis is memory bandwidth limited, so achieves poor performance. The "model" times listed in table 2 use a simple theoretical model to predict the evaluation time based on the number of floating point operations and the amount of memory transferred as,

$$\text{model time} = (\text{flops/point}) \times (\text{points})/(\text{processor speed}) + (\text{memory})/(\text{bandwidth}). \tag{10}$$

In this case, the processor speed is 1 Gflops/sec and the memory bandwidth is 550 MB/sec, as measured by the STREAM benchmark [10]. This model is useful to gauge how an algorithm can be expected to perform on given computer hardware. For instance, here the monomial basis cannot be expected to run faster than the model time of 127 ms, due to memory bandwidth limitations. For the Hermite and B-spline bases, there is also potential for improvement from the currently achieved performance to the theoretical model performance.

In 2D DIC, the spline function is often computed across the whole image as an initialization prior to computing any correlations. This would be expensive in 3D for two reasons: first, it requires storing the entire image in memory at once; second, it requires solving three linear systems with the entire image, one for each dimension, with transposes between each solve. The transposes in particular make this an expensive operation. Instead, we compute the 3D spline over just the current subset plus a small boundary region around it to accommodate minor perturbations in position and size during the minimization. This dramatically reduces our memory requirements and makes the algorithm scalable to large 3D images.

5 Scaling to Large Problems

For 2D DIC, storing two 1024×1024 images in memory is not a problem; they require 1 MB each if stored one byte per pixel. The coefficients necessary for bicubic splines require 8 MB, 32 MB, or 128 MB, depending on the scheme, using double precision floating point numbers.

For 3D DVC, however, two $1024 \times 1024 \times 1024$ images require 2 GB of memory. The coefficients necessary for tricubic splines require 8 GB, 64 GB, or 512 GB, depending on the scheme. This is more memory than most desktop computers have today, so loading the entire image is not feasible. 3D images are typically stored as a series of 2D images, each representing a single slice with constant value of the vertical coordinate z. Rather than attempting to load the entire 3D image, we developed a data structure that loads only those slices that are currently in use. This data structure makes the algorithm scalable to larger problem sizes, rather than being restricted by the amount of available RAM. It also has immediate benefits for parallel computing.

Our current implementation takes 5–20 seconds to compute each correlation point, depending on subset size, image quality, and other settings. Faster processors would reduce that time, but ultimately the cubic growth of 3D image data will exceed what a single processor can process in a reasonable amount of time. To reach our goal of a 100^3 correlation grid with 1,000,000 points, at 5 seconds each, would require 58 days of computing time. Using parallel computing, we aim to reduce this to a single day. Here we present a high level overview of a parallel algorithm for DVC.

Every correlation point is computed independently, apart from using results from neighboring correlation points to start the coarse search. To implement a coarse-grained parallel algorithm, we therefore assign different correlation points to different processors. A key question is how to assign correlation points to processors. In our storage scheme for 3D images, each processor reads only the slices it needs for the current subset, as shown in figure 1. Therefore, assigning correlation points in a plane with the same z coordinate to a single processor will maximize reuse of image data already in memory. This makes the algorithm scalable to large data sets because each processor reads only a fraction of the data, instead of every processor reading and storing the entire data set. Significant issues such as dynamic load balancing and alternative means of parallelization still require investigation.

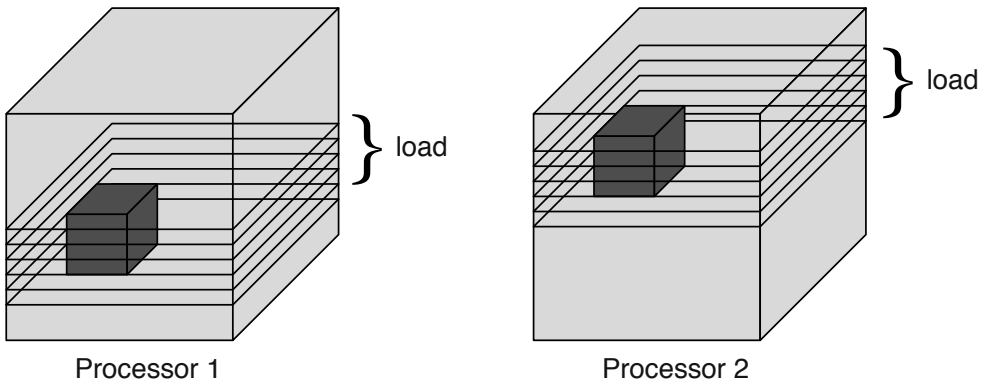

Figure 1: Each processor reads only slices required for its current subset. Different processors work on different subsets in parallel.

6 Results

We demonstrate the application of this improved high performance DVC code to detect the 3D deformation field around a spherical inclusion in a material under uniaxial tension. We use Goodier's analytical solution [7] for the displacement around a spherical rigid inclusion.

First, we do a baseline test between two images without any deformation, to determine the effects of noise

introduced by the scanner and the accuracy of the DVC method. We compute a 20^3 grid of 8000 correlation points, with 20 voxel spacing in all dimensions. The average baseline, i.e., no motion, measured displacements with one standard deviation error bars are $u = -0.084 \pm 0.221$, $v = -0.572 \pm 0.220$, and $w = -1.157 \pm 0.175$. The v and w displacements are greater than the 0.2 standard deviation, indicating they represent an actual rigid body motion, likely caused by mechanical perturbations of the tomograph rotation stage during its 360 degree motion. As a better alternative to simply averaging the baseline DVC results, and as a comparison with the deformation results to follow, we also use a least squares fit to rigid translation and rotations, assuming small angles. Table 2 shows we detected a similar rigid translation as the average results quoted above for all three directions.

After the baseline test, we take the first scan and apply an artificial deformation using the analytical solution for a spherical inclusion, then perform DVC between the first (deformed) and the second (undeformed) scans. We use a least squares fit between the displacements measured with DVC and the exact solution to determine the rigid body motion and the applied load T. The results shown in table 2 agree well with the rigid body motion detected for the baseline scan using the same original pair of images. We also detect the applied tension T with 0.4% accuracy. Figure 2 shows isosurfaces of DVC computed values for u, v, and w in 3D, showing zero displacement along the midplanes of the sphere and a bulge in displacement near the sphere, flattening to a linear displacement field far from the sphere. Note that since the signal to noise ratio is higher for the u values, they are captured much better, but nonetheless the v and w values are also captured in these results.

subset size	u_{rigid}	v_{rigid}	w_{rigid}	θ_x	θ_y	θ_z	T
baseline test							
31^3 voxels	-0.14	-0.43	-1.25	-4.3×10^{-4}	-1.8×10^{-4}	-2.2×10^{-6}	n/a
sphere test							
21^3 voxels	-0.15	-0.46	-1.03	-3.0×10^{-4}	-2.4×10^{-4}	2.5×10^{-5}	1.00408
31^3 voxels	-0.09	-0.48	-1.24	-4.1×10^{-4}	-9.1×10^{-5}	-1.7×10^{-5}	1.00424
41^3 voxels	-0.08	-0.48	-1.26	-4.1×10^{-4}	-5.4×10^{-5}	-6.8×10^{-6}	1.00436

Table 2: Least squares fit of displacements to exact solution, with rigid translation; small angle rotations about x, y, and z axes; and applied tension T. Exact applied tension T is normalized to 1.

7 Summary

We have developed a digital volume correlation method that minimizes twelve degrees-of-freedom, uses spline interpolation, and is scalable to large problem sizes. To make large scale 3D DVC problems tractable we developed and implemented improvements to the DIC/DVC algorithm. An analysis of different basis functions has led us to use either the Hermite or B-spline basis, the choice depending on the specific computer used and ease of implementation. We have shown how to optimize the spline implementation for DVC, for instance, by taking advantage of the fixed-width spacing of image data.

Our algorithm scales to large problem sizes because it reads only those slices required by the current subset. In particular, it is not constrained by the available memory. This layout has further advantages for parallel computing, since each processor can concentrate on a small set of data, without wasting resources duplicating the entire image on every processor.

For our PDMS samples with embedded particles, we achieved an accuracy of 0.2 voxels. We were able to detect and subtract out rigid motion that occurred from mechanical perturbations in the CT scanner. We were able to measure macroscopic quantities accurately, such as the applied load with 0.4% accuracy.

8 Acknowledgments

We are grateful to Charles Mark Bee and the Imaging Technology Group at the Beckman Institute for the use of the Skyscan MicroCT scanner, Prof. Nancy Sottos and Brett Beiermann of the Autonomic Materials Research Group at the Beckman Institute for help preparing PDMS samples, and Prof. Michael Sutton for

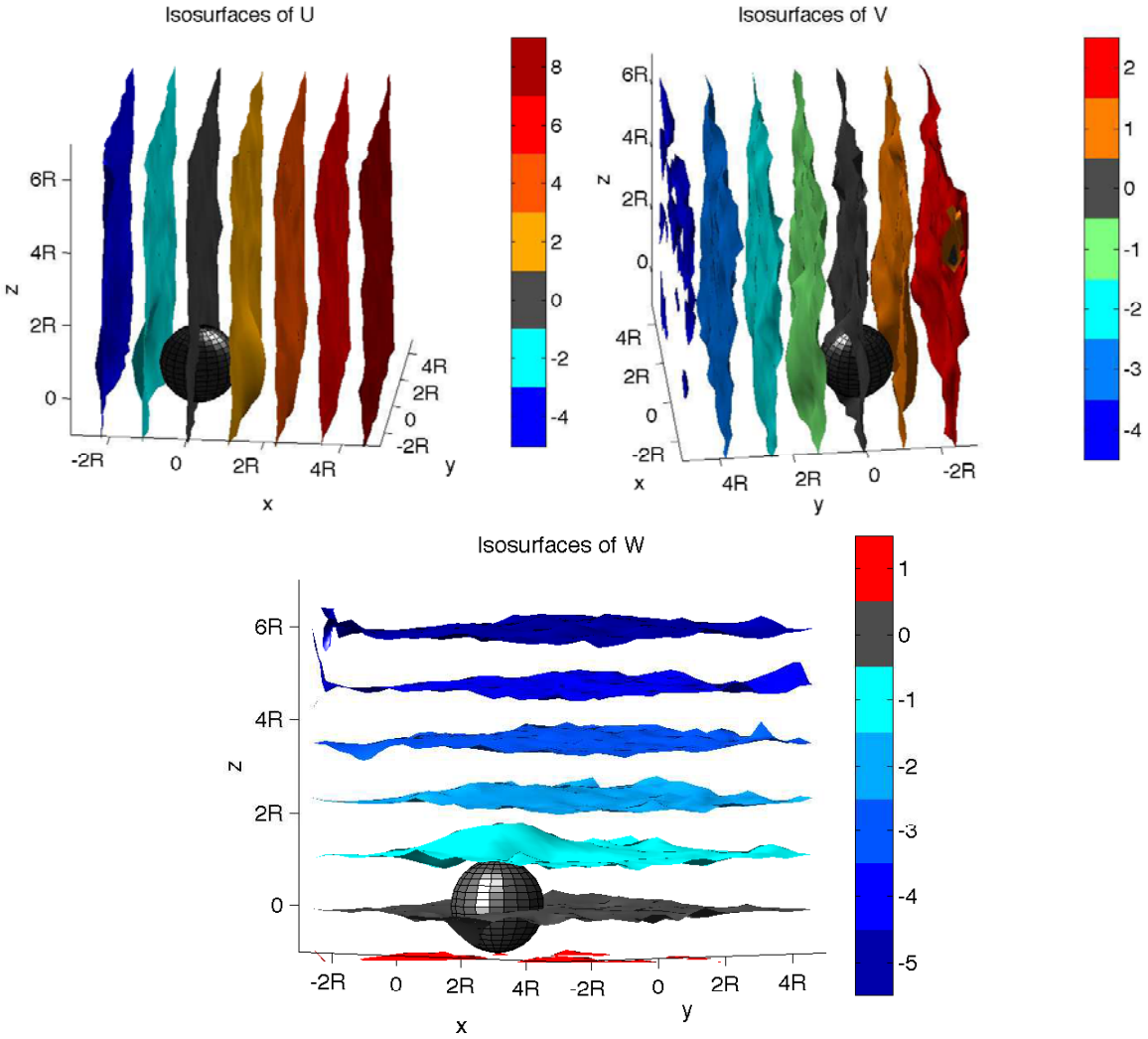

Figure 2: Isosurfaces of u, v, and w displacements, showing how they bulge out near the sphere and tend towards flat surfaces far away from sphere. Sphere has radius R. Results using 41 voxel subset. Applied loading is in x direction.

helpful discussions. This work was supported by the Center for Simulation of Advanced Rockets under contract number B523819 funded by the U.S. Department of Energy, by the Institute for Advanced Computing Applications and Technologies, and by a grant from the University of Illinois research board.

References

[1] B. K. Bay, T. S. Smith, D. P. Fyhrie, and M. Saad. Digital volume correlation: Three-dimensional strain mapping using X-ray tomography. *Experimental Mechanics*, 39:217–226, 1999.

[2] T. Chu, W. Ranson, M. Sutton, and W. Peters. Applications of digital-image-correlation techniques to experimental mechanics. *Experimental Mechanics*, 25:232–244, 1985.

[3] C. de Boor. *A Practical Guide to Splines*. Springer-Verlag, 1978.

[4] P. Dierckx. *Curve and Surface Fitting with Splines*. Oxford University Press, 1993.

[5] C. Franck, S. Hong, S. Maskarinec, D. Tirrell, and G. Ravichandran. Three-dimensional full-field measurements of large deformations in soft materials using confocal microscopy and digital volume correlation. *Experimental Mechanics*, 2007.

[6] A. Germaneau, P. Doumalin, and J. C. Dupré. 3D strain field measurement by correlation of volume images using scattered light: Recording of images and choice of marks. *Strain*, 43:207–218, 2007.

[7] J. N. Goodier. Concentration of stress around spherical and cylindrical inclusions and flaws. *Journal of Applied Mechanics*, 55(7):39–44, 1933.

[8] N. Lenoir, M. Bornert, J. Desrues, P. Bésuelle, and G. Viggiani. Volumetric digital image correlation applied to X-ray microtomography images from triaxial compression tests on argillaceous rock. *Strain*, 43:193–205, 2007.

[9] *MATLAB*. The MathWorks, Inc., Natick, MA, 2009.

[10] J. D. McCalpin. Memory bandwidth and machine balance in current high performance computers. *IEEE Computer Society Technical Committee on Computer Architecture (TCCA) Newsletter*, December 1995.

[11] I. J. Schoenberg. Contributions to the problem of approximation of equidistant data by analytic functions. *Quarterly of Applied Mathematics*, 4:45–99, 1946.

[12] H. W. Schreier, J. R. Braasch, and M. A. Sutton. Systematic errors in digital image correlation caused by intensity interpolation. *Optical Engineering*, 39:2915–2921, 2000.

[13] T. S. Smith, B. K. Bay, and M. M. Rashid. Digital volume correlation including rotational degrees of freedom during minimization. *Experimental Mechanics*, 42:272–278, 2002.

[14] E. Verhulp, B. van Rietbergen, and R. Huiskes. A three-dimensional digital image correlation technique for strain measurements in microstructures. *Journal of Biomechanics*, 37:1313–1320, 2004.

Proceedings of the SEM Annual Conference
June 7-10, 2010 Indianapolis, Indiana USA

Digital X-ray tomography Volume Correlation of Rock Wool During Compression

Eric Maire[a], Jerome Adrien[a], Francois Hild[b], Stephane Roux[b] and Jean-Francois Witz[b]

[a]Universite de Lyon, INSA-Lyon, MATEIS CNRS UMR 5510, F-69621 Villeurbanne, France
[b]Laboratoire de Mecanique et Technologie (LMT-Cachan), ENS Cachan/CNRS/UPMC/UniverSud Paris, F-94235 Cachan Cedex, France

Introduction

X-ray computed microtomography (XCMT) is increasingly being used to visualize the complete microstructure of various materials. One of its main advantages lies in the non-destructive way of obtaining three-dimensional (3D) views of various materials. By analyzing 3D reconstructed pictures, one has access, for instance, to the structure of biological or cellular materials, and sometimes to the way they deform by using in situ experiments analyzed by 3D correlation algorithms. In the present study, the reconstructed scans themselves are used to evaluate full displacement fields.

The aim of the present paper is to analyze a compression test on a stone wool sample by using XCMT performed with a lab tomograph to understand the way in which these materials deform internally. The standardized mechanical performance of these materials refers to a strain level well above the ‘‘elastic” limit. In that case, the strain field appears to be generically non-uniform, and it is important to characterize the regions that concentrate strains, and possibly identify morphological features that are responsible for such strain concentrations as they appear to be stress (and thus performance) limiting. Full 3D strain maps and morphology are therefore extremely valuable. A finite-element based approach to volume correlation [1] is used to measure displacement and evaluate strain fields during a compression test on stone wool. The studied material, the experimental configuration and the imaging system are presented. The experimental results are finally analyzed and discussed.

Material and experiment

Stone wool is an insulating material made of fibers with basalt-like composition. Fig. 1 shows a large scale scanning electron microscope (SEM) view of the studied material. The production process of stone wool, called REX, involves (among other mechanisms) a centrifugal instability of a molten rock layer deposited on rapidly spinning wheels. The destabilization of the viscous layer forms a tadpole whose bulky head is drawn by a hot gas burner and whose tail connected to the spinning wheel produces fibers. In the final product, as can be seen in Fig. 1a, the fibers are mixed with a fraction of so-called ‘‘shot” particles (the initial head of the tadpole). These shot particles are a signature of the production process. They increase the density of the final material, and play no role for insulation. The size of the fibers is mostly in the range 1–10 μm, while the shot particles are of the order of 50–100 μm in diameter. These shot particles will be used as a contrast support for the digital volume correlation. The sample has been compressed in situ in a standard laboratory tomograph for different values of the displacement. At each deformation step, a 3D tomographic scan has been acquired and subsequently used to calculate the displacement field by digital volume correlation using the method described in [2].

T. Proulx (ed.), *Application of Imaging Techniques to Mechanics of Materials and Structures, Volume 4*, Conference Proceedings of the Society for Experimental Mechanics Series 14, DOI 10.1007/978-1-4419-9796-8_40, © The Society for Experimental Mechanics, Inc. 2013

Fig. 1. Large scale SEM view of the analyzed sample showing the fibers and coarse shot particles.

Results

As shown in a previously published paper [2], the calculated displacement fields indicate that strong heterogeneities do exist in the local value of the displacement, with some regions of the sample being highly deformed while much less for some others. To better understand the spatial distribution of the measured displacement pattern, a 3D visualization showing the clustering of large strains in 3D, after thresholding is shown in Fig. 2a. The high strain regions are more or less oriented with an oblique angle compared with the compression direction, which is vertical in this figure. Fig. 2b shows for the same sample, oriented in the same way as in Fig. 2a, the outline of the regions where the density in the initial sample (i.e. before deformation) is low (the threshold is here applied to capture the darkest regions of the tomographic scan). Given the origin of the contrast in these images, low gray levels indicate low densities. The spatial pattern is again complex. The regions do not correspond perfectly but the specific oblique angle is the same in both figures. This indicates that the regions with a high deformation are regions where the density is rather small in the initial state.

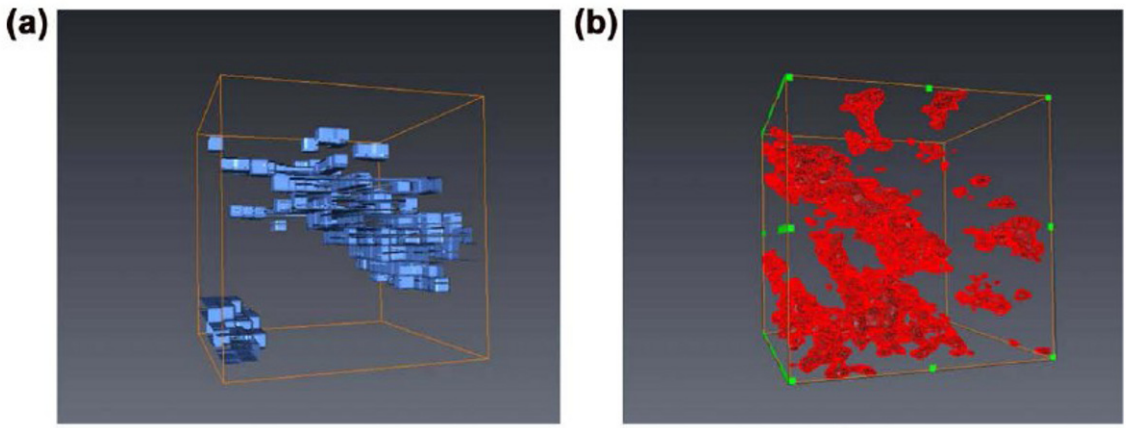

Fig. 2. 3D isosurface to highlight the regions where the measured compression strain is the highest (a), and where the gray level of the reconstructed images are low, i.e. with the smaller density (b). The strains were obtained by using the sample in its first deformed state, and the gray level for the sample in its initial state (i.e. before deformation).

References

[1] Roux S, Hild F, Viot P, Bernard D. Comp Part A (2008) **39**, 1253.
[2] Hild F, Maire E, Roux S, and Witz JF. Acta Materialia (2009) **57**, 3310.

Proceedings of the SEM Annual Conference
June 7-10, 2010 Indianapolis, Indiana USA

Recent progress in digital image correlation

Bing Pan[1,*], Zhaoyang Wang[2]

[1]Institute of Solid Mechanics, Beijing University of Aeronautics & Astronautics, Beijing, 100191, China

[2]Department of Mechanical Engineering, The Catholic University of America, Washington, DC 20064, USA

** Corresponding author: panb04@mails.tsinghua.edu.cn*

Abstract: In this paper, we report the following important progress recently made in the basic theory and implementation of digital image correlation (DIC) for deformation and shape measurement. First, we answer a basic but confusing question to the users of DIC: what is a good speckle pattern for DIC? We present a simple local parameter, called the sum of squared subset intensity gradient, and an easy-to-compute yet effective global parameter, called mean intensity gradient, for quality assessment of the local speckle pattern within each subset and entire speckle pattern, respectively. Second, we provide an overview of various correlation criteria used in DIC for evaluating the similarity of the reference and deformed subsets, and demonstrate the equivalence of three robust and mostly widely used correlation criteria, i.e., a zero-mean normalized cross-correlation (ZNCC) criterion, a zero-mean normalized sum of squared difference (ZNSSD) criterion and a parametric zero-mean normalized sum of squared difference (PZNSSD) criterion with two additional unknown parameters, which elegantly unifies these correlation criteria for pattern matching. Finally, to overcome the limitation of the existing DIC techniques, we introduce a robust and generally applicable reliability-guided DIC technique, in which the calculation path is guided by the ZNCC coefficients of computed points, to determine the genuine full-field deformation or shape of objects containing geometrical discontinuities and discontinuous deformation.

Keywords: Digital image correlation, deformation measurement, speckle pattern

1. Introduction

Digital image correlation (DIC) [1,2] is an effective and practical tool for full-field deformation measurement, which has been commonly accepted and widely used in the field of experimental mechanics. In essence, DIC is an image-based deformation measuring technique based on digital image processing and numerical computation. In the most widely used subset-based DIC technique, a reference square subset with sufficient intensity variations is selected from the reference image (or source image). Then, by means of a predefined criterion and a certain optimization algorithm, the DIC technique searches the deformed image for the target (or deformed) subset, whose intensity pattern is of maximum similarity (or minimum difference) with the reference subset. The differences between the reference subset and the target image yield the subset center's displacement vector.

To obtain reliable and accurate matching, the selected subset must contain sufficient intensity variations to ensure that it can be uniquely and accurately identified in the deformed image, which means that the test object surface has to be covered with speckle pattern (or more exactly, random gray level intensity variation). The speckle pattern deforms together with the specimen surface during deformation, and will be further used as a faithful carrier of surface deformation information in the subsequent matching process of DIC. Generally speaking, the speckle pattern on test object surface can be naturally occurred speckle patterns (i.e., the texture of the object surface) or artificial speckle patterns prepared by spraying white and/or black paints using an airbrush. Although the speckle pattern can be made with easy with various techniques, a fact is that the speckle pattern made by various techniques or by different people may demonstrate distinctly different gray distribution characteristics. As a consequence, the histogram distribution, image contrast and other statistical

T. Proulx (ed.), *Application of Imaging Techniques to Mechanics of Materials and Structures, Volume 4*, Conference Proceedings of the Society for Experimental Mechanics Series 14, DOI 10.1007/978-1-4419-9796-8_41, © The Society for Experimental Mechanics, Inc. 2013

parameters of these speckle patterns may be entirely different. It is observed that the errors of measured displacements using DIC are closely related to the quality of the speckle pattern [3-6]. In other words, the measured displacements of different speckle patterns using DIC technique may be different even though the deformation state of the specimen, the calculation parameters are the same. Consequently, how to assess the quality of the speckle pattern is undoubtedly an important but confusing problem to the users of DIC. In addition, an effective criterion for quality assessment of speckle pattern will provide clear guidance for sample surface preparation and is therefore helpful to the optimal use of the DIC technique.

Also, to evaluate the similarity or difference between the reference and target subsets, a criterion must be defined first before the implementation of DIC. The predefined criterion can be a cross-correlation criterion or a sum of squared difference criterion [1]. Since the matching process of DIC cannot be fulfilled without a predefined criterion, the correlation criterion (or matching criterion) is of fundamental importance in DIC. As pointed out by Sutton MA in a recent book: "*the digital image correlation method owes its name to the use of the normalized cross-correlation criterion* [2]", thus it can be seen that the significance of correlation criterion in DIC technique is self-evident. In literature, various criteria including cross-correlation (CC) criterion, sum of absolute difference (SAD), sum of squared difference (SSD), and parametric sum of squared difference (PSSD) [7] have been designed and used. It should be emphasized here first that the selection of correlation criterion for matching is not an important issue if the intensity of each pixel does not change in the deformed image (though the position of the same pixel changes due to external loading or other reasons). Recently, an evaluation of four SSD criteria for displacement and strain mapping was carried out by Tong W [8], and the result shows that various correlation criteria almost yield same results under the condition that the intensity value of each pixel remains unchanged in the deformed image. However, this ideal condition hardly holds true in practical experiments where the intensity of the deformed image may undergo potential undesired changes. In certain cases, the local intensity within the target image may differ significantly with that of the reference image, and the intensity changes between images recorded at different configurations may be induced by various reasons. For example, the illumination lighting may be uneven and fluctuate with time. The reflectivity of the test specimen surface may also change due to an increase of surface roughness accompanying the increasing strain. In particular, in 3D digital image correlation based on the stereovision principle, the same specimen surface image captured by different cameras may differ with each other due to different imaging orientations [2]. In all the above situations, a robust correlation criterion must be used to accommodate the variations in the intensity of the deformed image; otherwise, significant displacement measurement errors may occur due to the mismatch of intensity change model [7,8]. Based on the consideration of compensating for or eliminating the errors associated with intensity change of the target subset, a zero-mean cross correlation criterion (ZNCC), a zero-mean normalized sum of squared difference (ZNSSD) criterion, and a parametric sum of squared difference (PSSD) criterion with two additional unknown parameters (compared with conventional SSD criterion and called $PSSD_{ab}$ hereafter) have been highly recommended for matching the same subsets located in the reference image and the deformed image, as they are insensitive to the potential scale and offset changes of the target subset intensity. At a first glance, the mathematical expressions of the above-mentioned three correlation criteria are fully different. However, since these three correlation criteria have the same performance against the offset and scale changes in the deformed subset intensity, they must have certain relationships. Accordingly, understanding the transversal relationships among them is undoubtedly an interesting and meaningful issue and also useful to the optimal use of these matching criteria. In this work, we will focus on the ZNCC, ZNSSD and $PSSD_{ab}$ criteria and prove their equivalence.

In the practical implementation of DIC technique, to calculate the displacement components of each point of interest, a square subset centered at the current point is selected and used to determine its corresponding location in the deformed image. Subsequently, the matching is completed through optimizing the predefined correlation criterion. Although the technique is simple in principle and implementation, existing DIC technique

really has at least one evident deficiency. For example, it is evident that the subsets surrounding the points located near or at the boundaries of the specified ROI may contain unwanted or foreign pixels from other regions. Figure 1 shows an example of image correlation computation of a dog-bone specimen acquired in a simple uniaxial tensile test, and it is clear that the subsets centered at boundary points (e.g., the two squares highlighted in red) contain unwanted pixels of background image. In such a case, the local deformation distributions within these subsets are discontinuous and thus cannot be approximated with the commonly used continuous displacement mapping function. As a result, erroneous displacement calculations with relatively very low cross-correlation coefficient occur at these locations. In the existing DIC method, in order to achieve reliable and accurate measurement, these boundary points are either intentionally excluded from calculation or automatically discarded after calculation by use of a global threshold applied to the computed cross-correlation coefficients. In this sense, the existing subset-based DIC technique cannot be taken as a genuine full-field deformation methodology, as the deformation information of the boundary points of ROI is absent.

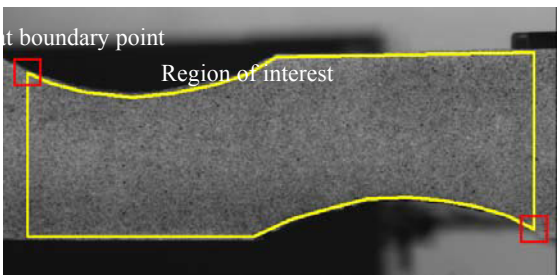

Fig. 1 An example of correlation calculation using conventional subset-based DIC algorithm: the two representative subsets surrounding the boundary points of the specified ROI contain unwanted points of background intensity

In this paper, we will define a novel, simple yet effective global parameter, called mean intensity gradient, for quality assessment of the speckle patterns used in DIC as well as estimating displacement measurement error related to speckle patterns. We will also give the mathematical proof of the equivalence of the ZNCC, ZNSSD and $PSSD_{ab}$ criteria. Besides, to compute the deformation of boundary points of the defined ROI, a modified ZNSSD criterion combined with a reliability-guided scanning scheme guided by ZNCC coefficient is described in the work. It should be noted first that all this progresses have been and will be published shortly and the originality is not claimed here. Interested readers can find more details in refs. [9-12].

2. What is a good speckle pattern for DIC?

Theoretical analysis of the displacement measurement error of DIC has conducted by various researchers. Based on the results obtained by Pan et al. [6] and especially Wang et al.[13], it is found that mean bias error and standard deviation of the computed displacements of DIC is closely related to the following novel global parameter, called mean intensity gradient of speckle pattern (denoted by δ_f), which is of the following form:

$$\delta_f = \sum_{i=1}^{W}\sum_{j=1}^{H}\left|\nabla f\left(\mathbf{x}_{ij}\right)\right| \Big/ \left(W \times H\right) \tag{1}$$

where W and H (in unit of pixels) are image width and height, $\left|\nabla f\left(\mathbf{x}_{ij}\right)\right| = \sqrt{f_x\left(\mathbf{x}_{ij}\right)^2 + f_y\left(\mathbf{x}_{ij}\right)^2}$ is the modulus of local intensity gradient vector with $f_x\left(\mathbf{x}_{ij}\right)$, $f_y\left(\mathbf{x}_{ij}\right)$ are the x- and y-directional intensity derivatives at pixel $\mathbf{x}_{ij}$, which can be simply computed using the commonly used gradient operator (e.g., a central difference algorithm).

Once the mean intensity gradient of the entire speckle pattern is determined, the sum of square of subset

intensity gradient (SSSIG) within a local subset of N by N pixels can be approximated as:

$$\sqrt{\sum_{i=1}^{N}\sum_{j=1}^{N}\left[f_x\left(\mathbf{x}_{ij}\right)\right]^2} \cong N\times\delta_f \tag{2}$$

It is obvious that a large subset size leads to more accurate approximation of Eq.(2). It is also shown in ref.[9] that both the mean bias error and standard deviation error of the estimated displacement are in inverse proportion to the SSSIG value of the subset according to the following relationships.

$$E\left(u_e\right) \cong \frac{\sum_{i=1}^{N}\sum_{j=1}^{N}\left[-h\left(\mathbf{x}_{ij}\right)\cdot f_x\left(\mathbf{x}_{ij}\right)\right]+\left(1-2\tau_x\right)\cdot N^2\cdot\sigma^2}{\sum_{i=1}^{N}\sum_{j=1}^{N}\left[f_x\left(\mathbf{x}_{ij}\right)\right]^2} \tag{3}$$

$$std(u_e) \cong \frac{\sqrt{2}\sigma}{\sqrt{\sum_{i=1}^{N}\sum_{j=1}^{N}\left[f_x\left(\mathbf{x}_{ij}\right)\right]^2}} \tag{4}$$

Thus, it is easy to find that the displacement measurement accuracy (i.e., mean bias error) and precision (i.e., standard deviation error) of DIC are in inverse proportion to the product of the subset size *N* and the mean intensity gradient of the speckle pattern. Since mean intensity gradient is a statistical parameter of the speckle pattern and directly affects the displacement measurement error of DIC when the subset size is fixed, it can be used as an effective global parameter for the quality assessment of the whole speckle pattern.

3. Equivalence of the correlation criteria used for pattern matching

In this section, the relationships among the ZNCC, ZNSSD, and $PSSD_{ab}$ criteria are described. It should be noted that the derivations can also be easily applied to other simpler correlation criteria, and similar relationships can be established. As we know, the correlation coefficient is computed between the reference subset and target subset. For a square subset containing *n* (=*N* × *N*) discrete pixels, let $f(x_i, y_i)$ and $g(x'_i, y'_i)$ denote the gray values of the *i*th pixel of the reference subset and the target subset, respectively. For the purpose of notation brevity and clarity, the gray values of $f(x_i, y_i)$ and $g(x'_i, y'_i)$ are further simplified as f_i and g_i [10]. The lower and upper bounds of summation are also omitted in all the following derivations for notation brevity.

First, the mathematical definitions of a ZNCC, a ZNSSD and a $PSSD_{ab}$ are provided in Eqs.(5),(6) and (7):

$$C_{ZNCC} = \frac{\sum \overline{f}_i \overline{g}_i}{\sqrt{\sum \overline{f}_i^2 \sum \overline{g}_i^2}} \tag{5}$$

where $\overline{f}_i = f_i - \overline{f}$ and $\overline{g}_i = g_i - \overline{g}$.

The ZNSSD criterion, which is insensitive to both offset and scale changes of the intensity of the target subset [8,14], is defined as

$$C_{ZNSSD} = \sum\left(\frac{\overline{f}_i}{\sqrt{\sum \overline{f}_i^2}} - \frac{\overline{g}_i}{\sqrt{\sum \overline{g}_i^2}}\right)^2 \tag{6}$$

The generalized $PSSD_{ab}$ coefficient considers two unknown parameters *a* and *b* to account for both the offset and scale changes of the intensity of target subset [1,2,7], and it is given as

$$C_{PSSDab} = \sum\left(af_i + b - g_i\right)^2 \tag{7}$$

3.1 From ZNSSD criterion to ZNCC criterion

Recently, it has been shown that the ZNSSD coefficient is directly related to the ZNCC coefficient [8,14] as follows,

$$C_{ZNSSD} = \sum\left(\frac{\overline{f}_i}{\sqrt{\sum \overline{f}_i^2}} - \frac{\overline{g}_i}{\sqrt{\sum \overline{g}_i^2}}\right)^2 = \sum\left(\frac{\overline{f}_i^2}{\sum \overline{f}_i^2} - 2\frac{\overline{f}_i\overline{g}_i}{\sqrt{\sum \overline{f}_i^2}\sqrt{\sum \overline{g}_i^2}} + \frac{\overline{g}_i^2}{\sum \overline{g}_i^2}\right)$$
$$= 2 - 2\frac{\sum \overline{f}_i\overline{g}_i}{\sqrt{\sum \overline{f}_i^2}\sqrt{\sum \overline{g}_i^2}} = 2\left(1 - C_{ZNCC}\right) \tag{8}$$

Eq. (8) evidently indicates that the ZNSSD and ZNCC criteria are equivalent. In practice, because the computation of ZNSSD coefficient is relatively easier than that of the ZNCC coefficient, ZNSSD criterion is usually employed.

3.2 From PSSDab criterion to ZNCC criterion

Although the $PSSD_{ab}$ coefficient defined by Eq. (7) has a substantially different form from the ZNCC coefficient defined by Eq. (5), we will show below that the $PSSD_{ab}$ criterion is equivalent to the ZNCC criterion.

By minimizing the $PSSD_{ab}$ coefficient with respect to *a* and *b*, we have

$$\begin{cases} \dfrac{\partial C_{PSSDab}}{\partial a} = 0 \\ \dfrac{\partial C_{PSSDab}}{\partial b} = 0 \end{cases} \Rightarrow \begin{cases} 2\sum\left[\left(af_i + b - g_i\right)f_i\right] = 0 \\ 2\sum\left(af_i + b - g_i\right) = 0 \end{cases} \tag{9}$$

Solving Eq. (9), the optimal estimates for *a* and *b* are determined as

$$a = \frac{\sum\left[\left(g_i - b\right)f_i\right]}{\sum f_i^2} \tag{10}$$

$$b = \frac{\sum\left(g_i - af_i\right)}{\sum 1} = \frac{\sum\left(g_i - af_i\right)}{n} = \overline{g} - a\overline{f} \tag{11}$$

Substituting Eqs. (10)(11) into Eq. (9), the unknown parameter *a* and *b* can be determined as

$$a = \frac{\sum \overline{g}_i\overline{f}_i}{\sum \overline{f}_i^2} \tag{12}$$

$$b = \overline{g} - \frac{\sum \overline{g}_i\overline{f}_i}{\sum \overline{f}_i^2}\overline{f} \tag{13}$$

By substituting Eqs. (12) and (13) into Eq. (7), the $PSSD_{ab}$ coefficient now can be further denoted as.

$$
\begin{aligned}
C_{PSSDab} &= \sum\left(af_i + b - g_i\right)^2 = \sum\left(af_i + \overline{g} - a\overline{f} - g_i\right)^2 \\
&= \sum\left(\frac{\sum \overline{g}_i\overline{f}_i}{\sum \overline{f}_i^2}\overline{f}_i - \overline{g}_i\right)^2 = \sum\left[\left(\frac{\sum \overline{g}_i\overline{f}_i}{\sum \overline{f}_i^2}\right)^2 \overline{f}_i^2 - 2\frac{\sum \overline{g}_i\overline{f}_i}{\sum \overline{f}_i^2}\overline{f}_i\overline{g}_i + \overline{g}_i^2\right] \\
&= -\frac{\left(\sum \overline{g}_i\overline{f}_i\right)^2}{\sum \overline{f}_i^2} + \sum \overline{g}_i^2 = \sum \overline{g}_i^2\left[1 - \frac{\left(\sum \overline{g}_i\overline{f}_i\right)^2}{\sum \overline{g}_i^2 \sum \overline{f}_i^2}\right] = \sum \overline{g}_i^2\left(1 - C_{ZNCC}{}^2\right)
\end{aligned}
\tag{14}
$$

Although the $PSSD_{ab}$ criterion doesn't have a linear relationship with the ZNCC criterion as explicitly shown in Eq.(14), mathematic deduction will show that their partial derivatives with respect to the desired deformation parameter vector has a simple linear relationship considering if we take $\sum \overline{g}_i^2$ as constant. Besides, upon a successfully subset matching using either the $PSSD_{ab}$ or ZNCC criteria, the value of $\sum \overline{g}_i^2$ can be readily determined by virtue of certain interpolation scheme (e.g., a bicubic interpolation).

4. Genuine full-field deformation measurement with reliability-guided DIC

4.1 Modified correlation criterion for boundary points

As mentioned earlier, the subsets centered at the points near the boundaries of ROI may contain less than (2*M* +1) × (2*M*+1) pixels as schematically illustrated in Fig.1. Because the valid points within ROI have already been labeled as 1 in a binary mask M_v after specifying the ROI, they can be easily identified and therefore used in the following calculation. Accordingly, the following modified ZNSSD criterion is defined for the boundary points to evaluate the similarity between the reference and target subsets [12]:

$$
C_{ZNSSD}(\mathbf{p}) = \sum_{x,y\in S}\left[\frac{f(x,y) - f_m}{\sqrt{\sum_{x,y\in S}[f(x,y) - f_m]^2}} - \frac{g(x',y') - g_m}{\sqrt{\sum_{x,y\in S}[g(x,y) - g_m]^2}}\right]^2 \tag{16}
$$

where *S* denotes the set of valid points within the interrogated subset, $f_m = \frac{1}{N_v}\sum_{x,y\in S}[f(x,y)]$ and $g_m = \frac{1}{N_v}\sum_{x,y\in S}[g(x',y')]$ are the mean intensity values of the reference and target subsets, respectively. N_v is the number of valid points within the subset.

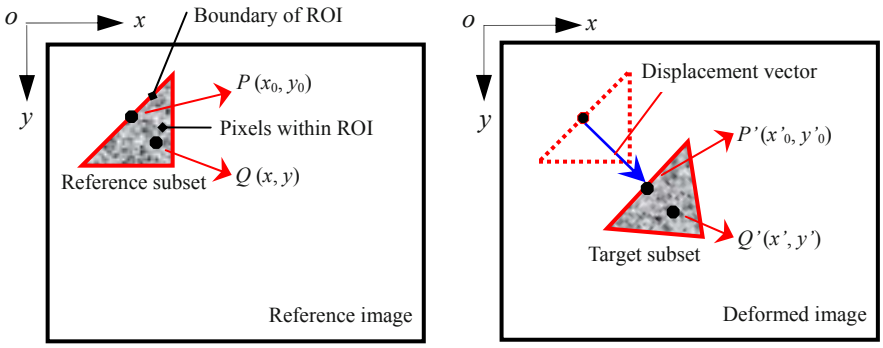

Fig. 2 Example of tracking a subset centered at a boundary point

Using the NR algorithm [14,15,16], the modified ZNSSD correlation coefficient can be optimized to minimum to determine the desired deformation parameter vector **p** provided that the number of valid points within the subset is larger than the number of desired unknowns (this can be always satisfied in real cases).

Because the pixels used for correlation coefficient optimization is less than (2M +1) × (2M+1) pixels, the accuracy and precision of the determined displacements is normally a little lower than that computed with a full square subset.

4.2 Reliability-guided digital image correlation

In the existing standard DIC algorithm, a ROI is defined and the computation generally starts from the upper left point of the ROI. Then, the correlation calculation is carried out point by point along each row or column. According to the continuous deformation assumption, the determined deformation parameters of the former point are used as the initial guess of the current point. This simple scanning strategy is normally quite effective and very easy to implement when a simple rectangular ROI is defined. However, in many practical applications, the test specimen may have complex shape containing various geometric discontinuities. In these cases, an irregular ROI, rather than a rectangular ROI, is normally specified in the reference image.

If a complex ROI is defined in the reference image to approximate the complex shape of the test object, the initial guess for some points will be a troublesome and challenging problem. In this case, if one point is wrongly computed, the incorrect result of deformation parameters will be passed on to the next point and lead to a propagation of error. In this work, a simple yet effective scanning strategy guided by the ZNCC coefficient of computed points is used for reliable initial guess transfer between consecutive points. Since the ZNCC coefficient value represents the reliability degree of the correlation analysis, the method is also called reliability-guided DIC method in our recent work [13]

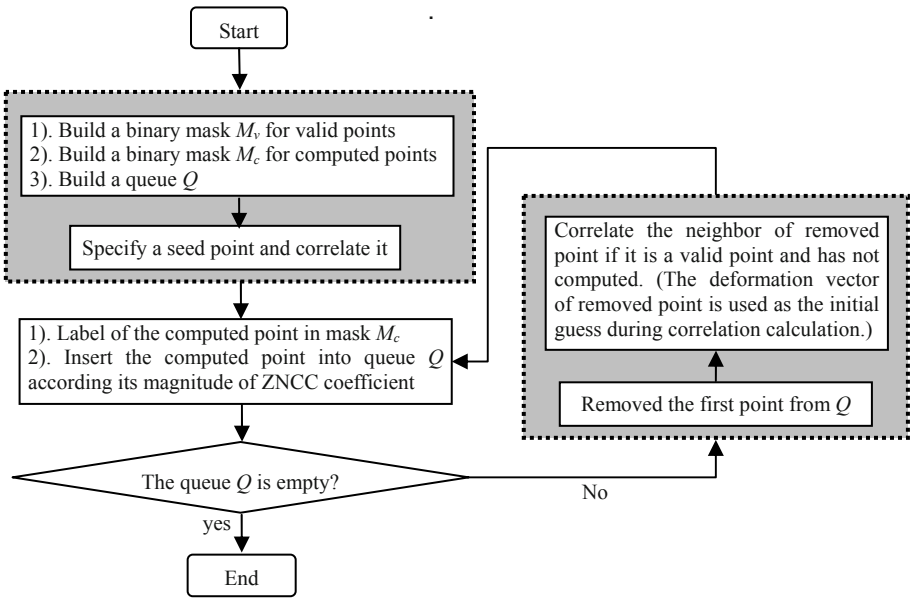

Fig. 3 Flowchart of the scanning strategy used in RG-DIC method

To clearly indicate the implementation procedure of the RG-DIC algorithm, a flowchart is plotted as shown in Fig. 3. Before the implementation of the RG-DIC method, a queue Q and two binary masks M_v and M_c with the same size as the digital images are built. After a point has been analyzed, it is subsequently inserted into the queue Q according to the magnitude of its correlation coefficient. The binary mask M_v is to identify the valid points (set to 1) to be included in the analysis and the invalid points (set to 0) to be excluded. The other binary mask M_c denotes the valid points that have been computed. The initial value of each pixel in M_c is set to 0; if one point has been computed, its corresponding position in M_c is set to 1. The implementation procedure of the proposed RG-DIC method comprises the following three steps:

Step 1: Specify a seed point (or starting point) in the reference image, which can be accurately and reliably searched in the deformed image. The deformation parameters and the ZNCC coefficient of the single seed point can be computed using the NR method. Afterwards, the correlated seed point is marked as 1 in the binary

mask Mc and inserted into queue *Q*.

Step 2: If the queue *Q* is not empty, remove the first point, which has the maximum ZNCC coefficient, from the top of the queue. Next, analyze each of its four (or eight) neighboring points: if it is a valid point (i.e., M_v =1) and has not been computed (i.e., M_c =0), it will then be computed using the NR method to obtain its deformation parameters and ZNCC correlation coefficient. Note that the computed deformation parameters of the removed point are used as initial guess for its neighbors. Then, each of the just calculated points is labeled as 1 in the binary mask M_c and inserted into the queue *Q* according to its ZNCC coefficient value.

Step 3: Repeat step 2 until the queue *Q* is empty, which means that all the valid points in the ROI have been computed and the image correlation computation is completed.

From the above description, it can be seen that the correlation analysis is always performed from the points with highest ZNCC coefficient to the points with lowest ZNCC coefficient. If a point has been incorrectly computed with a low ZNCC coefficient due to decorrelation or other reasons, the computation of its neighbors will be postponed to near the end of the processing. As a result of this approach, the unreliable results of these points will not affect the correlation of its neighbors, and thus, the possible error propagation of existing algorithm can be avoided.

4.3 Experimental verification

To verify the effectiveness and practicality of the proposed method, one representative image pairs of specimens with relatively complex shapes will be processed to reproduce the genuine full-field displacement fields within the specified ROI. In the following calculation, the NR algorithm with first-order displacement mapping function is employed to optimize the ZNSSD criterion to get the desired deformation parameters for each point; the subset used is 33×33 pixels and the grid step (i.e., the distance between neighboring calculation points) is set to 2 pixels.

In the validation test, a dog-bone shape specimen made of alumina with a size 2mm×8mm×0.13mm is used. Prior to the experiment, an artificial speckle pattern was made on the specimen by spraying white and black paints on its surface. The specimen was clamped tightly at both ends and the corresponding image was recorded as reference image. Afterwards, the horizontal uniaxial tensile loading was exerted on the right side and a deformed image was recorded. The image pair shown in Fig.4 will be processed with the proposed improved DIC technique to extract the full-field displacement fields.

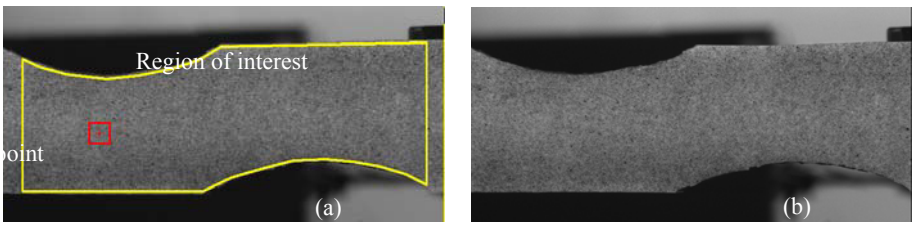

Fig. 4 Experimental images of a dog-bone specimen subjected to uniaxial tensile loading: (a) reference image, (b) deformed image. The inner square illustrates the arbitrarily selected seed point and its subset.

Since the specimen is of relatively complex shape with two semicircular cut-outs, the ROI is approximated with a polygon as shown in Fig.4(a). For the points within an irregular ROI, the conventional DIC method is prone to yield incorrect results at some locations. Using the proposed approach, the calculation starts from the seed point (the seed point and its surrounding subset are plotted in red in Fig. 4) and is then guided by the ZNCC coefficients of computed points. Figure 5 illustrates the computed full-field *u*-displacement, *v*-displacement and ZNCC coefficient distributions with the proposed technique and the existing standard technique. The computed contour maps have been imposed on the ROI of the reference image for an intuitive comparison. By use of the modified ZNSSD correlation coefficient defined in Eq. (5) and the ZNCC coefficient

determined by the rightmost side of Eq. (2), the algorithm can automatically discard the invalid points within each subset surrounding the boundary points. As a result, the displacements of the points located at or near the boundaries of ROI can be reliably and accurately determined, as clearly seen in Figs.5 (a) and (c). Also, from the ZNCC coefficient distributions shown in Fig.5 (e), it can be seen that the ZNCC coefficients of the boundary points are almost the same as those of the central points computed with a regular square subset. The relatively high ZNCC coefficients of the boundary points help to clearly prove the validity and practicality of the proposed approach. In contrast, the computational results obtained by using the existing standard DIC technique with the common ZNCC criterion are shown in the right side of Figs. 5. It is evident from Figs.5(b) and (d) that the computed *u*- and *v*-field displacements for the points located near the ROI boundaries are unreliable. The ZNCC coefficients of these boundary points shown in Fig.5 (f) are much lower than those in Fig. 5 (e), which clearly proves the advantage of the proposed technique.

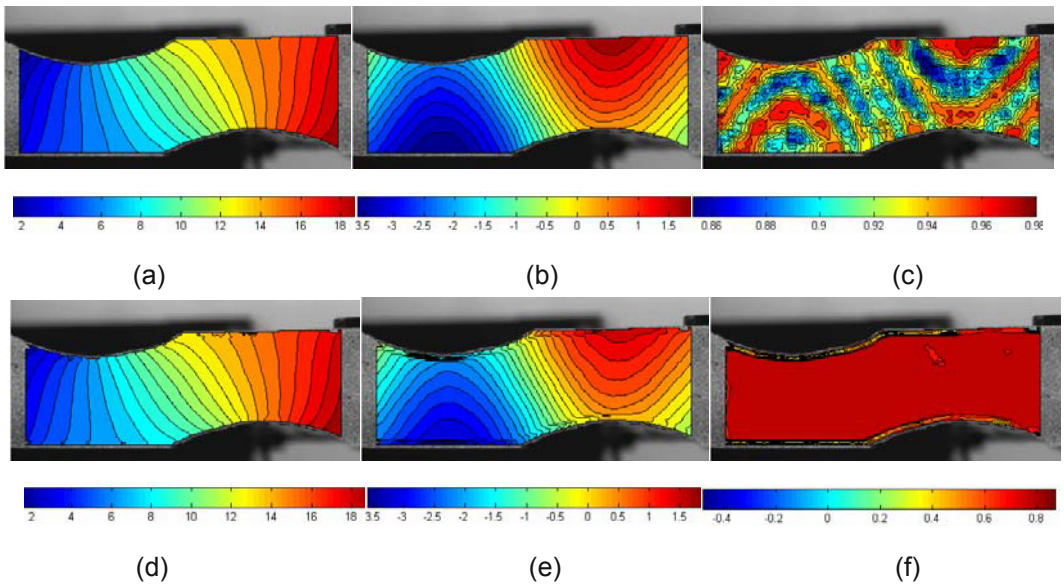

Fig. 5 Comparison of the results obtained with the proposed technique and existing technique: (a)(b) u-displacement field, (c)(d) v-displacement field, and (e)(f) ZNCC

5. Conclusion

In this paper, we report the following important progress recently made in the basic theory and implementation of subset-based DIC for deformation and shape measurement. First, in order to answer the basic but confusing question of what is a good speckle pattern for DIC, we present an easy-to-compute yet effective global parameter, called mean intensity gradient, for quality assessment of the local speckle pattern within each subset and entire speckle pattern. Second, we demonstrate the equivalence of three robust and mostly widely used correlation criteria, i.e., a ZNCC criterion, a ZNSSD criterion and a $PSSD_{ab}$ criterion with two additional unknown parameters, which elegantly unifies these correlation criteria for pattern matching. Finally, to overcome the limitation of the existing DIC techniques, we introduce a robust and generally applicable reliability-guided DIC technique, in which the calculation path is guided by the ZNCC coefficients of computed points, to determine the genuine full-field deformation or shape of objects containing geometrical discontinuities and discontinuous deformation. The effectiveness of the improved DIC technique is also demonstrated by processing experimental images with complex shape.

References

[1] Pan B, Qian KM, Xie HM, Asundi A. Two-dimensional Digital Image Correlation for In-plane Displacement and Strain Measurement: A Review. Measurement Science and Technology. 2009, 20: 062001.

[2] Sutton MA, Orteu JJ, Schreier HW. Image correlation for shape, motion and deformation measurements.

Springer, 2009.

[3] Lecompte D, Smits A, Bossuyt S, et al. Quality assessment of speckle patterns for digital image correlation. Opt Lasers Eng 2006; 44(11): 1132-1145.

[4] Haddadi H, Belhabib S. Use of rigid-body motion for the investigation and estimation of the measurement errors related to digital image correlation technique. Opt Lasers Eng 2008; 46:185-96.

[5] Sun YF, Pang HJ. Study of optimal subset size in digital image correlation of speckle pattern images. Opt Lasers Eng 2007; 45: 967-974.

[6] Pan B, Xie HM, Wang ZY, Qian KM and Wang ZY. Study on Subset Size Selection in Digital Image Correlation for Speckle Patterns. Opt Exp, 2008, 16(10): 7037-7048.

[7] Pan B, Asundi A, Xie HM, Gao JX. Digital Image Correlation using Iterative Least Squares and Pointwise Least Squares for Displacement Field and Strain Field Measurements. Opt Lasers Eng 2009; 47(7-8):865-874.

[8] Tong W. An evaluation of digital image correlation criteria for strain mapping applications. Strain, 2005, 41(4): 167-175.

[9] Pan B, Lu ZX, Xie HM. Mean intensity gradient: an effective global parameter for quality assessment of the speckle patterns used in digital image correlation. Optics and Lasers in Engineering. 2010, 48(4): 469-477.

[10] Pan B, Xie HM, Wang ZY. Equivalence and efficiency of digital image correlation criteria. Experimental Mechanics. (Under review).

[11] Pan B, Wang ZY, Lu ZX. Genuine full-field deformation measurement of an object with complex shape using reliability-guided digital image correlation. Optics Express.

[12] Pan B. Reliability-guided Digital Image Correlation for Image Deformation Measurement. Applied Optics, 2009, 48(8): 1535-1542.

[13] Wang YQ, Sutton MA, Bruch HA and Schreier HW. Quantitative error assessment in pattern matching: effects of intensity pattern noise, interpolation, strain and image contrast on motion measurement. Strain. 2009; 45: 160-178.

[14] Pan B, Xie HM, Guo ZQ, Hua T. Full-field strain measurement using a two-dimensional Savitzky-Golay digital differentiator in digital image correlation. Opt Eng, 2007, 46(3): 033601.

[15] Bruck. HA, McNeil SR, Sutton MA, Peters WH. Digital Image Correlation Using Newton-Raphson Method of Partial Differential Correction. Exp Mech, 1989, 29(3): 261-267.

[16] Pan B, Xie HM, Xu BQ, Dai FL. Performance of sub-pixel registration algorithms in digital image correlation. Measurement Science & Technology, 2006,17(6): 1615-1621.

Proceedings of the SEM Annual Conference
June 7-10, 2010 Indianapolis, Indiana USA

Analysis of Fractured Samples with Digital Volume Correlation

F. Hild,[a] J-Y. Buffière,[b] A. Gravouil,[c] N. Limodin,[b] J. Réthoré,[c] S. Roux,[a] W. Ludwig[b,d]

[a]LMT-Cachan, ENS Cachan / CNRS / Université Paris 6 / PRES UniverSud Paris,
61 avenue du Président Wilson, F-94235 Cachan Cedex, France
Email: hild@lmt.ens-cachan.fr
[b]MATEIS, Université de Lyon, INSA-Lyon / CNRS, Villeurbanne, France
[c]LaMCoS, Université de Lyon INSA-Lyon / CNRS, Villeurbanne, France
[d]ESRF, Grenoble, France

ABSTRACT

Synchrotron X-ray tomography was used to monitor *in situ* three dimensional (3D) fatigue crack propagation in a nodular graphite cast iron. Direct image analysis allows for the retrieval of the successive positions of the crack front, and the detection of local crack retardation, while volume correlation enables for the measurement of displacement fields in the bulk of the specimen. Stress Intensity Factors (SIF) are extracted from the measured displacement fields. It is possible to link the non propagation of a crack with crack closure in COD maps or with a local value of the measured SIF range.

INTRODUCTION

The availability of third generation synchrotrons has fostered the development of high resolution (voxel size around 1 µm) X-ray micro-tomography in the last 15 years [1]. A spatial resolution close to that of an optical microscope can now be achieved in 3D that re-opens wide areas of research. One of those areas is the characterization of three dimensional fatigue crack propagation.

In this work we focus on the effect of closure on 3D crack propagation. 3D displacement fields, COD maps, and SIFs have been obtained *in situ* by combining Digital Volume Correlation (DVC) and synchrotron X-ray tomography at different stages of fatigue life [2]. This complete 3D crack characterization in combination with image analysis and post-failure topography measurements allows for an interpretation of crack propagation / arrest. It is shown that a non uniform closure level along the crack front induces asymmetric crack arrest / propagation.

MATERIAL AND METHODS

The material studied herein is a ferritic nodular graphite cast iron (Fe - 3.4C - 2.6Si - 0.05Mg - 0.19Mn wt.%) containing a uniform distribution of nearly spherical graphite nodules (average diameter: 50 µm). The graphite nodules are easily imaged by tomography and used as natural markers for volume correlation of the 3D reconstructed images.

The tomography experiment was performed on ID19 beamline at the European Synchrotron Radiation Facility (ESRF) in Grenoble, France. A specially designed fatigue machine allowing for *in situ* loading and high frequency cycling of the specimens was used [3], see Figure 1. Small hourglass pre-cracked fatigue samples cut from larger specimens were used (see Reference [2] for a detailed description of the experiment). A 5.06 µm voxel size was chosen. This value, which is one order of magnitude larger than the best resolution

T. Proulx (ed.), *Application of Imaging Techniques to Mechanics of Materials and Structures, Volume 4*, Conference Proceedings of the Society for Experimental Mechanics Series 14, DOI 10.1007/978-1-4419-9796-8_42, © The Society for Experimental Mechanics, Inc. 2013

available at ID19, is much smaller than the graphite nodule average size in order to allow for good quality images to be obtained while it is also large enough for the size of the region of interest, focused around the crack, to be only 340 × 340 × 512 voxels in size. This limited data size enabled for DVC measurements to be performed on line during the tomography experiment.

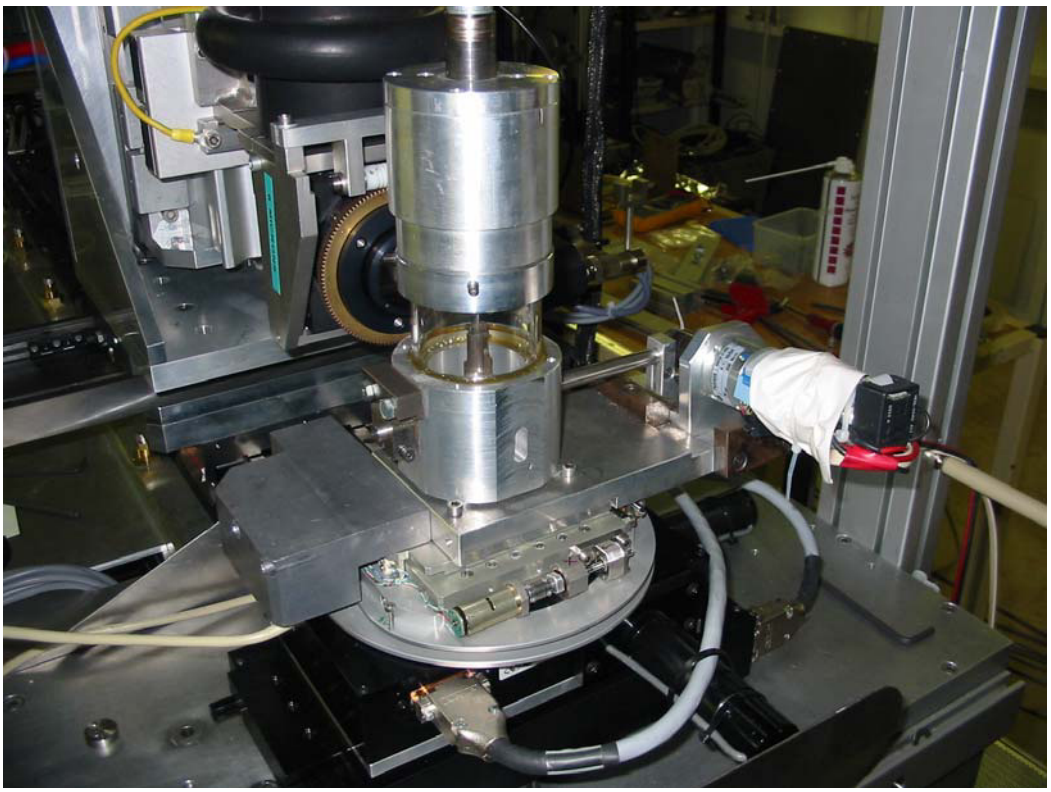

Figure 1. Experimental setup to perform in situ experiments.

At the beginning of the experiments scans were acquired at intermediate loading steps ranging between a minimum and a maximum load (R = 0.1). Then during the *in situ* fatigue experiment, scans were recorded at different time intervals with the specimen held under maximum load. When crack growth was detected in these images, another complete loading / unloading sequence was recorded. The fatigue experiment was conducted until the unbroken ligament became too short for further crack propagation.

DIGITAL VOLUME CORRELATION

3D displacements of any voxel in the reconstructed 3D volume are assessed by using a volume correlation technique. The principle of DVC is to analyze two images of the same specimen under different loading conditions, and to determine the displacement field in the bulk of the specimen by searching for the best match between the images. In the present case, 3D reconstructed volumes are considered, and 8-node cubic elements defined on a 3D mesh (tri-linear functions of x, y and z) are chosen (it is designated as C8-DVC [4]).

A Region Of Interest of 288 × 288 × 288 voxels was centered in the original 3D image. Elements with a 16-voxel edge were chosen as a good compromise between displacement uncertainty and spatial resolution of the measured displacement fields. For the selected element size, the displacement uncertainty was assessed to be about 0.04 voxel [5].

For a given loading / unloading cycle, correlation was performed between the image obtained at the minimum load of the current cycle and that at the load for which the displacement field was sought. However, for the images that were obtained at different time intervals at the maximum load of a given cycle only, using the reference image of the previous loading cycle was thought to be accurate enough, provided that the crack growth remained limited in the interval.

Due to the presence of the crack, the image obtained under higher load, i.e. the deformed image, cannot be perfectly matched to the reference image once it has been corrected for by the measured displacement field. The difference is the residual error that directly provides a 3D image of the crack surface [2]. Measurement of

the SIF along the crack front was carried out using a method introduced by Hamam et al. [6] and adapted to 3D images [7]. The residual error is used to retrieve the crack position while the 3D displacement fields obtained with DVC are fitted in each plane orthogonal to the crack front with relevant mechanical solutions in order to extract K_I, K_{II} and K_{III} SIF values along the crack front [2].

RESULTS AND ANALYSIS

In the specimen investigated, the crack has initially a fairly constant length throughout the sample thickness (Figure 2). However in spite of this limited variation in crack length, the measured SIF value increased in a markedly different way from the "short" to the "long" crack side (10 to 15 MPa√m respectively). During the first fatigue cycles, this large variation in ΔK_I along the crack front resulted in a large variation in crack growth rates with a crack that grew rapidly on the long crack side, while it was pinned on the short crack side where the ΔK_I value is locally below the crack growth threshold (~ 10 MPa√m). As shown in Figure 2, the crack propagation required 3,000 cycles to start on the short crack side. This corresponded to a local value of about 12 MPa√m for ΔK_I, i.e. a value close to that used for fatigue pre-cracking. Then, the difference in crack growth rates between both sides of the specimen progressively reduced.

An analysis of crack topography was performed to assess the possible influence of the roughness of the crack surfaces on crack propagation. After the fatigue tests, the specimens were broken in bending to allow for their analysis in a laser profilometer.

This analysis revealed a significant step of 85-µm in height, i.e. larger than the average size of the graphite nodules, on the short crack side. This step was inherited from the larger pre-cracked sample and the reasons for its occurrence could not be guessed from the observation of the microstructure inside the small tomography sample. However, it is clear that this asperity affected the propagation of the crack as there is a strong correlation between the crack front region where the crack was arrested for almost 3,000 cycles and this bifurcation in the crack path.

It is expected that the presence of the step in the crack plane induces mode II / mode III displacements with corresponding non-zero K_{II} / K_{III} values that have a shielding effect on mode I opening.

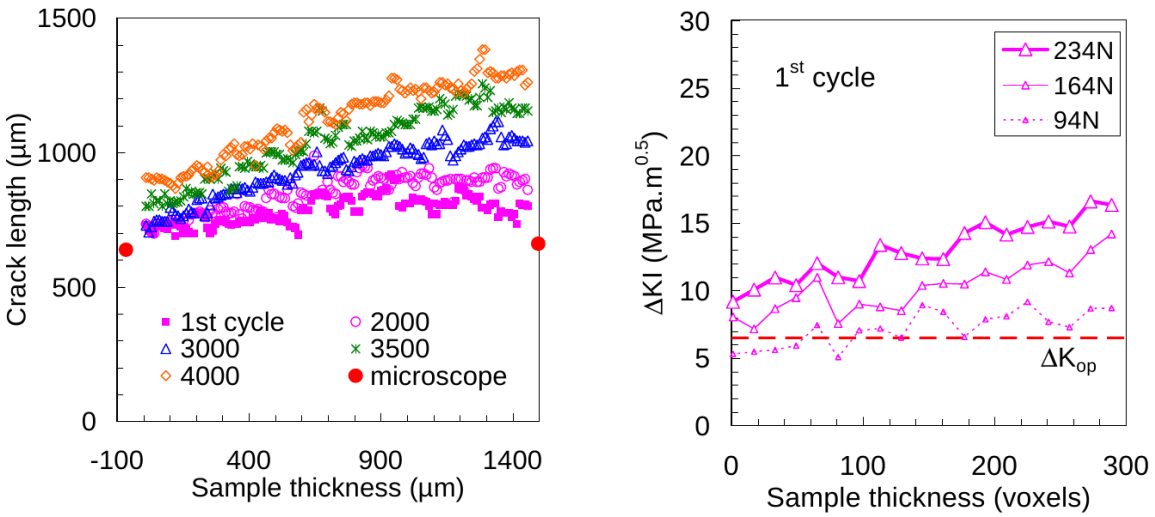

Figure 2. Crack front location as a function of fatigue cycles (left). Variation of the mode I stress intensity factor along the crack front for the first fatigue cycle for three different levels (right).

ACKNOWLEDGMENTS

This work was funded under the grant ANR-09-BLAN-0009-01 (RUPXCUBE Project). It was also made possible by an ESRF grant for the experiment MA-501 on beamline ID19.

REFERENCES

[1] S. R. Stock (2008) Recent advances in X-Ray microtomography applied to materials. Int. Mat. Rev. **53** [3], 129-181.

[2] J. Rannou, N. Limodin, J. Réthoré, A. Gravouil, W. Ludwig, M.-C. Baïetto-Dubourg, J.-Y. Buffière, A. Combescure, F. Hild and S. Roux (2010) Three dimensional experimental and numerical multiscale analysis of a fatigue crack. Comp. Meth. Appl. Mech. Eng. **199**, 1307-1325.

[3] J.-Y. Buffière, E. Maire, J. Adrien, J.-P. Masse and E. Boller (2010) In Situ Experiments with X ray Tomography: an Attractive Tool for Experimental Mechanics. Exp. Mech. **50** [3], 289-305.

[4] S. Roux, F. Hild, P. Viot and D. Bernard (2008) Three dimensional image correlation from X-Ray computed tomography of solid foam. Comp. Part A **39** [8], 1253-1265.

[5] N. Limodin, J. Réthoré, J.-Y. Buffière, F. Hild, S. Roux, W. Ludwig, J. Rannou and A. Gravouil (2010) Influence of closure on the 3D propagation of fatigue cracks in a nodular cast iron investigated by X-ray tomography and 3D Volume Correlation. Acta Mat., doi:10.1016/j.actamat.2010.01.024.

[6] R. Hamam, F. Hild and S. Roux (2007) Stress intensity factor gauging by digital image correlation: Application in cyclic fatigue. Strain **43**, 181-192.

[7] N. Limodin, J. Réthoré, J.-Y. Buffière, A. Gravouil, F. Hild and S. Roux (2009) Crack closure and stress intensity factor measurements in nodular graphite cast iron using 3D correlation of laboratory X ray microtomography images. Acta Mat. **57** [14], 4090-4101.

Proceedings of the SEM Annual Conference
June 7-10, 2010 Indianapolis, Indiana USA

Long term condition monitoring of tapestries using image correlation

Author: J. M. Dulieu-Barton, School of Engineering Sciences, University of Southampton, Highfield, Southampton, SO17 1BJ, UK, janice@soton.ac.uk

Co-Authors: D. Khennouf, A. R. Chambers, University of Southampton,

F.J. Lennard, D. D Eastop, Textile Conservation Centre

ABSTRACT

Digital Image Correlation (DIC) is used to extract non-contact full-field three-dimensional displacement and in-plane strains from an historic tapestries. A DIC-based approach is devised that allows the effect of RH variations on a tapestry to be quantified. A historical tapestry has been monitored in a closely controlled environment and in the natural environment. The results revealed that very small variations in RH can have significant effects on strain. An automated long term monitoring approach has been devised to allow strain data to be extracted in real time from tapestries in remote locations. The results show that DIC provides better understanding of the effect of RH fluctuations on strain which will ultimately lead to more insight into the degradation process of historical tapestries. The paper demonstrates the potential for using DIC as a condition monitoring tool.

1. Introduction

Tapestries are hand-woven textiles that are often large, have intricate designs, were very time consuming to produce and expensive to commission. Tapestry conservation is a key issue in the heritage sector so specialists are employed to examine the condition of tapestries and recommend conservation strategies that do not alter their intrinsic characteristics and maintain their appearance and function. Tapestries are produced by weaving on a loom where closely spaced, highly twisted yarns, i.e. warp yarns, are stretched and fixed in one direction. Less dense yarns are woven transverse to the warp yarns to produce the pattern, i.e. weft yarns. On completion the tapestry is hung so that the weft yarns support the weight of the tapestry. It is known that tapestry degradation is related to the environment, however the precise mechanics of the failure of tapestries has not been physically characterised and currently condition assessment is based on the observation of an experienced conservator. In this paper a means of determining the rate of tapestry deterioration is established that related the relative humidity (RH) changes directly to the strains induced in the tapestry.

T. Proulx (ed.), *Application of Imaging Techniques to Mechanics of Materials and Structures, Volume 4*, Conference Proceedings of the Society for Experimental Mechanics Series 14, DOI 10.1007/978-1-4419-9796-8_43, © The Society for Experimental Mechanics, Inc. 2013

Inappropriate humidity can have severe effects on many artefacts e.g. paintings and wooden furniture [1]. To a lesser degree, tapestries are also affected by humidity. For this reason, museums galleries, and historical houses normally control humidity to tight ranges (typically 50%± 5%RH [1]) using air conditioning systems that can be very expensive to run. However, it has not been established if this range provides the 'ideal' conditions for preserving and displaying textiles, this is still a subject of debate within the conservation community [2]. Therefore, if it can be shown that widening the 50%±5%RH range has little or no significant effect on textiles, the budgets spent on expensive humidity control systems can be allocated to other conservation activities.

As the moisture content of the air surrounding the tapestry changes, the tapestry responds rapidly to this change by altering its own moisture content to stay in equilibrium with the surrounding air. In [2] a tapestry was displayed and the weight of the tapestry, RH, and temperature were recorded regularly over a period of nine days. Two important observations can be made: there is a strong positive correlation between the weight of the tapestry and fluctuation in RH. Secondly and more importantly, in only one week, the weight of the tapestry had dropped by approximately 700 g then increased back to its initial weight. Although this change in weight did not cause any noticeable damage at the time, it is a fair assumption that this will cause deformation in the tapestry. Therefore the continual cycling of RH will cause cyclic deformation to occur and may lead to failure. The work in the present paper proposes a DIC-based continual monitoring approach for quantifying the effect of RH fluctuation not on weight, but on strain in a tapestry (which is more directly linked to material performance and hence damage). This monitoring approach has been applied to study the effect of RH fluctuation on tapestries in both controlled and uncontrolled humidity environments. Since DIC is a non-contact full-field deformation measurement tool, there is a strong potential for using the continual monitoring approach developed in this work to study the effect of RH fluctuation on other museum objects.

2. The tapestry and test set-up

The tapestry used in this work is known as the verdure fragment and was woven over 300 years ago. It is 185 x 165 cm x 1 mm thick and has a mass of about 5.8 kg. The warp material is wool and the weft materials are a mixture of wool and silk. It has a linen backing attached by stitching to the four edges. It has 24 weave repeats per cm^2 (3 warp and 8 weft). The tapestry is mounted by means of a Velcro strip attached to its top edge to a specialist display device that enables the tapestry to stand away from the wall.

An essential part of DIC is that sufficient contrast is available in the image so that the image processing algorithm can detect features that enable the correlation. For engineering structures this 'correlation device' usually takes the form of a painted 'speckle pattern' applied to the surface of the material using an aerosol spray. This approach is unacceptable for tapestries as the paint would cause permanent disfigurement. In previous work [3] the suitability of the regular weave pattern along with the natural random contrast in the fibre, inherent in all textiles, was shown to be suitable as a correlation device. Therefore the DIC readings are all taken directly from the surface of the tapestry.

The DIC system used in the current work is manufactured by LaVision, and comprises two 2-Megapixel CCD cameras. The images were processed using the standard features of DaVis 7.2 software (developed by LaVision) and the StrainMaster package to obtain full-field strain maps. The digital cameras were fitted Nikon 50 mm f/1.8D lenses.

The verdure fragment was monitored initially in a room where humidity was controlled to 50% ± 5% RH i.e. the same humidity level that tapestries are typically exposed to in the museum environment and then in the natural environment. The cameras were positioned approximately 0.6 m away from the tapestry. The angle between the cameras is approximately 40º and the distance between them is 0.5 m. Calibration was carried out using a LaVision Type 11 two-level calibration. A 120 × 90 mm region of interest was selected for monitoring within the central part of the tapestry. The DIC system was set to record one image every 5 minutes. An environmental sensor was positioned approximately 10 cm in front of the tapestry and was set to record RH and temperature at the same rate. Note that temperature was controlled to 22ºC in all the experiments that have been conducted in controlled environment. The DIC image acquisition and the RH/temperature data recording were started simultaneously. The room was closed and the monitoring process was checked remotely at regular intervals. Once recording is completed the images are processed using Davis 7.2 and global strain data are extracted from the region of interest using 128 x 128 interrogation cells that covered a region on the tapestry of about 0.5 cm^2.

3. Controlled humidity experiments

The tapestry was monitored for 48 hours and the humidity was controlled to 50% ± 5% RH. Figure 1 shows strain, temperature and RH plotted against time (temperature was controlled to 22ºC). Note that strain on the y axis has been magnified 105 times so that it can be plotted with RH on the same graph. For instance, the '20' mark on the y axis corresponds to 20% RH, 20ºC and 0.02% strain. The main observation from the results in Figure 1 is that longitudinal strain responded rapidly to fluctuation in RH, even though the test has been carried out in a controlled humidity environment. A variation of approximately 8% in RH has caused the longitudinal strain to fluctuate by more than 0.06%. Recalling the results of [2] as RH increases the mass of the tapestry increases. Likewise, in Figure 1 it can be seen that as RH increases the longitudinal strain increases.

It could therefore be concluded that the strain increase is directly related to the increase in mass (and therefore self-load) as a result of moisture uptake. Therefore, the increase in moisture content does not only affect the mass of the tapestry, but also the strain. In conducting this work it was not possible to measure the mass change as this would mean removing the tapestry from display and would affect the DIC readings. Furthermore, the mass change in the tapestry used in [2] was 700 g for a tapestry of mass 43 kg. The total mass of the verdure fragment is 5.8 kg so overall moisture uptake would be less and more difficult to measure accurately as it would be reasonable to assume fluctuations would be around 100 g.

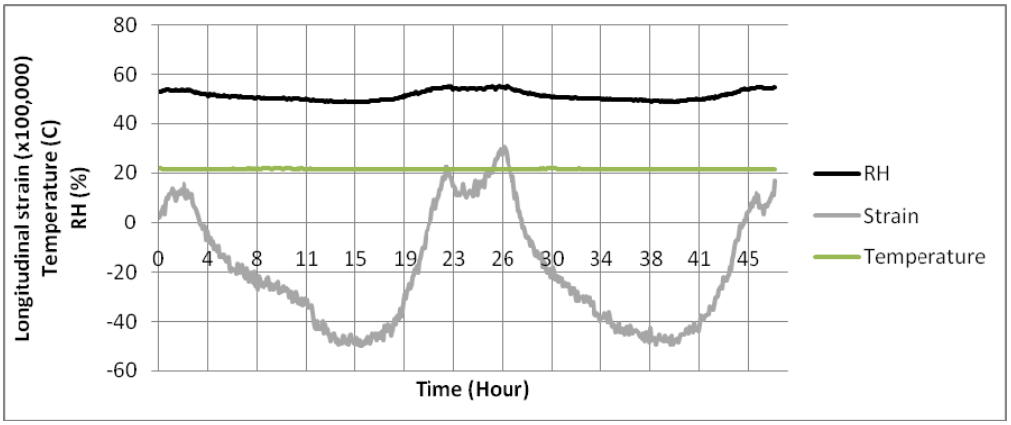

Figure 1: The effect of humidity fluctuation on longitudinal strain

Another experiment was conducted over a 130 hour period and this yielded similar results. The transverse strains were also calculated and these showed similar trends i.e. an increase in strain for increased humidity. The strong positive correlation between longitudinal strain and RH fluctuation can be seen more clearly in Figure 2 which plots strain in the longitudinal and transverse directions against RH in a scatter diagram for both the 48 hour and the 130 hour experiments. One of the main differences between the four plots is that they cross the x axis in different points. It is understandable that the two longitudinal strain plots cross the x axis at different points compared to the points at which the two transverse strain plots cross the x axis. However, since both experiments were carried out on exactly the same part of the tapestry, it would be expected that the two longitudinal strain plots would cross the x axis at the same point and the two transverse strain plots to cross the axis at the same point. It is clear from Figure 2 that this is not the case because the variations of RH in the two experiments do not have the same trends. While RH in the 48 hour experiment fluctuated within a range of [49% 55%], fluctuation in the 130 hour test was in the range of [45% 52%].

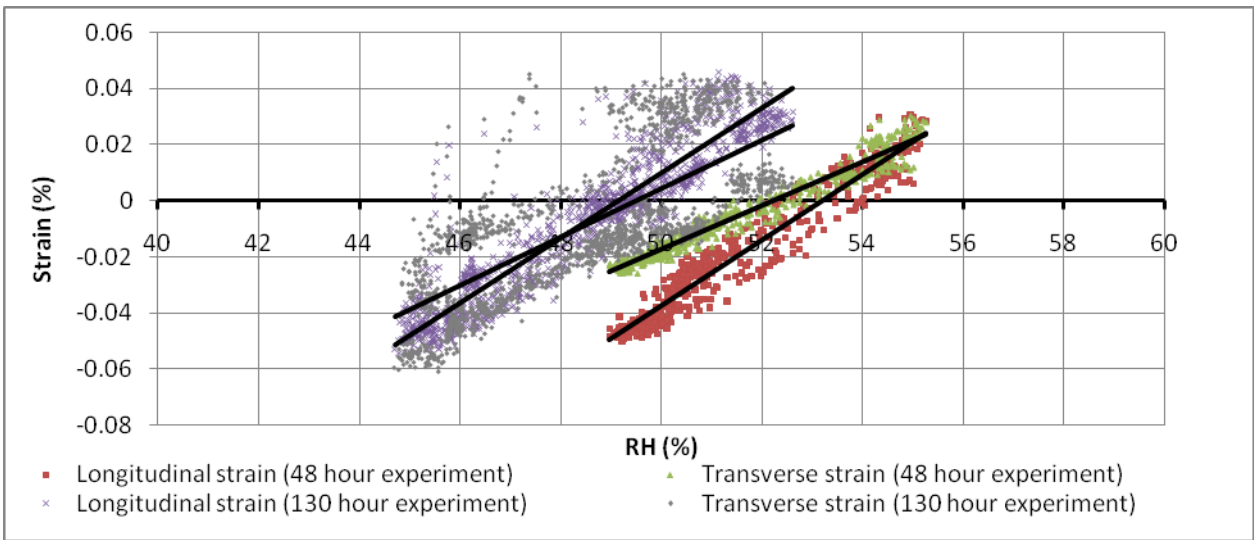

Figure 2: Comparison of the 48 hour and the 130 hour experiment results on the verdure fragment

Despite affecting the points at which the four plots cross the x axis, the difference in the ranges within which RH has fluctuated did not have any significant effect on the slopes of the trend lines. As illustrated in Table 1, in both experiments the longitudinal strain scatter plots had a slope of 0.011 and both of the transverse strain scatter plots had slopes that are approximately 0.008, clearly demonstrating the repeatability of such an approach.

Table 1: Slopes and coefficients of correlation from the 48 hour and 130 hour experiments

Experiment	**Slope**	***-x-* axis crossing**	**Coefficient of correlation (R^2)**
Longitudinal strain (48 hour experiment)	0.0117	53.20	0.9389
Transverse strain (48 hour experiment)	0.0078	49.90	0.9547
Longitudinal strain (130 hour experiment)	0.0114	47.20	0.9296
Transverse strain (130 hour experiment)	0.0087	47.60	0.5163

4. Continual in-situ monitoring in uncontrolled humidity

The experimental arrangement described above was used to monitor the verdure fragment for a period of 260 hours. The humidity was left uncontrolled in the room. RH over this period fluctuated between 48% and 34%, which is well below the 50% ± 5% RH range. The temperature during this period rose from 14ºC to 18ºC, which is most likely the reason for the reduction in of RH. Figure 3 depicts the effect that RH fluctuation had on the longitudinal strain. It is important to note that strain has been scaled by 104 times so that it can be plotted with RH (as opposed to 105 in the plots of the previous section). Therefore the 20 mark on Figure 3 refers to 20% RH and 0.2% strain. The main observation from the graph is that the longitudinal strain remained well below 0.1% until the 85th hour of the test where RH started to decline at a faster rate. The longitudinal strain immediately responded to this decrease reaching nearly -0.7% near the end of the experiment. This strain level is one order of magnitude higher than the strain observed in the controlled humidity experiments. Therefore, displaying or storing tapestries in uncontrolled humidity environment may have significant effects on the rate of tapestry degradation.

Figure 4 plots RH and longitudinal strain in a scatter diagram. The plot can be divided into two parts. In the part where RH was between 45% and 49%, the strain was below 0.1% and the slope was 0.0136. In the region of [34% 45%] RH on the other hand, the plot exhibits a different linear relationship between longitudinal strain and RH with a slope of 0.0514 RH. This linear part however contains two flat regions where strain remained constant at -0.3% and -0.6%, these correspond to the times when humidity was in the ranges of [41% 43%] and [36% 38%] respectively. These regions also correspond to the flat parts of the strain curve of Figure 3; the [125 170] and [220 250] hour ranges. Although the positive correlation between RH and strain can be explained using the moisture absorption properties of the yarns, no information has been found in the literature as to why the tapestries might behave differently in the [41% 43%] and [36% 38%] RH ranges. This requires further experiments to be carried out in where humidity can be controlled to these particular ranges.

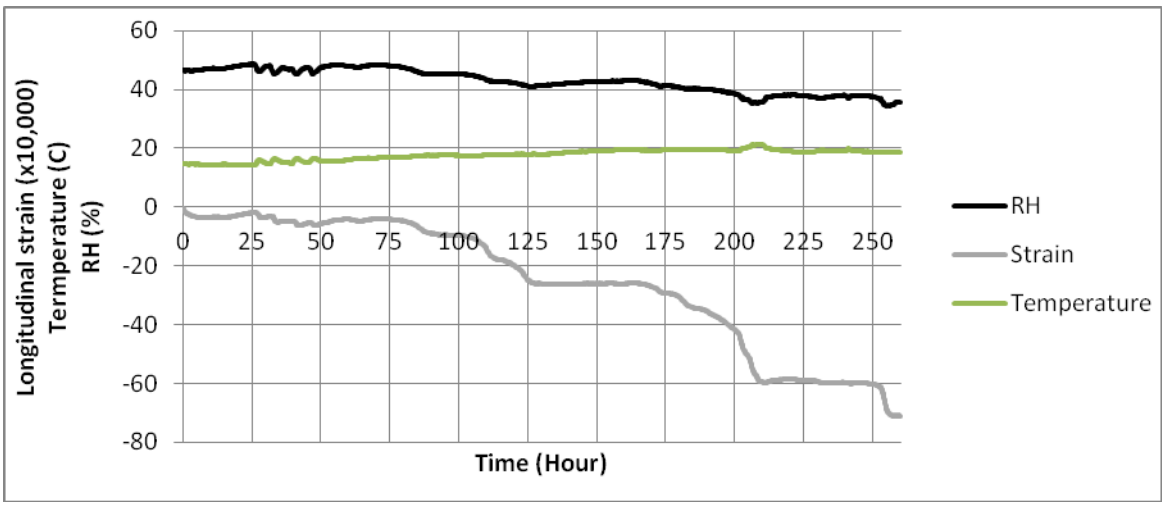

Figure 3: The effect of humidity fluctuation on longitudinal strain (verdure fragment 260 hour monitoring)

As humidity was within the 50%±5% RH range in the first 100 hours of the experiment, the slopes of the clusters of points in the controlled regions have been calculated. The slopes are 0.0136 and 0.0073 for the longitudinal and transverse strain scatter plots respectively, which agrees with the findings of the verdure fragment experiments conducted in controlled humidity conditions.

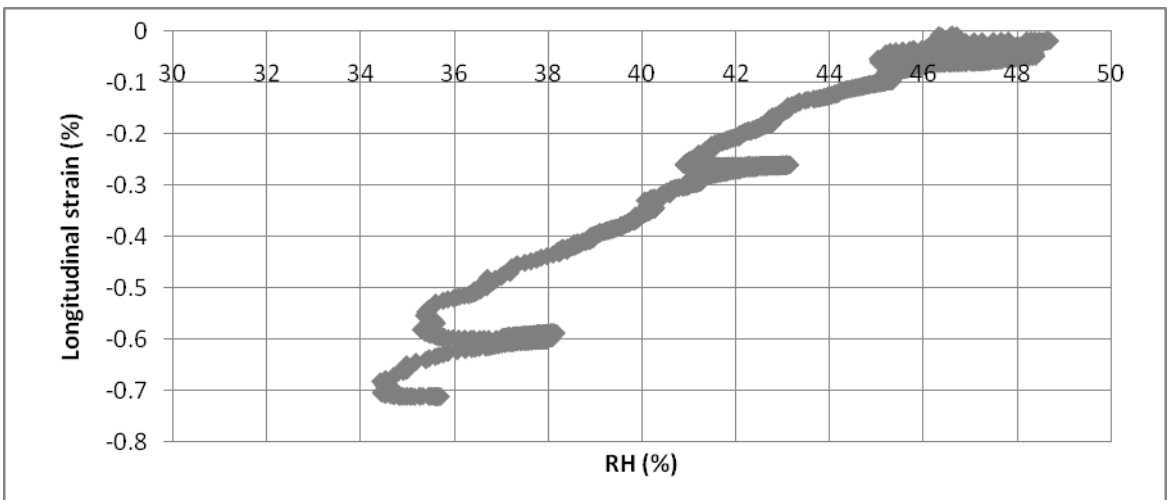

Figure 4: Scatter plot for RH against longitudinal strain

5. Definition of empirical models

From the monitoring experiments presented in this chapter, it would seem that although tapestries are complex mechanical structures, it is possible to approximate their strain response to RH changes using a linear mathematical model. To construct an empirical model for the three tapestries studied in this work for instance, a simple equation could be used of the form:

$$\varepsilon_{x,y} = k_{x,y} RH \quad (1)$$

where k is a constant that can be determined experimentally and RH is relative humidity.

Table 2 shows values of k obtained from the experiments described in this paper and on other tapestries in other conditions. By examining the top four rows it can be seen that the verdure fragment, displayed in the standard way in controlled humidity conditions has a k_x value of approximately 0.01265 ± 0.0013 and a k_y of 0.0078 ± 0.0006. Note how these constants varied considerably when the storage and display conditions have been changed. Also note how the values of k differ from one tapestry to another. By applying the monitoring approach described in this paper on a larger number of tapestries, a complete, detailed, and comprehensible database could be developed that will provide conservators with a great deal of information on the mechanical effects of RH on tapestries.

Table 2: Comparison of the slope values of the scatter diagrams from various tapestries

Experiment	**Slope (longitudinal strain)**	**Slope (transverse strain)**
Verdure fragment in controlled RH(48 h)	0.0117	0.0078
Verdure fragment in controlled RH(130 h)	0.0114	0.0087
Verdure fragment (260 h) - controlled RH region	0.0136	0.0073
Verdure fragment unrolled tapestry (48 h) - controlled RH	0.0139	0.0076
Verdure fragment rolled tapestry (48 h) - controlled RH	0.0191	0.0063
West Dean tapestry (480 h) – controlled RH region	0.0015	0.0101
Armorial tapestry in controlled RH (48 h)	0.0087	0.0103
Verdure fragment constrained from four edges (48 h)	0.0044	0.0025
Verdure fragment (260 h) - uncontrolled RH region	0.0514	0.0317
West Dean tapestry (480 h) – uncontrolled RH region	0.0092	0.0119

After quantifying the effect of RH variation on museum objects, the data can be used to construct empirical mathematical models for predicting the behaviour of tapestries in various humidity conditions. Table 2 shows that different tapestries have different responses to RH fluctuation. To determine the response, experimental data must be gathered for each tapestry to make the model; DIC is the tool to do this. One this has been established, historical data on humidity can be used to ascertain how many strain cycles have been experienced in the past. To establish the condition it is necessary to inform the model using accelerated ageing data from representative samples tested to failure. This could be achieved by using the model to design tests that accelerate the effects of RH on samples in the lab. Furthermore, the mathematical models can be used to determine the 'ideal' RH condition for the museum environment. This way the long term effect of the strain changes resulting from humidity fluctuations can be estimated and the most convenient humidity levels for museum objects can be determined.

6. Conclusions

A DIC-based continual monitoring approach has been demonstrated that allows the effect of RH on strain in tapestries to be quantified. An experimental programme has been conducted that demonstrates the approach. The main outcomes are:

- The relationship between strain and RH in tapestries can be approximated by a linear model in controlled humidity conditions.
- If a tapestry is moved to a region of uncontrolled humidity strain can be increased considerably. This confirms that controlling humidity in the museum environment is an effective preventive conservation technique.
- The continual monitoring approach can be used to compare the response of different tapestries to RH fluctuations. Comparison can be carried out based on curves of RH and strain variation against time and slopes of scatter plots of strain against RH.

Acknowledgements

The work in this paper was supported by the UK Arts and Humanities Research Council

References

1. Thomson, G., “The Museum Environment”, Butterworths, (1994), UK
2. Howell, D., “*Some mechanical effects of inappropriate humidity on textiles*”, James and James, London, , ICOM-CC 11th Triennial Meeting, (1996),692-8
3. Khennouf, D., Dulieu-Barton, J.M., Chambers, A.R., Lennard, F.J. and Eastop, D.E., “*Assessing the feasibility of monitoring strain in historical tapestries using Digital Image Correlation*”, Strain, 2010, 46, 19-32. DOI: 10.1111/j.1475-1305.2009.00637.x

Proceedings of the SEM Annual Conference
June 7-10, 2010 Indianapolis, Indiana USA

An Inverse Method for Analyzing Defects in Heterogeneous Materials

John M. Considine
Research Materials Engineer
US Forest Service
Forest Products Laboratory
Madison, WI
jconsidine@fs.fed.us

David W. Vahey
Research Materials Engineer
US Forest Service
Forest Products Laboratory

Don Matthys
Professor, Physics
Marquette University

Robert E. Rowlands
Professor, Mechanical Engineering
University of Wisconsin-Madison

Kevin T. Turner
Assistant Professor, Mechanical Engineering
University of Wisconsin-Madison

ABSTRACT
Evaluation of defects in heterogeneous materials, such as cellulose-fiber composites, can lead to methods for improving strength. Full-field displacement measurement techniques, *e.g.*, digital image correlation and electronic speckle pattern interferometry, provide useful information by which defects can be evaluated. Inverse Methods (IM) have been used to determine material properties from full-field displacement data. In homogenous materials, the resulting system of equations relating displacements with applied load and constitutive properties is overdetermined and is solved with traditional least squares methods. However, heterogeneous materials create an underdetermined system that cannot be addressed in the same way. Numerically simulated heterogeneous, orthotropic materials were evaluated in a 2-D finite element model, and the resulting nodal displacements were used as input to an IM algorithm. The algorithm determined local moduli, E_x and E_y, with errors, ranging from 9% to 20%. Errors in calculated G_{xy} were greater. Techniques for reducing error are provided. Simulations suggested IM can be an important tool in defect evaluation given full-field displacement measurements.

INTRODUCTION

All practical engineering materials contain strength-reducing defects. Defects increase local stresses above far-field applied stress through disorder, discontinuities, and material variability. For many years, measurement of strength reduction was a primary method of defect detection. In general, defects lower strength by concentrating stresses to levels that can be an order of magnitude greater than far-field stresses. Size, location, and frequency of defects in crystalline and ceramic materials have been an area of active research for many years. Hull and Bacon [1] described the stress fields caused by a variety of defects in crystalline solids.

Defect analysis of materials containing long-chain polymers, such as cellulose fibers in paper, has concentrated on fracture behavior [2-4]. However, papermaking also creates defects through variations in fiber alignment, fiber-to-fiber bonding, distribution of fiber lengths, and other parameters. As the density of native cellulose approaches 1500 kg/m^3 and paper density ranges from 600-800 kg/m^3, a large amount of void space is present that generates geometric defects with a range of sizes and shapes. As in crystalline materials [5], these defects can be detected through stress-distribution analysis.

One method of evaluating stress distribution is the use of inverse methods (IM). Avril and Pierron [6] reviewed several IM approaches and showed their general equivalency. IM can be generally described as the iterative adjustment of parameters in a numerical model, usually a FEM (finite element method) model, to minimize the

T. Proulx (ed.), *Application of Imaging Techniques to Mechanics of Materials and Structures, Volume 4*, Conference Proceedings of the Society for Experimental Mechanics Series 14, DOI 10.1007/978-1-4419-9796-8_44, © The Society for Experimental Mechanics, Inc. 2013

difference between an experimentally measured quantity and the numerically calculated quantity. For example, adjustable parameters may be constitutive properties and the measured quantities may be displacements.

By comparing FEM calculated out-of-plane displacements with those measured by shadow moiré, Le Magorou *et al.* [7] used IM to determine bending stiffness in composite wood panel. Molimard *et al.* [8] evaluated E_{xx}, E_{yy}, ν_{xy}, and G_{xy} of a composite material by minimizing the difference between moiré-measured displacements and those predicted by FEM in a perforated tensile plate. Similarly, Genovese *et al.* [9] used IM procedures to evaluate a truss system and a composite plate. Each of these references incorporated a specific type of IM entitled FEMU-U (finite element method updating–displacement).

With FEMU-U, the r.m.s. (root mean square) of displacement differences, also called a cost function, between measured values and those predicted by FEM are minimized by iteratively changing constitutive parameters in the FEM model. FEMU-U is attractive because displacements are first-order outputs of high-resolution full-field techniques of DIC and ESPI. Strain, a second-order output, has greater noise associated with numerical differentiation.

A common feature of these earlier investigations [7-9] is that only homogeneous materials were evaluated. The resulting system of equations was overdetermined. In 2-D models, the degree of freedom is (number of nodes) x 2 – (number of constitutive parameters) – 1. For homogeneous, isotropic materials, the number of constitutive parameters is two (E, ν); for homogeneous, orthotropic materials, the number of constitutive parameters is 4 (E_1, E_2, ν_{12}, G_{12}). For either case, the number of degrees of freedom is large and the problem has a unique solution based on minimizing least squares of the chosen cost function.

Quasi-heterogeneous material systems have been evaluated by Sutton *et al.* [10], who evaluated a weld-zone between two isotropic materials, and by Avril *et al.* [11], who identified the stiffness ratio between a high modulus spherical inclusion within a low modulus material. In these cases, a large portion of each specimen was homogeneous and isotropic.

Contrasted with isotropic cases, the system of equations associated with evaluating the constitutive parameters of heterogeneous, orthotropic materials is underdetermined in that there are many more parameters to evaluate than available inputs. A heterogeneous, orthotropic FEM model consisting of 100 four-node quadrilateral elements, arranged in a 5 x 20 array, has 126 nodes (252 displacement inputs) and 400 constitutive parameters to be determined. Underdetermined systems have an infinite number of solutions; the conventional least squares solution of an underdetermined system minimizes the appropriate cost function using the smallest value of constitutive parameters.

Heterogeneous, orthotropic models are important in defect analysis of composite materials. In fibrous composites like paper, defects can be attributed to items such as locally varying orthotropy ratios, fiber misalignment, low weight and poorly bonded regions, non-uniform fiber length, and incorporation of foreign materials. Each of these defects alters the surrounding stress field, creating regions of tensile and compressive stress concentration. Knowledge of local stress combined with local constitutive parameters provides the basis for defect analysis.

The goal of this work is to numerically simulate defects in heterogeneous, orthotropic materials and to use those simulations to evaluate the effectiveness of FEMU-U in determination of local constitutive parameters. These simulations reflect worst-case scenarios; material properties that limit variability, such as material characteristic length, were not incorporated in the simulations. Parasitic displacement noise was not included in this exploratory evaluation. The resulting system is underdetermined, but approaches are suggested for improving model conditioning.

Here defects are defined by any combinations of disorder, discontinuity, or variability that cause local stresses to exceed far-field applied stresses. This work describes two simulations: (1) a simulation to produce defects through local constitutive property variability and (2) a simulation to incorporate nodal displacements of a uniaxial tensile and biaxial tensile specimen in a FEM model from the first simulation in a FEMU-U algorithm to determine local constitutive properties.

METHODS

Evaluation of FEMU-U for heterogeneous materials was accomplished through numerical simulations of five parameters known to be associated with defects in paper materials and IM analysis of 100 randomly selected simulations. The five parameters included (1) principal elastic modulus, E_1, (2) COV (coefficient of variation) of E_1, (3) orthotropy ratio, $R = E_1/E_2$, (4) COV of misalignment angle, θ, between the principal material direction and direction of load application, and (5) COV of density, ρ. The following pseudo-code generates material properties for 100 elements as input for a FEM model.

→ *Let* E_1 *vary from 4 GPa to 10 GPa in 0.5 GPa increments [13 cases]*
  → *Let* COV(E_1) *vary from 10% to 40% in 10% increments [4 cases]*
  → *Generate 100* E_{11}*s randomly from normal distribution with mean* E_1 *and* COV(E_1)
    → *Let R (orthotropy ratio) vary from 2.0 to 5.0 in 0.25 increments [13 cases]*
    → *Generate 100* E_{22}*s randomly from normal distribution with mean* E_1/R *and* COV(E_1)
      → *Let* COV(θ) *vary from 10% to 40% in 10% increments (with* COV(θ) *evaluated at* θ*=45°[4 cases] (*see following discussion in text)*
      → *Generate 100* θ*'s randomly with mean 0° and* COV(θ)
        → *Let* COV(ρ) *vary from 10% to 40% in 10% increments [4 cases]*
        → *Generate 100* ρ*'s randomly with mean 1.0 and* COV(ρ)
          → *Let* ν_{12} *= 0.23 (common for cellulose materials)*
          → *Let* $\nu_{21} = \nu_{12} \cdot E_{22}/E_{11}$ *for each of 100 elements*
          → *Let* $G_{12} = \sqrt{E_{11}E_{22}} \Big/ [2(1+\sqrt{\nu_{12}\nu_{21}})]$ *for each of 100 elements* (see [12])
          → *Let* $[E'_{11}, E'_{22}, G'_{12}] = \rho \cdot [E_{11}, E_{22}, G_{12}]$
          → *Calculate* E_x, E_y, ν_{xy}, G_{xy} *from transformation of* $E'_{11}, E'_{22}, \nu_{12}, G'_{12}$ *with* θ *for each of 100 elements*

*Calculation of θ: 100 θ were randomly generated with a mean of 45° and the specified COV and 45° was subtracted from each of the 100 θ values.

The pseudo-code produces 10816 heterogeneous simulations, each with 100 elements. These simulations represent worst cases because large variations in material properties are allowed in adjacent elements. Such cases are justified by the large COV(ε), as great as 40%, measured by researchers [13-15] during tensile testing. Material characteristic length or correlation distance, which describes how rapidly material properties vary in space, is not included.

Here K_t, tensile stress concentration factor, is defined as the ratio of FEM-calculated element stress in the direction of far-field stress to far-field stress. K_c is defined as the ratio of FEM-calculated element stress in the direction orthogonal to far-field stress to far-field stress. A homogeneous, linear elastic tensile specimen has K_t equal to unity and K_c equal to zero.

Each of the 10816 heterogeneous simulations was used as input for two FEM models, shown in Figures 1a and 1b. The long model dimension corresponded with the y-direction because 2-direction properties are generally the most critical in applications involving paper materials. FEM analysis was performed within ANSYS® using PLANE42 (4-node quadrilateral) elements and an orthotropic material model. Nodal displacements were used as input to the FEMU-U solver. Parasitic noise was not added to nodal displacements but has been addressed in other simulations [6].

The particular inverse method used here is FEMU-U, finite element model updating via displacement gap. Through an iterative process that determines new constitutive parameters, the displacement difference between the simulation-produced nodal displacements and FEM nodal displacements is minimized. Nodal displacements come from the constitutive property variability simulations and are used as input to the FEMU-U algorithm.

The function to be minimized is

$$f(\hat{u}_{FEM}, P) = \|r\| \; where \; r = (\hat{u}^{Simulation} - \hat{u}^{FEM}) \tag{1}$$

where

$\hat{u}^{Simulation}$ = vector containing nodal u-, v-displacements determined by heterogeneous model simulation
$\hat{u}^{FEM}$ = vector containing nodal u-, v-displacements from FEM model
P = vector containing constitutive parameters, E_x, E_y, ν_{xy}, G_{xy}
$||r||$ = norm of r

Because Equation (1) is nonlinear with respect to P, iterative procedures are appropriate methods for minimization of $f(\hat{u}_{FEM}, P)$ and determination of P. LMA (Levenberg–Marquardt Algorithm) (*e.g.*, see [16]) is commonly used because it combines the benefits of Steepest Descent Method with Gauss–Newton Method. The LMA has the form

$$P_{i+1} = P_i - (J^T J + \lambda \cdot diag(J^T J)^{-1} J^T r \quad (2)$$

where

i = iteration number
J, J^T = Jacobian and Jacobian transpose, determined by backward difference, $J_{m,n} = \frac{\partial r_m}{\partial P_n}$; m = number of nodal displacements (number of nodes x 2 for planar models), n = number of constitutive parameters x number of elements (100 in this work)
λ = non-negative damping factor, adjusted each iteration step, adjusts between Steep Descent Method and Gauss–Newton Method.

The Jacobian, J, in Equation (2) is calculated by backwards finite difference. The primary disadvantage of LMA is the need for matrix inversion during each iteration. In most applications, reduced iterations compensate for the matrix inversion.

After calculating a new P_{i+1} the constitutive parameters are checked for validity, *e.g.*, a positive-definite stiffness matrix in the FEM model, and are adjusted if not valid. Invalid elements P_i are adjusted to global mean P_i. The validated P_{i+1} are inputs to a new FEM analysis and the resulting nodal displacements are used to determine f_{i+1}. If $f_{i+1} < f_i$, the constitutive parameters are updated, $P_{i+1} \rightarrow P_i$, λ is reduced by a factor of 10, and the next iteration begins. If $f_{i+1} > f_i$, then λ is increased by a factor of 10 and P_i is not updated. As $\lambda \rightarrow 0$, LMA becomes exactly the Gauss–Newton Method. Typically 10 iterations were required.

RESULTS AND DISCUSSION

Figure 2a compares maximum tensile stress concentration, K_t, and maximum absolute value of the compressive stress concentration, K_c, for each heterogeneous simulation used as input for the FEM model in Figure 1a. Compressive failure strength for cellulose materials is typically 25% of tensile failure strength for both 1- and 2-directions; therefore, the simulated defects appear sufficient to test the ability of IM to determine heterogeneous constitutive behavior. A randomly chosen 100-member subset of scenarios (shown in Figure 2b) was used for subsequent investigations.

The model system, as originally formulated, was underdetermined because it contained 400 unknowns (E_x, E_y, ν_{xy}, G_{xy} for each of the 100 elements) with 252 inputs (126 nodes with u-, v-displacements). A possibility to improve system conditioning is to increase node density, but ultimately this is not a practical solution. One would usually like to know local behavior at the smallest element size possible based on experimental measurement techniques. If a particular measurement technique can accurately provide displacement information within a 1-mm x 1-mm grid, a resulting FEM model using PLANE42 elements would have element size of 1 x 1 mm. An 8-node quadrilateral element, such as the ANSYS® PLANE82 element, would need to be 2 x 2 mm and the region over which the constitutive properties are determined for this element would be 4 times larger than for the PLANE42 element.

System conditioning was improved here following the example of other researchers, Avril *et al.* [17] for example, reduced the number of parameters by eliminating ν from iterations. This approach was employed here in that ν_{xy} was assumed to be a homogeneous 0.23, based on representative results from Baum *et al.* [18].

LMA requires two initial estimates of P in order to calculate J and begin iterations. Genovese *et al.* [9] evaluated the effect of initial estimates on the number of iterations using FEMU-U in an overdetermined system and found that poor initial estimates increased the iterations required for minimization, but minimization was eventually achieved. Although thorough evaluation of initial estimates is beyond the scope of this investigation, an informal

analysis showed lack of convergence for poor initial estimates, primarily because the rate of convergence was different for each of E_x, E_y, and G_{xy}. It was found that minimization could be achieved if the first initial estimate for each of E_x, E_y, and G_{xy}, was the same throughout and with each modulus estimated 2 times larger than expected. The second initial estimate assumed that each of the parameters was heterogeneous, with E_x and E_y approximated at their mean values with a COV of 10%, and randomly assigned to each of the 100 elements. The mean value initial guess for E_x and E_y was justified because these values are generated during the same experimental tests used to capture full-field displacements. The second initial estimate for element G_{xy} was calculated as in the pseudo-code, with ν_{xy} = 0.23, *i.e*,. $G_{12} = \sqrt{E_{11}E_{22}} \Big/ [2(1+\sqrt{\nu_{12}\nu_{21}})]$.

Figures 3a and 3b show some results of FEMU-U applied to 100 simulations of the uniaxial load model, illustrated in Figure 1a. Root mean square errors provide an estimate of global error and were calculated according to

$$\%RMS_e(P_i) = \frac{norm(P_i^{Simulation} - P_i^{FEM})}{\sqrt{number\ of\ elements} \cdot mean(P_i^{Simulation})} \cdot 100\% \quad (3)$$

where

P_i = one of E_x, E_y or G_{xy}

Some correlation appeared evident in Figure 3a between the errors of E_x and E_y; $\%RMS_e(E_x)$ increased with $\%RMS_e(E_y)$.This type of behavior was expected because error in E_x cannot be compensated in E_y. The converse is also true. Such an understanding has practical application in that usually some material behavior is known prior to evaluation. If an FEMU-U algorithm for an underdetermined system produces a result contrary to known behavior in E_x or E_y, all material parameters are likely inaccurate.

A similar correlation was not evident in Figure 3b. Errors in the calculation of G_{xy} were higher and had no general trend with errors in E_y. Shear-induced nodal displacement was minimal for the uniaxial loading in Figure 1a and was created by nearby property heterogeneity. Another factor increasing $\%RMS_e(G_{xy})$ was a poor initial estimate. Avril *et al.* [17] used an Iosipescu shear test for accurate determination of G_{xy} in a homogeneous, orthotropic material.

Simulations allowed freedom to investigate unrealistic test geometries, such as in Figure 1b. This geometry was included to determine if FEMU-U more accurately determines E_x, E_y, and G_{xy} with alternate loading configurations. Figures 4a and 4b show errors of moduli as determined with the biaxial load geometry. The errors were similar to those in Figures 3a and 3b. No significant improvement in E_x, E_y, and G_{xy} were observed.

It is encouraging to note that comparison of Figures 3a and 4a suggests that uniaxial testing is sufficient for E_x, E_y determination. However, accurate determination of local G_{xy} seems to require a test geometry with significant shear behavior.

Errors shown in Figures 3 and 4 may seem high considering the lack of parasitic noise in simulated nodal displacements. This type of noise was not introduced because it creates a specific length scale that can be accurately determined only when a specimen geometry and evaluation scale are determined.

Errors in moduli determination can be reduced by determination of ν_{xy}. In specific simulations with large orthotropy ratios, inaccuracy of ν_{xy} greatly increases errors in moduli. In applications, determination of local ν_{xy} may be important because locally negative values may exist.

We are working to improve the accuracy of FEMU-U in defect analysis in the following ways:

- Material correlation length—This length scale can be used to limit the gradient of moduli changes.
- Knowledge of defect location—Nodal displacements in the region of the defect can be weighted to improve moduli determination near that region.
- Moduli filtering—Similar to correlation length, filtering can be used to damp periodic large moduli fluctuations associated with displacement measurement errors.

CONCLUSION

Defect analysis of materials can be accomplished by the determination of stress concentrations within materials. Numerical simulations were performed to create a variety of heterogeneous models that exhibited tensile and compressive stress concentrations. Nodal displacements, as calculated by a heterogeneous, orthotropic FEM model, were used in a FEMU-U algorithm to determine its success in local moduli evaluation. The resulting system was underdetermined as it attempted to compute 300 moduli from 252 inputs. E_x and E_y, as determined by FEMU-U, had similar errors, from 9% to 20%. Calculations of G_{xy} had larger errors. Uniaxial and biaxial models had similar errors in moduli determinations. Some portion of the errors was attributed to the elimination of Poisson's Ratio in the FEMU-U algorithm.

REFERENCES

[1] Hull, D., and Bacon, D. J., 2001, Introduction to dislocations, Butterworth-Heinemann, Oxford [Oxfordshire] ; Boston.

[2] Westerlind, B. S., Carlsson, L. A., and Andersson, Y. M., 1991, "Fracture toughness of liner board evaluated by the J-integral," Journal of Materials Science, 26(10), pp. 2630-2636.

[3] Fellers, C., 1993, "Fracture toughness - a new paper property," Papier, 47(7), pp. A345-A352.

[4] Batchelor, W. J., and Wanigaratne, D. M. S., 2003, "A New Cyclic Loading Method for Measuring Sheet Fracture Toughness," International Journal of Fracture, 123(1-2), pp. 15-27.

[5] Chasiotis, I., and Knauss, W. G., 2003, "The mechanical strength of polysilicon films: Part 2. Size effects associated with elliptical and circular perforations," Journal of the Mechanics and Physics of Solids, 51(8), pp. 1551-1572.

[6] Avril, S., and Pierron, F., 2007, "General framework for the identification of constitutive parameters from full-field measurements in linear elasticity," International Journal of Solids and Structures, 44(14-15), pp. 4978-5002.

[7] Le Magorou, L., Bos, F., and Rouger, F., 2002, "Identification of constitutive laws for wood-based panels by means of an inverse method," Composites Science and Technology, 62(4), pp. 591-596.

[8] Molimard, J., Le Riche, R., Vautrin, A., and Lee, J. R., 2005, "Identification of the four orthotropic plate stiffnesses using a single open-hole tensile test," Experimental Mechanics, 45(5), pp. 404-411.

[9] Genovese, K., Lamberti, L., and Pappalettere, C., 2005, "Improved global-local simulated annealing formulation for solving non-smooth engineering optimization problems," International Journal of Solids and Structures, 42(1), pp. 203-237.

[10] Sutton, M. A., Yan, J. H., Avril, S., Pierron, F., and Adeeb, S. M., 2008, "Identification of heterogeneous constitutive parameters in a welded specimen: Uniform stress and virtual fields methods for material property estimation," Experimental Mechanics, 48(4), pp. 451-464.

[11] Avril, S., Huntley, J. M., Pierron, F., and Steele, D. D., 2008, "3D heterogeneous stiffness reconstruction using MRI and the virtual fields method," Experimental Mechanics, 48(4), pp. 479-494.

[12] Szilard, R., 1974, Theory and analysis of plates: classical and numerical methods, Prentice-Hall, Englewood Cliffs, N.J.,.

[13] Dodson, C., 1968, "A contribution to the development of a statistical rheology of bonded fibrous networks," Doctoral, Brunel University.

[14] Choi, D., Thorpe, J. L., and Hanna, R. B., 1991, "Image-analysis to measure strain in wood and paper," Wood Science and Technology, 25(4), pp. 251-262.

[15] Lyne, M., and Hazell, R., 1973, "Formation Testing as a Means of Monitoring Strength Uniformity," The Fundamental Properties of Paper Related to its Uses, *Trans. Vth Fund. Res. Symp.*, F. Bolam, ed., FRC, Manchester, UK, 2003, Cambridge, UK, pp. 74-100.

[16] Bun, M., 2009, "Applications of the Levenberg-Marquardt Algorithm to the Inverse Problem," http://www.math.washington.edu/~reu/papers/2009/mark/reupaper.pdf, p. 21.

[17] Avril, S., Bonnet, M., Bretelle, A. S., Grediac, M., Hild, F., Ienny, P., Latourte, F., Lemosse, D., Pagano, S., Pagnacco, E., and Pierron, F., 2008, "Overview of identification methods of mechanical parameters based on full-field measurements," Experimental Mechanics, 48(4), pp. 381-402.

[18] Baum, G. A., Brennan, D. C., and Habeger, C. C., 1981, "Orthotropic elastic constants of paper," Tappi Journal, 64(8), pp. 97-101.

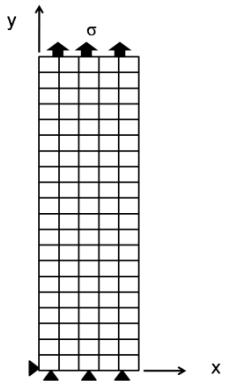

Figure 1a: FEM model for uniaxial loading.

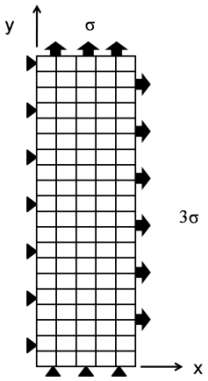

Figure 1b: FEM model used for biaxial loading.

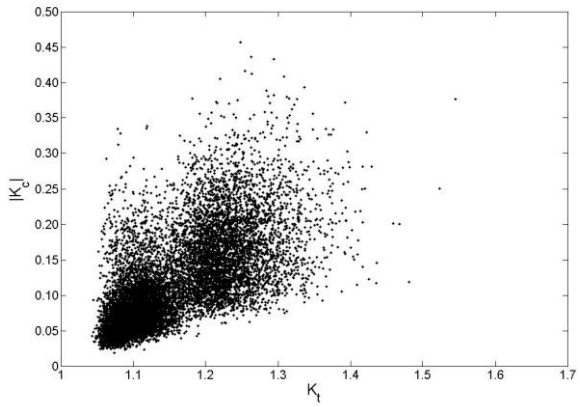

Figure 2a: Maximum tensile stress concentration compared to minimum compressive stress concentration for each simulation.

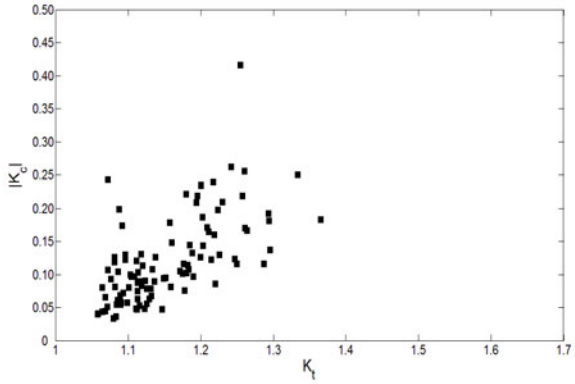

Figure 2b: A subset of 100 randomly chosen simulations from Figure 2a subsequently used for FEMU-U.

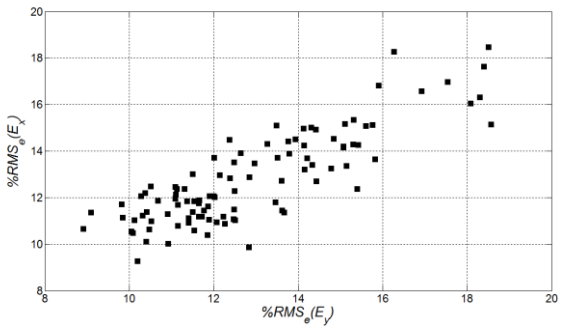

Figure 3a: Root mean square error of E_y and E_x for uniaxial loading, as a % of actual mean E_y and E_x.

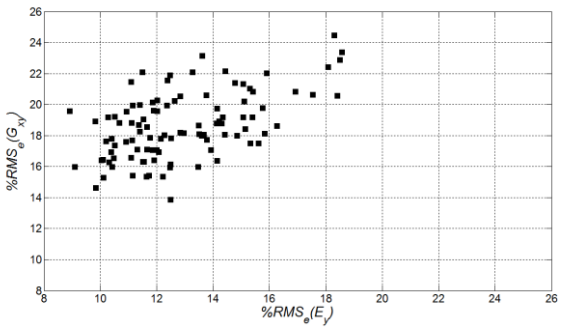

Figure 3b: Root mean square error of E_y and G_{xy} for uniaxial loading, as a % of actual mean E_y and G_{xy}.

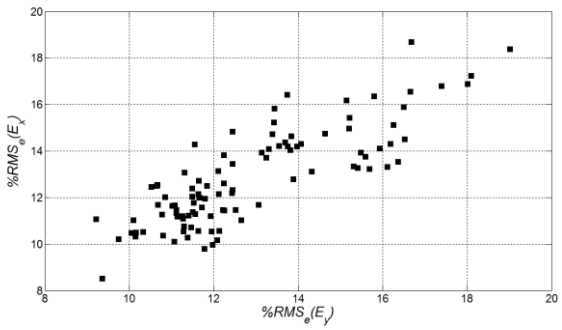

Figure 4a: Root mean square error of E_y and E_x for biaxial loading, as a % of actual mean E_y and E_x.

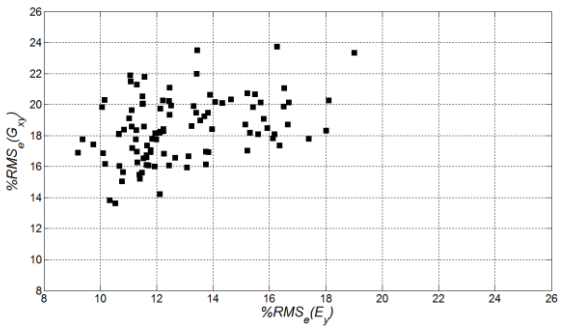

Figure 4b: Root mean square error of E_y and G_{xy} for biaxial loading, as a % of actual mean E_y and G_{xy}.

Proceedings of the SEM Annual Conference
June 7-10, 2010 Indianapolis, Indiana USA

Variation of Paper Curl due to Fiber Orientation

J. T. Decker[1], A. A. Khaja[1], M. T. Hoang[1], J. M. Considine[2], D. W. Vahey[2], K. T. Turner[1] and R. E. Rowlands[1,3]

[1] University of Wisconsin, Madison, WI, USA
[2] US Forest Service, Forest Products Laboratory, Madison, WI, USA
[3] Corresponding author, 3348 Engineering Hall 1415 Engineering Dr Madison, WI 53706, rowlands@engr.wisc.edu

ABSTRACT

Transverse deviations from the ideal flat surface in paper, or curl, can be a serious problem in the paper industry. The manufacturing of paper materials results in the material being orthotropic and laminar. Moreover, the dominant fiber orientation in a paper sheet can vary through the thickness of the sheet. Many paper structures are produced by lamination of paper plies. In these products directions of symmetry of the elastic properties, and coefficients of moisture and temperature expansion/contraction, consequently differ through the thickness of the laminated material. When subjected to humidity changes, the top and bottom portions of a paper laminate therefore expand or contract different amounts, causing the structure to curl. Paper products that curl are difficult to convert in packaging applications and print or copy in automated feeding mechanisms, leading to large costs for companies. It can become impossible to machine process and dispense paper products (such as stamps) that have curled. The present research involves determining the moisture induced curl in [0/15] and [0/45] Whatman paper laminates using a full-field 3-D laser scanner.

1. Introduction

Curl, being the deviation of a sheet from its flat surface, is a prevalent occurrence in paper materials and often results from moisture changes. Such deviations from flatness in these materials are sometimes significant with respect to planar dimensions and can result in serious manufacturing consequences, problems during converting and printing processes, as well as improper machine-dispensing. With laminated products such as postage stamps, the different plies often have very different coefficients of moisture expansion in different orientations so any environmental moisture change can cause the laminate to bend out of its plane resulting in curl and/or twist. Storing laminated paper products in uncontrolled conditions can aggravate the situation. This particular investigation involves measuring the out-of-plane deflections of laminated plies of Whatman filter paper when the environment relative humidity is changed from 0% to 50% RH. The curvatures, twist, and radii of curvature in two-ply Whatman laminates having stacking sequences of [0/15] and [0/45] are evaluated by measuring the transverse deflections using a 3-D laser scanner.

T. Proulx (ed.), *Application of Imaging Techniques to Mechanics of Materials and Structures, Volume 4*, Conference Proceedings of the Society for Experimental Mechanics Series 14, DOI 10.1007/978-1-4419-9796-8_45, © The Society for Experimental Mechanics, Inc. 2013

2. Background

Several previous studies have been reported on the modeling and/or measurement of the transverse flexure (curl, twist) of paper or related materials, as represented by references 1 through 11.

Various methods have been employed to evaluate the curl/twist of paper materials. Although early means of measuring the transverse displacements of paper sheets involved such rudimentary techniques as viewing the deformed sheet through a transparent mesh of known pitch, Eriksson and co-workers [5] employed a commercial unit which consisted of a non-contacting distance meter and an environmental chamber. Viitaharju and Niskanen [6] utilized a previously developed PC-controlled curl meter. Nordstrom, Carlsson et al [7-9] assembled a system for measuring the shape of vertically-supported paper sheets using a non-contacting laser displacement sensor. By attaching the laser sensor to a translation stage, they were able to record the transverse displacements, $W(x,y)$, at several preselected positions across the deformed paper sheet. The x- and y-positions of the translation table (hence relative sensor position and therefore location on the paper sheet being interrogated) were computer-controlled and the recorded W-displacements stored for subsequent processing. Many of these approaches are not portable and testing can be somewhat arduous to implement for routine analyses, thereby hampering their application for routine quality control in a manufacturing environment. Reis et al. [11] recently proposed a procedure for measuring the diagonal curl which involves measuring the maximum transverse displacement of a sheet which is suspended at its corners.

3. Laminate Preparation

The present laminated specimens were prepared by bonding two plies of Whatman filter paper (Whatman International, Maidstone, Kent, UK, identified as Chromotography paper, model 3MM CHR and is 100% cellulose) together with a sheet of heat-activated photo mount dry adhesive (Dry Mount, from laminationplus.com). The combination of top and bottom plies of paper, separated by a sheet of the dry adhesive, were pressed between heated platens (76°C) at load of 9000 N (2000 pounds) for 10 seconds. The platens reached the specified equilibrium temperature before applying the load; the much larger mass of the platen ensured constant temperature during pressing. An additional aluminum plate was placed between each of the top and bottom platens and the paper sheets. Care was taken to remove any adhesive exposed beyond the paper sheets to prevent bonding the paper to the aluminum plates. The laminate preparation was done at ambient temperature and humidity, but hot pressing the paper laminates brought them to essentially 0% RH. The prepared laminates were then stored for 24 hours at 50% RH at 23°C. Within a few minutes of being removed from the hot press, individual sheets of Whatman paper had 0.33 mm caliper and two-ply laminated structure had 0.73 mm caliper. The measured caliper of individual Whatman plies and their laminates after being at 50% RH for 24 hours were essentially the same as at 0% RH.

4. Specimen Configuration

The originally dry laminates (100 mm × 89 mm) were hung vertically during the 24 hours at 50% RH, Fig. 1. The specimens were clamped along the top edge, the other three edges being free. They were clamped using a traditional clip board except the board was cut away to enable the laminate to deflect either inwardly or outwardly. The [0/15] and [0/45] laminates were tested with the 0°-ply vertically downward towards the camera and the angle ply behind this 0°-ply, the off-axis angle of 15° or 45° is measured from the vertical downward direction.

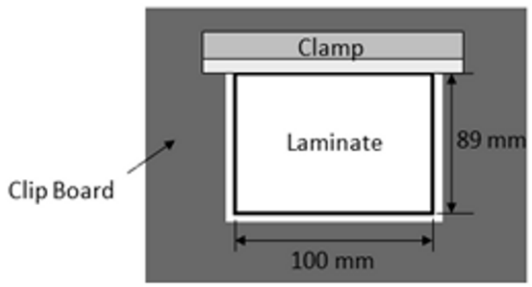

Fig. 1 Schematic of laminate loading

5. Deflection Measurements and Their Processing

The moisture-induced transverse deflections of the paper laminates were measured and recorded using a commercial 3-D laser scanner system (3-D REVscan scanner by Creaform, Levis, PQ, Canada; http://www.creaform3d.com). The scanner, which operates on the triangulation principle, consists of a laser which impinges light onto the surface of interest, and two cameras to capture the reflected light, Fig. 2. Triangles of known geometry are created by the fixed distance between the laser source and the cameras (dimension D in Fig. 2) and the angle created between the laser spot on the surface and cameras. Basic trigonometric principles are applied to calculate the distance between the scanner and the surface. A record of the surface in terms of relative transverse deflection is determined by repeating this triangulation process up to 20,000 times per second. The REVscan laser scanner is self positioning. It cannot directly create a scan; rather, it uses positioning features (targets) near the region of interest in order to be able to create a spatial model of the surface relative to the scanner's position in space. These "positioning features" or targets are small reflective circles which are placed near the scanned surface, Fig. 3. The accompanying VxScan software recognizes these targets, uses their relative placement to locate the scanner in space, and creates a reference frame in which the data may be collected and read. The targets should not be placed in a symmetrical fashion and the target array needs to be sufficiently dense so the scanner sees at least four targets at all times. The VxScan software is used to collect, analyze and store the scan data, and is a necessary part of every scan. Although the scanned data can be processed in a number of ways, Matlab® provides convenient options for manipulating the data and generating contour maps of a scanned surface, Figs. 4 through 6. The in-plane horizontal and vertical axes of all displacement images illustrated have units of mm.

Unlike many of the methods used previously to record transverse displacements, the 3-D REVscan laser scanner is highly portable, results are available almost instantaneously and the system indicates whether the transverse motion is towards or away from the camera. Accurate, quantitative results necessitate a preliminary calibration using a provided calibration plate.

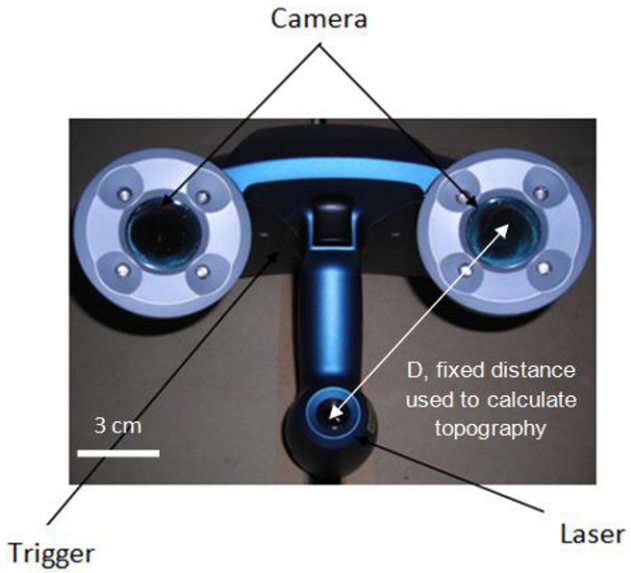

Fig. 2 Front view of laser scanner

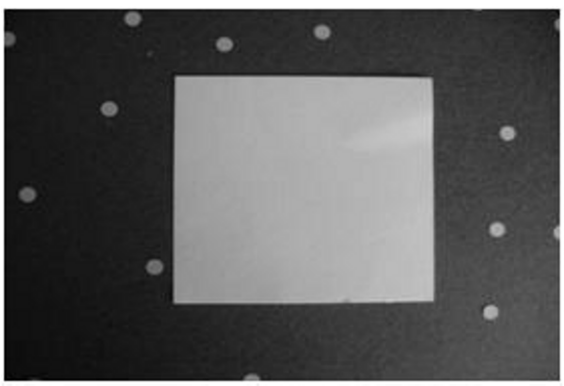

Fig. 3 Positioning features (targets) surrounding Whatman material

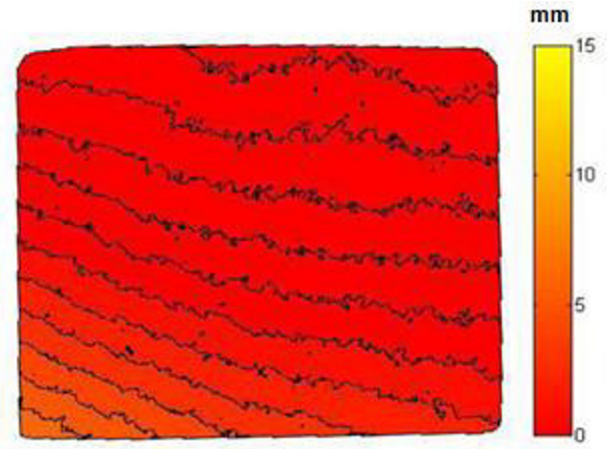

Fig. 4 Contour plot of transverse displacements in [0/15] laminated Whatman composite at 50% RH. The in-plane dimensions are 100 x 89 mm (Fig. 1).

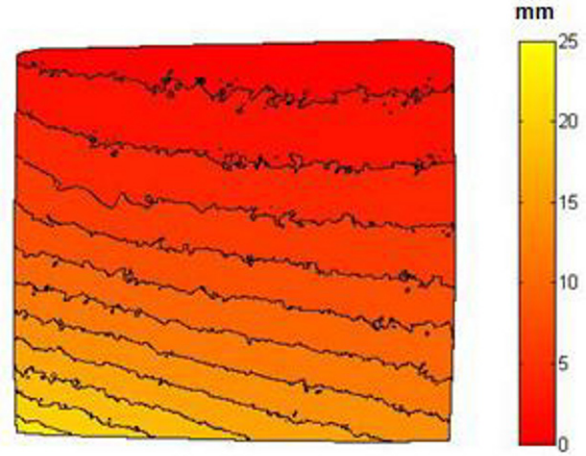

Fig. 5 Contour plot of transverse displacements in [0/45] laminated Whatman composite at 50% RH. The in-plane dimensions are 100 x 89 mm (Fig. 1).

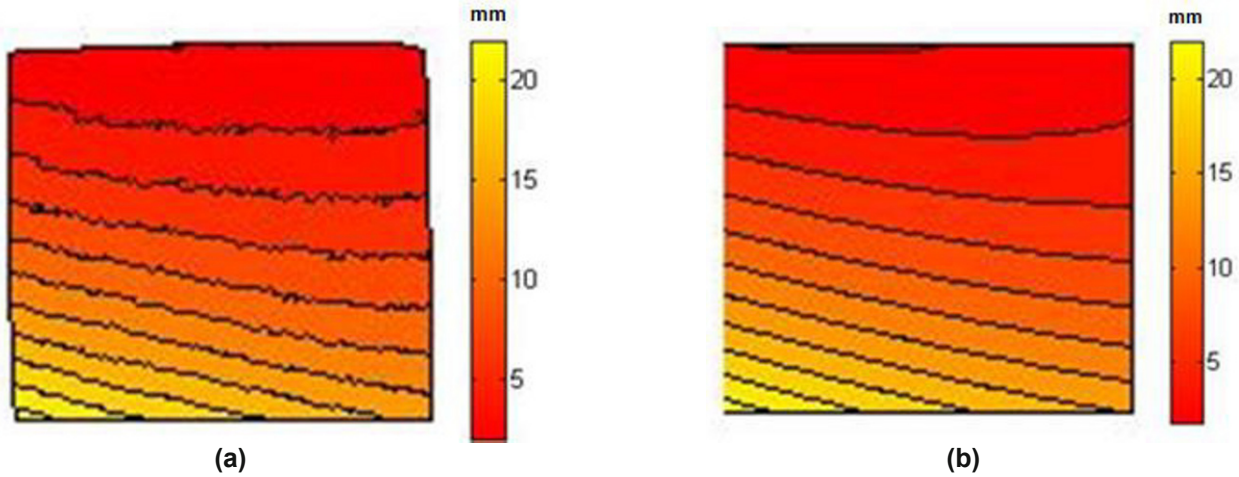

(a) **(b)**

Fig. 6 Contour plots of transverse displacements in [0/45] laminated Whatman Composite at 50% RH. The in-plane dimensions are 100 x 89 mm: (a) from VxScan software, (b) least-squares fit of eqn (1) to output from VxScan software.

The 3-D REVscan laser scanner has an accuracy of 0.05 mm (0.002") in each of the x, y and z directions. Although the resolution in the z-direction depends on the size of the object being scanned, and can be as fine as 0.1 mm, the data used in Figs. 4 through 6 were recorded at a z-resolution of 0.4 mm. Data for these displacement images were also collected at an in-plane resolution of 0.4 mm; that is, each data point originates no closer than 0.4 mm to any other point. Hence, the Matlab® generated contour plots of Figs. 4 through 6 are based on approximately 50,000 input data values. The contour plot of Fig. 6(b) is a least-squares fit of eqn (1) to the approximately 50,000 output values from VxScan. Comparing Figs. 6(a) and (b) demonstrates how well maps of $W(x, y)$ can be represented by fitting the data to the simple polynomial:

$$W(x, y) = C_1x^2 + C_2xy + C_3y^2 + C_4x + C_5y + C_6 \quad (1)$$

The curvatures, κ_{xx} and κ_{yy}, and twist, κ_{xy}, and the associated radii of curvatures are given by

$$\kappa_{xx} = -\frac{\partial^2 W}{\partial x^2} = -\frac{1}{R_x}, \qquad \kappa_{yy} = -\frac{\partial^2 W}{\partial y^2} = -\frac{1}{R_y}, \qquad \kappa_{xy} = -\frac{\partial^2 W}{\partial x \partial y} \quad (2)$$

and from eqn (1)

$$\kappa_{xx} = -2C_1, \quad \kappa_{yy} = -2C_3, \quad \kappa_{xy} = -C_2 \tag{3}$$

The sign conventions utilized in eqns (1) through (3) are compatible with those of reference 4.

6. Results

Based on eqns (1) through (3), the Cartesian components of curvature and twist for the [0/15] and [0/45] laminates of Figs. 4 through 6 are given in Table 1. The *x*-direction is horizontal and the *y*-direction is vertical. Values of Table 1 recognize the Mohr's Circle analogy for plates, Fig. 7, such that κ_{xx}, κ_{yy}, κ_{xy} are the curvatures and twists, respectively, with respect to the *x,y* coordinates, κ_1 and κ_2 are maximum and minimum values of the curvatures, and R_x, R_y, R_1 and R_2 are the associated radii [4].

Table 1 Scanner determined curvatures and radii of moisture induced curl in [0/15] and [0/45] laminates of Whatman paper material (moisture increased from 0 to 50% RH).

	Laminate	
	[0/15]	[0/45]
$\kappa_{xx} = -\frac{\partial^2 W}{\partial x^2} = -\frac{1}{R_x} = -2C_1$ (10^{-4} mm^{-1})	-5.76	-7.04
$\kappa_{yy} = -\frac{\partial^2 W}{\partial y^2} = -\frac{1}{R_y} = -2C_3$ (10^{-4} mm^{-1})	-7.64	-24.00
$\kappa_{xy} = -\frac{\partial^2 W}{\partial x \partial y} = -C_2$ (10^{-4} mm^{-1})	-4.27	-9.50
$\kappa_1 = \frac{1}{R_1}$ (10^{-4} mm^{-1})	-2.30	-2.80
$\kappa_2 = \frac{1}{R_2}$ (10^{-4} mm^{-1})	-11.10	-28.20
$\lvert R_1 \rvert$ (m)	4.35	3.60
$\lvert R_2 \rvert$ (m)	0.90	0.35

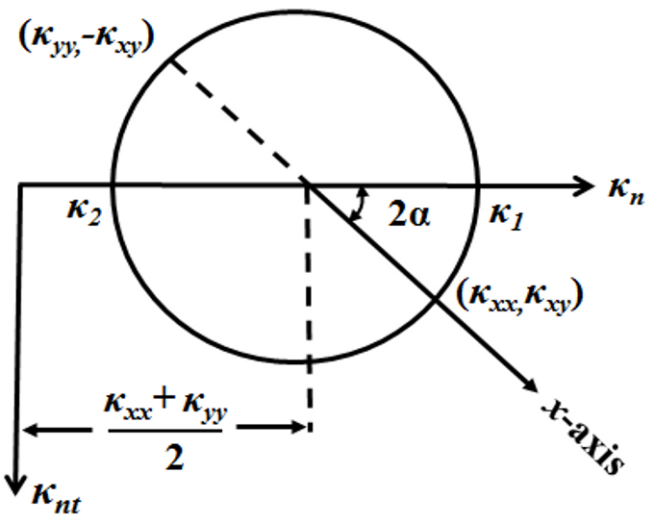

Fig. 7 Mohr's circle analogy for plate curvatures and twist [4].

7. Summary, Discussion and Conclusions

The 3-D REV scanner is well suited for measuring transverse deformations of thin flexed sheets. The scanner was used here to evaluate moisture-induced curl (curvatures, twist, and radii of curvature) in [0/15] and [0/45] Whatman laminates. Recognizing a paper ply has its greatest coefficient of moisture expansion in its cross-machine or 2-direction, the mismatch in moisture coefficients between the top and bottom plies of a laminate is greater for the [0/45] than the [0/15] stacking sequence. This is compatible with the smaller physical radius of curvature, $|R_2|$ = 0.35 m (associated with κ_2 in Table 1), for the [0/45] laminate, compared to 0.90 m for the [0/15] case. It is also consistent with the former's increased overall transverse displacement (Figs. 4 through 6). Future research will consider more stacking sequences, additional humidity changes and numerical predictions of the observed responses.

Acknowledgment

Financial support for this research was provided by the United States Postal Service. Funds for the purchase of the 3-D laser scanner were made available by the United States Postal Service and the College of Engineering at University of Wisconsin-Madison.

References

[1] Bortolin, G., Gutman, P. O. and Nilsson, B., On Modeling of Curl in Multi-ply Paperboard, *Journal of Process Control*, **16**, 419-429 (2006).

[2] Leppanen, T., Sovari, J., Erkkila, A-L and Hamalanen, J., Mathematical Modelling of Moisture Induced out-of-plane Deformation of Paper Sheet, *Modelling Simul. Sci. Eng.*, **13**, 841-850 (2005).

[3] Hyer, M.W., Calculations of the Room-Temperature Shapes of Unsymemtric Laminates, *J. Comp, Mat'ls*, **15**(7), 296-310 (1981).

[4] Hyer, M. W., Some Observations on the Cured Shape of Thin Unsymmetric Laminates, *J. Comp. Mat'ls*, **15**(3) 175-194 (1981).

[5] Eriksson, L. E., Cavlin, S., Fellers, C. and Carlsson, L. A., Curl and Twist of Paperboard – Theory and Measurement, *J. Nordic Pulp Paper Research,* **2**(2), 66-70 (1987).

[6] Viitaharju, P. H. and Niskanen, K. L., Chiral Curl in Thin Papers, *J. Pulp & Paper Science*, **20**(5) 148-152 (1994).

[7] Nordstrom, A., Carlsson, L. A. and Hagglund, Measuring Curl in Thin Papers, *J. TAPPI*, **80**(1), 238-244 (1997).

[8] Nordstrom, A., Gudmundson, P. and Carlsson, L. A., Influence on Sheet Dimensions of Curl of Paper, *J. Pulp & Paper Science*, **24**(1), 18-25 (1998).

[9] Lu, W. and Carlsson, L. A., Influence of Initial Deflections on Curl of Paper, *J. Pulp & Paper Science*, **27**(11), 373-378, (2001).

[10] Nordstrom, A. L., Gudmundson , P. and Carlsson, L. A., Influence of Gravity on Curl of Horizontal Paper Sheets, *J. TAPPI*, **84**(5), 1-18 (2001).

[11] Reis, M. S., Abreu, C. T., Heitor, M. J., Ataide, J. and Saraiva, P. M., A New Procedure for the Routine Assessment of Paper Diagonal Curl, *J. TAPPI*, **92**, 20-26 (2009).

Proceedings of the SEM Annual Conference
June 7-10, 2010 Indianapolis, Indiana USA

A MOIRÉ-DEFLECTOMETRY BASED BULGE/CONTACT TEST FOR TRANSPARENT THIN FILMS

Dewei Xu, Kenneth M. Liechti, Dan Yang and Joshua McNalley
Research Center for the Mechanics of Solids, Structures and Materials
Department of Aerospace Engineering & Engineering Mechanics
The University of Texas at Austin
Austin, TX 78712
dwxu@mail.utexas.edu

Bulge tests have been widely used to characterize mechanical properties of thin films. In this technique, mechanical properties are extracted from the analytically or approximately obtained pressure-deflection response. The determination of the out-plane deflection is critical for bulge tests and to date, this has been implemented by using optical microscopy with a calibrated vertical displacement, laser interferometry and shadow moiré. All these techniques rely on reflected light from the bulged film surface, so films with relatively smooth and reflective surfaces are required. Consequently, these techniques are less applicable to transparent polymeric thin films.

The problem that is addressed here is that of a pressurized circular membrane in contact with a rigid substrate. A closed-form membrane analysis with Hertz, JKR, DMT and Maugis contact is developed to describe the relationship between pressure, contact radius and contact force. Both the variation in the slope of the deflection profile of the portion of the membrane outside the contact zone and the contact radius itself are measured by an apparatus based on moiré deflectometry. In this arrangement, collimated beams are refracted by the lens structure and transmitted through a pair of Ronchi gratings placed at a set distance from each other. The rotation between resulting fringe patterns determines the local slope. Contact experiments with several thin films and a glass substrate show that these analyses predict both the slope field and contact radius well.

There is considerable flexibility to the technique which allows for a wide range of film sizes and accuracy due to the range of gratings and optical parameters that can be selected.

T. Proulx (ed.), *Application of Imaging Techniques to Mechanics of Materials and Structures, Volume 4*, Conference Proceedings of the Society for Experimental Mechanics Series 14, DOI 10.1007/978-1-4419-9796-8_46, © The Society for Experimental Mechanics, Inc. 2013

Proceedings of the SEM Annual Conference
June 7-10, 2010 Indianapolis, Indiana USA

OOF3D: An Image-Based Finite Element Solver for Materials Science

Valerie R. Coffman†, Andrew C. E. Reid, Stephen A. Langer, Gunay Dogan

Information Technology Laboratory
National Institute of Standards and Technology
100 Bureau Drive, Mail Stop 8910
Gaithersburg, MD, 20899

†valerie.coffman@nist.gov

ABSTRACT

Recent advances in experimental techniques (micro CT scans, automated serial sectioning, electron back-scatter diffraction, synchrotron radiation x-rays) have made it possible to characterize the full, three dimensional structure of real materials. Such new experimental techniques have created a need for software tools that can model the response of these materials under various kinds of loads. OOF (Object Oriented Finite Elements) is a desktop software application for studying the relationship between the microstructure of a material and its overall mechanical, electromagnetic, or thermal properties using finite element models based on real or simulated micrographs. OOF provides methods for segmenting images, creating meshes of complex geometries, solving PDEs using finite element models, and visualizing 3D results. We discuss the challenges involved in implementing OOF in 3D and use finite element simulations of trabecular bone as an illustrative example.

1 Introduction

Future advances in computational materials science will come from integrating simulations and experiments. One of the key challenges of realizing this lies in finding computationally tractable representations of complex geometries such as multiphase material microstructures and biological materials. In this paper, we describe OOF3D (named for "Object Oriented Finite-Elements", in three dimensions), a forthcoming software package for addressing this challenge. Previous publications describe the current and previous two dimensional versions of OOF [1, 2, 3, 4, 5, 6].

The 2D OOF tool has been used successfully in a wide variety of applications, including studying the relationship between thermal properties and the structure of plasma-sprayed zirconia coatings [7], the effects of microstructure on the macroscopic mechanical properties of glass-matrix composites [8], the role of texture in the macroscopic response of polycrystalline piezoelectric materials [9], and the modeling and design of electrode microstructures in rechargeable lithium-ion batteries [10].

When the OOF project began fully 3D microstructure characterization data was rare. Since then, advances in experimental techniques such as automated serial sectioning [11], 3D electron back-scatter diffraction (EBSD) [12], and synchrotron x-rays [13, 14], have produced an abundance of fully 3D microstructure characterization data. The new data sets have created a greater need for software tools that can model the properties of materials with complex microstructure geometries.

Most meshing algorithms require as input numerical representations of straight lines, flat planes, and simple curves that make up the boundaries of the structure to be simulated. But for material microstructures, converting the boundaries to a simple numerical representation by hand is a tedious task. Another method for forming a finite element mesh from an

T. Proulx (ed.), *Application of Imaging Techniques to Mechanics of Materials and Structures, Volume 4*, Conference Proceedings of the Society for Experimental Mechanics Series 14, DOI 10.1007/978-1-4419-9796-8_47, © The Society for Experimental Mechanics, Inc. 2013

image is to do so directly, defining a cube element for each voxel [15, 16, 17, 18]. This has two major pitfalls. First, it usually creates too many elements – homogeneous regions can adequately be described by larger elements. Second, it introduces jagged edges where the boundary in the real material is smooth, which can lead to artificial features such as stress concentrations at voxel corners.

OOF3D avoids these pitfalls by using a unique, image-based, adaptive meshing technique, a 3D generalization of the two dimensional technique described in detail in [5]. This meshing scheme begins with a coarse, regular, well-formed, space-filling mesh of tetrahedra on the image, and then brings that mesh into correspondence with the image by a series of mesh-modifying steps which preserve the space-filling and well-formed character of the mesh. Mesh modifying steps may refine elements, replacing them with smaller elements, or may move nodes and boundaries around to align them with image features. Because the well-formed, space-filling character of the mesh is preserved, unmeshable voids cannot arise, and illegal (inverted) elements can be avoided. These mesh-modify steps use two heuristics of mesh quality: element shape quality and element homogeneity. The homogeneity is a measure of how close an element is to enclosing a region that contains a single material and is defined as the ratio of element volume occupied by the dominant material category to the total volume of the element.

Simulations with OOF3D follow the same general procedure as with OOF2: the user loads a set of experimental or simulated images or EBSD data constituting slices of the volumetric microstructure sample, groups the voxels into material categories, assigns properties to material components, generates a finite element mesh, and performs virtual experiments. OOF is used to visualise the microscopic response of the microstructure to external conditions, to compute effective macroscopic material properties, or to design material microstructures with desired characteristics. For a brief description of using OOF2 to analyse a particular 2D microstructure, see [6].

As with OOF2, OOF3D runs on Linux and Mac OSX. The installation requirements include a C++ compiler, Python interpreter, X11 windows system, and GTK. A new requirement of OOF3D is VTK [19], which is used for 3D visualization of microstructures, meshes, and numerical results.

In this paper, we discuss the key differences in implementing OOF in 3D with a focus on meshing. We discuss simulations of trabecular bone as an illustrative example to show how OOF meshing methods improve upon previous methods such as voxel to brick conversion.

2 3D Image-based Meshing

As with OOF2, the OOF3D meshing scheme begins with image or EBSD data that has been segmented, that is, broken up into distinct sets of voxels that correspond to the material phases of the microstructure. Image segmentation is a rich topic beyond the scope of this paper. For our purposes here, we will assume that a segmentation of the image exists, and also treat “voxel group”, “voxel category”, and “material” as synonyms, although they have slightly differing technical meanings within the OOF3D program.

While OOF2 allows mixed meshes of triangles and quadrilaterals, the current OOF3D code allows only tetrahedra. As discussed in [5], finding measures of shape quality that are consistent for different element types poses a significant challenge. In 3D, this challenge becomes greater as mixed meshes require at least three types of elements (tetrahedra, hexahedra, and wedges, for instance). It is not clear that the benefits of mixed meshes outweigh the difficulties. For this reason, we have implemented only tetrahedral meshes though our methods could feasibly be extended to hexahedral meshes as well.

2.1 Mesh Quality

In order for the mesh modification routines to make decisions between various possible local modifications, two mesh quality measures are introduced: element homogeneity, which reflects the degree to which the mesh represents the microstructure, and shape quality, which aids in good convergence behavior in the finite-element solution steps.

We define two element functionals which we call “energies”. The homogeneity energy measures how well the mesh matches the voxel regions, and the shape energy quantifies the quality of the shapes of elements. We use the word “energy” because some of our mesh modification routines, such as the Anneal routine [5], move the mesh nodes as if they were physical particles with potential energies given by the shape and homogeneity functionals. If the weighted average of the two energies, summed over elements, is low, the mesh is a good finite element representation of the microstructure.

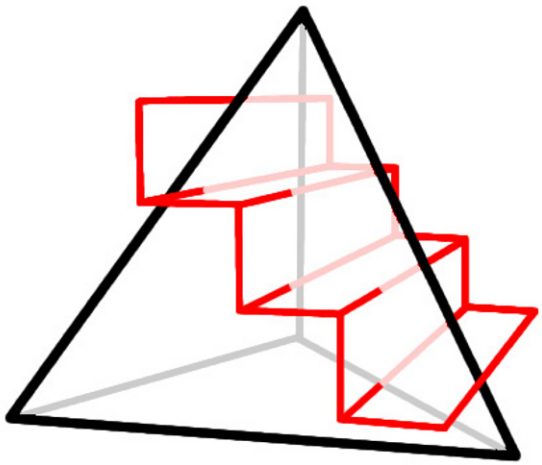

Figure 1: The black lines represent the tetrahedral element and the red lines represent a boundary between two voxelized material regions. The homogeneity is the ratio of the maximum element volume occupied by one material to the total element volume. Calculating this requires finding the volume overlap of the tetrahedron with the voxelized region corresponding to each material.

The homogeneity (see Figure 1) is a measure of how close an element is to enclosing a region that contains a single material:

$$H = \frac{\max_i \{v_i\}}{V} \tag{1}$$

where v_i is the volume within the element that belongs to material i and V is the total volume of the element. (Note that v_i includes the fractional volume of voxels that intersect the element boundaries so that the functional is a continuous function of the node positions.) If an element is filled with only one material, $H = 1$. The corresponding homogeneity energy is defined by

$$E_{\mathsf{hom}} = 1 - H \tag{2}$$

Calculating the element homogeneity in 3D involves a challenging computational geometry problem: finding the volume intersection of a tetrahedral element with a non-convex, voxelized material region of an image. We have developed an algorithm that ignores the shared internal faces of contiguous material regions and uses careful bookkeeping of topological data to find the element homogeneity in a way that is fast and robust. This algorithm is essential for OOF3D to quickly create efficient and well-formed meshes of complex geometries directly from experimental data and will be described in detail in a future publication [20].

For the shape energy, it is useful to have an energy function which has high values for tetrahedra that have high aspect ratios, resembling needles or plates. These elements can lead to slow convergence of the finite element solver[21]. For tetrahedral elements, the shape energy is taken to be

$$E_{\mathsf{shape}} = 1 - \frac{3^{\frac{7}{4}}}{2^{\frac{3}{2}}} \frac{V}{A_{rms}^{\frac{3}{2}}} \tag{3}$$

where A_{rms} represents the root-mean-square face area of the tetrahedron. E_{shape} is zero for regular tetrahedra and 1 for flat tetrahedra. This measure is chosen because it is scale-invariant and varies smoothly with node positions [22, 21].

These two measures can be combined into an effective element energy

$$E = \alpha E_{\text{hom}} + (1 - \alpha) E_{\text{shape}} \tag{4}$$

where α is a tuneable parameter. In several of the mesh adaptation routines, the user may adjust α according to whether the priority is improving shape quality or homogeneity.

2.2 Adaptive Methods

The two primary categories for mesh adaptation routines used in OOF3D are routines that (1) move nodes but preserve the connectivity or topology of the starting mesh (*e.g.* Anneal, Snap Nodes), and (2) routines that change the topology by adding, removing, or reconnecting nodes (*e.g.* Refine, Snap Refine). Mesh modifiers in the first category that also do not depend on predetermined snapping rules (Anneal, Relax, Smooth, Fix Illegal, and Manual node motion) generalize in a straightforward way for OOF3D by simply allowing the nodes to move in all three dimensions. OOF2 mesh modification routines that are specific to triangles and quadrilaterals (*e.g.* Split Quads, Swap Edges, and Merge Triangles) have not been generalized for OOF3D.

In the following sections, we describe the 3D generalizations of the routines described in [5] that are significantly different from their 2D counterparts including Snap Nodes, Fix Illegal Elements, Refine, Snap Refine, and Rationalize.

2.2.1 Snap Nodes

Snap Nodes attempts to move element nodes directly to the boundaries of voxel categories. In OOF3D, Snap Nodes follows a similar general procedure as in OOF2:

1. Loop over the elements to identify transition points between voxel categories along each segment of each element.
2. Find all possible snap movements involving one, two, three, or all four nodes (as opposed to only one or two nodes in 2D) and assign a priority to each.
3. Starting with the highest priority, and choosing randomly from snaps with equal priorities, choose a node move, if any, considering the user chosen criterion for acceptance or rejection.

A key difference in Snap Nodes in 3D versus 2D is the number of possible moves. In 2D, there were five marking types (topologically equivalent sets of edges marked by a transition point) for two element types and a total of 10 different snapping rules. In 3D, there are eight different possible edge marking types (one for one edge, two for two edges, three for three edges, and two for four edges) and a total of 142 different snapping rules.

2.2.2 Refine and Snap Refine

Refine and Snap Refine subdivide tetrahedral elements into smaller tetrahedra, creating more degrees of freedom in the mesh. This is done in two steps. First the elements are marked for subdivision. For Refine, the segments are subdivided according to user criterion whereas for Snap Refine, the positions of the new nodes are chosen to be the transition points along the element segments. Second, each element with marked edges is replaced with a set of smaller elements. While the Refine method in OOF2 allowed trisection and bisection of elements as well as the choice to preserve only quadrilaterals or triangles, in OOF3D, only bisection for tetrahedra are allowed and the rules used by

Refine and Snap Refine are the same. As with Snap Nodes, the set of predetermined rules is much greater for 3D than for 2D. In 3D there are 10 different edge marking types and a total of 60 different refinement rules.

In 3D, refinement has the extra requirement that the element refinements of neighbors much have consistent face refinements. For certain marking types, if all the neighbors have already been refined, this can create a situation where the best way to refine the element is to add a node to the center. Since this leads to a greater number of degrees of freedom, which we wish to minimize, elements with markings that have the potential to fall into this trap are sorted out during the edge marking step and handled first.

2.2.3 Rationalize

Rationalize fixes badly shaped tetrahedra by performing local remeshing. Unlike OOF2, Rationalize in OOF3D does not have subalgorithms. Rationalize searches for tetrahedra that have extreme angles in the triangular faces, extreme dihedral angles between pairs of faces, or extreme solid angles at nodes. For elements with small face-corner angles or dihedral angles, the nodes opposite the small angle are merged, removing all elements that shared the removed segment. For an element with one node that has a large solid angle, the element and the neighboring element that shares the face opposite the node with the large angle, are rearranged into three elements. For elements for which all four nodes are nearly in the same plane, with two segments that nearly form an 'X', a node is added where the segments nearly intersect and all neighbors that share one of these segments is divided in half.

3 Trabecular Bone

Figure 2: 3D micro CT scan of a trabecular bone biopsy taken from the femoral neck of a 61 year old human male. This sample is 100 $\times$ 100 $\times$ 100 voxels and represents approximately 2mm $\times$ 2mm $\times$ 2mm. The solid bone is represented in white and the pink fog is included to add a perception of depth.

Trabecular bone is comprised mostly of calcium hydroxyapatite in a complex, sponge like microstructure that is difficult to mesh. Figure 2 shows a sample of trabecular bone visualized with OOF3D. This data set was collected by Perilli et. al. and provided publicly to other research groups [23, 24].

Recent studies suggest that the risks of osteoporosis are linked not only to bone density, but that the microscale structure of trabecular bone also plays an important role [17]. Previous finite element studies of trabecular bone have used

meshes created by converting voxels to brick elements which has the pitfalls described above: too many elements, and the resolution of voxelization artifacts [17, 18]. These studies are limited to length scales less than about 5mm and to simulating linear elastic and yield properties.

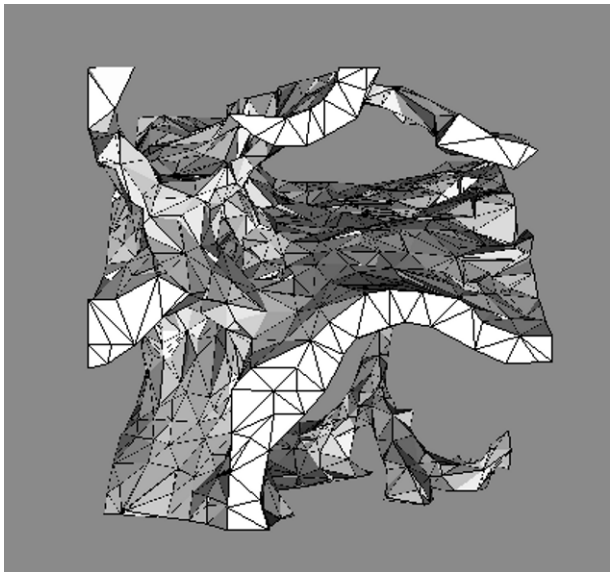

Figure 3: A finite element mesh created with OOF3D from the data shown in figure 2. The Refine, Snap Nodes, Rationalize, and Snap Refine routines were used.

Preliminary OOF3D data shows that we can achieve up to a 50-fold improvement in the number of elements needed to mesh trabecular bone. The mesh shown in figure 3 was created with OOF3D from the data shown in figure 2 and has a total of about 20,000 elements compared to 10^6 voxels. This will drastically increase the scope of possible simulations. With more powerful meshing capabilities, we will be able to perform larger scale simulations with a greater range of physical phenomena including plasticity, fracture and remodeling (the process by which bone is broken down and rebuilt).

4 Conclusion

We have described the updates to measures of mesh quality and mesh modification routines from [5] necessary to generalize the OOF tool to three dimensions. We have demonstrated our three dimensional image-based meshing technique on trabecular bone and found a 50-fold improvment in mesh efficiency versus meshing techniques that create a number of elements on the same order as the number of voxels.

Future plans include adding interface properties for cohesize zone models of fracture [25, 26, 27] and integrating the multiscale method of Overlapping Finite Elements and Molecular Dynamics (OFEMD) [28] with the 3D image based meshing of OOF3D. The result will be the capability to perform fully atomistic, fully continuum, or multiscale fracture simulations based on realistic geometries. If the microstructure characterization technique is nondestructive, such fracture simulations can be compared directly to fracture experiments done on the same sample. By refining simulation techniques through direct comparisons to experiments, we could potentially create a simulation method that can accurately predict the fracture behavior of a microstructure allowing us to not only gain greater insights into which structural features of microstructures determine fracture properties, but to design new material microstructures with desired properties.

5 Acknowledgments

The OOF2 program, including source code, is available at http://www.ctcms.nist.gov/oof/oof2/. OOF2 was produced by NIST, an agency of the U.S. government, and by statute is not subject to copyright in the United States. Recipients of the software assume all responsibilities associated with its operation, modification and maintenance.

We also acknowledge the valuable contributions of Seung-Ill Haan, Rhonald C. Lua, R. Edwin García, Craig Carter, and Ed Fuller to previous versions of OOF on which OOF3D is based.

To be notified when OOF3D is available, add yourself to the OOF email list. http://www.ctcms.nist.gov/oof/mail.html

References

[1] Stephen A. Langer, Edwin R. Fuller, Jr, and W. Craig Carter. Oof: An image-based finite-element analysis of material microstructures. *Computers in Science and Engineering*, 3(3):15–23, 2001.

[2] Stephen A. Langer, Andrew C. E. Reid, R. Edwin García, Seung-Ill Haan, Rhonald C. Lua, W. Craig Carter, Edwin R. Fuller, Jr, and Andrew Roosen. Oof: Analysis of real material microstructures. Webpage. http://www.ctcms.nist.gov/oof/index.html.

[3] Stephen A. Langer, Andrew Reid, Seung-Ill Haan, and R. Edwin García. The oof2 manual. website. http://www.ctcms.nist.gov/~langer/oof2man/index.html.

[4] R. Edwin García, Andrew C. E. Reid, Stephen A. Langer, and W. Craig Carter. Microstructural modeling of multifunctional material properties: The oof project. In Dierk Raabe, Franz Roters, Frédéric Barlat, and Long-Qing Chen, editors, *Continuum Scale Simulation of Engineering Materials*. Wiley-VCH, 2004.

[5] Andrew C. E. Reid, Stephen A. Langer, Rhonald C. Lua, Valerie R. Coffman, Seung-Ill Haan, and R. Edwin García. Image-based finite element mesh construction for material microstructures. *Computational Materials Science*, 43:989–999, 2008.

[6] Andrew C. E. Reid, Rhonald C. Lua, R. Edwin García, Valerie R. Coffman, and Stephen A. Langer. Modelling microstructures with oof2. *Int. J. Materials and Product Technology*, 35(3/4), 2009.

[7] A. D. Jadhav, N. P. Padture, E. H. Jordan, M. Gell, P. Miranzo, and Edwin R. Fuller, Jr. Low-thermal conductivity plasma-sprayed thermal barrier coatings with engineered microstructures. *Acta Materialia*, 54(12):3343–3349, 2006.

[8] V. Cannillo, T. Manfredini, M. Montorosi, and A.R. Boccaccini. Investigation of the mechanical properties of moreinforced glass-matrix composites. *Journal of Non-Crystalline Solids*, 344:88–93, 2004.

[9] R. Edwin García, W. Craig Carter, and Stephen A. Langer. The effect of texture and microstructure on the macroscopic properties of polycrystalline piezoelectrics: Application to barium titanate and pzn-pt. *Journal of the American Ceramic Society*, 88(3):750–757, 2005.

[10] R. Edwin García, Yet-Ming Chiang, W. Craig Carter, Pimpa Limthongkul, and Catherine M. Bishop. Microstructural modeling and design of rechargeable lithium-ion batteries. *Journal of the Electrochemical Society*, 152(1):A255–A263, 2005.

[11] Jonathan E. Spowart. Automated serial sectioning for 3-d analysis of microstructures. *Scripta Materiala*, 55:5–10, 2006.

[12] Anthony D. Rollett, S.-B. Lee, R. Campman, and G.S. Rohrer. Three-dimensional characterization of microstructure by electron back-scatter diffraction. *Annual Review of Materials Research*, 37(1):627–658, 2007.

[13] Donald H. Bilderback, Charles Sinclair, and Sol M. Gruner. The status of the energy recovery linac source of coherent hard x-rays at cornell univerity. *Synchrotron Radiation News*, 19(6):30, 2006.

[14] K.D. Finklestein, I.V. Bazarov, M. Liepe, Q. Shen, D. Bilderback, S. Gruner, and A. Kazimirov. Energy recover linac: A next generation source for inelastic x-ray scattering. *Journal of Physics and Chemistry of Solids*, 66:2310, 2005.

[15] E.J. Garboczi, D.P. Bentz, and N.S. Martys. Digital images and computer modeling. In Po-Zen Wong, editor, *Methods in the Physics of Porous Media*, pages 1–41. Academic Press, San Diego, CA, 1999.

[16] A.P. Roberts and E.J. Garboczi. Elastic properties of model porous ceramics. *J. Am. Ceram. Soc.*, 83:3041–3048, 2000.

[17] Babul Borah, Gary J. Gross, Thomas E. Dufresne, Tim S. Smith, Michael D. Cockman, Paula A. Chmielewski, Mark W. Lundy, James R. Hartke, and Earl W. Sod. Three-dimensional microimaging (mrμi and μct) finite element modeling, and rapid prototyping provide unique insights into bone architecture in osteoporosis. *The Anatomical Record*, 265:101–110, 2001.

[18] B. van Rietbergen, H Weinans, R Huiskes, and A. Odgaard. A new method to determine trabecular bone elastic properties and loading using micromechanical finite-element models. *Journal of Biomechanics*, 28(1):69–81, 1995.

[19] W. Schroeder, K. Martin, and Bill Lorensen. *The Visualization Toolkit: An Object-Oriented Approach to 3D Graphics*. Prentice Hall, 2006.

[20] Valerie R. Coffman, Andrew C.E. Reid, and Stephen A. Langer. Element homogeneity: calculating the intersection of finite elements with voxelized regions. *In Preparation*, 2010.

[21] J.R. Shewchuck. What is a good linear element? interpolation, conditioning, and quality measures. In *Eleventh International Meshing Roundtable*, pages 115–126, Ithaca, New York, 2002. Sandia National Laboratories.

[22] J.R. Shewchuck. What is a good linear finite element? interpolation, conditioning, anisotropy, and quality measures. *preprint*, 2002.

[23] E. Perilli, F. Baruffaldi, M. Visentin, B. Bordini, F. Traina, A. Cappello, and M. Viceconti. MicroCT examination of human bone specimens: effects of polymethylmethacrylate embedding on structural parameters. *JOURNAL OF MICROSCOPY-OXFORD*, 225(2):192–200, FEB 2007.

[24] X-ray microct scans of human bone biopsies. Webpage. http://www.biomedtown.org/biomed_town/LHDL/Reception/datarepository/repositories/BelRepWikiPages/XRayMicroCTScansOfHumanBoneBiopsies.

[25] X. P. Xu and A. Needleman. Numerical simulations of fast crack groth in brittle solids. *Journal of the Mechanics and Physics of Solids*, 42(9):1397–1434, 1994.

[26] G. T. Camacho and M. Ortiz. Computational modelling of impact damage in brittle materials. *International Journal of Solids and Structures*, 33:2899–2938, 1996.

[27] Viggo Tvergaard and John W. Hutchinson. The relation between crack growth resistance and fracture process parameters in elastic-plastic solids. *Journal of the Mechanics and Physics of Solids*, 40(6):1377–1397, 1992.

[28] Valerie R. Coffman, James P. Sethna, Jeff Bozek, Anthony Ingraffea, Nicholas P. Bailey, and Erin I. Barker. Challenges in continuum modeling of intergranular fracture. *to appear in Strain*, 2010.

Proceedings of the SEM Annual Conference
June 7-10, 2010 Indianapolis, Indiana USA

Prediction of Landslide by Displacement Measurement using Sampling Moiré Method

Yoshiharu Morimoto[1,a], Motoharu Fujigaki[2,b], Akihiro Masaya[2,c],
Yuji Sasatani[2,d] , Hiroyuki Kondo[2,e] and Makiko Nakabo[2,f]

[1]Moire Institute Inc., 2-1-4-804, Hagurazaki, Izumisano, Osaka 598-0046, Japan
[2]Wakayama University, Sakaedani, Wakayama 640-8510, Japan
[a]morimoto@moire.or.jp, [b]fujigaki@sys.wakayama-u.ac.jp, [c]masaya@sys.wakayama-u.ac.jp,
[d]sasa0721@center.wakayama-u.ac.jp, [e]s102023@sys.wakayama-u.ac.jp,
[f]s112039@sys.wakayama-u.ac.jp

Abstract
In sampling moiré method, a specimen grating pattern on an object is recorded by a digital camera. A moiré fringe pattern appears by sampling the recorded grating pattern with a constant pixel pitch. The phase analysis of the moiré patterns obtained from one grating pattern provides accurate results of displacement values of the grating. Meanwhile, it is very important to keep our life safely by predicting landslides. If the small displacement of land before the landslide is detected, it is possible to put out an alert before the disaster happens. In this paper, a measurement system for small displacement of landslide by sampling moiré method is developed.

INTRODUCTION

In sampling moiré method or scanning moiré method [1, 2], a specimen grating pattern on an object is recorded by a digital camera. Though the digitized image shows only the specimen grating, a moiré fringe pattern appears by thinning-out the pixels, i.e., sampling the image with a constant pixel pitch. This method was extended to a phase analysis method for a fringe pattern [3]. It is very simple and the accuracy is very high. This method is, therefore, suited for practical uses. The authors also applied this method to shape, deformation and strain measurement [4,5,6]. If the sampling pitch is changed, the moiré pattern is changed. If the phase of the sampling, i.e., the start pixel of the sampling is changed, the phase of the moiré pattern is changed. By using the phase-shifted moiré patterns, the phase distributions of the moiré fringes are analyzed. This sampling moiré method is very easy to use. It will be a new tool for experimental mechanics and health monitoring for measuring shape, displacement and strain distributions of materials and structures.

Meanwhile, landslide disaster occurred 803 times in Japan in 2009. The damage due to the landslide disaster was large. It is requested to develop methods to predict landslides. The landslide includes fatal possibility because it is sudden disaster. A small displacement occurs before the sudden landslide [7]. If the small displacement is detected, it is possible to make an alert just before the disaster happens. It is necessary to measure small displacement of slope and cliff with high reliability and in real time. There are some methods for detection of the landslide. For example, the method of determining the tension of wire between two piles, and method using optical fiber are used [8]. However the cost is high and it requires measuring devices on the land. It is required to develop a real-time measurement method with low cost, easy-to-use and high reliability. In this paper, the sampling moiré method is applied to predict landslides. It is very fine to predict a small displacement of land without

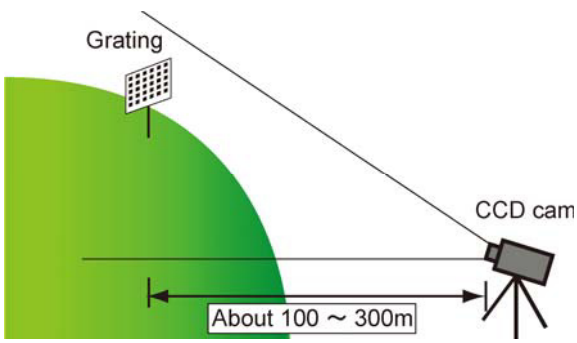

Fig.1 Displacement measurement of slope

T. Proulx (ed.), *Application of Imaging Techniques to Mechanics of Materials and Structures, Volume 4*, Conference Proceedings of the Society for Experimental Mechanics Series 14, DOI 10.1007/978-1-4419-9796-8_48, © The Society for Experimental Mechanics, Inc. 2013

electric wires used in strain gage method.

Figure 1 shows a conceptual view of a displacement measurement method proposed for detecting small displacement of a slope. A stake with a grating is set on the slope. The displacement of the stake is measured at long-range by the sampling moiré method. The cost of the system is low because only a stake with a grating, a camera and a PC are necessary.

In this paper, a detection system for small displacement of landslide by sampling moiré method is developed and the experimental results are shown.

PRINCIPLE OF SAMPLING MOIRE METHOD

In sampling moiré method [4,5,6], a specimen grating pattern on an object is recorded by a digital camera. Though the digitized image shows only the grating, a moiré fringe pattern appears by thinning-out the pixels, i.e., by sampling the image with a constant pixel pitch. Figure 2 illustrates the appearance of moiré fringe patterns by sampling moiré method. In this figure, though only three vertical pixels of the recorded image are shown, the sampling pixel number is corresponding to the number of the camera resolution such as 640, 1280 pixels, etc in actual case. Figure 2(a) shows deformed grating pattern attached on the specimen. The pitch of the grating in this figure is 1.125 times larger than that of the sampling points. Then, the recorded image by the camera is shown in Fig. 2(b), in which no moiré fringe pattern can be discerned. Figure 2(c) shows the moiré fringe patterns when the recorded image is sampled at every N-pixel (in the figure, N = 4). The four images of Fig. 2(c) are obtained by sampling at the first, second, third and fourth pixels of Fig. 2(b) as the sampling start point. This process is corresponding to the phase-shifting of the fringe pattern. At the pixels without data of these images shown in Figs. 2(c), the brightness values are obtained by interpolating the neighboring sampled data. Then, the four phase-shifted moiré images shown in Fig. 2(d) are obtained from single picture of Fig. 2(b). From the phase-shifted moiré images, the phases of the moiré pattern are calculated as follows.

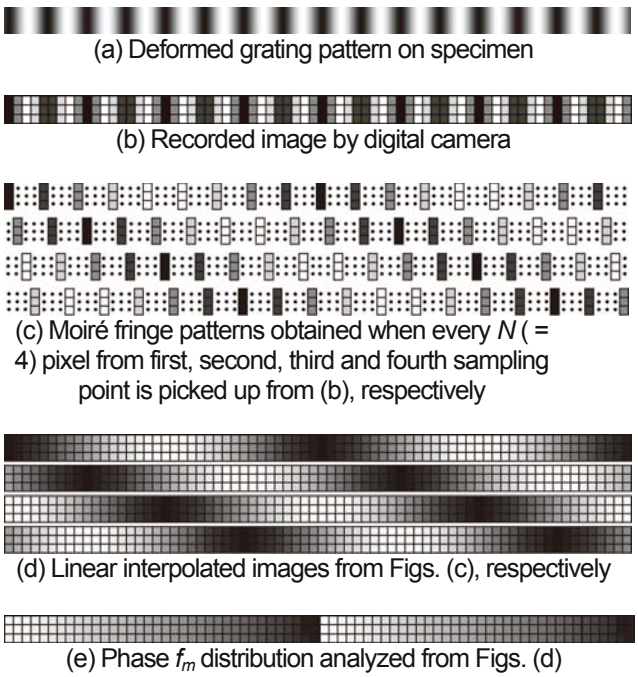

Fig. 2. Principle of phase-shifting moiré method

The k-th phase-shifted images can be expressed approximately as follows:

$$I_k(i,j) = I_a(i,j)\cos[\phi(i,j) + k\frac{2\pi}{N}] + I_b(i,j) \qquad (k = 0,1,...,N-1) \tag{1}$$

Where $I_b(i,j)$ represents background brightness in the image, which are insensitive to the change in phase; $I_a(i,j)$ represents the amplitude of the grating brightness and $\phi(i,j)$ is the initial phase value. The phase distribution of the moiré pattern can be obtained by Discrete Fourier transform (DFT) algorithm using Eq. (2) or phase-shifting method using Fourier transform (PSM/FT) [9] as follows:

$$\phi(i,j) = -\tan^{-1}\frac{\sum_{k=0}^{N-1} I_k(i,j)\sin(k\frac{2\pi}{N})}{\sum_{k=0}^{N-1} I_k(i,j)\cos(k\frac{2\pi}{N})} \tag{2}$$

The phase analysis of the moiré pattern provides accurate results of displacement values of the grating. If the number N of the phase-shifted moiré patterns is larger, the phase analysis becomes more accurate.

The phase ϕ_m of the moiré pattern is the difference between the grating phase ϕ_s and the reference phase ϕ_r of the grating (i.e., the sampling phase) as follows:

$$\phi_s = \phi_r - \phi_m \tag{3}$$

When the object is deformed, the relationship between the phase-differences $\Delta\phi_s$ and $\Delta\phi_m$ of ϕ_s and ϕ_s, respectively before and after deformation is obtained as follows:

$$\Delta\phi_s = -\Delta\phi_m \tag{4}$$

Therefore, the phase-difference $\Delta\phi_s$ of the grating pattern can be calculated from the phase-difference $\Delta\phi_m$ of the moiré pattern.

From the moiré phase difference between before and after movement of the grating, the displacement of the grating is obtained. The relationship between the displacement Δx and the phase difference $\Delta\phi_m$ is expressed in Eq. (5).

$$\Delta x = \frac{\Delta\phi_m}{2\pi} \times p \tag{5}$$

where p is the pitch of the grating.

EXPERIMENTS AND RESULTS

In order to check the accuracy of sampling moiré method for landslide, three experiments for the distance from a camera to a target in the case of close (3m), middle (17m) and long (140m) ranges are performed.

Close Range Experiment

Experimental Setup

The accuracy of the displacement measurement by sampling moiré method at close range is confirmed by this experiment. Figure 3 shows a schematic view of the experiment. L in Fig. 4 is the distance between the grating and the CCD camera. L is 3 m in this experiment.

Figure 4 shows a target plate set on a moving linear stage. A one-dimensional grating and a two-dimensional grating are put on the plate. Ronchi gratings with two values black and white are used. That is, one has a one-dimensional rectangular brightness distribution and the other has a two-dimensional rectangular brightness distribution. All of the pitches of the gratings are 15 mm. The gratings are fixed on a moving stage. The accuracy of the moving stage is 3 μm.

The target plate is moved in the x-direction from 0.0 mm to 5.0 mm at intervals of 0.5 mm by the moving linear stage.

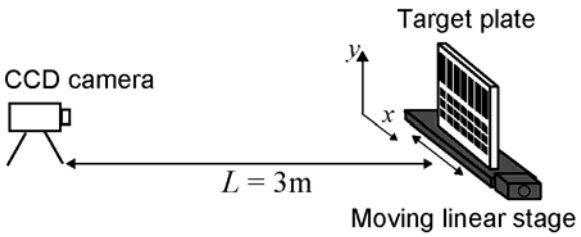

Fig. 3 Experiment scenery

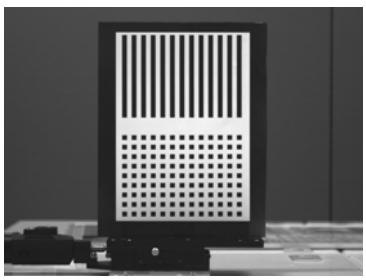

Fig. 4 Image of target plate

Experimental Results

Figure 5 (a) is a recorded image. In this image, the grating pitch N is almost 28 pixels. Figure 5 (b) shows the moving averaged image for the y-directional 28 pixels of Fig. 5 (a). This image shows that the two-dimensional grating image is changed into a one-dimensional grating image. Figure 5 (c) shows the phase distribution of the moiré pattern obtained by sampling moiré method before movement. Figure 5 (d) shows the displacement distribution between before and after movement of the target plate. The displacement was calculated as the average in the analyzed area size, 230 x 120 pixels. The analyzed areas are shown as rectangles in Figure 5 (d).

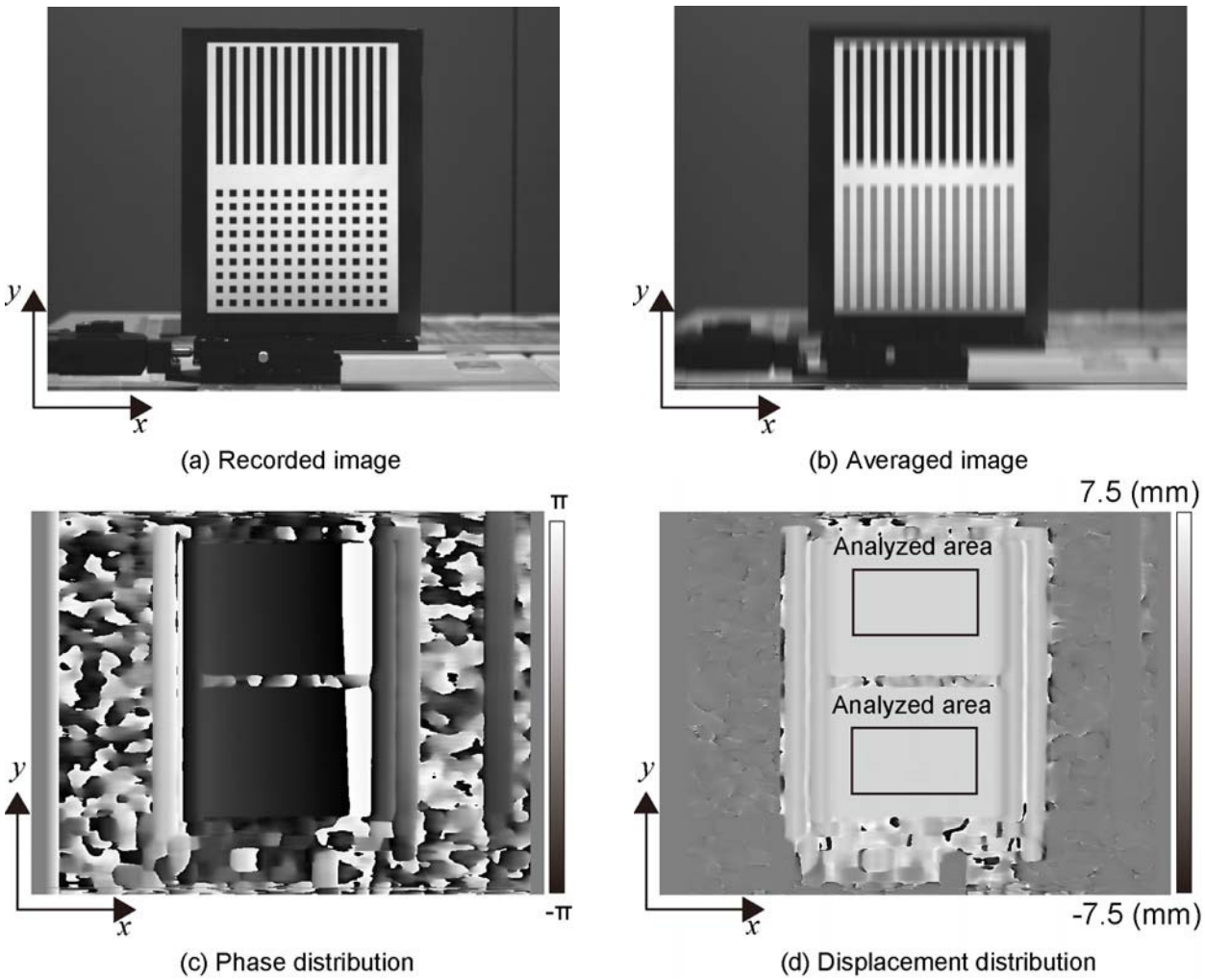

Fig. 5 Process of experiment

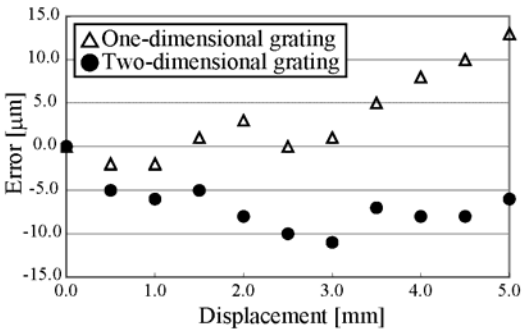

Fig. 6 Error of displacement measurement

Table 1: Average and standard deviation of errors [μm]

	Average error	Standard deviation
One-dimentional grating	3.7	5.2
Two-dimentional grating	-7.4	2.0

Figure 6 shows the error distribution of the result of the *x*-directional displacement measurement. Table 1 shows the average of the errors. The average errors were 4 μm and -7 μm for one-dimensional grating and two-dimensional grating, respectively. The analyzed displacement was very accurate.

Middle Range Experiment

Experimental Setup

The accuracy of the displacement measurement by sampling moiré method at middle range is confirmed. The distance L between the grating and the CCD camera as shown in Fig. 4 is 17 m in this experiment. The target plate is moved in the x-direction from 0.0 mm to 5.0 mm by the moving linear stage and stopped at intervals of 0.5 mm for a few hundred second.

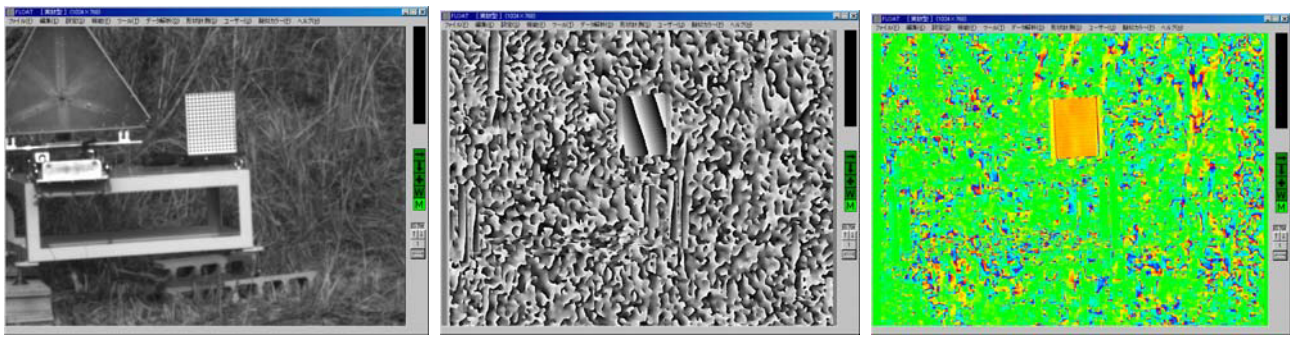

(a) Target with grating on stage (b) phase distribution (c) Displacement distribution

Fig. 7 Process of experiment

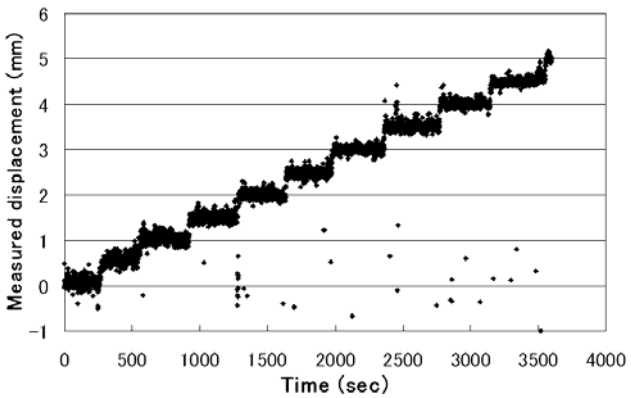

Fig. 8 Measured displacement values while displacement is given at every 0.5mm with time

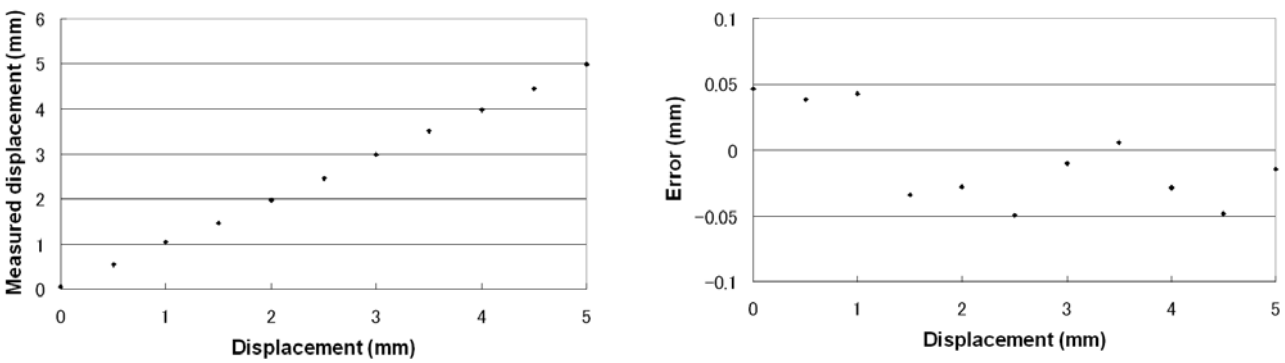

(a) relationship between given displacement and measured displacement

(b) Error for given displacement

Fig. 9 Results of displacement measurement

In this case, only a two-dimensional grating with a rectangular brightness distribution is used. The pitch of the grating is 15 mm. The grating is fixed on the moving stage.

Experimental Results

Figure 7 (a) shows a recorded image. In this image, the grating pitch N is almost 10 pixels. The analyzed area is 147x185 pixels. By averaging this image in the y-direction, the x-directional phase distribution of the moiré is obtained using the sampling moiré method. Figure 7 (b) shows a phase distribution during moving the target plate with a two-dimensional grating. Figure 7(c) shows the displacement distribution when the x-directional displacement is 5mm. Figure 8 shows the measured displacement change with time. The displacement was obtained by averaging 30 data for each stopping. The relationship between the averaged displacement and the given displacement is shown in Fig. 9 (a). Figure 9(b) shows the error distribution of the displacement measurement. The average errors were less than 50 μm. The analyzed displacement was very accurate.

Long Range Experiment

Experimental Setup

The accuracy of the displacement measurement by sampling moiré method at long range is confirmed by this experiment. Moreover the availability of averaging is confirmed by this experiment.

A plate with a grating and the moving stage are used in a long range experiment. Figure 10 shows a conceptual view of the experiment. The distance L' between the target and the CCD camera is 140 m in this experiment. Figure 11 shows a CCD camera and a telescopic lens fixed at the wall on the fourth floor of a building. The focus length of the lens is 500mm. Figure 12 shows a moving stage, a target plate with a two-dimensional grating and a fixed plate. The target plate is moved in the x-direction from 0.0 mm to 5.0 mm at intervals of 0.5 mm with the moving linear stage.

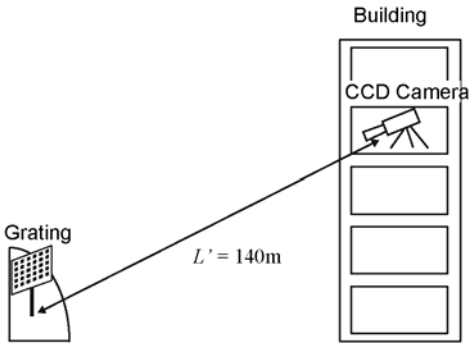

(a) Schematic view of experiment

Photo from grating to building

Fig. 10 Experiment scenery

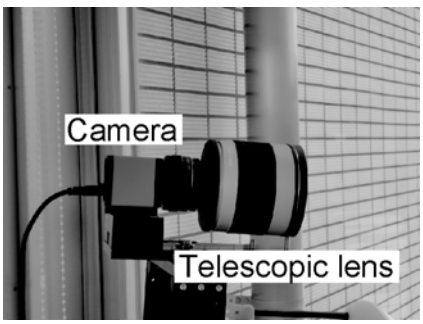

Fig. 11 Camera and lens

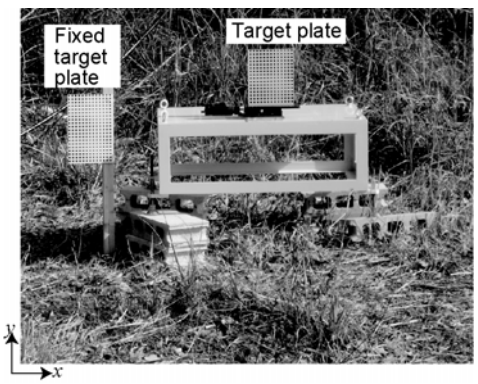

Fig. 12 Moving stage and target

Experimental Results

Since the grating image was captured with a telescopic lens, fluctuation of air appeared in the recorded image. In this case, the displacement was calculated from one image and also from the averaged image of 25 images which were recorded at every 400 msec, as shown in Fig. 13.

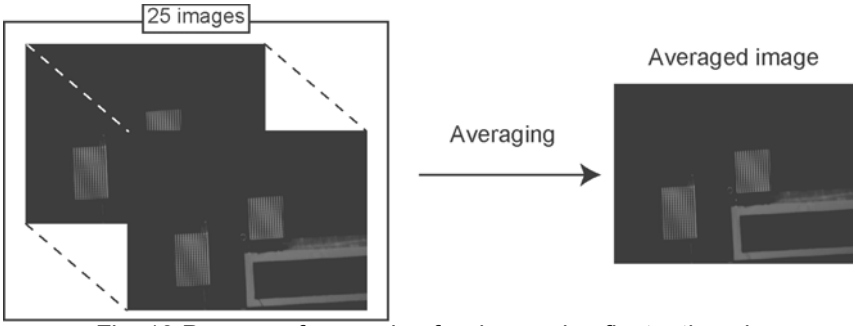

Fig. 13 Process of averaging for decreasing fluctuation air

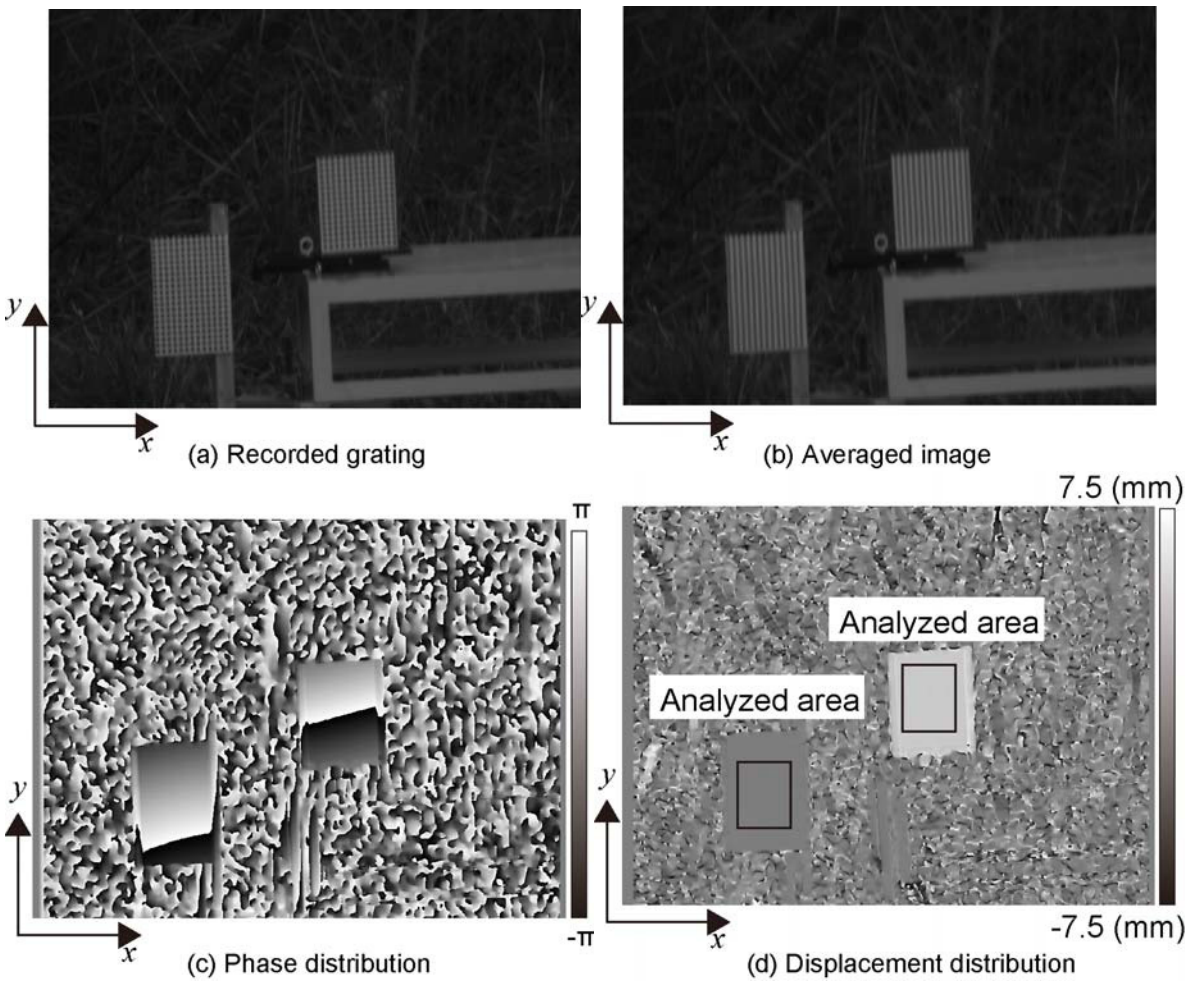

Fig. 14 Process of experiment

Figure 14(a) shows the recorded images of the two-dimensional grating with about 11 pixel pitch. In order to extract the x-directional grating of Fig. 14(a), the image was averaged in the y-direction and then Fig. 14(b) was obtained. Figure 14(c) shows the phase distribution of the moiré obtained by sampling moiré method. The target plate was moved with moving stage. Figure 14(d) shows the displacement distribution after the movement. The displacement was averaged in the rectangular area with100x125 pixels shown in the figure.

Figure 15 shows the measured displacement values and error values. Table 2 shows the error and the standard deviation of the measured displacement.

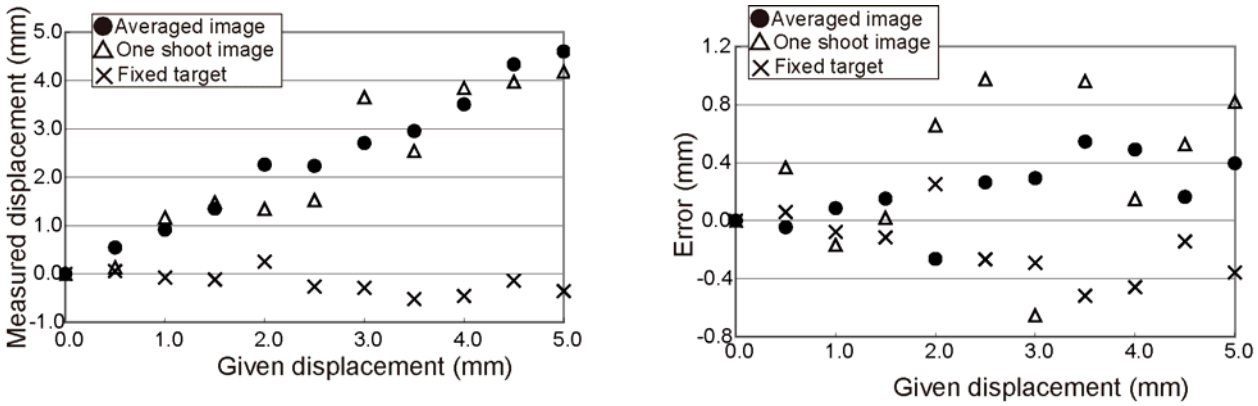

(a) Measured displacement (b) Error of measured displacement

Fig. 15 Results of experiment

Table 2 Error and standard deviation of measured displacement (μm)

	Moving target		Fixed target
	One image	Average of 25 images	Average of 25 images
Average error	330	190	170
Standard deviation	510	240	230

CONCLUSIONS

The displacement measurement by sampling moiré method was proposed. It was confirmed that the accuracy of the analyzed displacement was less than 10 μm at close-range and 50 μm at middle-range. At long-range, the influence of air fluctuation was problem. The error due to the fluctuation was decreased into 230 μm by averaging of 25 pictures. It is confirmed that the sampling moiré method is useful to detect small displacement of the land just before landslides.

REFERENCES

1. Morimoto, Y. and Hayashi, T., Deformation Measurement During Power Compaction by a Scanning-moiré Method, Experimental Mechanics, 24 (2), p.112-116 (1984)
2. Morimoto, Y. Yang, I.-H. and Gu, C.-G., Scanning Moiré Method for Obtaining Smooth Fringe Patterns, Optics and Lasers in Engineering, 24p.3-17 (1996)
3. Arai, Y., Yokozeki, S, Shiraki, K and Yamada, T. High Precision Two-Dimensional Spatial Fringe Analysis Method, *Journal of Modern Optics*, 44(4): 739-751 (1997).
4. Fujigaki, M., Iwai, K. and Morimoto, Y., Shape Measurement with Grating Projection Using Sampling Moiré Method, *3rd International Symposium on Advanced Fluid/Solid Science and Technology in Experimental Mechanics(ISEM2008)*, #145(CD-ROM) (2008).
5. Ri, S., Fujigaki, M. and Morimoto, Y. Sampling Moiré Method for Accurate Small Deformation Distribution Measurement," *Exp. Mech.*, DOI 10.1007/s11340-009-9239-4x, (2008) and 50-501-508 (29010)
6. Shimo, K., Fujigaki, M., Masaya, A. and Morimoto, Y., Development of Dynamic Shape and Strain Measurement System by Sampling Moiré Method, *ICEM2009* (2009).
7. Fujita, T., *Landslide-geology of disaster in mountain district,* Kyoritsu Publishing, Chapter 6, 107 (1990).
8. Chigira, M., *An introduction to disaster geology,* Kinmiraisha, Chapter 7, 190 (1998).
9. Morimoto, Y. and Fujisawa, M., Fringe Pattern Analysis by a Phase-shifting Method Using Fourier Transform, Optical Engineering, 33(11), p.3709-3714. (1994)

Proceedings of the SEM Annual Conference
June 7-10, 2010 Indianapolis, Indiana USA

INVESTIGATION OF THE COATING PARAMETERS FOR THE LUMINESCENT PHOTOELASTIC COATING TECHNIQUE

Ergin Esirgemez, Daniel R. Gerber and James P. Hubner
Aerospace Engineering and Mechanics Department
The University of Alabama, Tuscaloosa, AL
esirg001@crimson.ua.edu, drgerber@crimson.ua.edu, phubner@eng.ua.edu

ABSTRACT

The luminescent photoelastic coating (LPC) technique is an optical method to measure the full-field strain on 2D and 3D structural components. The maximum shear strain—or separated principal strain when oblique incidence is performed—and its corresponding principal strain direction are related to the relative changes in emission magnitude with respect to analyzer position. The amplitude of the emission change is termed optical strain response, OSR, and is a function of maximum shear strain, γ_{max}, in the plane perpendicular to light propagation and two coating calibration parameters: the polarization efficiency, φ, and the coating characteristic, η. Determining the coating parameters plays an important role since they affect the accuracy of the measurement. Generally, the coating parameters are calibrated *in-situ* with strain gage measurements and assumed independent of surface inclination. A better theoretical understanding of the two calibration coefficients, specifically the polarization efficiency, φ dependence on oblique excitation or emission inclination is necessary to improve full-field, strain-separation accuracy of the measurement. This study investigates and reports the effects of the coating parameters on OSR, and the current methods to determine the coating parameters.

Key Words: luminescence, photoelastic coating, polarization efficiency, strain measurement

1. INTRODUCTION

The luminescent photoelastic coating (LPC) technique is a full-field strain measurement technique that has been developed to measure the strain field on 2D and 3D structures [1]. LPC incorporates both a luminescent dye and absorption dye within a photoelastic binder. The luminescent dye emits at higher wavelength than the excitation and partially preserves the stress-induced polarization of the coating. The absorption dye limits the penetration depth of the excitation and effectively eliminates the coating thickness dependency once a threshold thickness is achieved [2]. The LPC technique uses circular polarized illumination from a light emitting diode (LED) lamp to excite the coating and a charged-couple device (CCD) camera to image the corresponding luminescent emission at different analyzer angles for loaded and unloaded conditions. Images are then stored and analyzed using software to measure the maximum effective in-plane shear strain relative to the LED and CCD position and principal strain direction. A schematic of basic LPC instrumentation is shown in Fig 1.

An LPC measures the maximum shear strain (principal strain differences) and the principal strain direction on the model surface in the plane perpendicular to the propagation of the excitation and emission. Separation of the principal strains requires measurement of the emission intensities at oblique incidence angles and correction of the polarization changes due to the refraction of light [3]. Compared to a reflective photoelastic coating (RPC) which provides a higher absolute-intensity measurement, an LPC provides a higher relative-intensity measurement at oblique angles as shown in Fig. 2. The increased

T. Proulx (ed.), *Application of Imaging Techniques to Mechanics of Materials and Structures, Volume 4*, Conference Proceedings of the Society for Experimental Mechanics Series 14, DOI 10.1007/978-1-4419-9796-8_49, © The Society for Experimental Mechanics, Inc. 2013

relative signal strength at oblique angles of the LPC enhances the ability to separate the principal strains on 3D specimens.

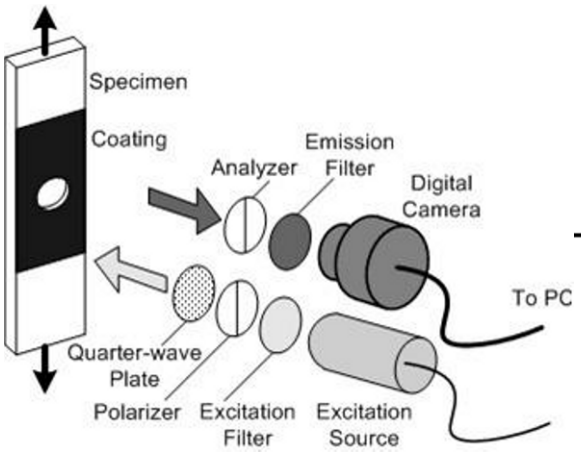

Figure 1. Schematic of basic instrumentation for an LPC system [1].

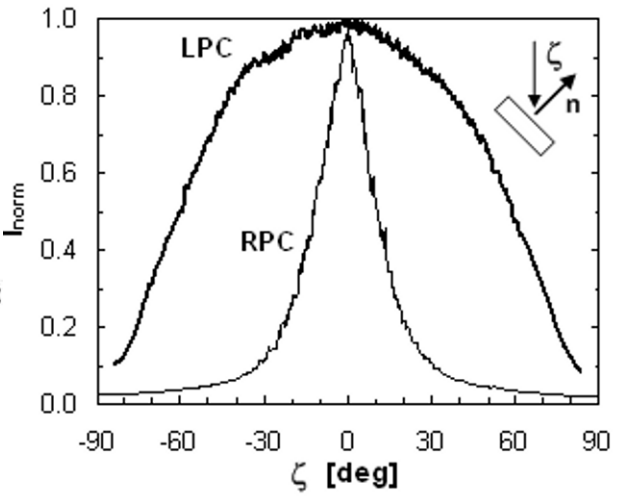

Figure 2. The normalized measured intensity of an LPC and RPC with respect to surface inclination angle, ζ [3].

2. THEORY

The theoretical response of an LPC and the methodology to separate principal strains using oblique incident excitation is detailed in Refs. [1-2] and [3-4], respectively. The generalized intensity response for the LPC technique is

$$\frac{I}{I_{avg}} = 1 + Fsin(2\alpha - 2G)\ , \tag{1}$$

where I is the measured pixel intensity, I_{avg} is the average pixel intensity over a π (180°) analyzer rotation, α is the analyzer angle, *F* is the amplitude and *G* is the phase of the normalized intensity response with respect to initial position of the analyzer angle. For the LPC technique, the amplitude, *F*, termed total optical response (TOR) and the phase, *G*, are the coupled terms that contain the relative retardation in the plane perpendicular to light propagation (due to the strain field), the relative transmission attenuation (due to surface inclination and refraction), the principal strain direction and the excitation incidence plane orientation. In a 2D application, the relative change in emission intensities is a function of the maximum in-plane strain and is called the optical strain response (OSR) and defined as

$$OSR = \varphi\left[\frac{\left(\gamma_{eff}/\eta\right)}{1+\left(\gamma_{eff}/\eta\right)^2}\right] \tag{2}$$

where γ_{eff} is the effective maximum in-plane shear strain (combined retardation effect in the planes perpendicular to excitation and emission), φ is polarization efficiency, and η is the coating characteristic, which is a function of coating absorptivity, a, and the penetration depth, h^*; $\eta = ah^* = a\frac{\lambda^*}{2\pi K}$. For normal excitation and emission, $\gamma_{eff} = \varepsilon_1 - \varepsilon_2$ where 1 and 2 are the principal strain directions in the surface plane and G is the principal direction relative to the zero analyzer position.

The absorptivity is a property of the absorption dye; higher absorptivity decreases the penetration depth of the excitation and reduces the coating thickness required for thickness-independent measurements [2]. The effective wavelength, λ^*, depends on the excitation and emission wavelengths of the luminescent dye and, thus, the excitation and emission filters used by the optical measurement system. The optical sensitivity coefficient, K, of a photoelastic coating is a measure of the birefringent response of the binder

to strain [5]. For an *in situ* calibration, these values are not measured independently but collectively as the coating characteristic. This is similar to the gage factor of an electrical-resistant strain gage being a function of alloy Poisson ratio and resistivity. The coating characteristic can be thought of as a characteristic strain value that affects the curvature and sensitivity of the OSR. The value of η corresponds to the maximum shear strain of the peak OSR. A larger coating characteristic decreases the OSR sensitivity but extends its range, as shown in Fig. 3. The polarization efficiency of the coating is related to the polarization retention of the luminescence. If the luminescence does not retain the strain-induced polarization changes of the excitation passing through the coating, then the emitting intensity will be depolarized and the measured intensity with respect to the analyzer position will be constant. For this case, φ = 0. Changes in the value of the polarization efficiency affect the maximum value the OSR curve attains. The polarization retention of luminescence depends on processes such as photoselection and depolarization [6].

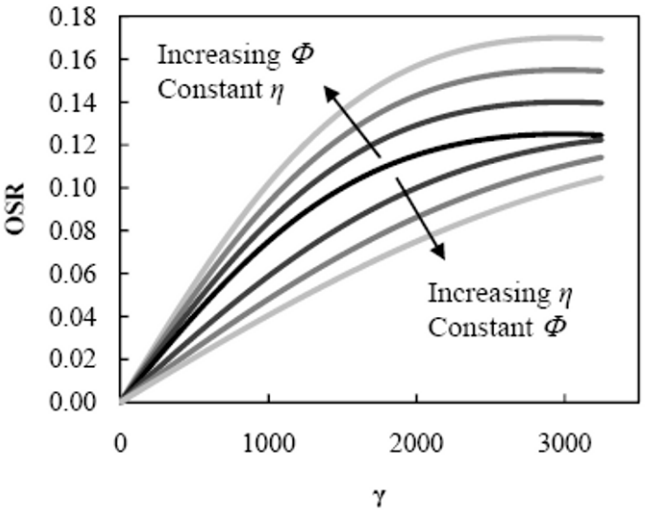

Figure 3. OSR vs maximum shear strain for various values of ϕ and η.

In a 3D application, the relative transmission attenuation of obliquely propagating light creates a change in polarization due to the refractive index change between the coating and the air. This effect, governed by the Fresnel equations, is called the optical Fresnel response (OFR) and must be considered for the full-field 3D measurement or oblique 2D measurement to separate the principal strains. OFR is defined as

$$OFR = \frac{1-T}{1+T}. \tag{3}$$

where the luminescent transmission ratio, *T*, is a function of the refraction index of the coating, n_c, and the incident angle, ζ_i,

$$T = cos^4\left\{\zeta_i - sin^{-1}\left(\frac{1}{n_c} sin\,\zeta_i\right)\right\}. \tag{4}$$

The corresponding direction of the OFR is in the plane defined by the incident excitation and the surface normal. The TOR (F in Eq. 1) can be approximated as a vector sum of the OSR and OFR [3]:

$$\overrightarrow{\mathrm{OSR}} \cong \overrightarrow{\mathrm{TOR}} - \overrightarrow{\mathrm{OFR}}\,. \tag{5}$$

The TOR is measured when a load is applied to the test specimen. The TOR includes residual coating strain, applied strain and the refraction effects.

Separation of principal strains requires measuring the OSR for two or more excitation angles [3-4]. OSR is a function of the maximum shear strain in the plane perpendicular to the propagation of the excitation and emission; therefore, for non-normal incidence, the out-of-plane strain component must be considered. The strain induced retardation depends on the local maximum shear strain, γ_{max}. In general, two LED orientations are defined: one when the excitation (LED) and emission (CCD) propagation vectors are parallel and one when they are oblique. Using principles of photogrammetry [7], image intensities are resectioned onto and analyzed in the domain of a representative FEA-style grid of the specimen [4].

From the grid representation of the specimen, the surface normal vector of a mesh cell can be exploited to calculate the relative surface inclination with respect to the excitation and emission propagation vectors. These propagation vectors depend on the positioning of the LED and CCD as well as the refraction of excitation and emission into and out of the coating. The planes perpendicular to the excitation and emission in the coating are found by a rotation of the grid cell relative to the surface normal. The directions of the new rotated coordinate systems are found using strain coordinate transformation principles [8]. In short, the effective maximum shear strains for parallel and oblique cases can be written in terms of principal strains. Eq. 6 provides the maximum shear strain of the measured OSR. The result is two equations representing the parallel and oblique cases [4]:

$$\gamma_{eff,p} = \gamma' = \sqrt{(K_1\varepsilon_1 + K_2\varepsilon_2)^2 + (K_3\varepsilon_1 + K_4\varepsilon_2)^2} = OSR_p \frac{\eta}{\varphi} \tag{6a}$$

$$\gamma_{eff,o} = \frac{\gamma''}{\tilde{\lambda}_{ex}} + \frac{\gamma'}{\tilde{\lambda}_{em}} \frac{\cos\psi'_{em}}{\cos\psi'_{ex,o}} = \frac{1}{\tilde{\lambda}_{ex}} \sqrt{(K_1\varepsilon_1 + K_2\varepsilon_2)^2 + (K_3\varepsilon_1 + K_4\varepsilon_2)^2}$$
$$+ \frac{1}{\tilde{\lambda}_{em}} \frac{\cos\psi'_{em}}{\cos\psi'_{ex,o}} \sqrt{(K_5\varepsilon_1 + K_6\varepsilon_2)^2 + (K_7\varepsilon_1 + K_8\varepsilon_2)^2} = OSR_o \frac{\eta}{\varphi} \tag{6b}$$

where ψ', is the excitation or emission refracted propagation angle relative to the surface normal, $\tilde{\lambda}$ is the excitation or emission wavelength relative to the effective wavelength, and the terms, K_1-K_8, are the coefficients derived for the transformation of the strains for each grid cell. These coefficients are dependent of the specimen's shape and determined automatically using the surface information of the structural grid. Eqs. 6a and 6b are nonlinear equations and can be solved using Newton-Raphson method [9] to determine the separated principal strains on each node of the 2D or 3D grid. These equations are valid for 2D or 3D structures.

3. EXPERIMENTS and CALIBRATION PROCEDURES

In the LPC method, a series of images using circular polarized light are acquired at various analyzer angles for specimen unloaded and loaded conditions. Images are acquired in the dark, except for the excitation light. A dark-field image (no excitation light) is also captured to correct for the offset noise of the CCD camera. The images of the unloaded condition are used to quantify the residual strains in the coating and other measurement biases. Application of the technique for 3D structures may require a correction if the surface inclination changes relative to the LED and CCD orientation between the loaded and unloaded conditions, e.g. when torque is applied to a cantilever beam. This change in surface inclination causes a change in the measured polarization as modeled by the Fresnel equations—not a photoelastic effect. To account for the Fresnel response in the image processing, a sequence of images (in both loaded and unloaded conditions) is acquired using unpolarized excitation of the coating.

Image warping techniques (2D polynomial or trigonometric transformations) or image resectioning techniques (direct linear transformation) are implemented to align surface target points, which are marked on the surface before the experiment, between the images for the loaded and unloaded conditions. The raw intensities at each pixel of the images over π rotation of the analyzer are fitted to the sinusoidal function in Eq. 1 using the nonlinear Levenberg-Marquardt algorithm.

As an example of a 2D application of the LPC method, an anodized bar (6061-T6 Aluminum, 1 in x 0.25 in x 11 in) coated with an LPC was subjected to the tension. The tension was gradually increased until the bar broke. OSR was measured at each load level. The coating parameters (polarization efficiency, φ, and the coating characteristic, η) was calibrated using a strain gage located on the uncoated surface (backside) of the specimen. Figure 4 shows the theoretical OSR and the experimental results of the aluminum bar. The maximum value of the shear strain measured in the experiment was 11400 με, and the minimum value was 87 με. The root mean square (RMS) error was 2.7%.

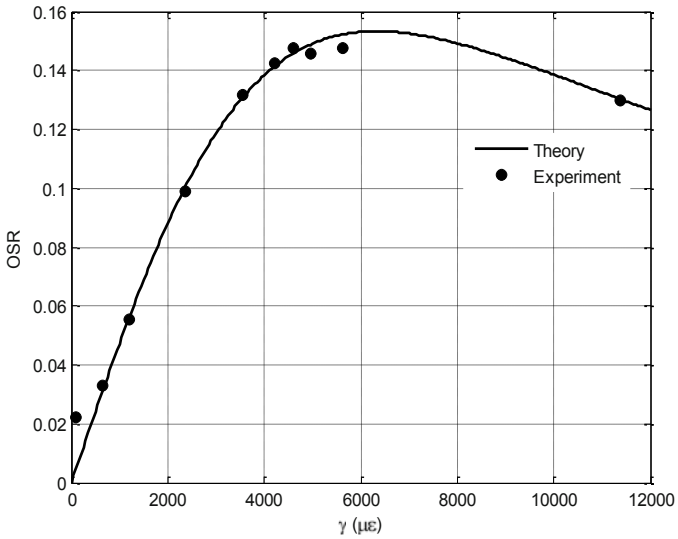

Figure 4. OSR of an LPC coating for the tension test.

It is observed, from Fig. 4, that the sensitivity of the OSR is nonlinear (strain dependent) as predicted by Eq. 2. While effectively linear at low maximum shear strain levels, the sensitivity decreases and eventually becomes negative at higher strain levels. This is analogous to the thickness-dependent, sub-fringe response of an RPC in which the strain dependence is sinusoidal. Because of the lower sensitivity at higher strain levels, higher experimental error will occur for a given measurement accuracy of the OSR.

The current LPC technique typically relies on an *in situ* strain gage measurement to calibrate the OSR to the maximum shear strain. Either a uniaxial gage aligned along a known principal axis or a rosette gage is used to determine the calibrating maximum shear strain. The former requires knowledge of the material's properties. Various approaches of calibration are possible including gage measurements acquired on 1) an identical uncoated specimen if available or 2) the coated specimen after measuring the OSR and then removing an area of the coating, applying the gage, and reloading the specimen. For simplified geometries with known analytical solutions, e.g. a cantilever beam—as is the case in this investigation—or a disk in compression, the OSR can be calibrated to the theoretically calculated maximum shear strain.

In most applications, the specimen is tested in its elastic response range. The measured strain values for calibration are usually less than the coating characteristic value: $\gamma/\eta < 0.6$. Because of the existence of camera shot-noise as well as other measurement uncertainties, a nonlinear, least-squares regression fitting the OSR to the corresponding maximum shear strain, Eq. 2, can lead to a range of coefficient pairs (φ, η) that provide a reasonable calibration of the coating response. This is shown in Fig. 5 where the mean square error (MSE) topology of the OSR fit shows a large region of ordered pairs (φ, η) that correspond to a low MSE (the dark trough extending from lower left to upper right). In this theoretical example, $(\varphi, \eta/\eta_o)$ = (0.3,1.0) is the true state; however, a lower φ value (0.28, 0.9) will also produce a low MSE. Because of the shallow MSE gradient and the presence of measurement noise, it is possible to calculate values for both parameters using a two-parameter, nonlinear regression that minimizes the MSE but fails to accurately calculate each parameter individually.

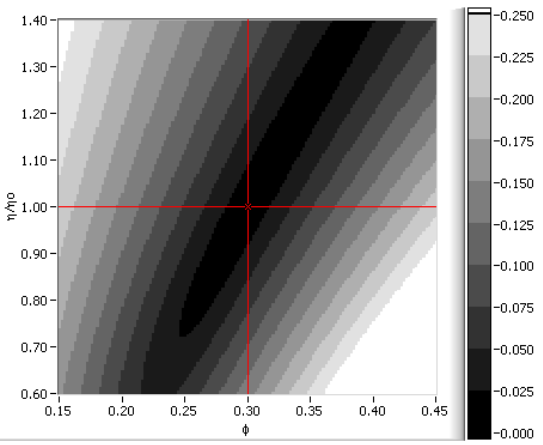

Figure 5. Mean square error topology of a fitted data set for φ = 0.3.

Gerber and Hubner [10] demonstrated experimentally that at the polarization efficiency is effectively modeled by the emission anisotropy, providing a better physical underpinning of the calibration coefficient. The emission anisotropy [6], *r*, is

$$r = \frac{1-I_{\perp}/I_{\parallel}}{1+2\left(I_{\perp}/I_{\parallel}\right)} \tag{7}$$

where $I_{\perp}$ represents the average intensity of an image taken with the emission analyzer orientation perpendicular to a linear excitation polarizer orientation and $I_{\parallel}$ represents the average intensity of an image where the two orientations are parallel. Emission anisotropy originates due to the selective absorption and emission of a luminophor relative to the polarization state of the excitation and the transition moment of the luminophor [6]. While a single luminophor can achieve an anisotropy of 1.0, the maximum anisotropy for randomly distributed luminophors without depolarization effects is 0.4 due to photoselection: the process of exciting luminophors that are partially aligned with the polarization of the excitation. Depolarization effects such as light scattering and reabsorption can further increase or decrease the response, respectively. Because the polarization efficiency depends on the polarization retention of the luminescent dye and anisotropy is an intensity-independent measure of polarization, these are expected to be related.

4. FACTORS AFFECTING THE COATING PARAMETERS

4.1. Surface Inclination Effect

To observe the surface inclination effect on the anisotropy, an anodized bar specimen (6061-T6 aluminum, 1 in x 0.25 in x 11 in) was coated with LPC and placed in the in the test fixture, as shown in Fig. 6a. Three different cases were considered. In Case I, the CCD-LED pair were located next to each other such that excitation and emission propagation angles are parallel to the surface normal of the bar (parallel incidence), and then, the bar was rotated along its longitudinal axis (y) at increments of 10°. In Case II, while the surface normal of the bar and emission propagation remained parallel, the LED was rotated about the longitudinal axis of the bar at 10° increments such that excitation propagation created an oblique angle with the surface normal. This is termed the oblique incidence case and used if strain separation is demanded. In Case III, the excitation propagation and surface normal remained parallel, and the CCD was rotated around the bar at 10° increments. These three cases are shown schematically in Figs. 6b-d. For each case, $I_{\perp}$, and $I_{\parallel}$ were measured without load and the anisotropy was calculated at each angle increment using Eq. 7.

Figure 7 shows how the anisotropy normalized by the 0º orientation changes for the three different cases. When the angle between emission propagation (CCD) and surface normal increases (Case I and Case III), the normalized calculated anisotropy decreases dramatically; however, when the angle between the excitation propagation (LED) and the surface normal increases (Case II), the decrease in normalized anisotropy is not significant—2% decrease in anisotropy at 60°. The results indicate that the emission anisotropy is dependent on the relative CCD position to the surface normal but not the LED position. This apparaent dependency on the relative CCD position likely stems from the polarization change with the surface inclination or the change of the luminescent transmission ratio which is the function of surface inclination angle and the refraction index of the coating as shown in Eq 4. The theoretical luminescent transmission ratio for coating refraction index, $n_c = 1.5$, exhibits the similar pattern as the emission anisotropy as shown in Fig. 8. If the response in Fig. 7 is due to refraction, then the polarization efficiency is assumed independent of surface inclination. Further investigation is needed to understand the relationship between polarization efficiency and the emission anisotropy and why no relationship is present for the oblique excitation case.

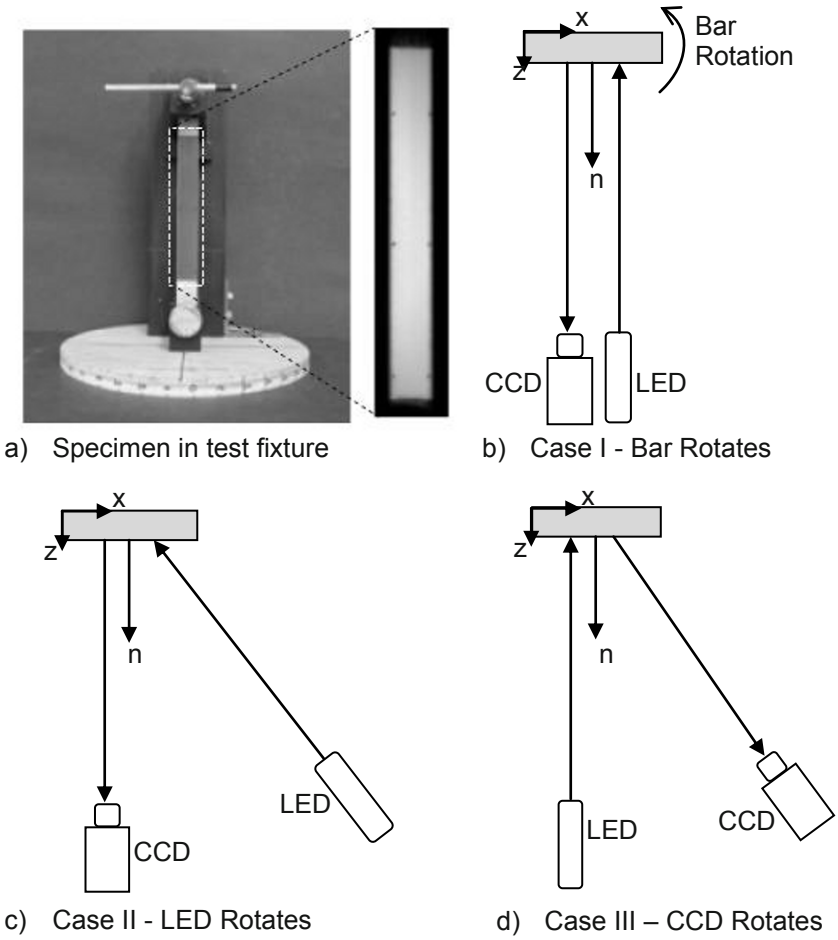

Figure 6. Schematic of the experimental set-up cases.

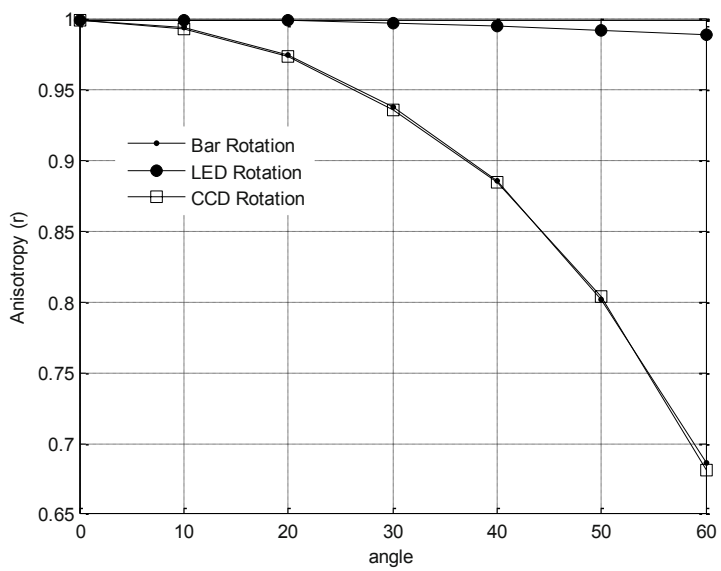

Figure 7. Surface inclination effect on anisotropy

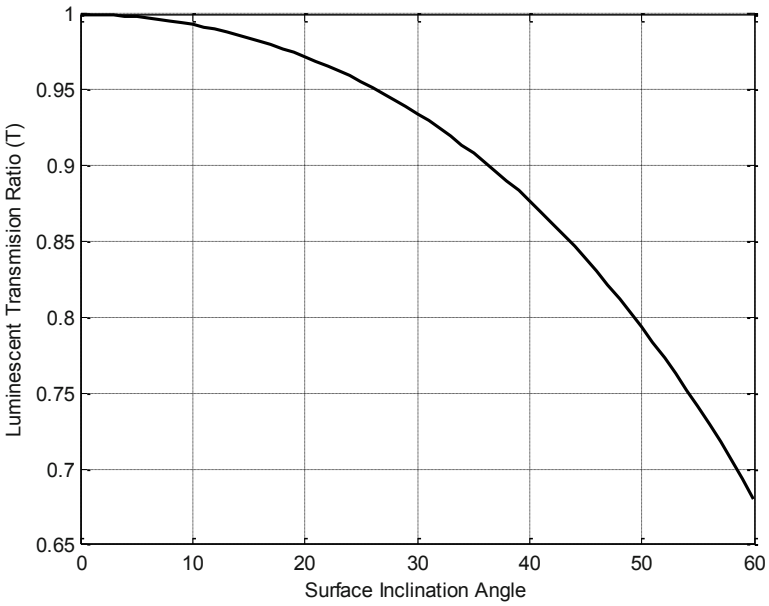

Figure 8. Theroetical luminescent transmission ratio for $n_c = 1.5$.

4.2. Other Effects

Gerber and Hubner investigated the effects of other four factors on the coating parameters by designing an experiment in a 2^k factorial method with k=4 [10]. The four factors were

A: the substrate reflectance (either the specimen is anodized or not),

B: luminescent dye concentration (either normal amount of dye or 50% of the regular amount),

C: absorption dye (either normal amount of dye or 100% above),

D: cure time (either 6 hours or 12 hours).

In their factorial design experiment, a specimen was coated with each of the possible factor combinations for 16 total specimens.

Surface background was studied because previous tests showed that the reflectance of the emission can affect the measured OSR. This will likely manifest in the polarization efficiency due to the increase in the imaged intensity and decrease in polarization retention when the substrate is more reflective. The luminescent dye concentration was lowered by 50% to determine if the polarization retention would increase due to a decrease of excitation crosstalk between luminophors. A direct effect of lowering the luminescent dye concentration is a decrease in emission intensity, thus, longer exposure times. The absorption dye was increased 100% by weight relative to the normal concentration to increase the coating absorptivity. That will result in increasing the value of the coating characteristic. The expected affect of absorptivity on polarization efficiency is unknown. The fourth factor, cure time, was decreased to determine if preparation time could be reduced. If the coating is not completely cured, then the optical sensitivity, *K*, would be less, creating a larger coating characteristic value.

To measure the OSR, the coated aluminum beam specimens were placed in a cantilever bending rig (Fig. 6) with a bending moment arm of 10 in. The specimens were tested in a randomized order to protect against systematic errors. The OSR and the emission anisotropy for each specimen were measured. Initially, to calibrate the coating parameters, a nonlinear regression that employed the Levenberg-Marquardt (LM) algorithm was performed to calculate the best-fit values for both the polarization efficiency and the coating characteristic by minimizing the mean square error between the fitted and measured

OSR. The theoretical maximum shear strain was calculated based on the linear beam theory. Figure 9 shows an example of the fit.

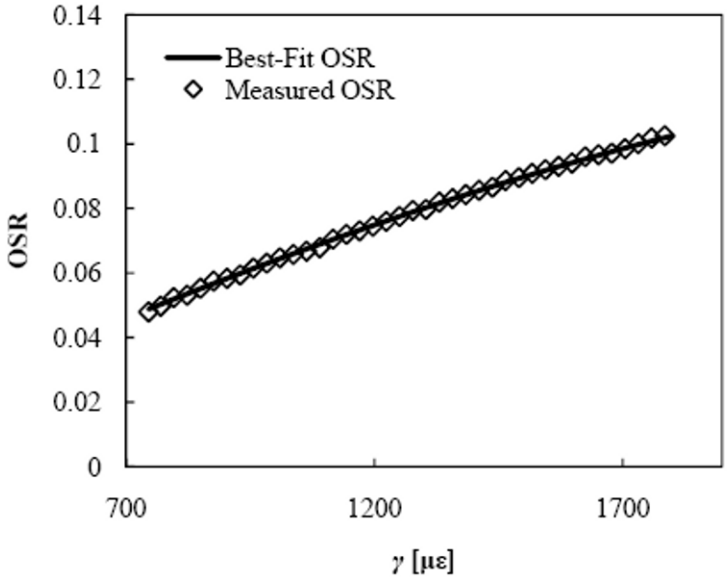

Figure 9. Measured OSR and best fit curve based on Eq. 2.

In short, the independent two-parameter fit did not yield accurate reduced-order regression models of the significant effects on the polarization efficiency and coating characteristic. However, when the polarization efficiency was set equal to the emission anisotropy and only the coating characteristic was free to fit the measure OSR, the reduced-order regression models of the significant factors produced much better results. Why the polarization efficiency should be equal to or closely approximated by the emission anisotropy is not fully understood.

Figure 10 shows the corresponding half-normal probability plots for the case of $\varphi = r$. Table 1 presents statistical results of the analysis including the effect size, t-value and p-value for each significant factor or interaction. For the polarization efficiency, where four factors are significant, the t-value for significance is 2.20. For the coating characteristic, the t-value is 2.16. Also listed in Table 1 is the absolute uncertainty in the φ and η measures. In terms of percentage relative to the average polarization efficiency and coating characteristic of the sample, the uncertainties are 1.3% and 3.6%, respectively.

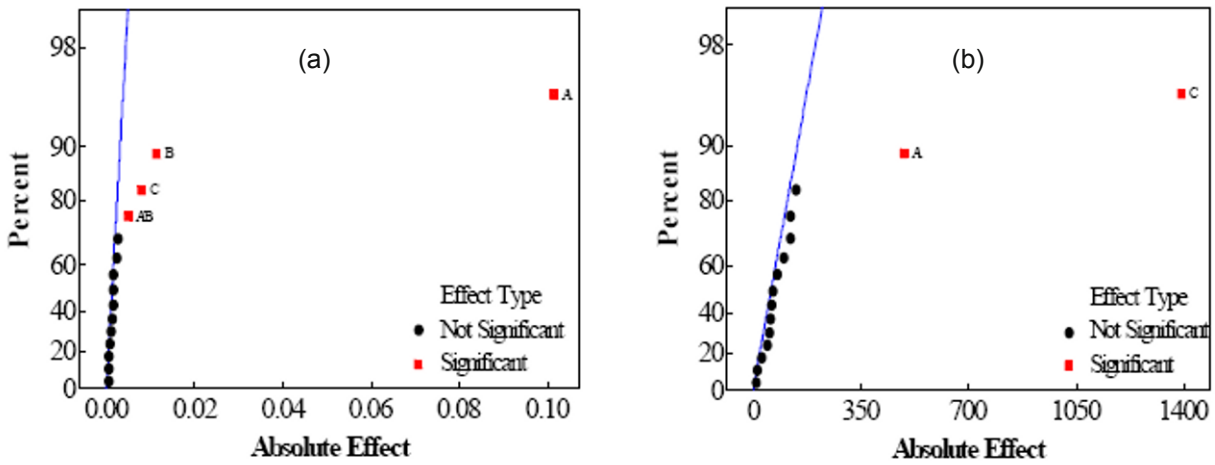

Figure 10. Half-normal % probability plot for a) the polarization efficiency and b) for the coating characteristic when the polarization efficiency is set equal to the emission anisotropy [10]

Table 1. Effect size and statistics of significant parameters when $\varphi = r$.

Parameter	Factor	Effect	t-value	p-value	Uncertainty
φ	A	0.1014	73.29	< 0.001	0.0031
φ	B	-0.0114	-8.22	< 0.001	
φ	C	0.0079	5.69	< 0.001	
φ	AB	-0.0049	-3.52	0.005	
η	A	491	6.24	< 0.001	170
η	C	1394	17.71	< 0.001	

Figures 11a and 11b show the residuals for the polarization efficiency and coating characteristic, respectively, for both analyses: φ fit and $\varphi = r$. The residuals appear structureless, indicating a reasonable assumption of independence, except for a slight upward trend in the polarization efficiency residuals when $\varphi = r$. The residuals for the two-coefficient fit are larger on average. When normalized by the standard error, the residuals for both analyses fall within two standard errors except for one point of the coating characteristic when $\varphi = r$.

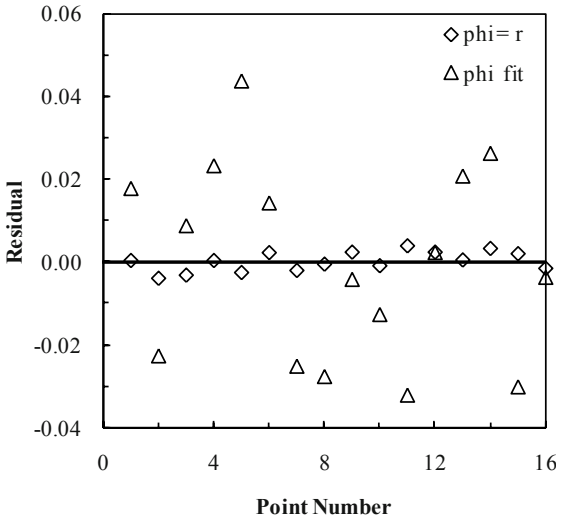

Figure 11a. Polarization efficiency residual plot for both analysis procedures

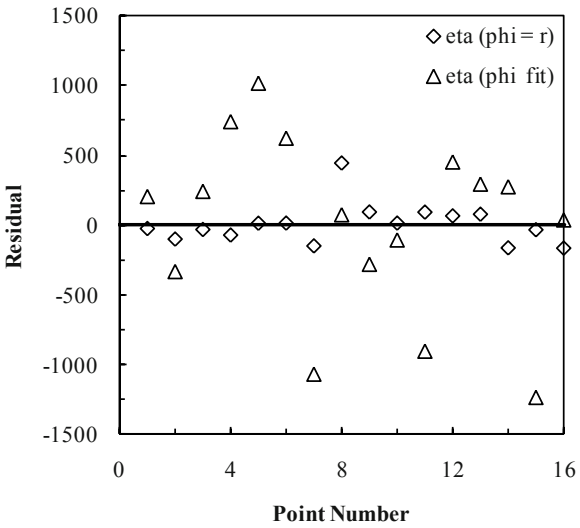

Figure 11b. Coating characteristic residual plot for both analysis procedures

For the polarization efficiency, the substrate reflectance and luminescent dye concentration have major effects while the absorption dye concentration and the reflectance-luminescence interaction have minor effects. Higher polarization efficiency exists when the specimen is anodized. The higher polarization efficiency increases the sensitivity of the OSR to maximum shear strain. The lower polarization efficiency for the metallic specimens indicates that the reflection of the luminescence partially destroys the polarization. While the absolute image intensity increases for the metallic surface, the sensitivity is less. A flat black undercoat should provide the same effect as an anodized surface but compatibility and adhesion are other important factors to consider with an undercoat.

The luminescent dye is the second strongest effect on polarization efficiency, and the negative t-value indicates an inverse correlation. Thus, in terms of sensitivity, lower concentration is preferred; however, decreased concentration will proportionally decrease the absolute measured intensity. This will increase relative imager shot-noise unless longer exposures times are used. The nature of this effect is possibly similar to the surface reflectance in that the stronger the luminescence (higher concentration) causes more surface reflection to be captured in the image. It could also be related to luminescence self-quenching at higher concentrations. The interaction effect of these two factors has a minor but significant negative correlation with polarization efficiency; the absorption dye concentration shows a minor positive correlation.

For the coating characteristic, the absorption dye concentration has a major effect and the substrate reflectance has a minor effect. The positive correlation with absorption dye concentration is expected; adding more dye increases the excitation absorption. This effect decreases the OSR sensitivity but increases the range. The surface reflection affecting the coating characteristic is unexpected. While it cannot be determined from the design of this experiment how or if the reflected luminescence specifically affects the optical sensitivity or the effective wavelength of the coating, the increase of the reflected luminescence of the metallic specimens causes a decrease in the coating characteristic.

All effects and interactions not listed in Table 1, including cure time and all its interactions, were deemed insignificant. The probability that these insignificant effects were judged as such erroneously—and they actually are significant (type II error)—was calculated with the highest order interaction (ABCD) neglected. For the polarization efficiency, the highest type II error was 5.5% (D-cure time). For the coating characteristic, the highest type II error was 3.0% for the CD interaction.

5. STRAIN SEPARATION

A simple strain separation test using the oblique excitation approach was conducted on a bending bar specimen. The bar specimen (6061-T6 aluminum, 1 in x 0.25 in x 11 in) was anodized and coated with LPC for the bending test. The specimen was placed in the test fixture shown in Fig. 6, and the bending force was applied 10 in from the fixed, cantilever support. Applied bending force was 19.5 lbs (deflection of 0.5 in), and the corresponding theoretical maximum in-plane shear strain at the base (10 in from the load) using the linear elastic beam theory was 2543 με. Images were acquired at two CCD/LED orientations: parallel and oblique. Figure 12 shows the schematic view of the CCD/LED orientations for parallel and oblique excitation.

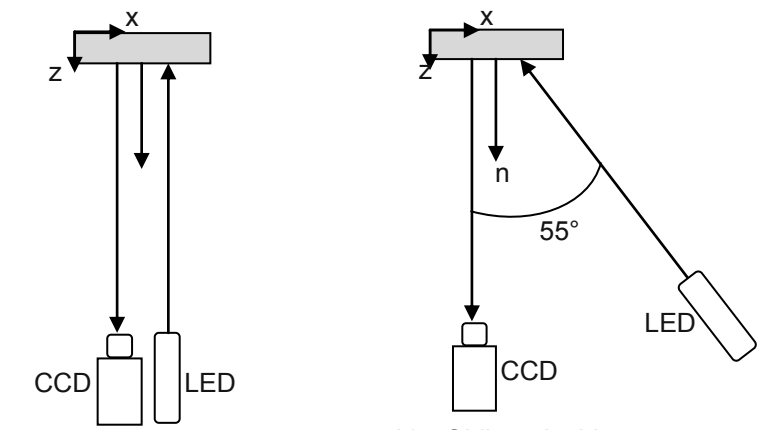

Figure 12. Schematic view of CCD/LED orientations

The OSR was measured for parallel and oblique incidence and calibrated using the theoretical values computed based on linear bending beam theory. Two calibrations were performed. First, the coating parameters (φ, η) were determined separately using the LM algorithm. Second, the emission anisotropy was measured for parallel and oblique incidence, and then the values of emission anisotropy were set equal to the polarization efficiency $(\varphi = r)$. The remaining parameter, coating characteristic (η), was determined by regression fit using the LM algorithm.

Figure 13 shows the OSR measured and calibrated for normal and oblique incidence by determining two coating parameters separately. The two-parameter fit, Eq. 2, exhibits more curvature than the experimental data. The coating parameters were determined to be $\varphi = 0.24$, and $\eta = 3582$ for parallel incidence and $\varphi = 0.27$, and $\eta = 4636$ for oblique incidence. The root mean square (rms) errors for the fitted OSR were 0.15% for parallel incidence and 0.10% for oblique incidence. Since there is no change in the coating or specimen between the two excitation orientations, it was not expected that the coating characteristic would change, increasing by 30%.

Once the OSR for parallel and oblique incidences were calibrated, the separated principal strains were determined using the Eqs. 6a and 6b. Figure 14 shows the comparison between measured and theoretical separated principal strain. The measured principal strain were in good agreement with the theoretical values and the root mean square (rms) errors are 41 με for ε_1 and 13 με for ε_2.

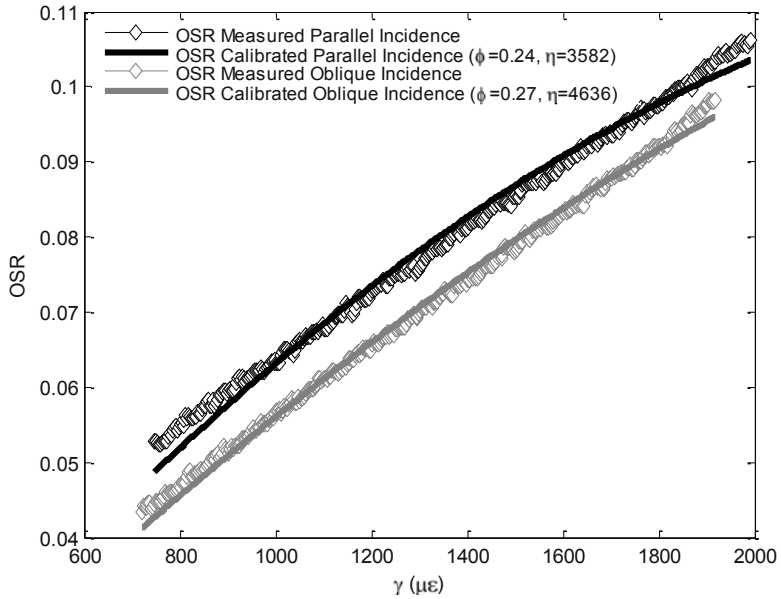

Figure 13. Calibrated and measured OSR when (φ, η) are determined individually.

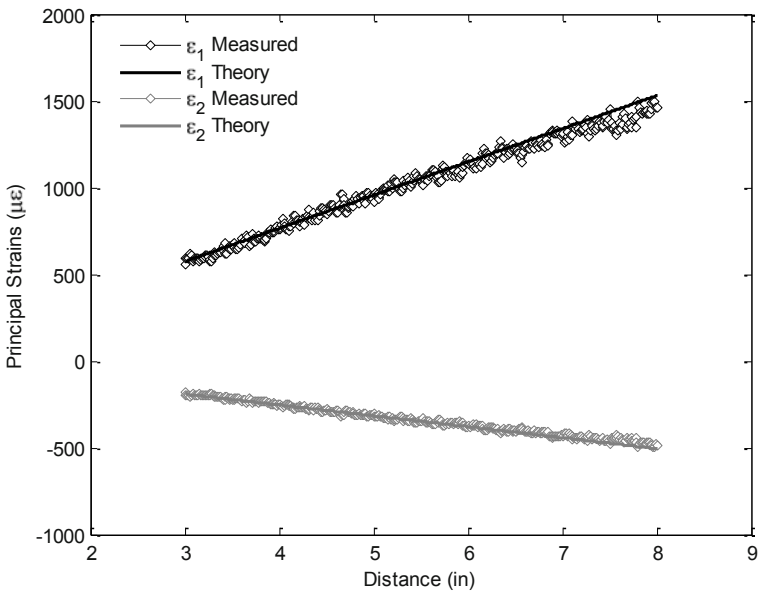

Figure 14. Separated principal strains when (φ, η) are determined individually.

Next, the measured emission anisotropy for parallel and oblique incidence were set equal to the value of polarization efficiency and the coating characteristic was free to fit the measured OSR. In this case the coating parameters were $\varphi = r = 0.29$, and $\eta = 4511$ for parallel incidence and $\varphi = r = 0.28$, and $\eta = 4805$ for oblique incidence, as shown in Fig. 15. Note that the polarization efficiency was slightly lower for oblique excitation case, which is consistent as shown in Fig 7 (bar rotation). In addition the difference between the normal and oblique value of the coating characteristics was less (6%). The rms error was greater than the two-parameter fit case: 0.23% for parallel incidence and %0.10 for oblique incidence. However, the value of the rms error are still low when compared to the uncertainty on OSR due to the camera shot-noise, which is about 0.4% [11]. Separation of principal strains was performed

again using the new calibrated OSR values. Figure16 shows the separated principal strains are also in good agreement with the theoretical values. In this case, the rms errors are 58 με for ε_1 and 19 με for ε_2, slightly higher than when both coating parameters were determined by the regression. The increase in the rms error stem from the poorer fit of OSRs for parallel and oblique incidence; however, 17 με increase for ε_1, and 6 με increase for ε_2 are small when compared to the maximum shear strain value for the bar; 0.6% for ε_1 and 0.2% for ε_2.

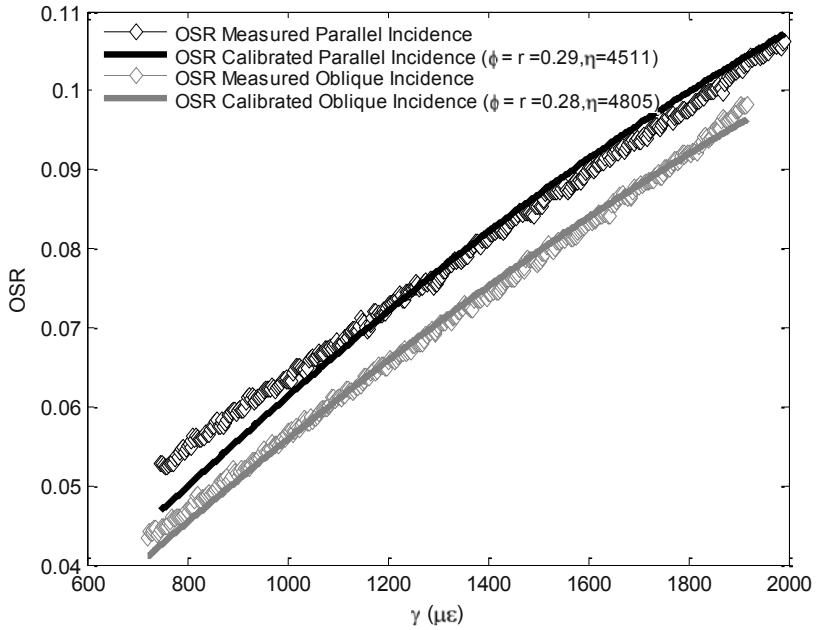

Figure 15. Calibrated and measured OSR when ($\varphi = r$) and only η is determined.

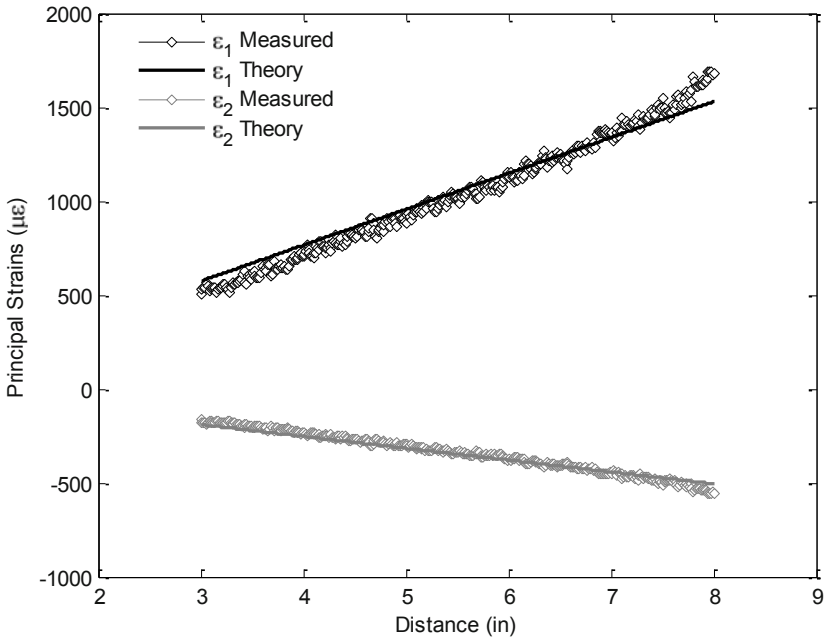

Figure 16. Separated principal strains when ($\varphi = r$) and only η is determined.

6. CONCLUSION

The OSR of the LPC technique is modeled as a nonlinear function of maximum in-plane shear strain, and the coating parameters: the polarization efficiency, φ, and the coating characteristic, η. The effect of surface inclination and other factors on the measured anisotropy was investigated. Experiments demonstrate that the measured anisotropy decreases when surface inclination angle changes relative to the emission propagation. This is likely, however, related to the refraction of emission out of the coating. The effect of surface inclination angle relative to the excitation propagation is minor. The strain separation of the aluminum bar was performed using two different OSR calibration approaches: first, the coating parameters (φ, η) were calibrated using a two-parameter regression and, second, the polarization efficiency set equal to the measured anisotropy and the coating characteristic was determined using a one-parameter regression. The results show that when (φ, η) are determined separately, the separated principal strains are in good agreement with the theoretical values. The rms errors in this case are 41 με for ε_1 and 13 με for ε_2. However, it was noted that this calibration procedure leads two different coating characteristic value for different excitation angle: $\eta = 3582$ for parallel incidence and $\eta = 4636$ for oblique incidence (a 30% difference). This is thought to be an erroneous result since η is expected to be independent of the excitation angle. The different values for the coating characteristic likely arises due sensitivity of the theoretical response to measurement noise. When the calibration procedure is repeated with the value of polarization efficiency is equal to the measured anisotropy for parallel and oblique excitation, the separated principal strains shows also good agreement with the theoretical values but are slightly larger. The rms errors for this case are 58 με for ε_1 and 19 με for ε_2. However, the values of the coating characteristic for the two different excitation cases were closer to each other: $\eta = 4511$ for parallel incidence and $\eta = 4805$ oblique incidence (a 6% difference), supporting the approach of setting the polarization efficiency equal to the emission anisotropy.

7. ACKNOWLEDGEMENTS

This project is supported by NSF contract CMMI-0643170: Dr. Shih-Chi Liu program manager.

8. REFERENCES

[1] Hubner, JP, PG Ifju, KS Schanze, Y.Liu, L Chen, and W El-Ratal, “Luminescent Photoelastic Coatings,” *Experimental Mechanics*, **44**(4), 416-424 (2004).

[2] Hubner, JP, L Chen, Y Liu, K Schanze, J Nicolosi, P Ifju, and W El-Ratal, “Characterization of a New Luminescent Photoelastic Coating,” *Experimental Mechanics*, **45**(2), 137-143 (2005).

[3] Hubner, JP, and L. Chen, “Coupled Strain and Fresnel Response of Photoelastic Coatings at Oblique Incidence,” *Experimental Mechanics*, **47**(4)**,** 549-560 (2007)

[4] Esirgemez, E, and Hubner, JP, “Luminescent Photoelastic Coating Image Analysis and Strain Separation on a Three-dimensional Grid,” *Proceedings of SPIE Sensors and Smart Structures Technologies for Civil, Mechanical, and Aerospace Systems 2010*, ed. Ronald G. Driggers, Paper: 100005 (2010).

[5] Zandman, F, S Redner and JW Dally, *Photoelastic Coatings*, Iowa State University Press, Ames, IA, 31-35 (1977).

[6] Lakowicz, JR, *Principles of Fluorescence Spectroscopy*, 3rd ed, Springer, 353-366 (2006).

[7] Abdel-Aziz, YI, and HM Karara, “Direct Linear Transformation form Comparator Coordinates into Object Space Coordinates,” *ASP Symposium on Close Range Photogrammetry*, 1-18 (1971).

[8] Dally, JW, and WF Riley, *Experimental Stress Analysis*, 4th ed., College House Enterprises, Tennessee, 9-11 (2005)

[9] Chapra, SC, and RP Canale*, Numerical Methods for Engineers with Software and Programming Applications*, 4th ed., McGraw-Hill Inc, New York, 601-604 (2002).

[10] Gerber, DR, and JP Hubner “Factorial Design Experiment to Analyze the Response of a Luminescent Photoelastic Coating” 48th Aerospace Sciences Meeting and Exhibit, AIAA Paper 2010-0188, January (2010).

[11] Esirgemez, E, and JP Hubner (2009) “Temperature Dependence of the Luminescent Photoelastic Coating Technique,” *Journal of Strain Analysis*, **44**(8), 699-711 (2009).

Proceedings of the SEM Annual Conference
June 7-10, 2010 Indianapolis, Indiana USA

Highly Compact and Robust 3D Imaging and Shape Measurement System

Dung A Nguyen, Minh Vo, Zhaoyang Wang*, Thang Hoang
*Department of Mechanical Engineering, The Catholic University of America
Washington, DC 20064
wangz@cua.edu

ABSTRACT

The fringe projection profilometry (FPP) is one of the most widely used techniques for three-dimensional (3D) imaging and 3D shape measurements. In this paper, a FPP-based compact, portable, easy-to-implement yet robust 3D imaging and shape measurement system is explored and established. The system utilizes a series of advanced electronic devices, such as a single board computer, a credit-card sized projector, and a USB camera. It employs a number of novel techniques including ultrafast phase unwrapping with multi-frequency fringes, effective gamma correction of digital projection, arbitrary setup of system components, automatic system calibration with a least-squares inverse approach, and multi-thread parallel processing for 3D shape acquisition, reconstruction and display. The system not only provides full-field 3D information with high accuracy and fast speed, but also possesses remarkable features including but not limited to high compactness, easy implementation, and superior capability of dealing with multiple objects with complex shapes in a wide measurement range.

INTRODUCTION

Fringe projection profilometry (FPP), also called fringe projection technique, is one of the most widely used techniques in practical applications of three-dimensional (3D) shape measurements, including object detection, digital model generation, object replication, reverse engineering, rapid prototyping, product inspection, quality control, etc. A 3D FPP-based imaging system generally comprises of a high speed CMOS camera, a DLP projector and a computing unit, as shown in Figure 1. In the past two decades, numerous FPP-based 3D shape measurement approaches [1]-[11] have been developed to posses the following combined technical features: high accuracy, fast speed, easy implementation, capability of measuring multiple objects, and capacity of measuring complex shapes. However, those systems usually have complex system set up and are also non-portable due to their size and weight. This paper aims to introduce a new portable and super compact dedicated projecting system, which can be easily brought anywhere along with a laptop, which has built-in webcam, to practice 3D measurement. Along with advanced, well developed 3D algorithm, it gives great promise of satisfying the critical demands of enormous applications in various fields, especially in future 3D teleconference and entertainment.

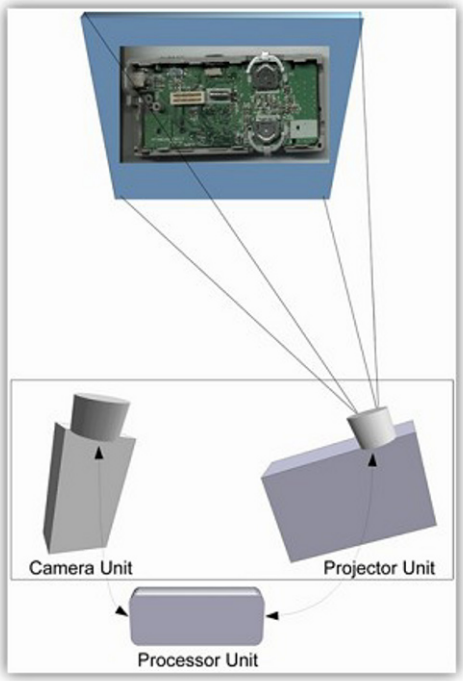

Figure 1. Typical FPP-based 3D imaging system

T. Proulx (ed.), *Application of Imaging Techniques to Mechanics of Materials and Structures, Volume 4*, Conference Proceedings of the Society for Experimental Mechanics Series 14, DOI 10.1007/978-1-4419-9796-8_50, © The Society for Experimental Mechanics, Inc. 2013

1. SYSTEM DESIGN

1.1. Portable, Dedicated and Compact Projecting System with DLP Pico Projector and Beagleboard

In recent few years, DLP projector industry has observed a new evolution of compact and portable Pico projectors with the size smaller than a credit card such as white Samsung Pico projector or Optica PK-100 in Figure 1. These projectors provide us a new approach to highly packed 3D imaging system that is much more portable, handy and convenient in applications of many fields, especially in communication system.

(a) (b)

Figure 1. New generation of portable and compact DLP Pico projectors: (a) White Samsung Pico Projector and (b) Optima PK-100.

After taking careful survey about Pico projector market, we realize that with this kind of projector, another significant improvement to the 3D system can be made if the DLP Pico projector from Texas Instruments (TI) is utilized. Instead of relying on a computer to generate the fringe patterns, we develop a dedicated compact system for patterns' generation and projection with this TI projector. In order to do so, a low-cost, fan-less and small single-board computer, 3in x 3in Beagleboard [3], is adopted as a separated processing unit for projection control. Figure 2 (a) and (b) show the amazingly small size of TI pico projector and the Beagleboard respectively. Figure 2 (c) illustrates the combined dedicated projecting system which can be built into a 4in x 4in x 2in box. Despite the tiny appearance, TI projector is capable of projecting a high quality image with up to 0.17 in HVGA resolution while the Beagleboard is running with 600Mhz superscalar ARM Cortex-A8 processor, which allows graphics accelerator capable of rendering 10 million polygons per second with OpenGL ES 2.0.

1.2. USB Camera/ Webcam for Capturing

With the dedicated projecting system described above, simply a laptop with a built-in webcam or a USB camera is sufficient enough to practice 3D measurement. This approach greatly reduces the complexity of the 3D system. In order to synchronize the projecting process with capturing process for real time measurement, a USB adapter is needed to connect the Beagleboard with the employed laptop or computer. Most consumer webcams are capable of providing VGA-resolution video at a frame rate of 30 frames per second. Many newer devices can produce video in multi-megapixel resolutions, and a few can run at high frame rates such as the PlayStation Eye, which can produce 320×240 video at 120 frames per second. The proposed approach allows us to take advantage of those features and promote traditional 2D teleconference to a new level of 3D communication.

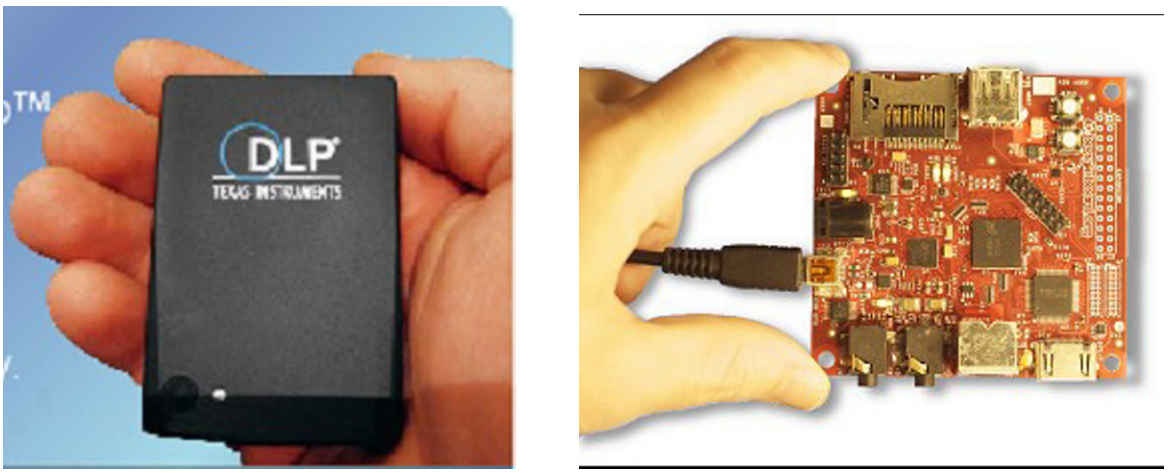

(a) (b)

(c)

Figure 2. Portable, compact projecting system includes (a) DLP Pico Projector and (b) Beagleboard. Figure (c) illustrates the combined dedicated projecting system.

2. 3D DETERMINATION ALGORITHM

2.1. Phase-Shifted Patterns with Gamma Correction

During the 3D measurement, a set of fringe patterns are projected onto the surfaces of the objects of interest. The surface height/depth information is naturally encoded into the distorted fringe patterns. To extract the 3D surface profiles easily, the initial fringe patterns being projected are always straight, vertical (or horizontal) oriented, and equally spaced. Since phase shifting scheme is typically employed to achieve automatic and full-field data processing, the fringe patterns (for vertical fringes) are normally generated in a numerical way with a simple sinusoidal function. However, in reality, a digital projector often applies gamma-decoding correction to the images and videos to enhance the visual effect. This internal gamma-decoding of the DLP projector outputs undesired non-sinusoidal patterns. This problem has been well considered in our previous paper [31], in which a more complex equation was suggested to take into account the gamma factor. It is expressed as:

$$I = 2I_0\left[\frac{1}{2}+\frac{1}{2}\cos\left(2\pi k\frac{x}{w}+\delta\right)\right]^{\frac{1}{\gamma}} \quad (1)$$

where I is the pattern intensity at the point whose horizontal pixel coordinate is x, w is the width of the pattern image, k is the number of fringes in the image, δ is the phase shifting amount, I_0 is normally set to 127.5 to obtain a desired intensity in the range of 0-255 for gray scale images, and the decoding gamma factor γ, which is usually in the interval 2.2-2.6. This approach deals with the gamma problem at the source, i.e., the digital projection part; therefore, it provides a direct, simple yet effective solution, and does not introduce any additional calculation in the 3D shape determination part.

2.2. 3D Shape Determination Algorithm

To obtain the 3D shapes of an object or object system, both the in-plane and out-of plane dimensions must be determined. Due to the fact the 2D in-plane dimension can be directly calculated from the corresponding digital image through a simple transformation with acknowledgement of the camera-object distance, the primary task of the 3D shape determination algorithm is actually to rigorously determine the out-of-plane height and depth information. The mathematical derivation of the governing equation for the 3D shape determination based on an arbitrary or generalized setup involves a very tedious procedure. The derivation has been elaborated in Ref[[22]], and this paper puts emphasis on the practical implementation of the technique. Basically, the governing equation of the out-of-plane shape determination can be simplified as:

$$z = \frac{1 + C_1\phi + (C_2 + C_3\phi)i + (C_4 + C_5\phi)j + (C_6 + C_7\phi)i^2 + (C_8 + C_9\phi)j^2 + (C_{10} + C_{11}\phi)ij}{D_0 + D_1\phi + (D_2 + D_3\phi)i + (D_4 + D_5\phi)j + (D_6 + D_7\phi)i^2 + (D_8 + D_9\phi)j^2 + (D_{10} + D_{11}\phi)ij} \tag{2}$$

where z is the out-of-reference-plane height or depth at point (x, y), and ϕ is the projection fringe phase at the same point. In the equation, the coefficients C_1-C_{11} and D_0-D_{11} are constants determined by the geometrical and other system parameters and have to be determined first. The relevant details are discussed in later section. Compared with the existing FPP techniques which use specific setups, the above approach based on arbitrary and generalized setup of system components is much easier to implement; more importantly, it can cope with the numerous uncertainties in practice of FPP.

2.3. Multiple Frequency Approach for Phase Detection

When the object or object system of interest involves complex shapes and/or multiple separated objects, the phases of the projection fringes on each object and among different objects are often discontinuous. For a correct phase determination, such discontinuities of fringe phases must be detected correctly. FPP-based techniques generally employ phase shifting scheme to obtain the full-field wrapped phase distributions of the projection fringes. The wrapped phase must then be unwrapped to obtain the real phase distributions, which are essential for the 3D shape determination. In actual applications, a notable challenge is how to correctly and quickly perform the phase unwrapping when fringe discontinuities are present. This issue can be well addressed by the following approach based on multi-frequency fringe projection. The algorithm can be expressed as:

$$\phi_i^{uw} = \phi_i^{w} + INT\left(\frac{\phi_{i-1}^{uw} \cdot \dfrac{f_i}{f_{i-1}} - \phi_i^{w}}{2\pi}\right) \cdot 2\pi \qquad (i = 2,3,...,n) \tag{3}$$

where the subscript i indicates the ith projection fringe pattern, and the superscripts uw and w denote unwrapped phase and wrapped phase, respectively. In the equation, n is the number of fringe frequencies and $n \geq 2$; f is the relative fringe frequency or the number of fringes in the projection pattern, and $f_n > f_{n-1} > \cdots > f_1 = 1$; INT represents an operator to take the rounding integer of a decimal number; the wrapped phase ϕ^w is obtained from the traditional or advanced phase shifting algorithm, and $\phi_1^{uw} = \phi_1^{w}$ for the lowest-frequency fringe pattern with one fringe or less in the entire field.

The direct phase unwrapping approach based on multi-frequency fringe projection can obtain the full-field unwrapped phase distributions in an ultrafast manner. Furthermore, the approach is suitable for measuring multiple objects with complex shapes without any additional processing.

2.4. Least-squares Inverse Approach for System Calibration

To calculate the absolute out-of-reference-plane height or depth *z* using Eq. (6), the coefficients C_1-C_{11} and D_0-D_{11}, which are determined by geometrical and other relevant parameters of the measurement system, must be determined in advance. The calibration approach involves minimizing the linear least-squares error defined as:

$$S = \sum_{k=1}^{m} \left[F_C - F_D z_k^g \right]^2 \tag{4}$$

where

$$\begin{aligned} F_C &= 1 + C_1\phi_k + (C_2 + C_3\phi_k) i_k + (C_4 + C_5\phi_k) j_k + (C_6 + C_7\phi_k) i_k^2 + (C_8 + C_9\phi_k) j_k^2 + (C_{10} + C_{11}\phi_k) i_k j_k \\ F_C &= D_0 + D_1\phi_k + (D_2 + D_3\phi_k) i_k + (D_4 + D_5\phi_k) j_k + (D_6 + D_7\phi_k) i_k^2 + (D_8 + D_9\phi_k) j_k^2 + (D_{10} + D_{11}\phi_k) i_k j_k \end{aligned} \tag{5}$$

and z_k^g denotes the absolute out-of-reference-plane heights of the reference plane (height is zero) and gage blocks, *k* is the ordinal number of each valid point, *m* is the total number of datum points on the reference plane and gage blocks used in the calculation, and a larger *m* generally yields more reliable results. The least-squares criterion [[29]-[30]] requires

$$\begin{cases} \dfrac{\partial S}{\partial C_p} = 0, \quad p = 1,2,\cdots 11 \\ \dfrac{\partial S}{\partial D_q} = 0, \quad q = 0,1,\cdots 11 \end{cases} \tag{6}$$

Eq. (10) yields a group of linear equations, which will be employed to solve for the coefficients C_1-C_{11} and D_0-D_{11}.

It is noted that although the above FPP-based 3D shape measurement technique provides measurements of the out-of-plane dimension relative to a reference plane, the reference plane does not have to physically exist in actual applications except for the system calibration purpose; additionally, the reference plane is not necessarily the background plane nor necessarily located behind the objects of interest. The above feature indicates that a rigid-body translation and rotation of the entire camera-projector system will not affect the governing parameters and the virtual reference plane.

3. EXPERIMENTS

To demonstrate the validity and applicability of the described system in FPP implementation, a few experiments have been carried out and one of them is presented here. In this experiment, the proposed dedicated projecting system, which includes TI Pico Projector and Beagleboard, is used along with iSight webcam and a Macbook Pro to practice 3D measurement. The iSight webcam has the resolution of 640x480 pixels and capturing speed of 30 fps. The plate with different high gages, as shown in figure 3, is used to calibrate the system.

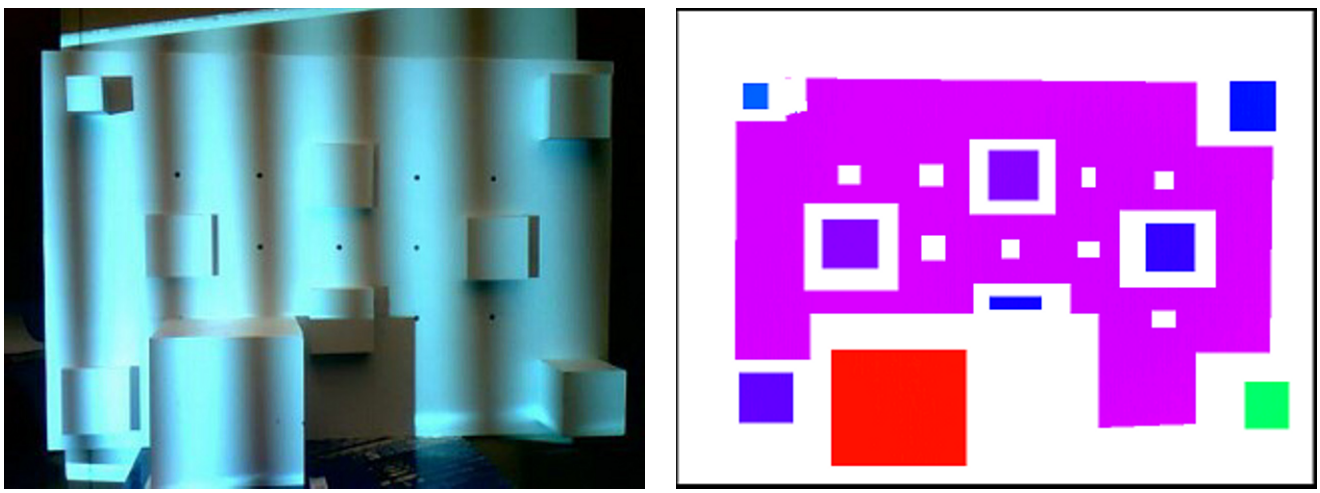

(a) (b)

Figure 3. The calibration plate with different high gage blocks (a) and the result of calibration process (b)

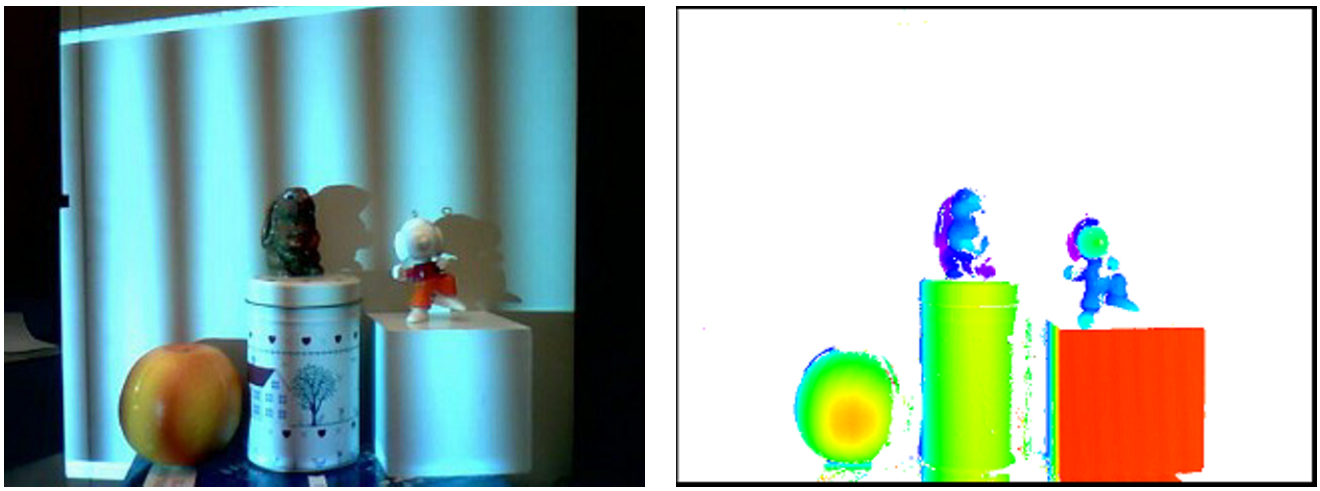

(a) (b)

Figure 4. Demonstration with proposed projecting system and webcam to analyze several separated and complex-shaped objects (a) and the corresponding result(b).

Figure 4 illustrates one of our experiments in which several objects, including an orange, a shiny snoopy and a dark-colored rabbit are used to test the proposed system. The corresponding result is shown in Figure 4 (a). The difference in colors represents the high difference. This experiment has shown great capability of the system even with shiny, complex-shaped and dark-colored objects.

4. CONCLUSION

This paper presents a new implementation for 3D FPP-based imaging system by introducing a dedicated, portable and compact projecting system with TI Pico Projector and Beagleboard along with the use of webcam or USB camera to capture images, which are then analyzed by a laptop. In addition, some of the best recent advances in FPP-based 3D shape measurements, along with simple but robust solutions are also employed to give great promise of providing measurements with high accuracy, easy implementation, capability of measuring multiple complex-shaped objects. The validity and practicability of the proposed approach have been verified by experiments. As technologies evolve, there have been high demands for the 3D shape measurement techniques to posses a number of advanced technical features, and the technique presented in this paper is capable of satisfying the various critical demands in enormous scientific, engineering and entertaining applications.

ACKNOWLEDGMENTS

This work was supported by Burns Fellowship at the Catholic University of America, National Collegiate Inventors and Innovators Alliance (under grant 5205-07), and National Science Foundation (under grant 0825806).

REFERENCES

[1] F. Chen, G. Brown, and M. Song, “Overview of 3-D shape measurement using optical methods,” Optical Engineering, 39, 10–22 (2000).

[2] W. Schreiber and G. Notni, “Theory and arrangements of self-calibrating whole-body 3-D measurement systems using fringe projection technique,” Optical Engineering, 39, 159–169 (2000).

[3] L. Salas, E. Luna, J. Salinas, V. Garcia, and M. Servin, “Profilometry by fringe projection,” Optical Engineering, 42, 3307–3314 (2003).

[4] Q. Hu, P. Huang, Q. Fu, and F. Chiang, “Calibration of a three-dimensional shape measurement system,” Optical Engineering, 42, 487–493 (2003).

[5] R. Legarda-Sáenz, T. Bothe, and W. Juptner, “Accurate procedure for the calibration of a structured light system,” Optical Engineering, 43, 464–471 (2004).

[6] C. Tay, C. Quan, T. Wu, and Y. Huang, “Integrated method for 3-D rigid-body displacement measurement using fringe projection,” Optical Engineering, 43, 1152–1159 (2004).

[7] T. Peng, S. Gupta, and K. Lau, “Algorithms for constructing 3-D point clouds using multiple digital fringe patterns,” Computer-Aided Design and Applications, 2, 737-746 (2005).

[8] J. Pan, P. Huang, and F. Chiang, “Color-coded binary fringe projection technique for 3-D shape measurement,” Optical Engineering, 44, 023606, (2005).

[9] H. Guo, H. He, Y. Yu, and M. Chen, “Least-squares calibration method for fringe projection profilometry,” Optical Enging, 44, 033603, (2005).

[10] S. Zhang, X. Li, and S. Yau, “Multilevel quality-guided phase unwrapping algorithm for real-time three-dimensional shape reconstruction,” Applied Optics, 46, 50–57 (2007).

[11] S. Zhang and S. Yau, “Generic nonsinusoidal phase error correction for three-dimensional shape measurement using a digital video projector,” Applied Optics, 46, 36–43 (2007).

[12] H. Guo, H. He, and M. Chen, “Gamma correction for digital fringe projection profilometry,” Applied Optics, 43, 2906-2914 (2004).

[13] Z. Li, Y. Shi, C. Wang, and Y. Wang, “Accurate calibration method for a structured light system,” Optical Engineering, 47, 053604 (2008).

[14] R. Tsai, “A versatile camera calibration technique for high accuracy 3D machine vision metrology using off-the-shelf TV cameras and lenses,” IEEE J. Robotics and Automation, 3, 323–344 (1987).

[15] Z. Zhang, “A flexible new technique for camera calibration,” IEEE Transactions on Pattern Analysis and Machine Intelligence, 22, 1330–1334 (2000).

[16] L. Chen and C. Quan, “Fringe projection profilometry with nonparallel illumination: a least-squares approach,” Optics Letters, 30, 2101–2103 (2005).

[17] L. Chen and C. Quan, “Reply to comment on "fringe projection profilometry with nonparallel illumination: a least-squares approach"," Optics Letters, 31, 1974–1975 (2006).

[18] Z. Wang and H. Bi, “Comments on fringe projection profilometry with nonparallel illumination: a least-squares approach,” Optics Letters, 31, 1972–1973 (2006).

[19] Z. Wang and H. Bi, “Practical fringe projection profilometry with a LCD projector,” Proceedings of Photomechanics 06: International Conference on Full-field Measurement Techniques and Their Applications in Experimental Solid Mechanics, 2006.

[20] Z. Wang, H. Du, and H. Bi, “Out-of-plane shape determination in fringe projection profilometry,” Optics Express, 14, 12122–12133 (2006).

[21] H. Guo, M. Chen, and P. Zhang, “Least-squares fitting of carrier phase distribution by using a rational function in fringe projection profilometry,” Optics Letters, 31, 3588-3590 (2006).

[22] H. Du and Z. Wang, “Three-dimensional shape measurement with arbitrarily arranged fringe projection profilometry system,” Optics Letters, 32, 2438-2440 (2007).

[23] C. Coggrave and J. Huntley, “High-speed surface profilometer based on a spatial light modulator and pipeline image processor,” Optical Engineering, 38, 1573–1581 (1999).

[24] L. Kinell, “Spatiotemporal approach for real-time absolute shape measurements by use of projected fringes,” Applied Optics, 43, 3018-3027 (2004).

[25] J. Tian and X. Peng, “Three-dimensional vision from a multisensing mechanism,” Applied Optics, 45, 3003-3008 (2006).

[26] W. Osten, W. Nadeborn, and P. Andra, “General hierarchical approach in absolute phase measurement,” Proc. SPIE, 2860, 2-13 (1996).

[27] W. Nadeborn, P. Andra, and W. Osten, “A robust procedure for absolute phase measurement,” Optics and Lasers in Engineering, 24, 245–260 (1996).

[28] J. Burke, T. Bothe, W. Osten, and C. Hess, “Reverse engineering by fringe projection,” Proc. SPIE, 4778, 312-324 (2002).

[29] Z. Wang and B. Han, “Advanced iterative algorithm for phase extraction of randomly phase-shifted interferograms,” Optics Letters, 29, 1671–1673 (2004).

[30] Z. Wang and B. Han, “Advanced iterative algorithm for randomly phase-shifted interferograms with intra- and inter-frame intensity variations,” Optics and Lasers in Engineering, 45, 274–280 (2007).

[31] Z. Wang, D. Nguyen, J. Barnes, “Recent advances in 3D shape measurement and imaging using fringe projection technique,” *Proceedings of the SEM Annual Congress and Exposition on Experimental and Applied Mechanics*, Albuquerque, New Mexico, 2009.

Proceedings of the SEM Annual Conference
June 7-10, 2010 Indianapolis, Indiana USA

Experimental Limitations of Phase Shifting Interferometry

N. Ansari[a,*] and W. R. Ashurst[a]
[a]Department of Chemical Engineering, Auburn University, Auburn, AL 36849 USA
[*]Corresponding author: ansarna@auburn.edu (N. Ansari)

Abstract

Digital Phase Shifting Interferometry (PSI) is widely used in optical testing to determine the surface topography of a continuous surface. The height profile obtained using PSI is derived from intensity measurements made at different phases, which are seperated by a definite phase step. The unreliable piston travel of the peizo in response to a definite actuating signal is the main source of phase step and hence height errors in the height profile derived using PSI. The five frame sequence suggested by Hariharan et. al. for intensity measurements makes PSI relatively insensitive to both positive and negative phase step errors (as large as 50% of the single desired phase step). However, we report on significant errors in the PSI derived height profile that can result if a mathematically equivalent but experimentally different sequence than that suggested by Hariharan et. al. is employed for intensity measurements.

1. Introduction

Since its introduction in 1974 by Bruning et. al., PSI has been widely used in optical testing [1]. PSI combined with appropriately designed test structures and analysis routines is routinely used by the MEMS community to determine important material properties such as stress gradient in structural layers used to fabricate useful micromechanisms [2]. Hurst et. al. recently reported a technique, which uses PSI derived height profile of an actuated cantilever beam to determine apparent in-plane work of adhesion between contacting in-plane MEMS surfaces [3]. Using PSI, the height profile of a surface is determined by calculating the original optical phase difference (ϕ) or path length difference between two interfering beams at every point on the surface. In order to determine ϕ between the two interfering beams, the phase difference between them is varied and interferograms are collected at each phase step for every point on the surface. Intensity measurements corresponding to atleast three phase shifts coupled with knowledge of the phase shifts are used to determine ϕ between the interfering beams. In most of the commonly used interferometers, one of the surfaces (reference or sample) is mounted on a piezoelectric transducer (PZT) and phase shifts are introduced by applying suitable voltages to the PZT.

Most of the analysis techniques that use PSI are extremely sensitive to the height profile derived using it. It is therefore very important to identify and eleminate all possible sources of systematic errors in PSI. While factors like extraneous fringes and spatial noise due to scattered light do introduce certain errors, it is widely accepted that the most prominent source of systematic errors in PSI is deviation in the phase steps from their predetermined nominal values due to non-linearity and dependence of PZT on variables like its age and temperature. Several approaches reported in literature to address this issue include acuator calibration schemes and novel shifting hardwares, etc. [1]. Several algorithms like the equistep algorithm in which the phase step need not be known accurately but should be equal are developed to address the uncertainity associated with phase steps [1]. Greivenkamp suggested a generalized algorithm which allows unequal phase steps as long as the applied phase steps can be accurately known [1]. However, the additional hardware required to accurately determine the applied phase steps makes his approach unattractive [1]. Farrell et. al. reported two algorithms, which although do not require the phase steps to be known or equal, but require a significantly higher computational effort as comapred to algorithms that require predetermined fixed phase steps [1]. The algorithm suggested initially by Schwider et. al. and later by Hariharan et. al. is one of the most simple, robust and reliable algorithms for PSI. The computational effort required by this algorithm, which implicitly evaluates the actual phase shifts and uses them to calculate the original phase difference between the interfering beams is also significantly less [4]. In this paper, we report a mathematically equivalent but experimentally different five frame sequence for collecting the interferograms than that suggested by Hariharan et. al. While the sequence suggested by Hariharan et. al. is extremely insensitive to phase step errors, the sequence reported by us in this paper results in significant

T. Proulx (ed.), *Application of Imaging Techniques to Mechanics of Materials and Structures, Volume 4*, Conference Proceedings of the Society for Experimental Mechanics Series 14, DOI 10.1007/978-1-4419-9796-8_51, © The Society for Experimental Mechanics, Inc. 2013

errors in the PSI derived height profile. Therefore, the five frame sequence for collecting interferograms for PSI should be selected cautiously, since an experimentally easily executable sequence can result in significant errors in the height profile derived using it.

2. Five Frame Sequence for PSI

The self-calibrating five frame sequence (referred to as H) suggested by Hariharan et. al. is given by Eqs. 1-5 shown below, where I_1, I_2, I_3, I_4 and I_5 are the intensity measurements made at phase steps of $+2\alpha$, $+\alpha$, 0, $-\alpha$, -2α respectively [4].

$$I_1 = A + B + 2\sqrt{AB}\cos(\phi + 2\alpha) \tag{1}$$

$$I_2 = A + B + 2\sqrt{AB}\cos(\phi + \alpha) \tag{2}$$

$$I_3 = A + B + 2\sqrt{AB}\cos(\phi) \tag{3}$$

$$I_4 = A + B + 2\sqrt{AB}\cos(\phi - \alpha) \tag{4}$$

$$I_5 = A + B + 2\sqrt{AB}\cos(\phi - 2\alpha) \tag{5}$$

A sequence of five frames (referred to as NH), which is mathematically equivalent to the sequence H is given by Eqs. 6-10 shown below, where I_1, I_2, I_3, I_4, I_5 are the intensity measurements made at phase steps of 0, $-\alpha$, -2α, -3α, -4α respectively.

$$I_1 = A + B + 2\sqrt{AB}\cos(\phi) \tag{6}$$

$$I_2 = A + B + 2\sqrt{AB}\cos(\phi - \alpha) \tag{7}$$

$$I_3 = A + B + 2\sqrt{AB}\cos(\phi - 2\alpha) \tag{8}$$

$$I_4 = A + B + 2\sqrt{AB}\cos(\phi - 3\alpha) \tag{9}$$

$$I_5 = A + B + 2\sqrt{AB}\cos(\phi - 4\alpha) \tag{10}$$

The two sequences H and NH are mathematically equivalent since both of them consist of five frames seperated by four phase steps of α each. Also, ϕ between the two interfering beams is given by the same Eq. 11 for both the sequences when the predetermined phase step (i.e., α) is 90°.

$$\frac{\tan\phi}{2} = \frac{I_2 - I_4}{2I_3 - I_1 - I_5} \tag{11}$$

However, it is clearly evident from Eqs. 1-5 and Eqs. 6-10 that the two sequences are experimentally executed differently. While for sequence H, the PZT is stepped in both directions (i.e., forward and backward) from its starting position for collecting the interferograms, for sequence NH, it is stepped only in one direction. In other words, for sequence H, the interferogram corresponding to the original optical phase difference of the interfering beams (i.e., with no additional phase step added) is collected in the third frame, while for sequence NH, it is collected in the first frame. Error ($\Delta\phi$) in ϕ as a result of a small error (ϵ) in each phase step is to a first approximation given by Eq. 12 and Eq. 13 for sequences H and NH respectively. It is clearly evident from Eq. 12 and Eq. 13 that sequence NH is much more sensitive to the phase step error (ϵ) than sequence H.

$$\Delta\phi = \frac{\epsilon^2}{8}\sin 2\phi \tag{12}$$

$$\Delta\phi = 2\epsilon \tag{13}$$

3. Experimental Details

A long working distance, incoherent light interference microscope, similar to that reported by Sinclair et. al. in reference [2] is used to collect the interferograms. A green LED (supplied by Nichia Corp.), which has a characteristic wavelength (λ_{max}) of 525 nm, is monochromated using a monochromator which transmits 532 nm and used as the illumination source. The interferometer is interfaced with a computer and the PZT, which is used for varying the optical phase difference between the interfering beams is controlled using a scripting environment. Both the reflecting surfaces used in all the experiments are 8 mm $\times$ 8 mm Si(100) chips. In order to validate the authenticity of the data collected, a relative tilt is introduced between the two reflecting surfaces for all the experiments. A CCD camera attached to the interferometer is used for recording the interferograms.

Before investigating the effect of phase step errors on error in the determination of ϕ, the error in ϕ associated with vibrational disturbance in the experimental setup is determined. This is done using two sets of five interferograms each, collected using sequence H. For this experiment, no intentional phase step error was added to the nominal phase step. In order to collect interferograms using sequence H, an initial voltage of 1 V is applied to the PZT to move it to a position from where it can be moved in both the directions to collect the interferograms as required by sequence H. Interferograms are then collected at nominal phase steps of 90°. For collecting ineterferograms using sequence NH, the PZT is initially moved four phase steps forward. Interferograms are then collected at every phase step while pulling the PZT back to its original position. To study the effect of phase step errors, sets of five interferograms each are collected with a different phase step error added to the nominal phase step for each set. These experiments are done using both the sequences. These interferograms are compared to the corresponding interferograms, which are collected using the same sequence and with no intentional phase step error added to the nominal phase step, to estimate the error in the determination of ϕ due to phase step errors.

4. Results and Discussion

The rms error in ϕ due to vibrational disturbance in the interferometer is determined to be 6.77°, which corresponds to a rms height error of 5 nm. Six sets of five interferograms each are collected using both the sequences. The first set is collected with no intentional phase step error added to the nominal phase step. For each successive set, the intentional phase step error is incremented by 10% of the nominal phase step. Fig. 1a and Fig. 1b show $\Delta\phi$, the rms error in determining ϕ as a function of percentage phase step errors (of the nominal desired phase step) for both the sequences. It is clearly evident from the two figures that sequence H is highly insensitive to phase step errors and results only in small errors in ϕ even for phase step errors as large as 60% of the nominal desired phase step. On the contrary, sequence NH is highly sensitive to phase step errors and results in significantly large errors in ϕ, which increase with the increase in phase step errors. A phase step error of 60% results in rms errors of 8.12° and 121.8° in ϕ for sequences H and NH respectively. These correspond to rms height errors of 6 nm and 90 nm respectively. Also, positve phase step errors result in larger errors in ϕ than the corresponding negative phase step errors as seen from Fig. 1a and Fig. 1b respectively. This could be attributed to a small positive phase step error inherently present in the response of the PZT to an actuating signal, which adds to the externally applied intentional positive phase step errors, thereby increasing them and subtracts from the externally applied intentional negative phase step errors, thereby decreasing them.

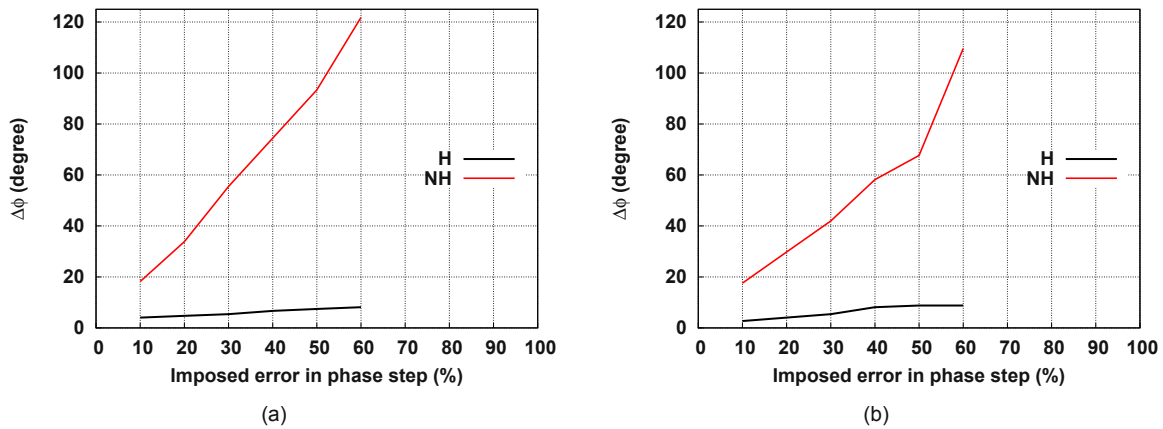

Figure 1: Error in ϕ for different imposed percentage (a) positive and (b) negative error in α.

5. Conclusions

We have shown clear evidence of the presence of significant errors in the PSI derived height profile obtained using a mathematically equivalent but experimentally different five frame interferogram collecting sequence than that suggested by Hariharan et. al. A significantly high rms error of 90 nm is observed in the height profile derived using sequence NH when the phase step error is 60% of the nominal desired phase step. In contrast, sequence H is extremely insensitive to phase step errors and even for a high phase step error of 60%, rms error of 6 nm, which is only marginally greater than the rms error in the height profile due to vibrational disturbances, is observed in the height

profile derived using it.

6. Acknowledgments

The authors gratefully acknowledge the financial support given by Auburn University.

References

[1] C. T. Farrell, M. A. Player, Phase-step insensitive algorithms for phase-shifting interferometry, Meas. Sci. Technol., 5, 648–652, 1994.

[2] M. B. Sinclair, M. P. de Boer, A. D. Corwin, Long-working-distance incoherent-light interference microscope, Applied Optics, 44 (36), 7714–7721, 2005.

[3] K. M. Hurst, C. B. Roberts, W. R. Ashurst, A New Method to Determine Adhesion of Cantilever Beams Using Beam Height Experimental Data, Tribology Letters, 35, 9–15, 2009.

[4] P. Hariharan, B. F. Oreb, T. Eiju, Digital phase-shifting interferometry: A simple error-compensating phase calculation algorithm, Applied Optics, 26 (13), 2504–2506, 1987.

Proceedings of the SEM Annual Conference
June 7-10, 2010 Indianapolis, Indiana USA

Mechanical Characterization and Modeling of X- and K-cor Composites

C. Sharkey, S.W. Kwon, S.W. Lee, and H.A. Bruck
Departments of Aerospace and Mechanical Engineering
University of Maryland

A. Rahman and D. Barrett
NAVAIR-Pax River

Abstract

This research is focused on developing appropriate macro-mechanical models that account for the microstructural details unique to X- and K-cor composite sandwich panels. Digital Image Correlation (DIC) is used to elucidate on the details of the deformation fields within the sandwich structure. These details are used to enhance the models by providing critical details on the failure initiation mechanisms and the subsequent load redistribution that occurs in these structures. The effects of environmental conditions on the mechanical behavior of these composite materials are also being investigated.

I. Specimen Fabrication

All specimens have Rohacell foam cores implanted with truss structures of pultruded carbon fiber pins. The provided specimens were excess material, so they were not made to our specifications. However they do provide a range of pin densities and core thicknesses that were sufficient to begin experimental tests to provide data for the model development, and for identifying specifications that would be needed for further testing. It is important to note that in higher density core materials the thickness of the core was also increased, so test specimens differed geometrically as well.

For specimens being manufactured at UMD, face sheets were ordered from Dragonplate. The sheet is comprised of five layers of carbon-fiber weave with orientations of 0/90, +45/-45, 0/90, +45/-45, and 0/90, giving a total thickness of 1 mm. Two 4" x 6" pieces of the face sheet were bonded to samples of the different types of foam core of the same sizes using West System epoxy resin and hardener. The samples were then vacuum cured for 48 hours and oven cured for another 48 hours at 80° C before being cut into test specimens. An example of a K-Cor specimen can be seen in *Figure 1*.

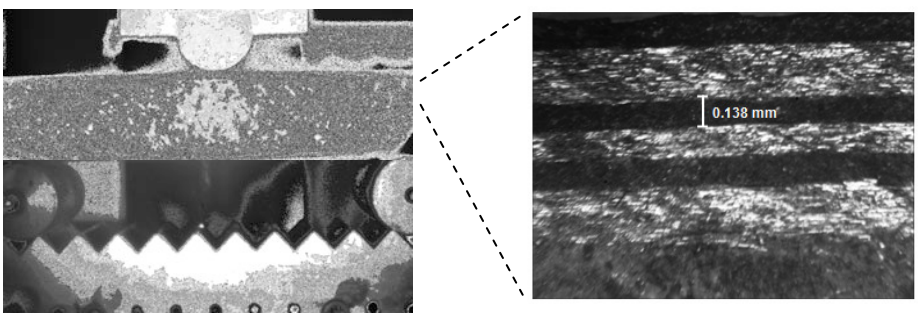

Figure 1. K-Cor specimen with exploded view of laminated carbon-fiber epoxy face sheet

II. Modeling

Finite Element Specimen Model

The K-Cor computational model was developed using the sample in *Figure 1*. It has a thickness of 12 mm and a pin density of 1.8 lb/ft^3. Details of the pin configuration used in the finite element model can be seen in *Figure 2*. The resulting finite element model for the K-Cor specimen can be seen in *Figure 3*. Previous

T. Proulx (ed.), *Application of Imaging Techniques to Mechanics of Materials and Structures, Volume 4*, Conference Proceedings of the Society for Experimental Mechanics Series 14, DOI 10.1007/978-1-4419-9796-8_52, © The Society for Experimental Mechanics, Inc. 2013

experimental results have indicated that for test specimens with smaller widths relative to the size of the unit cell, pin locations are different and also the number of pins in a specimen is different depending on where cuts are made.

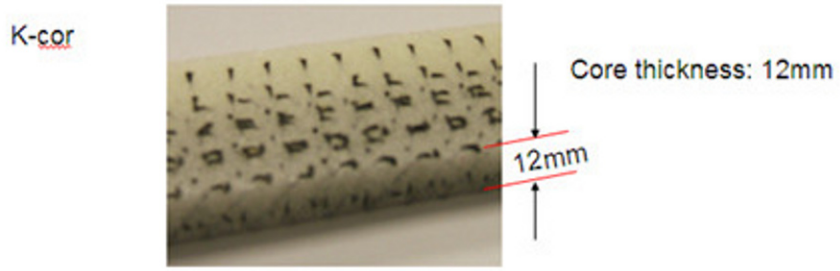

Figure 2. K-Cor composite with pin density of 1.8 lb/ft^3 used to develop finite element model.

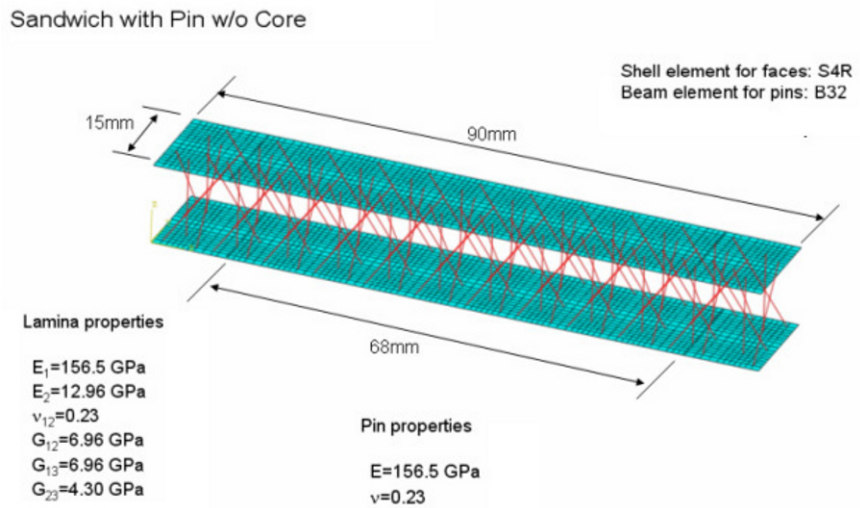

Figure 3. Three different models for investigating the effects of pin location.

3. Experimental Results and Comparison with FEA Simulation for Three-point Bending

Figure 4 shows axial and transverse displacement fields obtained with DIC during three point bending test results that were compared with the results of the FEA simulations under a loading of 102 kg applied on the center line of top plate. A displacement gage recorded a max transverse displacement of 0.80 mm, while DIC indicated 0.36 mm which is 45% of the displacement gage reading. Therefore, three models with different pin locations were used to determine if the experimental results could be correlated with the FEA simulations.

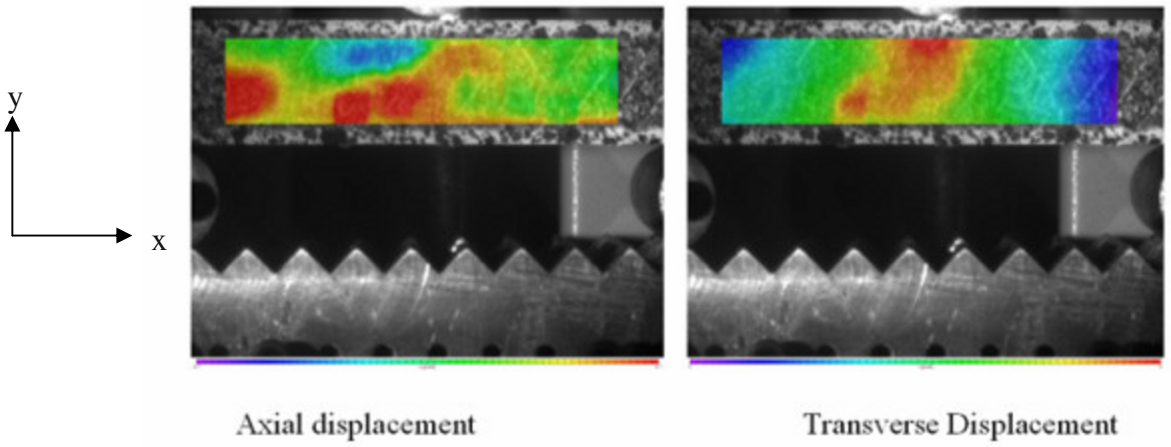

Figure 4. Axial and transverse displacement fields determined using DIC from specimen with artificial speckle pattern at peak load of 102 kg.

For the comparison, the foam core is modeled and inserted into the model described previously. To distinguish from the pins only model, the letter "C" is added to the model name such as "Model 3C" where "C" stands for the foam core. The finite element model of Model 1C and Model 2C are similar except that pin locations are different due to differences in specimen cutting. The foam core is modeled with 3D solid elements with two elements along the thickness direction. The maximum transverse displacement U_3 for the three models are calculated and compared with experimental results. *Figure 5* shows the contour plots for transverse displacement of the three models. The maximum transverse displacements of Model 1C, Model 2C and Model 3C are 0.6991mm, 0.5591mm and 0.5504 mm, respectively. The summary of comparison is shown in *Table 1*. All three calculated values are between the displacement gage reading and the DIC reading.

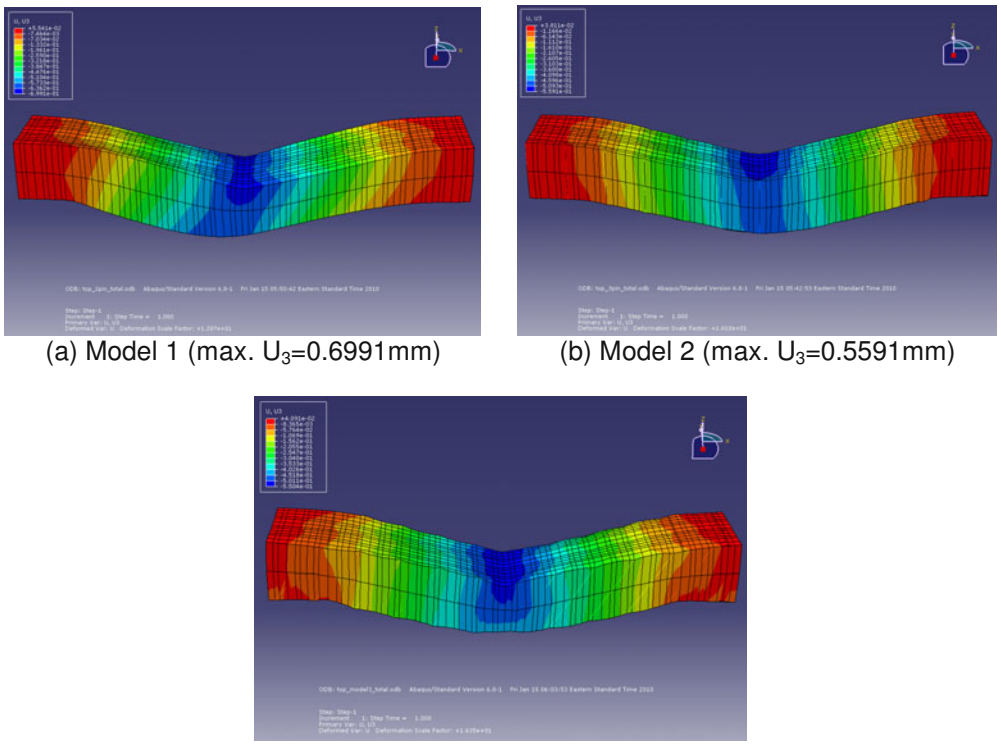

(a) Model 1 (max. U_3=0.6991mm) (b) Model 2 (max. U_3=0.5591mm)

(c) Model 3 (max. U_3=0.5504mm)

Figure 5. Maximum transverse displacement of the three pin location models with foam core.

Model	Max. U_3			
	Displacement gage	DIC	FE Analysis	FE Analysis (pins only)
Model 1C	0.80mm	0.36mm	0.6991mm	0.7466mm
Model 2C			0.5591mm	0.6047mm
Model 3C			0.5504mm	0.5862mm

Table 1. Summary of model comparisons for pin location effects.

Among the three models, the Model 3C seems to be quantitatively closest to the actual test specimen that has oblique pins on the edge surface (See *Figure 4*). However, it cannot be guaranteed that all oblique pins on the surface are secure and can sustain the loading because some pins could have been damaged during specimen cutting and preparation. In fact, one can observe some pins on the surface are missing in certain specimens.

To investigate the effect of damaged or missing pins on the surface, a model that has no pins on the surface is considered as an extreme case. This model is constructed by removing two rows of oblique pins at the edges from Model 3C. This model is named Model 4C and there are only 7 rows of pins in this model. *Figure 6* shows the maximum transverse displacement of the Model 4C is 0.8086mm, which is closer to the displacement gage reading and results in a 47% increase in the predicted displacement. Accordingly, the maximum transverse displacement would be somewhere between 0.5504~0.8086mm. The best way to prevent the effect of damaged pins is to use a specimen that is cut between the pin rows.

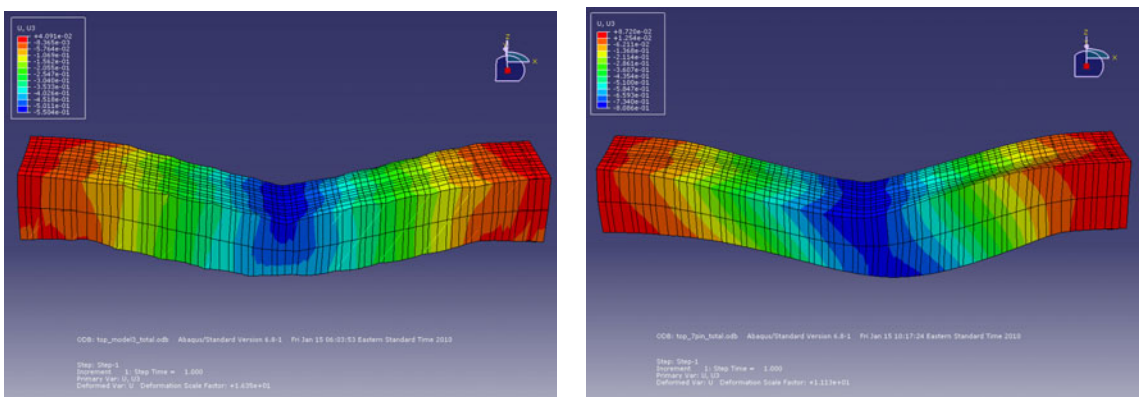

(a) Model 3C (max U_3=0.5504mm) (b) Model 4C (max U_3=0.8086mm)

Figure 6. Comparison of transverse displacement fields (a) with no missing or damaged pins in Model 3C, and (b) with missing or damaged pins in Model 4C indicating qualitative changes that are similar to the displacement fields measured experimentally.

3. Three Point Bend Failure Modes

In materials with such a complex structure, there are many different ways for the material to experience failure, a number of which were seen in the tests performed. These can be seen in photographs taken of the specimen as well as through DIC analysis which can show strain concentrations and potentially show where a failure is imminent before it actually occurs. One way in which the material can fail is through core shear. This means that the shear stress in the specimen limits the maximum load the specimen can take, and the core will start to essentially tear into separate pieces. It is interesting to note that in these materials, the core shear failure often happens along one of the angled pins or where one of the pins should have been present but was not. This is

confirmed through DIC, which shows concentrations of strain along the lengths of the pins within the material. *Figure 8* shows a core shear failure photograph and the corresponding axial strain DIC field.

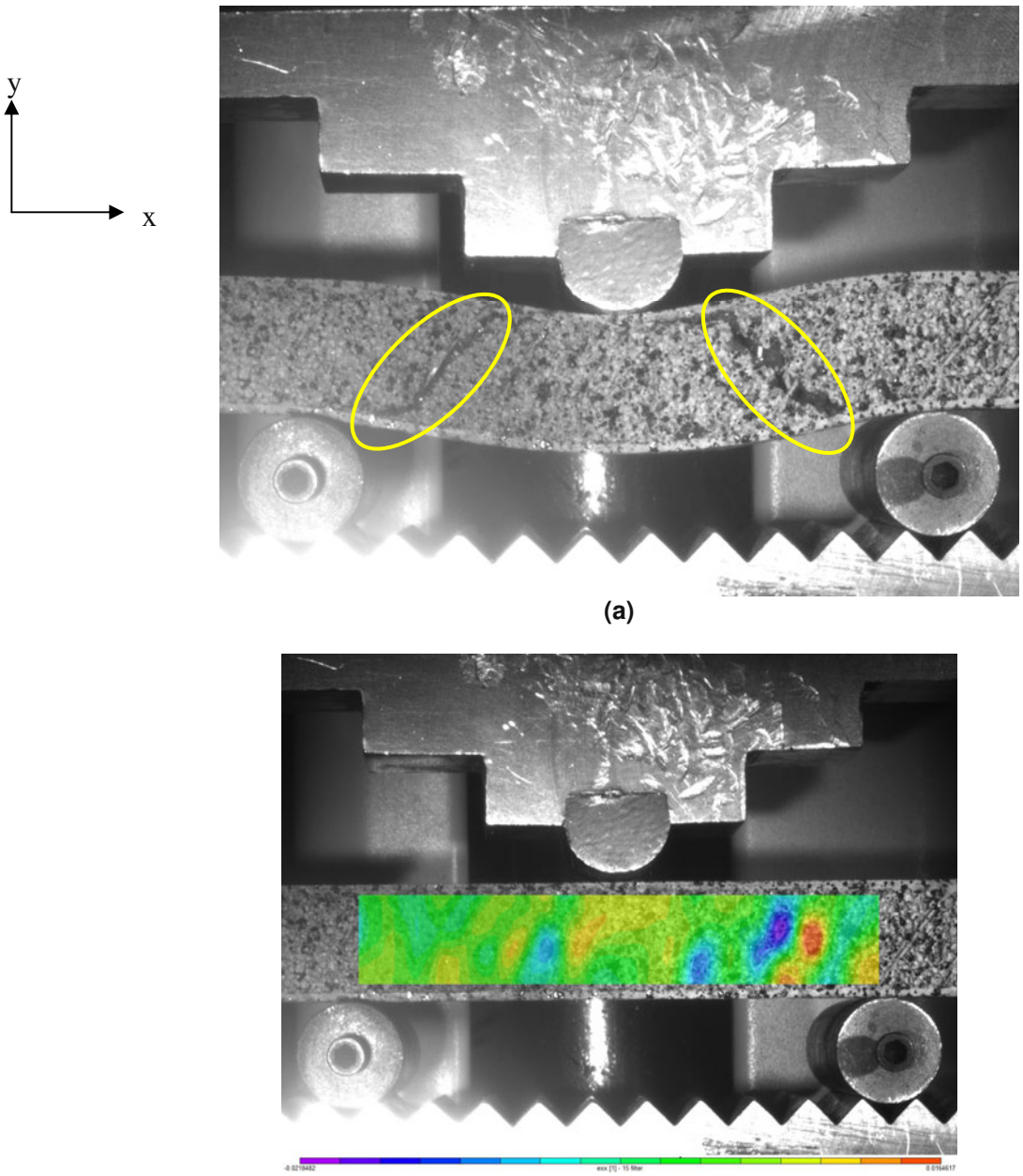

Figure 8. Core shear failures in 1.8 lb/ft^3 material.

Another common failure mode in this type of material is pin buckling, leading to pin failure. This happens when the stress on any given pin or group of pins becomes too large for the pin(s) to handle, so they will begin to deform and eventually break. *Figures 9 a, b, c, and d* show the progression of a pin buckling failure and the associated DIC image, which shows strain concentrations on both sides of the pin that is about to buckle and fail.

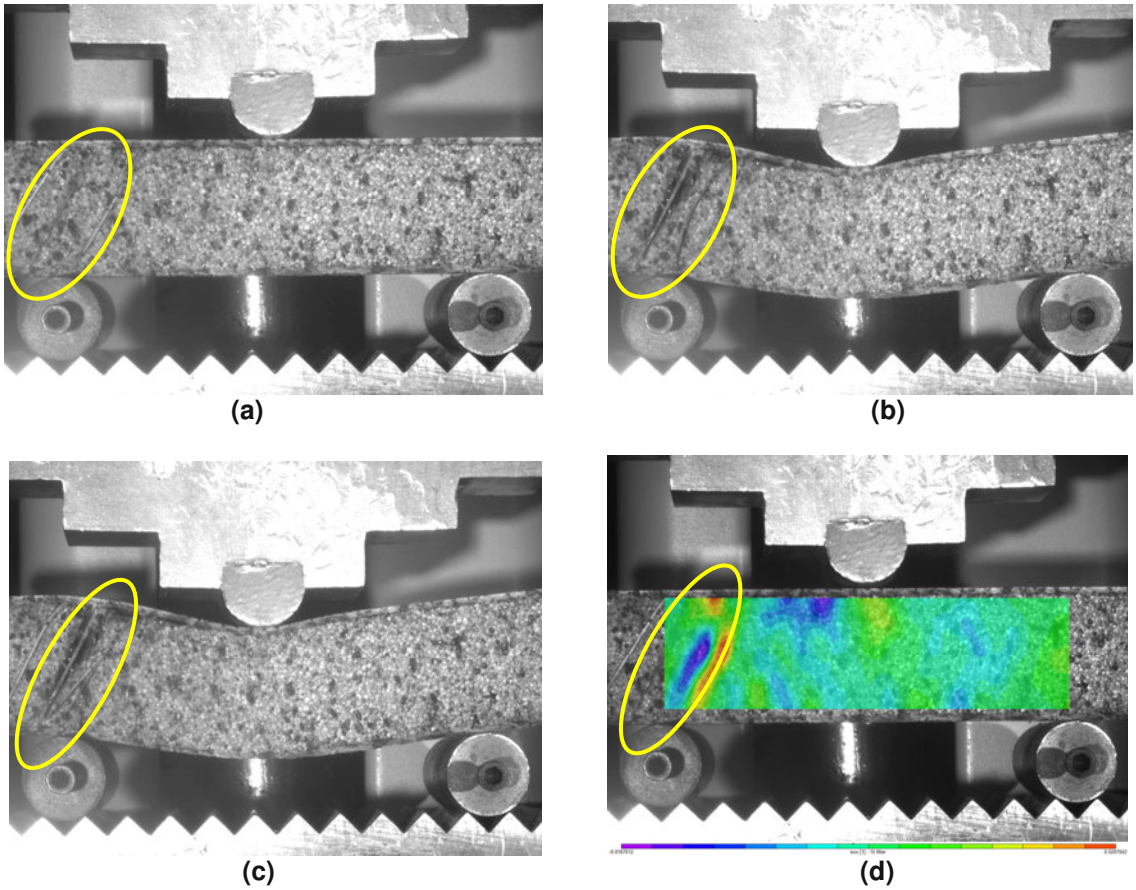

Figure 9. Pin buckling in 4 lb/ft^3 material. (a) Undeformed pin, (b) Severely deformed pin, (c) Fractured pin, and (d) DIC image.

Delamination is another common failure mode in any laminated composite. This occurs when the stresses in the material bonding layers together becomes greater than the strength of that adhesive, so the layers begin to peel apart from each other. *Figures 10 a, b, c, and d* show the process of a delamination failure. As shown in the pictures, in the lower left side of the specimen, the bottom face sheet begins to separate from the core material. This is also shown in the DIC image with the transverse strain concentration along the bottom face sheet.

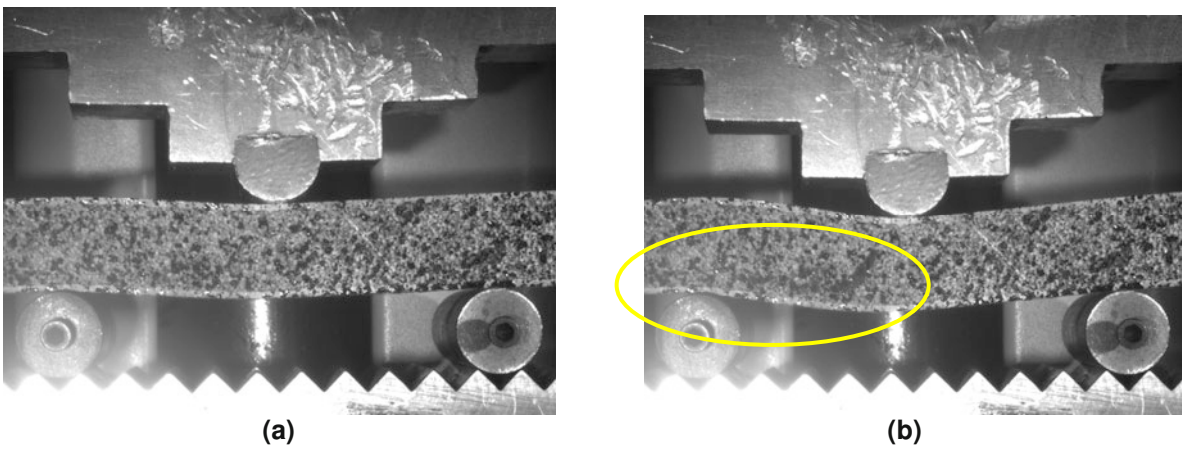

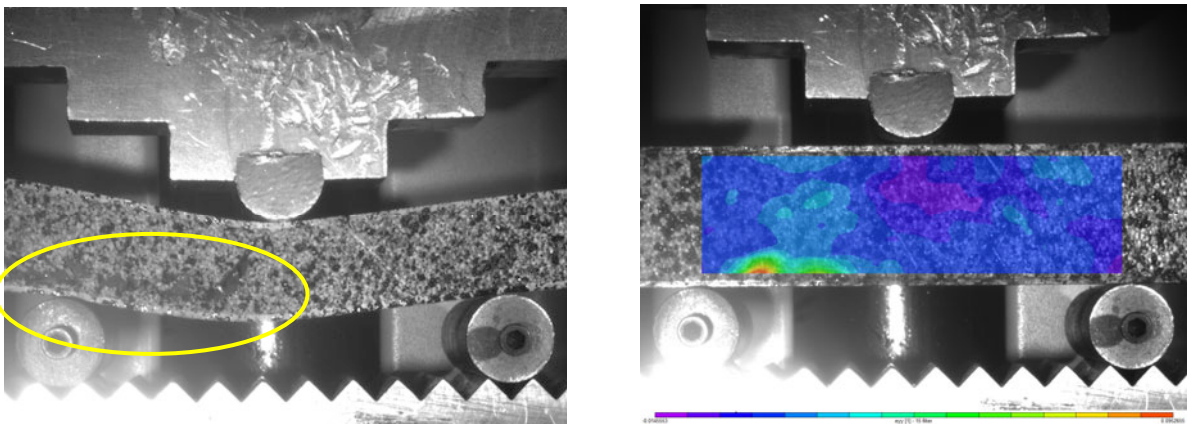

(c) (d)

Figure 10. Delamination in 1.8 lb/ft^3 and 4 lb/ft^3 material. (a) Onset of delamination, (b) Propagation of delamination, (c) Delamination failure, and (d) DIC transverse strain.

Lastly, this type of material can fail by indentation, which occurs when the loading element presses into the top of the material while very little or no deformation is occurring at the bottom of the specimen. *Figure 11* shows a comparison of an undeformed specimen and one that has experienced indentation. In both the pictures and the DIC image, it is clear the center of the top face sheet of the material deforms more vertically than the same point on the bottom face sheet.

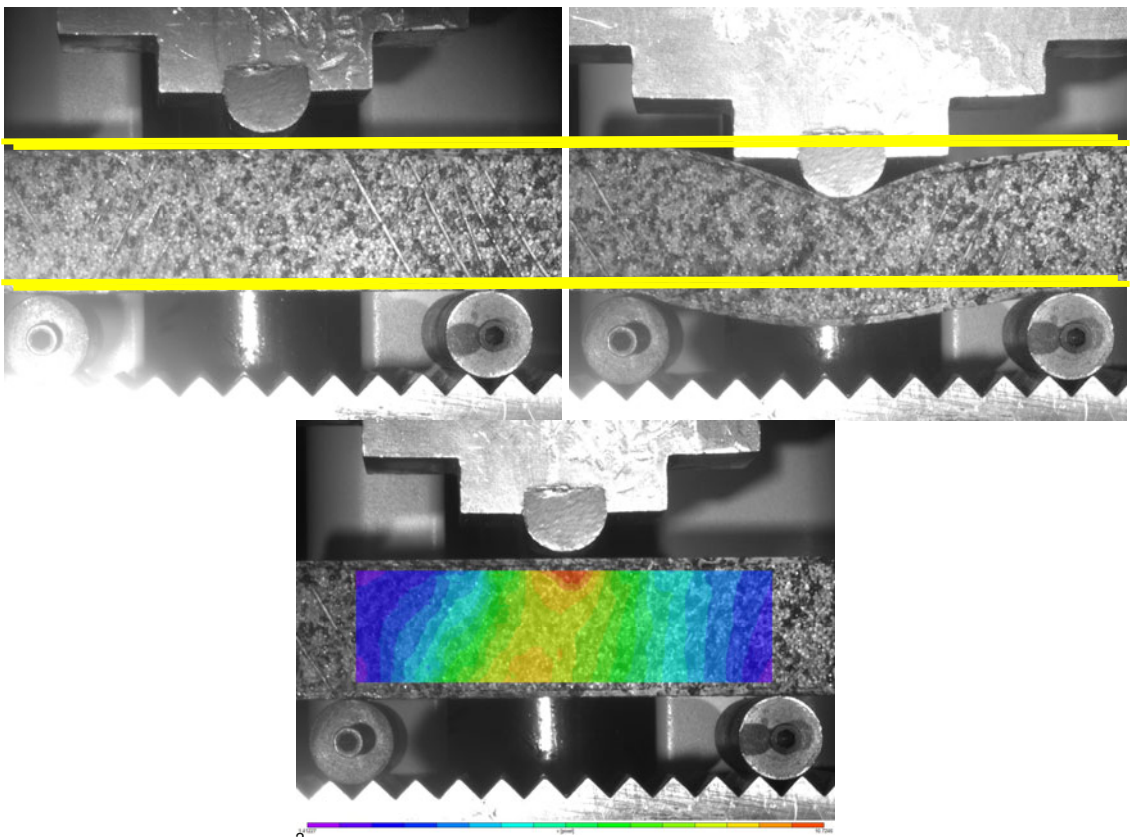

Figure 11. Indentation in 8 lb/ft^3 material. Undeformed specimen (left), failure by indentation (right), and DIC vertical deformation (bottom).

DIC can also be used as a tool to predict failure types and locations before any damage is visible to the naked eye. At low load levels, strain concentrations often form in the DIC images in the same area as the eventual failure. *Figure 12* shows an example of this phenomenon.

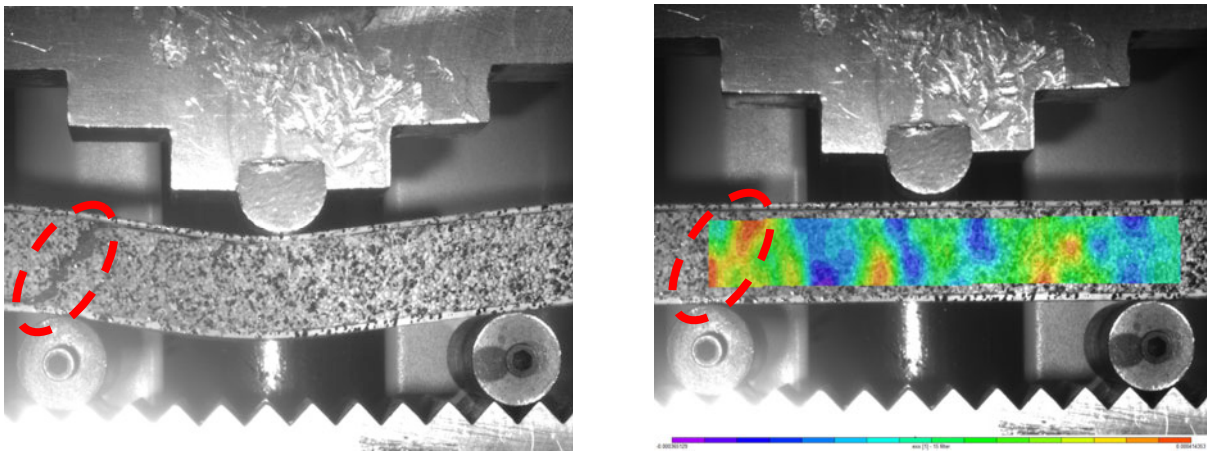

Figure 12. Comparison of failure location and ε_{yy} from DIC at approximately 10% of maximum load level

4. Effects of Incremental Damage in Three-point Bending

To investigate the effect that incrementally damaging the specimen would have on the elastic response of the material, the specimen was loaded until the first cracking sound was heard and then immediately unloaded. This occurred at approximately 100 kg. This same procedure was also repeated five times to examine the effects of increased damage on the specimen. *Figures 13 a, b, and c* show the results of increasing damage on the properties of the specimen. As the plots show, the elastic modulus of the specimen is significantly reduced each time the specimen is loaded and unloaded with a 41% reduction after 0.5% inelastic strain. The cause of this is inelastic damage in the specimen, most likely in the form of a partially or fully broken pin in the core material or the development of a crack in the face sheet.

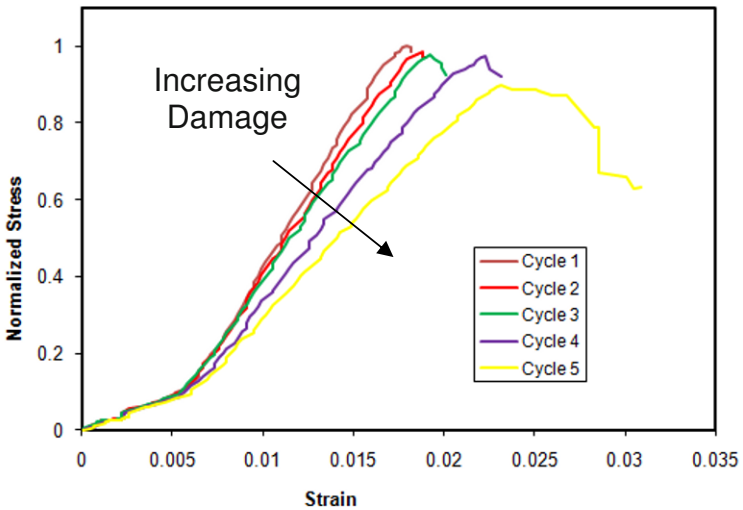

Incremental Inelastic Strain	Relative Young's Modulus
0	1
0.0005	0.91
0.001	0.83
0.003	0.72
0.005	0.59

Figure 13. Incremental damage stress-strain curves and changes in elastic modulus

5. Conclusions

The mechanical behavior of X- and K-Cor composites have been characterized using DIC. The experimental results have been used to refine the developed of a FEA model consisting of isotropic beam elements for the pultruded carbon fiber pins, orthotropic shell elements for the laminated face sheets, and isotropic solid elements for the foam core. Experimental three-point bend DIC results were compared with FEA simulations for different arrangements at a given pin density and configuration in order to provide the best correlation. Corresponding damage mechanisms were then quantified using DIC, which could be used to identify potential failure locations and modes at very low loading levels. Finally, degradation in elastic modulus due to incremental damage was quantified,.

Proceedings of the SEM Annual Conference
June 7-10, 2010 Indianapolis, Indiana USA

Novel Insert Design for Thick Single Lap Bolted Composite Joints

Brandon Bouchard, Bryon Hall, Gaetano Restivo, Gary Cloud
Composite Vehicle Research Center, Michigan State University
2727 Alliance Drive, Lansing, MI 48910

ABSTRACT

Mechanical fastening is a popular choice in joining composites because of the ability to transfer high loads and the ease of assembly and disassembly. However, drilling operations expose the fibers to environmental factors, and the high contact stresses between the bolt and the hole lead to localized delaminations, decreasing the joint strength. A new insert design, proposed here, seals the joint and increases the contact area between the bolt and the hole. This design is also low-cost and compatible with current machining techniques.

With the novel design, a phase changing liquid is injected into the empty region between the bolt and the hole. The liquid is then allowed to cure. The tests then performed are on non-reinforced joints and joints reinforced with both machined isotropic inserts and the novel design. Initial tests in the elastic range are analyzed by using Digital Image Correlation. The joints are also tested to ultimate failure to determine any trends. From these tests and other preliminary considerations, it can be concluded that the novel design has tremendous potential for applications involving thick composite joints.

INTRODUCTION

Composite materials are being used in greater frequency as they can provide weight and strength advantages. Many aerospace applications already exist for such materials, but as larger structures and vehicles are designed, better understanding of thick composite joints is necessary. Bolted joints provide many advantages including the ability to be easily assembled, disassembled, and transfer high loads. These characteristics are important because many applications require the joining of dissimilar materials, such as a composite to an isotropic material. This type of joint also allows the lighter composites to be joined to a strong substructure creating lighter and more effective assemblies.

There have been a large number of studies [1-6] aimed at investigating the effects of the joint geometry on the failure of thin composite joints. Failure modes of bearing, shear out, net tension and cleavage were shown to depend on the geometry of the joint and position. In all of the tests, bearing was seen to be the ideal failure mode because it is not a catastrophic failure and continues to carry load after failure. Through these studies optimum design qualities remained consistent with width-to-hole diameters W/D and edge to hole diameter E/D being above 4 and 3 respectively.

Thick composites have also been studied [7-9]. Failure was studied in a similar way as with thinner joints. In a study on 3D scaling of joints, failure has only been seen [7-8] for thick composites to occur in net tension. This was proposed to be caused by the higher thickness constraints that exist. Strain has been studied in similar joints through the thickness [9]. This was accomplished with the use of photoelasticity and strain gages mounted through the thickness. The main conclusion was that most of the stress is due to the tilting of the bolt.

In addition to the properties of hole position and thickness of the composite, other studies [11-14] have focused on performance in relation to preload of bolts and washers clearances. Increases in the preload showed improvement in the stiffness and the failure loads seen by the joint.

The use of inserts has been found to provide stress relieving and failure resistance [15-17] in thin composites. These studies have focused on thin composites with preformed isotropic inserts. The inserts have been found to

T. Proulx (ed.), *Application of Imaging Techniques to Mechanics of Materials and Structures, Volume 4*, Conference Proceedings of the Society for Experimental Mechanics Series 14, DOI 10.1007/978-1-4419-9796-8_53, © The Society for Experimental Mechanics, Inc. 2013

decrease the stresses seen in the composite by reducing the stress concentrations. Improvements have been seen to be as high as 50%.

In proposal of the novel insert, the advantages seen from the isotropic inserts can be built upon. Specialized bolt designs will allow different materials to be injected into the gap between the materials being fastened and the fastener. A preformed insert must be machined specifically for each diameter and shape of the hole. An injected insert would be able to conform to a variety of hole shapes and diameters without the need for precise machining. An injecting the insert would also seal the fastening system, preventing water or other liquids from entering the joint area. It also conforms to the hole, no clearance will exist in the joint, minimizing long term fatigue due to bolt clearance. Additional advantages can be achieved by the adhesive effects of an injected insert. In essence, the joint becomes both adhesive and mechanical. While the adhesive bond is much weaker, it can seal the system and create a locking mechanism between the nut and bolt, reducing the possibility of the bolt loosening.

Thus this study looks to compare use of preformed isotropic inserts to the novel insert in a thick composite joint. To perform the study, multiple sizes of inserts both preformed isotropic and novel are tested. Digital Image Correlation and failure testing are used to test the mechanical behavior of the inserts.

EXPERIMENTAL METHODS

Composite laminates made from glass/epoxy were investigated in this study. A large panel was purchased from McMaster-Carr. It was a .5” (12.7 mm) thick composite panel with a [0/90] layup, and it was constructed of Grade G-10 Garolite to Military standard MIL-I-24768. This material was selected for its strength characteristics and machinability. All samples in this study were created from a single panel.

Material properties for the Garolite were experimentally determined to be $E_x = E_y = 25612$ MPa and $v_{xy} = 0.155$. Dimensions for the joint were evaluated with FEM analysis to ensure no interaction between the area of study and the clamped portion. The samples were then cut to the size of 4” x 8” (101.6 x 203.2 mm). The width of 4” (101.6 mm) was decided upon to ensure that the width to diameter ratio would remain within a reasonable range prescribed in literature. The length of 8” (203.2 mm) ensures no interaction between the loading end and area of interest. After the samples were cut, the holes were drilled in a mill to ensure accurate positioning. The location of the center hole was chosen to have a ratio of diameter to edge distance of 4; this ratio has been shown to exhibit bearing failure in thin composites. Bearing failure is ideal because it has the highest yield strength compared to other joint failure modes but [9] concludes that the thickness constraint will fail in net tension. Dimensions and test setup are shown in Figure 1.

The testing fixture shown in Figure 1 was used with an offset to allow for a single lap shear test. The authors used Digital Image Correlation (DIC) to measure the strain fields that are developed in the specimens as a result of the loading configuration. The DIC setup for these experiments used a single Charge-coupled Device (CCD) camera. A light source consisting of sixteen light emitting diodes (LED) was used to evenly illuminate the desired surface. The light source used green LEDs to complement the sensitivity of the CCD camera. The camera and light source were mounted on a common tripod to provide stability during the experiment.

The samples were bolted into the fixture. The entire sample was loaded into a MTS 810 universal testing machine. Load from the MTS is transferred via the bolts through the specimen clamp and sample. An aluminum plate was used as the second plate in the lap joint. It was connected to the sample by a bolt torqued to 25 in lbs (2.82 Nm). The torque was kept constant based on the recommendation from [15]. The test was then setup to run at a constant ramp of 1mm/min providing a quasi static loading condition. The tests run in the elastic range with DIC specimens were loaded from 0 N to 30,000 N; images were captured at increments of 5,000 N. The images were transmitted to a personal computer for processing to calculate the full-field strain distribution in each specimen. When running failure tests, the only measured readings were the time, displacement, and force as recorded by the software program.

To test the effects of inserts, composite samples were produced with different hole diameters. For a point of comparison, isotropic inserts were prepared and tested in the same configuration as the Figure 1. Four different inserts were produced, in two different sizes and two different materials. All of the inserts were machined to fit a .5” (12.2 mm) bolt and sit flush in the hole of the lap joint. The outer diameters of the inserts used were .625”

(15.9 mm) and .75” (19 mm). For materials, Aluminum E = 71.7 GPa and Steel E = 210 GPa were chosen to give the joint either a ductile with the aluminum or stiffer reaction with the steel.

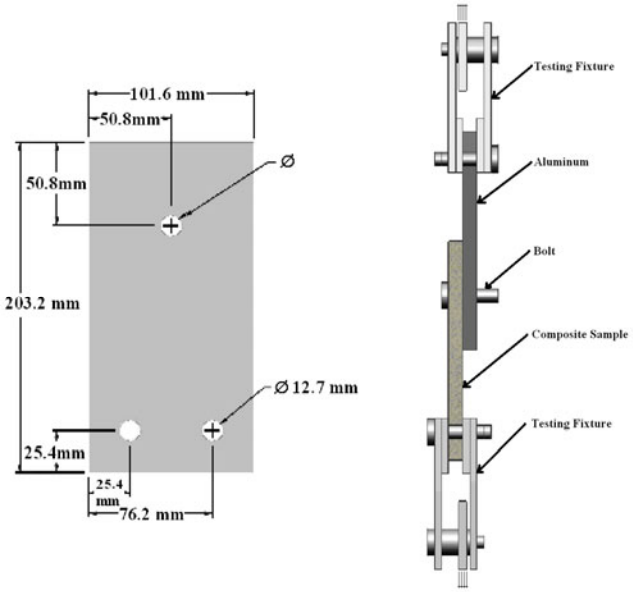

Figure 1: Sample Dimensions and Test Configuration for Single Lap Shear Joint Testing.

For the novel insert design, an insert is formed by injecting a liquid into a fastened single lap bolted joint using a specially designed injection bolt. The liquid is then allowed to cure until a soft insert has formed. The injection bolt is a standard grade 8 hex bolt that has been machined so a liquid can be injected through the bolt into the joint. Figure 2 shows the schematics of such a design; the grayed area represents the injection channels.

It was necessary to test the effectiveness of different bolt channel designs. Two different parameters were chosen as variables for the design of the injection bolt; channel diameter and channel quantity. Using the parameters, three different designs were initially developed. The first design contains two thru-channels. The channels are perpendicular to each other and are equally spaced through a 1” (25.4 mm) length. The second design contains one thru-channel; centrally located within the 1” (25.4 mm) length. The third design contains two half-channels; the channels are parallel to each other and are equally spaced through a 1” (25.4 mm) length. The channels of all three designs are 0.125” (3.17 mm) in diameter. A length of 0.25” (6.35 mm) of the vertical injection channel has been enlarged to 0.1875” (4.76 mm) to accommodate the injection device. In testing, after epoxy has been injected into the joint, the injector will be removed from the bolt.

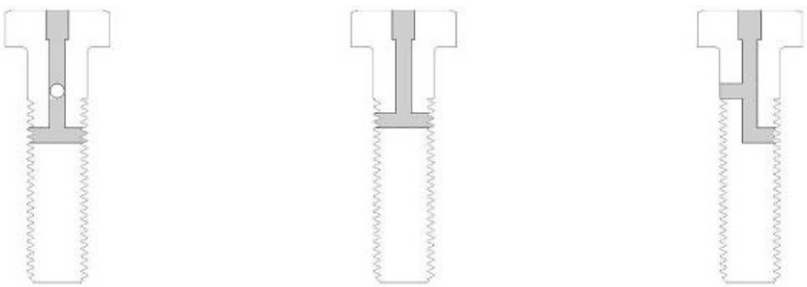

Figure 2: Bolt Configurations (1) Dual Thru-Channel (2) Single Thru Channel (3)Dual Half-Channel

A disposable 1oz (30 ml) syringe with a tapered nozzle was chosen as the best option for injection of the resin in the experiments. The bolts were centered in the holes with clearances of .125 in (3.12 mm) and .25 in (6.35 mm). The samples were then clamped and torqued to the 2.5 in lbs (2.82 Nm). The dual thru-channel bolt was chosen for testing because it would allow for the fastest injection of the resin with the least amount of voids. After the setup was tightened the thin epoxy resin was injected into the bolt.

RESULTS FROM DIGITAL IMAGE CORRELATION

Digital Image Correlation (DIC) was used to measure the in-plane strain fields that were developed as a result of the loading configuration as well as to understand the effects of each type of insert on the in-plane strain fields. The area of interest for the joint is the area directly around the hole. The surface strains will help in determining the strain relief provided by the various inserts. Initial DIC experiments were performed on un-reinforced single-lap bolted joints to provide a baseline for comparison. A sample before being prepared with the speckle pattern is displayed in Figure 3. The grid displayed at the lower portion consists of 5 mm blocks and the shaded area presents the area analyzed by DIC.

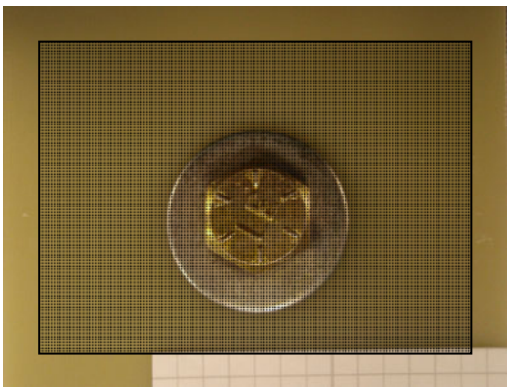

Figure 3: Shaded area displays the field studied by Digital Image Correlation.

Figure 4 and 5 show the full-field strain distribution in the horizontal and vertical directions of the un-reinforced single-lap bolted joint. The specimen is loaded in the downward direction resulting in a compressive stress against the top portion of the bolted connection. From Figure 4a it is seen the primary horizontal normal strain (1.5 mm/m) occurs at the contact point between the bolt and composite plate. From Figure 4b it is seen the primary vertical normal strain (0.5 mm/m) occurs at a point 45 degrees from the center point of the bolted connection.

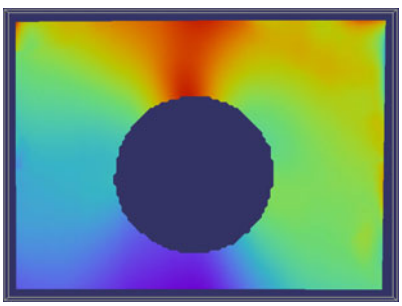

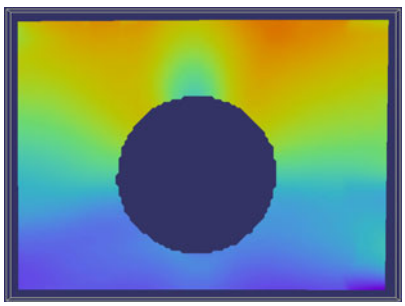

Figure 4a (left): Horizontal Normal Strain for Un-reinforced joint at 30 kN
Figure 4b (right): Vertical Normal Strain for Un-reinforced joint at 30 kN

A second baseline was performed on preformed inserts. The purpose of these experiments was to correlate with similar research performed on thin composite plates as well as to provide a secondary baseline with which to compare the injected inserts. These tests used 1144 steel and 7075 aluminum inserts with a 0.50 in. (13 mm) inner diameter and wall thicknesses of 0.0625 in. (1.59 mm) and 0.125 in. (3.18 mm). As the 0.0625 in. (1.59 mm) wall thickness inserts resulted in an increased strain distribution and as both the steel and aluminum 0.125 in. (3.18 mm) wall thickness inserts showed decreased strain distributions, for purposes of brevity, only the results of the 7075 aluminum are given; these results are shown below in Figure 5a and Figure 5b. Comparing Figure 5a to Figure 4a shows a a7075 aluminum insert resulted in a 66% reduction in the strain distribution. Although a similar result is not shown by a comparison of Figure 3b to Figure 3a, the aluminum insert redistributed the strain field, reducing the strain field gradient around the connect area between the bolted connection and the composite plate.

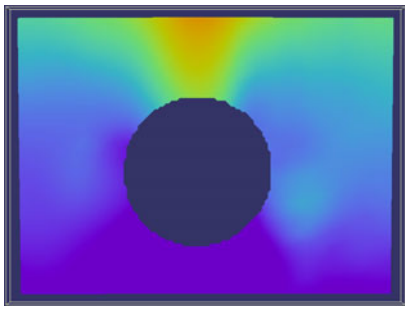
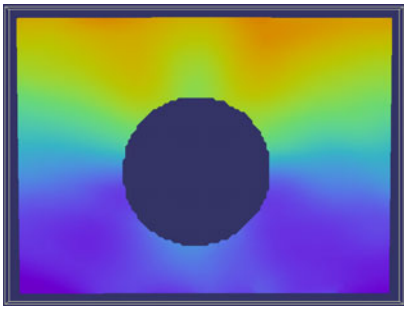

Figure 5a (left): Horizontal Normal Strain for 7075 aluminum insert reinforced joint at 30 kN
Figure 5b (right): Vertical Normal Strain for 7075 aluminum insert reinforced joint at 30 kN

The third set of experiments was performed on bolted connections using the injected inserts. The injection bolts were machined from bolts similar to those used for the previous experiments. Inner diameters equivalent to 0.50 in. (13 mm) and wall thicknesses equivalent to 0.0625 in. (1.59 mm) and 0.125 in. (3.18 mm) were tested. The injection fluid consisted of a thin epoxy resin with a medium rate hardener. After injection, the joint was allowed to cure for 24 hours before applying loading to the samples. Although both samples showed a decrease in the strain fields, for brevity, only the results of the sample with a 0.125 in. (3.18 mm) wall thickness is shown; these results are shown in Figure 5a and Figure 5b. Figure 6a and Figure 6b show a decrease in the strain field as compared to both the un-reinforced baseline as well as the preformed insert baseline.

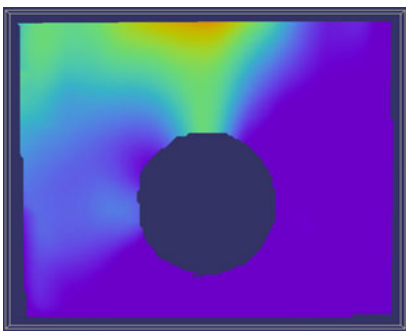
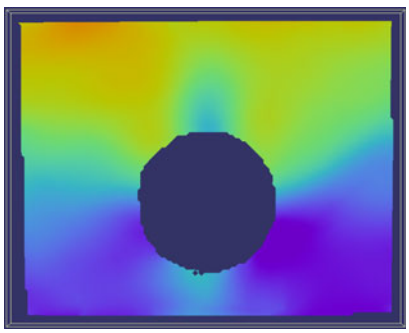

Figure 6a (left): Horizontal Normal Strain for injected insert reinforced joint at 30 kN
Figure 6b (right): Vertical Normal Strain for injected insert reinforced joint at 30 kN

FAILURE RESULTS

The following are the results from the experiments run to failure. As can be seen from the Figure 7, the baseline tests were run to final catastrophic fiber failure with just a simply bolted lap joint. Figure 8 plots the load against the displacement for the failure testing. The graph begins as non linear as the slack is removed from the fixture. The initial building of load between 10 and 35kN was seen to be linear; from these regions the stiffness of the joint was calculated. When the load displacement breaks from linearity it is assumed delamination and initial fiber failure begins. This is also the point where delamination can be seen on the outer face. This delamination can be seen at the far left of Figure 7. When the slope of the curve goes to zero, delamination becomes better defined and a crack breaks through on the surface. After the break through occurs, the delamination continues to progress and at the final plateau the fibers begin to fail in the form of net tension. The ultimate failure occurs at the end of the graph due to catastrophic net tension failure, as shown on the far right of Figure 7.

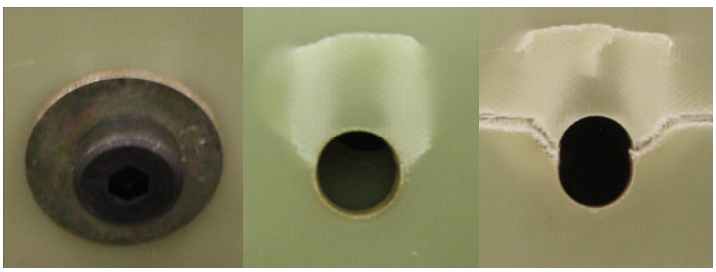

Figure 7: Pictures corresponding to Initial Delamination, Crack Breakthrough, and Final Net Tension.

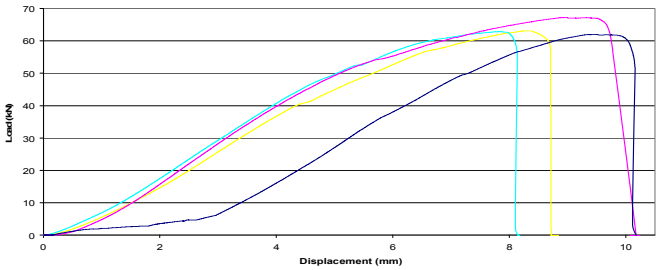

Figure 8: Baseline testing results.

Testing for the inserts continued in the same setup as the baseline tests. Results from the isotropic inserts are shown in Figures 9 and 10. Inserts with an outer diameter of .625" are displayed with a dashed line and the results for the .75" outer diameter are shown as solid.

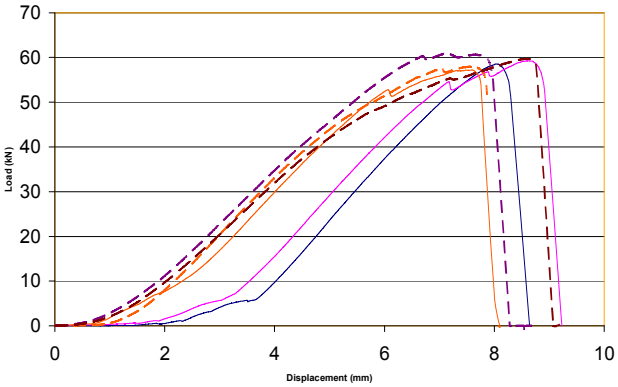

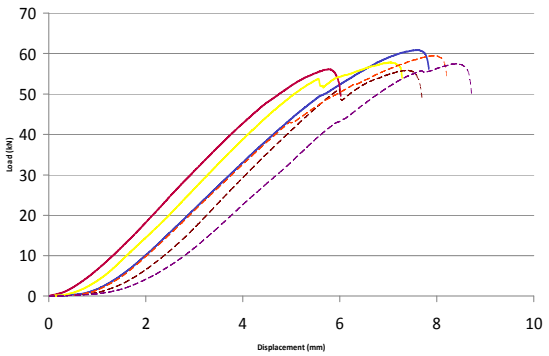

Figure 9 (left): Steel Insert Results
Figure 10 (right): Aluminum Insert Results

From the data provided during testing, several values were calculated for each test. Averages are presented below in Table 1.

Table 1: Failure Test Averages.

	Stiffness N/mm	Ultimate Load (kN)	Failure Stress (MPa)	Bearing Stress (MPa)
Base	9771	64.8	57.4	402
AL625	13890	57.6	54.9	238
AL75	11972	58.3	53.5	181
ST625	18426	58.6	55.9	242
ST75	1608	58.3	53.6	181
Novel 625	15464			
Novel 75	15637			

It is important to note that the novel bolts failed at approximately 45kN. This failure occurred along one of the grooves as shown in Figure 11. As also shown in Figure 11, the resin had failed. The resin failing created an impulse which caused the bolt to fracture. This is why there is no data provided for these inserts in Table 1.

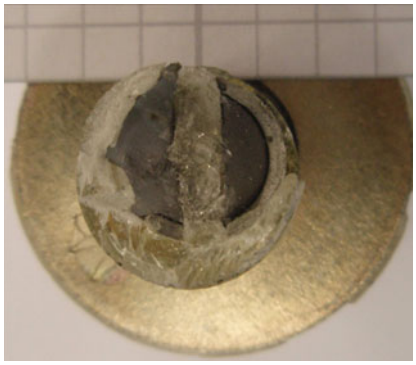

Figure 11: Failure of Injection Bolt.

DISCUSSION

The experiments provide information useful in the optimization of a reinforced single-lap bolted joint. Similar to research performed on thin composite joints, the experiments show that both the wall thickness and moduli of elasticity of the insert change the effectiveness of the insert at reducing the strain fields in the vicinity of the bolted connections. However, differing from thin-plate composite research in which materials stiffer than the composite are the most effective at reducing stress concentrations, these experiments suggest that softer materials, such as the epoxy resin used in these experiments, are most effective at reducing strain concentrations in thick plate composites.

It is seen that the stiffness of all of the inserts increases. This is expected as the joint has more material. Although failure of the composite was not achieved for the novel insert, the data shows that inserts in general do provide relief to the joint and offset the initial failures. This offset is believed to be caused by the increase in ductility compared to use of only the bolts. Allowing for deformation in the inserts allows for loads to be transferred more uniformly through the thickness of the hole. It can be seen in the graphs that this allows the cross section to fail initially in progressive sections before final catastrophic failure. Unfortunately no improvements in the ultimate load for any of the inserts are made. This can be assumed that because of the nature of the net tension failure, removal of more material from the joint will provide less overall strength.

CONCLUSION

Injected inserts provide a new, novel concept of reinforcing bolted connections utilizing composite plates. Compared to the method of using a preformed insert to reinforce the joint, the injected insert has several possible advantages. Injected inserts will decrease the strain fields around the bolted connection and increase the stiffness of the joint. This is important because with the use of inserts the initial failure can be accounted for providing a longer operating range. In addition, injected inserts require less restrictive tolerances as they conform to the shape of the hole and will also seal the joint against environmental factors. However, injected inserts do have a disadvantage. The removal of material for the bolt to create the injection channels can weaken the strength of the bolt to below that of the composite plate. In conclusion, once the failure load of the bolt can be increased, the injected insert could serve as a viable alternative to the traditional method of using preformed inserts to increase the strength and performance of bolted connections using composite plates.

REFERENCES

[1] Atas, Cesim. "Bearing strength of pinned joints in woven fabric composites with small weaving angles." *Composite Structures* 88 (2009): 40-45.
[2] Baba, B. "Behavior of Pin-loaded Laminated Composites." *Experimental Mechanics* 46 (2006): 589-600. Print.
[3] Kweon, Jin-Hwe, Jae-Woo Jung, Tae-Hwan Kim, Jin-Ho Choi, and Dong-Hyun Kim. "Failure of carbon composite-to-aluminum joints with combined mechanical fastening and adhesive bonding." *Composite Structures* 75 (2006): 192-98.
[4] Pekbey, Y. "The bearing strength and failure behavior of bolted E-glass/epoxy composite joints." *MECHANICS OF COMPOSITE MATERIALS* 44.4 (2008): 397-414.
[5] Riccio, A., Marciano, L. (2005) “Effects of Geometrical and Material Features on Damage Onset and Propagation in Single-Lap Bolted Composite Joints under Tensile Load: Part 1 – Experimental Studies.” Journal of Composite Materials 39: 2071-2090.
[6] Yilmaz, Taner, and Tamer Sinmazcelik. "Effects of Geometric Parameters on the Pin-bearing Strength of Glass/Polyphenylenesulphide Composites." *Journal of Composite Materials* 43.20 (2009): 2239-253.
[7] Hou, L., and D. Liu. "Three-dimensional size effects in composite pin joints." *EXPERIMENTAL MECHANICS* 43.2 (2002): 115-23.
[8] Hou, L., and D. Liu. "Size effects and thickness constraints in composite joints." *JOURNAL OF COMPOSITE MATERIALS* 37.21 (2003): 1921-938.
[9] Lancu, F., X. Ding, G. Cloud, and B. Raju. "Three-dimensional Investigation of Thick Single-lap Bolted Joints." *Experimental Mechanics* 45.4 (2005): 351-58.
[10] Eriksson, Ingvar. (1990) “On the Bearing Strength of Bolted Graphite/Epoxy Laminates.” Journal of Composite Materials 24: 1246-1269.
[11] Cooper, C., and G. J. Turvey. "EFFECTS OF JOINT GEOMETRY AND BOLT TORQUE ON THE STRUCTURAL PERFORMANCE OF SINGLE BOLT TENSION JOINTS IN PULTRUDED GRP SHEET MATERIAL." *COMPOSITE STRUCTURES* 32.1-4 (1995): 217-26.
[12] Herrington, P.D., Sabbaghian, M. (1992) “Effect of Radial Clearance between Bolt and Washer on the Bearing Strength of Composite Bolted Joints.” Journal of Composite Materials 26: 1826-1843.
[13] Khashaba, U., H. Sallam, A. Al-Shorbagy, and M. Seif. "Effect of washer size and tightening torque on the performance of bolted joints in composite structures." *Composite Structures* 73 (2006): 310-17.
[14] Sayman, Onur, Ramazan Siyahkoc, Faruk Sen, and Resat Ozcan. "Experimental determination of bearing strength in fiber reinforced laminated composite bolted joints under preload." *JOURNAL OF REINFORCED PLASTICS AND COMPOSITES* 26.10 (2007): 1051-063.
[15] Camanho, P.P., Tavares, C.M.L., et al. (2005) “Increasing the efficiency of composite single-shear lap joints using bonded inserts.” Composites Part B: engineering 36: 372-383.
[16] Herrera-Franco, Pedro J., Cloud, Gary L. (1992) “Strain-Relief Inserts for Composite Fasteners –An Experimental Study.” Journal of Composite Materials 26: 751-768.
[17] Nillsson, Sören. (1989) “Increasing Strength of Graphite/Epoxy Bolted Joints by Introducing an Adhesively Bonded Metallic Insert.” Journal of Composite Materials 23: 642-650.

Proceedings of the SEM Annual Conference
June 7-10, 2010 Indianapolis, Indiana USA

Smoothing Measured Displacements and Computing Strains Utilizing Finite Element Method

S. Yoneyama and S. Kobayashi
Department of Mechanical Engineering, Aoyama Gakuin University, 5-10-1 Fuchinobe, Sagamihara, Kanagawa 229-8558, Japan. yoneyama@me.aoyama.ac.jp

ABSTRACT

A method for smoothing measured displacements and computing strains utilizing a finite element method is proposed. Nodal displacement values of a finite element model are determined by fitting the interpolation functions of finite elements to measured displacement values using the method of least-squares. Then, the smoothed displacement distributions are obtained. The displacements in the region where the measurement values are not obtained or unreliable are determined by solving finite element equations. The validity is demonstrated by applying the proposed method to displacements of a plate with a hole obtained by finite element method. Results show that the displacements and the strains can be determined accurately by the proposed method. Furthermore, the strains near free boundaries can be determined easily. As strains can be evaluated easily and accurately, it is expected that the proposed method can be applied to various problems in solid mechanics.

INTRODUCTION

Optical methods such as speckle interferometry, holographic interferometry, and digital image correlation are widely used for the measurement of surface deformation in solid mechanics [1-5]. Generally, these experimental techniques provide only the information of surface displacements. In other word, stresses or strains cannot be obtained directly by these methods. Therefore, it is required to differentiate the displacement distributions to obtain stresses or strains.

The derivatives of displacements at a point can be estimated from the values of displacements at neighboring points. The use of finite difference method, however, has the disadvantage that the errors in the measured values give rise to even greater errors in their derivatives. For this reason, a least-squares method has long been widely used for the numerical differentiation in the calculation of in-plane strains from the displacements [6-8]. In this case, a polynomial is fitted to displacement values in a small local region by a least-squares method to reduce the effect of the measurement errors in displacements. The average strains in the region are obtained from the coefficients of the approximated polynomial. Then, the strain distributions are obtained by repeating this procedure for the whole field. The major drawback of this technique is the difficulties of the data processing near boundaries. It is difficult to evaluate the strains at the boundary accurately by this technique because the measured displacement used for the least-squares approximation does not exist beyond the boundary. In addition, the measured displacements at the boundary frequently contain relatively large errors compared with those inside the boundary. Furthermore, it is difficult for this technique to evaluate the strains near the crack tip because the small local region for the least-squares method sometimes overlap crack faces that have opposite displacements.

Another approach to the calculation of the strains from the measured displacements is the use of a finite element method (FEM) [9,10]. The measured displacements are used as the nodal displacements in a finite element method. Then, the strains inside the elements are calculated easily using a displacement-strain relationship. In this method, the errors arising the differentiation of the measured displacements still exist. Therefore, various data smoothing and other techniques for inputting the data to the finite element method have been proposed

T. Proulx (ed.), *Application of Imaging Techniques to Mechanics of Materials and Structures, Volume 4*, Conference Proceedings of the Society for Experimental Mechanics Series 14, DOI 10.1007/978-1-4419-9796-8_54, © The Society for Experimental Mechanics, Inc. 2013

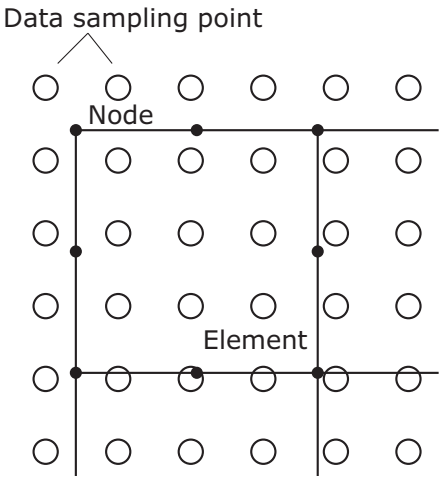

Fig. 1 Data sampling points, elements and nodes

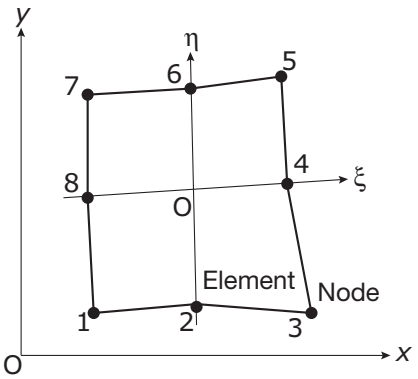

Fig. 2 8-noded isoparametric element

[11,12]. The disadvantage of the techniques utilizing a finite element method is the preparation of a finite element model. However, the strains at the boundary and the crack tip are easily obtained by utilizing the finite element method. In addition, hybrid analysis can be performed easily. That is, the displacements at the region where the measurement values cannot be obtained or unreliable can be obtained by solving the finite element equation [9,10,13]. Other hybrid methods that utilize the measured values only at the boundary of a finite element model have also been proposed by several researchers [9,10,14-16].

In the present study, an alternative method for smoothing measured displacements and computing strains utilizing a finite element method is proposed. Nodal displacement values of a finite element model are determined by fitting the interpolation functions of finite elements to measured displacement values using a least-squares method. Then, the smoothed displacement distributions are obtained. The displacements in the region where the measurement values are not obtained or unreliable are determined by solving finite element equations. The validity is demonstrated by applying the proposed method to displacements of a plate with a hole obtained by finite element method. Results show that the strains can be determined accurately by the proposed method. Furthermore, the strains near free boundaries and strain concentration region can be determined easily. As strains can be evaluated easily and accurately, it is expected that the proposed method can be applied to various problems in solid mechanics.

SMOOTHING DISPLACEMENTS AND COMPUTING STRAINS

The locations of data points where displacements are measured do not usually coincide with those of the nodal points. Therefore, the displacements at the nodal points are determined by the displacements at neighboring points using interpolation in conventional data processing technique with finite element [10]. In the proposed method, on the other hand, the nodal displacements are determined using a least-squares method. Figure 1 schematically shows the relationship between the locations of the nodes of an element in a finite element model and the data sampling points. It is considered that the in-plane displacements at the data sampling points are measured by optical methods. The displacements at the nodal point are determined from the measured displacements inside the element.

Figure 2 shows an 8-noded isoparametric element. In this figure, ξ and η are the local coordinates that lie in the ranges of $-1 \le \xi \le 1$ and $-1 \le \eta \le 1$. In a finite element method, the x- and y-displacement components u and v inside the element are interpolated by the nodal displacements of the element as

$$u = \sum_{i}^{n} N_i u_i^{\text{node}}$$
$$v = \sum_{i}^{n} N_i v_i^{\text{node}}, \tag{1}$$

where u_i^{node} and v_i^{node} are the element displacements at its nodes, i is the node number and n is the number of the node, that is, $n = 8$ when 8-noded isoparametric element is used. N_i is the shape function that can be represented by the local coordinates ξ and η.

The experimental values of the displacement at the points inside the element can be expressed from Eq. (1) as

$$u_j^{\text{exp}} = \sum_{i}^{n} N_i u_i^{\text{node}}$$
$$v_j^{\text{exp}} = \sum_{i}^{n} N_i v_i^{\text{node}}, \tag{2}$$

where u_j^{exp} and v_j^{exp} are the measured displacement values at the data sampling points inside the element and j is the data index. In Eq. (2), u_j^{exp} and v_j^{exp} are known values because they are measured. The shape function N_i can also be known from the location of the data points. Therefore, the nodal displacement values can be determined using a least-squares method if the number of data points inside an element is greater than the number of the nodes of the element. The relationship between the measured displacement and the nodal displacement of a whole finite element model can be represented from Eq. (2) as

$$\mathbf{u}^{\text{exp}} = \mathbf{N}\mathbf{u}^{\text{node}}, \tag{3}$$

where

$$\mathbf{u}^{\text{exp}} = \begin{Bmatrix} u_1^{\text{exp}} \\ v_1^{\text{exp}} \\ u_2^{\text{exp}} \\ v_2^{\text{exp}} \\ \vdots \\ u_M^{\text{exp}} \\ v_M^{\text{exp}} \end{Bmatrix}, \quad \mathbf{u}^{\text{node}} = \begin{Bmatrix} u_1^{\text{node}} \\ v_1^{\text{node}} \\ u_2^{\text{node}} \\ v_2^{\text{node}} \\ \vdots \\ u_N^{\text{node}} \\ v_N^{\text{node}} \end{Bmatrix}.$$

In above equations, M is the number of the data points, N is the number of the node of the whole finite element model, and $\mathbf{N}$ is the $2M \times 2N$ matrix that is composed of the shape function. The nodal displacement vector $\mathbf{u}^{\text{node}}$ can be determined using the least-squares method as

$$\mathbf{u}^{\text{node}} = (\mathbf{N}^T\mathbf{N})^{-1}\mathbf{N}^T\mathbf{u}^{\text{exp}}. \tag{4}$$

Because the values of $\mathbf{u}^{\text{node}}$ are determined from the measured values within the elements by the method of least-squares, the nodal displacements by above procedure are smoothed and they can be considered as the appropriate values. After determining the displacement vector, the strains can be calculated as

$$\varepsilon_x = \sum_{i}^{n} \frac{\partial N_i}{\partial x} u_i^{\text{node}}$$
$$\varepsilon_y = \sum_{i}^{n} \frac{\partial N_i}{\partial y} v_i^{\text{node}} \tag{5}$$
$$\gamma_{xy} = \sum_{i}^{n} \left(\frac{\partial N_i}{\partial y} u_i^{\text{node}} + \frac{\partial N_i}{\partial x} v_i^{\text{node}} \right)$$

The stresses can also be calculated using a constitutive relation. In the above procedure, a finite element equilibrium equation is not solved. The finite element method is utilized only for computing strains from the measured displacements.

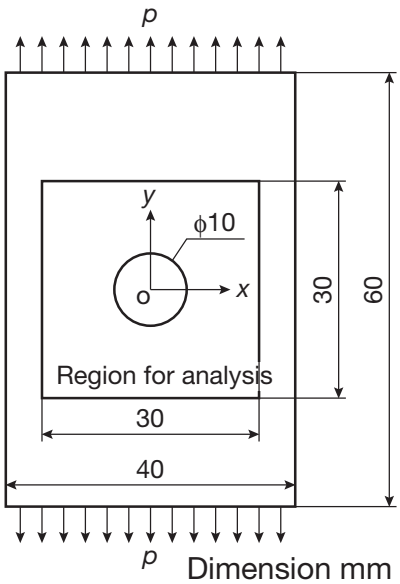

Fig. 3 Specimen geometry used in simulation

HYBRID ANALYSIS

Because the proposed method utilizes a finite element model for evaluating strains, a hybrid analysis can be introduced if necessary. In other words, the displacements in the region where the measurement values are not obtained or unreliable are determined by solving the finite element equation [9,10,13]. The finite element equilibrium equations for the whole model is written as [17]

$$\mathbf{KU} = \mathbf{F} \tag{6}$$

where **K** is the stiffness matrix, **U** represents the displacement vector, and **F** gives the nodal force vector. In the hybrid method, the displacements determined by the proposed method are used as the boundary condition for solving Eq. (6). Therefore, the nodal force vector **F** becomes zero vector. Equation (6) is rewritten as

$$\begin{bmatrix} \mathbf{K}_{uu} & \mathbf{K}_{uk} \\ \mathbf{K}_{ku} & \mathbf{K}_{kk} \end{bmatrix} \begin{Bmatrix} \mathbf{U}_u \\ \mathbf{U}_k \end{Bmatrix} = \begin{Bmatrix} \mathbf{F}_k \\ \mathbf{F}_u \end{Bmatrix} \tag{7}$$

where $\mathbf{U}_u$ and $\mathbf{U}_k$ are the unknown and known displacement vectors, and $\mathbf{F}_k$ and $\mathbf{F}_u$ represents the known and unknown nodal force vectors, respectively. $\mathbf{K}_{uu}$, $\mathbf{K}_{uk}$, $\mathbf{K}_{ku}$ and $\mathbf{K}_{kk}$ are the corresponding stiffness matrices. Uk is determined from the measured values by the proposed method as described in previous section and $\mathbf{F}_k$ is zero vectors. Equation (7) can be rewritten as

$$\mathbf{K}_{uu}\mathbf{U}_u = \mathbf{F}_k - \mathbf{K}_{uk}\mathbf{U}_k \tag{8}$$

Therefore, the unknown displacement vector $\mathbf{U}_u$ can be determined by solving Eq. (8).

VERIFICATION BY SIMULATION

In order to validate the effectiveness of the proposed method, the strains are computed by the proposed method from the displacements obtained by the finite element direct analysis. A plate with a hole under tension shown in Fig. 3 is analyzed to generate the displacement distributions to be used in the simulation. In Fig. 3, the model is subjected to the traction p in the y-direction on the upper and lower boundaries. The material in this simulation is assumed to be steel; the elastic modulus is E = 210 GPa and the Poisson's ratio is ν = 0.3. The displacement distributions are calculated under the condition of the traction of p = 30 MPa. The values of displacements on the surface are obtained at the points on the two-dimensional grid of 0.5 mm in interval. Then, the random noise of ±20 nm is given to the displacements to simulate the measurement errors. Figure 4 shows the displacement distributions used as the data input into the algorithm by the proposed method.

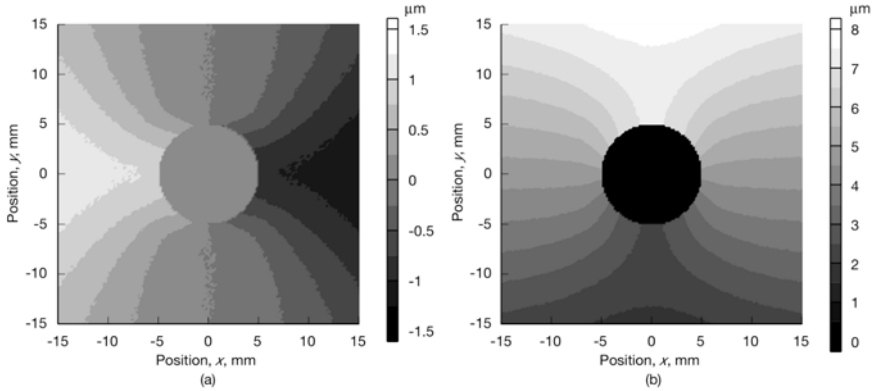

Fig. 4 Displacements used as input data in simulation: (a) u; (b) v

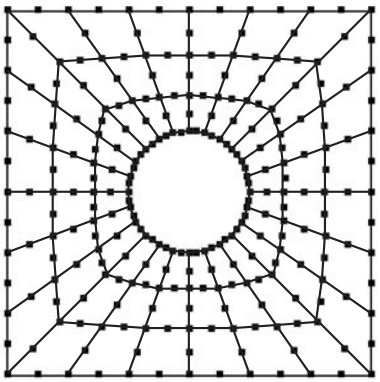

Fig. 5 Finite element model for computing strains

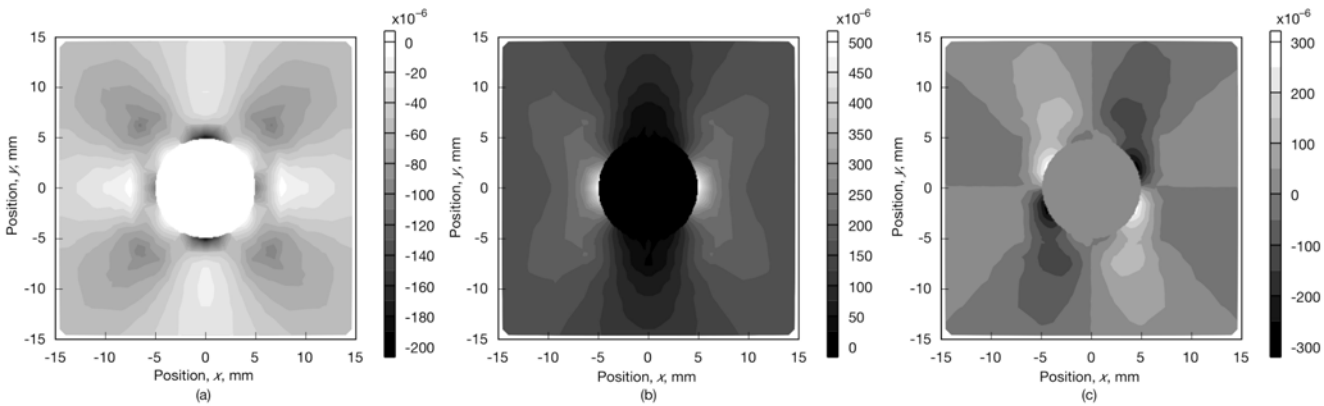

Fig. 6 Exact strain distributions: (a) ε_x; (b) ε_y; (c) γ_{xy}

The region for computing strains is 30 mm × 30 mm area shown in Fig. 3. Figure 5 shows the finite element model of the 30 mm × 30 mm region for computing strains. In this model, 8-noded isoparametric elements are used. The numbers of the elements and the nodes are 72 and 264, respectively. The strains are computed from the displacements in Fig. 4 by the proposed method using this model. In addition, the strains are also computed by giving the displacements to the all nodes directly to compare the results.

The strain distributions obtained by the finite element direct analysis are shown in Fig. 6. These distributions are treated as the exact strains for validating the strains obtained by the proposed method. The strains obtained by supplying the displacements into the all nodes in the model are shown in Fig. 7. Comparing these results to the

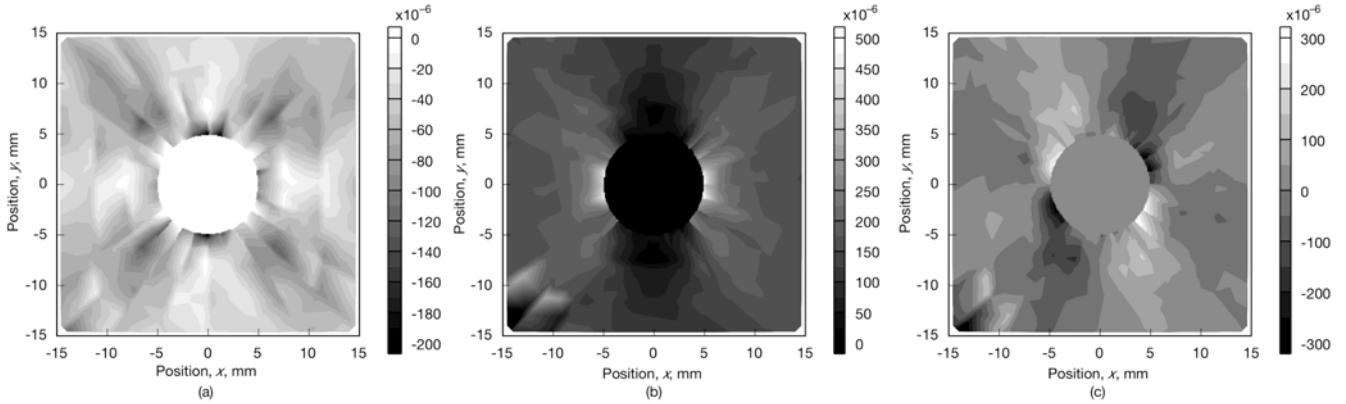

Fig. 7 Strain distributions obtained by supplying displacements to all nodes directly: (a) ε_x; (b) ε_y; (c) γ_{xy}

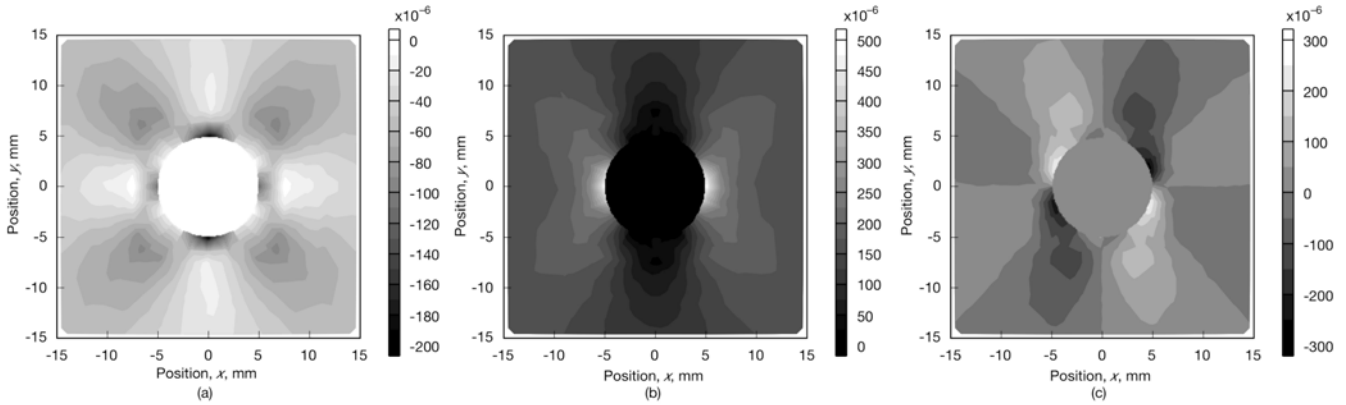

Fig. 8 Strain distributions obtained by the proposed method: (a) ε_x; (b) ε_y; (c) γ_{xy}

exact distributions in Fig. 6, it is understood that these strain distributions are different from the exact strains. Because the strains are computed from the displacements with random errors, the strain distributions in Fig. 7 contain much error. Figure 8 represents the strain distributions obtained by the proposed method. It is observed that the strain distributions obtained by the proposed method are in good agreement with the exact distributions in Fig. 6. The displacements are smoothed by the least-squares method in the proposed method, and then the smoothed strain distributions are obtained. In addition, the strains on the free boundary where the computing strain is sometimes difficult are also obtained. The average difference between the strains obtained by the proposed method and exact ones is 2.7×10^{-6}, the maximum difference is 83×10^{-6}, and the standard deviation is 6.9×10^{-6}. As shown in these results, the smoothed strains are obtained easily by the proposed method. The proposed method can be used as one of the data processing methods for optical methods.

CONCLUSIONS

In this study, a method for smoothing measured displacements and computing strains utilizing a finite element method is proposed. Nodal displacement values of a finite element model are determined by fitting the interpolation functions of the finite elements to the measured displacement values. Then, the strains are calculated using displacement-strain relationship. The validity is demonstrated by applying the proposed method to displacements of a plate with a hole obtained by finite element method. Results show that the displacements and the strains can be determined accurately by the proposed method. Furthermore, the strains near free boundaries can be determined easily. The proposed method can be used as one of the data processing methods for optical methods.

REFERENCES

1. Moore, A.J. and Tyrer, J.R., Phase-stepped EPSI and Moiré Interferometry for Measuring Stress-intensity Factor and J Integral, Experimental Mechanics, **35**(4), 306–314 (1995).
2. Gong, X.L. and Toyooka, S., Investigation on Mechanism of Plastic Deformation by Digital Speckle Pattern Interferometry, Experimental Mechanics, **39**(1), 25–29 (1999).
3. Suzuki, S., Sakaue, K. and Iwanaga, K., Measurement of Energy Release Rate and Energy Flux of Rapidly Bifurcating Crack in Homalite 100 and Araldite B by High-speed Holographic Microscopy, Journal of the Mechanics and Physics of Solids, **55**(7), 1487–1512 (2007).
4. Mekky, W. and Nicholson, P.S., The Fracture Toughness of Ni/Al2O3 Laminates by Digital Image Correlation I: Experimental Crack Opening Displacement and R-curves, Engineering Fracture Mechanics, 73(5), 571–582 (2006).
5. Lee, D., Tippur, H., Kirugulige, M. and Bogert, P., Experimental Study of Dynamic Crack Growth in Unidirectional Graphite/Epoxy Composites Using Digital Image Correlation Method and High-speed Photography, Journal of Composite Materials, 43(19), 2081–2108 (2009).
6. Bossaert, W., Dechaene, R. and Vinckier, A., Computation of Finite Strains From Moiré Displacement Patterns, Strain, **3**(1), 65–75 (1968).
7. Pan, B., Xie, H., Guo, Z. and Hua, T., Full-field Strain Measurement Using a Two-dimensional Savitzky-Golay Digital Differentiator in Digital Image Correlation, Optical Engineering, **46**(3), 033601 (2007).
8. Yoneyama, S., Kitagawa, A., Kitamura, K. and Kikuta, H., In-plane Displacement Measurement Using Digital Image Correlation with Lens Distortion Correction, JSME International Journal, Series A, **49**(3), 458–467 (2006).
9. Morton, J., Post, D., Han, B. and Tsai, M.Y., A Localized Hybrid Method of Stress Analysis: A Combination of Moiré Interferometry and FEM, Experimental Mechanics, **30**(2), 195–200 (1990).
10. Tsai, M.Y. and Morton, J., New Developments in the Localized Hybrid Method of Stress Analysis, Experimental Mechanics, **31**(4), 298–305 (1991).
11 Sutton, M.A, Turner, J.L., Bruck, H.A. and Chae, T.A., Full-field Representation of Discretely Sampled Surface Deformation for Displacement and Strain Analysis, Experimental Mechanics, **31**(2), 168–177 (1991).
12. Segalman, D.J., Woyak, D.B. and Rowlad, R.E., Smooth Splike-like Finite-element Differentiation of Full-field Experimental Data Over Arbitrary Geometry, Experimental Mechanics, **19**(12), 429–427 (1979).
13. Jayarama Rao, G., Pathinam, P. and Narayanan, R., Development of Hybrid Method Coupling Moiré Interferometry and Finite Element Method, Computers and Structures, **60**(3), 433–440 (1996).
14. Weathers, J.M., Foster, W.A., Swinson, W.F. and Turner, J.L., Integration of Laser-speckle and Finite-element Techniques of Stress Analysis, Experimental Mechanics, **25**(1), 60–65 (1985).
15. Nishioka, T., Kurio, K. and Nakabayashi, H., An Intelligent Hybrid Method to Automatically Detect and Eliminate Experimental Measurement Errors for Linear Elastic Deformation Fields, Experimental Mechanics, **40**(2), 170–179 (2000).
16. Fujikawa, M. and Takashi, M., Modified Intelligent Hybrid Technique Reducing Experimental Error Over the Entire Target Area, Experimental Mechanics, **45**(6), 541–549 (2005).
17. Bathe, K.-J., Finite Element Procedures, Prentice-Hall, 338–484 (1996).

Proceedings of the SEM Annual Conference
June 7-10, 2010 Indianapolis, Indiana USA

Diagnostic Use of Digital Image Correlation in High-Speed, Explosive Experiments

Franco J. Gagliardi, gagliardi7@llnl.gov
Bruce J. Cunningham, cunningham1@llnl.gov
Louis Ferranti, Jr., ferranti1@llnl.gov

Lawrence Livermore National Laboratory
Energetic Materials Center
P.O. Box 808, L-282, Livermore, CA 94550, USA

ABSTRACT: Digital image correlation (DIC) was used as a diagnostic tool in two series of scaled explosive experiments. In this paper, we focus on the use of DIC as a tool to obtain full-field displacement measurements during high-speed events. From the displacement records we were able to obtain full-field strains, strain-rates and velocity data. The experiments discussed in this paper involved explosive charges submerged in aquarium-like structures, one side of which consisted of a 6061-T6 aluminum plate. In each experiment, the outside of the aluminum plate was patterned so that it met the requirements for use with the DIC system. Two different plate preparation techniques were used in the experimental series and both resulted in the acquisition of quality data. While both techniques were effective, each proved to have unique advantages. The details of plate preparation and a discussion of the performance of each method are included in the paper. The displacement, strain and velocity data are discussed and the output capabilities of the DIC system are demonstrated. In addition to the high-speed, transient data acquired during the deformation events, static, surface-profile measurements of the post-test, deformed plates were made using the DIC system. A discussion of the static measurements is also presented.

INTRODUCTION

Explosive blast mitigation is an area of research that is important because it can be used to make better structural designs that are less susceptible to malicious activity [1-6]. Computer models are often used in the design process in an effort to predictively characterize the behavior of a design to certain forms of energetic input, such as that experienced when a structure is impacted with the pressure released from the detonation of a high explosive material. To ensure that computer models are reliable, they need to be validated and tuned with experimental data to ensure that they are properly accounting for the complex nature of the physical phenomena associated with the experiments. This combination of experimental data and computer models is a valuable asset in the fight against those seeking to do damage. Ideally, full-scale models of proposed structures would be tested to determine their response to various stimuli but cost and space are usually prohibitive for evaluating this type of structure. Due to the impracticality of doing explosive tests on full-scale structures to determine their response, scaled experiments are conducted. Much thought is needed in order to develop scalable tests because of the complexity related to the boundary conditions and the pressure application.

This paper reports the results from two series of laboratory-scale experiments in which several forms of blast mitigation were used in order to validate and tune models that will be used to model a large-scale structure. The tests reported include six tests that used one of two different models of an aquarium-like structure. The so-called aquariums had one of their sides made from aluminum 6061-T6. The outside surfaces of the aluminum plates

T. Proulx (ed.), *Application of Imaging Techniques to Mechanics of Materials and Structures, Volume 4*, Conference Proceedings of the Society for Experimental Mechanics Series 14, DOI 10.1007/978-1-4419-9796-8_55, © The Society for Experimental Mechanics, Inc. 2013

were prepared for use with digital image correlation (DIC) and were imaged using high-speed photography during the explosive event. The dynamic deformation was monitored and the post-test plastic deformation of each plate was measured using DIC. The results from the two series are presented in the following sections.

EXPERIMENTS

Two series of tests were run to evaluate several blast mitigation techniques in which digital image correlation was used as a primary diagnostic tool. The first series used a cube-like aquarium volume of about 11.5-liters of de-ionized water mixed with a small weight percent of surfactant. The second series used an aquarium-like structure that held a volume of about 265-liters. The experimental assembly is discussed for each in the following subsections.

Small Aquarium Series: Set-up and Tank Configuration

The first series of experiments consisted of the small aquarium variant of the explosive assembly. This assembly, except for the fourth experiment, was made up of a five-walled container, four walls of which were made out of 6.35-mm Lucite and the fifth made out of 3.2-mm thick aluminum 6061-T6. The fourth aquarium had another Lucite wall added so that the Lucite portion alone could contain the water, which would provide the opportunity for a purely air barrier to be created as will be discussed below. The assembled container had a volume of approximately 11.5-liters. The aluminum plate used as one side of the aquarium was 61-cm wide by 61-cm tall. The plate had holes drilled through it so that when attached, the Lucite portion of the aquarium would be centered. Additional holes were drilled near the top and bottom of the plate so that it could be reinforced with Unistrut® beams.

In all of the small aquarium experiments the explosive material used was LX-14, which is composed of 95.5% of the explosive HMX and 4.5% of the polymer binder Estane. The charges each weighed about 6.3-g and were in the shape of right-circular cylinders. The explosive charge was positioned in the assembly so that there was a standoff of about 7-cm. Fig. 1 shows a side-view diagram of each of the small aquariums highlighting the blast mitigation technique used. In the first experiment, represented in diagram 1, no mitigation was used, and thus only water existed between the explosive train (LX-14 main charge, shown in purple, and the detonator, shown in black) and the aluminum plate. In the second experiment, shown in diagram 2, air-filled plastic tubes were used as the mitigation type. The tubes had a nominal outer diameter of 6.35-mm and a wall thickness of about 1-mm. The tubes were arranged in an array about 7-cm thick and they were stacked the full height of the aquarium (represented by the colored rectangles). Diagram 3 illustrates the use of an approximately 130-μm thick Mylar sheet that created an air pocket for blast mitigation in the third experiment. The rightmost diagram, 4, shows the aquarium rotated 90˚. This change made it possible to have only air between the charge and the aluminum plate.

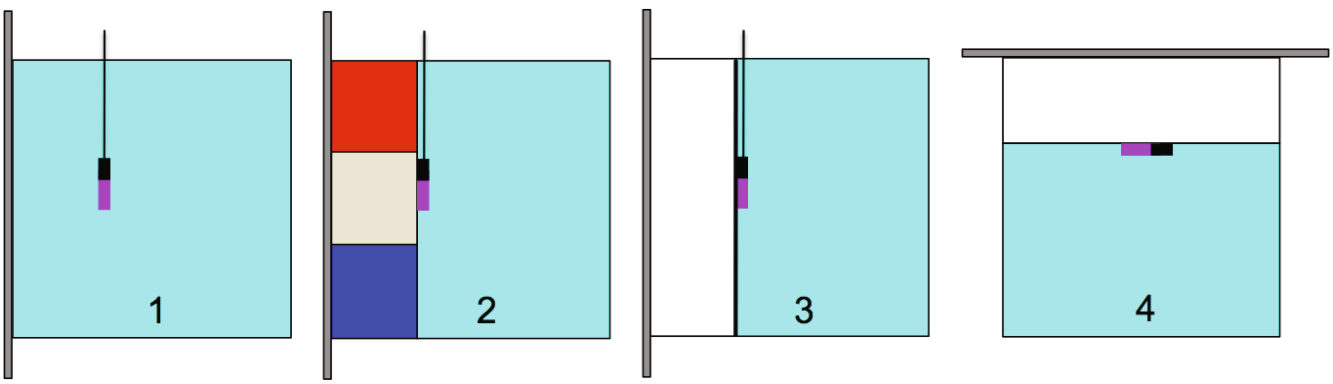

Figure 1. Side-view diagrams of the four small aquarium assemblies demonstrating the various blast mitigation techniques observed with DIC system: 1) no mitigation, 2) air-filled plastic tubes stacked in an array about 7-cm thick extending the full height of the aquarium, 3) air-pocket created with the use of a Mylar sheet (~130-μm thick), 4) air, achieved by turning the structure on its side. In all four scenarios the explosive charges are represented by the purple rectangles and the detonators are represented by the black rectangles.

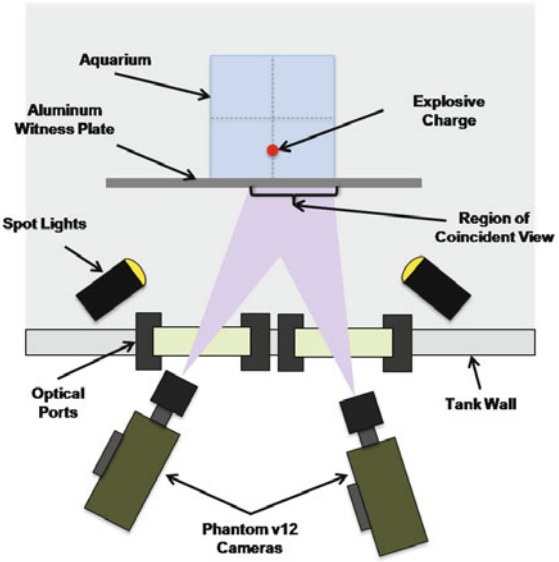

Figure 2. Diagram showing the experimental layout used for the small aquarium shots that incorporated DIC. Note that the diagram is not to scale.

All four small aquarium shots were conducted in the Gun Tank in the High Explosives Applications Facility (HEAF) at LLNL. The Gun Tank is a large blast chamber that has several ports located on its side in which 38.1-mm quartz windows were installed to allow video capture of the explosive event. Two Vision Research Phantom v12 cameras were setup outside of the chamber so that they each could view the area of interest of the aluminum plate. Fig. 2 shows a diagram of the small aquarium shot setup highlighting the general relationship between the explosive assembly, the tank wall, the spot lights, the optical ports and the cameras. Also, the diagram shows the region selected for coincident view. Note that the diagram is not to scale.

The Phantom v12 cameras have a fixed selection of frame rate versus resolution options. The relationship is such that as the cameras acquire images at higher speeds the available resolution decreases. For example, at a frame rate of 20,978 frames per second (fps) the best resolution available is 512 pixels by 512 pixels while at a rate of 66,997-fps the best resolution is 256 by 256. This inverse relationship made resolution vs. frame rate optimization necessary. For the small aquariums an adequate frame rate was estimated to be ~40,000 frames per second, a rate at which the cameras could acquire images with a maximum resolution of 256 by 512 pixels. This rectangular viewing area presented us with the opportunity to either look at the whole plate with significant wasted viewing area around the edges, given that our target was square, or to assume half-symmetry about the vertical axis centered on the horizontal axis. After considering the boundary conditions and our desire to maximize the information we acquired the half-symmetry option was chosen.

Once the general area of interest was chosen our attention was focused on determining the appropriate speckle size. Given the size of the aquarium, viewing half of it encompassed an area about 13-cm wide by 26-cm tall. This meant that we had 256 pixels distributed over 13-cm, making each pixel account for 0.26-mm^2 (0.51-mm x 0.51-mm). Our goal was that each spot in our speckle pattern would be at least 3 pixels (1.5-mm) across so we chose to produce a stencil that had many randomly drilled 3-mm holes. The stencil was made from a thin aluminum plate that had hundreds of holes drilled through it. The drilled plate had aluminum bar stock adhered to its edges to help keep it flat.

The 61-cm by 61-cm aluminum plates used as the target surface for the DIC were prepared prior to each shot using a multi-step process. The first step used was an allodyning treatment. This was done in an effort to make the surface more susceptible to paint adhesion. The next step in the process was spraying a thin layer of white Rust-Oleum® flat white paint as the background. The final step in the process involved spraying flat Rust-Oleum® black paint through the stencil onto the white background. The stencil did not cover the whole area of interest so the stencil had to be moved around the area of interest and sprayed until the total area was covered. Fig. 3 is a sequence of images showing different stages in the small aquarium shot sequence. Image 1 shows a section of the 61-cm by 61-cm aluminum 6061-T6 plate speckled with Rust-Oleum® spray paint. Image 2 shows an image of the aquarium assembly illuminated in the blast chamber. Multiple spots of light coming from the 1000-Watt Altman 1000Q Follow Spotlights can be seen overlapping in an effort to evenly light the target. Image 3 is a Phantom camera image taken during the calibration sequence. Image 4 is a Phantom camera image of the prepared surface in place in the blast chamber prior to detonation.

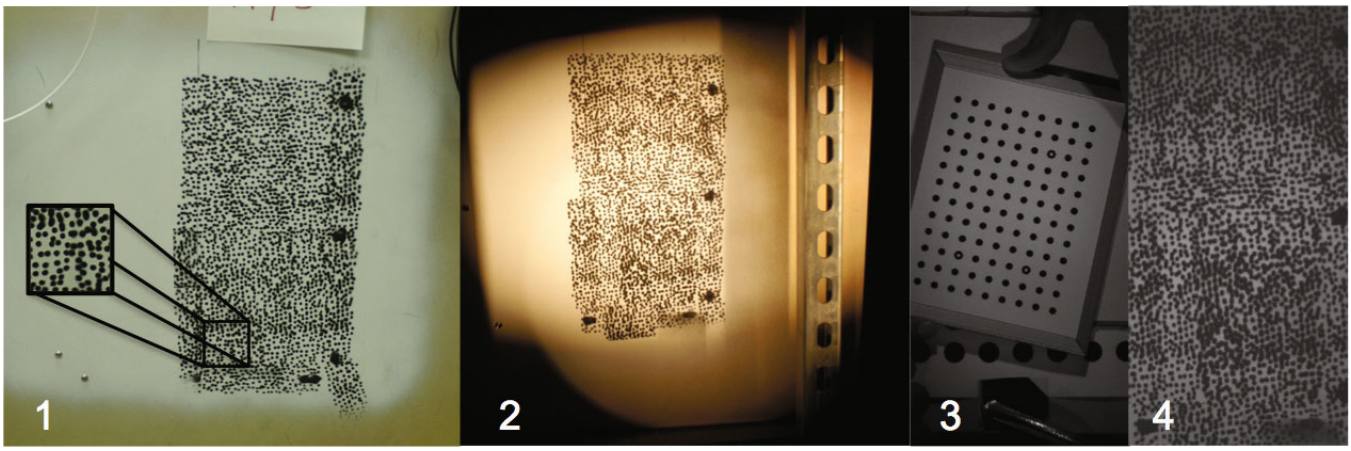

Figure 3. Images showing different stages in the small aquarium shot sequence. Image 1 shows a section of the 61-cm by 61-cm aluminum 6061-T6 plate speckled with Rust-Oleum® spray paint. Image 2 shows an image of the aquarium assembly illuminated in the blast chamber. Multiple spots of light can be seen overlapping in an effort to evenly light the target. Image 3 is a Phantom camera image taken during the calibration sequence. Image 4 is a Phantom camera image of the prepared surface in place in the blast chamber prior to detonation.

Large Aquarium Series: Set-up and Tank Configuration

The second series of experiments consisted of the large aquarium version of the explosive assembly. Similar to the small aquariums the large assembly was made up of a five-walled container, four walls of which were made out of 9.5-mm thick Lexan and the fifth wall made out of 15.9-mm thick aluminum 6061-T6. The assembled container had a volume of approximately 265-liters. The aquarium was approximately 72-cm wide by 55-cm tall. The aluminum plate used as one side of the aquarium was 1.22-m wide by 1.22-m tall. The plate had holes drilled through it so that when it was assembled the Lexan portion would be centered. Like the small aquarium version the aluminum plate was reinforced with Unistrut® beams.

LX-14 was also the explosive material used in the large aquarium experimental series. The charges in this case weighed about 146.5-g and were in the shape of right-circular cylinders. The explosive charge was positioned 17.5-cm from the aluminum plate. In the first large experiment no mitigation was used between the explosive and the aluminum plate. In the second experiment air-filled plastic tubes were used as the mitigation type.

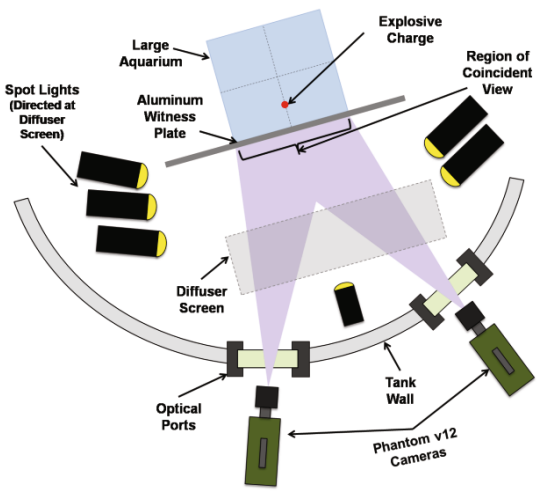

Figure 4. Diagram showing the experimental layout used for the large aquarium shots that incorporated DIC. Note that the diagram is not to scale.

The two large aquarium shots were conducted in the Spherical Tank in HEAF. Due to the increased size of the assembly and the need for extra space for additional lighting, the Spherical Tank was used because it had a more accommodating layout for our experiments. Like the Gun Tank, the Spherical Tank had 38.1-mm thick quartz optical ports installed to allow video capture of the explosive event. The ports on the Spherical Tank are located 45˚ apart around the spherical center of the tank. The Phantom cameras were setup outside of the tank and were focused so that they each were viewing the same area of interest of the aluminum plate. Fig. 4 shows a diagram of the large aquarium shot setup highlighting the general relationship between the explosive assembly, the tank wall, the spot lights, the optical ports and the cameras, with the noted difference from the small series that the lights were primarily reflected off of a diffuser screen prior to illuminating the target. This was done because illuminating the target with direct lighting resulted in uneven illumination with significant glare.

The length of the event for the large aquariums was calculated to take longer than the event for the small aquariums and thus a

slower frame rate was deemed acceptable. Lowering the frame rate made it possible for us to increase the resolution from 256 x 512 to 512 x 512. The frame rate of 20,978 fps was available at the resolution of 512 pixels by 512 pixels. Having a square field of view with the cameras allowed us to image the whole plate.

The plate preparation used for the large plate was different than the technique that was used for the small plates. Instead of using spray paint 3M Controltac™, which is a thin, white, adhesive-backed film, was used. This material was purchased to use in conjunction with a large printer but it turned out that the ink was not compatible with the Controltac™ surface. Instead of printing the speckle pattern from a computer file, the speckle pattern was drawn by hand by several of the authors of this paper. Prior to the addition of the permanent black ink speckling, the white surface was buffed to remove some of its gloss. After buffing the surface of the Controltac™ the speckle pattern was applied using the same principle as was used with the small aquariums, i.e., each speckle should be at least 3-pixels wide. Next, the film was cut in half and applied to the freshly cleaned surface of the aluminum witness plate, one side at a time, making sure that no bubbles or creases were formed during the application process.

The large area of interest and relatively low resolution made calibration somewhat difficult. When imaging a small area with a low resolution (due to high frame rates) one has the option of reducing the frame rate and increasing the resolution to calibrate the camera system. This has the benefit of getting crisp calibration images that can be used to calibrate the system even though the actual event will be captured at a much lower resolution (effectively looking at a small portion of the pixels). When imaging large objects, like these aquarium assemblies, the technique of increasing the resolution is not as practical. Instead, Correlated Solutions, Inc. Target Generator Software was used to create a large (50.8-mm between dots) calibration grid. The grid was printed out on a large printer and adhered to a 46-cm by 66-cm thin, flat plate of steel. The large-scale grid was then used as the traditionally used smaller grids are in other applications to calibrate the system. Fig. 5 show a sequence of images taken during the setup of one of the large aquarium shots. Image 1 is a photograph of the plate prior to final assembly but after the adhesive film had been applied. Image 2 shows a photo from one of the Phantom cameras taken during the calibration process. Image 3 is a picture from one of the Phantom cameras prior to the initiation of the explosive material.

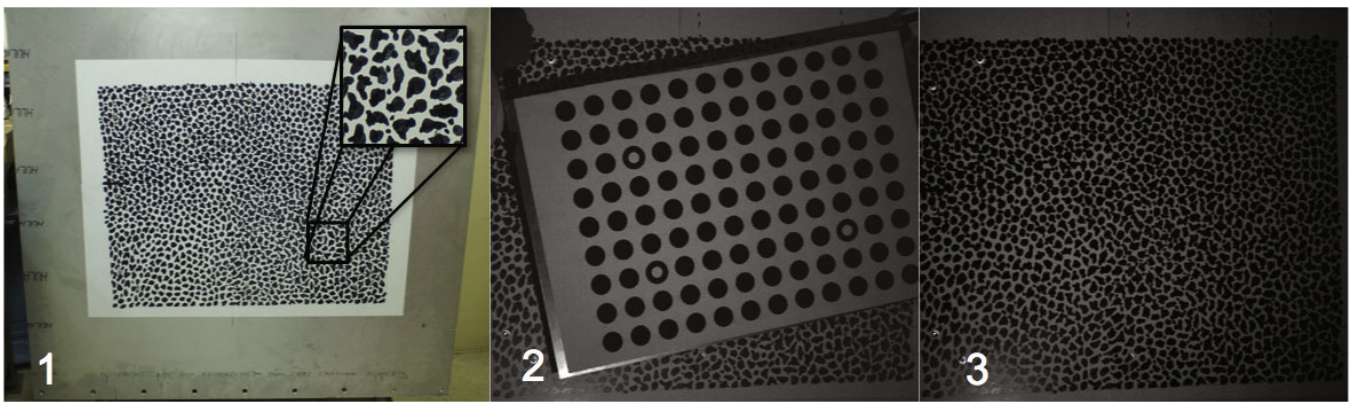

Figure 5. Images showing different stages in the large aquarium shot sequence. Image 1 shows the 1.22-m by 1.22-m aluminum 6061-T6 plate with the speckled 3M Controltac™ adhesive film attached. Image 2 shows an image from one of the Phantom cameras during the calibration sequence using a large array of calibration dots from Correlated Solutions, Inc. calibration software. The large dot array was printed on white paper and adhered to a large flat steel plate. Image 3 is a Phantom camera image of the prepared surface in place in the blast chamber prior to detonation.

RESULTS

Each attempt to use DIC as a diagnostic to watch the aluminum plate portion of the aquarium deform during the explosive event resulted in an abundance of useful data. Included in the results are output data files that include information regarding full-field displacement information, strain, strain-rate and velocity. The displacement data came in the form of color contour files that had the ability to have any point or group of points interrogated

independently and plotted one experiment versus the other. A selection of output resulted have been selected to shown the breadth of data acquired during this experimental series.

For the first three aquarium tests the out-of-plane displacement (*w*) was measured across a lineout taken at the mid-point of the plate as shown in Fig. 6. The lineout data was available at every frame but for the sake of comparison has been chosen at 0.1, 0.3 and 0.5-msec and is plotted also in Fig. 6. For the first and third small aquarium tests the paint on the plate nearest the explosive charge spalled off as a result of the displacement wave. The paint spall resulted in some localized loss of data but the overall picture of the displacement phenomena remained clear. The unmitigated shot (#1) and the air pocket/Mylar (#3) shots experienced significantly more deformation than did the air-filled plastic tube mitigated shot (#2). Due to the boundary conditions present in the experiments the plate rigidly moved during the deformation event. However, Vic3D, the Correlated Solutions, Inc. Software was used to remove the rigid body displacements prior to plotting the data shown below.

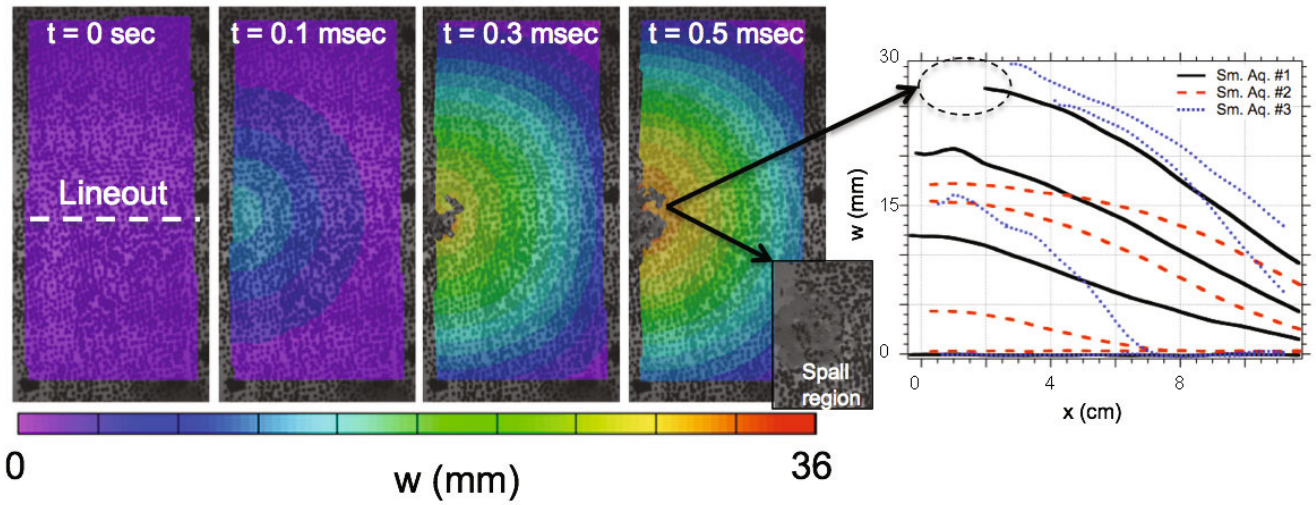

Figure 6. Color contour images showing the displacement progression in Small Aquarium #1, the unmitigated shot, alongside the lineout of out-of-plane displacement data in millimeters for the three small aquarium shots. A small region of paint spall is also shown inset in the figure and correlated with an area of data loss in the plot on the right bound by the dashed oval.

Out-of-plane displacement data was also collected for the large aquariums shots and is shown in Fig. 7. In the figure the top row shows the w-displacement in millimeters at 0.5-msec intervals for the first 1.5-msec of the unmitigated large test. The bottom row of the figure shows the analogous data for the air-filled plastic tube mitigated test. Both data sets are shown on the same scale and the magnitude differences are quite clear. The fact that the maximum w-displacement occurs around 1-msec is also clear in both image sequences.

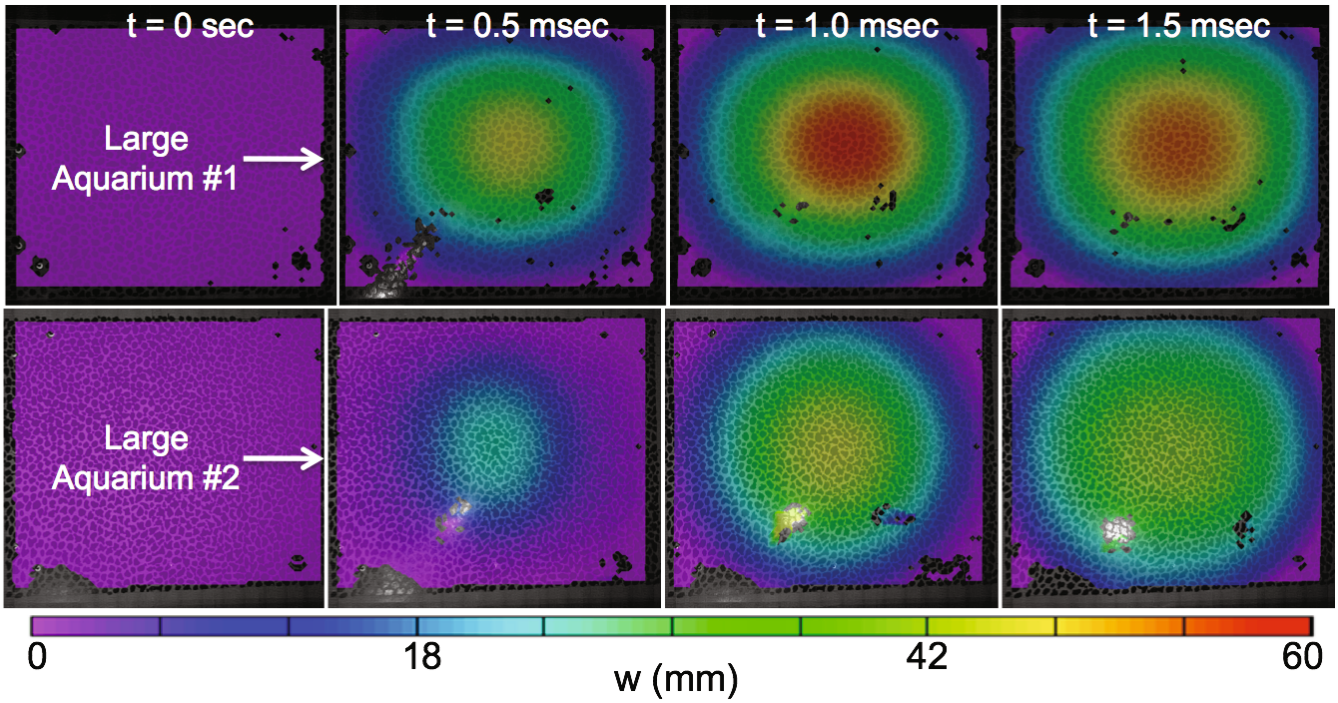

Figure 7. Comparison of the color contour output plots for Large Aquarium #1 and #2 over the first 1.5-msec of the deformation event. The top row shows the displacement results for Lg. Aq. #1, which had no mitigation in the water between the explosive charge and the aluminum plate. The bottom row shows the displacement results for Lg. Aq. #2, which had air-filled plastic tubes stacked in an array between the explosive charge and the aluminum plate.

In addition to the full-field data shown in the color-contour plots, data from a small region near the center of the two large aquarium shots was extracted and compared. The out-of-plane displacement, the strain, and the velocity are all plotted in Fig. 8 as a function of time. In all cases the unmitigated shot shows a greater effect from the explosive blast than the mitigated shot.

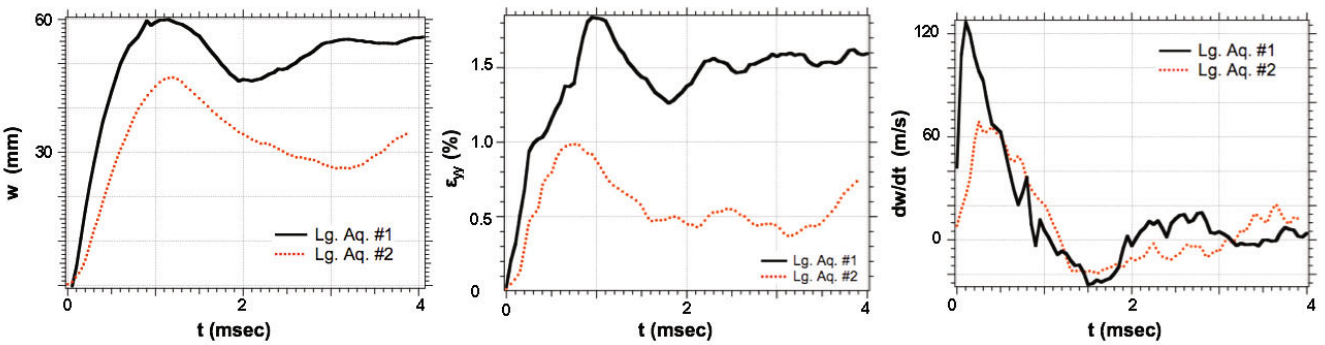

Figure 8. Displacement, w (mm), strain, e_{yy} (%) and velocity, dw/dt (m/s) for a small region taken from the central location of each of the aluminum plates used in the Large Aquarium tests.

Post-test permanent deformation measurements of the witness plates were also acquired using the DIC system. The measurements were possible through the use of a projector hooked up to a lap top computer, a computer image file that had a random, high contrast speckle image and standard DIC components (e.g. cameras and software). The system was calibrated as usual and then the static images were taken and correlated. The correlation resulted in the spatial dimensions of the plate from which the shape could be determined. The measurement was done for all of the plates and the permanent deformation from each plate was compared to the

other plates that had used different blast mitigation techniques. Fig. 9 shows an example of the Large Aquarium #1 imaged in two ways. The first, shown on the right, included the view of the entire plate. This included regions of the plate not witnessed during the deformation event and areas of the plate outside of the region immediately connected to the aquarium. The second view, shown on the left, was a reduced view of the larger plate and corresponds with the area adjacent to where the aquarium was located. Each view provided information that was useful to the modelers.

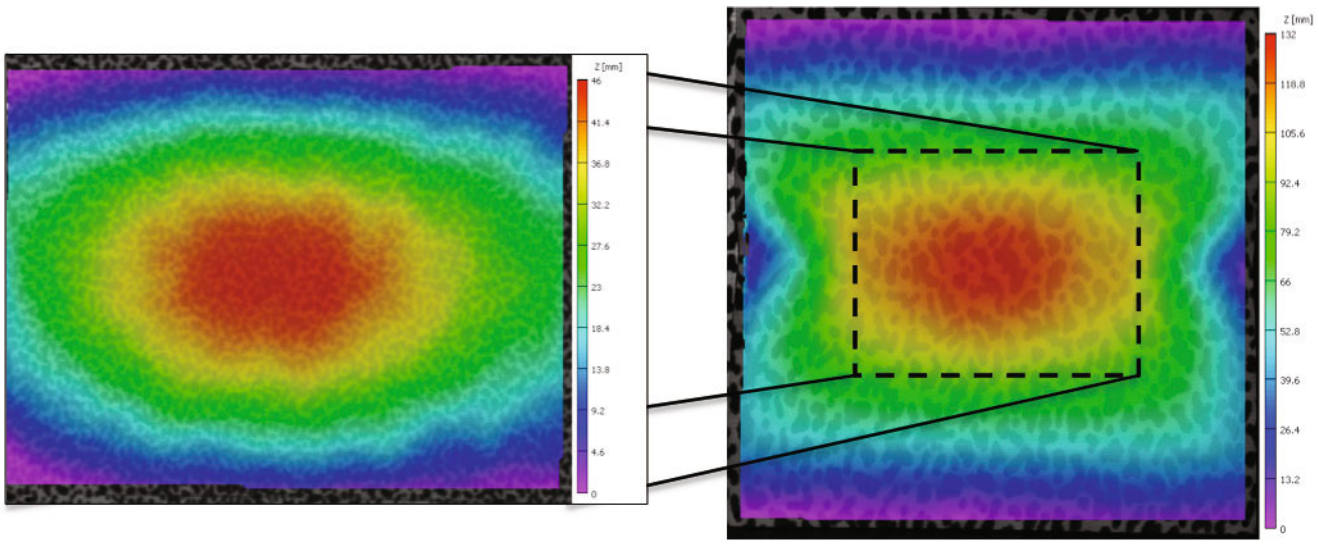

Figure 9. Two views of the post-test, static plate shape showing the full plate (on the right) and the central region closest to the aquarium (on the left). Each image has its own scale, set appropriately to demonstrate the amount of deformation seen in each case.

DISCUSSION

The six experiments reported in this paper show the effectiveness of digital image correlation for deformation events captured at rates from 20,000-40,000 fps. The out-of-plane deformation seen in the small aquarium shots was on the order of tens of millimeters and peaked in about 0.5-msec. The unmitigated shot and the air-pocket mitigated shot showed the most deformation in the small aquarium series. These results showed that the air-filled plastic tubes provided the best mitigation technique. The application of a speckle pattern using the spray paint technique was effective in that it resulted in a nicely contrasted image that did not have glare issues. The application was not technically challenging although the fabrication of the stencil and the application of the paint was time consuming. The biggest drawback to the paint technique was that in cases of unmitigated or under-mitigated blasts the paint spalled off the surface. The loss of paint resulted in the loss of data in the centermost region of the plate. While it was undesirable to lose this data the general displacement trend is still clear in the data.

The large aquariums were prepared using the 3M Controltac™ speckle technique. As mentioned previously, this method was done to avoid paint spall and so that the speckle pattern could be printed from a computer file. However, due to film and ink mismatch the automatic printing was not possible. This fact led to the need to hand speckle, which resulted in a well-controlled speckle pattern that took a long time to prepare. The glossiness of the Controltac™ also proved to be a challenge and required that the surface be buffed with an abrasive prior to speckling in an effort to reduce the glare. The high intensity lights located in close proximity to the surface resulted in cases of uneven lighting and a lot of glare. The solution to the problem of uneven lighting and glare was the introduction of a diffuser screen. This helped even the lighting and reduce the glare although it did not fully eliminate the glare. In order to get enough light on the target surface one of the more wide-angled lights was left directly pointed at the target. This did not prove to be an issue until the plate began to move as a rigid body after the blast impact. As the plate moved forward, pivoting and translating, the glare from the light began to interfere with the images in localized areas. Like the data loss from the paint spall, the glare caused localized data loss, but unlike the paint spall the data loss was not in the central region of the plate. In addition, the large aquariums were viewed in their entirety instead of using half-symmetry so the deformed plate stayed in the region

of coincident view longer than the deforming small aquarium plates. The deformation data, the strain and the velocity data were obtained for the large aquarium shots. The maximum out-of-plane deformation ranged between 40 and 60-mm with the unmitigated shot showing much more displacement than the shot done with air-filled plastic tube mitigation. The velocity and strain magnitudes were likewise diminished in the case of the air-filled tube mitigation.

SUMMARY

Six high-speed explosively driven deformation events were imaged with Phantom cameras and analyzed using digital image correlation. The details of the experiments including tank assembly and the preparation of the aluminum plates viewed with the cameras were discussed. Displacement, strain and velocity data were acquired for the small series and large series of aquarium shots. The data showed that air-filled plastic tube blast mitigation technique was superior to no mitigation and also to air mitigation. The benefits of spray paint speckling and hand drawn speckling were discussed as well as the drawbacks associated with each technique. Post-test static plate measurements were performed and example data was shown.

AKNOWLEDGEMENTS

The authors would like to thank LLNL's Dan Greenwood, Frank Garcia and Greg Silva for their assistance with the operation of the cameras, the development of proper lighting conditions, assembly preparation and the calibration of the digital image correlation system. Discussions with David Backman of the National Research Council of Canada were also very helpful.

This work was performed under the auspices of the U.S. Department of Energy by Lawrence Livermore National Laboratory under Contract DE-AC52-07NA27344.

REFERENCES

1. Nansteel, M. W. and Chen, C. C., "High-Speed Photography and Digital Image Correlation for the Study of Blast Structure Response," *ITEA Journal*, Vol. 30, pp. 45-56, 2009.

2. Neuberger, A., Peles, S. and Rittel, D., "Scaling the response of circular plates subjected to large and close-range spherical explosions. Part I: Air-blast loading," *Int. J. of Impact Engineering*, Vol. 34, pp. 874-882, 2007.

3. Neuberger, A., Peles, S. and Rittel, D., "Scaling the response of circular plates subjected to large and close-range spherical explosions. Part II: Air-blast loading," *Int. J. of Impact Engineering*, Vol. 34, pp. 859-873, 2007.

4. Tiwari, V., Sutton, M. A., Shultis, G., McNeill, S. R., Xu, S., Deng, X., Fourney, W. L. and Bretall, D., "Measuring Full-field Transient Plate Deformation Using High Speed Imaging Systems and 3D DIC" *Proceedings of the SEM Annual Conference*, Albuquerque, NM, June 2009.

5. Reu, P. L. and Miller, T. J., "The Application of High-Speed Digital Image Correlation," *J. of Strain Analysis*, Vol. 43, pp. 673-688, 2008.

6. Reu, P. L. and Miller, T. J., "The Application of High-Speed and Ultra-Speed Digital Image Correlation," presented at the SEM Fall Conference, Columbia, SC, 2009.

Proceedings of the SEM Annual Conference
June 7-10, 2010 Indianapolis, Indiana USA

Dynamic Deformation of Copper-Jacketed Lead Bullets Captured By High Speed Digital Image Correlation

S. P. Mates[1] and R. Rhorer
National Institute of Standards and Technology
100 Bureau Drive Stop 8553, Gaithersburg, Maryland 20899-8553
[1]Corresponding Author, smates@nist.gov

ABSTRACT

The development of high fidelity simulations of lead-cored bullet impacts on soft body armor, motivated by the need for improved armor designs and performance standards for law enforcement, requires accurate models for both the armor and the deformable bullet. This paper examines the ability of the Johnson-Cook constitutive model to predict the dynamic deformation of a 0.357 caliber copper-jacketed lead-cored slug subjected to a direct-impact Kolsky Bar test. A high speed 3D Digital Image Correlation (DIC) technique is used to measure the deformation history of the slug subject to an impact velocity of 15.3 m/s and an impact energy of 62.5 J, which is about 6.5 % of the impact energy required in NIJ Standard 0101.04 for testing Type II body armor with this bullet. The DIC results and force history data are compared to finite element simulations of the test. A sensitivity analysis of the material parameters is carried out to determine their relative influence on the deformation and force history response, and improved parameter values are identified and compared to the baseline values.

INTRODUCTION

Accurate mathematical analyses of the ballistic resistance of soft body armor are currently sought in order to design more resistant next-generation armors and to understand the performance current ones. Realism in finite element simulations requires knowledge of both the armor structural behavior and the bullet structural behavior under dynamic loading. Structural behavior depends of course on both material behaviors (viscoelastic and viscoplastic response) and on geometric and interfacial factors such as friction.

Theoretical and numerical studies on the ballistic resistance of woven fabric armors often involve rigid projectiles [1-3], which is appropriate given the highly complex nature of the structural response of woven soft body armor compared to the relatively simpler behavior of a deforming bullet. Some of these studies have relied on experimental data in which projectile specifics are hidden due to the classified nature of the work [4]. However, ultimate accuracy is attainable only if the deformation of the projectile is also considered, since the evolving contact zone between the deforming bullet and the armor may play a critical role in penetration. In high velocity impact (> 100 m/s), it is believed that the local strength of the fibers determines the resistance to penetration rather than the supporting structure [5,6]. Further, the resistance of the armor depends mainly on only those fibers that pass directly through the impact zone because the transmission of elastic wave energy across fibers is limited [7]. Thus the size of the contact zone determines the number of fibers involved in arresting the projectile. Its importance is reinforced by experimental observations that show bullet tip shape (conical versus blunt, for example) has an important effect on penetration performance and failure mechanisms in woven armor [5,8]. For a deforming projectile, especially a lead-cored slug, the growth of the contact area during impact will influence how many fibers are involved in defeating the projectile. Thus, understanding the shape evolution of the bullet as it deforms during impact is an important aspect of the soft body armor ballistic resistance problem.

A recent study on the penetration of light steel armors by a small-arms projectile [9] has highlighted the problem that there is a limited amount of literature data on the viscoplastic response of the materials used in small arms ammunition, including lead-antimony and copper-zinc alloys. Further, these data may not reflect the behavior of the actual bullets, whose constituent materials may undergo significant work hardening and texture evolution during manufacturing, as shown by recent research [10]. Tests performed on samples extracted from bullets have

T. Proulx (ed.), *Application of Imaging Techniques to Mechanics of Materials and Structures, Volume 4*, Conference Proceedings of the Society for Experimental Mechanics Series 14, DOI 10.1007/978-1-4419-9796-8_56, © The Society for Experimental Mechanics, Inc. 2013

shown departures from expected behavior [11], with significant variations observed depending on where the sample is taken [10]. This paper therefore focuses on the behavior of whole bullets in order to help address this gap.

Specifically, we use an advanced 3D digital image correlation (DIC) technique [12] to optically measure the full-field deformation history of a 0.357 Jacketed Soft Point (JSP) bullet (a specified test round in NIJ 0101.04 [13]) as it is subjected to a controlled impact test using a Kolsky bar. The measurements are compared to a finite element simulation using literature-derived constitutive constants to determine how well the actual bullet deformation is captured. Then, the sensitivity of the results to the model constants are examined by performing repetitive simulations using design-of-experiments techniques, and improved solutions are sought. DIC methods are becoming widely used in so-called identification problems or inverse problems [14], in which material constants are deduced from full-field DIC strain or deformation data and along with load-time or load-displacement data obtained from mechanical tests and with finite element simulations of those tests. The greatly increased quantity of data supplied by the DIC technique is a key enabler for making inverse problems of this kind considerably more tractable than in the past. The advantage of the present approach of testing entire bullets is that the stress-states and structural response of the bullet which are captured by the test and simulations are naturally more representative of real bullet impacts for which the test results are intended to help understand. Therefore, if the identification effort is successful, and more accurate material models are “identified” by this method, these models will have inherent validity that traditional uniaxial test data would lack. Success in this endeavor is complicated by the non-linear, path-dependent nature of plasticity, which makes such problems considerably more difficult than elasticity problems for which inverse methods are more often successfully applied [14].

In our test, the bullet is impacted by a striker bar with an impact velocity of 15.3 m/s and an impact energy of 62.5 J, which is about 6.5 % of the impact energy specified in NIJ Standard 0101.04 for testing Type II body armor with this bullet type. Finite element simulations are first performed using literature-derived material model for the copper alloy jacket, and an in-house developed model for the lead-antimony core. The simulation results are compared to the 3D DIC shape data and to force history data measured by a strain gage mounted to the transmission bar. Then, Design-of-Experiments (DOE) methods are used to explore the sensitivity of the simulation results to the material model constants and relevant friction coefficients, and to attempt to identify an improved set of constants that better describes the observed deformation behavior of the bullet. This example is used as a first step toward the development of a methodology to assess the ability of literature-derived material models to capture the controlled, dynamic deformation of deformable bullets. If found lacking, improved material models will be developed in order to increase confidence in simulating impacts of deformable bullets against soft body armor.

EXPERIMENTAL AND NUMERICAL METHODS

Kolsky Bar Direct Impact Test

The bullet sample investigated is a 0.357 caliber magnum Jacketed Soft Point (JSP) projectile with a mass of 10.2 g (158 grains), shown in Fig. 1. The bullet consists of a lead alloy core (containing up to 10 % Sb by wt.) surrounded by a copper alloy jacket (containing up to 30 % Zn by weight, also referred to as brass).

The NIST compression Kolsky bar is used to subject the bullet to a controlled, dynamic compression event by firing the striker bar directly into the nose of the bullet. A Kolsky bar, also known as a Split Hopkinson Pressure Bar (SHPB) [15], is a high strain rate mechanical testing device in which a test specimen is sandwiched between two long, thin elastic bars and deformed rapidly by the impact of a striker at the end of one of the elastic bars (called the incident bar). In a direct impact test, however, the specimen is placed at the struck end of the incident bar, which also serves as the transmission (second) bar in this test, and impacted directly by the striker. This method increases the amount of strain that can be achieved in the specimen, with the drawback that the usual method of deducing the strain and stress in the specimen cannot be used. Instead, the deformation in the specimen is measured optically by digital image correlation, and the transmitted bar strain gage signal is used to deduce the load history during impact.

In the test, the striker bar, which is made of maraging steel, is 375 mm long and 15 mm in diameter, and matches the acoustic impedance of the maraging steel incident bar (e.g. it is also 15 mm). The incident/transmission bar

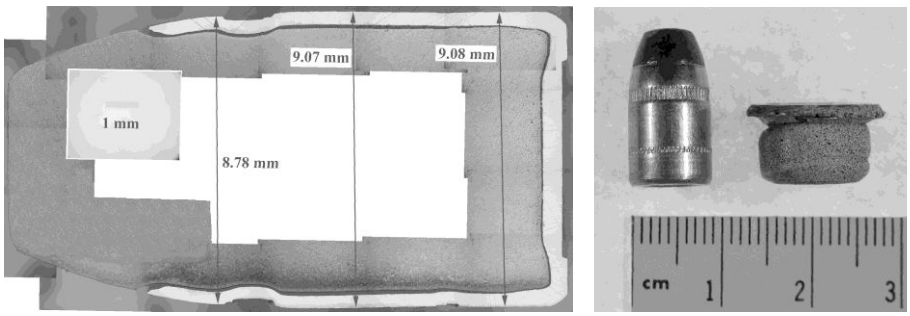

Fig. 1 Left: 0.357 magnum JSP 158 grain bullet in cross-section. Right: Untested and tested bullets.

combination (henceforth called simply the transmission bar) has a length of 3000 mm. Foil strain gages mounted to the bars measure the bar strain history, which is yields the load-time history experienced by the bullet during the test. The striker impacts the bullet at 15.3 m/s, yielding a kinetic energy of 62.5 J, or about 6.5 % of the energy of an NIJ standard soft body armor shoot test for this bullet type (reference velocity of 436 m/s, bullet weight of 10.2 g, kinetic energy of 969 J). The striker impact produces a total axial compressive engineering strain of 0.49 in the bullet (see Figure 1). Compared to a real ballistic impact, in which the bullet essentially turns inside out, the strains developed in this test are considerably smaller, as are the maximum strain rates. Our test is limited by the size of the striker and the maximum velocity it can be fired at without damaging the striker or incident bar. However, the amount of plastic strain produced in the bullet nevertheless provides a significant test for the material models under study.

Digital Image Correlation

Three dimensional image correlation shape measurements are performed on stereo image pairs using commercially available software. The stereo image pairs are recorded at 62,500 frames per second with a resolution of 128 x 400 pixels and a magnification yielding 0.063 mm per pixel. The high speed digital cameras are fitted with 90 mm macro (1:1 magnification) lenses with the apertures stopped down 2 positions for adequate depth-of-field. The working distance is 30 cm. The DIC surface patterns are manually sprayed on using a flat white primer coat with 100 % coverage followed by flat black speckles to about 50 % coverage. Full coverage with the white base coat was needed to avoid specular reflections from the incident lighting that ruins the correlation analysis. Tests were conducted almost immediately after applying the speckled coating to limit curing and thereby

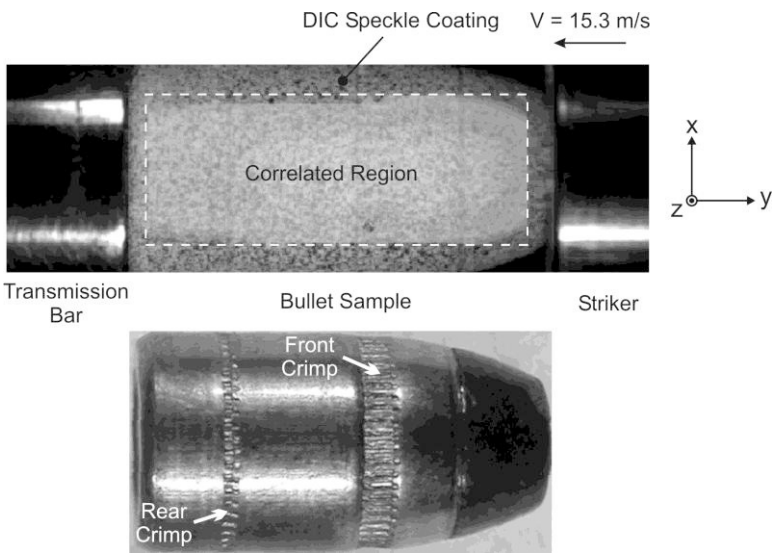

Fig. 2 3D DIC measurement during a direct impact Kolsky Bar test of a 0.357 JSP bullet.

maintain pliability in the coating so as to avoid cracking and spalling during the test. Uncertainties in the displacement measurements, determined from translation experiments involving a rigid cylinder under similar optical conditions and DIC analysis parameters used in the experiment, were ± 0.02 mm (2 σ) covering random image noise, and up to 0.05 mm bias error due to coordinate system misalignment. Fig. 2 shows the typical extent of the correlation region on the test bullet. Correlation performance was found to be good using the default software analysis settings (21 pixel windowing, 5 pixel overlap, with default smoothing) and no systematic attempts to vary these settings were made to improve upon this performance.

Finite element model

ABAQUS/Explicit[1] is used to solve the simulation geometry shown in Fig. 3. Only a portion of the entire computational domain, which includes the entire 375 mm long striker bar and the 3000 mm long transmission bar, is shown. The dimensions of the bullet cross section were taken from measurements of a sectioned bullet (Fig. 1). Axisymmetric CAX4R and CAX3 elements are used throughout. The mesh density is highest in the bullet sample and at contact interfaces, and it is kept to a minimum in the striker and transmission bars. A minimal mesh density was needed to minimize computation time required for each simulation since the DOE studies require up to 300 repeat simulations to be completed in a reasonable time on a quad-core desktop computer (about 20 hours). The forward jacket crimp was modeled simply as a depression in the jacket, while the rear crimp (see Fig. 2) was ignored. Table 1 includes some material parameters for the bullet and the Kolsky bar that are fixed in this study.

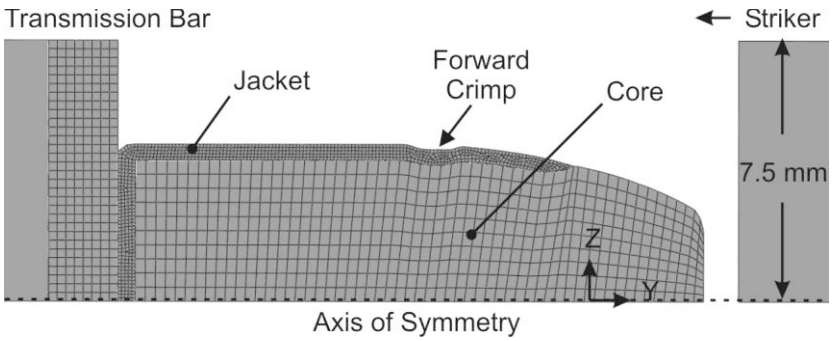

Fig. 3 A portion of the finite element mesh used to simulate the direct impact test.

Table 1. Properties for bullet and Kolsky bar used in the simulations.

Material	Elastic Modulus [GPa]	Poisson Ratio	Density [kg/m3]
Brass	79	0.3	8520
Lead	14	0.42	10740
Maraging steel	200	0.29	8048

The behavior of the lead and brass is modeled using the Johnson-Cook relation [16] which assumes an isotropic, viscoplastic (rate-sensitive) response:

$$\sigma = (A + B\varepsilon^n)\left(1 + C ln(\dot{\varepsilon_o})\right)(1 - \bar{T}^m) \qquad (1)$$

[1] Commercial products are identified in this work to adequately specify certain procedures. In no case does such identification imply recommendation or endorsement by NIST, nor does it imply that the materials or equipment identified are necessarily the best available for the purpose.

Here σ is stress, ε is strain, $\dot{\varepsilon}_o$ is the normalized strain rate (here normalized to a strain rate of 1.0), and $\bar{T}$ is the normalized temperature. The behavior for specific materials is obtained by specifying material constants *A*, *B*, *n*, *C* and *m*. In this study, thermal softening effects are ignored by setting $\bar{T}$ to 0.

Baseline constants for the lead-antimony core material could not be found in the literature. Instead, a baseline set was developed from in-house compression tests carried out at three strain rates (0.0014 s^{-1}, 0.13 s^{-1} and 2500 s^{-1}) on 9 mm by 4.5 mm thick cylindrical specimens cut from individual bullets. Details of these tests will be reported elsewhere. No attempts were made to produce test specimens from the bullet jacket. Instead, baseline constants were chosen from the literature for cartridge brass [16]. Table 2 lists the baseline constants for both materials. We assume, based on the manufacturer's MSDS information for this bullet, that the jacket contains 30 % zinc by weight, and is comparable to cartridge brass with the designation C260 (equivalent to UNS 26000). The initial state of the brass material from which the baseline constants were developed in [16] is unknown. ASTM Standard B927 [17] indicates a wide range of strengths are possible for this material, depending on temper and work hardening state. It lists range of yield strengths between 83 MPa to 345 MPa and tensile strengths between 276 MPa to 483 MPa, depending on temper. In addition, work hardening can increase the flow stress by 50 % to over 100 %. In light of this, there is less confidence in the baseline brass model compared to the baseline lead model, which is based on measurements of material extracted from the bullets directly. Finally, friction between the external bullet surfaces and the bar and internal friction between the bullet jacket and the bullet core are modeled using hard contact and Coulomb friction coefficients. Baseline values for these coefficients are given in Table 2.

Objective Functions for DOE calculations

The DOE approach is adopted first to explore the sensitivity of the simulation results to variations in the material constants and friction coefficients. A commercial software package called ISight[1] is used to automatically perform the DOE, which involves controlling the parameter variation, writing the necessary input files for the finite element code, parsing the output values for the desired quantities and controlling the computation of the objective functions. Of interest to this study is how well the simulation compares numerically with the experimental data, namely the shape history provided by the DIC measurement and the transmitted load history provided by the data from the strain gage mounted on the transmission bar. Numeric residuals between the simulation results and the data are computed using two objective functions, one for the shape history, Φ_S, and the other for the bar strain (or transmitted force) history, Φ_F. The objective functions are as follows:

$$\Phi_S = \sum_{t=1}^{N} \sum_{i=1}^{M} \sqrt{\left(\frac{Z_{i,t}^{FEA} - Z_{i,t}^{DIC}}{Z_{i,t}^{DIC}} \right)^2} \qquad (2)$$

$$\Phi_F = \sum_{t=1}^{P} \sqrt{(LE_t^{FEA} - LE_t^{EXP})^2} \qquad (3)$$

In Equation 2, *Z* is the out-of-plane surface position of the bullet, while in Equation 3 *LE* is the elastic strain in the transmission bar measured by the strain gage. The superscript *FEA* refers to the simulation, while the superscripts *EXP* and *DIC* represent experimental data. Φ_S is summed over space (index *i*) then time (index *t*), while Φ_F is summed over time only (using a separate time index), to arrive at single values representing the discrepancy between the data and each simulation run.

Φ_F is calculated by linearly interpolating the LE^{FEA} at the locations in time where LE^{EXP} is available. The calculation is performed by an add-on software component purchased separately with ISight[1]. Φ_S is computed using an in-house developed code that extracts Z_i^{DIC} data along the center of the correlation zone following the bullet axis at each time step. The code then extracts the nodal positions of the bullet surface, Z_i^{FEA}, from the simulation results at the same time step, and interpolates the simulated surface position at the y-locations of the DIC data points using a spline fitting routine. This shape residual estimation method admits the possibility that the two data sets being compared do not cover the same range of y values. In these cases, Z^{FEA} can be undefined at the non-overlapping end. To avoid unrealistically large residuals resulting from extrapolating the spline fit outside its defined range, these points are not considered in the residual sum. This will tend to reduce the sensitivity of

the shape residual function to large discrepancies in the total elongation of the bullet between the model and the data, but this is not viewed as a serious problem for the moment. Finally, the residual method assumes that the bullet axis and the x-axis of the DIC measurement are well aligned.

At present, uncertainties in the measured quantities are ignored in the development of the objective functions, with the exception that the four nodes on the extremes of the DIC surface data are dropped from the residual calculation as these data are less reliable than the interior points. The remaining points are weighted equally. Further, both objective functions are given equal weight in identifying improved solutions.

RESULTS

Fig. 4 provides a detailed view of the tested bullet, showing excellent agreement between the DIC measurement and the final shape of the bullet jacket. This figure is also used to highlight the breakdown in axisymmetry that occurs during dynamic compression. It is characterized by two fractures in the front of the jacket and an obvious asymmetry in the shape of the rear of the jacket. Lacking strict axisymmetric behavior in the experiment means that the numerical simulations to which the DIC data are compared will differ even if the constitutive parameters are exactly right. Nevertheless, we proceed with attempting to investigate the effect of the material models on the agreement between the simulation and the experiment. Further tests are being conducted to assess the repeatability of the deformation using this particular bullet type and impact energy.

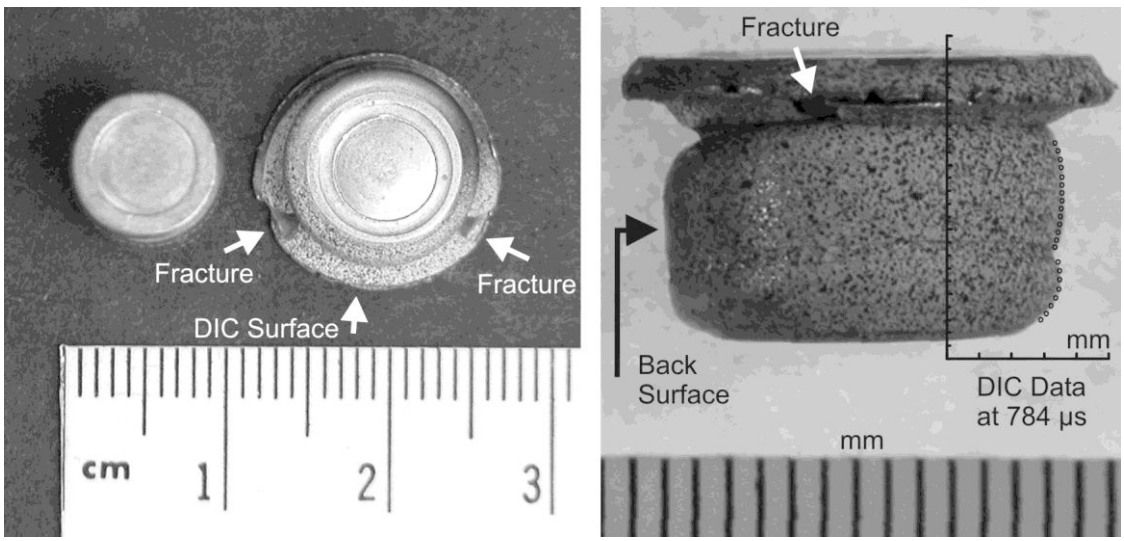

Fig. 4 Rear view of jacket fractures occurring on one side of tested bullet in relation to DIC surface measurement (left) and image highlighting contour difference between DIC surface and rear surface of bullet after test (right).

Fig. 5 compares the baseline simulation against the experimental shape history and bar strain history data from the experiment. The simulation indicates more extensive bullet deformation toward the bullet tip, and somewhat lower transmitted forces early in the test, compared to the experiment. Assuming as we do that the discrepancy is mainly due to incorrect material parameters, the result indicates that the real materials are somewhat stronger and more resistant to deformation than the baseline simulation predicts. Clearly, however, structural features of the bullet, such as the rear crimp that causes the cusp in the jacket toward the end of the test observed in Fig. 5, cannot be matched by the current simulation geometry. In the next phase of the study, the simulation geometry will be refined to more faithfully represent the role of the crimped regions on the structural response of the bullet. Of further note is that, due the extreme deformation of the bullet tip, DIC information cannot be resolved for the lead tip and the forward portion of the brass jacket beyond about 368 µs, or about half way through the compression test. Therefore, for the purpose of computing shape residuals for the DOE calculations, only the DIC measurements behind the front crimp on the jacket are used since this data is available through the entire test.

However, when comparing the “improved” solution to the data and the baseline solutions graphically, as in Fig. 5, all of the available data are used.

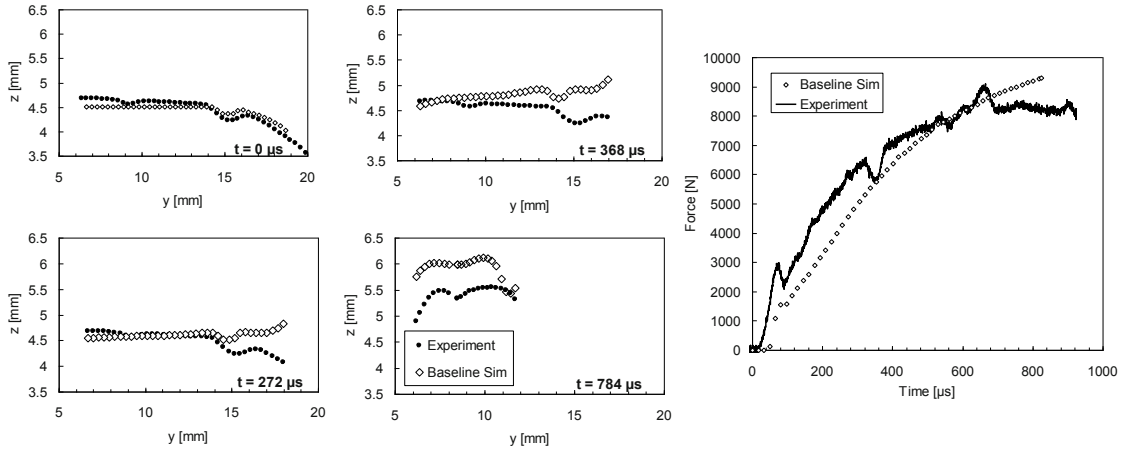

Fig. 5 Comparison of baseline simulation results with experiment. Objective function values for the baseline solution are: Φ_S = 0.031416 and Φ_F = 3.61986e-8.

To explore the effect of the material parameters and friction on the force and shape histories, an initial DOE, DOE1, was performed with parameter ranges listed in Table 2 using an Optimal Latin Hypercube (OLH) method with a fixed seed and 300 design points. The ten parameters include four each that describe the yield, strain hardening behavior and rate sensitivity of the lead and brass according to Equation 1, and two for the external and internal friction coefficients. The range on each parameter was fixed at ± 75 %. The primary purpose of this calculation is to determine the dominant parameters affecting the values of Φ_S and Φ_F.

The main effects determined from DOE1 are identified in Fig. 6, which examines the relative influence of each factor as well as the interaction and quadratic terms on Φ_S and Φ_F. The results indicate that the dominant parameters are those that describe the yield and strain hardening behavior of the brass and lead, with interaction terms having a strong effect. In contrast, the friction coefficients and the rate sensitivities have less effect on the objective functions.

Table 2. DOE1 (Optimal Latin Hypercube method) factors and bounds.

Material	Factor	Baseline Value	Lower Bound (-75 % of baseline)	Upper Bound (+75 % of baseline)
Brass	*A* [MPa]	112.3	28.1	196.5
	B [MPa]	505	126.3	883.8
	n	0.42	0.105	0.735
	C	0.009	0.0018	0.0158
Lead	*A* [MPa]	5.59	1.40	9.78
	B [MPa]	43.6	10.9	76.3
	n	0.216	0.054	0.378
	C	0.016	0.004	0.028
friction	f_e	0.1	0.025	0.175
	f_i	0.5	0.125	0.875

A second DOE, DOE2, was performed using only the six yield and hardening parameters for the brass and lead, while keeping the remaining parameters fixed to baseline values. The purpose of DOE2 is to explore a parameter space that is more likely to achieve better agreement with the experiment, namely one that results in stronger plastic response from the lead and/or brass. As indicated in Fig. 6, both the lead core and the brass jacket have strong influences on the shape and force objective functions. As such, the parameter space for DOE2, given in

Table 3, is balanced, with the same limits chosen for the brass and lead responses as were used in DOE1. DOE2 uses the Optimal Latin Hypercube method with a fixed seed and a limit of 150 simulations.

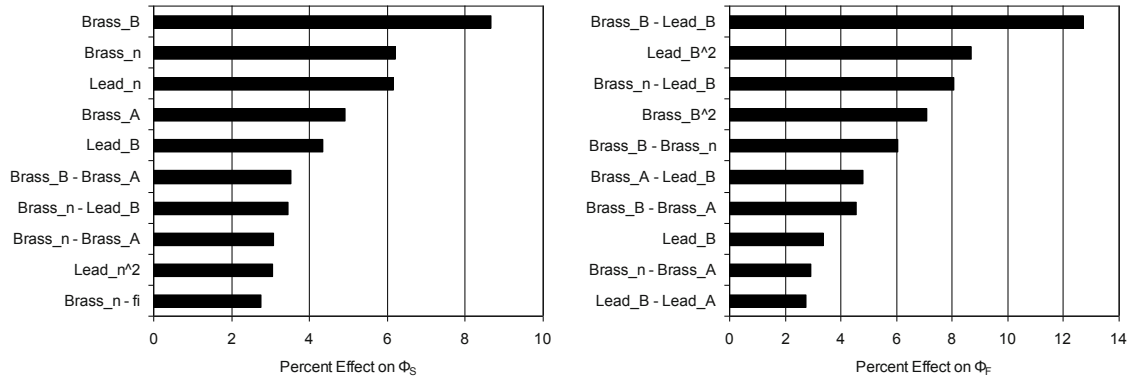

Fig. 6 Main effects for DOE1 (300 simulations).

Table 3. DOE2 (Optimal Latin Hypercube method) factors and bounds.

Material	Factor	Baseline Value	Lower Bound (-75 % of baseline)	Upper Bound (+75 % of baseline)
Brass	*A* [MPa]	112.3	28.1	196.5
	B [MPa]	505	126.3	883.8
	n	0.42	0.105	0.735
	C	0.009	-	-
Lead	*A* [MPa]	5.59	1.40	9.78
	B [MPa]	43.6	10.9	76.3
	n	0.216	0.054	0.378
	C	0.016	-	-
friction	f_e	0.1	-	-
	f_i	0.5	-	-

Fig. 7 plots the values of the two objective functions against one another for DOE2. This scatter plot, which is referred to as a Pareto plot, helps identify improved simulation results and, potentially, more accurate parameter values that better describe the dynamic deformation of the bullet than the baseline literature ones. Five simulations, indicated by labels in Fig. 7, were examined for further analysis. They are all on or near the so-called Pareto front, which contains solutions that are not dominated by any other solutions in the set. One solution is dominated by another solution only if both objective function values are equal or superior to it. This technique is used to discriminate results in multi-objective optimization, where trade-offs between the various objectives must be evaluated to find an optimal solution.

The chosen set includes one result, simulation #31, which was selected as having an optimally low combination of objective functions values. The shape and force residual histories for simulation #31, which represents the author's interpretation of the best available simulation, not the best possible solution, are compared to the experimental data and the baseline simulation in Figure 7. Both the shape history agreement and the force history agreement are modestly improved compared to the baseline values. Values for the material parameters corresponding to simulation #31 are compared to baseline values in Table 4 along with the corresponding values of Φ_S and Φ_F.

Fig. 9 plots the baseline stress-strain curves against the improved solution #31 and three neighboring solutions on the Pareto front. The plot illustrates the variation in the stress-strain curves that have produced this family of potentially improved solutions, mindful that #31 is considered the best while the others are all improvements over the baseline solution. A widely scattered set of curves would indicate that very different material responses could all produce similarly good solutions. This would be a bad result, since it would argue that our test method is not capable of identifying the true (unique) material model. As Fig. 9 shows, there are two families of solutions that

provide better results than the baseline. One family, consisting of simulations #4 and #126, suggest a much stronger lead response coupled with a much weaker brass response compared to baseline levels. On the contrary, simulations #31 and #40 suggest about the same or moderately stronger lead response, and a mild to significant increased brass strength. Clearly there is a tradeoff in the strengths of the two materials when approaching more accurate solutions. However, since there is more confidence in the lead baseline that was developed from actual measurements as opposed to the brass baseline which comes from the literature, solutions #31 and #40 are more likely to be pointing to the correct conclusion that the brass behavior may be significantly stronger than the literature indicates, perhaps due to cold work that is introduced during manufacturing.

That neither objective function is very sensitive to the strain rate can be explained by the fact that the brass response, which dominates the problem, is not a highly rate sensitive material. The lead, being a bit more rate

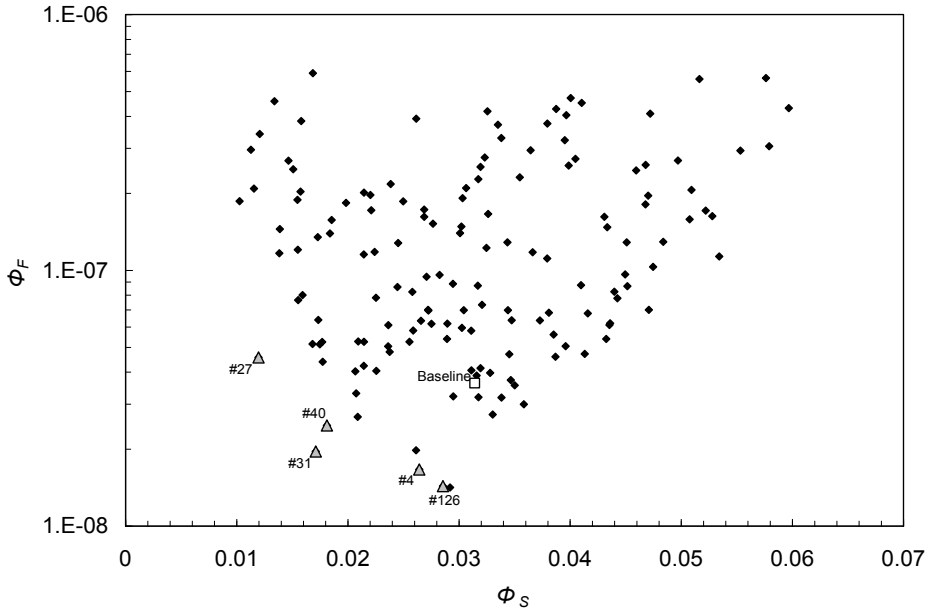

Fig. 7 Pareto plot of Φ_F against Φ_S for DOE2 (150 simulations). Note: ordinate is a log scale. Labeled shaded triangles are "improved" simulations in the region around the Pareto front.

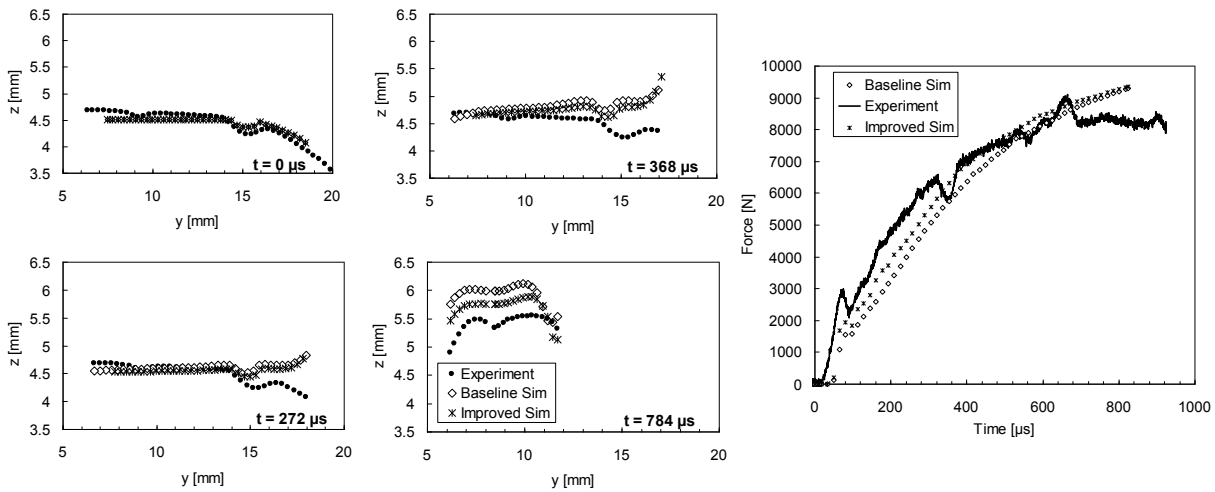

Fig. 8 Comparison of baseline and improved (#31) simulation results from DOE2 and experiment. Improved objective function values are: Φ_S = 0.017116 and Φ_F = 1.957 x 10^{-8}.

sensitive than brass (*C* value of 0.016 against 0.009 for brass), is still not considered highly rate sensitive. Pure iron, a very rate sensitive material, has a *C* value of 0.06 [16]. One might therefore expect to achieve similar results using a low strain rate testing machine.

The next steps in this research effort will be to investigate the use of multi-objective optimization techniques to identify an optimal solution, which will necessarily include a more comprehensive uncertainty analysis of the shape measurements in particular, and of a more thorough stability and uniqueness assessment of the optimized solutions. Further testing of this particular bullet type is also needed to resolve the asymmetrical behavior of the bullet during the test and to assess the repeatability of its behavior in compression. In addition, efforts will be made to more faithfully model the crimped regions of the jacket, which were observed to have a significant influence on the shape evolution in the experiment that could not be captured by the simulations. Ultimately the goal of this work is to develop a test and inverse modeling methodology to assess the dynamic mechanical response of small arms projectiles, including the constitutive responses of the individual materials and accounting for frictional effects, to provide more reliable material and structural descriptions that can be used in simulations of actual ballistic impacts against soft body armor.

Table 4. Comparison of material parameters and objective function values for baseline and improved simulation (#31).

Material	Factor	Baseline Value	Improved Value (#31)
Brass	A [MPa]	112.3	191
	B [MPa]	505	528
	n	0.42	0.58
	C	0.009	0.009
Lead	A [MPa]	5.59	4.66
	B [MPa]	43.6	43.4
	n	0.216	0.078
	C	0.016	0.016
friction	f_e	0.1	0.1
	f_i	0.5	0.5
Objective Function	Φ_S	0.031416	0.017116
	Φ_F	3.61986×10^{-8}	1.957×10^{-8}

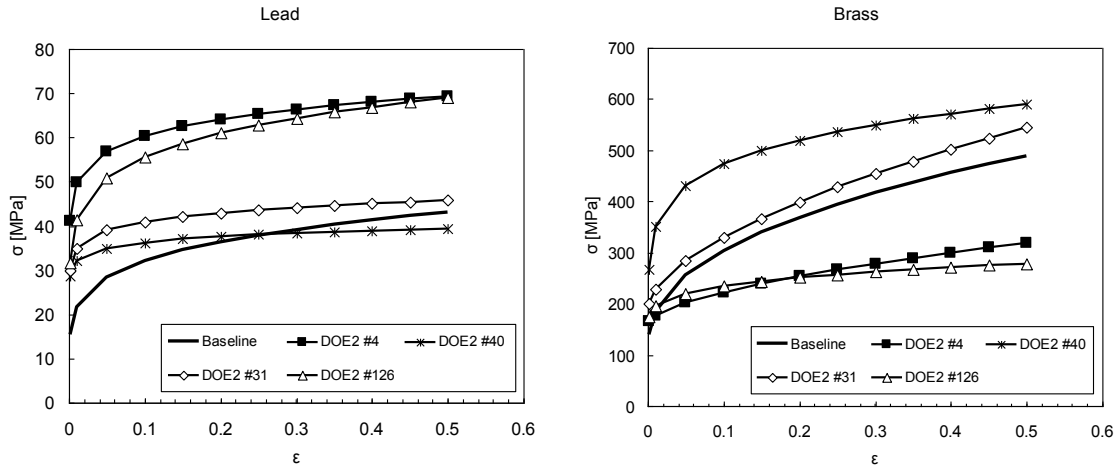

Fig. 9 True stress-true strain curves for brass and lead for improved simulation (#31) and close neighboring simulations from DOE2 compared with baseline values.

CONCLUSIONS

A method is being developed to examine the dynamic mechanical response of whole bullets using high speed 3D digital image correlation shape measurements and finite element modeling. The goal is to provide more accurate models for bullets that can be used to simulate soft body armor impacts. A test case was presented in which a 0.357 magnum 158 grain JSP bullet, consisting of a lead-antimony core and brass jacket, was deformed dynamically using a direct impact Kolsky bar test. The shape and load histories during the test were compared to a finite element simulation using baseline constitutive parameters for the lead, developed from in-house testing, and for the brass jacket from the literature. A commercial DOE/optimization software package was used to identify the most important material constants affecting the shape and load histories during dynamic compression. The initial DOE showed that the jacket and lead strength parameters dominate the problem, while friction and rate sensitivities have relatively less effect. Improved solutions obtained from a second DOE in which only the strength of the lead and brass were varied pointed to stronger brass response compared to the literature baseline value. Limitations of the model in matching the shape evolution due to the role of the crimping on the jacket, and on the asymmetric deformation observed in the experiment will be address by more detailed jacket modeling and further experiments.

ACKNOWLEDGEMENTS

Support for this work was provided by the NIST Office of Law Enforcement Standards under K. Rice. In addition, the efforts of M. Kennedy in the laboratory and S. Banovic for metallurgical characterization are gratefully acknowledged.

REFERENCES

[1] Phoenix SL and Porwal PK, Int. J. Solids Struc., 40 (2003), 6723-6765.
[2] Lim CT, Shim VWP and Ng, Int. J. Impact Engng., 28 (2003), 13-31.
[3] Iannucci L and Willows ML, Composites: Part A, 37 (2006), 2041-2056.
[4] Cunniff PM, Textile Res. J., 62 (1992), 495-509.
[5] Cantwell WJ and Morton J, Composites 20 (1989), 545-551.
[6] Navarro C, Key Engineering Materials 141-143 (1998), 383-400.
[7] Roylance D, Fibre Science and Technology, 13 (1980), 385-395.
[8] Cheeseman BA and Bogetti TA, Composite Structures 61 (2003), 161-173.
[9] Børvik T, Dey S and Clausen AH, Int. J. Impact Engrg., 36 (2009), 948-964.
[10] Cheng, CL, “Mechanical and Microstructural Characterization of Copper Microsamples after Cold Drawing,” MS Thesis, UMBC, May 2008.
[11] Andersen Jr CE, Burkins MS, Walker JD and Gooch WA, Comp. Modeling in Engrg. and Sci., 8 (2005), 91-104.
[12] Sutton MA, Orteu JJ and Schreier HW, Image Correlation for Shape, Motion and Deformation Measurements, (Springer, New York, 2009).
[13] NIJ Standard-0101.04. Ballistic Resistance of Personal Body Armor. Washington, DC (USA): U.S. Department of Justice, 2000.
[14] Avril S et al., Exp. Mech, 48 (2008), 381-402.
[15] Gray III GT, ASM Handbook Vol 8 (The American Society for Metals, Materials Park, Ohio, 1990) pp.462-476.
[16] Johnson, G.R., et al., ASME J. Eng. Mat. and Tech., 105 (1983) 42-47.
[17] ASTM Standard B927

Proceedings of the SEM Annual Conference
June 7-10, 2010 Indianapolis, Indiana USA

High Speed Imaging in Dynamic Tensile Testing of Fabric-Cement Composites

Deju Zhu [1], Alva Peled[2], Barzin Mobasher*[3]

[1] Graduate Research Associate, Department of Civil and Environmental Engineering, Arizona State University, Tempe, AZ, 85287, E-mail: Deju.Zhu@asu.edu
[2] Senior lecturer, Structural Engineering Department, Ben Gurion University, Beer Sheva, 84105, Israel, E-mail: alvpeled@bgu.ac.il
[3] Professor, Ph.D., P.E., Department of Civil and Environmental Engineering, Arizona State University, Tempe, AZ, 85287, corresponding author, E-mail: Barzin@asu.edu

ABSTRACT

Dynamic tensile tests were conducted using a high speed servo-hydraulic testing machine on three types of fabric reinforced cement composites. A good correlation was found between the properties of the fabrics and the composites in high speed tensile tests. The carbon composite exhibits the highest strength, followed by the AR-glass composite and then PE composite in high speed tensile tests. The cracking evolution and patterns of the composites were recorded by a high speed digital camera at a sampling rate of 10000 fps. Images showed that multiple cracking behavior was predominant for the carbon and glass fabric-cement composites, indicating good stress transfer within these systems. However, for the carbon, only the filaments at the bundle perimeter were bonded to the cement matrix as the inner filaments completely pulled out during loading. No multiple cracking was observed with PE fabric-cement composite as a single major crack was detected. This major crack opened and widened until the fabric was completely broken.

Keywords: Dynamic tensile testing; Fabric-cement composites; High speed imaging;

1. Introduction

Cementitious materials may be subjected to dynamic loading for variety of reasons including: blast explosions, projectiles, earthquakes, fast moving traffic, wind gusts, wind driven objects, and machine vibrations. Due to the inherent brittleness and low tensile strength of most cement-based elements, dynamic loading can cause severe damage and cracking [1]. In order to accurately analyze and design structures that are subjected to dynamic loading, it is necessary to utilize the mechanical properties associated with the strain rates to which the structural components are subjected. Testing dynamic properties is a challenge since the results are highly dependent on the loading rate, method of testing, and the geometry of the tested element [2]. Fiber reinforcement is undoubtedly one of the most effective means of enhancing the resistance, strength, and energy absorption of cement based materials subjected to dynamic loading. To date, dynamic properties of cement composites have been studied mainly for short fiber composites under impact condition. Fabric-cement composites clearly demonstrate a significant improvement in the energy absorption capacity under static loading as compared to plain concrete materials and other fiber cement composites [3, 4, 5, 6]. Recent work on their impact behavior clearly showed the potential of such components under high speed loading [7]. In spite of recent activity in the study of impact resistance of cement composites, the dynamic tensile behavior is still not well understood. Characterization of dynamic tensile properties of materials is challenging as the failure process is affected by the mode and manner of testing. Problems appear at high rate loading due to inertial effect, non-uniform loading, and difficulties in measuring reliable mechanical characteristics of the materials. The use of servo-hydraulic machines in medium strain rate tensile testing was reported for composite materials [8] and woven fabrics [9, 10], but few applications exist in cement based composites[11].

T. Proulx (ed.), *Application of Imaging Techniques to Mechanics of Materials and Structures, Volume 4*, Conference Proceedings of the Society for Experimental Mechanics Series 14, DOI 10.1007/978-1-4419-9796-8_57, © The Society for Experimental Mechanics, Inc. 2013

This paper presents the development of a high speed tensile testing system for laminated cement composites reinforced with various fabrics. Three types of fabric were used, i.e. Alkali Resistant (AR) glass, polyethylene (PE) and carbon. The cement based composites reinforced with these three fabrics were tested to obtain the dynamic material properties, including Young's modulus, tensile strength, toughness, and maximum strain. Typical stress-strain curves representing the tensile behavior of individual composites were compared. Crack patterns and failure behavior of each composite were observed.

2. High Speed Tensile Test Methodology

2.1 Dynamic Tensile Test Procedure

The dynamic tensile tests were conducted using a MTS high rate servo-hydraulic testing machine which can operate in closed-loop and open-loop at a maximum speed of 14 m/s with a load capacity of 25 kN. The development of this test method was addressed in earlier works [12, 13]. The speed of the actuator is controlled by the opening of the servo-valve of hydraulic supply. By manually setting the level of opening of the servo-valve, the rate of flow of hydraulic fluid and hence the actuator speed can be controlled.

The setup of the dynamic tensile testing is presented in Figure 1(a). As the system starts to run, the actuator accelerates to reach and maintain the preset speed. During this range of travel, the conical portion of the sliding bar contacts the slack adaptor (hollow tube) which is connected with the actuator and transfers the force to the specimen. The hollow tube travels freely with the actuator at the specified velocity before making contact with the sliding bar. This eliminates the inertia effect of the actuator and the lower grip during the acceleration stage. The stainless steel grips are shown in Figure 1(b) and weigh approximately 1500 g. A specimen was installed between two steel wedges with serrated faces. In this study, the load was measured by a Kistler 9041A piezoelectric force link (load washer) with a capacity of 90 kN and rigidity of 7.5 kN/μm and frequency response of 33 kHz. The load signal was amplified through a Kistler 5010B dual mode charge amplifier. A high speed digitizer (up to 10 mega-samples per second) collected the force signal from the piezoelectric force link, and the actuator LVDT signal as the deformation of the specimen. A Phantom v.7 high speed digital camera with a sampling rate of 10000 fps captured the cracking and failure behavior of the different composites. The camera was placed in front of the specimen observing its full size in between the grips.

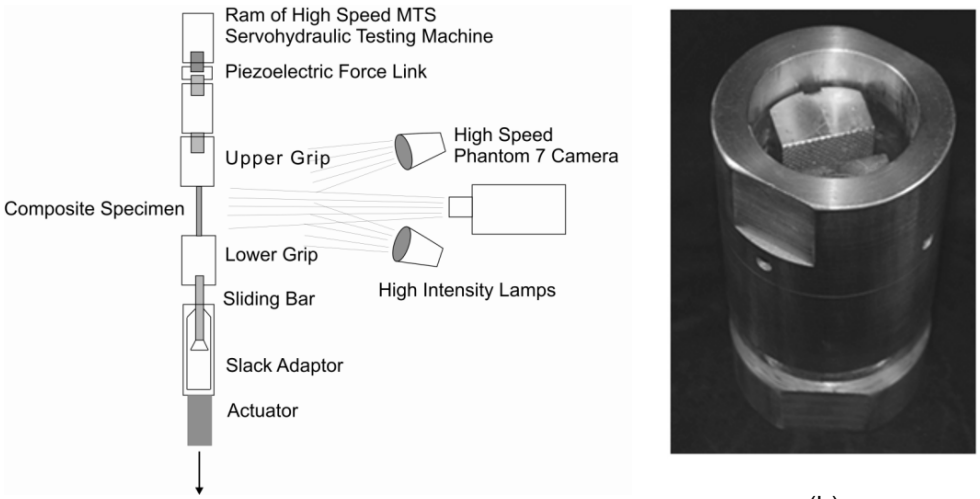

(a) (b)

Figure 1- (a) schematic diagram of test set-up for dynamic tensile testing and (b) one grip set

2.2 Data Processing

Processing of the dynamic data is quite cumbersome compared to the quasi-static tests. The signals from the piezoelectric force link and the LVDT of actuator were recorded at a sampling rate of 250 kHz and contained high frequency noise which was filtered using a low-pass filter with a cut-off frequency of 3 kHz to obtain the specimen response. An example of the recorded responses of carbon fabric reinforced cement composite generated by the high speed testing setup after applying the low-pass filter is given in Figure 2(a). The figure presents the recorded

force and displacement of actuator versus time histories of the entire test. A constant velocity of 1150 mm/s is obtained by linearly fitting the section of displacement history curve just prior to loading the specimen. Due to the resistance provided by the test specimen, the test duration took less than 15 milliseconds at an average velocity of 500 mm/s. Using the cross-sectional area and gage length of the specimen, the nominal stress versus strain curve can be calculated as shown in Figure 2(b). The behavior of the composite has three distinct ranges during loading: elastic region, stain-hardening region, and post-peak region. In the elastic region, the stress-strain curve is linear with Young's modulus of the composite defined as the slope of the stress-strain curve in this region. As the composite specimen starts to fail and distributed cracking forms, this leads to a quasi-strain-hardening behavior that is extended until the peak stress, defined as tensile strength. The post-peak region is characterized as the sudden drop in stress, indicating the total failure of the specimen. Toughness is evaluated using the total area under the stress-strain curve. The stress-strain curves were calculated for all specimens and the Young's modulus, tensile strength (peak stress), maximum strain and toughness.

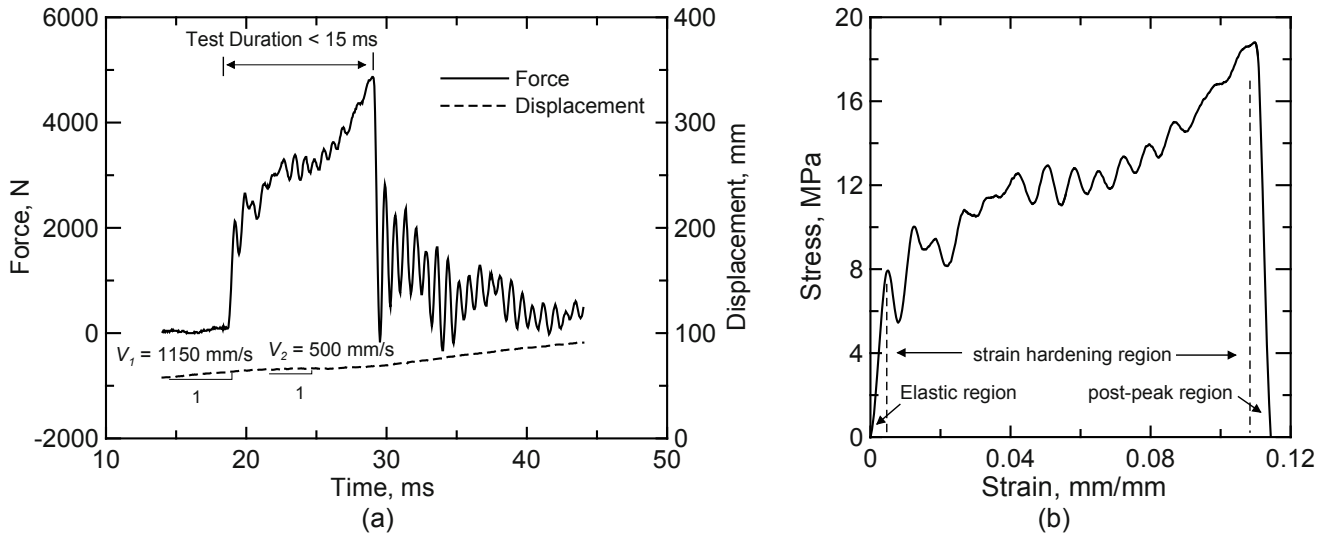

Figure 2-(a) Force and displacement of actuator versus time curves at nominal velocity of 1150 mm/s, using carbon fabric reinforced cement composite, and (b) stress-strain curve

3. Experimental

3.1 Materials

Fabrics studied in this program contained three different fiber materials: AR-glass, PE, and carbon. Their structure and mechanical properties of yarns are given in Table 1.

- The AR-glass was in the form of leno bonded fabric, in which, a perpendicular set of yarns (warp and weft) are glued together at junction points, with four yarns per cm in both directions. This fabric was coated with sizing.
- The PE was in a form of short weft warp knitted fabric, in which the warp yarns are knitted into stitches and bind together a set of yarns that are laid-in intermittently in both weft and warp directions. The loops are placed as three stitches (reinforcing yarns) per cm in the reinforcing direction of the composite.
- The carbon fabric is in the form of a weft insertion warp knitted, where yarns in the warp direction are knitted into stitches to assemble straight yarns in the weft and warp directions, having two yarns per cm in both directions. The weft yarns are the reinforcing yarns in the composite.

Table 1: Properties of Yarns Made up the Fabric (under Static Condition)

Yarn type	Yarn nature	Strength (MPa)	Young's Modulus (MPa)	Filament size (mm)	Bundle diameter (mm)
PE	Monofilament	240	1760	0.250	0.25
AR-Glass	Bundle	1372	72000	0.014	0.30
Carbon	Bundle	2200	240000	0.008	1.15

The laminated fabric-cement composites were prepared using the pultrusion process with cement paste of 0.4 water/cement ratio. In this process the fabric passes through a slurry infiltration chamber to get coated, and then pulled through a set of rollers to squeeze the paste in between the fabric openings while removing excessive paste [3]. The fabric-cement composite were then formed on a plate shaped mandrel resulting in laminated sheets with 250 × 300 mm and thickness of about 7-12 mm (depending on fabric type). Cement boards were made with 4 layers of fabrics. The reinforcing yarns in the composite of each fabric were placed along the pultrusion direction. After forming the samples, constant load of about 50 N was applied on the surface of the fabric-cement sheet to improve penetration of the matrix in between the yarn and fabric openings.

All boards were cured in water at room temperature for 28 days and then cut to the specimens of 25 mm in width and 150 mm in length. The average thickness of carbon, AR-glass, PE composites were 11 mm, 6.6 mm, and 12 mm, respectively. Five replicate fabric-cement specimens were used for each fabric category. Aluminum plates of dimensions of 25×50×1 mm were glued onto the gripping edges of the specimen to minimize localized damage and provide better load transfer from the grips to the specimen during the high speed tensile test. The gauge length of each specimen was 50 mm.

3.2 Mechanical behavior of composites under high speed loading

Figure 3 compares typical stress-strain behavior of the composites with the different fabrics under high rate loading condition. The highest load carrying capacity is demonstrated by the carbon composite followed by the AR glass composite and then PE composite. These trends correlate well with the tensile properties of the fabrics (Table 1). In the case of the PE and AR-glass composites, there is a linear behavior almost up to the peak and then a reduction in composite strength is observed at relatively low strain, very soon after reaching the peak. On the other hand, the behavior of the carbon composite is quite different. There is a stiff linear behavior up to the Bend-Over-Point (BOP), at stress value of about 6 MPa and strain value of 0.005 mm/mm. Beyond this point, a complete and pronounced change in the slope of the stress-strain response occurs and the stress increases with a reduced stiffness to as high as 17 MPa. These differences in tensile behavior of the various fabric composites indicate the role of each fabric under high rate loading. Table 2 summarizes the material properties of each composite during high speed loading.

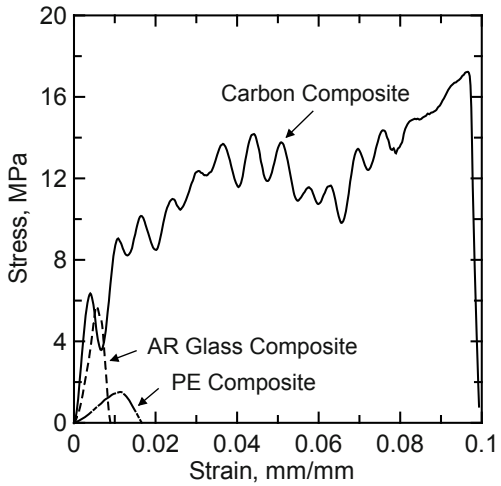

Figure 3- Comparison of typical stress-strain curves of cement based composites

Table 2: Composites Properties under High Rate Loading
(The values in parenthesis are standard deviation)

Composites	Strain Rate (1/s)	Young's Modulus (MPa)	Strength (MPa)	Toughness (MPa)	Maximum strain (mm/mm)
PE	23 (4)	140 (24)	1.31(0.17)	0.016(0.007)	0.021(0.007)
AR-Glass	18(3)	1176(323)	5.56(0.51)	0.032(0.009)	0.01(0.002)
Carbon	10(1)	2247(463)	17.86(0.82)	1.21(0.14)	0.10(0.014)

3.3 Cracking and Failure Behavior

The cracking patterns were recorded using a high speed digital camera. Typical images were chosen to present the cracking behavior of each composite. In the case of the AR-glass composite three stages are presented as shown in Figure 4. Figure 4(a) represents the intact specimen, and Figure 4(b) represents the end of the multiple cracking process, i.e., where beyond this point no new cracks are formed. The behavior of successive cracking was indicative of stress transfer mechanism at the fabric-cement interface to be sufficient for load transfer and

composite action. After this stage, the strain increased and cracks opened uniformly until a point of bifurcation where one of the cracks becomes the dominant one that continues to open, while the load begins to decrease. Only this dominant crack was observed and all other cracks were not visible by naked eye [Figure 4(c)-(e)]. The main crack continues to widen under load for the duration of the test. At this point the forces were mainly carried by the fabric bridging the main widening crack until all its yarns were completely broken, leading to a complete failure of the tested specimen. Yarn breakage was clearly demonstrated in Figure 4(e).

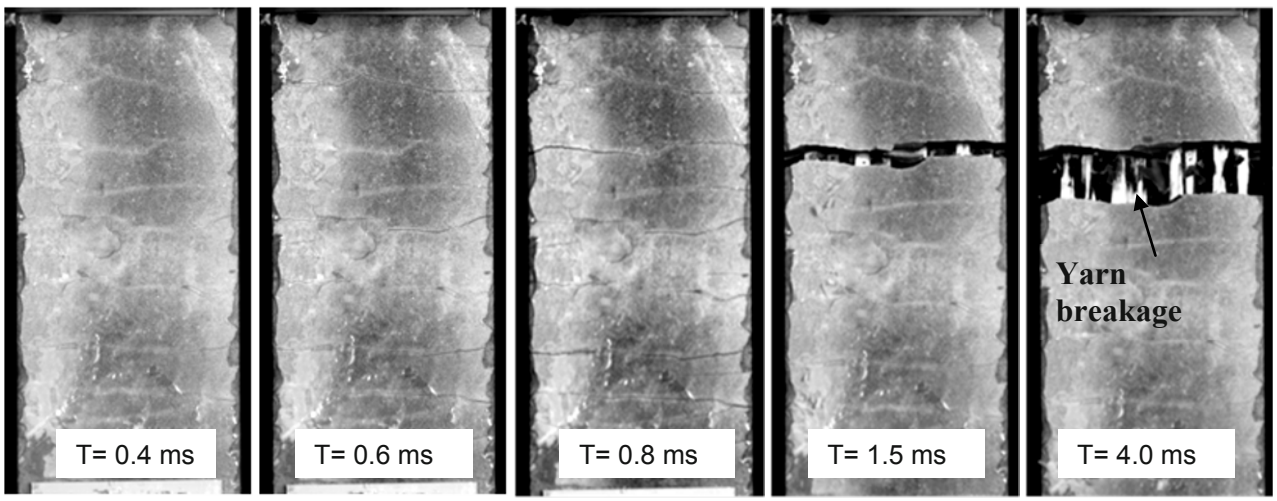

Figure 4- AR glass composites: (a)-(c) multiple micro-cracking, (d) main crack widening and other micro-cracks closing, (e) complete failure

Similar multiple cracking behavior was also observed for the carbon composites as shown in Figure 5. Figure 5(a) represents the intact specimen, and Figure 5(b)-(e) represented the development of multiple cracking. At the end of the multiple cracking region in this system, the developed crack spacing was larger than that of AR-glass composite, indicating less efficient bonding. No brakeage of fibers could observe after 6 ms of testing [Figure 5(e)]. In Figure 6, the carbon composites developed few of visible cracks, then failed near the grip section, the yarns were mainly pulled out from the cement matrix.

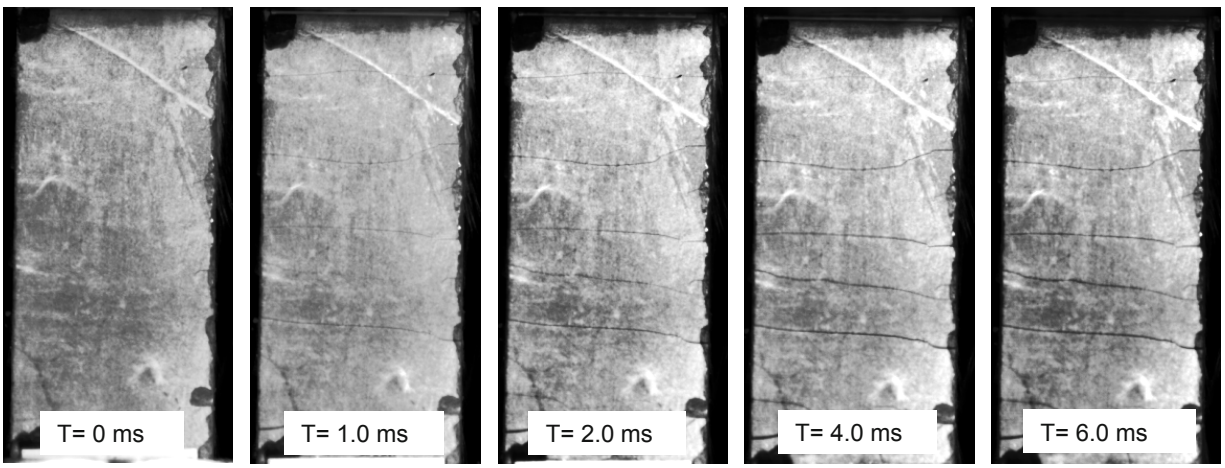

Figure 5- Carbon composites (multiple cracking): (a) intact, (b) multiple cracking, (c)-(e) multiple crack widening

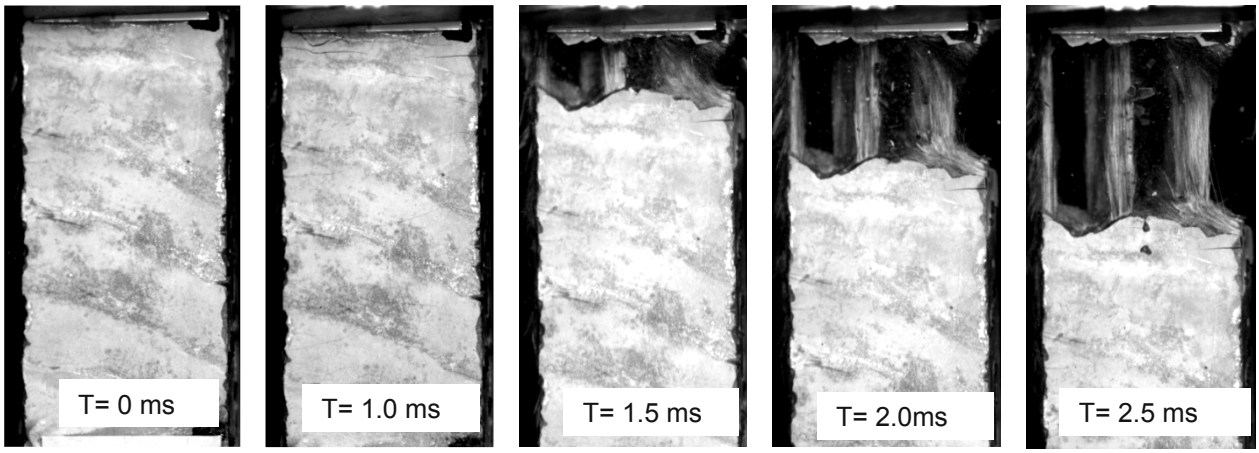

(a) (b) (c) (d) (e)

Figure 6- Carbon composites (failure near the grip section): (a) intact, (b) few of visible cracks, (c)-(e) yarn pullout

Figure 7(a)-(e) represents the cracking behavior of PE composite during the high rate loading process. No multiple cracking was observed with this fabric composite as a single major crack was detected. This major crack opened and widened until the fabric was completely broken. The cement matrix was broken into several smaller segments at the fracture surface as soon as the crack was developed and widened, which were not observed with the other two composites.

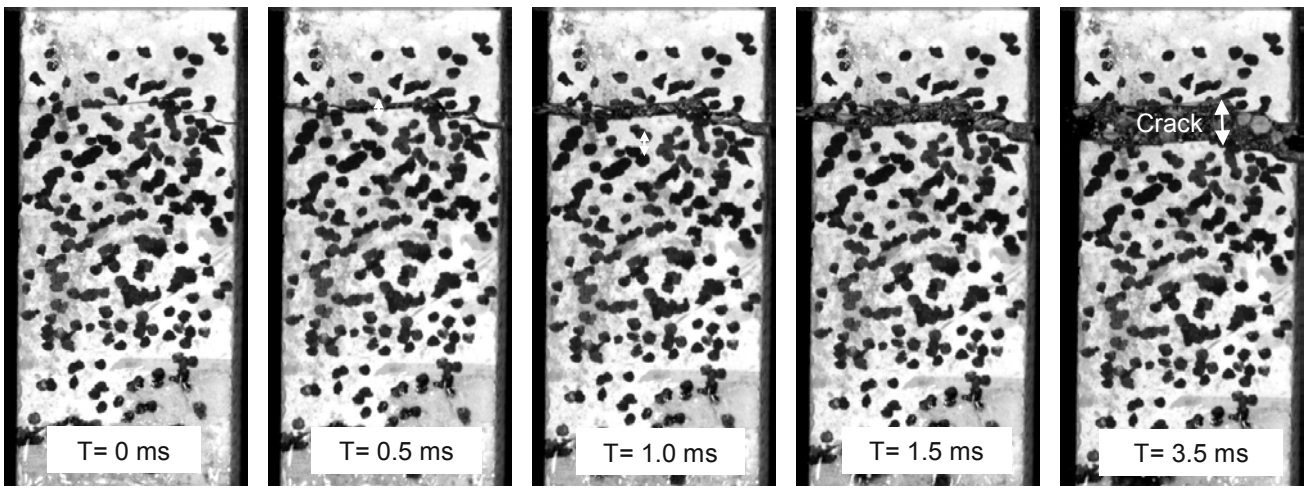

(a) (b) (c) (d) (e)

Figure 7- PE composites: (a) intact, (b) single cracking, (c)-(d) crack widening, (e) total failure.

4. Conclusions

High speed tensile tests of three types of fabric-cement composites were successfully performed at this study. A fairly uniform tensile behavior was clearly observed of all composite systems, demonstrating the reliability of the high speed testing method for cement-based composites. The test results obtained here can provide tools to design composite elements that are expected to be subjected to extreme loading conditions during their service life. A good correlation was found between the properties of the fabrics and the composites, with the carbon composite exhibiting the highest strength, followed by the AR-glass composite and then PE composite. Multiple cracking behaviors were observed for the carbon and glass fabric-cement composites, indicating good stress transfer within these systems. However, for the carbon, only the filaments at the bundle perimeter were bonded to the cement matrix as the inner filaments were fully pulled out during loading providing ductile behavior of the composite. This is opposed to the AR-glass fabric-cement composite, where the bundle was coated with sizing and therefore the entire bundle is glued together and no slippage of individual filaments occurs, leading to more brittle behavior. No such cracking pattern was seen for the PE fabric-cement composite.

Acknowledgements

The authors would like to thank Nippon Electric Glass Co., Ltd. USA, SAERTEX GmbH & Co. KG, Germany and Polysack Ltd. Israel for their cooperation for providing the fabrics used in this study. The BSF (United States Israel Binational Science Foundation) program 2006098 acknowledged for the financial support in this research.

References

[1] Gupta P. and Banthia N. Fiber Reinforced Wet-mix Shotcrete under Impact, *J. of Materials in Civil Engineering (ASCE),* 81-90, 2000.

[2] Bharatkumar, B.H. and Shah, S.P. Impact Resistance of Hybrid Fiber Reinforced Mortar. I*nternational RILEM Symposium on Concrete Science and Engineering: A Tribute to Arnon Bentur*, e-ISBN: 2912143926, RILEM Publication SARL, 2004.

[3] Peled, A., and Mobasher, B. Tensile Behavior of Fabric Cement-Based Composites: Pultruded and Cast, ASCE, *J. of Materials in Civil Engineering*, 19(4), 340-348, 2007.

[4] Mobasher, B., Peled, A., and Pahilajani, J. Distributed Cracking and Stiffness Degradation in Fabric-Cement Composites, *Materials & Structure (RILEM)* J. 39(3), 317-331, 2006.

[5] Peled, A. and Bentur, A. Fabric Structure and Its Reinforcing Efficiency in Textile Reinforced Cement Composites, *Composites, Part A*, 34, 107-118, 2003.

[6] Kruger, M. Ozbolt, J., and Reinhardt, H.W. A New 3D Discrete Bond Model to Study the Influence of Bond on Structural Performance of Thin Reinforced and Prestressed Concrete Plates." Proc., High *Performance Fiber Reinforced Cement Composites (HPFRCC4)*, RILEM, Ann Arbor, MI, 49-63, 2003.

[7] Zhu, D., Gencoglu, M., Mobasher, B. Low Velocity Impact Behavior of AR Glass Fabric Reinforced Cement Composites in Flexure. *Cement and Concrete Composites*, 31(6), 379-387, 2009.

[8] Fitoussi, J., Meraghni, F., Jendli, Z., Hug, G., and Baptiste, D. (2005). Experimental Methodology for High Strain Rates Tensile Behavior Analysis of Polymer Matrix Composites. *Composite Science Technology*, 65, 2174–2188.

[9] Zhu, D., Mobasher, B., and Rajan, S. D. High Strain Rate Testing of Kevlar 49 Fabric. Society for Experimental Mechanics - *11th International Congress and Exhibition on Experimental and Applied Mechanics*, v1, p.34-35, 2008.

[10] Zhu, D., Bansal, S., Mobasher, B., Rajan, S. D., and Pereira, J.M. Experimental Development of a Constitutive Model for High-Speed Impact Containment Fabrics. *Proceedings of the 11th International Conference on Engineering, Science, Construction, and Operations in Challenging Environments,* 2008.

[11] Silva, F., Zhu, D., Soranakom, C., Mobasher, B., Toledo Filho, R. High Speed Tensile Behavior of Sisal Fiber Cement Composites. *Materials Science and Engineering: A*, 527(3), 544-552, 2010.

[12] Zhu, D., Mobasher, B., and Rajan, S.D. Dynamic Tensile Testing of Kevlar 49 Fabrics. *ASCE Journal of Materials in Civil Engineering*. (In review), 2008.

[13] Zhu, D., Mobasher, B., Rajan, S.D. Image Analysis of Kevlar 49 Fabric at High Strain Rate. In: Society for Experimental Mechanics, 11th International Congress and Exhibition on Experimental and Applied Mechanics, v2, p. 986-991, 2008.

Proceedings of the SEM Annual Conference
June 7-10, 2010 Indianapolis, Indiana USA

Ultra high speed DIC on a three point bending test mounted on a Hopkinson bar

Prof. F. Pierron[*], Prof. M.A. Sutton[**], Dr V. Tiwari[**]

[*] Laboratoire de Mécanique et Procédés de Fabrication, Arts et Métiers ParisTech,
Rue Saint Dominique, 51006 Châlons-en-Champagne, France
fabrice.pierron@chalons.ensam.fr
[**] Department of Mechanical Engineering, University of South Carolina,
Columbia, SC, USA, sutton@sc.edu

ABSTRACT

This paper deals with the analysis of an aluminium beam impacted in a three point bending configuration using a Hopkinson bar device. Full-field deformation measurements were performed using Digital Image Correlation on images captured with an ultra high speed camera (16 frames at a time resolution of 10 μs). The performance of the deformation and strain measurements were evaluated and the measurements were then used quantitatively to analyse the very complex dynamic behaviour of the beam. It was shown that the deformation of the beam was controlled by the interaction between the striker and the flexural bending wave triggered by the initial shock. The principle of virtual work was used to reconstruct the impact force from the shear strains and to analyze how this impact force relates to the acceleration of the specimen (inertia forces) and the development of the bending stresses. The results are in good agreement with expectations. This opens up new perspectives in the quantitative use of full-field measurements to extract elasto-plastic constitutive parameters from such impact tests.

INTRODUCTION

Camera based computer vision techniques to measure full-field strains in deformed solids are now widely used throughout the scientific community working on mechanics of materials and structures. In static or slow events, standard CCD or CMOS cameras provide very good quality data and significant work is now underway to invent new test procedures to take full advantage of such a wealth of experimental data ([1,2], for instance). However, for ultra high speed events (impact, Hopkinson bar tests), this area of research is still very much in its infancy. One of the reasons is that the single CMOS sensor camera technology is presently limited to frame rates less than 10 kHz for a full 1 Mpixel spatial resolution. Therefore, such applications require the use of so-called ultra high speed cameras with multiplexed sensor technologies (see [3], for instance). In such cases, the quality of the images is much poorer and strain measurement resolutions are usually low. As a consequence, high strain rate testing methodologies have not yet evolved to make full use of such full-field data. The objective of the present paper is to show how full-field strain measurements can be used advantageously to process test data on more complex test configurations. It is shown that acceleration forces can be used in the identification process and that impact force can be reconstructed from the full-field measurements. However, the paper is rather seminal in nature and it is clear that very significant research efforts are required for such methodologies to be fully operational, including the improvement of ultra high speed digital imaging devices.

T. Proulx (ed.), *Application of Imaging Techniques to Mechanics of Materials and Structures, Volume 4*, Conference Proceedings of the Society for Experimental Mechanics Series 14, DOI 10.1007/978-1-4419-9796-8_58, © The Society for Experimental Mechanics, Inc. 2013

EXPERIMENTAL SET-UP

Mechanical set-up

A schematic of the mechanical set-up is shown on Figure 1. It consists of a three-point bending configuration mounted onto a Hopkinson bar fixture. A projectile fired by an air gun is used to produce the loading. It impacts the bar which then strikes the specimen. Clearly, the usual analysis to retrieve the load does not apply here so the strain gauges signal will not be considered and the bar is just used to introduce the load. The specimen is a 6 mm thick 6061T6 aluminium bar, 110 mm long, 10 mm wide with a 90 mm distance between the supports.

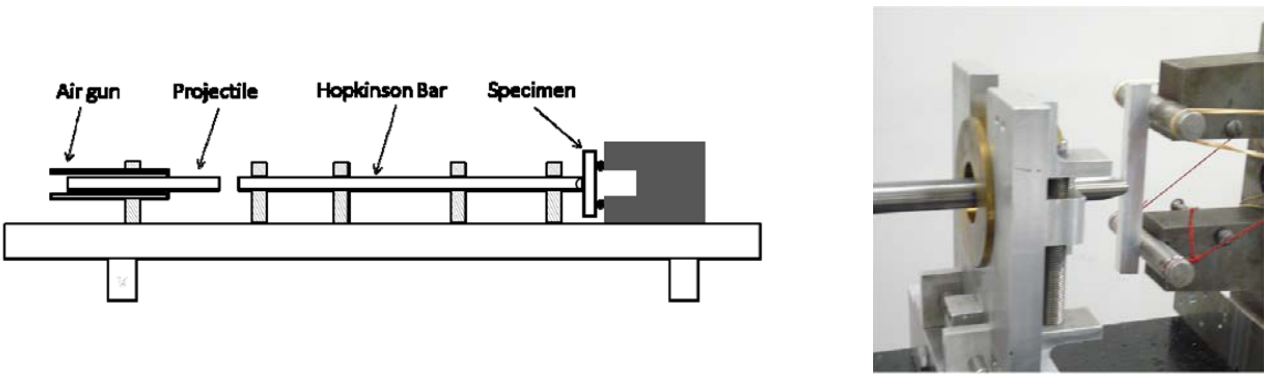

Figure 1. Schematic of the test set-up and photograph.

Image capturing and processing

An IMACON 200 camera has been used to record images of a speckle pattern deposited onto the specimen. The field of view is centred on the loading point and comprises a length of about 14 mm. The frame rate used here is 10 μs. The IMACON camera enables the recording of 16 images at this rate. The idea was to focus the attention on the early stages of loading when plasticity initiates. A lens was used to reach a pixel size of 20 μm. The size of the active area is about 500 by 800 pixels. Figure 2 shows four images extracted from the film of the test, including the first and last images. The reference time is the contact between the projectile and the input bar. From the speed of the compression wave in the bar, the time of impact between bar and specimen was computed and the corresponding delay time entered into the camera triggering system.

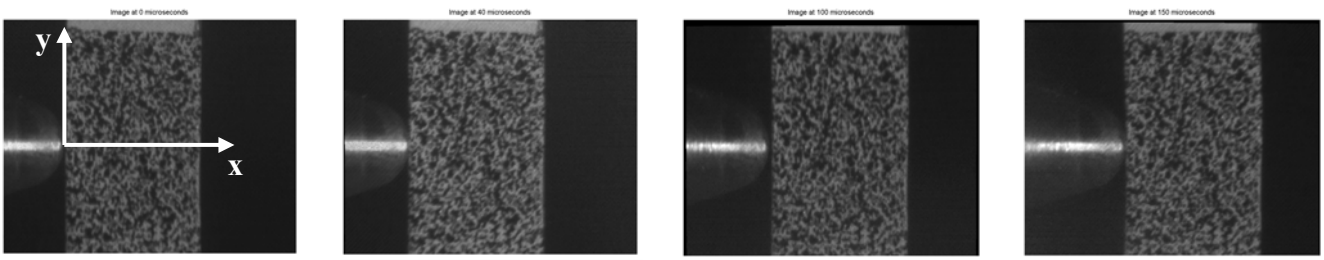

(a) 0 μs (b) 40 μs (c) 100 μs (d) 150 μs

Figure 2. A selection of images from the test.

From the images captured by the camera, the objective is to extract displacement fields by using an image correlation algorithm. However, because of the technology of the camera, a flat-field correction has to be performed (to have more details, see [3]). A correction for lens distortion was also applied using a parametric bi-cubic spline model identified on rigid translation movements, as detailed in [3]. From these corrected images, displacement data are computed using the VIC2D image correlation algorithm [4]. A correlation window of 31 by 31 pixels was selected here, with a 5 pixels shift, which are typical values for this type of problem. It is clear that these parameters will impact the performance of the results, with a larger correlation window providing better resolution at the cost of spatial resolution. The shift of five will provide extra data between two windows but the data will not be independent. The spatial resolution of the displacement measurements is therefore 31 pixels (i.e.,

0.62 mm). From the displacement maps, strains are derived by a smoothing / differentiation procedure in order to enhance the strain resolution. For this purpose, the diffuse approximation procedure detailed in [5,6] has been used, with several radii: 8, 12, 16, 20 and 24 measurement points. These radii represent the size of the window over which the second order polynomial fit is performed. The diffuse approximation procedure exhibits a very good smoothing / reconstruction compromise, hence the rather large radii used here.

Performance evaluation

In order to evaluate the resolution of the measurements both in displacement and strain, 16 images of the still specimen have been taken before the test. In fact, in order to reduce the sensor to sensor variability, two sets of still images were recorded and the correlation was performed between the images provided by each individual sensor taking the first image as reference and the second as the "deformed" image. The parameters described above were used to produce displacements and strains. Figure 3 shows the displacement resolution without (a) and with (b) smoothing. These resolutions have been obtained from the standard deviation of the displacement maps. The first thing that can be seen on Figure 3(a) is that there is a strong sensor to sensor variability. The resolution lies between 0.1 and 0.2 pixels, which is one order of magnitude higher than what is usual with standard CCD cameras. Smoothing clearly improves the resolution (Figure 3(b)), dividing it by a factor of about 2 for a radius of 24. From the local second order fitting of the displacement, strain components are obtained directly and the strain resolution can be computed in the same way as for the displacement. When no smoothing is applied (Figure 4(b)), the strain resolution is about 0.01 which is very poor. It should be noted that these values are higher than that reported in [3] which means that the set-up is probably not optimal. Smoothing obviously improves the strain resolution. With a radius of 8 points, the strain resolution already drops to about 4.10^{-3} and this decreases down to about 1.10^{-3} for a radius of 24. This value will be retained here. As for the spatial resolution, one can evaluate it to about 4 times the correlation window, i.e. 2.4 mm even if this value would need to be estimated more carefully. A procedure to evaluate this with the diffuse approximation filtering is presently under evaluation.

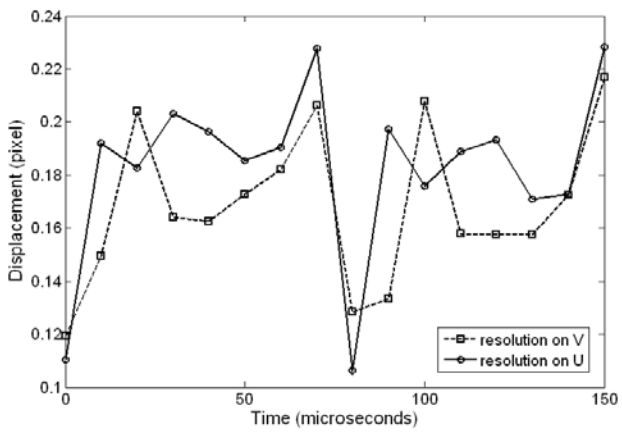

(a) Displacement resolution - raw

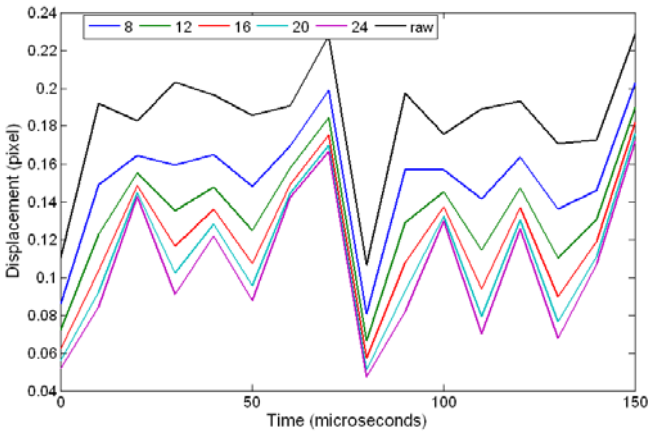

(b) Displacement resolution – filtered (U)

Figure 3. Displacement resolution on raw data (a) and after smoothing (b) for several diffuse approximation radii.

RESULTS AND ANALYSIS

The 16 images that have been recorded during the impact loading of the aluminium specimen were processed with the procedure described above (window of 31 pixels, shift of 5, smoothing with a radius of 24). It should be noted that each image was correlated with the reference image coming from the same sensor from the shot of the still scene before the impact. Figure 5 shows raw and smoothed displacement maps for the last image (150 μs), and Figure 6 shows the strains at the same stage. The displacement map patterns are consistent with the bending impact load and so are the strains with ε_x showing Poisson's effect related to the bending strains ε_y. The shear strains are also consistent with the change of shear force sign (negative on the top part and positive on the bottom part. The bending strains reach several percents, so it can be said that the plastic regime has been reached at the end of the recording.

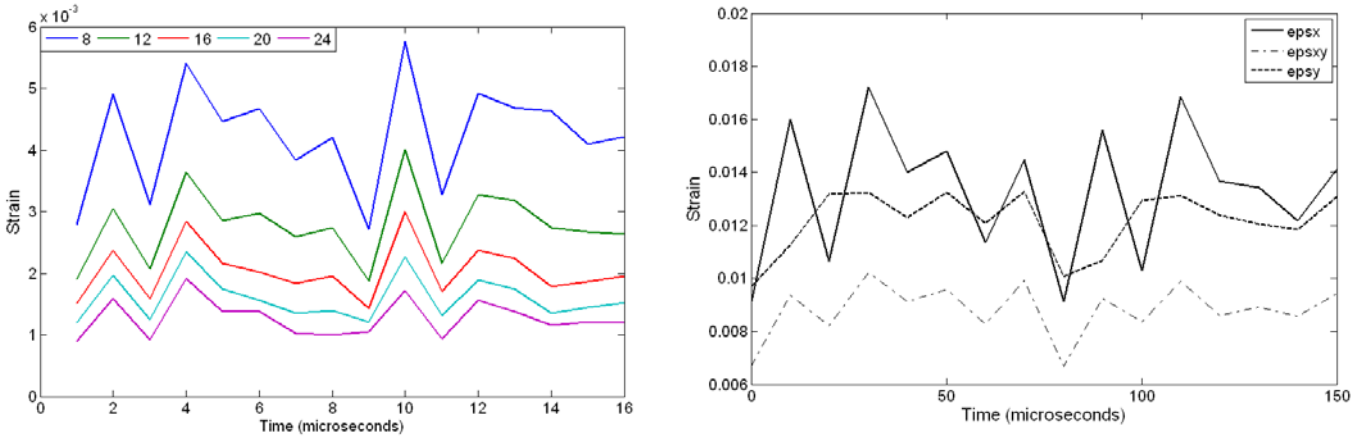

(a) ε_x strain resolution

(b) ε resolution without smoothing

Figure 4. Strain resolution for several diffuse approximation radii (a), and for direct differentiation (b).

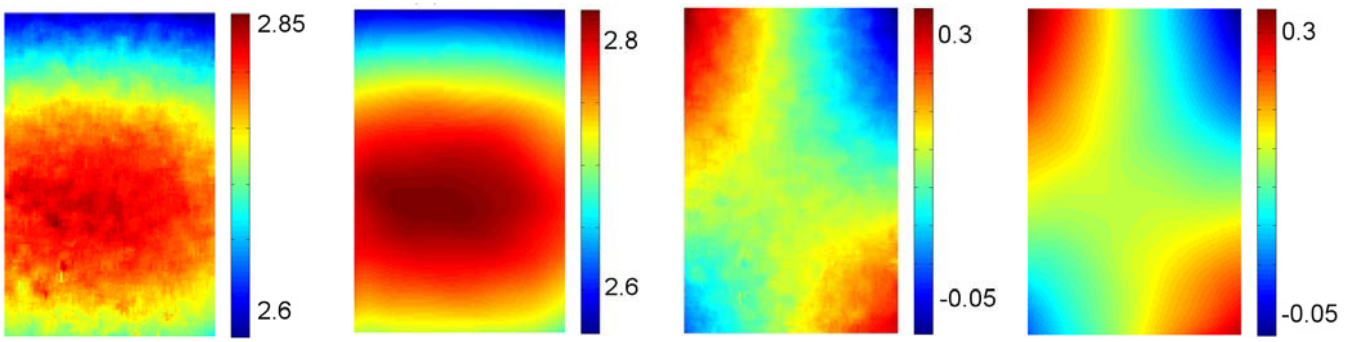

(a) u_x (raw)

(b) u_x (smoothed, r=24)

(c) u_y (raw)

(d) u_y (smoothed, r=24)

Figure 5. Displacement maps (in mm) for the last image (150 μs).

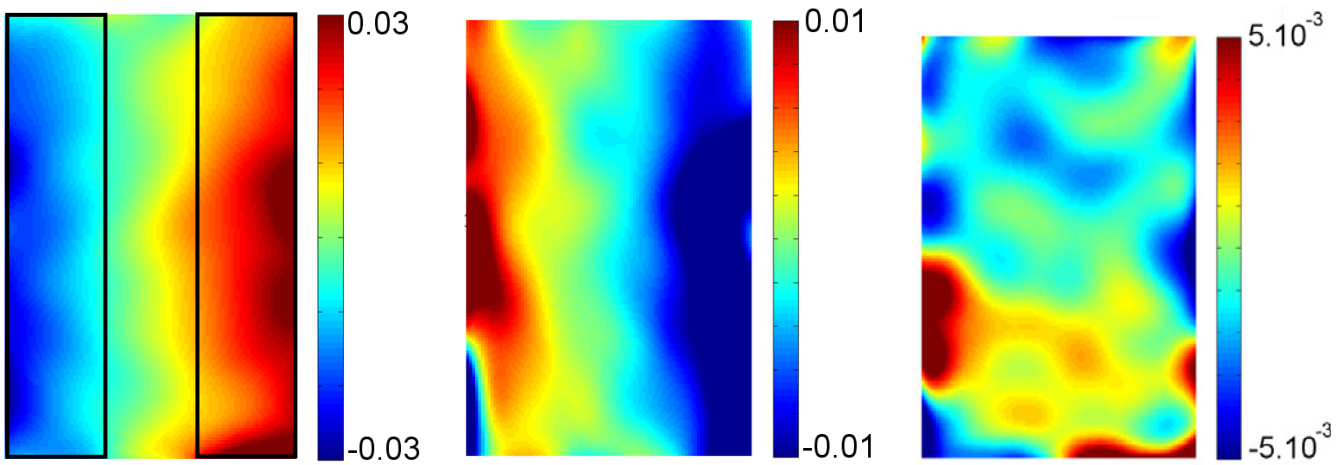

(a) ε_y

(b) ε_x

(c) ε_{xy}

Figure 6. Strain maps for the last image (150 μs).

From the displacement maps, speed and acceleration can be calculated by numerical time differentiation:

$$v_\alpha(n) = \frac{U_\alpha(n) - U_\alpha(n-1)}{\Delta t}; a_\alpha(n) = \frac{U_\alpha(n+1) + U_\alpha(n-1) - 2 \times U_\alpha(n)}{\Delta t^2}, \alpha \in \{x, y\}. \quad (1)$$

Clearly, only 14 acceleration maps can be reconstructed because of missing data for the first and last images. As for the speed, the data represent average speed between two images. Figure 7 shows the spatial averaged speed and acceleration along the test. One can see that the y acceleration can be neglected with respect to the x component (along the impact direction), which is hardly surprising. This is also the reason why only the x-component of the speed was represented for the sake of clarity. One can also see a periodic pattern on the acceleration with a first peak at 30 μs and a period around 45 μs (the second peak seems to occur between images at 70 and 80 μs. Actually, if one considers the bending wave that produces stresses in the y direction, then if one considers the top surface (where the bar hits the specimen), a compressive wave is created. It will travel to the free end at y=+55 mm and will be reflected to become tensile. When arriving back at y=0, it will be reflected again (by encountering the wave that has travelled along the negative y side), reach the y=+55 mm free end again and travel back to y=0 when one consider that one period of the wave is reached (the specimen is in the same state as when the wave started travelling. Considering a speed of $c = \sqrt{E/\rho}$ with E=70 GPa and a density of 2700 kg.m^{-3}, the wave speed is about 5100 m.s^{-1}. The period of the wave is then 2l/c where l is the length of the beam, which gives a period of about 43 μs, consistent with the experimental observations. One can also see that the acceleration reaches up to 1.5.10^{-6} m.s^{-2} which is considerable. It is to be expected that the inertia forces will not be negligible in the present case. This will be confirmed later on in the paper. As for the evolution of the speed, it follows that of the acceleration, increasing when acceleration is positive, constant when it is near zero and reducing when there is deceleration (between 80 and 120 μs).

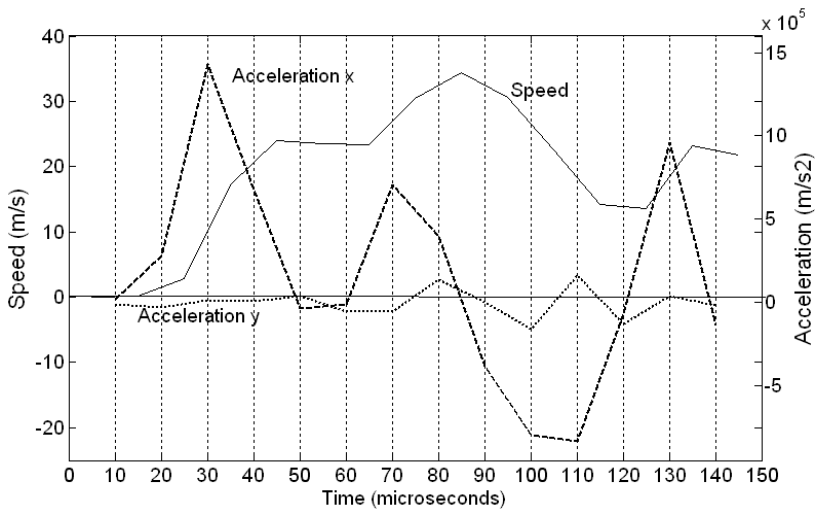

Figure 7. Spatial acceleration average along the test

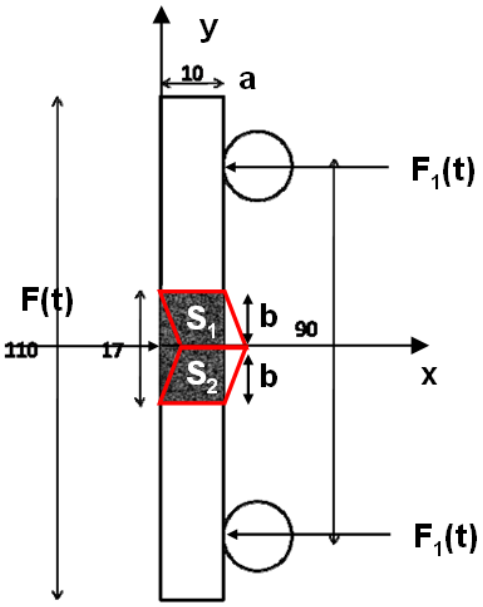

Figure 8. Schematic of the specimen (units in mm)

Force reconstruction

One of the interesting possibilities of the present test is to use the strain data to reconstruct the impact force. Indeed, let us apply the principle of virtual work with the following virtual field (see Figure 8 for axes and dimensions):

$$\text{On } S_1 \begin{cases} u_x^* = -y + b \\ u_y^* = 0 \end{cases} \quad \begin{cases} \varepsilon_x^* = 0 \\ \varepsilon_y^* = 0 \\ \varepsilon_s^* = -1 \end{cases} \qquad \text{On } S_2 \begin{cases} u_x^* = y + b \\ u_y^* = 0 \end{cases} \quad \begin{cases} \varepsilon_x^* = 0 \\ \varepsilon_y^* = 0 \\ \varepsilon_s^* = 1 \end{cases} \tag{2}$$

The effect of this virtual field is represented in red on Figure 8. It is a virtual shear strain field. The principle of virtual work writes in general:

$$-\int_V \sigma : \varepsilon^* dV + \int_{\partial V} T.u^* dS = \int_V \rho a.u^* dV \tag{3}$$

where σ is the stress tensor, T the surface density of boundary forces, ρ the density, a the acceleration vector and the star quantities the virtual displacement and strain fields. With the virtual field of Eq. 2, the different terms of this equation become (assuming linear elastic isotropy and plane stress conditions):

$-\int_V \sigma : \varepsilon^* dV = Gt\int_{S1} \varepsilon_s dxdy - Gt\int_{S2} \varepsilon_s dxdy$ where G is the shear modulus and t the specimen thickness.

$\int_{\partial V} T.u^* dS = Fb$. Thanks to the virtual field, the reaction forces F_1 are not involved in the equation, only the unknown impact force F.

$$\int_V \rho a.u^* dV = t\rho\int_{S1} a_x(-y+b)dS + t\rho\int_{S2} a_x(y+b)dS$$

The continuous integrals can be approximated by discrete sums. For instance:

$$\int_{S1} \varepsilon_s dxdy = S_1\bar{\varepsilon}_s^{S_1} = ab\bar{\varepsilon}_s^{S_1} \; ; \; \int_{S1} a_x(-y+b)dV = ab.\overline{a_x(-y+b)}^{S_1}$$

where the bar indicates the spatial average over the considered surface. Finally, the force can be expressed as a function of the measured quantities:

$$F = atG(\bar{\varepsilon}_s^{S_2} - \bar{\varepsilon}_s^{S_1}) + \rho at.\overline{a_x(-y+b)}^{S_1} + \rho at.\overline{a_x(y+b)}^{S_2} \tag{4}$$

The interesting thing is that although the bending strains are well into the plastic range, the shear strains are much smaller (see Figure 6(c)) and remain below the elastic limit much longer than the bending strains which justifies the present approach. Figure 9 shows the reconstructed impact force with and without the acceleration terms. Because of the small volume involved in the equation, the two terms in Eq. 4 containing the acceleration remain small compared to the shear strain term. However, the acceleration terms ccount for the reduction to zero of the force when contact is lost. Since the shear strains are negative on S_1 and positive on S_2, they add up in the first term of Eq. 4. G was assumed from the E value reported above (70 GPa) and ν=0.3.

Discussion

One can see that there is a force peak at around 40 μs, certainly related to the first acceleration peak (often referred to as the inertia peak in impact testing). Then the force steadily decreases to reach near zero between 80 and 120 μs and then shoots up again. Interestingly, one can see on the grey level images that there is a loss of

contact between the striker and the specimen during the same time interval, see Figure 2(c) for the grey level image at 100 μs where the loss of contact is clear. The start of this loss of contact corresponds to the maximum of the specimen speed between 80 and 90 μs caused by the second acceleration peak caused by the bending wave. At this stage, the specimen centre moves faster than the striker and contact is lost. The deceleration of the specimen caused by the negative part of the bending wave causes the striker to catch up with the specimen and contact is established again at around 120 μs where the force increases again. So basically, the stress state in the specimen is governed by the interaction between the movement of the striker (itself influenced by the specimen through the contact) and the bending vibration caused by the initial impact. These two effects either combine (like at 120 μs) or compensate each other, like at 50 μs. At that instant, if the specimen was free, the negative part of the bending wave would decelerate the specimen but at that stage, the specimen speed is not high enough and the striker is still in contact with the specimen resulting in a near zero acceleration. Whereas at 90 μs, the specimen speed results in loss of contact and the acceleration is free to become negative. It shows the complexity of the phenomenon but also clearly underlines the faculty of full-field measurements to give enough experimental information to analyse such a complex behaviour. Another interesting point is that between 80 and 120 μs, when contact is lost and the shear force should clearly be zero from Eq. (4), it is not zero. This is probably caused by some plastic shear strains. Indeed, the static yield stress in shear of 6061T6 is about 200 MPa, which corresponds to an engineering shear strain of about 7.10^{-3} (that is, $3.5.10^{-3}$ tensorial shear strain), which is clearly reached near the striker to specimen contact zone at the maximum force level (40 μs), as can be seen on Figure 10. This plastic residual strain corresponds to about 1.10^{-3} on average. This suggests here that the reconstructed force is certainly slightly overestimated after the first force peak.

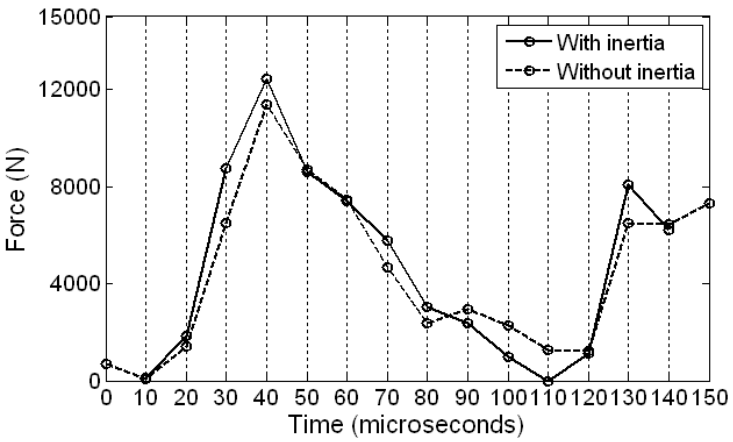

Figure 9. Reconstructed impact force

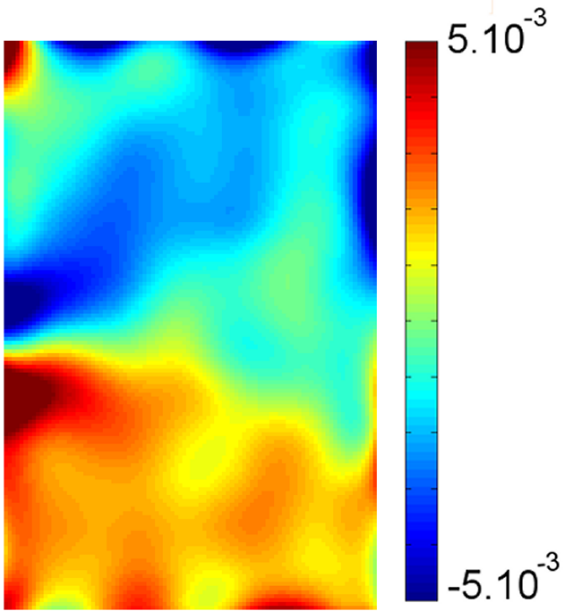

Figure 10. Tensorial shear strain at 40 μs

Finally, it is interesting to analyse the bending effects. For that purpose, a bending virtual field will be used (see Figure 11 for the axes and the virtual deformed shape):

$$\begin{cases} u_x^* = \frac{1}{2}(c^2 - y^2) \\ u_y^* = xy \end{cases} \qquad \begin{cases} \varepsilon_x^* = 0 \\ \varepsilon_y^* = x \\ \varepsilon_s^* = 0 \end{cases} \tag{5}$$

The choice of $\mathbf{u}_x^*$ is such that the virtual shear strain is zero (virtual Bernoulli bending), and such that it is zero for y=±c in order to filter out the unknown reaction forces. Inputting this virtual field into the principle of virtual work:

$$\frac{\mathbf{Fc}^2}{\mathbf{2t}} = \rho \int_S \mathbf{a}_x \mathbf{u}_x^* \mathbf{dS} + \int_S \sigma_y \mathbf{x dS} \tag{6}$$

It should be noted that the y-component of the acceleration has been neglected here. One of the problems is that the measurement zone does not cover the whole of the specimen. This means that none of the right hand-side terms can be computed directly. This is also why this configuration cannot be used to extract material constitutive parameters such as in [7-8], for instance. Another configuration will have to be used, such as a cantilever beam for instance, where the measurement area could cover the whole specimen length. This is presently underway. Nevertheless, it is possible to estimate the first second hand-side term from the measured acceleration. Assuming a quadratic form of the beam deflection (and therefore, of the acceleration), and calling $\mathbf{a}_x^{max}$ the maximum acceleration at y=0 (in fact, this is calculated by the average of $\mathbf{a}_x$ over a small slice centred on y=0 in order to improve the signal to noise ratio), it can be shown by direct integration that:

$$\frac{\rho}{2} \int_S \mathbf{a}_x (\mathbf{c}^2 - \mathbf{y}^2) \mathbf{dS} = \frac{\mathbf{8\rho w c}^3}{\mathbf{15}} \mathbf{a}_x^{max} \tag{7}$$

Finally, Eq. 6 becomes:

$$F = \frac{16\rho w c t}{15} a_x^{max} + \frac{2t}{c^2} \int_S \sigma_y x dS = F_i + F_d \tag{8}$$

where F_i stands for 'inertia force and F_d for 'deformation force'. Eq. 8 shows that the force is consumed either to accelerate the specimen (first right hand side term) or to create bending stresses (second right hand side term). Figure 12 shows a plot of the inertia force F_i, on the same plot as the force F reconstructed from the shear strains. The first thing that can be seen on this plot is that the maximum load reconstructed from the shear strains match the peak of inertia obtained from the acceleration (about 12 kN). This confirms that the very high load at 40 μs is indeed caused by specimen acceleration (inertia peak). From Eq. 8, one can see that the bending stresses (and therefore strains) will build up when $F-F_i$ is positive. This will happen three times during the test. First between 40 and 80 μs. The acceleration drops because of the bending wave and the force bends the specimen. The second time is between 90 and 120 μs. This is a purely inertial effect. The applied force is zero (no specimen to striker contact) and the bending wave is solely responsible for the increase of bending stress. The final bending stress increase is at the end of the test (140 to 150 μs) when the striker catches up with the specimen. After the third bending wave peak, the force deforms the specimen.

In order to confirm this analysis, the average of the bending strains were calculated over the top and bottom parts of the beam. One third of the width was considered for this average (see rectangles on Figure 6(a)). These average bending strains are represented on Figure 13 together with F_d ($F-F_i$) obtained from Eq. 8. This plot clearly shows that the bending strains build up in a stepwise manner, following the increase of bending moment, as explained above. Because of hardening, the strains (largely plastic here) tend to increase when the bending moment slope is positive only.

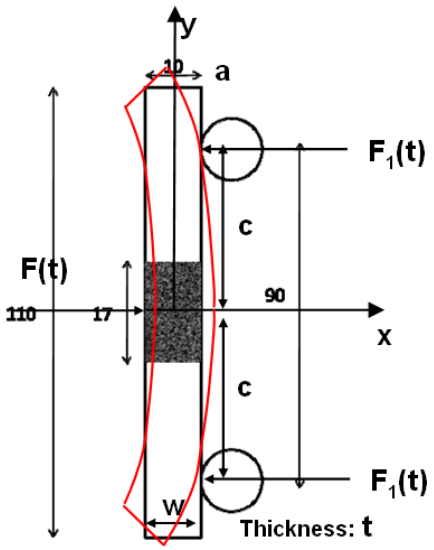

Figure 11. Configuration for virtual bending strain analysis

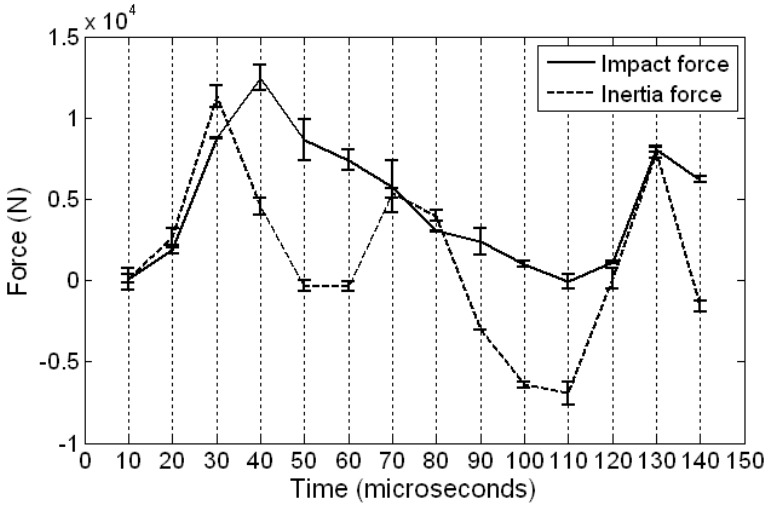

Figure 12. Impact and inertia forces

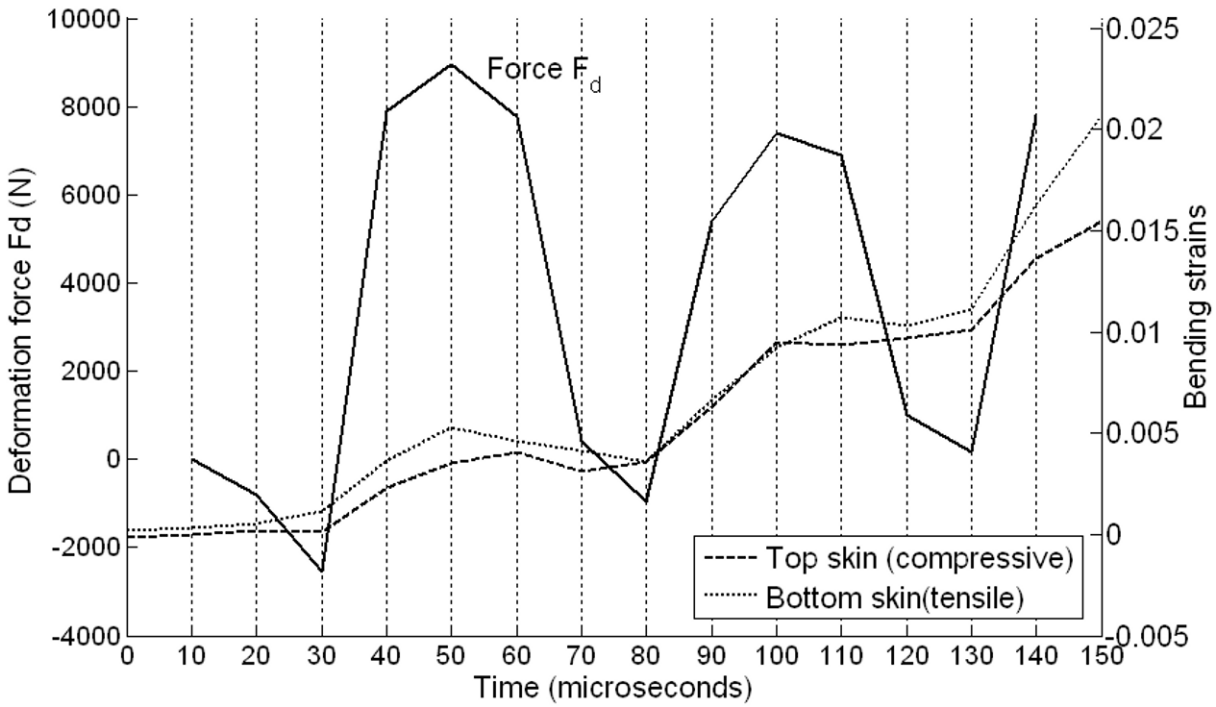

Figure 13. Average bending strains together with average bending force from Eq. 8 (compression bending strains have been multiplied by -1 for presentation purposes)

CONCLUSION

In this paper, it was shown how full-field strain measurements can be used to analyse the very complex behaviour of an aluminium beam impacted in a three point bending configuration. The principle of virtual work was used to reconstruct the impact force from the shear strains and to explain the stepwise built-up of the bending strains. It is clear that this paper is only a first attempt at trying to analyse a more complex impact test than the usual uniaxial

Hopkinson bar configuration by using full-field deformation measurements. It is interesting to note how the complex interaction between striker and bar produces a more complex load path that contain more information on the elasto-plastic material behaviour than the standard tests. By reducing the striker bar length, one could also include the wave reflection in the striker itself to produce even more complex load paths. There is certainly scope for novel test configuration design to take full advantage of the full-field measurements. By adapting specimen dimensions and load configuration, the whole specimen could be imaged and the data used to identify an elasto-plastic constitutive law in the same spirit as in [7]. And since the stress state is heterogeneous, the strain rate map will also be non uniform, with possibilities to extract some information about strain rate sensitivity on one single test, as shown in [8].

Nevertheless, many difficulties are still ahead of the scientific community to reach this goal. Among many others, the quality of the images should be increased. This is very dependent on the technology of ultra-fast imaging devices. The use of another type of camera (see [9]) enabled to obtain better resolution together with the grid method. Also, the design of a suitable test configuration will also be very challenging. This paper aims at providing some initial thoughts to guide future researchers in this area.

REFERENCES

[1] Grédiac M., The use of full-field measurement methods in composite material characterization: Interest and limitations, *Composites Part A: Applied Science and Manufacturing*, 35 (7-8):751-761, 2004.

[2] Pierron F. and Lo Y.-L. Editors, Special issue on ‘inverse problems in experimental mechanics’, *Experimental Mechanics*, 48(4), 2008.

[3] Tiwari V., Sutton M.A., McNeill S.R., Assessment of high speed imaging systems for 2D and 3D deformation measurements: methodology development and validation, *Experimental Mechanics*, 47(4):561-579, 2007.

[4] VIC 2D image correlation package, www.correlated-solutions.com

[5] Avril S., Feissel P., Pierron F., Villon P., Estimation of the strain field from full-field displacement noisy data: comparing finite element global least squares and polynomial diffuse approximation, *European Journal of Computational Mechanics,* vol. 17, n° 5-7, pp. 857-868, 2008.

[6] Avril S., Feissel P., Pierron F., Villon P., Comparison of two approaches for controlling the uncertainty in data differentiation: application to full-field measurements in solid mechanics, *Measurement Science and Technology*, vol. 21, 015703 (11 pp), 2010.

[7] Avril S., Pierron F., Pannier Y., Rotinat R., Stress reconstruction and constitutive parameter identification in elastoplasticity using measurements of deformation fields, *Experimental Mechanics*, 48(4):403-420, 2008.

[8] Avril S., Pierron F., Yan J., Sutton M.A., Identification of viscoplastic parameters and characterization of Lüders behaviour using Digital Image Correlation and the Virtual Fields Method, *Mechanics of Materials*, 40:729-742, 2008.

[9] Moulart R., Pierron F., Hallett S., Wisnom M., Full-field strain measurements at high rate on notched composites tested with a tensile Hopkinson bar, Annual SEM (Society for Experimental Mechanics) conference, 1-4 June 2009 in Albuquerque (NM), USA.